The inhibitory microcircuit in mouse presubiculum : from interneuron properties to input-output connectivity

Mérie Nassar

THÈSE DE DOCTORAT
DE L'UNIVERSITÉ PIERRE ET MARIE CURIE

Spécialité Neurosciences
École doctorale Cerveau-Cognition-Comportement

Présentée par:
Mérie Nassar

Pour obtenir le grade de
DOCTEUR DE L'UNIVERSITÉ PIERRE ET MARIE CURIE

Sujet de la thèse:

The inhibitory microcircuit in mouse presubiculum: from interneuron properties to input-output connectivity

Soutenue le 16.09.2016
devant le jury composé de:

Dr Jean Christophe Poncer	Président du jury
Pr Matthew Nolan	Rapporteur
Pr Marlene Bartos	Rapportrice
Pr Dietmar Schmitz	Examinateur
Dr Desdemona Fricker	Directrice de thèse

Abstract

Spatial orientation and navigation are controlled by specific neuronal circuits and elements. The presubiculum, a transitional cortical area of the parahippocampal formation, is located between the hippocampus and the entorhinal cortex, and it participates in spatial navigation in animals and humans. More than half of presubicular neurons are head direction cells that fire as a function of the directional heading. The presubiculum is thought to be a crucial node for transferring directional heading information to the entorhinal-hippocampal network, and feeding back visual landmark information to upstream regions of the head directional circuit. Despite its functional importance, information processing within the 6-layered presubicular microcircuit remains not completely understood.

During my PhD, I studied inhibitory neurons of the presubicular microcircuit in the slice preparation using patch-clamp recordings. I characterized their anatomo-physiological properties as well as their functional connectivity with local principal neurons.

In the first part, I examined the diversity of two major populations of GABAergic neurons, the parvalbumin (PV) and somatostatin (SOM) expressing interneurons in mouse presubiculum. Using transgenic mouse strains Pvalb-Cre, Sst-Cre and X98, where interneurons were fluorescently labeled, I showed the existence of typical PV fast-spiking basket-like interneurons mainly in the Pvalb-Cre line and SOM low-threshold spiking Martinotti cell-like interneurons in the X98 and Sst-Cre line. Unsupervised cluster analysis based on electrophysiological parameters further revealed a transitional group containing interneurons from either Pvalb-Cre or Sst-cre lines with quasi-fast-spiking properties and heterogeneous morphologies. A small subpopulation of ~6% of interneurons co-expressed PV and SOM in mouse presubiculum. The presubiculum appears to share the whole complexity of other cortical areas in term of inhibition.

In the second part, I investigated the integration of thalamic inputs by principal neurons as well as PV and SST interneurons in the presubiculum using double patch-clamp recordings. I found that thalamic axons selectively innervated superficial layers and made direct synaptic contacts with pyramidal neurons that project to medial entorhinal cortex and also with PV interneurons in superficial layer 3. In contrast, SST interneurons were indirectly recruited by presubicular pyramidal cells in a facilitating and frequency dependent manner. They may mediate lateral inhibition onto nearby principal cells, and at the same time, preserve sustained firing of principal neurons. In paired recording experiments, I found that PV cells inhibit neighboring pyramidal neurons with a high connection probability. PV interneurons are rapidly recruited by thalamic excitation and mediate feed-forward inhibition in presubicular pyramidal neurons.

My PhD work brought fundamental knowledge about the presubicular inhibitory microcircuit. It has unraveled different populations of GABAergic interneurons and revealed canonical feedforward and feedback inhibitory motifs that are likely to be recruited at different times during head direction signaling.

Acknowledgments

First of all, I would like to thank Jean Christophe Poncer, Matthew Nolan, Marlene Bartos and Dietmar Schmitz for being part of my thesis jury.

Je remercie tout naturellement Desdemona de m'avoir permise de travailler avec elle au cours de ces trois dernières années. J'ai eu beaucoup de chance d'avoir une directrice de thèse toujours présente pour moi à n'importe quel moment. Sans ta présence, je n'aurais pas pu avancer dans mes projets aussi vite que j'ai ainsi pu le faire. Tu m'as laissée une certaine liberté de réflexion tout en sachant à la fois me guider dans ma démarche quand je te le demandais. Face à mes doutes concernant les bonnes expériences à réaliser, les protocoles et les analyses à faire, j'ai eu souvent besoin de conseils et tu as su être là. Ton optimisme face à mon découragement m'a toujours rassurée et réconfortée dans la poursuite de mes projets. Je te remercie pour ta compréhension par rapport à mes projets futurs et pour ton soutien permanent. Enfin, tu as été d'une grande aide et disponibilité pour la rédaction de ce manuscrit : tes conseils, corrections et relectures ont été très utiles. Encore une fois, je te remercie pour tout cela.

Je remercie Richard qui m'a accueillie dans son laboratoire thèse. Merci pour tous les précieux conseils que vous m'avez donnés tout au long de ces années. Je tiens à vous remercier pour votre présence et votre soutien inconditionnels. Vous avez toujours su déceler mes humeurs changeantes et me remonter le moral en fin de journée après des manips décevantes. J'ai également apprécié nos conversations scientifiques et extra-scientifiques. Enfin, vous avez su être un vrai médiateur par rapport aux problèmes administratifs qui ont concerné le déménagement.

Je remercie Mathieu et toute son équipe de nous avoir récemment accueilli dans son laboratoire. Je te remercie pour le soutien, la disponibilité et la compréhension dont tu as fait preuve dès le début. Le meilleur est à venir.

Je remercie Jean qui m'a formée au cours de mon stage de Master 2 et les premières années de la thèse. Travailler avec toi n'a pas souvent été très facile, je l'avoue, mais j'ai eu la chance d'avoir une personne qui a enduré tous les problèmes de la thèse avant moi. Je te remercie d'avoir partagé avec moi ton expérience de la recherche en me prodiguant tes conseils et les aides nécessaires pour avancer au mieux dans mes projets. Je te remercie pour ton aide avec les analyses: tes routines Matlab m'ont permis de gagner un temps considérable. Enfin, merci

pour l'exigence scientifique que tu as su me transmettre et qui a certainement influencé ma façon de travailler.

Merci à tous les membres de l'équipe Miles : Farah, Maja, Ivan, Bertrand, Giampaolo, Caroline, Etienne, Mélanie, Juliane et Katia. Merci pour les échanges, les réunions, déjeuners et les sorties et que l'on a pu avoir tous ensemble. Merci à Farah, mon amie et confidente de l'équipe, tu m'as beaucoup apportée tant sur le plan scientifique qu'humain. Je te remercie pour ta présence et ta gentillesse. Merci également à Maja avec qui j'ai pu partager de très bons moments au labo. Merci à Bertrand pour son travail et sa disponibilité, sans qui je n'aurais pas pu maîtriser aussi bien les injections stéréotaxiques. Merci à Giampaolo dont j'ai fait la connaissance que très récemment mais avec qui j'ai passé des moments agréables en cette dernière période d'écriture.

Merci à l'équipe Bacci avec qui j'ai énormément interagi et qui m'ont très vite intégrée dans leur équipe. Merci à Giulia avec qui j'ai passé les meilleurs moments de ma thèse que ce soit lors des déjeuners ou des pauses café. Nos discussions diverses et variées, et surtout nos fous rires m'ont permis de décompresser au cours de ses années. J'ai eu la chance d'avoir à ma disposition tes choco princes pour me remonter le moral. Enfin, merci à Charlotte avec qui j'ai beaucoup discuté de mes problèmes de souris, de tranches mais aussi des soucis de la vie. Tu as été toujours présente pour m'écouter et me soutenir à n'importe quel moment.

Merci à l'équipe des Charpier. Merci à Tristan, Mark et Adrien ainsi qu'à mes autres collègues avec qui j'ai passé de très bons moments au cours des divers évènements organisés à l'ICM.

Merci à mes amis du master et de la thèse. Merci à Marie, Pauline, Léa mais aussi Virginie, Céline et plein d'autres que j'oublie surement…Je tiens à remercier Marie qui a été d'une aide précieuse et qui avait souvent les solutions à mes problèmes. J'ai beaucoup apprécié nos discussions ainsi que le partage de tes découvertes et connaissances scientifiques avec moi. Je pense, par exemple, à ta chambre à interface qui, a considérablement facilité mes enregistrements.

Merci à mon ami Romain. Tu as su être présent pour moi dans les bons comme dans les mauvais moments malgré la distance qui nous sépare. Merci pour ton soutien.

J’aimerais remercier mes amis proches qui ont vécu indirectement cette thèse avec moi et qui ont su m’écouter, m’encourager et parfois me supporter. Merci à Léa, Shirin, Philippine, Sze-mung, Elise, Thomas, et Anthony.

Enfin, je tiens à remercier ma famille et notamment mes parents, mon frère et ma sœur. Merci de m’avoir encouragée durant toute cette thèse. Merci à ma petite sœur Léa qui a toujours été là pour moi. Cette thèse n’aurait pas vu le jour sans votre soutien.

Table of Contents

LIST OF ABBREVIATIONS

Anatomy

ADN	anterodorsal thalamus
AVN	anteroventral thalamus
ATN	anterior thalamic nuclei
AM	anteromedial thalamus
AV	anteroventral thalamus
CA	corpus ammonis
DG	dentate gyrus
HF	hippocampal formation
HD	head direction
DTN	dorso tegmental nucleus
LDN	laterodorsal thalamus
LMN	lateral mammillary nucleus
MEC	medial entorhinal cortex
MS	medial septum
LEC	lateral entorhinal cortex
PHR	parahippocampal region
PaS	parasubiculum
PrS	presubiculum
PER	perirhinal cortex
POR	postrhinal cortex
PoS	postsubiculum = dorsal part of PrS
RSC	retrosplenial cortex
Sub	subiculum

Physiology

EPSP/EPSC	excitatory post-synaptic potential/current
FS	fast spiking
IPSP/IPSC	inhibitory post-synaptic potential/current
LT	late spiking
LTS	low threshold spiking
RS	regular spiking
BS	burst spiking
PPR	paired-pulse ratio

Others

AAV	adeno-associated virus
AMPA	alpha-amino-3-hydroxy-5-methyl-4-isoxazolepropionic acid
Arch	archaerhodopsin
CB	calbindin

CCK	cholecystokinin
ChAT	choline acetyltransferase
ChR2	channelrhodopsin-2
CR	calretinin
CTB	Cholera toxin B
DTX	dendrotoxin
GABA	gamma aminobutyric acid
HIPP	hilar perforant path associated
IN	interneuron
LBC	large basket cell
MC	martinotti cell
NBC	nest basket cell
NMDA	n-Methyl-D-aspartic acid
NpHR	natronomonas pharaonic halorhodopsin
NPY	neuropeptide
O-LM	oriens lacunosum moleculare
PCR	polymerase chain reaction
PN	pyramidal neuron
PV	parvalbumin
SBC	small basket cell
scRT-PCR	single cell reverse transcription
SOM	somatostatin
TTX	tetrodotoxin
VIP	vasoactive intestinal peptide

INTRODUCTION

1- The Hippocampal-Parahippocampal system: Anatomy, Connectivity and Function

1.1 Gross anatomy of the hippocampal-parahippocampal region

The cortex that forms the hippocampal formation (HF) has a three-layered appearance also called Allocortex. In the HF, three distinct subregions can be distinguished: the subiculum, the dentate gyrus (DG), the hippocampus proper (consisting of Ammon's horn divided in CA3, CA2 and CA1) (Van Strien et al., 2009). The parahippocampal region (PHR) is generally described as having 6 layers, classified as Periallocortex, a transitional zone between the Allo- and Neocortex. Lying adjacent to the HF, it is divided in 5 subregions which are the presubiculum (PrS), the parasubiculum (PaS), the entorhinal cortex (EC) consisting of medial (MEC) and lateral (LEC) cortices, peri- (PER) and postrhinal (POS) cortices (Witter et al., 2000; Van Strien et al., 2009) (**Fig. 1**).

1.2 Hippocampal-Entorhinal connectivity

A complex picture of the rodent connectivity within and between the HF and the PHR has emerged over the years and has provided new elements for understanding its functions. Overall, the entorhinal cortex is commonly perceived as a major input and output structure of the hippocampal formation, entertaining the role of the nodal point of cortico-hippocampal circuits (**Fig. 2A**). The perforant pathway provides a connectional route from the entorhinal cortex to all fields of the HF including the DG, all CA fields and the subiculum. Indeed, entorhinal layer 2 neurons project to the dentate gyrus and also directly to CA3. EC layers 3, 5 and 6 also contribute to this projection, although to a lesser extent (Canto et al., 2008). In the molecular layer of the DG and the stratum lacunosum-moleculare of CA3, projections from the EC converge onto the apical dendrites of dentate principal cells and interneurons (Canto et al., 2008). Entorhinal layer 3 projects to CA1 and the subiculum (Amaral and Witter, 1989). CA2 region is considered as the convergence point of direct projection from EC layer 2 and 3 (Chevaleyre and Siegelbaum, 2010; Rowland et al., 2013) even though a lack of direct projections from entorhinal layer 3 projections to CA2 pyramidal cells has been recently described (Kohara et al., 2014).

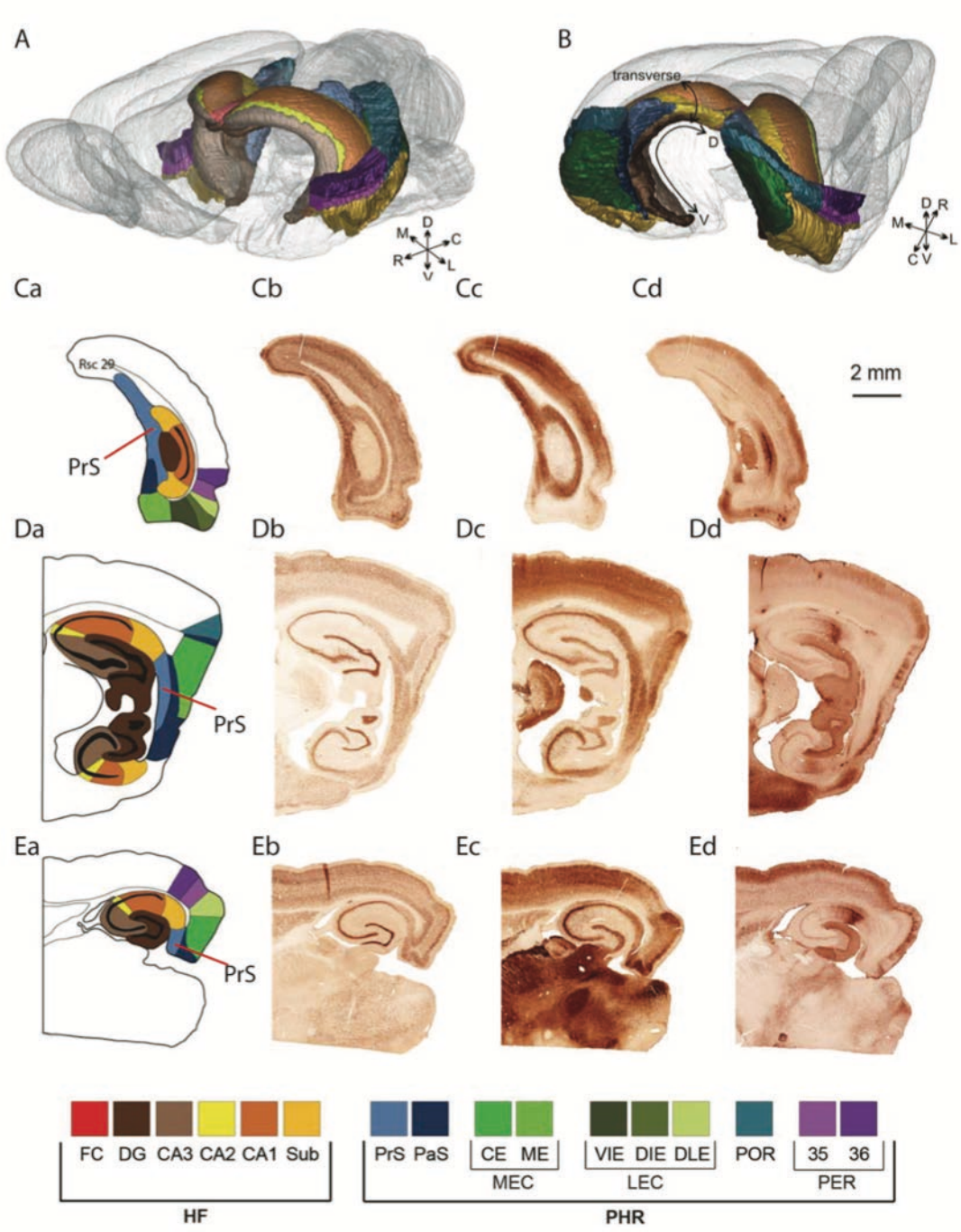

Figure 1: Views of the hippocampal region of the rat brain. **A**. 3D oblique frontal view embedded in a transparent rat brain. **B**. Oblique occipital view. **C**. Coronal sections. **D**. Sagittal sections. **E**. Horizontal sections. **(a)** Schematic color coded delineation of divisions of the hippocampal region. Color code as presented in the lower panel. **(b)** NeuN-stained sections. **(c)** PV-stained sections. **(d)** CB-stained sections. Abbreviations: CA1–3, Cornu ammonis 1–3; CB, Calbindin; DG, Dentate Gyrus; EC, Entorhinal Cortex; HF, Hippocampal Formation; LEC, Lateral Entorhinal Cortex; MEC, Medial Entorhinal Cortex; PaS, Parasubiculum; PER, Perirhinal Cortex; PHR, Parahippocampal Region; POR, Postrhinal Cortex; PrS, Presubiculum; PV, Parvalbumin; Sub, Subiculum; 35, Perirhinal Area 35; 36, Perirhinal Area 36. Adapted from Boccara et al. (2015).

More generally, there are reciprocal connections between the EC and CA1/the subiculum (Amaral and Witter, 1989). Projections from the PaS and PrS convey monosynaptic inputs in all layers of the MEC (Canto et al., 2012). The HF output to the PHR arises from CA1 and the subiculum and, according to the standard view, terminates primarily in the deep layers of the EC (Canto et al., 2008) and to a much lesser extent in the superficial layers of the EC (Van Groen et al., 2003). Other PHR subregions have also been observed to project to the HF directly, although less strongly than the EC. CA1 projections to the dorsal part of the presubiculum have been described (Van Groen and Wyss, 1990c), but countered thereafter by another study (Cenquizca and Swanson, 2007).

1.3 Spatial navigation and its neuronal schemes

Given its fundamental role in memory processing and formation, spatial navigation, emotional processing and learning, many studies have been conducted to understand the flow of information into, through, and out of the various fields that comprises the hippocampal-parahippocampal region. On the neuronal level, various types of spatially tuned cells have been identified in the HF-PHR **(Fig. 2B)**: place cells (O'Keefe and Dostrovsky, 1971), grid cells (Hafting et al., 2005), border cells (Solstad et al., 2008) and head direction cells (Taube et al., 1990 a,b).

Place cells are principal neurons in the hippocampal formation that discharge for discrete locations (place field). Place cells have been recorded throughout the hippocampus (CA1, CA3), the subiculum and the entorhinal cortex, but whether these recordings represented actual place cells or individual nodes of a periodic grid such as found in grid cells, remains to be verified (Boccara et al., 2010).

The grid cell system (Hafting et al., 2005) has been first described in the entorhinal cortex and then in pre- and parasubiculum of the rat (Boccara et al., 2010). Grid cells have periodically spaced firing fields that span the entire environment in a grid-like fashion. The vertices of the firing fields define a triangular or hexagonal array.

Border cells, which are active only close to the environmental borders, were identified in the entorhinal cortex (Solstad et al., 2008) and the presubiculum (Boccara et al., 2010). Some cells encode a conjunctive representation of position, direction, and velocity in the entorhinal

cortex (Sargolini et al., 2006) and presubiculum (Boccara et al., 2010). Border cell activity is often co-localised with grid- and head directional-activity (Solstad et al., 2008).

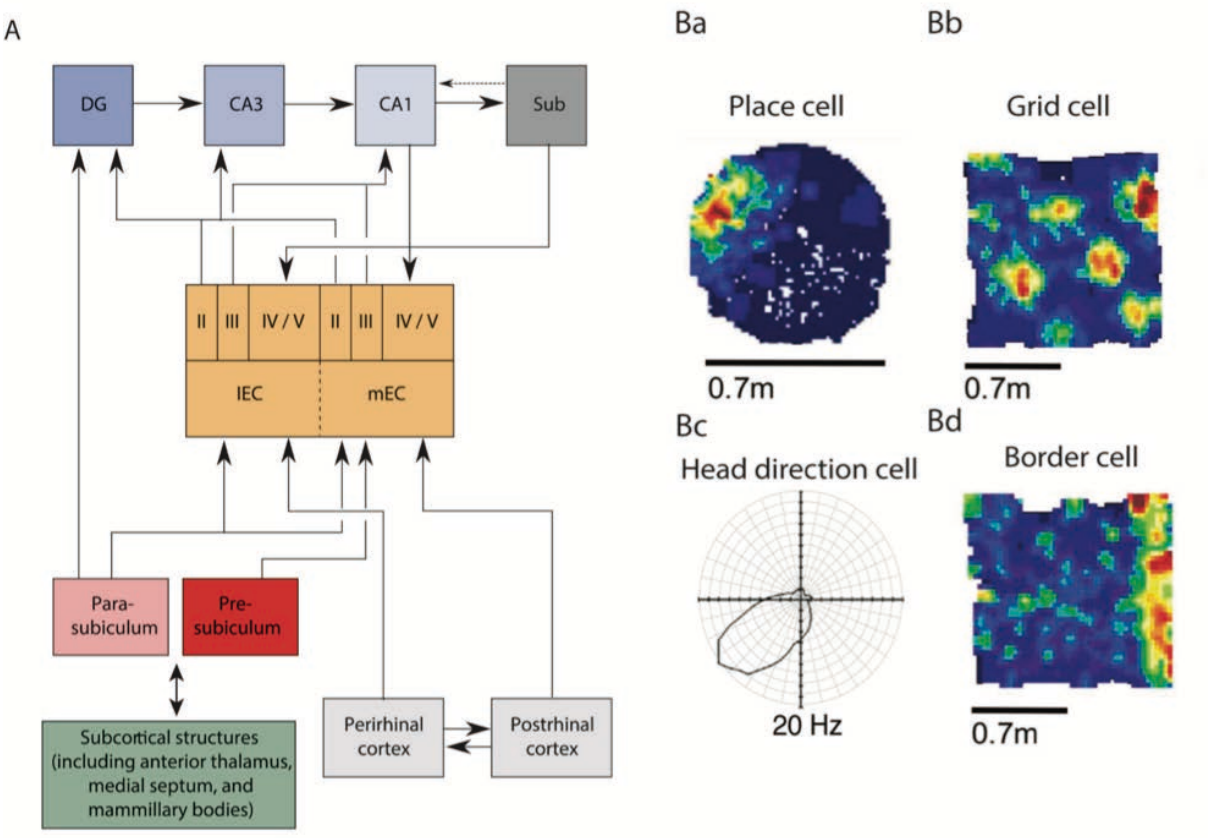

Figure 2: Connectivity of the hippocampal-parahippocampal region and its spatially tuned cells. **A**. Subcortical structures-including the medial septum, mammillary bodies, and anterior thalamus–project to all subfields of the hippocampal-parahippocampal formation. Post- and perirhinal cortices provide neocortical input to medial entorhinal cortex (MEC) and lateral entorhinal cortex (LEC), respectively. The presubiculum projects to MEC, whereas the para-subiculum projects to MEC, LEC, and dentate gyrus (DG). Both MEC and LEC provide input to the DG, CA3, and CA1 subfields of the hippocampus proper via the perforant path. Within the hippocampus proper, DG sends mossy fiber projections to CA3, CA3 sends Schaffer col-lateral projections to CA1, and CA1 sends output projections to the deep layers of MEC and LEC both directly and via the subiculum, adapted from Bush et al. (2014). **B**. Typical firing patterns of the major cell types in the cognitive map. Color-coded rate maps for a hippocam-pal place cell **(a),** a medial entorhinal grid cell **(b)** and a medial entorhinal border cell **(d)** (Red, maximum firing rate; blue, minimum firing rate), adapted from Clark and Taube. (2012). **(c)** A head direction cell with a preferred firing direction to the Southwest of the enclosure, adapted from Marozzi and Jeffery. (2012).

Head direction cells fire when the animal's head points to a specific direction regardless of the animal's position in an environment and its ongoing behaviour. They have first been described in the dorsal part of the presubiculum (Ranck, 1984; Taube et al., 1990 a,b) of the rat, also known as the postsubiculum, where they are particularly abundant, but have been observed in a number of cortical and subcortical regions since.

Since the discovery of grid cells in the MEC, grid cells are considered substrate for path integration-based navigation, particularly for place cell formation (McNaughton et al., 2006; Moser and Moser, 2013, Fyhn et al., 2004). A recent study, showing entorhinal grid cells projecting directly onto the hippocampus supports this theory showing a possible direct influence onto place cells (Zhang et al., 2013). Conversely, place signals may also be necessary for grid cells to emerge. Excitatory drive from CA1 hippocampus is crucial for grid pattern in the MEC: 1) loss of firing rate and of grid structure itself was observed when the hippocampal region was silenced with muscimol, 2) without hippocampal excitation, entorhinal grid cells turn into head direction cells (Bonnevie et al., 2013).

2-The Presubiculum: Anatomy, Function and Connectivity

2.1 Anatomy of the presubicular cortex

2.1.1 Anatomical delineation

The presubiculum, as part of the parahippocampal formation, is located in the brain's temporal lobe. The presubiculum (PrS) corresponds to Brodmann's area 27 and 48 (Brodmann, 1909) and is in direct continuation with the septo-temporal axis in rodents. PrS has been divided into a dorsal and a ventral portion referring to slight differences in connectivity. The dorsal portion of the PrS corresponding to Brodmann's area 48 is also known as postsubiculum (Van Groen and Wyss, 1990c). In the proximo-distal axis, PrS borders anteriorly the subiculum (Sub) and posteriorly, follows the parasubiculum. Subiculum, pre- and parasubiculum form the so called "subicular complex". At the dorsal-lateral extreme, PrS borders the retrosplenial cortex (Ding and Rockland, 2001). PrS architecture based mainly on connectional patterns, gene expression and neurochemical markers is overall conserved across rodents, monkeys and humans (Ding, 2013).

2.1.2 Laminar organization

The presubicular Periallocortex, which consists of inner and outer lamina, separated by lamina dissecans (Witter et al., 1989) shares classical features of cortical laminar organization described earlier by Ramon y Cajal, in 1899 in terms of neuronal content and cellular density (**Fig. 3A**). The molecular layer 1 is a relatively cell-free plexiform layer that contains some putative interneurons and glial cells. PrS is distinguishable by its layer 2, easily well marked in Nissl or NeuN stained sections as a densely and small packed pyramidal cell layer. Layer 2 combines to layer 3 to form superficial layers of the PrS. Layer 3 is broader than layer 2 with a much lower neuronal density and is composed of pyramidal neurons, presenting a looser cell arrangement. A cell-sparse lamina dissecans or layer 4 separates the superficial from the deep layers. The main cytoarchitectonic characteristic differentiating deep layers from each other is that layer 5 contains one or two rows of large pyramidal cells whereas layer 6 harbors smaller fusiform pyramidal cells (Van Groen and Wyss, 1990c). The presubicular deep layers are in continuum with the pyramidal cell layer of the subiculum and the deep layers of the parasubiculum and entorhinal cortex (Amaral and Witter, 1989).

Presubiculum exhibits both interlaminar and intralaminar connections (Funahashi and Stewart, 1997b). Excitatory neurons in deep layers are highly interconnected with each other, generating bursting behavior which distinguishes them from superficial layer neurons (Funahashi and Stewart, 1997b). Neuroanatomical tracing experiments showed that interlaminar connections are almost exclusively in the direction of superficial to deep in contrast with a weak connectivity from deep to superficial layers (Honda et al., 2008). Projections from layer 2 cells are bilateral and confined to layers 2 and 5 whereas projections from layer 5 cells are ipsilateral with fewer projections mostly to layer 2 (**Fig. 8D;** Honda et al., 2008). Deep layer 5 excitatory neurons consist of at least six types of cortical projection neurons with various patterns of collateralization distributing output signals to different regions such as the subiculum (Sub), parasubiculum (PaS), retrosplenial cortex (RSC), medial entorhinal cortex (MEC) and recurrently to the PrS, (Honda et al., 2011) and thus, are thought to coordinate networks of brain areas involved in spatial signaling.

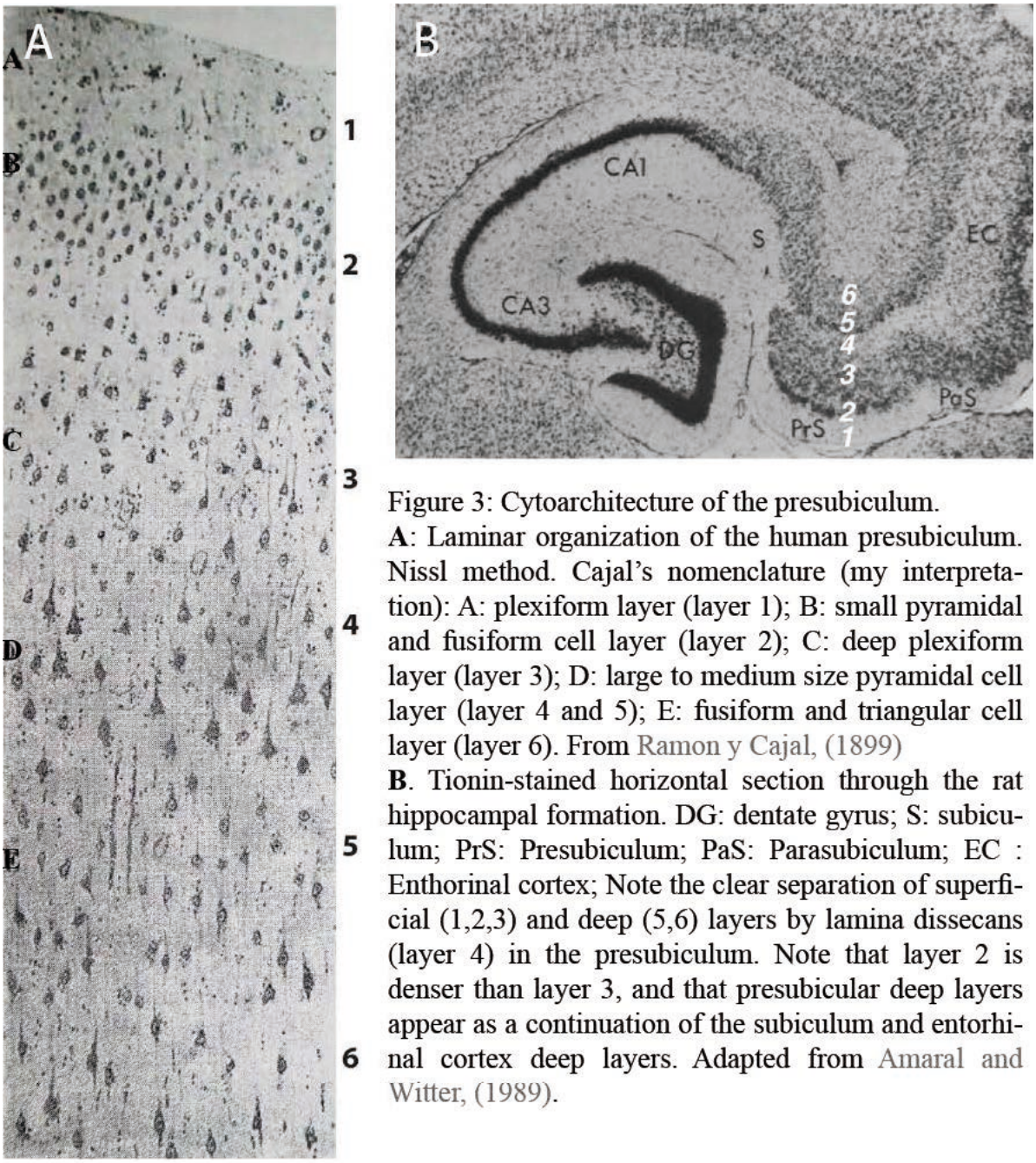

Figure 3: Cytoarchitecture of the presubiculum.
A: Laminar organization of the human presubiculum. Nissl method. Cajal's nomenclature (my interpretation): A: plexiform layer (layer 1); B: small pyramidal and fusiform cell layer (layer 2); C: deep plexiform layer (layer 3); D: large to medium size pyramidal cell layer (layer 4 and 5); E: fusiform and triangular cell layer (layer 6). From Ramon y Cajal, (1899)
B. Tionin-stained horizontal section through the rat hippocampal formation. DG: dentate gyrus; S: subiculum; PrS: Presubiculum; PaS: Parasubiculum; EC : Enthorinal cortex; Note the clear separation of superficial (1,2,3) and deep (5,6) layers by lamina dissecans (layer 4) in the presubiculum. Note that layer 2 is denser than layer 3, and that presubicular deep layers appear as a continuation of the subiculum and entorhinal cortex deep layers. Adapted from Amaral and Witter, (1989).

Generally, the presubiculum is easily distinguishable from neighboring regions by the characteristics of its cytoarchitecture (**Fig. 3B**). Along most of the long axis of Sub, the subicular cell sheet is distally continuous with the deep layers of PrS. The precise border between Sub and the deep layer of PrS is generally crescent-shaped and characterized by a subtle change from a homogeneous layer of cells in Sub to a more radially organized cell layer in PrS. Borders of PrS and PaS can be defined on the basis of the larger size of the parasubicular neurons. Also, parasubiculum is lacking the densely packed layer 2 of presubiculum and there is no clear laminar separation between superficial layers 2 and 3. Parvalbumin immunoreactivity

may contribute to establishing the PaS/PrS borders with a quite homogeneous neuronal distribution in superficial layers of PrS contrasting with a higher number and uniformly bigger PV in the superficial layers of PaS (Boccara et al., 2015). The calcium binding protein calbindin shows a strong reactivity along most of the extent of the presubicular layer 2 contrasting with the absence of reactivity for calbindin in Sub and PaS (Boccara et al., 2010).

2.1.3 Modular structures

During early post-natal stage, superficial layers of the presubiculum transiently exhibit cortical columns (Nishikawa et al., 2002). The development of functional modules has been attributed to reelin secreted by Cajal–Retzius cells, seemingly cooperating with the influences of early serotonergic projections (Nishikawa et al., 2002; Janusonis et al., 2004). At the adult stage, the presubiculum is characterized by pronounced cell islands confined to the upper layer 2, that co-localize with anatomical modules or « patches ». This patchy organization is revealed by immunostaining with several markers, such as the calcium binding proteins calretinin, calbindin, parvalbumin or markers for myelin and cytochrome oxidase (Preston-Ferrer et al., 2016; Ding and Rowland, 2001). These labeling patterns are also convenient marker for the boundary between the presubiculum and the retrosplenial cortex. In the most dorsal part of mouse presubiculum, layer 2 cell bodies were unstained with AchE staining and tend to form clusters separated by fiber stripes (Slomianka and Geneser, 1991). More recently, these modules have been linked to the grid like arrangement of calbindin positive theta-modulated layer 2 pyramidal neurons found in the entorhinal cortex (Ray et al., 2014) conserved in size and periodicity in five mammalian species including human entorhinal cortex (Naumann et al., 2015).

2.2 Presubiculum and spatial orientation

2.2.1 Sense of orientation

Spatial orientation and its related function, navigation, represent fundamental cognitive functions that mammals depend on for survival. To navigate an environment successfully requires the integration of multimodal sensory information, the maintenance of an accurate world model, and the ability to localize oneself and recover from mistakes. Mammalian brains show a remarkable ability to navigate through their environment. For many species, they cover large regions of the local terrain in search of a goal (food, mates, etc.) and are able to return

immediately and safely to their nesting spot. The neuronal representation of space enables two fundamental processes: path integration and landmark navigation. Path integration (often referred to as "dead-reckoning") uses internally self-movement generated information to keep track of current position and directional heading. This information is referred to as "idiothetic": idiothetic cues include vestibular, proprioceptive and motor inputs. By contrast, landmark navigation (often referred to as piloting) involves the use of environmental/external cues (landmarks) relying on visual, auditory and olfactory modalities to establish current position relative to familiar terrain.

2.2.2 Properties of presubicular head direction neurons

A head direction (HD) cell fires whenever the animal's head is pointed in a particular direction in the horizontal plane irrespective of the animal's location (**Fig. 4A**; Taube et al., 1990a). Cell firing will continue whether the animal is moving or still and is largely independent of the animal's ongoing behavior: discharge will persist without adaptation as long as the preferred head orientation is maintained. Within the range of the cell's preferred direction, the firing rate follows a triangular or Gaussian tuning curve so that the firing rate is the highest in the middle of the range, and falls off symmetrically around that center (Blair and Sharp 1995, Taube. 1998) (**Fig. 4B**). The direction at which the cell fires maximally (the « peak firing rate ») is referred to as the cell's preferred firing direction. When the animal's head is not pointing in a cell's preferred firing direction, basal firing rate is at or close to zero. The range of head directions in which the firing rate is above the cell's baseline firing rate ranges from 60° to 150° (average 90°) around the preferred direction (Blair and Sharp, 1995; Taube, 1995). Different HD cells have different preferred directions and all directional headings are represented within a population of HD cells. The overall set of HD cells, therefore, acts as a compass that signals head orientation. Peak firing rates vary for different HD cells in the same or different brain areas ranging from 5 to 120 Hz (Taube, 2007).

HD cells receive and utilize information from both external landmark cues and internal cues. Visual landmarks dominantly control the preferred direction of the HD cell in order to stabilize, correct the signal and avoid drifts (Zugaro et al., 2003). Visual cue card rotations cause equal rotations of firing fields corresponding to deviations of the firing fields **(Fig. 4E)**. Interestingly, card removal leaves firing fields and the peak firing rate intact but can drift over time (**Fig. 4F**). In addition to cue card shifts, changing the shape of the testing enclosure from a cylinder to a square or rectangle also caused changes in the preferred direction (Taube et al., 1990b). Goodridge et al., (1998) looked at the role of sensory modalities other than vision on

the firing of head direction cells. Whereas a simple auditory cue, such as a localized series of clicks or bursts of noise, was ineffective, a localized smell did exert a small but significant control over the preferred direction.

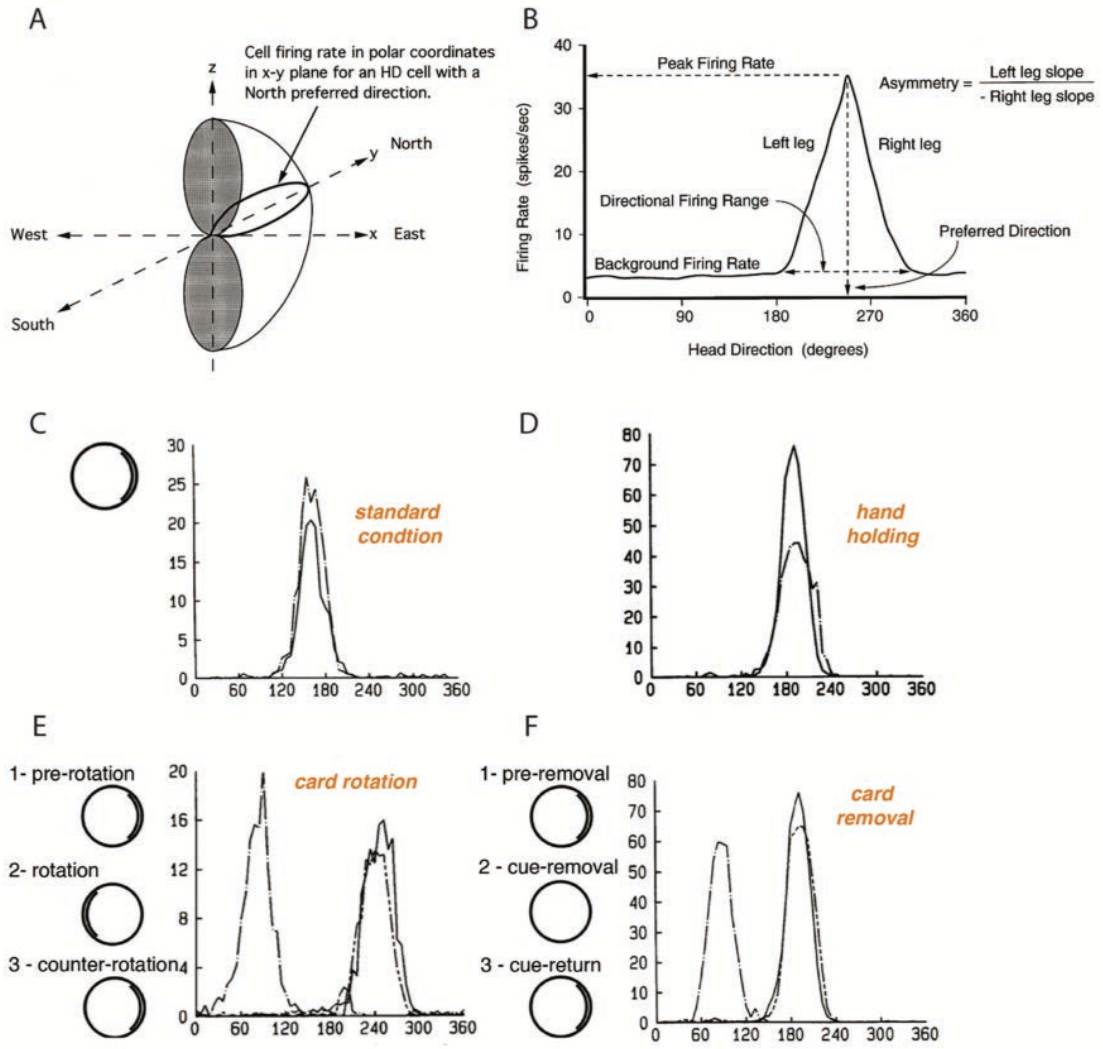

Figure 4: Basic features of presubicular head direction cells. **A**. Three-dimensional model of HD cell firing. The surface of the hemi-torus-shaped figure represents the maximum firing rate of the cell as a function of azimuth and height. Note that there are abrupt transitions from high firing rates to directions where the cell ceases responding. **B**. Firing rate vs head direction tuning curve for a hypothetical HD cell. Five parameters are measured to study the firing properties of the cell: (1) preferred firing direction, (2) peak firing rate, (3) directional firing range, (4) background firing rate, (5) asymmetry score, from Taube. (1998). **C**. Stability of head direction cell firing across two recording sessions, one (dashed line) recorded 15 days after the other (solid line). In standard condition, a prominent cue card is disposed as a polarizing cue on one side of the open field wall. **D**. Carrying the animal by hand and moving it around in the arena (dashed line) only decreased peak firing rate compared to standard condition (solid line). **E**. Cue card rotation causes a corresponding shift in preferred direction. The same head direction was recorded in standard condition (1, solid line), after a 180° clockwise

rotation of the cue card (2, dash-dot line) and after the equivalent counter rotation putting the card in its initial position (3, line with 2 short dashes). **F**. Drift of preferred direction following card removal. The same head direction was recorded in standard condition (1, solid line), after cue card removal (2, dash-dot line) and after cue card return to its initial position (3, line with 2 short dashes), adapted from Taube et al. (1990a,b).

While the HD signal appears to be generated from the self-movement information that arises from the vestibular system, proprioceptive and/or motor efference cues also play a major role in updating the signal during movement. Motor activity is likely to improve signal quality without affecting its generation: preventing an animal from moving reduces peak firing rate with no changes in preferred direction and directional firing (**Fig. 4C-D**) (Taube et al., 1990b).

2.2.3 Head Direction Circuit

With the discovery of head direction cells in the postsubiculum, a succession of following studies explored the existence and characteristics of HD cells in several brains areas that are part of the Papez circuit (1937), connected directly or indirectly with the postsubiculum, forming a head direction macrocircuit.

Head directional activity has been described in numerous brain regions: the anterodorsal thalamic nucleus (ADN), the anteroventral thalamic nucleus (AVN) together forming the anterior thalamic nuclei (ATN) (Taube, 1995), the nucleus reuniens of thalamus (Jankowski et al., 2014), the lateral mammillary nucleus (LMN) (Stackman and Taube, 1998), the medial entorhinal cortex (MEC) (Sargolini et al., 2006), the retrosplenial cortex (both granular and agranular regions) (Chen et al., 1994; Cho and Sharp, 2001), the lateral dorsal thalamus (LDN) (Mizumori and Williams, 1993) and the dorsal striatum (Wiener, 1993). Smaller numbers of head direction cells have been described in the dorsal tegmental nucleus (DTN) (Basset and Taube, 2001) and the hippocampal area CA1 (Leutgeb et al., 2000). These areas are hierarchically interconnected, starting from vestibular system to DTN, LMN, ADN, PrS and finally MEC (**Fig. 5A**), and contain head direction cells that contrast in their specific tuning properties. One striking parameter is the directional range that is narrower for presubiculum and retrosplenial cortex compared to ADN, LMN and DTN (**Fig. 5B**). Along the dorsoventral axis, no topographical organization of directional tuning was observed in the presubiculum, contrasting with a loss of sharply tuned cells from dorsal to ventral position in the MEC (Giocomo et al., 2014). Interestingly, head direction cells in the ADN and LMN were found to

exhibit anticipatory firing in that they predicted the animal's future head direction few (25) msec in advance (Blair and Sharp, 1995).

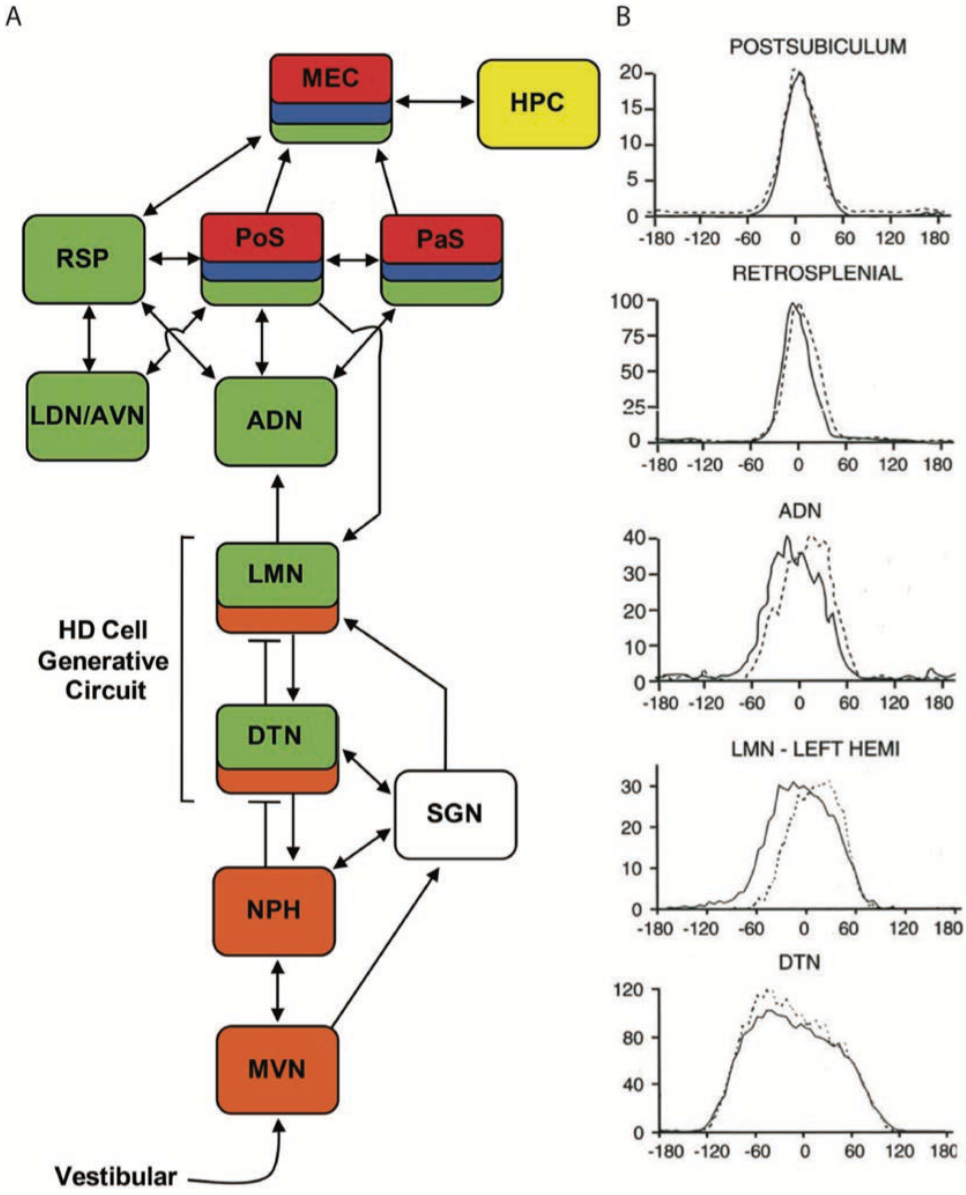

Figure 5: The head direction circuit. **A**. Circuit diagram showing the principle connections between brain regions containing place cells (yellow), grid cells (red), border cells (blue), HD cells (green), and angular velocity cells (orange). Arrows indicate excitatory projections, and lines that end with a bar represent inhibitory projections. ADN, anterodorsal thalamus; AVN, anteroventral thalamus; DTN, dorsal tegmental nucleus; HPC, hippocampus; LDN, laterodorsal thalamus; LMN, lateral mammillary nuclei; MEC, medial entorhinal cortex; MVN, medial vestibular nuclei; NPH, nucleus prepositus hypoglossi; PaS, parasubiculum; PoS, postsubiculum; RSP, retrosplenial cortex; SGN, supragenual nucleus, from Clark and Taube. (2012). **B**. Typical tuning curves of head direction cells in presubiculum (postsubiculum), retrosplenial cortex, ADN, left LMN and DTN. Solid lines represent tuning curves during clockwise, dashed lines during counterclockwise head turn, adapted from Wiener and Taube. (2005).

2.2.4 Subcortical source of head direction signal

Generation of the head direction signal takes place in subcortical regions from information provided by the vestibular system composed of the semicircular canals and the otolith organs that detect angular and linear acceleration respectively. Semicircular canals are necessary for head direction cell activity in ATN (Muir et al., 2009; Clark and Taube, 2012; Valerio and Taube, 2016) whereas the otolith organs provide robustness and stability for HD signal (Yoder and Taube, 2009). All along the integrative pathway, from the vestibular organ to the DTN, vestibular information is carried by angular head velocity cells that fire as a function of head rotation speed and direction (Bassett and Taube, 2001; Sharp et al., 2001b). These cells are tonically active when the head is still, but increase their firing rate during one kind of turn (clockwise versus counterclockwise) and decrease their firing rate during the opposite kind of turn. The angular velocity signal is received by the DTN from the vestibular nuclei via the supragenual nucleus and the nucleus prepositus. The generation of the HD signal is thought to occur within the reciprocal connections between the dorsal tegmental nuclei (DTN) and lateral mammillary nuclei (LMN) transforming angular head velocity signals into HD signals (Bassett et al., 2007; Clark and Taube, 2012).

Several theoretical models have been developed to simulate the spatial firing properties of HD cells and show how such cells might be combined to form a compass-like directional system (Skaggs et al., 1995; Redish et al., 1996; McNaughton et al., 2006). Particularly, attractor network-based models are a class of neural networks that are considered to be a good approximation to those in the HD system (**Fig. 6**). In these models, HD cells are arrayed in a circle with the location of each cell on the circle representing the preferred direction of that cell. An estimate of current HD is accomplished by a vector summation of the angular displacement and the animal's previous HD. Nearby HD cells with similar preferred directions are connected with strong excitatory synapses and fire together within a temporally correlated group of HD neurons (activity packet). The activity packet is believed to move on a virtual ring as the animal turns its head. Cells that are far apart on the ring with greatly different preferred directions are suppressed by lateral inhibitory synapses. This symmetric connectivity creates a single « bump » of excitation (a "hill" of activity) on the ring whose shape is determined by the connections weight, and position guided by the external inputs (Knierem et Zhang, 2012). Recent studies of Peyrache et al., (2015) revealed that the postulated attractor network was preserved in both ADN and presubiculum during sleep and wake states.

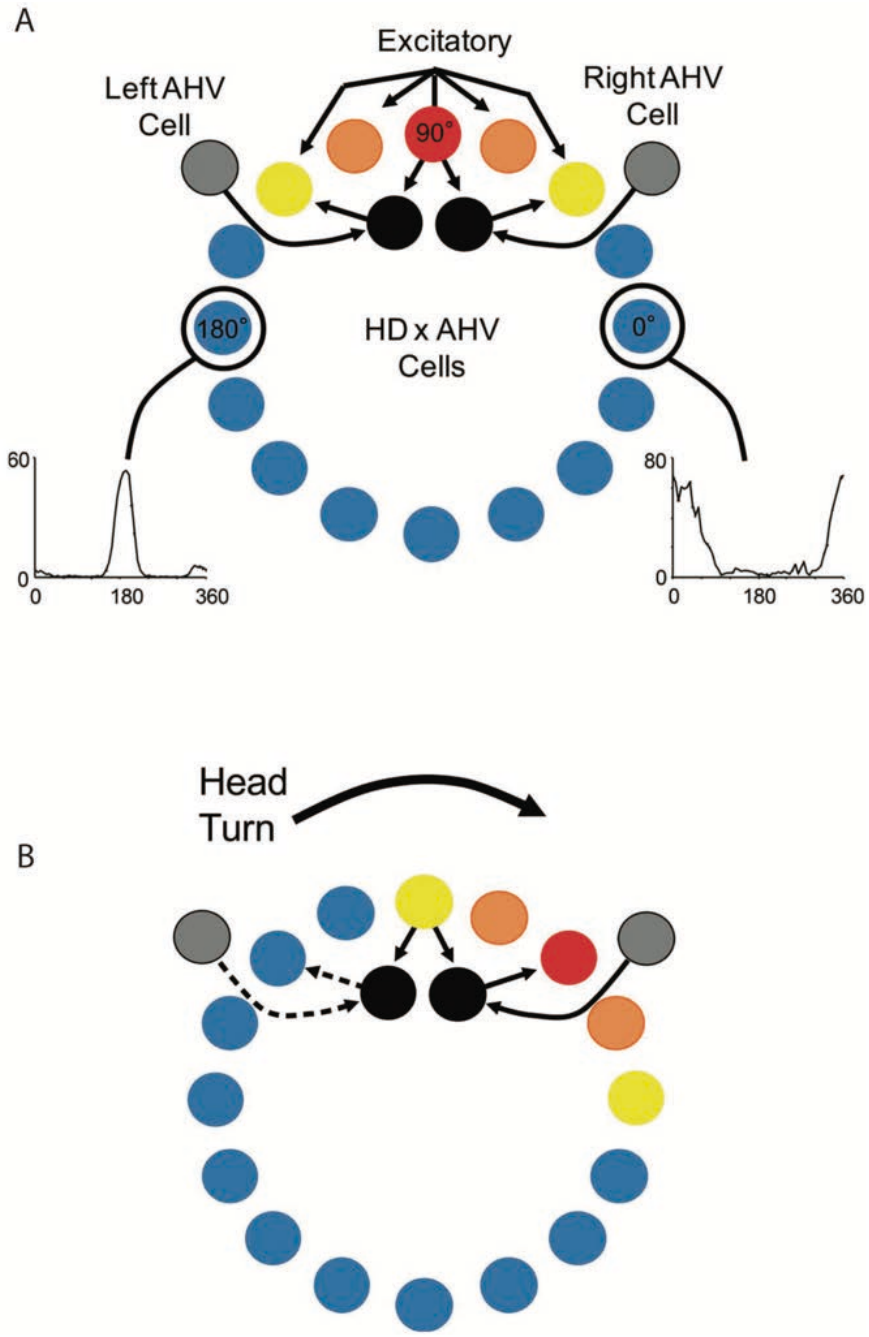

Figure 6: A continuous attractor network model of head direction signal generation. **A**. In this model, HD cells are arranged in a circle or ring with each HD cell (colored circles) positioned according to their corresponding preferred tuning direction. Each HD cell sends strong excitatory axons to nearby neurons, and weaker excitatory inputs to more distant neurons. Inhibitory projections (not shown) within the network limit net activity resulting in a focused point, or a "hill", of high activity (warm colors). Movement of the activity hill corresponding to an animal's head movements is achieved by two additional neural signals: one that is sensitive to changes in an animal's angular head velocity (AHV) (gray circle), and another that conjunctively encodes current HD × AHV (black circle). **B**. Following a head turn, conjunctive HD × AHV cells drive the activity hill in the appropriate HD. A right head turn would engage HD × AHV neurons that are specifically sensitive to clockwise head turns (solid arrows). These neurons would in turn activate HD cells to the right of the hill and drive activity to the animal's current HD, adapted from Clark and Taube. (2012).

Thus, the coordinated activity in the HD system is not only shaped by incoming sensory signals, but is also strongly influenced by internal self-organized mechanisms.

Combined lesion and recording studies have critically elucidated how the head direction signal is transmitted from one region to the next. Bilateral lesions of the LMN abolish the HD signal in the ATN (Bassett et al., 2007). HD cell activity is conveyed in both directions between the ATN and the PrS. But only the ATN is a crucial and necessary upstream element in the head direction circuit since its lesion abolished head direction cells activity in presubiculum (Goodridge and Taube, 1997) and other areas including parasubiculum and superficial layers of the medial entorhinal cortex (Clark and Taube, 2012; Winter et al., 2015). In contrast, lesions of the PrS had very subtle effect on direction-specificity of ADN neurons but rather influences ADN HD neurons by increasing the extent of anticipation in ADN and disrupt visual landmarks based cue control in the ADN (Goodridge and Taube, 1997).

2.2.5 Functional importance of presubiculum in spatial coding

Spatial navigation engages a wide brain circuit and coding for the animal's head direction is considered a pivotal component of the brain's navigation system. Presubiculum appears to be a crucial node where directional heading information and visual landmarks are transferred to the entorhinal-hippocampal network that participates in spatial cognition (Yoder and Taube, 2011).

The dorsal part of the presubiculum is a crucial entry point for integrating visual landmark information in the HD circuit. PoS receives direct input from primary and secondary visual cortices (Vogt and Miller, 1983) and projections from retrosplenial cortex, relaying information from visual cortex (Vogt and Miller, 1983; Van Groen and Wyss, 1990a; Jones and Witter, 2007), from LDN (Bett et al., 2013; Clark and Harvey, 2016) and associative visual cortical areas, such as posterior parietal and postrhinal cortices (Yoder et al., 2011). The importance of the PrS in processing landmark information into subcortical generators of the HD signal is demonstrated in PrS lesioned rats that severely altered landmark control of HD cell's in both ADN (Yoder and Taube, 2011; Goodridge and Taube, 1997) and LMN (Yoder and Taube, 2011; Yoder et al., 2015). Thus, the PoS is well suited to exert feedback control on its efferent destinations ADN and LMN but also the retrosplenial cortex (Wyss and Van Groen, 1992), LDN (Van Groen and Wyss, 1990b, c) or medial entorhinal cortex (Honda et al., 2008)

by refining the local HD signal with visual information (Goodridge and Taube, 1997). Recent work has shown that the PrS is an important component for providing direct landmark control to the HD signal in the LMN and also contributes to its path integration maintenance when familiar visual landmarks are unavailable (Yoder et al., 2015).

Compared to grid and place signals, head direction signal maturation occurs earlier during post-natal development (Bjerknes et al., 2015; Langston et al., 2010; Wills et al., 2010). Thus, head direction cells do not require place and grid cell information of the hippocampal-entorhinal circuit. The early maturation of the head-direction signal is thought to guide the development of spatial representations in entorhinal cortex and hippocampus later on. Following hippocampal silencing of place cell activity and dissolution of the grid map, former grid cells developed a preference to spike when the animal pointed its head in a certain direction (Bonnevie et al., 2013) indicating that the grid cell signal somehow carries a head direction signal. Inactivation or lesion of ATN significantly reduced the spatial periodicity of grid cells with a decrease in direction-specific firing properties and number of HD cells in the parahippocampal region (**Fig. 7A**; Winter et al., 2015). Taken together, these findings suggest that there are multiple excitatory inputs to grid cells, from both the hippocampus and regions that carry head-direction signals. The plausible source of a directional signal for grid cells is the presubicular head direction cells. Indeed, many studies have hypothesized that the PrS (and PaS) by providing strong bilateral inputs to MEC may be required for the generation of grid and place cells (Van Groen and Wyss, 1990c; Caballero-Bleda and Witter, 1994; Honda and Ishizuka, 2004). Particularly, ipsi- and contralateral projections from presubiculum reach layer 2/3 of entorhinal cortex (Honda et al., 2008), where grid cells are found.

Visual landmarks influence head direction cells, grid cells and place cells because rotation of a visual landmark produces an equivalent rotation of grid, place and preferred direction fields (**Fig. 7B**; Knierim et al., 1995; Sargolini et al., 2006). Particularly, the presubiculum was shown to be important for the landmark control of place cells in the hippocampus: place fields from PrS-lesioned were not controlled by the cue and shifted randomly between sessions (**Fig. 7C**). Visual landmarks no longer influenced place fields when PrS, but not ADN, was lesioned (Calton et al., 2003). Behaviorally, PoS lesions impaired performance on spatial memory tasks, such as the water and radial arm mazes, where the use of landmark cues is necessary for task completion (Taube et al., 1992).

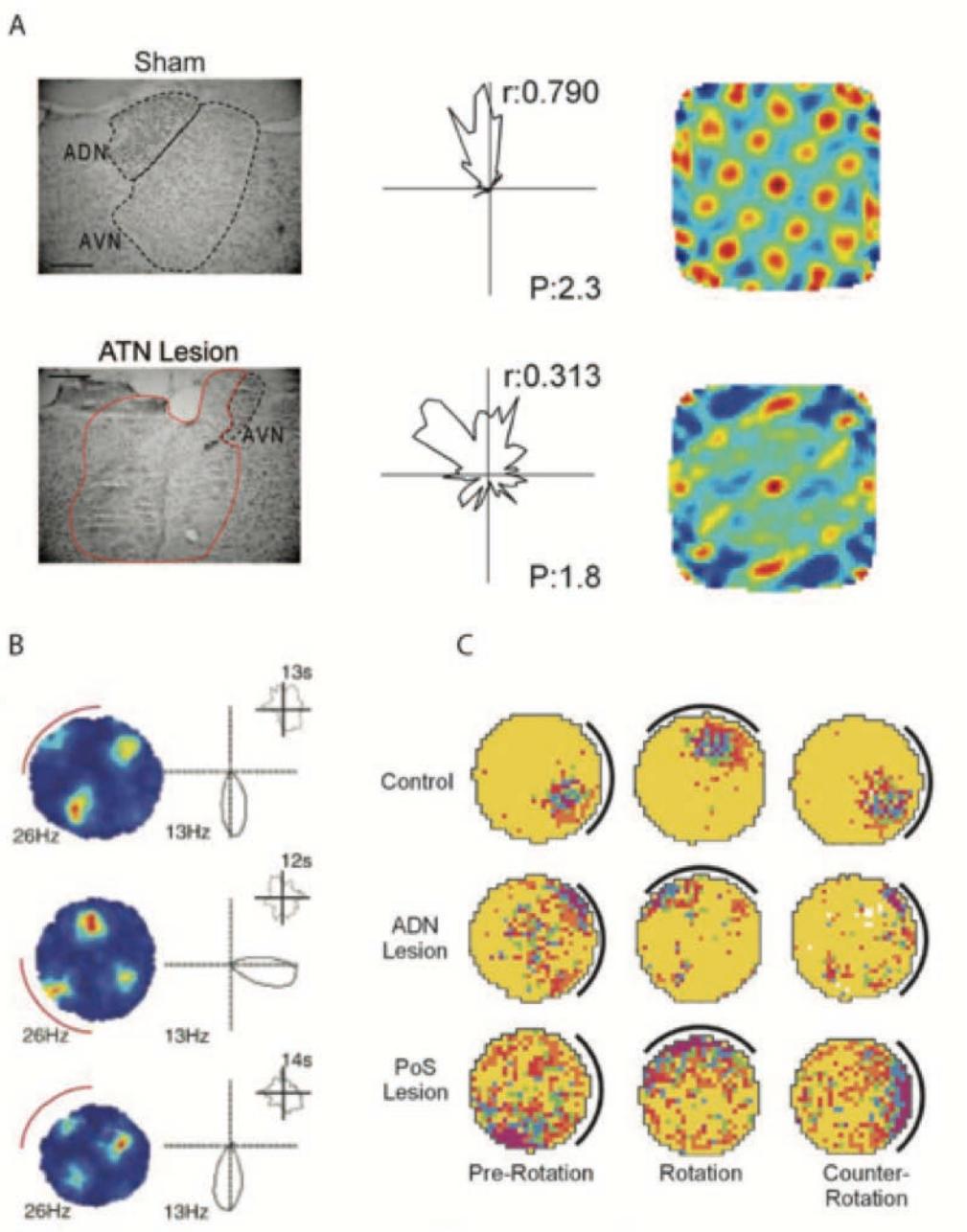

Figure 7: Presubiculum as a relay for generation and landmark control of HD circuit. **A**. ATN region from sham (top, left) and ATN large lesion (bottom left) animals. Only the right hemisphere is illustrated; however, this example is representative of bilateral damage in animals with ≥85% damage. Scale bars, 0.5 mm. Middle, Examples of HD cells from sham (top) and ATN large lesion (bottom) animals. HD cell from ATN lesion animals has less robust polar plots, with lower r and P. Right, two grid cells from a sham animal (top) and from an ATN large-lesion animal (bottom), adapted from Winter et al. (2015). **B**. Rate map for a grid cell (left) and polar plot for a head-direction cell (right) recorded simultaneously in layer 6 of MEC after rotation of a polarizing cue card on the wall of the circular environment (red arc). Top and bottom, cue card in original position. Middle panel, cue card rotated 90°. Insets show distribution of time across head directions, from Sargolini et al. (2006). **C**. Place/rate plots showing the response of representative place cells from each condition during the three sessions of the cue-rotation experiment, from Calton et al. (2003).

Thus, PoS is likely to play a role in selecting which cues to use as landmarks that would require the use of spatial memory.

2.3 Neuronal components of the presubiculum

2.3.1 Intrinsic excitability of presubicular neurons

Despite anatomical characterization that highlights functional uniqueness of this region, basic electrophysiological properties of cells in the PrS, relative to neighboring MEC and hippo-campus, have been addressed in only a handful of studies (Fricker et al., 2009; Funahashi and Stewart, 1997a; Menendez de la Prida et al., 2003; Simonnet et al., 2013, Abbassi. 2014, 2015; Tukker et al., 2015; Preston-Ferrer et al., 2016).

Funahashi and Stewart, (1997a) were the first to examine the presubicular neurons physiology and morphology. They found that pyramidal neurons in layer 3 and 5, as well as stellate cells in layer 2 and 5 were regular spiking neurons (Funahashi and Stewart, 1997a). Menendez de la Prida et al., (2003) found a large variability of cellular types classified according to their response to current injection in the subicular complex such as bursting (involving both Ca^2+ and persistent Na+ components), regular-spiking and fast-spiking cells. In our laboratory, Jean Simonnet provided a full description of principal neurons in all 6 layers of presubiculum using unsupervised cluster analysis based on the somatic location, morphology and firing pattern (**Fig. 8A**; Simonnet et al., 2013). Superficial cells that fired regularly (layers 2 and 3, cluster 1) were separated from deep cells (layers 5 and 6; cluster 3), burst firing pyramidal neurons of layer 4 emerged as a distinct third group. Burst firing layer 4 neurons had depolarized resting potential, hyperpolarized firing thresholds, expressed the Ih current strongly consistent with previous work (Yoshida and Hasselmo, 2009), and their apical dendrites extended to layer 1. Deep layer neurons fired regularly and had little frequency adaptation consistent with a role in maintained signaling of head position. Soon afterwards, another group published a similar study focused specifically on superficial layers (Abbasi and Kumar, 2013). The description of the electrophysiological properties of superficial layers covered much of the existing diversity and showed that superficial layers 2 and 3 contain a neuronal population more diverse than previously reported, even though it was not systematically correlated with morphology. The same group showed that in the context of temporal lobe epilepsy, only a subset of superficial layer 2 and 3 neurons undergoes alterations in their firing profiles and synaptic drive (Abbasi and Kumar, 2014).

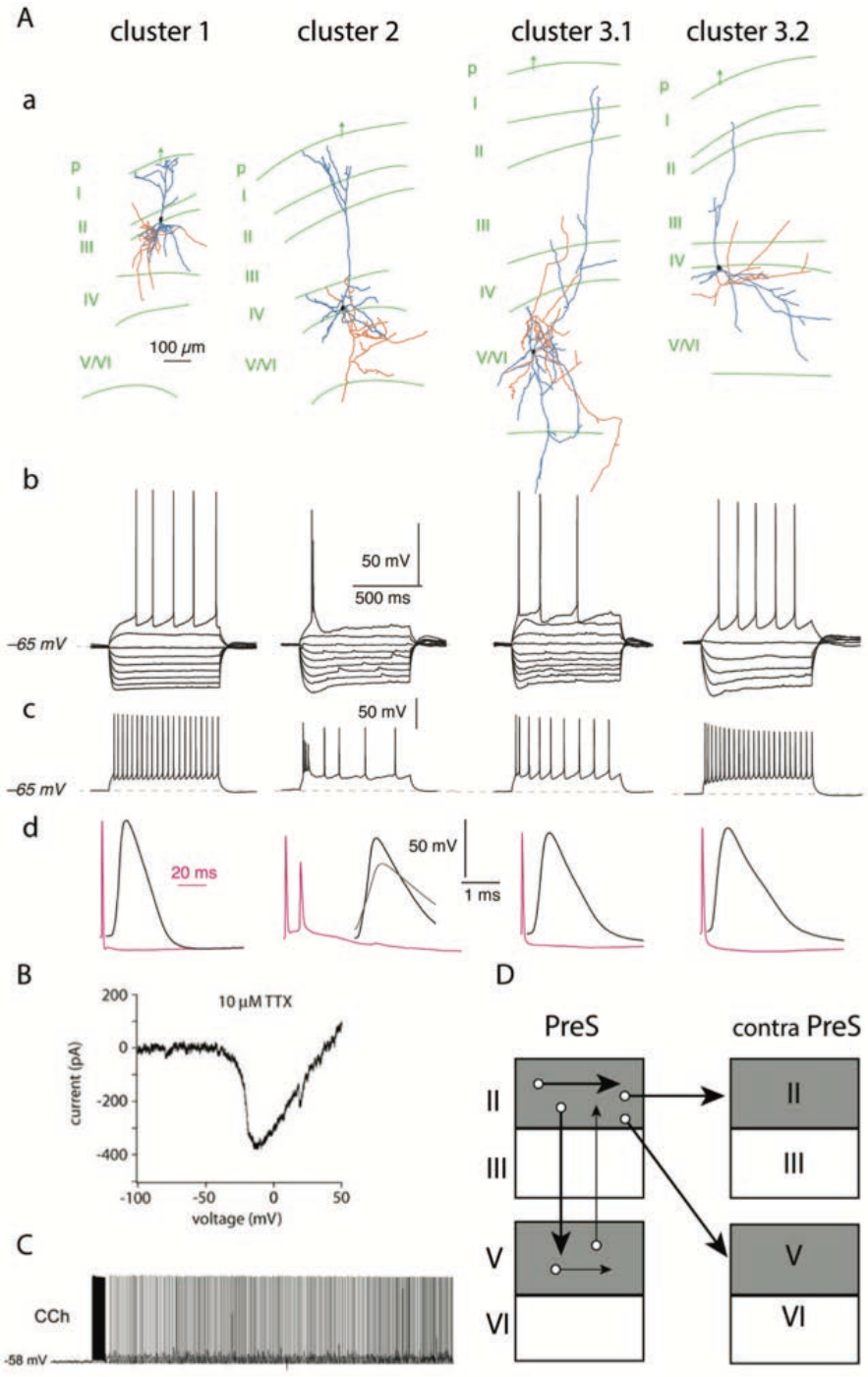

Figure 8: Physiological properties and connectivity of presubicular pyramidal neurons. **A**. Cluster neurons with somata in presubicular layers 2, 3, 4 and 5/6. (**a**) Reconstructions of biocytin-filled neurons in superficial and deep layers of the presubiculum. Axons in red, dendrites in blue, with layer limits and the pial surface in green. (**b**) Current-clamp records of responses to 800 ms hyperpolarizing and depolarizing current steps. (**c**) Regular or burst firing induced by + 100-150 pA step current injections. (**d**) Action potential (AP) waveforms. Adapted from Simonnet et al. (2013). **B**. A TTX-insensitive sodium current with slow acti-

vating and inactivating kinetics in presubicular principal neurons, from Fricker et al. (2009). **C**. Persistent firing was induced by the current injection (2 s, 50 pA) in the presence of carbachol (10 μM) in a postsubicular neuron. Bottom trace shows frequency of persistent firing. From Yoshida and Hasselmo, (2009). **D**. Summary of interlaminar and intralaminar connections of the presubiculum. Projections from layer 2 cells are bilateral and confined to layers 2 and 5, whereas those from layer 5 cells are ipsilateral and confined largely to layer V, with fewer projections to layer 2, from Honda and Ishizuka, (2004).

The presubiculum appears to carry the HD information via excitatory pyramidal cells, possibly also involving FS interneurons, without using a theta-rhythmic temporal code (Boccara et al., 2010; Tukker et al., 2015), at least not in layer 3 (Preston-Ferrer et al., 2016). The underlying mechanisms for the non-adapting HD signal still remain unknown. Intrinsic cellular properties may support persistent firing, such as a tetrodotoxin (TTX)-insensitive sodium current with slow kinetics in superficial layer presubicular neurons (**Fig. 8B**; Fricker et al., 2009), or a calcium-sensitive nonselective cation current (**Fig. 8C**; Yoshida and Hasselmo, 2009). Persistent activity may also depend on network properties, recurrent synapses and facilitating synapse dynamics (Goldman-Rakic, 1995; Wang, 2001; Major and Tank, 2004).

2.3.2 Input- and output regions of the presubicular microcircuit

Information processing in the presubiculum must be determined by the physiological and anatomical features of its local connections as well as the integrative properties of these neurons in response to afferent inputs. Combining the neuronal description studies with the anatomical and functional connectivity with incoming and outgoing pathways, a clearer picture of the presubicular organization will emerge. Here, I will review the major input/output pathways of the presubiculum that I have focused on during my thesis (i.e ATN, RSC, LMN and MEC).

The ATN and the retrosplenial cortex are considered to provide major inputs to presubiculum (Yoder et al., 2011). The projections from retrosplenial cortex to the entire dorsoventral axis of both superficial and deep layers of PrS have been described (Van Groen et al., 1990a; Van Groen et al., 1992a; Van Groen and Wyss, 2003; Jones et al., 2007; Sugar et al., 2011; Sugar and Witter, 2016). Projections depend on the parts of the retrosplenial cortex since it is divided into agranular (Van Groen et al., 1992a) and granular (a and b) regions (Van Groen et al., 1990a; Van Groen and Wyss, 2003). More specifically, direct inputs from retrosplenial cortex have been shown to project onto superficial layer 3 presubicular neurons (Kononenko and Witter, 2012).

In turn, deep layers of the presubiculum project to the retrosplenial cortex (Vogt and Miller, 1983; Wyss and Van Groen, 1992). The ATN projects to layers 1, 3 and 4 in the presubiculum (Van Groen and Wyss, 1990b, c; Van Groen and Wyss, 1995). In turn, the presubiculum-to-ATN projections originate from the deep layers of the ipsilateral presubiculum (Van Groen and Wyss, 1990b, c).

The presubiculum-to-LMN projection emanates only from the thin layer 4 (**Fig. 9**; Yoder and Taube, 2011) containing pyramidal cells with intrinsic bursting properties (Simonnet et al., 2013). Presubicular superficial layer neurons constitute the major output toward ipsilateral and contralateral medial entorhinal cortices (MEC), mainly targeting their superficial layers (Honda and Ishizuka, 2004; Canto et al., 2012; Tukker et al., 2015; Preston-Ferrer et al., 2016). However, some projections originate from deep layer neurons of the presubiculum and target deep layers and layer 1 of the ipsilateral MEC (Honda and Ishizuka, 2004). Projections from MEC back to PrS are sparse: Wyss (1981) described projections from MEC to layer I of the presubiculum.

Because most studies of inputs to presubiculum are anatomical, the identity of the main postsynaptic target types within presubiculum has remained uncertain. In particular, superficial layer neurons (mostly superficial layer 3 neurons) of the presubiculum are likely to relay the visual and vestibular information directly to the entorhinal cortex. A part of my thesis work has addressed the functional connectivity of thalamic-to-presubicular layer 3 MEC projecting neurons and interneurons (Nassar et al., in prep). We also examined whether projection-specific neurons possess distinct biophysical and anatomical properties (Huang et al., in prep.). These data are presented in the results section.

3-GABAergic neurons of a cortical network

The cortex is a complex, but relatively stereotypic organized network, composed of multiple cell types forming micro- to large-scale neuronal circuits (DeFelipe and Fariñas, 1992; Silberberg et al., 2002; Varela et al., 2001). Information flows through synapses in a finely organized network composed of afferent fibers and local cell bodies of diverse neurons. The cortex is composed of two main neuronal groups, glutamatergic pyramidal neurons (PN) and GABAergic interneurons (IN), which are distributed across different cortical layers. The lam-

inar organization of the cortex, largely conserved across mammalian species, is based on cytoarchitectonic criteria that define six layers, horizontally to the cortical surface (Douglas and Martin, 2004; Nieuwenhuys, 1994). PNs and INs from a specific layer can interact within their home layer and across layers. Inter-laminar connections are the anatomical framework of the cortical columns that form functional entities of interconnected neurons (Adesnik and Scanziani, 2010; Hubel and Wiesel, 1962; Mountcastle, 1957).

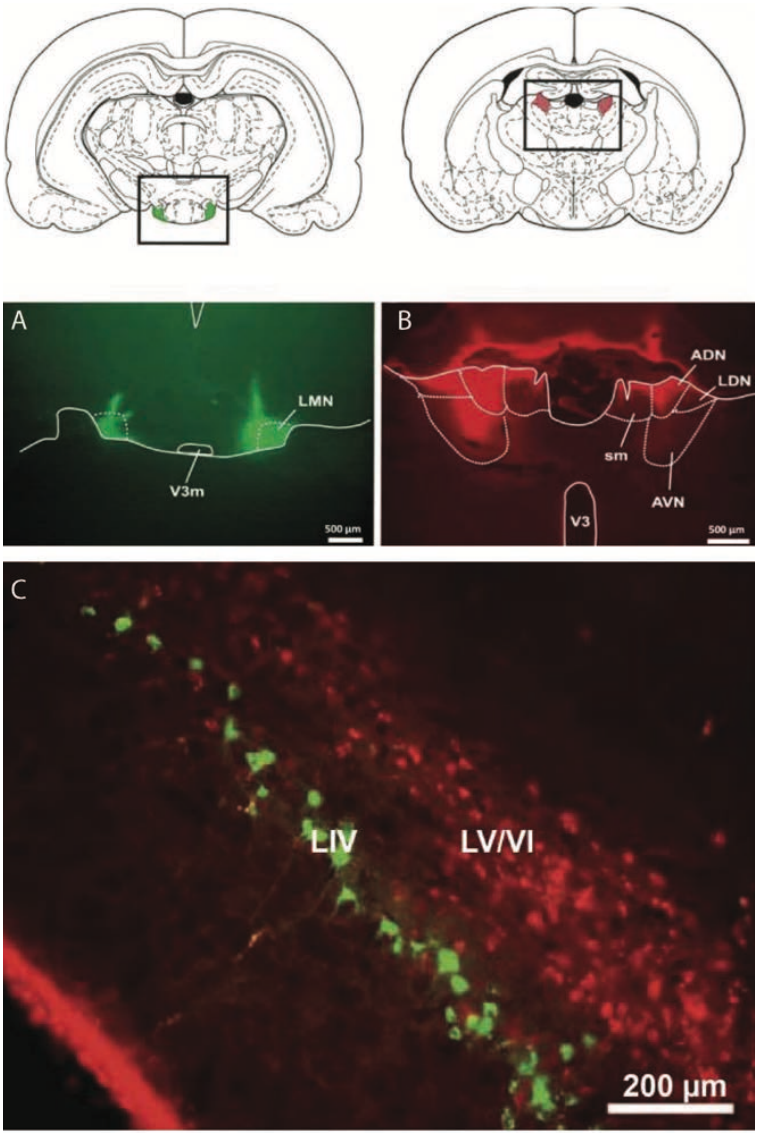

Figure 9: Projection specific neurons in layer 4 and deep layers (5/6). **A**. Cholera toxin-Alexa Fluor 488 (CTB-488) injection sites in LMN. The left LMN is partially filled with CTB-488, whereas the right LMN is completely filled with CTB-488. Dashed lines indicate LMN, corresponding to LMN (shaded areas in rectangle) in diagram above. V3, third ventricle; V3m, third ventricle, mammillary recess. **B**. CTB-594 injection sites in the ADN. CTB-594 is present in the ADN and surrounding areas including the anteroventral (AVN) and laterodorsal thalamic (LDN) nuclei. Dashed lines indicate ADN and surrounding nuclei, corresponding to the rectangle in the diagram above. **C**. Tracers migrated retrogradely in non-overlapping neu-

ronal populations in the presubiculum. Somata of layer 4 neurons show green labeling (green) as injected tracer in LMN. Somata of layer 5-6 neurons show labeling following tracer injection (red) into the right ADN. ADN, Anterodorsal thalamus; AVN, Anteroventral thalamus; LMN, Lateral mammillary nucleus; sm, stria medullaris; V3, third ventricle; V3m, third ventricle, mammillary recess. Adapted from Yoder and Taube, (2011).

To understand the functions of a microcircuit one also needs to understand its structural frame. What kind of neurons form a cortical circuit? How do these elements participate in information processing? How do individual neurons integrate one or multiple inputs to produce their firing? During my PhD, I aimed to answer these questions, focusing on the inhibitory microcircuit of the presubciulum. I examined the diversity of the multiple inhibitory neuronal components, their anatomical and functional connectivity with local principal neurons and incoming inputs from the thalamus. In this chapter, I will review the characteristics and the specificity of the different INs that constitute hippocampal and cortical circuits.

3.1 GABAergic neuron types

GABAergic neurons represent about 15-30% of cortical neurons located in all cortical layers (DeFelipe, 2002). They were first classified by Ramon y Cajal as 'short axon cells' in Golgi studies of human visual cortex (Ramón y Cajal, 1899) because they are almost exclusively involved in local neuronal networks due to their restricted axonal and dendritic arborizations. They were therefore called interneurons (INs). Some features distinguish them from pyramidal shaped principal neurons (PN); indeed, most mature inhibitory interneurons have aspiny dendrites and receive both excitatory and inhibitory synapses onto their somata. Their axon terminals form symmetrical synapses, corresponding to Gray's type 2, as opposed to glutamatergic, asymmetrical synapses of PNs, corresponding to Gray's type 1 (Gray, 1959). Cortical inhibitory INs are highly diverse and comprise many types according to their anatomy, electrophysiology and molecular diversity (Ascoli et al., 2008; DeFelipe et al., 2013; Gupta et al., 2000; Markram et al., 2004; Kubota, 2014; Kubota et al., 2016). Remarkably, individual INs selectively target distinct compartments of PNs (dendrites, soma or axon initial segment) or other IN types. Some INs are electrically coupled through Gap junctions (Beierlein et al., 2000; Bartos et al., 2002; Hestrin and Galarreta, 2005; Ma et al., 2011; Hu et al., 2011). Importantly, none of the anatomical, neurochemical or electrophysiological criteria alone can reliably classify cortical inhibitory INs. Therefore, many studies have applied multidimensional analyses to detect associations between these features. (Cauli et al., 1997; Markram et

al., 2004). More recently, the developmental origin and genetic makeup has been investigated (Kepecs and Fishell, 2014; Taniguchi, 2014; Tasic et al., 2016), and ultimately, we wish to further consider complexity across different brain structures and define interneuron types by their circuit specific function (Hangya et al., 2014).

3.1.1 Morphological properties and postsynaptic targets

Using Golgi based-impregnation methods, Cajal showed that cortical INs greatly vary in their somatic, dendritic and axonal morphologies. With his colleague Lorento de No, they demonstrated that dendritic arbors are a variable element and cannot define the interneuron types but rather predict the possible sources of afferent inputs. However, the pattern of axon arborization of an interneuron can provide strong evidence of its postsynaptic targets. In the hippocampus and the neocortex, some INs preferentially innervate perisomatic regions, proximal dendrites or axon initial segments, whereas others target more distal dendrites (**Fig. 10**; Freund, 2003; Freund and Katona. 2007; Markram et al., 2004; Kubota, 2014; Kubota et al., 2016). Some INs have been described as specialized in targeting other cortical INs (Acsády et al., 1996; Gulyas et al., 1996, Freund and Buzsáki, 1996; Somogyi et al., 1998; Staiger et al., 1997). The specialization of IN connectivity is thought to contribute largely to their functional specificities (Gentet et al., 2012; Isaacson and Scanziani, 2011; Jiang et al., 2015).

Basket cells innervate the somata and proximal dendrites of PNs, representing the largest populations of interneurons (about 50%). In the hippocampus, their bitufted dendritic tree extends towards all layers and their axon is confined to the stratum pyramidale (Freund and Buzsáki, 1996). Basket cells can be further subdivided into several classes based on their soma size, frequency of axonal branching, axo-dendritic morphology and firing properties (i.e., large (LBC) or small basket cells (SBC) and nest basket cells (NBC)) (Karube et al., 2004; Krimer et al., 2005; Markram et al., 2004; Uematsu et al., 2008; Kubota, 2014; Kubota et al., 2016). Basket cells are mutually interconnected via chemical and electrical synapses (Cobb et al., 1995; Gibson et al., 1999; Fukuda, 2007; Somogyi et al., 1998, Bartos et al., 2002; Hestrin and Gallaretta, 2005; Baude et al., 2007). The axo-axonic cells (Somogyi, 1977) are also called chandelier cells because their axon terminals form multiple climbing-fiber-like contacts resembling candlesticks on a chandelier. Originally described in neocortex, chandelier cells have also been found in the CA3, CA1 and dentate gyrus regions of the hippocampus. They target specifically the axon initial segment of PNs (Karube et al., 2004; Krimer et al., 2005; Markram et al., 2004; Kubota, 2014; Kubota et al., 2016). Thus, they are positioned at a cru-

cial site to override both dendritic integration and somatic gain, « updating » the action potential output.

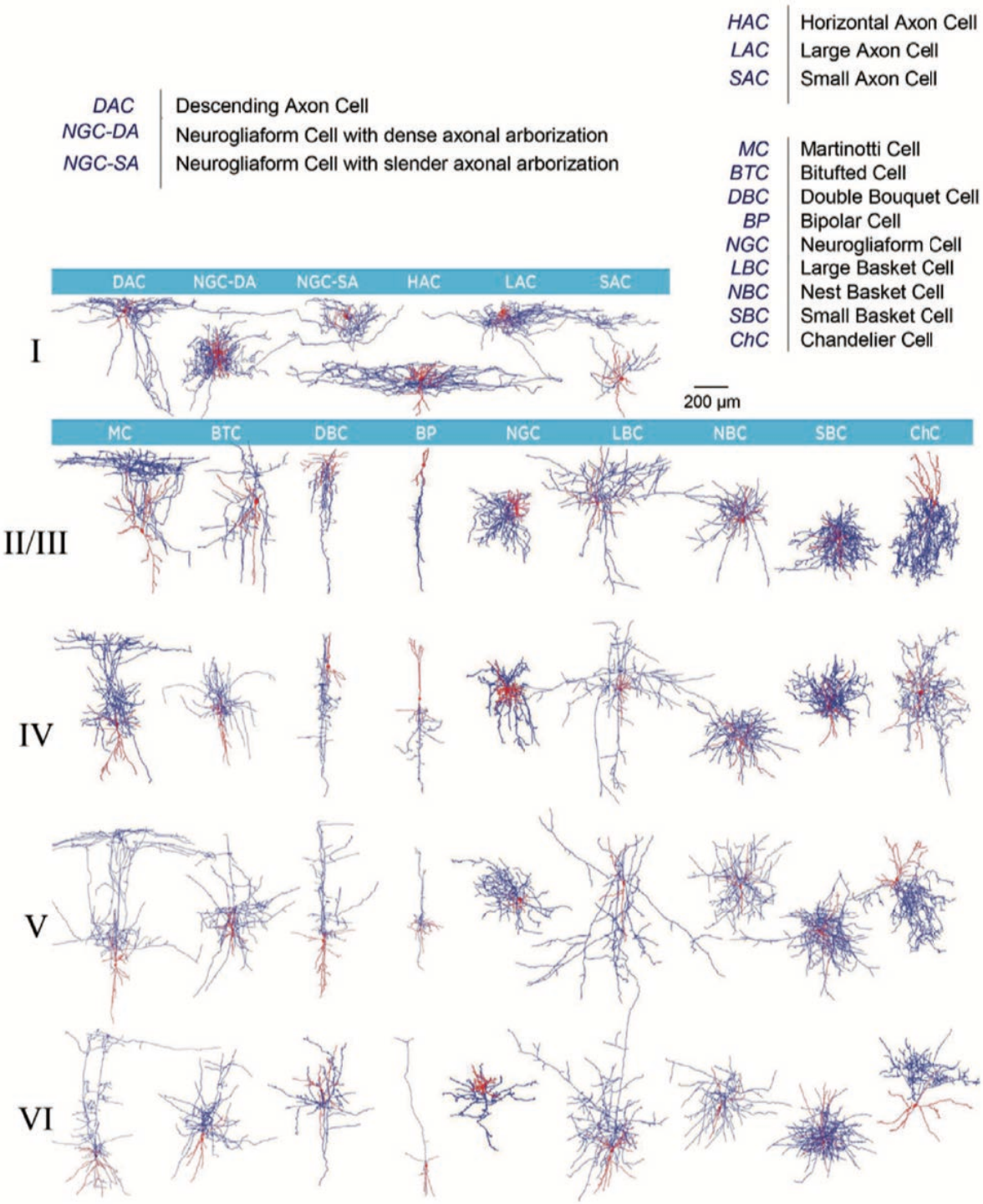

Figure 10: Morphologies of neocortical interneurons. Exemplar 3D reconstructions of 55 morphological types. Morphologies in L2 and L3 are not separated. Axon in blue, dendrites in red. Full morphologies are not always shown. From Markram et al. (2015).

The dendrite-targeting cells can be subdivided into several cell types: bipolar, double bouquet, bitufted and neurogliaform cells. The bipolar, double bouquet and bitufted cells present bipolar and bitufted dendrites but are differentiated by their axonal orientation or morphology (Markram et al., 2004). The neurogliaform somata can be found in all cortical layers and in the stratum lacunosum moleculare (Muralidhar et al., 2014; Capogna, 2011). Neurogliaform cells present a spherical dendritic field and thin and dense intertwined axonal arbors, forming electrical synapses with INs from the same or different type (Markram et al., 2004).

The dendritic and tuft-targeting cells are divided in Martinotti (MC) and layer 1 cells. The MCs have often bitufted dendrites with ascending axons composed of two parts, one near the cell body and the other projecting at variable distance innervating PNs tuft-dendrites in layer 1 (Markram et al., 2004). Oriens lacunosum moleculare (O-LM) cells and SOM hilar perforant path associated (HIPP) cells found in the hippocampus (stratum oriens and hilus) have axons ascending to stratum lacunosum moleculare or innervating dendritic tree of granule cells in the molecular layer respectively (Freund and Buzsáki, 1996; Houser, 2007). The layer 1 cells are confined to layer 1 and are divided in two groups. The first one corresponds to Cajal-Retzius multipolar cells (Druga, 2009) mostly present during development whose axons are confined to layer I making horizontal collaterals. The second class comprises the heterogeneous group of small, multipolar interneurons with diverse axonal arbors (Muralidhar et al., 2014).

3.1.2 Molecular markers and gene expression

Interneurons contain GABA-synthesizing enzymes GAD65 and GAD67 (Martin and Rimwall, 1993), and different neurochemical markers allow to divide the interneuron populations into subgroups. Several populations of interneurons contain different Ca2+ binding proteins or peptides. The most widely used interneuron markers are calcium-binding proteins such as parvalbumin (PV), calretinin (CR) and calbindin (CB) and neuropeptides such as somatostatin (SOM), vasoactive intestinal peptide (VIP), cholecystokinin (CCK), and neuropeptide Y (NPY). Besides, molecules such as the ionotropic serotonin receptor 5HT3a, reelin, nitritic oxide synthase or choline acetyltransferase (ChAT) can be used. Morphologically- or physiologically-defined interneuron types can co-exist and overlap in a single neurochemically identified subgroup (**Fig. 11**). Some interneurons co-express up to seven different molecular markers and patterns of co-expression differ between regions and species.

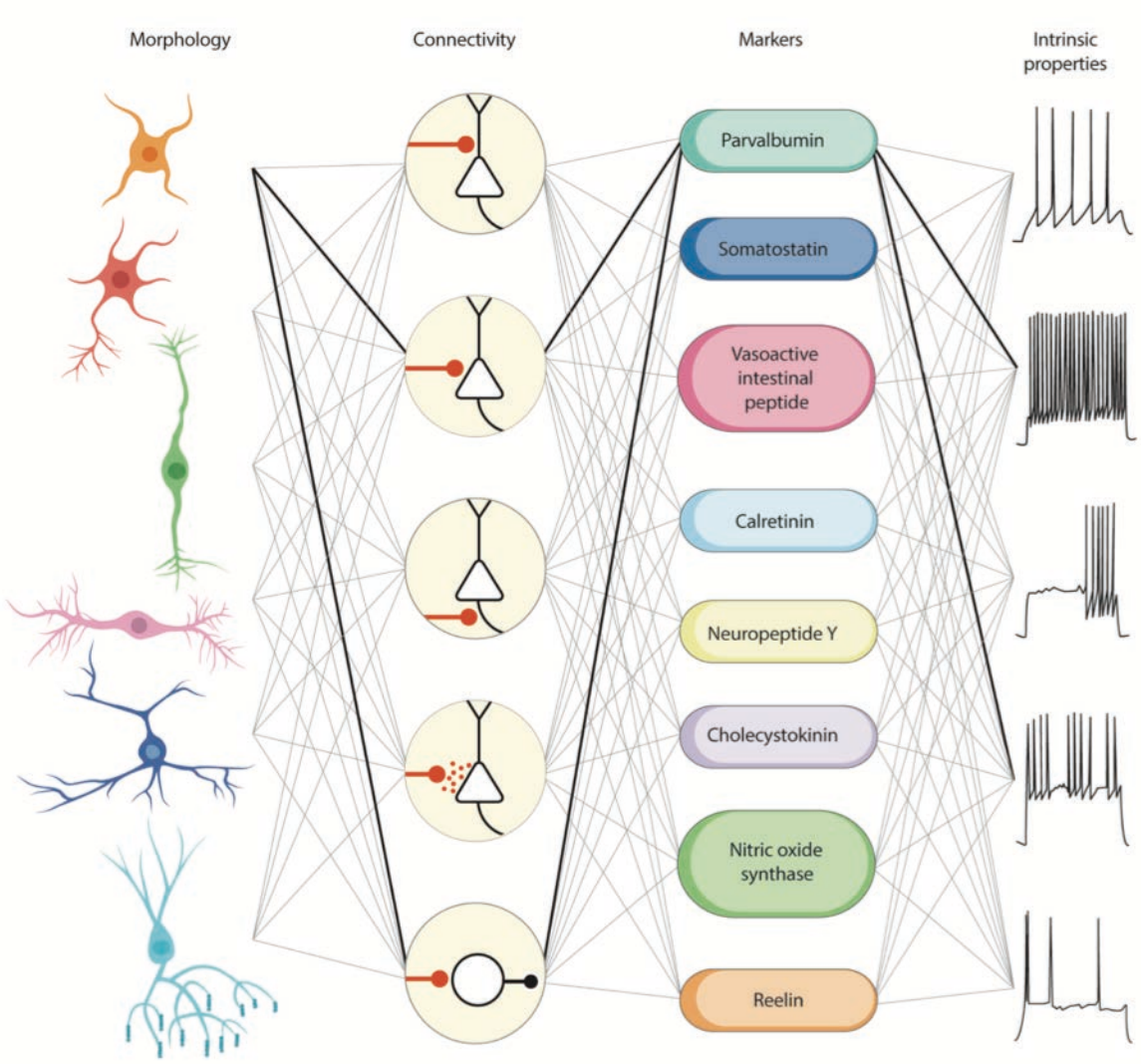

Figure 11: Multiple dimensions of interneuron diversity. Interneuron cell types are usually defined using a combination of criteria based on morphology, connectivity pattern, synaptic properties, marker expression and intrinsic firing properties. The highlighted connections define fast-spiking cortical basket cells, from Kepecs and Fishell. 2014.

PV is expressed in all compartments of basket and axo-axonic cells in the rat cerebral cortex and in the hippocampus (Celio, 1986; Kosaka et al., 1987). PV immunopositive neurons account for 40-50% of GABAergic neurons in rodents. A property of PV neurons is that they do not stain with antibodies against CR, SOM, VIP, CCK, NPY or ChAT (Gonchar et al., 2008; Uematsu et al., 2008) even though the overlap between PV mRNA and others from CB and peptides is much more extensive meaning that PV mRNA is not translated in many neurons (Cauli et al., 1997**).** Two types of basket cells are classically recognized: those expressing both PV and CB (Hartwich et al., 2009) and those expressing CCK (Freund et al., 1986; Kubota and Kawaguchi, 1997; Somogyi et al., 2004).

CB positive neurons are distributed in all cortical layers except layer 1 and exhibit vertically oriented morphology of DBCs and bipolar-bitufted cells. In rat, calbindin is expressed by a majority of neocortical SOM neurons (70%) and to a lesser proportion in PV cells (12%) (Kubota et al., 1994; Gonchar and Burkhalter, 1997). Unlike PV, CR and SOM that are only expressed in interneurons, CB is also found in pyramidal neurons (Kubota et al., 1994; Gonchar and Burkhalter, 1997). In the rodent entorhinal cortex, 88 % of calbindin positive neurons are glutamatergic (Peterson et al., 1996) and form discrete cell clusters in layer 2 (Fujimaru and Kosaka, 1996; Ray et al., 2014) similarly to what has been described in the presubiculum (Preston-Ferrer et al., 2016; cf. section 2.1.3).

CR INs represent about 20% of GABAergic neurons in the rodent cortex (Gonchar et al., 2008; Uematsu et al., 2008; Xu et al., 2010). CR INs can co-express different neuropeptides such as NPY, VIP and CCK (Kubota et al., 1994; Cauli et al., 1997), and present dendrite-targeting and layer 1 cell morphologies. CR INs interact preferentially with other INs in superficial layers and with PNs in deep layers (Druga, 2012; Meskenaite, 1997; Somogyi et al., 1998). CR expressions is species dependent; indeed, immunostaining in rats has shown that SOM and CR constitute non overlapping populations (Rogers, 1992**;** Kubota et al., 1994; Gonchar and Burkhalter, 1997), however in adult mouse cortex, SOM and CR are co-expressed in 20-40% of GABAergic neurons **(**Halabisky et al., 2006**;** Xu et al., 2006**;** Gonchar et al., 2008**)**.

Neuropeptides are expressed in different INs populations: bipolar cells express CR and VIP; double bouquet cells express CB/CR/VIP/CCK but not PV/SOM/NPY; bitufted cells express CB/CR/NPY/VIP/SOM/CCK but not PV (Gonchar et al., 2008; Markram et al., 2004; Xu et al., 2010). Interestingly, VIP is preferentially expressed in SOM negative bipolar and bitufted cells that display vertically descending axons controlling information across layers. They are absent in LBC, NBC and MC. VIP-expressing INs represent respectively around 10-20% of GABAergic cells of the rodent cortex (Gonchar et al., 2007; Uematsu et al., 2008; Xu et al., 2010) and can express the ionotropic serotonin receptor 5HT3a (Rudy et al., 2010).

Similar to CR, CCK expression is also species and regions dependent. CCK neurons co-express VIP and CR and lack NPY in rat frontal cortex (Kawaguchi and Kubota, 1997). In mouse visual cortex, CCK neurons contain CR and NPY but not VIP and they are negative

for PV and SOM. Some of the CCK neurons are basket cells with multiple boutons on other cortical cell bodies (Freund et al., 1986).

SOM expression is found in MCs, in a small fraction of SBCs and NBCs and also in some bipolar, double-bouquet and bitufted cells (Toledo-Rodriguez et al., 2004; Wang et al., 2004; Ma et al., 2006). Interestingly, SOM expressing interneurons not only innervate dendritic compartments but also form 1.2% of axo-axonic synapses onto PNs in rat and monkey visual cortex (Gonchar et al., 2002).

Among the different neurochemical expression patterns, PV, SOM and 5HT3aR-expressing VIP have been described as three non-overlapping subpopulations that account for the majority of GABAergic cells (Rudy et al., 2010). However, a few reports clearly show co-localization of SOM and PV in mouse and rat hippocampus (Jinno and Kosaka, 2000; Klausberger et al., 2004; Katona et al., 2014). Finally, the Petilla Interneuron Nomenclature Group has proposed a classification that distinguishes five different main groups of INs: (1) the PV INs, including chandelier and basket cells; (2) the SOM INs, such as MCs; (3) those expressing NPY but not SOM; (4) those expressing VIP; and (5) those expressing CCK but not SOM or VIP (Ascoli et al., 2008).

Since GABAergic cells originate from multiple embryonic sources, the mapping of the origins of distinct interneuron classes can help to comprehend interneuron diversity (Kepecs and Fishell, 2014). Hippocampal and neocortical interneurons have similar origins for homologous interneuron subtypes: the medial ganglionic eminence progenitors give rise to interneurons expressing PV and SOM while the caudal ganglionic eminence-derived interneurons are defined by CCK, VIP, CR, and Reelin expression (**Fig. 12;** Xu et al., 2004; Butt et al., 2005; Fogarty et al., 2007; Miyoshi et al., 2007; Gelman and Marin, 2010).

With the recent advent of the single cell RNAseq technique, transcriptomic profiling has revealed 23 GABAergic neuron types in visual cortex (Tasic et al., 2016). This cellular taxonomy indicates that there are indeed 4 major interneuron types with molecular markers SST, PV, VIP and Ndnf (neuron-derived neurotrophic factor), which segregate into further subtypes, with some rare interneuron types. Identifying molecular markers not only helps for classifications, but also gives relevant tools to visualize and study INs properties in transgenic

mouse lines (Madisen et al., 2010). The molecular classification is expected to be functionally discriminating.

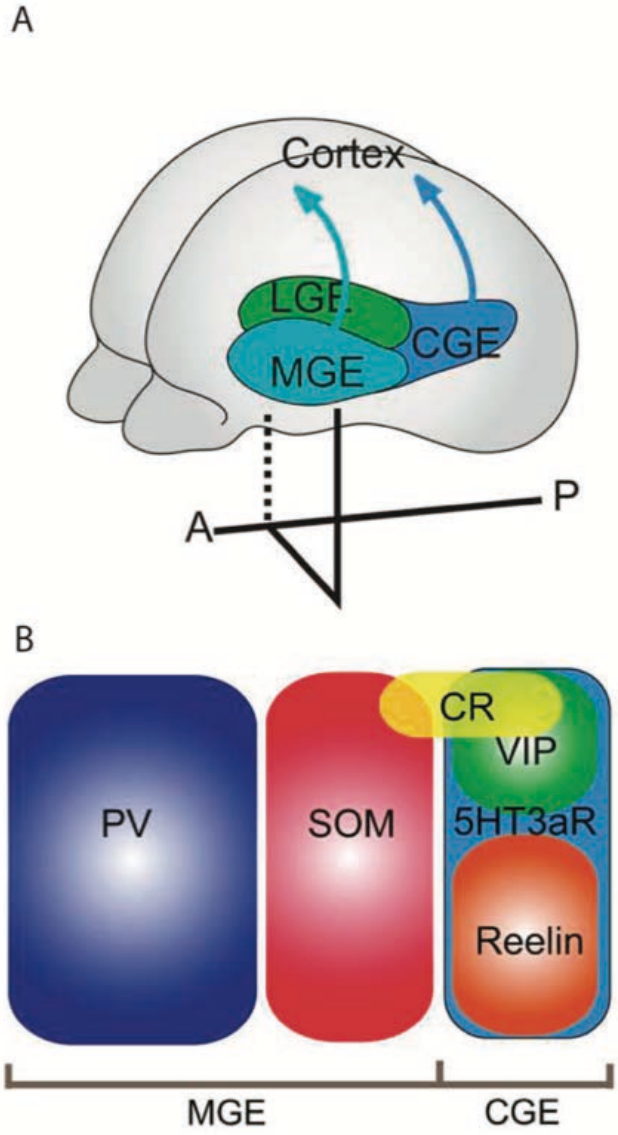

Figure 12: Embryonic origins of cortical interneurons. **A**. Cortical GABAergic interneurons are largely derived from the medial and caudal ganglionic eminence (MGE and CGE), and the preoptic area (POA), of the ventral forebrain. **B**. Three largely non-overlapping major interneuron subtypes. Interneurons subtypes are divided into PV, SOM, and 5HT3aR. PV- and SOM-expressing neurons and 5HT3aR-expressing neurons are generated from the MGE and the CGE, respectively, adapted from Taniguchi. 2014

3.1.3 Physiology: firing patterns and intrinsic properties

Morphological approaches have been associated with intracellular recordings in brain slices to allow the characterization of physiological and synaptic properties of interneurons (Cauli et al., 1997; Karube et al., 2008; Kubota, 2014; Jiang et al., 2015). Original intracellular recordings in rodent cerebral cortex have provided evidence that pyramidal neurons and interneurons have different intrinsic properties and firing patterns. Indeed, Connors and Gutnicks, 1990 and Kawaguchi, 1993 described the fast-spiking properties of some INs and non-fast-spiking with frequency adaptation for other INs. Four main IN electrophysiological profiles have been identified: a) fast spiking (FS), b) late spiking (LS), c) regular spiking (RS) and d) burst spiking (BS) or low threshold spiking (LTS) (Kawaguchi and Kubota, 1993, 1996, 1997).

FS INs display short duration spikes, brief afterhyperpolarisations and the ability to sustain a high frequency of discharge without accommodation (Kawaguchi, 1995). More detailed studies have described fast-spiking cells with continuous, delayed or stuttering firing properties. The fast spiking profile has been linked to PV chandelier and basket cells, however, not all basket cells are fast spiking INs (Karube et al., 2004; Kawaguchi and Kubota, 1997; Krimer et al., 2005; Uematsu et al., 2008; Wang et al., 2002). LS INs show a slow depolarizing ramp occurring around the spike threshold, delaying the onset of action potentials. This profile corresponds to neurogliaform or some basket INs (Karube et al., 2004; Kawaguchi and Kubota, 1997; Krimer et al., 2005; Uematsu et al., 2008). Finally, RS and BS INs, characterized by two or more spikes on slow depolarizing humps emitted in burst or not, correspond to a range of IN morphologies and include SOM expressing MCs, LBC positive for CCK and VIP-containing double bouquet cells (Kawaguchi and Kubota, 1996, 1997).

Voltage-gated ion channels are differently expressed across different interneuron subpopulations. Their activation generates the characteristics of the action-potential waveform and determines the spiking phenotype. PV fast-spiking interneurons, for example, express distinct voltage-dependent Kv currents (Lien et al., 2002; Lien and Jonas, 2003). Outward currents through delayed rectifying Kv3 channels (Erisir et al., 1999; Lien and Jonas, 2003) keep action potentials brief by activating at potentials close to the action potential peak, repolarizing the membrane voltage rapidly and limiting the duration of the after-hyperpolarization. High firing frequencies can be achieved because Kv3 channels can facilitate the recovery of both Na+ channels and transient A-type K+ channels from inactivation (Erisir et al., 1999). In PV neurons, dendritic K+ channels are likely to accelerate the decay time course of uEPSPs, lead-

ing to rapid and temporal precise activation by converging and spatially separated inputs (**Fig. 13A-B**; Hu et al., 2010). A high density of Na+ channels compensate for the morphological properties of BC cell axons allowing fast AP propagation and high frequency repetitive firing (**Fig. 13C-D-E**; Hu and Jonas, 2014).

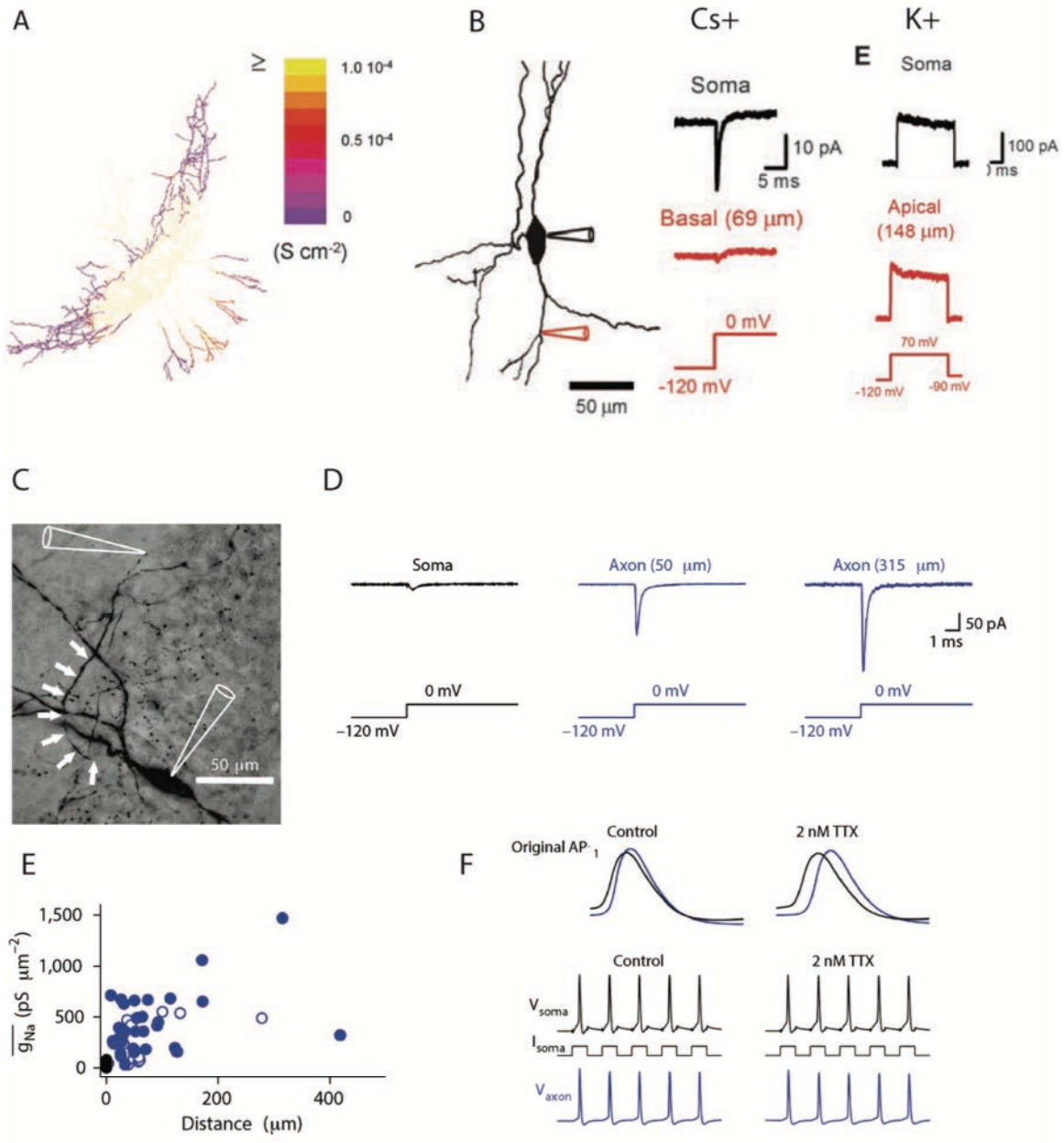

Figure 13: Dendritic K+ channels and axonal Na+ channels contribute to fast-spiking phenotype. **A**. Simulation of channel activation in a basket-cell 2 ms after the onset of a somatic current stimulus triggering an AP. Color code (right) shows density of activated K+ conductance. **B**. Difference between somatic and dendritic Na+ or K+ channel density in the same cell. (Left) Location of somatic and dendritic recording pipette, superimposed with morphological reconstruction of the somatodendritic domain of the BC. Na+ currents (middle) and K+ currents (right) recorded in outside-out patches isolated from these locations by using two patch pipettes pulled from same glass capillary. Na+ and K+ currents were recorded with Cs+

and K+ internal solution respectively. From Hu et al., (2010). **C**. Biocytin filled cell during recording and labeled with 3,3-diaminobenzidine as chromogen. White arrows indicate the axon trajectory. Recording pipettes are illustrated schematically. **D**. Na+ current in an outside-out patch in the soma, proximal axon (50 µm) and distal axon (315 µm from the soma). Na+ currents were evoked by a sequence of a prepulse to −120 mV followed by a test pulse to 0 mV (bottom). Black trace, somatic patch; blue traces, axonal patches. **E**. Summary plot of Na+ conductance density (g_{Na}+) against distance from the soma. Data from 48 axonal recordings and 24 somatic recordings. **F**. Top, simultaneous axon-soma recordings in control conditions, in the presence of 2 nM TTX. Traces are displayed at absolute voltage scale. Bottom, Effects of 2 nM TTX on reliability of AP propagation during a high-frequency train (five stimuli at 100 Hz; 5 ms, 0.7 nA). From Hu and Jonas. (2014).

In hippocampal SOM O-LM cells, voltage-gated Na+ channels in dendrites can initiate and mediate active propagation of action potential along the somato-dendritic tree with a constant amplitude, high velocity and reliability (Martina et al., 2000). Intrinsic currents also influence the BS or LTS behavior of some INs. In three subsets of SOM containing interneurons, Ma et al., (2006) detailed how the hyperpolarization-activated cationic current Ih influenced the electrophysiological properties, the sag and rebound burst. Taken together, the presence of specific sets of voltage-gated ion channels may have electrophysiological implications and correlate with firing patterns of interneuron types. The Petilla Interneuron Nomenclature Group distinguished firing patterns depending on firing rate (fast or, non-fast spiking), regularity (facilitating, regular, and accelerating) and bursting activity (**Fig. 14**; Ascoli et al., 2008). In my work, I used this classification of spiking patterns for presubicular interneuron types.

3.2 Other characteristics of interneuron populations

3.2.1. Interneuron input connectivity

Interneurons receive inputs from several intrinsic and extrinsic sources. In hippocampus, the relation between interneuron type and its input connectivity has been studied in some detail. Gulyas et al., 1999 quantified differences in dendritic morphology and in the density and distribution of afferent synapses onto PV, CR and CB expressing interneurons in CA1: a) PV cells received much more excitatory inputs and b) low proportion of inhibitory synapses com-pared to CR and CB INs, c) the pattern of excitatory innervation also varied among the three cell types : CB INs are activated in a feed-forward (FF) manner by Schaffer collateral afferents whereas PV and CR INs receive additional FF inputs from the EC and local feedback from recurrent collaterals.

More generally, Klausberger and Somogyi, (2008) have distinguished at least 21 types of interneurons in the hippocampal CA1 area (**Fig. 15**), by combining interneuron connectivity data with neurochemical, electrical and morphological interneuron characteristics. In neocortex, the inputs to interneurons and principal cells have recently been studies with optogenetics approaches. PV cells receive lots of direct excitation from long range inputs in contrast to SOM cells; VIP interneurons are well-known for their disinhibitory effect (Cruikshank et al., 2007, 2010; Gonchar and Burkhalter, 2003; Yang et al., 2013; Lee et al., 2013; Karnani et al., 2014).

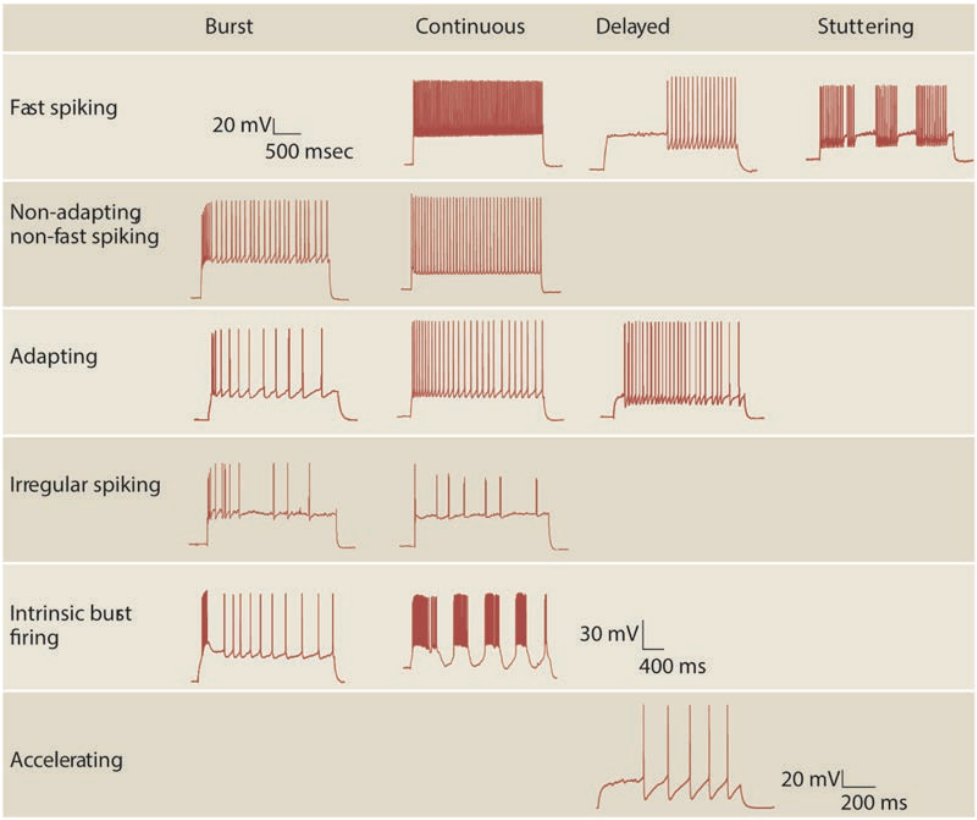

Figure 14: Petilla terminology: types of firing patterns. Cortical GABAergic INs display a vast repertoire of discharge responses. These samples are representative of the most common responses to standardized intrasomatic step-current injections in the rat neocortex. The features of firing patterns in response to step-onset, organized in columns, include bursts, delays and continuous firing, which is neither burst nor delayed. Steady- state patterns, displayed in rows, can be fast spiking, non-adapting non-fast spiking, adapting, irregular spiking, intrinsic burst firing or accelerating. Fast spiking neurons can also display a stuttering or 'Morse-code-like' discharge that is characterized by high-frequency spike clusters that are intermingled with unpredictable periods of silence for a wide range of long, sustained, somatic-current injections. Blank areas of the table and boxes containing only scale bars correspond to firing patterns that have not yet been characterized in neocortical INs. The scale bar at the top left refers to the traces in the first four rows; the scale bars in the fifth and sixth rows refers to the traces in the fifth and sixth rows, respectively. From Ascoli et al. (2008).

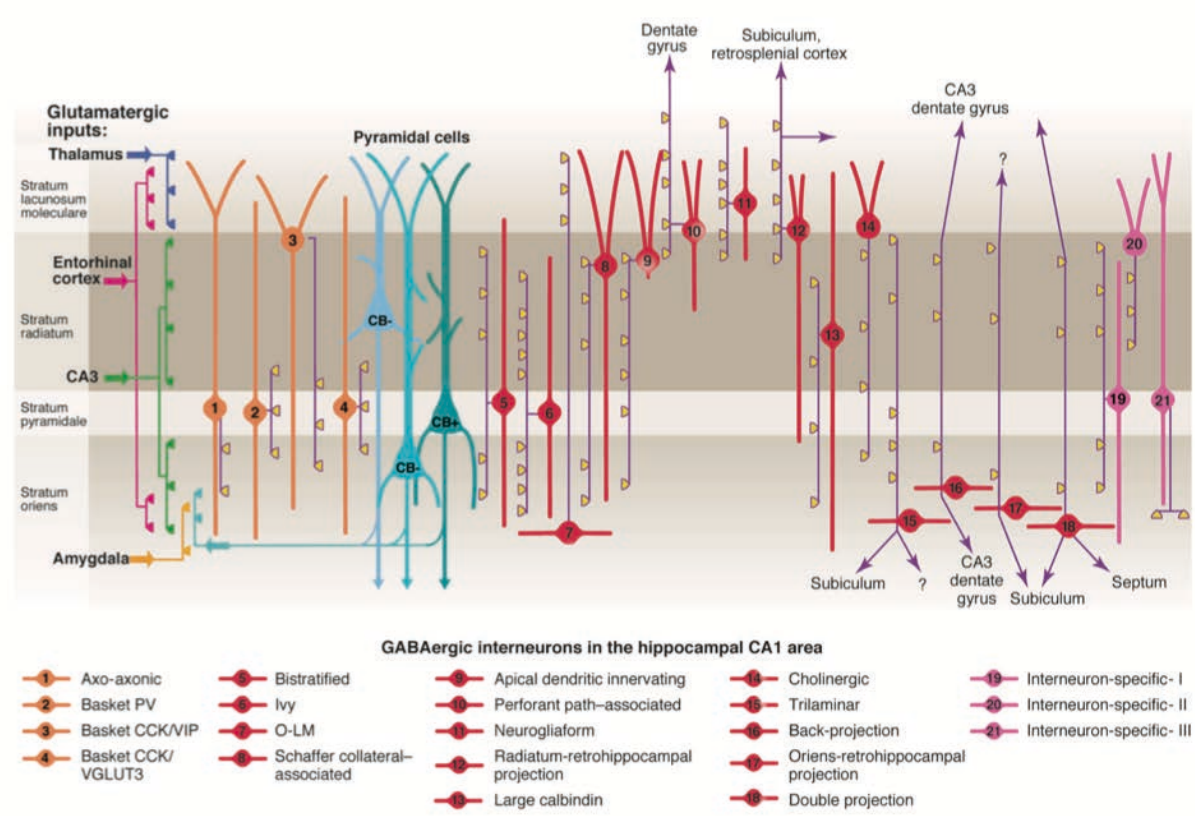

Figure 15: Three types of pyramidal cell are accompanied by at least 21 classes of interneuron in the hippocampal CA1 area. The main termination of five glutamatergic inputs are indicated on the left. The somata and dendrites of interneurons innervating pyramidal cells (blue) are orange, and those innervating mainly other interneurons are pink. Axons are purple; the main synaptic terminations are yellow. Note the association of the output synapses of different interneuron types with the perisomatic region (left) and either the Schaffer collateral/commissural or the entorhinal pathway termination zones (right), respectively. VIP, vasoactive intestinal polypeptide; VGLUT, vesicular glutamate transporter; O-LM, oriens lacunosum moleculare. From Klausberger and Somogyi. (2008).

3.2.2. Synaptic excitation of interneurons

Interneurons express different types of ionotropic glutamate receptors (Dingledine et al., 1999), which can be related to specific afferent pathways (Tóth and Mcbain, 1998). At excitatory synapses on interneurons, the AMPA-receptor-mediated excitatory postsynaptic current (EPSC) rises and decays rapidly, and so ensures fast and reliable activation of inhibitory cells. Glutamate released at excitatory synapses on interneurons may also co-activate kainate receptors and NMDA receptors. Both types of receptors activate and deactivate more slowly than AMPA receptors: kainate receptors are gated on a timescale of tens of milliseconds whereas NMDA receptors operate on a timescale of hundreds of milliseconds. Interneuron types with

"fast" or "slow" EPSP kinetics affect spike timing and synaptic integration differently (Maccaferri and Dingledine, 2002).

Interneurons also express a wide repertoire of other receptors, such as noradrenaline, muscarine, serotonin, mGluRs (Parra et al., 1998) and GABAb receptors (Mott et al., 1999) that excite or inhibit them. Receptor expression might differ among interneuron subtypes and plays a crucial role in setting their excitability and integrative properties.

The dynamic properties of excitatory glutamatergic synaptic transmission also differ for different interneurons. Neocortical SOM-positive cells (Reyes et al., 1998, Beierlein et al., 2003) receive facilitating EPSPs as do hippocampal O-LM cells (Lozonscy et al., 2002). Excitatory connections in most other interneurons comprising the PV+ fast-spiking INs result in depression of synaptic transmission during a train (Ali et al., 1998; Beierlein et al., 2003). This type of activity-dependent short-term plasticity is cell-type specific. Some heterogeneity has also been observed for given morphological types of interneuron in O-LM cells (Lozonscy et al., 2002) and bitufted SOM (Zilberter et al., 1999) rat neocortical neurons which display depressing synapses. Functionally, PV and SOM cells play complementary roles in the regulation of cortical network excitability. They are sequentially recruited to produce a shift of recurrent inhibition along the somato-dendritic axis (Pouille and Scanziani, 2004). PV interneurons are recruited transiently at the onset of a spike train, they mediate fast, strong and rapidly decreasing inhibition. SOM interneurons are recruited later, and thus mediate a slow and increasing inhibition, if PN activity is sustained.

3.2.3. Interneuron outputs

The dynamics of GABA release at interneuron-pyramidal cell connections can be either facilitating, depressing or a combination of both. The synaptic phenotype depends on the interneuron type, but also on the identity of the postsynaptic cell (Gupta et al., 2000). GABAergic neurotransmission is usually inhibitory, mostly via hyperpolarization, sometimes it is also shunting (Vida et al., 2006). Depending on the cellular and network properties, the GABAergic transmission can also be depolarizing (Szabadics et al., 2006; Sauer et al., 2012).

At the microcircuit level, GABAergic inhibition can either form a "blanket of inhibition" characterized by an unspecific and homogenous matrix covering PCs (Karnani et al., 2014; Packer and Yuste, 2011; Fino and Yuste, 2011) or can selectively innervate specific excitato-

ry neurons depending on their laminar location or cortical projection (Otsuka and Kawaguchi, 2009; Lee et al., 2014; Krook-Magnuson et al., 2012; Jiang et al., 2015). The computational roles of interneurons will be discussed in more detail in section 4.

The impact of interneuron activity can also extend beyond local circuit regulation and project to distant brain regions. Several long-range GABAergic neurons that project within the PHF-HF and neocortical areas have been described (Vida et al., 1998; Klausberger et al., 2005; Jinno et al., 2007; Miyashita and Rockland, 2007; Melzer et al., 2012). To date our classification schemes do not include molecular markers and morphological parameters that would allow to identify these long-range GABA neurons. Functional implications of these interneurons will be examined in section 4.

3.3. Toward a classification of interneuron diversity

Ramon y Cajal used only the Golgi impregnation to achieve the classification of neurons based on their anatomy. Nowadays, interneuron taxonomy includes physiological and molecular properties as well as their connectivity. However, interneurons still have defied a generalized classification system. The first aim of my thesis work consisted in describing the morphological and physiological properties of PV and SOM interneurons (Nassar et al., 2015) using unsupervised clustering in mouse presubiculum. This study was facilitated by the availability of mouse lines expressing dtTomato (PvalbCre*::*dtTomato, SSTCre*::*dtTomato) and GFP (X98 GFP) allowing specific labelling of PV and SOM expressing interneurons.

Several recent studies have relied on multidimensional mathematical cluster analysis, to compare multiple sets of parameters to achieve interneuron classification. Multidimensional analysis often reveals a high degree of individual variability and the biological usefulness of such classifications largely depends on the appropriate choice of parameters. Cluster analysis can be performed either on electrophysiological properties comparing multiple parameters such as passive, active or action properties (Ma et al., 2006; Helm et al., 2013) or may also include morphological parameters (McGarry et al., 2010; Dumitriu et al., 2007). Ma et al., (2006) studied a group of somatostatin (SOM)-expressing interneurons in mouse somatosensory cortex and two separate groups emerged: stuttering cells, which project mainly to layer 4 and low threshold bursting MCs. Dumitriu et al., (2007) have determined the synaptic properties of mouse visual cortical neurons, which express the green fluorescent pro-

tein in PV, SOM and NPY immuno-positive neurons and found that these 3 groups of interneurons are distinguished from each other in dendritic and axonal morphologies and also differ in the frequencies, am-plitude, and kinetics of the spontaneous excitatory and inhibitory synaptic currents they receive. Other studies have combined whole-cell current clamp-recordings, single cell reverse transcription (scRT-PCR) and biocytin labeling to define distinct subclasses of NPY in rat barrel cortex (Karagiannis et al., 2009) or GABAergic neurons in layer VI of mouse barrel cortex (Perrenoud et al., 2013). More recently, Hosp et al., (2014) revealed five classes of interneurons in the dentate gyrus using cluster analysis based on morphology and physiologi-cal properties of INs.

Whether interneurons truly divide into discrete classes, or whether they form a continuum has long been a matter of debate. Some archetypes of interneurons can clearly be identified, and « atypical » interneurons at the edge between archetypes might exist as well (Battaglia et al., 2013). Within a specialized cortical area, neurons with different functions may also be organized in a laminar or graded fashion (Otsuka and Kawaguchi. 2009; Lee et al., 2014; Beed et al., 2013).

In fine, interneurons will need to be defined functionally. We need to keep in mind that interneurons may switch roles in the network according to brain states (Klausberger et al., 2003, 2008). It appears from recent in vivo work, that interneurons can also be recruited at specific behavioral events (Hangya et al., 2014). For a deeper understanding of the function of interneurons in a microcircuit, one must identify the anatomy, physiology and molecular markers, but also the local and long-range connectivity and synaptic integration in relation to specific brain areas. In the future, we need to aim at dissecting connectivity and network motifs, and directly address the role of interneurons for flow-control and network coordination.

4-How inhibition shapes cortical information processing: functional importance of PV and SOM interneurons

Understanding the interactions between excitation and inhibition, as two indivisible components of a circuit is essential for elucidating the mechanisms of cortical function (Isaacson and Scanziani, 2011). Cortical information processing relies on the coordinated activity of interconnected neurons. When coupled to the excitatory neurons and depending on its location (somatic or dendritic) and timing of its action, inhibition counters excitation, modulates the gain, timing, tuning, bursting properties of pyramidal cell firing, and exerts selective filtering of synaptic excitation (Miles et al., 1996; Pouille and Scanziani, 2004; Isaacson and Scanziani, 2011; Atallah et al., 2012; Gentet et al., 2012; Lee et al., 2012; Royer et al., 2012; Wilson et al., 2012). Concomitant occurrence of excitation and inhibition happens during spontaneous cortical oscillations (Klausberger and Somogyi, 2008; Atallah and Scanziani, 2009) or "up and down states" (Haider et al., 2006; Neske et al., 2015) as well as following a simple sensory stimulus, like a whisker deflection (Okun and Lampl, 2008; Swadlow, 2002; Wilent and Contreras, 2005) or an oriented bar in the visual field (Anderson et al., 2000; Monier et al., 2003). During these local and external perturbations, excitation and inhibition fluctuate together: the ratio between excitation and inhibition is initially tilted toward excitation, and then shifts toward inhibition. This phenomenon is a necessary transient imbalance for sending messages and modifying network connections.

New tools help to dissect the role of interneurons in cortical processing (cf. section 5). Genetically distinct interneuron types can now be targeted and their activity can be observed and manipulated. Optogenetic tagging and awake juxta/intracellular recording techniques have led to a better understanding of how interneurons coordinate networks and relate to behavioral functions (Hangya et al., 2014).

In this section, I will summarize current views of how inhibition regulates the function of cortical neurons in behaving rodents. Specifically, I will focus on the contributions of PV+ and SOM+ interneurons in the hippocampal-entorhinal circuit and neocortex during network oscillations, spatial navigation and behavioral tasks.

4.1 Building blocks of the inhibitory circuit

Inhibition onto a single principal neuron or an assembly of excitatory neurons can be made in canonical arrangements by feed-forward and feedback inhibition (Buzsáki, 1984; Sheperd, 2004). Disinhibition occurs when GABAergic neurons target other GABAergic neurons (Acsády et al., 1996).

Excitatory inputs arising from cortical and subcortical regions can diverge onto both principal cells and interneurons, giving rise to feed-forward inhibition (**Fig. 16A**). Feed-forward inhibition can arrive in time before the principal cell's membrane can be charged to threshold and prevent the occurrence of action potentials, or it can prevent at least the occurrence of multiple spikes (Buzsáki, 1984) by competing with dendritic excitation or reducing output spiking (Cruikshank et al., 2007; Gabernet et al., 2005). This form of inhibition involves an inhibitory shaping of excitatory events. If the principal cell does emit an action potential, there is only a short time window within which this is possible, giving rise to very high temporal precision of evoked spiking (Pouille and Scanziani, 2001). This circuit motif dominates the signal transmission in barrel cortex for example (cf. section 4.4) and could be important in presubicular head direction coding during fast head turns (Nassar et al., in prep.).

Feedback inhibitory motifs can be divided into recurrent (**Fig. 16B**) and lateral inhibition (**Fig. 16C**). Recurrent inhibition involves a loop in which afferent glutamatergic axons activate principal cells first; then, through their axon collaterals, principal cells activate, in turn, interneurons that feedback inhibition to the neurons that brought about its excitation (Silberberg and Markram, 2007). Lateral inhibition affects the proportion of principal cells that do not provide excitation to interneurons but receive inhibition from a given interneuron (Kapfer et al., 2007; Silberberg and Markram, 2007; Berger et al., 2009). This circuit motif is used for surround inhibition in visual cortex (cf. section 4.3) and it could be important for maintained head directional signaling during immobility or slow head turns (Simonnet et al., under review).

A form of «direct» inhibition provided by GABAergic afferents from a distant area to a local microcircuit can also exist (**Fig. 16D**; Freund and Antal, 1988; Tóth et al., 1993; Jinno et al., 2007; Melzer et al., 2012). Such long range GABA connections may be important for synchronizations and network oscillations across the brain (cf. section 4.2.1). My initial results

suggest the existence of long range GABAergic connection between PrS and thalamus (cf. results), where they might contribute to the coherence of the head direction signal.

GABAergic interneurons also make inhibitory, often reciprocal, contacts onto each other (Gibson et al., 1999; Galarreta and Hestrin, 2002; Chamberland et al., 2010; Pfeffer et al., 2013; Xu et al., 2013). Interneurons that target only other interneurons are called interneuron specific interneurons (Gulyas et al., 1996; Hájos et al., 1996). They may express the calcium-binding protein calretinin (CR), the vasoactive intestinal peptide (VIP), or a combination of both. Their interactions can induce network synchrony (Cobb et al., 1995; Hu et al., 2011) and mediate disinhibition of principal cells (Xu et al., 2013) (**Fig. 16E**). My work has revealed some reciprocal connections between SOM and PV cells in presubiculum, and their functional importance remains to be explored.

Finally, PV, SOM and VIP interneurons accomplish within-population co-activity by means of conserved network mechanisms that receive each distinct subset of local excitatory inputs, as if they are specialized to operate as groups (Karnani et al., 2016b). Such various units of function may be beneficial to circuit operation by amplifying a type of inhibition (dendrite targeting, perisomatic, or disinhibitory) provided by the population and may interact together to deliver widespread and increased inhibition when excitation is about to overwhelm the circuit.

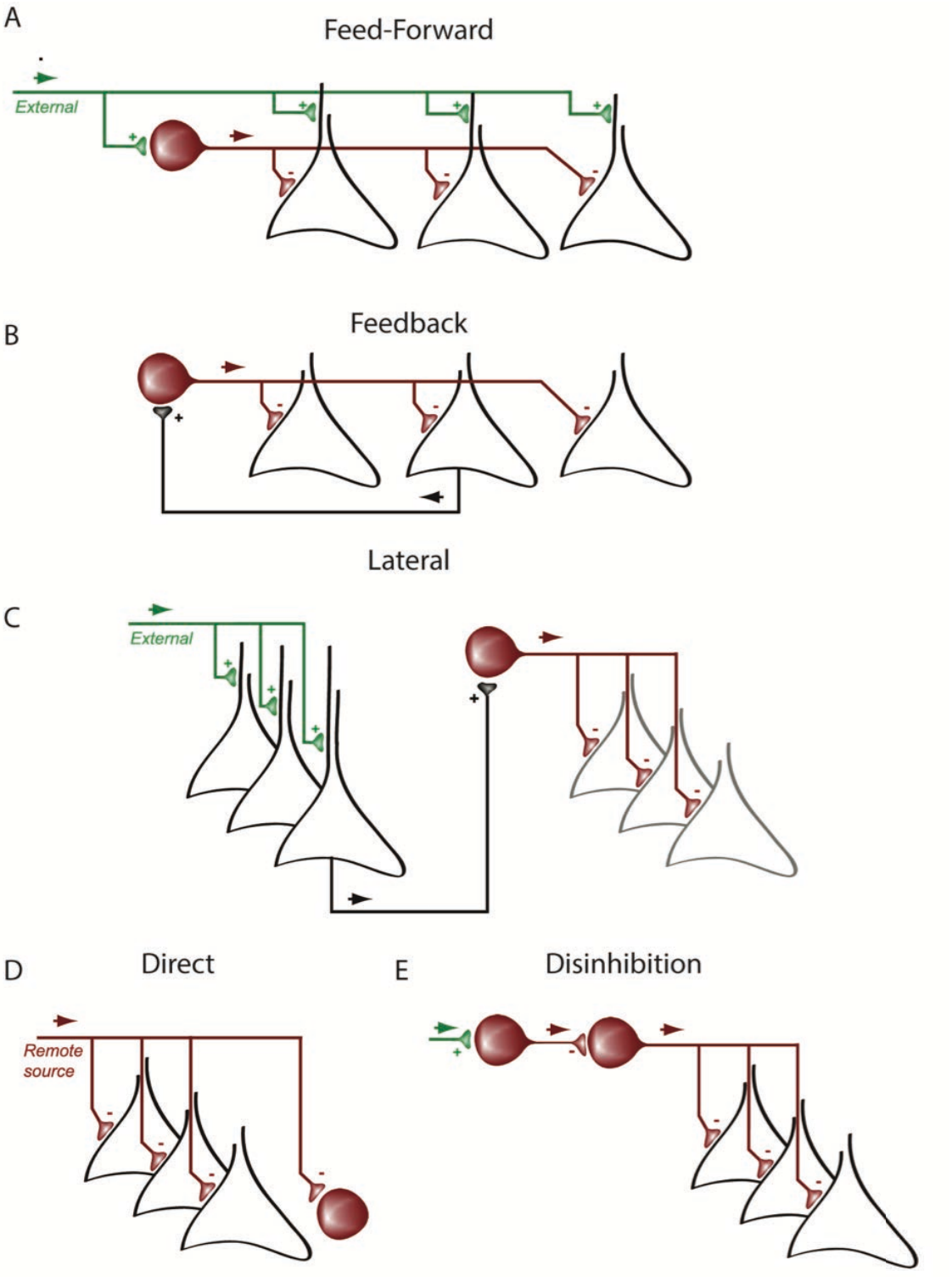

Figure 16: Main forms of inhibitory motifs. **A**. Feed-forward inhibition **B**. Feed-back inhibition. **C**. Lateral inhibition. **D**. Lateral inhibition. **E**. Disinhibition. Interneurons in red, afferent excitatory inputs from an external source in green and local principal neurons in black. From Roux and Buzsáki. (2015).

4.2 The hippocampal-entorhinal circuit

4.2.1 Behavioral states and oscillations

Network oscillations are crucial for synchronizing the activity of populations of neurons at different frequency that vary from slow oscillations in the delta (0.5–3 Hz) and theta (3–8 Hz) ranges to fast oscillations in the gamma (30–90 Hz) and ultrafast (90–200 Hz) ranges (Buzsáki and Draguhn, 2004). Gamma rhythms and theta rhythms occur throughout the neocortex and archicortex and can coexist or occur separately in the hippocampal-parahippocampal formation (Chroback and Buzsáki, 1998). Rhythmic oscillations vary as a function of brain state and behavior (Buzsáki and Draguhn, 2004) and local as well as long-distance GABAergic interneurons play a key role in coordinating such network activities.

The generation of gamma rhythms in the hippocampus depends on synaptic GABAergic inhibition. A gamma generator has been identified in dentate gyrus where dentate gyrus PV-positive BCs are connected in a tight network that is sufficient for generating oscillations in the gamma range (Bartos et al., 2001, 2002); and another in the CA3-CA1 regions where it initially emerges in the CA3 recurrent system which entrains the CA1 region via its interneurons (**Fig. 17C**; Csicsvari et al., 2003). Particularly, the FS-PV basket cells are essential for the generation of gamma oscillations both in vivo and in vitro in the CA3 region (**Fig. 17A-B**; Bragin et al., 1995; Hájos and Paulsen, 2009). Their firing activity is synchronized primarily by recurrent excitation derived from the local CA3 collaterals of pyramidal cells (Mann et al., 2005) and then by reciprocal interactions between each other (Galarreta and Hestrin, 2002). Inhibition at synapses between basket cells is fast, strong and shunting: network activity might induce intracellular accumulation of chloride which may result in a shift of the synaptic reversal potential in the depolarizing direction (Vida et al., 2006). Shunting inhibition might confer robustness to gamma oscillations in hippocampal interneuron networks leading to homogenizing firing rates by accelerating weakly activated interneurons and decelerating the strongly activated ones (Vida et al., 2006). Selective reduction of phasic excitation, but not inhibition, on fast-spiking basket and axo-axonic cells disrupts gamma oscillations (**Fig. 17D**; Fuchs et al., 2007; Wulff et al., 2009). When perisomatic inhibitory cells discharge synchronously, pyramidal cell activity is temporarily suppressed by strong synaptic inhibition; after the effect of inhibition disappears, the population discharge of pyramidal cells would again take place, and a new gamma cycle is initiated (Bartos et al., 2007). Thus, such oscillations

impose a periodic fluctuation of the membrane potential of PNs close but below the threshold ensuring a precise spike timing of the neurons.

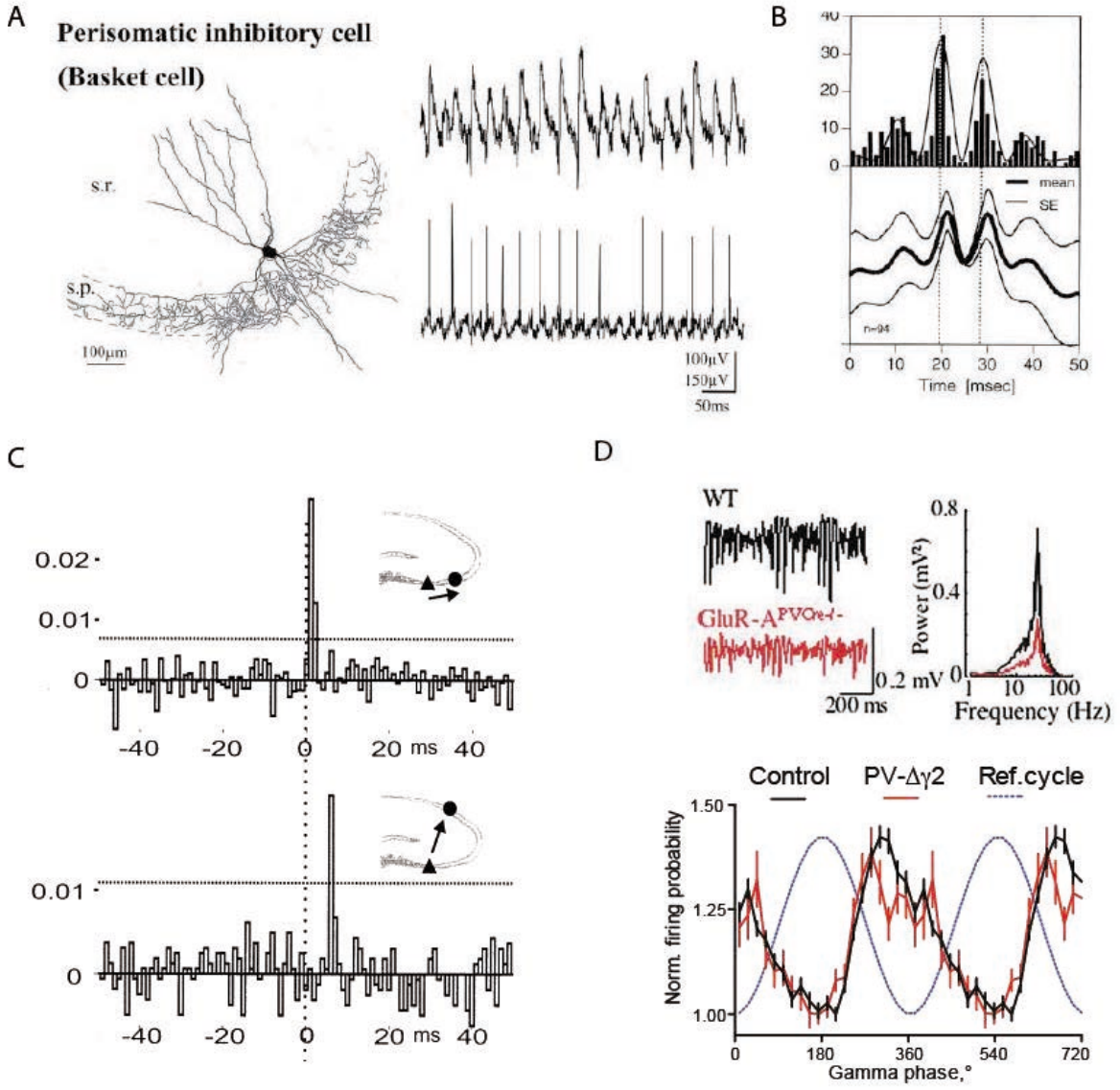

Figure 17: Role of PV INs in hippocampal gamma rhythms. **A**. Field potential (right, top) and cell-attached recording (right, bottom) from a multipolar basket cell (left) in stratum lucidum in CA3 region, adapted from Hájos et al. (2004). **B**. Spike timing histogramm (top) and averaged wide field activity of a putative hippocampal fast-spiking basket cell in the dentate gyrus in the behaving rat. The interneuron is phase-locked to the gamma oscillations and fires during the ascending phase (dotted lines), adapted from Bragin et al. (1995). **C**. Monosynaptic activation of a CA3 interneuron (top) or CA1 interneuron (bottom) by CA3 pyramidal cells. Cross-correlograms between the pyramidal neurons and interneurons recorded by two nearby tetrodes, adapted from Csicsvari et al. (2003). **D**. Top, example traces show 1 s of stratum radiatum field gamma oscillations in the presence of 200nM kainate. Graph shows pooled power spectra (n = 5, 60 s data epochs) for gamma rhythms induced by 200nM kainate in slices from control (black) and GluRA$^{PVCre-/-}$ (red) mice. Adapted from Fuchs et al. 2007. Bottom, preserved gamma oscillations in PV-Δγ2 mice. Rhythmic modulation of pyramidal cell discharge during theta-associated gamma oscillation. Adapted from Wulff et al. (2009).

During exploratory behavior, theta activity is the characteristic network pattern of the hippocampus (Wilson et al., 1993). Changes in firing rate and theta phase tend to occur when the animal crosses the place fields: as an animal moves from the periphery toward the center of a place field, the action potentials in pyramidal neurons shift to earlier phases of the theta cycle (O'Keefe and Recce, 1993). Using a combination of juxtacellular labeling and recordings from head-fixed animal running or not on a spherical treadmill, Varga et al., (2012) show a stereotypical temporal coding in which PV derived perisomatic inhibition is followed by O-LM cell-targeting distal dendritic inhibition during different network oscillations including theta in CA1: inhibition shifted from axon initial segment to soma, onto proximal dendrites (bistratified SOM) and finally distal dendrites (O-LM SOM) of pyramidal neurons in CA1 during each cycle of the theta oscillations (**Fig. 18A**; Katona et al., 2014; Lapray et al., 2012; Varga et al., 2012). Experiments performed in head-fixed awake mice engaged in a navigation task using silicon probe recordings combined with optogenetic silencing of either perisomatic PV or dendrite-targeting SOM INs showed an increase in the rate firing at the beginning and the end of the CA1 place field respectively; PV and SOM interneurons preferentially regulate spike timing and spike bursts of place cells, respectively (Royer et al., 2012). Recently, in an intact hippocampus preparation that robustly and spontaneously expresses theta rhythms (Goutagny et al., 2009), Amilhon et al., (2015) optogenetically silenced PV interneurons in the hippocampal preparation, and found that both the frequency and power of the ongoing theta oscillations were diminished; whereas the optogenetic silencing of SOM interneurons had limited effect on intrinsically generated theta oscillations but rather weakly modulate EC inputs (**Fig. 18B**).

4.2.2 Long-range GABAergic neurons

The hippocampal-entorhinal circuit activity is under the control of the medial septum (MS). It has reciprocal connections with the hippocampus (Tóth et al., 1993) and plays a pivotal role in the generation of theta oscillations (Vertes and Kocsis, 1997). The septo-hippocampal pathway is formed by cholinergic (Frotscher and Léránth, 1985) and parvalbumin-immunoreactive (PV) GABAergic neurons of the medial septum (Freund, 1989), and the latter are known to selectively innervate GABAergic interneurons in the hippocampus (Freund and Antal, 1988). As a result, activation of septal GABAergic afferents produces a silencing of interneurons and is associated with disinhibition of pyramidal cells (**Fig. 19A-B-C**; Tóth et al., 1997). Particularly, MS inhibitory input is able to provide large-amplitude sustained perisomatic inhibition to O–LMs (**Fig. 19D-E**; Chamberland et al., 2010), and therefore, is

ideally suited for suppressing O–LM activity at the positive peak of the theta wave (Borhegyi et al., 2004).

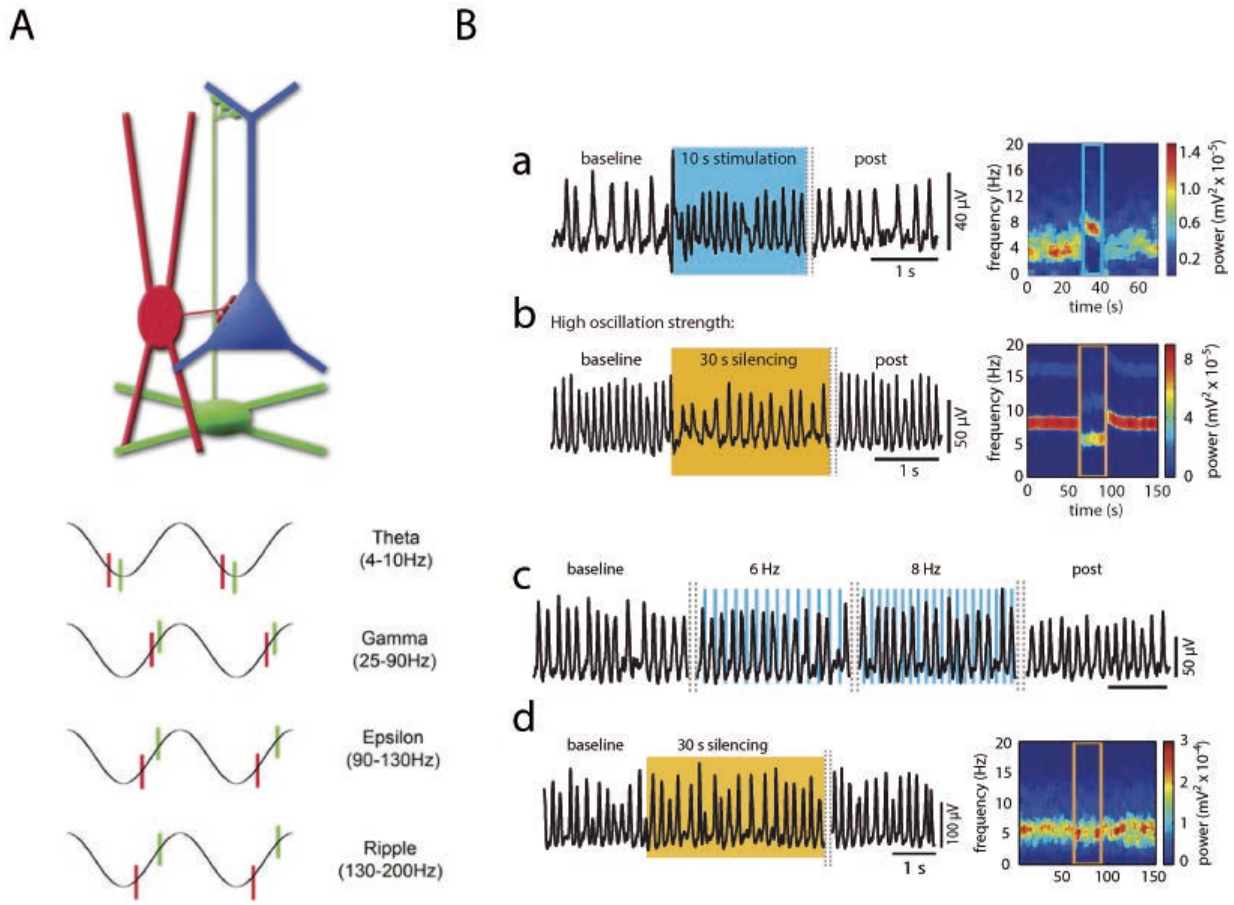

Figure 18: Implications of PV and SOM INs in theta rhythms. **A.** Top, schematic of the oscillation GABAergic inputs to the perisomatic region and distal apical dendrites of CA1 pyramidal cells delivered by PV BCs and OLM cells. Bottom, preferential phase locking of PV BCs (red) and O-LM cells (green) to theta, gamma, epsilon, and ripple oscillations. Adapted from Varga et al. (2012). **B**. (**a**) Tonic activation of PV interneurons triggers theta, and (**b**) tonic silencing disrupts the endogenous rhythm. (**c**, **d**) SOM Interneurons weakly participate in in-trinsic theta modulation. Adapted from Amilhon et al. (2015).

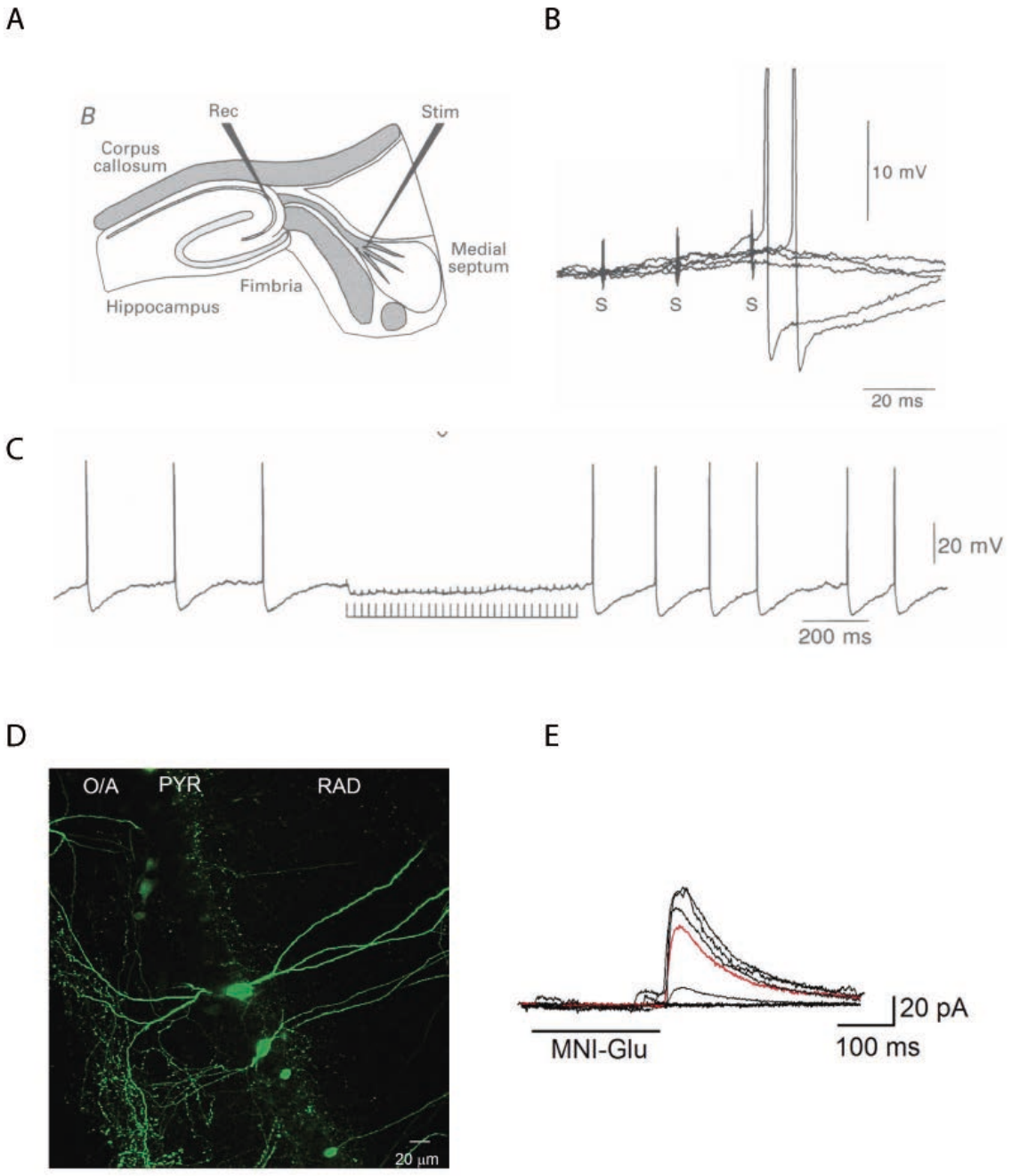

Figure 19: The septo-hippocampal pathway: evidence for long range GABA INs. **A**. Schematic of the septal nuclei and the hippocampus in a combined slice. **B**. At resting membrane potential, septal stimulation (3 shocks at 20ms intervals) induce firing of the CA3 pyramidal cell. Firing latencies varied between 20 and 80 ms after the first septal shock. **C**. Repetitive stimulation of septo-hippocampal fibers at 20 Hz suppressed spontaneous firing of the inhibitory cell. Adapted from Tóth et al. (1997). **D**. Two-photon z-stack acquired in the CA1 region of the hippocampus of a VIP-eGFP mouse, showing bipolarly oriented VIP-positive INs with a cell body inside the stratum pyramidale (PYR) and at the border between the PYR and the stratum radiatum (RAD). **E**. IPSCs evoked in O-LM IN by photostimulation of the VIP-positive cell with glutamate uncaging. Adapted from Chamberland et al. (2010).

The MS also projects to the MEC (Mitchell et al., 1982). Intraseptal lesions or inactivation in rats abolished theta oscillations and grid-like firing patterns in MEC (Brandon et al., 2011; Koenig et al., 2011). Similarly to the hippocampus, the septo-entorhinal pathway also involves long-range GABAergic projections: optogenetic activation of MS axons induced monosynaptic GABAergic responses in both FS and LTS interneurons in all layers of the MEC. No connections were found onto layer 2 stellate cells (**Fig. 20A-B**; Gonzalez-Sulser et al., 2014; Rowland et al., 2013). Medial septal projections target different interneuron types: septal PV cells inhibit preferentially FS neurons in the MEC, while septal CB neurons inhibit LTS neurons (**Fig. 20C-D-E-F**; Fuchs et al., 2016).

A bidirectional GABAergic connection between the MEC and the hippocampus has been identified (Germroth et al., 1989; Melzer et al., 2012). In particular, a combination of electrophysiological, neuronal tracing and optogenetic approaches revealed that a MEC GABAergic projection originating primarily from PV cells can preferentially target interneurons located in the O-LM (Melzer et al., 2012). In turn, long-range projecting hippocampal SOM interneurons target superficial layers in the MEC (Melzer et al., 2012). These long-range projecting GABAergic neurons in the hippocampal-entorhinal formation are likely well suited to precisely coordinate theta activity between the hippocampus and the entorhinal cortex (Mizuseki et al., 2009; Melzer et al., 2012).

4.2.3 Importance of interneurons in grid cell activity

Stellate cells and pyramidal cells are the principal neurons in layer 2 MEC (Gatome et al., 2010; Ray et al., 2014). More than 50 % of recorded layer 2 neurons are considered grid cells (Boccara et al., 2010) and show strong theta modulation with spatially modulated responses (Burgalossi et al., 2011). They are, thus, potential candidate of grid cell activity in MEC layer 2 even though, a recent study using Ca^{2+} imaging in freely moving mice showed that grid cell responses appeared in both stellate cells and pyramidal cells in similar proportions (Sun et al., 2015). Compared to deep layers in which excitatory cells directly communicate with high probability with one another (Dhillon and Jones, 2000), multiple simultaneous whole-cell recordings from stellate cells failed to detect any direct excitatory connections, while stimulation of interneurons reliably evoked monosynaptic inhibitory postsynaptic responses in stellate cells (Couey et al., 2013; Pastoll et al., 2013). Stellate cells are indirectly connected mostly through fast-spiking interneurons and thus, are integrated in a predominantly recurrent inhibitory network, driven by synchronous activity of stellate cells (**Fig. 21A**).

Considering the presence of intrinsic subthreshold membrane potential oscillations (Dickson et al., 2000; Yoshida et al., 2011), the Ih currentpresent in stellate cells (Pastoll et al. 2012), and the predominance of inhibitory network interactions within layer 2 of the MEC (Couey et al., 2013), it was proposed that inhibition enhances the excitation and firing of entorhinal neurons in a timely manner via rebound spikes (**Fig. 21C**; Hasselmo, 2014; Shay et al., 2016) that come at specific phases of oscillation in the membrane potential (Shay et al., 2016; Ferrante et al., 2016; Tsuno et al., 2015). These properties of rebound spikes and oscillations could help MEC cells to code spatial and temporal information allowing for the emergence and modulation of grid cell firing.

Couey et al., (2013) proposed an attractor network model where stable hexagonal grid patterns can emerge from a simple recurrent inhibitory network: inside a cluster (a "patch"; not to be confounded with patches of CB positive pyramidal cells of MEC layer 2; Ray et al., 2014), neurons inhibit each other via their connections with local interneurons and also interneurons from neighboring patches. Only a synaptic excitatory drive is able to overcome this inhibition and make a neuron fire. Neurons between two active patches, in contrast, are highly inhibited by all neurons of surrounding patches, and the external drive is not sufficient to overwhelm the inhibition. In such a connectivity scheme, grid cells connect only onto GABAergic interneurons, which in turn project back only onto grid cells; feedback inhibition likely to be provided by PV INs may serve as a clock signal for the temporal grid cell code. Optical stimulation of MEC layer 2 stellate cells and FS cells at theta frequency produced nested gamma-frequency synaptic activation in stellate cells (**Fig. 21B**; Pastoll et al., 2013). Beed et al., 2013 showed an inhibitory gradient together with a gamma power gradient that decreased along the dorso-ventral axis. Recent work from Buetfering et al., 2014 challenged the attractor network models by showing that PV interneurons do not display grid-like firing patterns but rather integrate inputs from grid cells with various phases and exhibit low sparsity, thus providing phase-dependent recurrent inhibition (**Fig. 21D**; Buetfering et al., 2014) in which PV INs could possibly control the gain of grid-cell output.

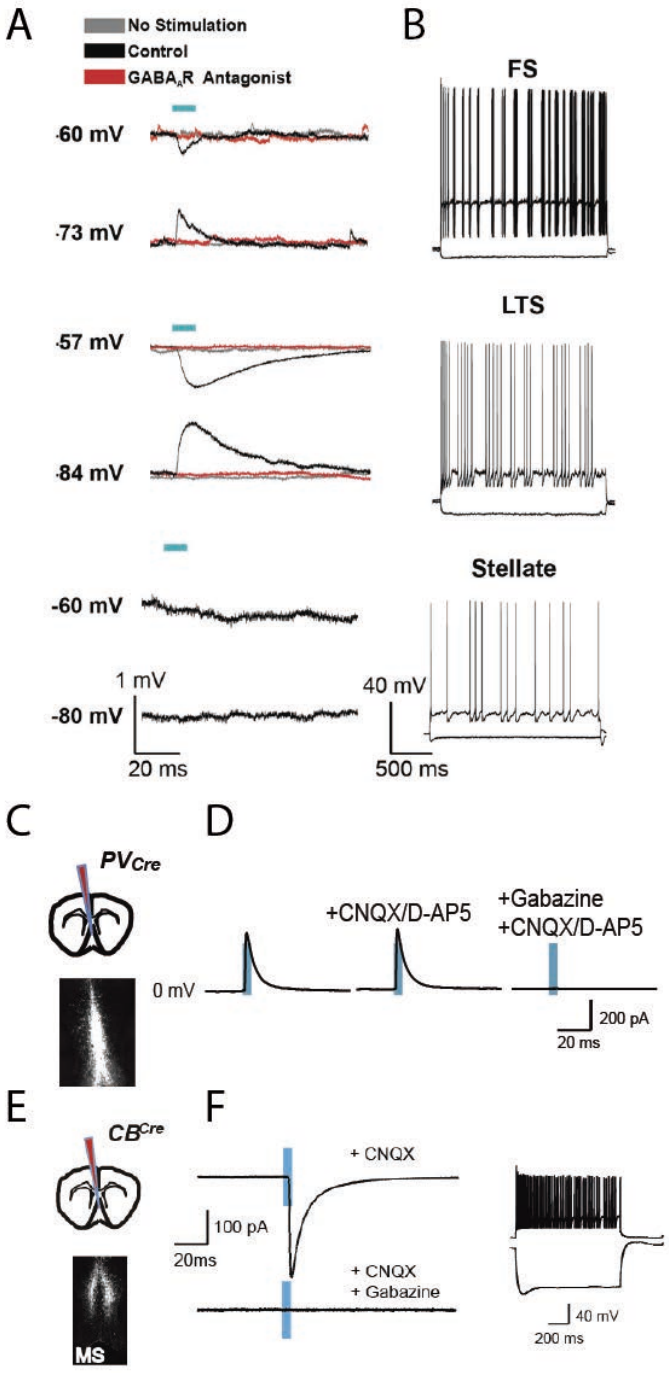

Figure 20: Long-range medial septal interneurons and their synaptic targets in the MEC.
A. Evoked IPSPs following photostimulation (blue bar) of ChR2-positive MS axons recorded at holding potentials on either side of the chloride reversal potential., No stimulation (gray) and $GABA_AR$ (red) blockade traces are also shown. **B**. Responses of fast-spiking (FS) interneurons, low-threshold spiking (LTS) interneurons, and stellate cells (SCs) to hyperpolarizing and depolarizing current injections, adapted from Gonzalez-Sulser et al. (2014). mCherry expression following AAV DIO ChR2-mCherry injection into the MS of a PVCre mouse (**C**) or CBCre mouse (**E**). **D.** Evoked responses of a targeted FS cell in MEC layer 2 at 0 mV in control and in the presence of antagonists after single laser pulses. **F**. Left, evoked IPSCs recorded after 5ms laser pulses (blue bar). Right, firing pattern of the targeted LTS interneuron, adapted from Fuchs et al. (2016).

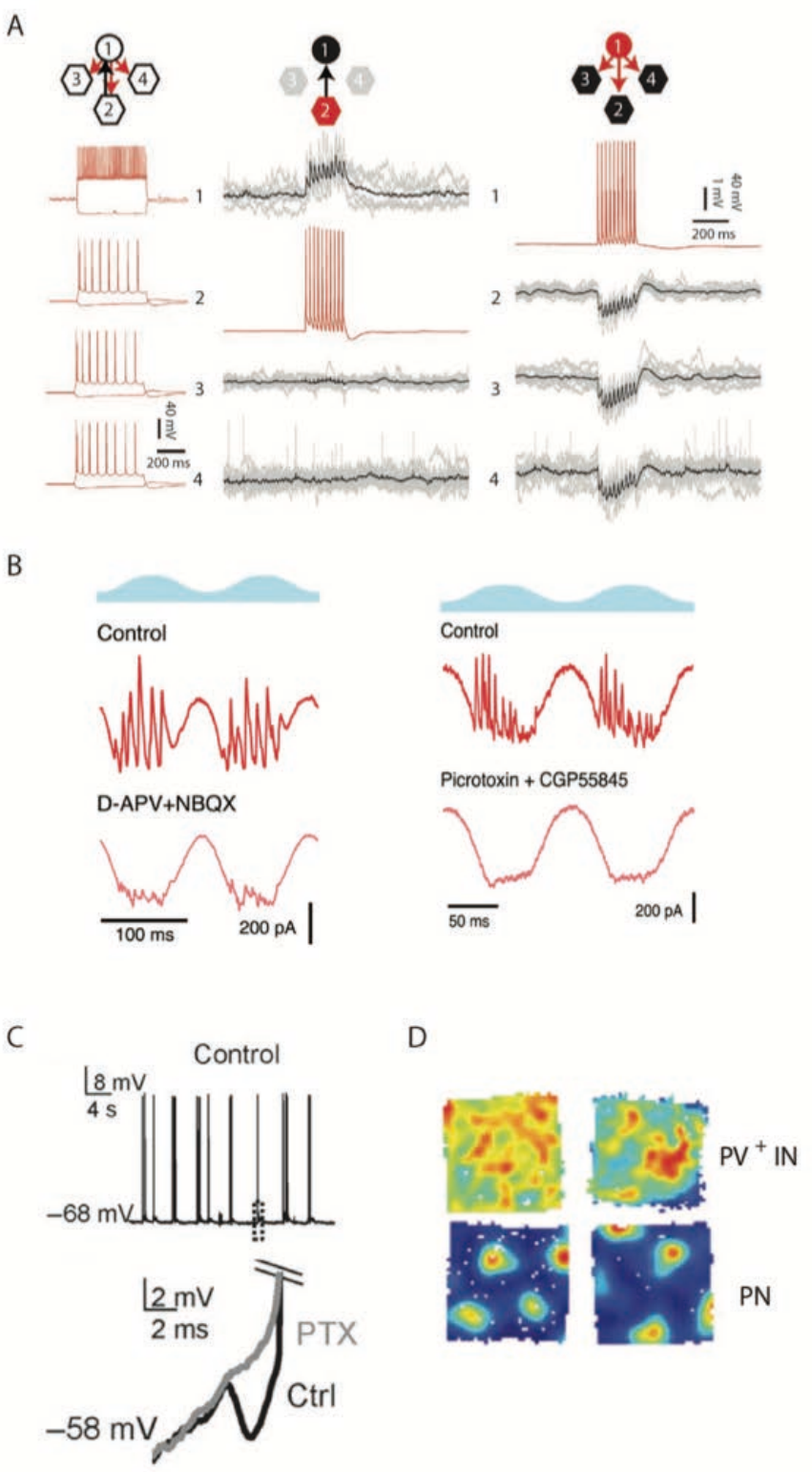

Figure 21: Role of PV interneurons in grid cell activity. **A**. Feedback inhibition in the entorhinal cortex . Simultaneous recording from one fast-spiking (putative PV) interneuron and three layer-two stellate cells. (Left) reciprocally connected cell pair consisting of one fast-spiking interneuron (1) and one stellate cell (2). Middle, action potentials in a stellate cell evoked EPSPs in the putative PV interneuron. Right, Action potentials in the interneuron evoked IPSPs in all three stellate cells. Adapted from Couey et al. (2013). **B**. Nested gamma oscillations require feedback inhibition mediated by inhibitory neurons. Right, local field potentials recorded from a stellate cell before (control) and during blockade of iGluRs (left) or

$GABA_A$ and $GABA_B$ receptors (right). Adapted from Pastoll et al. (2013). **C**. Post-inhibitory rebound spikes. Top, perithreshold voltage traces showing spontaneous action potentials in control condition. Bottom, higher magnification of the spikes from the marked rectangle in control (black) and in the presence of picrotoxin (PTX, grey). Adapted from Ferrante et al. (2016). **D**. Grid cell firing of entorhinal cortex neurons. Putative PV interneurons have broader spatial fields than principal neurons. Adapted from Buetfering et al. (2014).

4.3 Visual processing

What is the role of synaptic inhibition in the tuning of cortical neurons to visual stimuli? How do different interneuron subtypes influence the input-output transformation in pyramidal cells of the primary visual cortex?

Principal neurons in the visual cortex fire selectively in response to visual stimuli that have a particular orientation or direction (Anderson et al., 2000; Monier et al., 2003). Inhibitory neurons may be sensitive to orientation as well. Experiments in visual cortex of anesthetized mice have reported a broad orientation tuning of inhibitory neurons including PV, SOM and VIP interneurons in layers 1 and 2/3 (Kerlin et al., 2010). Some groups have reported tuned firing of SOM interneurons (Ma et al., 2010) or a subset of PV interneurons (Runyan et al., 2010, Runyan and Sur. 2013). Experiments performed on anesthetized mice using optogenetic tools indicated that PV cells strongly modulate layer 2/3 pyramidal cell gain or spiking in responses to visual stimuli while only modestly affecting their tuning properties (Atallah et al., 2012). In contrast, SOM optogenetic activation was shown to induce a sharpening of orientation tuning in pyramidal neurons (Wilson et al., 2012). In awake mice, however, optical activation of PV interneurons in V1 enhances the orientation selectivity of PNs, whereas activation of SOM or VIP interneurons did not (Lee et al., 2012).

Different findings for changes in orientation tuning and gain modulation observed in all these studies could be due to differences in targeting and recording methods, as well as differences in transgenic mouse lines, recording techniques (Liu et al., 2011; Kerlin et al., 2010; Ma et al., 2010, Lee et al., 2012; Cottam et al., 2013), diversity of interneurons within a given subclass (Markram et al., 2004) and local excitatory inputs (Bock et al., 2011; Hofer et al., 2011). If inhibitory neurons receive strong local inputs from nearby cells (Bock et al., 2011; Hofer et al., 2011), this could explain why orientation selectivity of PV neurons is correlated with the orientation distribution of cells in their local neighborhood.

Interneurons in the visual cortex also mediate lateral inhibition. Recordings in awake head-fixed mice found that SOM interneurons in V1 contribute to surround suppression (Adesnik et al., 2012) of PNs firing. Disinhibitory connectivity motifs also exist in primary visual cortex: SOM and PV interneurons make inhibitory connections with each other (Pfeffer et al., 2013; Jiang et al., 2015).

Given the role of PV and SOM interneurons in the visual cortex, we might ask whether similar organizing principals exist for head directional coding in the presubiculum. It will be interesting to test whether 1) the sharpening of head direction tuning could depend on specific interneurons and 2) the existence of a lateral inhibition might suppress neurons that have different directional tuning in the presubicular microcircuit.

4.4 Somato-sensation

Pyramidal neurons in the barrel cortex of rodents respond very precisely to whisker deflections (Okun and Lampl, 2008; Swadlow, 2002). Feedforward inhibition effectively suppresses sustained firing of spiny neurons to input from the thalamus. FFI is mediated by PV interneurons, it sharpens the timing of suprathreshold responses to thalamocortical inputs, and limits the window for integration of excitatory inputs (Wilent and Contreras, 2005; Cruikshank et al., 2007; Gabernet et al., 2005; Higley and Contreras, 2006). FS-PV interneurons of the barrel cortex receive rapid and more powerful thalamic inputs than do spiny cells (Cruikshank et al., 2007; Gabernet et al., 2005). Their feed-forward inhibitory responses onto spiny cells are of large amplitude and most effective for low frequency whisker deflections (Cruikshank et al., 2007; Gabernet et al., 2005). The synaptic responses to repetitive thalamocortical inputs are depressing and transient in PV neurons. On the contrary, responses of GFP-expressing X94 SOM neurons are delayed, strongly facilitating and produce sustained firing in the barrel cortex (Tan et al., 2008). Previous reports have indicated that layer 4 SOM neurons receive very weak thalamic input (Beierlein et al., 2003; Cruikshank et al., 2010) and are likely to mediate disinhibition of layer 4 excitatory neurons by targeting FS interneurons (Xu et al., 2013).

Interestingly, sensory processing and membrane potential dynamics in the barrel cortex differ dramatically between quiet and active behavioral states (Crochet and Petersen, 2006). Interneurons are much more active than excitatory neurons during different brain states (**Fig. 22A**; Gentet et al., 2010). Experiments conducted in layer 2/3 demonstrated that fast-spiking GA-

BAergic neurons (putative PV) dominate during quiet wakefulness, while during active wakefulness non-fast-spiking GABAergic neurons depolarize and fire action potentials at increased rates (**Fig. 22A**; Gentet et al., 2010). However, SOM interneurons were hyperpolarized during whisker deflections. Optogenetic suppression of SOM interneurons during quiet wakefulness caused burst spiking in PCs resembling their activity during active whisking (Gentet et al., 2012).

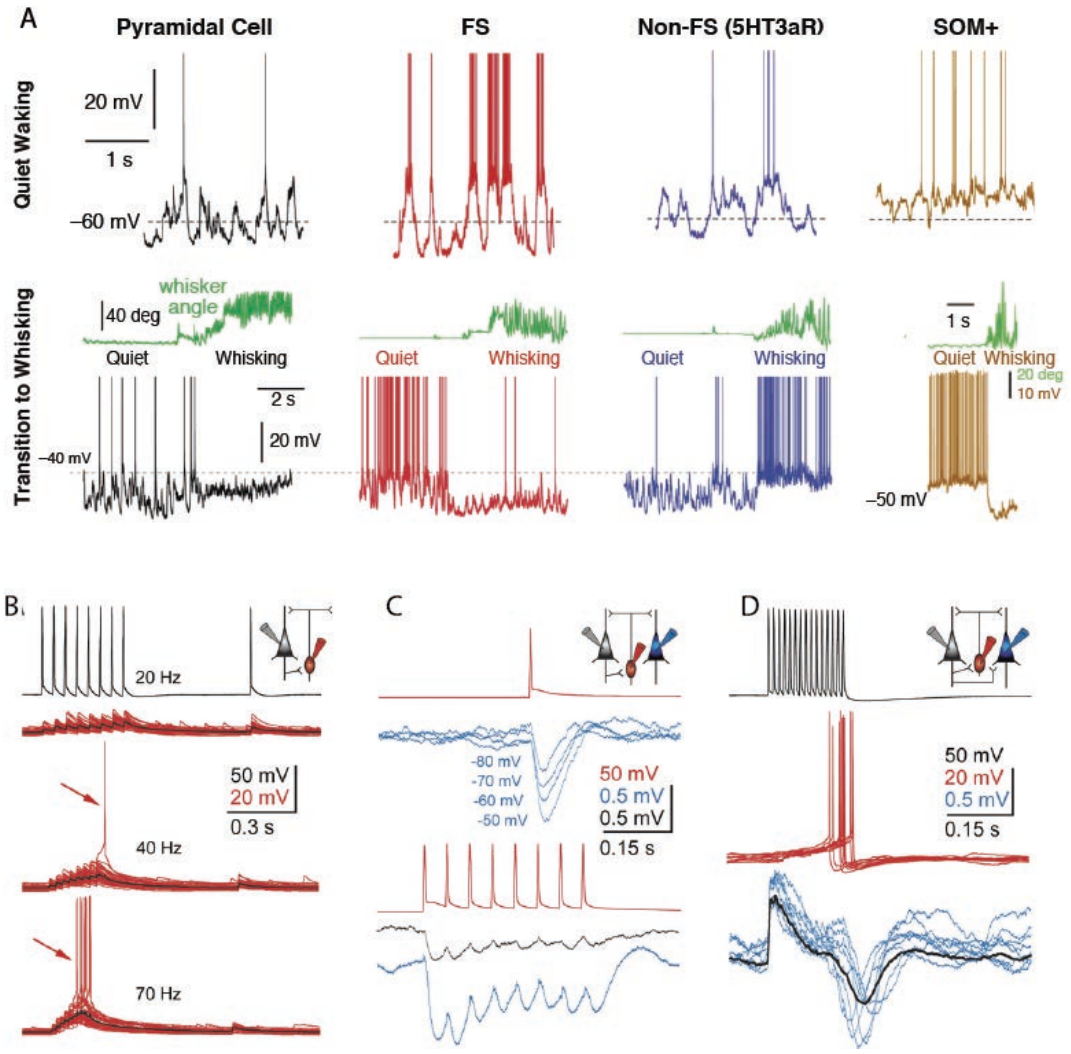

Figure 22: Role for PV and SOM interneurons in the somatosensory cortex. **A**. Membrane potential dynamics and firing during quiet waking versus active whisking for different neuronal classes: excitatory pyramidal cell, FS interneuron, non-FS putative 5HT3aR-expressing interneuron, and SOM+ interneurons. Adapted from Gentet et al. (2010). **B**. The pyramidal cell (PC) to Martinotti cell (MC) facilitating synapse. **C**. The MC to PC depressing synapse. **D**. Disynaptic connections: evoked action potential trains in the presynaptic PC induce a facilitating excitatory connection in the postsynaptic MC, which resulted in IPSPs in the postsynaptic neighboring PC. PC: black traces; MC: blue traces, average in black). Adapted from Silberberg and Markram. (2007).

A phenomenon, called the frequency-dependent disynaptic inhibition (FDDI) has been shown to be a dynamic and activity-dependent synaptic pathway in layer 5 and layer 2/3 of the primary somatosensory cortex (Kapfer et al., 2007; Silberberg and Markram, 2007). Indeed, layer 5 and layer 2/3 SOM-MCs, are selectively activated by high frequency action potential trains from single pyramidal cells and distribute inhibition to several neighboring pyramidal neurons (**Fig. 22B-C-D**; Kapfer et al., 2007; Silberberg and Markram, 2007) onto their distal dendritic tufts in layer 1 (Silberberg and Markram, 2007). Because layer 1 is an important target of sensory inputs such as whisker motor cortex (Petreanu et al., 2009), inhibition by MCs may therefore modulate the integration of top-down layer 1 inputs within the columnar network (Gentet et al., 2012).

These findings demonstrate that distinct interneuron types can contribute to different aspects of sensory processing by cortical neurons. PV interneurons mediate early onset transient inhibition and are involved in gain control (Gabernet et al., 2005) of firing whereas SOM get activated with a delay and modulate dendritic excitability (Silberberg and Markram, 2007) in rodent's somatosensory cortex.

Similarly, in the presubiculum, our results demonstrate the recruitment of PV interneurons in a feed-forward manner by thalamic inputs (Nassar et al., in prep). In contrast, SOM interneurons were indirectly recruited by thalamic inputs in a feedback manner during sustained firing of local principal neurons (Simonnet et al., under review).

4.5 VIP interneurons - Influence of disinhibition

Connections between excitatory and inhibitory neurons provide a framework that controls spontaneous and evoked neocortical activity, upon which sensory information is transformed into neuronal representations. One strategy for PV and SOM interneurons maybe to provide a global "blanket of inhibition" to nearby PNs (Fino and Yuste, 2011; Packer and Yuste, 2011; Karnani et al., 2014). Along with PV and SOM interneurons, VIP neurons constitute a major fraction of neocortical interneurons (Rudy et al., 2011), specialized in making synapses onto other interneurons, potentially serving to facilitate increases in cortical activity (Acsády et al., 1996; Hájos et al., 1996). VIP target specifically SOM and to a lesser extent, PV INs in the hippocampus and neocortex (**Fig. 23**; Chamberland et al., 2010; Lee et al., 2013; Pi et al.,

2013; Pfeffer et al., 2013). All three interneuron types (PV, SOM and VIP) receive cortical, thalamic and cholinergic inputs; however, VIP interneurons received more overall synaptic input from throughout the brain (Wall et al., 2016).

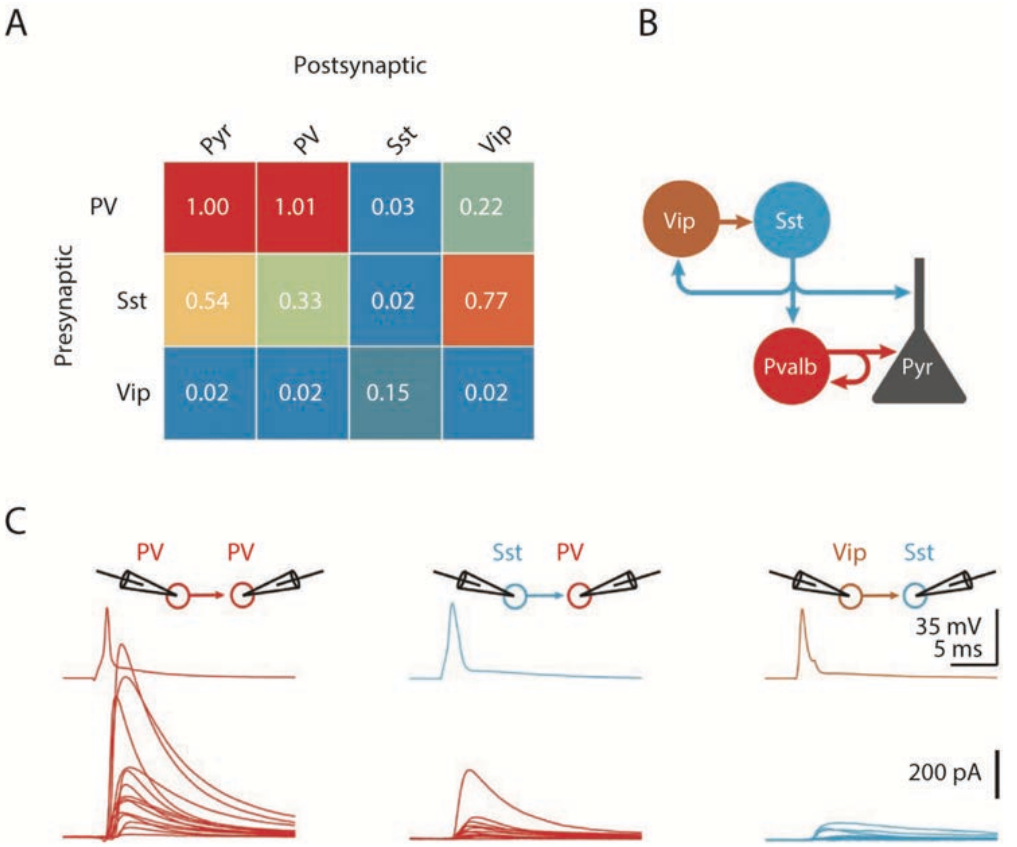

Figure 23: Interneurons connectivity patterns. **A**. Contributions of the three presynaptic interneuron types onto PV, SST, VIP interneurons and pyramidal cells. **B**. Schematic of the inhibitory connections between the three largest classes of interneurons (PV, SST, VIP) and pyramidal cells. **C**. Schematics of paired recordings between different interneuron types. Average uIPSC recorded in interneurons (bottom) in response to an action potential evoked in a presynaptic interneuron (top). Adapted from Pfeffer et al. (2013).

In vitro and *in vivo* recordings in V1 in awake mice (**Fig. 24C-D**; Karnani et al., 2016a) showed that VIP disinhibit the PNs under SOM lateral inhibition, thus making local and transient "holes" in the blanket (Karnani et al., 2014; Karnani et al., 2016a). The disinhibitory motif may serve as a switch to release the inhibitory break from the target neurons and shift the excitation–inhibition balance towards less inhibition. In the visual cortex of anesthetized mice, VIP neurons were broadly tuned, functionally similar to PV neurons with the exception of delayed responses (Mesik et al., 2015). VIP interneurons are also engaged in network ac-

tivity during specific behaviors (**Fig. 24A-B**; Lee et al., 2013; Pi et al., 2013; Fu et al., 2014). In the visual cortex, the activity of VIP cells was highly increased during locomotion, in which cholinergic input to VIP interneurons results in inhibition of SOM interneurons (**Fig. 24B**; Fu et al., 2014). In the somatosensory cortex, the firing rates of VIP interneurons increased during active whisking while those of SOM interneurons decreased, and this relationship was dependent on activity in primary motor cortex (Lee et al., 2013).

Taken together these data suggest a generalizable disinhibitory role of VIP+ neurons exerting a state independent facilitation of spontaneous and evoked neocortical activity during locomotion, non-locomotion, visual stimulation and under anesthesia (Jackson et al., 2016). Functionally, VIP interneurons may be specialized in controlling the intracortical gating of information during different brain states, resulting in an increase of excitatory neuron responses. The disinhibition of the cortex via VIP cells, which inhibit SOM cells, might be a general feature of long-distance corticocortical and thalamocortical circuits. In the presubiculum, the wiring and functional role of VIP neurons is currently unknown.

In conclusion, the association of interneuron classes with network oscillations, gain modulation or disinhibition during different brain states or behavior might rely on canonical circuit motifs conserved across neocortical regions. Other specific circuit functions such as precisely timed somato-sensation or maintained working memory could require specifically tailored circuit elements.

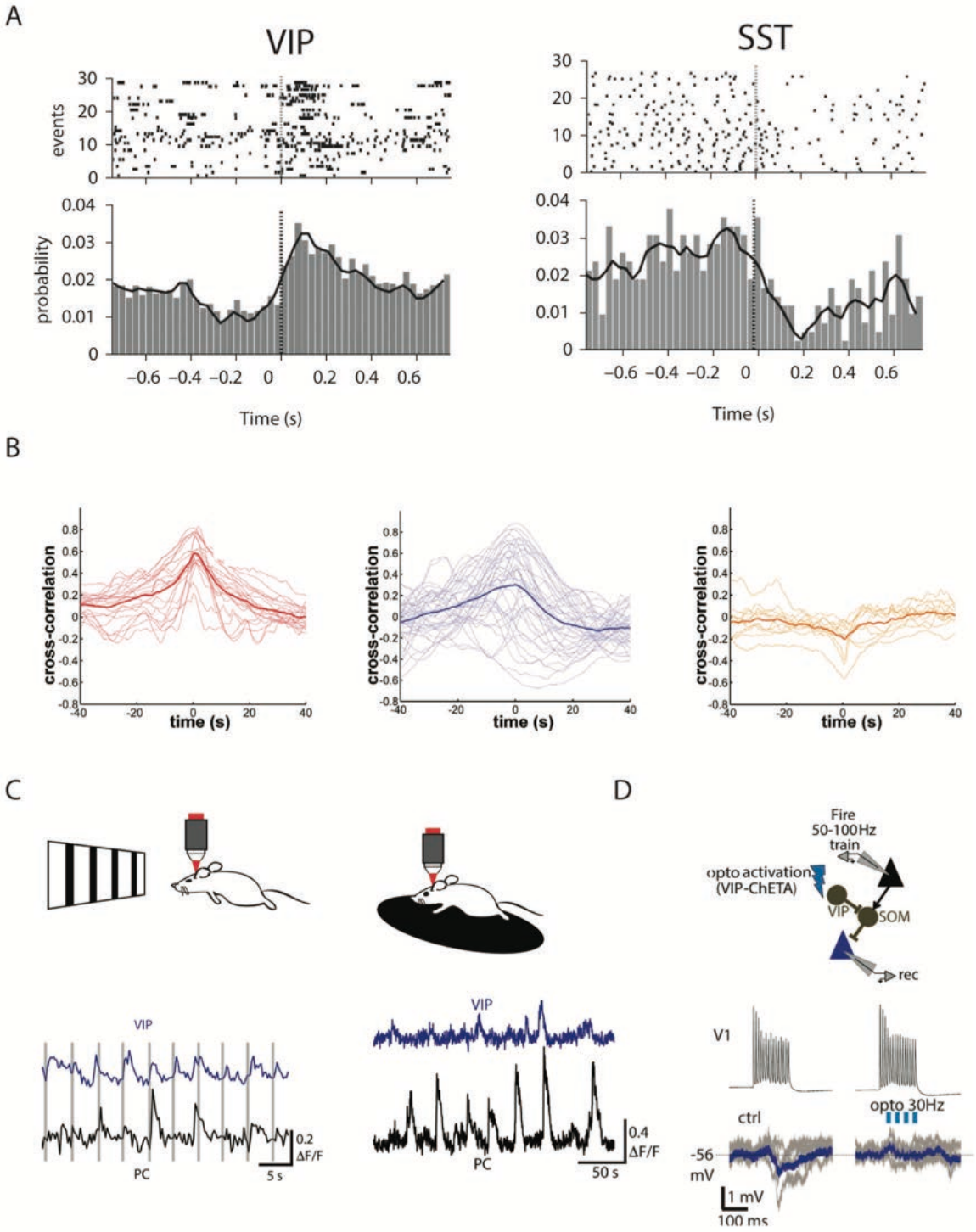

Figure 24: VIP-mediated disinhibition during behavioral states. **A**. Spiking activity of VIP interneurons (left) and SST interneurons (right) in S1 during active whisking, from Lee et al. (2013). **B**. Modulation of VIP (left, red), PV (middle, blue) and SST (yellow, right) during locomotion. Cross-correlogramm between the GCaMP6s calcium signal and running speed chart for the three interneurons types, from Fu et al. (2014). **C**. Visual stimulus-evoked (left) and spontaneous (right) correlations between VIPs and putative PCs. **D**. (top) Schematic of experimental model with an excitatory opsin (ChETA) in VIPs (bottom). Current-clamp recordings from V1 in control versus optical activation of VIP cells (blue), from Karnani et al. (2016a).

5-Novels methods for investigating the functional connectivity

The major aim of systems neuroscience is to understand how the brain processes information, encodes perception and generates behavior. These operations are determined by the structure of the neural circuits, the physiological and anatomical features of their local and external connections as well as the integrative properties of neurons that compose them. Critical steps toward the comprehension of neuronal circuits are the identification of the inputs of the circuit's diverse neuron types, and an understanding of their interaction within the circuit. Several neuronal tracing techniques exist to chart anatomical connections within the nervous system. Anterograde and retrograde neuronal tracers have allowed us to gain information about connectivity between different cortical and subcortical areas. However, when used alone, they appear insufficient to reveal connectivity at finer levels of complexity. In recent years, a toolbox of genetically encoded molecules has emerged and has enabled us to target specific cell types and control their electrical activity in a temporally precise fashion by pulses of light. Modern tracing strategies combined with innovative optical methods work in concert to reveal multisynaptic pathways and allow to identify connections to and from particular cell types.

In this section, I will briefly describe neuronal tracers such as Retrobeads, Cholera toxin B as well as the optical tools that I have used during my PhD.

5.1 Neuroanatomical tracers

Neuronal tracing techniques are based on the principle of axonal transport. With regard to the direction of transport, the notion of anterograde and retrograde transportation of tracer material can be distinguished. For retrograde transport, the tracer material enters from the cell axons (usually by endocytosis) and is transported back to the cell body. For anterograde transport, the uptake mechanisms involve the cell soma and/or its dendrites, and the tracer is carried along the axonal microtubular system to the cell's synaptic terminals.

5.1.1 Retrobeads

Fluorescently tagged microspheres or beads, first introduced by Katz et al., (1984), are 20-200nm large polystyrene (Molecular Probes) or latex (Lumafluor) microspheres labeled with dyes of different colors. Those from Lumafluor are red (rhodamine-labeled) or green (fluorescein-labelled) (Katz et al., 1984; Katz and Iarovici, 1990). They are suitable to trace both local and long-range connections, depending on the injected volume of tracer solution. They diffuse very little into the surrounding brain tissue and produce sharply defined injection sites. Rhodamine and fluorescein are fluorescent proteins that are soluble in water, as well as ethanol and methanol. The microbeads are taken up by axon terminals within the injection site and are transported retrogradely into the soma. The uptake mechanism is not completely understood (possibly a latex-triggered endocytosis); however, size and surface properties seem to play an important role. Retrograde transport is fast since the labelling increases until 48h after injection and is then persistent for several weeks. In retrogradely labeled pyramidal neurons, beads fill the cell soma and the proximal trunk of the apical dendrites. Latex microspheres are not cytotoxic for the animal, and no phototoxicity for labeled cells after illumination has been described. Latex microspheres can also be combined with immunohistochemistry, intracellular injections, immunofluorescence, Golgi silver impregnation or in situ hybridization. Under illumination, the fluorescence is stable and latex beads are directly visible without the need of further staining techniques, which makes them suitable for *in vitro*, *in vivo* and cell culture experiments. The possibility to record from labeled neurons or identify specific afferents makes the beads a marker of choice for functional connectivity studies. Severed fibers of passage, but not intact ones, seem to show some uptake of marker material. Once sectioned and mounted, beads fade over time because of their sensitivity to glycerol unless antifading specific mounting media are used. Beads in retrogradely labelled cells appear as granular dots in the cytoplasm. The rhodamine and fluorescein components are best excited with a light source of 540nm and 490nm wavelength respectively, while the maximum emission lies at 590nm and 520nm for red and green labelling respectively (Katz et Iarovici, 1990). Due to their overlapping wavelengths, cells brightly labelled with red beads can, however, interfere with the identification of cells that are more weakly labelled with green beads (Köbbert et al., 2000).

5.1.2 Cholera toxin B

Cholera toxin is comprised of two subunits, A and B, forming a hexameric complex. The A subunit consists of a single copy and is considered as a ADP-ribosyltransferase enzyme, which disrupts the G protein signaling leading eventually to dehydration of the cell (Finkel-

stein and Dorner, 1985). The nontoxic B subunit arranged as a pentameric ring is important to the protein complex as it allows the protein to bind to cellular surfaces via the pentasaccharide chain of ganglioside G_{M1} membrane receptor facilitating its internalization. Cholera toxin B (CTB) is an axonally transported marker and has proven to be a powerful tool for retrograde labeling of neurons. It has been recently used as a marker of lipid rafts (membrane microdomains enriched in cholesterol and sphingolipids) involved in cell signaling and protein trafficking (Janes et al., 1999). Historically, CTB has been limited to single-labeling techniques using bright-field horseradish peroxidase and DAB staining (Luppi et al., 1990). Recently, CTB conjugated with fluorescein- or rhodamine fluorochromes has been used to trace the connections of multiple brain areas. Fluorescently conjugated-CTBs are made from the pure original recombinant cholera toxin subunit B and completely free of the toxic A subunit (Conte et al., 2009a). Even at low concentrations (0.5%), dye-labeled CTB is very effective and sensitive and only a slight increase in background labeling was observed at higher concentrations (1%) (Conte et al., 2009b). Labeling is photostable and resists photobleaching for several months after coverslipping. After axonal transport, labeling is preferentially localized to soma and proximal dendrites. Because CTB remains in vesicles, labeled somata appear granular. Labelling is optimal after 2-4 days of survival even though it varies from 1 to 10 days depending on the age of the animal (Angelucci et al., 1996). CTB may be taken up by non-terminal passing fibers (Chen and Jones, 1995), which is a common problem for most neuronal tracers. Mostly considered as a retrograde tracer, some anterograde transport has been described (Angelucci et al., 1996).

5.2 Optogenetics

Electrical stimulation has been widely used with great efficacy to both control and probe the function of discrete brain regions. However, it is not possible to target genetically specified cell types, a disadvantage that can be overcome with genetically encoded molecules. A recent innovation in experimental neuroscience has been the development of light-activated channels or pumps, derived from microbial photosynthetic systems, to modulate neural activity. The expression of these photosensitive molecules is driven through genetic manipulation of the target cells, which is why these tools are referred to as optogenetics. These optogenetics tools allow for activation or silencing of neurons with high temporal precision and specificity. One frequently used approach to express light sensitive molecules in neurons is the use of lentivi-

rus or adeno-associated virus (AAV) for viral transduction in vivo. During my PhD, I used AAV virus vectors for *in vivo* delivery of plasmids containing ChR2 and a fluorescent reporter. Delivered through stereotactic injection in the brain, this method allows to target a spatially restricted brain area. Cell type specificity depends on the serotype and promoter used. This approach can lead to high level of protein expression within short periods of time.

5.2.1 Adeno-associated virus

AAV is a 20-30 nm diameter non-enveloped (no phospholipid coat), single-stranded, small DNA virus belonging to the Parvovirus family. It is a non-pathogenic virus with a genome of approximately 4.7kb flanked by two 145 base inverted terminal repeats (ITRs) on the 5' and 3' ends. The AAV genome consists of two open reading frames (ORFs) that encode four replication proteins (Rep), three capsid proteins (Cap/VP) and other assembly proteins (AAPs) (Murlidharan et al., 2014). ITRs are the only cis-acting elements necessary for successful encapsidation and replication of the virus. AAV provides a source for recombinant gene vectors derived from AAV (or rAAV) that carry no protein coding sequences. Wild type AAV virus requires co-infection by adenovirus or herpes simplex virus for efficient replication in their host, and will, in the absence of helper virus, stably integrate into the host cell genome. AAV vector genomes remain primarily episomal in target cells and have a low (if any) frequency of integration (https://www.med.upenn.edu/gtp/vectorcore/BiosafetyInformation.shtml). AAV demonstrates relatively low immunogenicity, and can be produced in large quantities with high purity and thus, is useful for long-term and high level of expression in the nervous system. Compared to lentiviral vectors, AAVs lead to greater spatial spread due to their small particle diameter (100nm compared to 20-30nm for AAVs). AAVs enter the cell through interaction between the capsid and the AAV membrane receptors (Pillay et al., 2016), preferentially the cell surface glycans (Asokan et al., 2012), which leads to vector internalization (**Fig. 25;** Russel and Kay, 1999). The vector DNA is then released in the cytosol and translocated to the nucleus (Russel and Kay, 1999). The different serotypes have different sequences in their ITRs and in their capsid proteins. The ITR serotype is the number listed first in the name of an AAV vector, while the capsid type is the second number. AAV serotypes noted from AAV2/1 to AAV2/9 exhibit a range of properties related to antigenicity, in vivo tropism, and receptor interactions based on their different capsid structures (Burger et al., 2005). In addition, the speed of onset of viral gene expression for maximal number of cells can vary up to several weeks or months among serotypes (Aschauer et al., 2013).

Particularly, the efficiency, tropism and extent of axonal transport vary widely among serotypes: in fact, AAV2/9 has been shown to travel in both anterograde and retrograde directions (Masamizu et al., 2011; Castle et al., 2014; Salegio et al., 2013), whereas AAV2/5 is more specifically anterograde (Soo-Hyun Lee, personal communication; Watakabe et al., 2014). In particular, rAAV vectors using Cre-dependent expression switches show a robust capacity for retrograde infection in a payload dependent manner (Rothermel et al., 2013). In order to achieve cell type-specific expression, the vector constructs include a recombinant promoter coding for a gene that is expressed only in the targeted cell type. Neuron-specific promoters are the promoters of the genes coding for synapsin (hSyn) or neuron-specific enolase (NSE). Pyramidal cell–specific expression can be achieved with the promoter for calcium/ calmodulin-dependent protein kinase II (CaMKII) even though the expression of CAMKII is not fully restricted to pyramidal neurons.

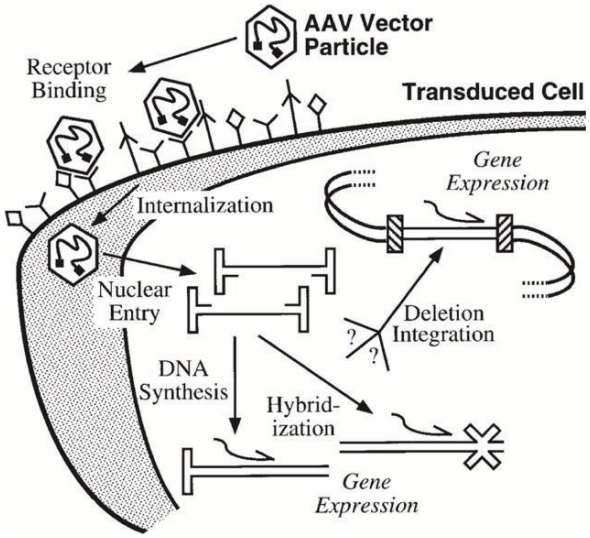

Figure 25: Steps for transduction by AAV vectors. Interaction with diverse membrane receptors on the cell surface allow the internalization of the viral vector followed by the nuclear entry, release and hybridization of its single stranded genome for further gene expression. Adapted from Russel and Kay. (1999)

5.2.2 Microbial opsins

Opsins are found in an extensive variety of organisms ranging from archaebacteria to mammals. These proteins are composed of a seven-transmembrane-helix-domain (7TM) covalently linked retinal, the aldehyde of vitamin A. Opsins are separated into two groups, depending on their primary sequence, type I (microbial) and type 2 (animal). Microbial-type opsins are found in archaea, eubacteria, fungi and algae, whereas animal-type 2 opsins are encountered in the mammalian retina photoreceptor cells. Optogenetics takes advantage of this dissocia-

tion by expressing de novo microbial opsins, for example in mammalian cells, conferring them new light sensitivity. Two classes of microbial opsins have been described: the light-driven ion pumps, including the chloride pumps halorhodopsins (HR) and the proton pumps bacteriorhodopsins (BR), and the light-driven ion channels channelrhodopsins (ChR) (**Fig. 26**). The first microbial opsin applied both *in vitro* and *in vivo* to excite neurons was channelrhodopsin-2 (ChR2), a member of the channelrhodopsin (ChR) family. Channelrhodopsins are light-gated nonspecific cation channels, conducting Na^+, K^+ and Ca^{2+} ions, derived from the green algae C. Reinhardtii (Nagel et al., 2003). Channelrhodopsins possess a molecule of all-trans retinal (ATR) bound at the core as a photosensor. Upon illumination with maximum excitation at 470 nm (blue light), ATR isomerizes and triggers a conformational change to open the channel pore, thus depolarizing expressing neurons and inducing single action potentials (Boyden et al., 2005). The main limitation of ChR2 is the high level of desensitization that decays by 80% from the peak to a steady-state response (Nagel et al., 2003). At high expression levels, ChR2 can form intracellular aggregates instead of trafficking to the membrane, extra spikes can occur (two spikes following one light pulse) and cells can enter "depolarization block" (repetitive stimulation does not allow repolarization of the membrane). A variant of ChR2 with a mutation at position H134R leads to a modest reduction in desensitization, but also to a slight increase in light sensitivity and slower channel closing, favoring depolarization block (Nagel et al., 2005; Lin et al., 2009). The E123T mutation in ChR2 (ChETA) creates faster kinetics, reduces extra-spikes and allows for temporary sustained spike trains up to 200Hz (Gunaydin et al., 2010). ChR2 application was quickly followed by the development of the inhibitory halorhodopsin (Chow et al., 2010) that could hyperpolarize and therefore silence expressing neurons upon illumination with 580 nm yellow light via an inward chloride flux with NpHR derived from the archaeon Natronomonas pharaonic. Multichannel photoinhibition and photostimulation can drive high-fidelity sequences of hyperpolarizations and depolarizations in neurons simultaneously expressing yellow light-driven HR and blue light-driven ChR2, allowing for the first time manipulations of neural synchrony without perturbation of other parameters such as spiking rates (Han and Boyden, 2007). The light-activated Halorubrum sodomense archaerhodopsin (Arch) is a light-driven proton pump. Once expressed in neurons and activated with yellow or green light, Arch pumps positive charge H+ out of the cells, hyperpolarizing them. It possesses strong photocurrents and can mediate complete silencing of neuronal activity in awake behaving mice (Chow et al., 2012). For ease of identification of transfected cells, optogenetic molecules can be tagged by fluorescent marker proteins such as eYFP, mCherry or tdTomato, on its C-terminal.,

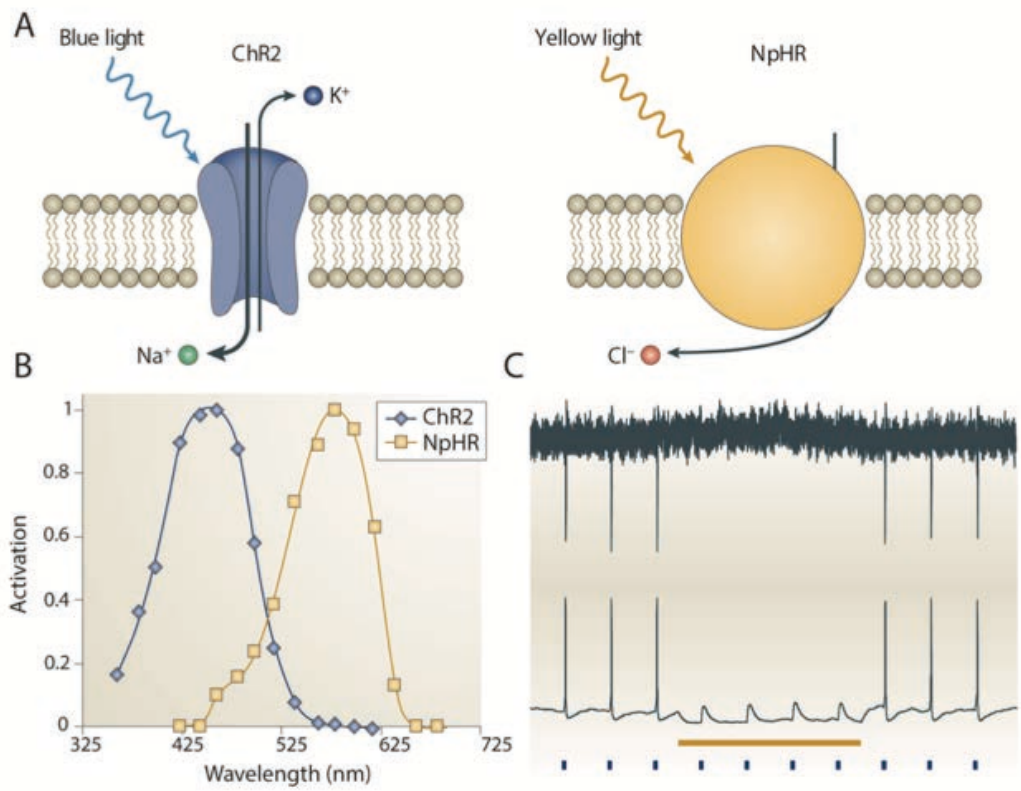

Figure 26: Properties of ChR2 and NpHR. **A**. Schematic of ChR2 (left) and NpHR (right). Following blue light illumination (~470 nm), ChR2 opening allows the entry of cations. Following yellow light illumination (~580 nm), NpHR pumps chloride ions into the cell, from Zhang et al. (2007a). **B**. Action spectra of ChR2 (blue) and NpHR (yellow). **C**. Cell-attached (top) and whole-cell current-clamp (bottom) recordings from hippocampal neurons activated (blue bar) and inhibited (yellow bar) following activation of ChR2 and NpHR respectively, from Zhang et al. (2007b).

6- Aims of the thesis

The presubiculum is a transitional cortical area that is part of the parahippocampal region. As presented in the introduction, despite its functional importance in spatial coding, many aspects of the structural and functional organization of the presubiculum have remained poorly understood. Specifically, inhibitory components and their functional connectivity within the microcircuit are still unexplored. My supervisor, Desdemona Fricker, therefore proposed me a thesis project whose aim was to elucidate the information processing at the level of the inhibitory microcircuit in mouse presubiculum.

The presubiculum contains head direction cells, which fire as a function of the animal's directional heading. The anterior thalamic nuclei, together with the visual and retrosplenial cortex are major inputs to the presubiculum and greatly contribute to the generation and the refinement of the head direction signal in this area. The role of the presubiculum is to distribute a visual landmark control to subcortical areas and it is considered a major drive to the downstream entorhinal cortex where it contributes to spatially tuned firing. It is likely that information in the presubiculum is actively integrated and refined.

In this framework, the aims of my thesis were 1) to determine the cellular components and 2) the local and afferent connectivity of the inhibitory microcircuit, 3) to contribute experimental data on connectivity and synaptic properties of interneurons for computational models and to gain insight in the function of GABAergic interneurons in HD signaling.

To achieve this, I took advantage of transgenic mouse lines that specifically label PV and SOM interneurons, the PVCre::dtTomato, SSTCre::dtTomato and X98 GFP to study the main inhibitory elements of the microcircuit. Using dual or single whole-cell patch-clamp recordings in combination with optogenetic tools that specifically activated afferent inputs and retrograde tracers that label presubicular efferent projections, I wished to examine the anatomy, electrophysiology and the input-output connectivity of inhibitory presubicular neurons.

METHODS

Animals

For interneuron identification, I used specific mouse strains expressing fluorescent proteins in interneuron populations. Pvalb-Cre mice (Jax n008069; Hippenmeyer et al., 2005) or Sst-IRES-Cre mice (Jax n013044; Taniguchi et al., 2011) were crossed with the Ai14 Cre reporter line (Jax n007914; Madisen et al., 2010). Cre-mediated recombination resulted in the expression of red fluorescent tdTomato (RFP) labeling in subsets of GABAergic neurons. I also used the transgenic mouse line X98-SST (Jax n006340), in which the GAD67 promoter drives GFP expression. Random insertion of the transgene in the genome has allowed the labeling of a subset of somatostatin positive neurons with axonal arborizations in layer I (Martinotti-type morphology in neocortex; Ma et al., 2006).

Slices

During my PhD, I was always striving to improve my slicing procedures. In order to perform electrophysiological recordings, the quality of slices was a crucial point and depended on the age of the animal. From the preparation of solutions to the dissection and slicing, every step has to be controlled and performed meticulously. Many recipes and advices are found in www.BrainSliceMethods.com. Animals were anesthetized with ketamine hydrochloride (Imalgene®) and xylazine (Rompun®) (100 and 15 mg.kg−1, respectively). The mixture is prepared as followed: I first added 1mL of Imalgene and 0.5 mL of Rompun, then I added 8.5 mL of NaCl to get a final volume (10mL) of 1/8 diluted solution. The injected volume depended on the weight of the animal (100µL of mixture per 10g). 100 µL of Choay heparine was injected intraperitoneally on the opposite side after anesthesia. When the mouse was deeply anesthetized (no response to nociceptive stimulation), another 100 µL of Choay heparine was injected in the left ventricle before perfusion and the descending aorta was clamped. Animals were then perfused through the heart by gravity flow with a sucrose-based solution with 125 NaCl, 25 sucrose, 2.5 KCl, 25 $NaHCO_3$, 1.25 NaH_2PO_4, 2.5 D-glucose, 0.1 $CaCl_2$, 7 $MgCl_2$ (in mM) cooled to 4◦C and equilibrated with 5% CO_2 in O_2. A perfusion needle was inserted into the left ventricle and after 5 seconds, the right atrium was cut with small scissors. A perfusion was judged to have worked when the animal lungs and rib cage bones turned white. The volume of perfusion varied from 20 to 50 mL. The speed was adjusted so that the solution came out of the perfusion needle by dripping.

Cutting 10X	MW	mM	1L	Units	
NaCl	58.44	125	73.0500	g	
Sucrose	342.3	25	85.5750	g	
KCl	74.56	2.5	1.8640	g	
NaH_2PO_4	119.98	1.25	1.4998	g	
$NaHCO_3$	84.01	25	21.0025	g	
Glucose	180.16	2.5	4.5040	g	
Cutting 1X			1L		
Stock 10X			100	mL	
$CaCl_2$	147.02	0.1	0.1	mL	of 1M solution
$MgCl_2$	203.31	7	7	mL	of 1M solution

Table 1: Ingredients and preparation of the sucrose-based solution

The stock solution could be kept at 4°C for two months. Cutting solution was prepared from 100 mL of 1L of 10X stock solution. Then, it was put in ice or in the freezer to decrease the temperature until 0-4°C. The day of the experiment, I started to oxygenate the cutting solution for at least 1 minute before adding 0.1 mM $CaCl_2$ and 7 mM of $MgCl_2$ in order to avoid their precipitation. $CaCl_2$ and $MgCl_2$ were always added in the final cutting solution but never in the stock solution. pH and osmolarity were then measured. Sucrose-containing solution was prepared from MilliQ water (Elix®, Millipore; resistance of 18.2µΩ).

A good perfusion significantly improves the slice quality with animals older than 25 days. Animals were decapitated and horizontal 280–320µm thick brain sections were cut in the same solution using a vibratome (Leica VT1000S or Microm HM650V). To obtain horizontal slices, the cerebellum was chopped off, then the dorsal part of the brain was stuck on the slicer platform using superglue. Cutting started from the ventral side, the parahippocampal area with the entorhinal cortex turned towards the blade. Some ice was put around the chamber to keep the cutting solution as cold as possible during slicing (usually between 0-4°C). Compared to coronal and parasagittal angles, horizontal slicing appeared more appropriate for preserving neuronal health and integrity of the presubicular tissue. Slices were stored for 20 min at 37°C in a holding immerged chamber filled with ACSF containing (in mM): 124 NaCl, 2.5 KCl, 26 $NaHCO_3$, 1 NaH_2PO_4, 2 $CaCl_2$, 2 $MgCl_2$, and 11 D-glucose, bubbled with 5% CO_2 in O_2 (pH 7.3, 305–315 mOsm/L).

Storing at physiological temperatures appeared to improve slicing quality for older animals. Then, they were stored for at least 45 min at room temperature in the same solution gently

bubbled with 5% CO_2 in O_2. I noticed that warming and storing acute slices in an interface chamber (designed with the help of Marie Goutierre, a PhD student in Jean Christophe Poncer lab) significantly improved neuronal health and facilitated my recordings from retrobeads-labeled neurons.

ACSF 10X	MW	mM	1L	Units	
NaCl	58.44	124	72.4656	g	
KCl	74.56	25	1.8640	g	
NaH_2PO_4	119.98	10	1.1998	g	
$NaHCO_3$	84.01	262	22.0106	g	
Glucose	180.16	110	19.8176	g	
ACSF 1X			1L		
Stock 10X			100	mL	
$CaCl_2$	147.02	2	2	mL	of 1M solution
$MgCl_2$	203.31	2	2	mL	of 1M solution

Table 2: Ingredients and preparation of the ACSF solution

The stock solution was kept at 4°C for two months. All components (listed in table 2) except $CaCl_2$ and $MgCl_2$ were added in the final stock solution. Cutting solution was prepared from 100 mL of 1L 10X stock solution only the day of experiment. Before adding 2 mM of $CaCl_2$ and 2 mM of $MgCl_2$, I started to oxygenate the solution for at least 1 minute to avoid their precipitation. pH (7.3) and osmolarity (305–315 mOsm/L) were then measured. ACSF was prepared from MilliQ water (Elix®, Millipore; resistance of 18.2μΩ).

Patch-clamp recordings

Slices were then transferred to a recording chamber (volume 2–3 mL, temperature 33–35◦C) mounted on a BX51WI microscope (Olympus, France). Fluorescently labeled PV, SST or X98 interneurons were identified using LED illumination with appropriate emission/excitation filters (OptoLED, blue (470nm) and yellow (580nm) LED, Cairn Research, Faversham, UK). Cf. **figure 27** for additional information. Recordings were made with glass pipettes pulled using a Brown–Flaming electrode puller (Sutter Instruments) from borosilicate glass of external and internal diameter of 1.5 mm and 0.86, respectively (Harvard Apparatus, UK; reference: GC150F-10). The electrode resistance, when filled with the internal solution was 3–8 MΩ. Dual recordings were easier to perform with higher resistance pipettes. For electrophysiological recordings, we used a MultiClamp 700B amplifier, a Digidata 1440a, a ISO-S-1.5G microelectrode holder (G23 instruments), pCLAMP software (Molecu-

ar Devices, Union City, CA, USA), Luigs and Neumann micromanipulators and a heated chamber. The motorized table was commanded by Morgentau software (custom written by Michael Bendels, Bendels et al., 2008), used to position a lattice of light stimulation sites across the presubiculum. During my PhD, I used one kind of internal solution. The potassium-gluconate solution contained (in mM) 135 K-gluconate, 1.2 KCl, 10 HEPES, 0.2 ethylene glycol tetraacetic acid (EGTA), 2 $MgCl_2$, 4 MgATP, 0.4 Tris-GTP, and 10 Na_2-phosphocreatine.

	mM	MW	mg/100mL	mg/25mL
K-gluconate	135	234.2	3161.7	790.425
KCl	1.2	74.56	8.9472	2.2368
HEPES	10	238,3	238.3	59.575
EGTA	0.2	380.4	7.608	1.902
$MgCl_2$	2		200 µL	50 µL (of 1M solution)
MgATP $2H_2O$	4	568.2	227.28	56.82
Na_3-GTP $2H_2O$	0.4	628.2	25.128	6.282
Na_2-phosphocreatine	10	255.1	255.1	63.775

Table 3: ingredients of the internal solution stock

The internal solution stock (25mL) was prepared from distilled water (Gibco™, Life technologies) in cold temperature (4°C) to keep ATP and GTP stable. The components were added in the same order as listed in table 3. pH (7.3) was then measured and adjusted with KOH if necessary. Osmolarity (290 mOsm/L) was measured thereafter and adjusted with distilled water (if too high) or K-gluconate (if too low). Aliquots of 1 mL were then stored at -20°C. Fresh aliquots were always used for each day of experiment.

Recordings were usually very stable with this internal solution after performing a gigaseal followed by a whole cell patch. Low EGTA did not alter stability and allowed calcium dependent physiological modifications. In order to study the inhibitory/excitatory conductance, 2mM QX 314 bromide (Tocris) was added the day of the experiment to an aliquot of 1mL of internal solution (and agitated), thus allowing to depolarize membrane potential to +40mV and eliminating action current in voltage-clamp mode. In order to perform double recordings, the two pipettes were positioned at the top of the slice, just above the targeted neurons that were carefully chosen by eye. Then, I patched one cell after another in whole-cell configuration. The protocol for testing the connectivity is described in Nassar et al. (in prep).

Analysis of electrophysiological data

Details concerning the analysis of the electrophysiological data will not be fully described here, as they are specifically depicted in the methods of the different studies. Electrophysiological parameters were analyzed with the following softwares: AxoGraph X (http://www.axograph.com/) for manual analysis, Spikoscope (a Labview based software developed by Ivan Cohen) and routines developed with Matlab (the Mathworks) by Jean Simonnet for computerized analysis.

Unsupervised cluster analysis for neuronal classification

As previously reviewed in the introduction section, interneurons can be classified according to many parameters such as the molecular content, morphology, intrinsic electrophysiological properties, their post-synaptic targets, their recruitment by specific inputs or as well as their specific behavioral-related activity (Ascoli et al., 2008).

Classification of neocortical interneurons is a crucial step in understanding cortical circuits as each subtype of interneuron likely has a different function. Classifications have been based on one or a combination of descriptors chosen arbitrarily, often using qualitative criteria (e.g. shapes of the axo-dendritic tree or somatic layer location). Therefore, interneuron classifications can change depending on which descriptors are used by the experimenter. It appears difficult to know which set of descriptors are the most relevant to determine a neuronal class and, more generally, how many classes of interneurons actually exist.

Unsupervised clustering analysis is becoming a widely used method to identify neuronal classes without predefining an initial group. This method uses algorithms to seek objective classification of neuronal populations. It classifies objects by attributing the same weight to each parameter, thus, facilitating the grouping with a standardized nomenclature. Each neuron is thus represented by one point in a multidimensional space (the number of dimension equals the number of parameters) and the closest neurons in this space are then grouped together.

I collaborated with Jean Simonnet to perform unsupervised cluster analysis in order to classify presubicular interneurons (Nassar et al., 2015). Interneurons were grouped based on similarities of 17 electrophysiological parameters obtained from 159 recorded neurons. Our clustering was based on Ward's method (Ward Jr, 1963), as previously used to classify neuronal populations (Cauli et al., 2000). Cluster analysis was implemented using the statistics toolbox of MATLAB (The Mathwork). Centering and reducing all values allowed the standardization

of all values. At each step, the two nearest points that represented neurons were associated together using the matrix of their Euclidean distances and then used for the consecutive steps. The mean within-cluster distance was calculated. This value typically decreased as the number of clusters increased. The Thorndike procedure (Thorndike, 1953), where jumps in distances within clusters indicate prominent differences between groups, was used to examine resulting clusters. Final clusters were defined from statistical and biological parameters.

Neuronal morphology

To examine the morphology, I always added 1-3 mg/mL of biocytin in the internal solution for the patch-clamp recordings either in the internal stock solution preparation or in 1 aliquot during the day of the experiment. Biocytin was dissolved by agitation and no change in the pH and osmolarity was observed after measurement. To get a sufficiently complete axo-dendritic neuronal arborization, recordings should not exceed more than 20 min in order to avoid background staining. In addition, depending on the amount of biocytin, the staining can be more or less efficient. Indeed, the higher the amount of biocytin, the better is the staining. Slices containing filled cells were fixed in 4% paraformaldehyde (PFA) in 0.1M sodium phosphate buffer (PBS) overnight at 4°C. Slices were then rinsed in PBS (3×3 min) and cryo-protected in 30% sucrose at 4°C overnight. I noticed that it is possible to store slices in 30% sucrose for several weeks without altering the staining.

Before starting biocytin revelation, membranes were permeabilized by three cycles of freezing/thawing. To perform this, slices were put on a slide, in a small drop of sucrose. Then, the slide was disposed on dry ice until sucrose is frozen. The experimenter palm was then used as a warm surface until full thawing. The procedure was repeated three times. Slices were then washed with PBS (2×30, then 1×60 min at slow agitation and room temperature) to completely remove the remaining sucrose. Slices were agitated in saturation buffer containing 2% milk powder (Carnation) and 1% Triton X-100 in PBS 0.1M for 3 h at room temperature. The Triton helps to permeabilize the membranes for the subsequent incubation. High concentration of Triton does not alter the staining and improves membrane permeabilization: slices are thick enough not to be degraded. Milk proteins are used to saturate the non-specific fixation sites, thus limiting the background staining. To reveal the biocytin staining, sections were gently agitated with Streptavidin–Cy3 or Cy5 conjugate (diluted at 1:500, Invitrogen, Eugene, OR, USA) and DAPI (1/1000) in the saturation buffer overnight at 4°C. DAPI is used as a nuclear marker to reveal tissue structure and define boundaries as well as layers of the presubiculum.

After washing with PBS (2×30 min, 1×60 min), slices were mounted on coverslips using anti-fade Prolong Gold medium (Life technologies). The position of the revealed neuron was checked to set the good orientation of the slice on the coverslip before mounting**.**

Filled cells were visualized with a QImaging Retiga EXI camera on an inverted Olympus IX81 microscope. Structured images were acquired with an Optigrid system and Volocity software (Improvision, Perkin-Elmer, Coventry, UK). Stacks of 75–250 images (*z*-step 0.7µm) were acquired with a 20X, 0.9NA oil immersion objective. Stacks were exported from Volocity as RGB tif stacks, converted into 8 bit tif stacks using ImageJ then imported to the Neurolucida software (Microbrightfield, Williston, VT, USA) for three-dimensional reconstruction. Images were always acquired with a X4 NA 0.16 objective to get a general overview of the presubiculum and its neighboring areas. Dendrites had typically bigger diameters compared to the axons. Compared to pyramidal neurons, interneurons had no dendritic spines. The "layer length" analysis feature of the Neurolucida software was used to measure dendritic and axonal lengths in specific layers. No correction for tissue shrinkage was applied (negligible shrinkage in the x-y axis and about 50% shrinkage in the z-axis).

Immunohistochemistry

Mice were anesthetized intraperitoneally with ketamine hydrochloride and xylazine (100 and 15 mg.kg− 1, respectively). They were then perfused transcardially with 20-30 mL of 0.9% saline containing heparin (1mL of Choay heparin (100–200 UI/mL) in 50mL of NaCl) followed by 30–50 mL of a fixative solution containing 4% paraformaldehyde in 0.1M sodium phosphate buffer (PBS) under a hood. Pump speed was adjusted to get a dripping output. Dissected brains were post-fixed overnight in the same solution at 4◦C, rinsed three times for 3 min, and then placed in a 30% sucrose solution at 4◦C for at least 24 h.

Horizontal sections of thickness 60 µm were cut in 0.1 M PBS using a slicing vibratome (Microm HM650 V), then transferred in 24 -well cell culture plates (2 to 3 slices per well). Membranes were permeabilized by three cycles of freeze-thawing slices on dry ice in a 30% sucrose containing solution.

Sections were washed three times (2×30 min, 1×60 min) in PBS 0.1M (BupH^{TM} Phosphate Buffered Saline Packs, Thermo Fisher Scientific). BupH Phosphate Buffered Saline Packs are pouches of dry-blend powder that are each sufficient to make 500 mL of sodium phosphate buffer (PBS). When dissolved in 500 mL of water, each pack makes 0.1M sodium phosphate,

0.15M NaCl with pH 7.2 Sections were then transferred to a saturation buffer containing 2% milk powder and 0.3–0.4% Triton X-100 in PBS 0.1M, and agitated for 2 h at room temperature. Decreasing the amount to 0.3-0.4% allowed to avoid the deterioration of the cell membranes during the immunostaining procedure as the small thickness of the slices makes them very delicate.

Sections were then transferred into primary antibody solution of 0.1 M PBS, 2% milk powder and 0.3–0.4% Triton X-100 and gently agitated, overnight at 4°C (24-well cell culture plates, 1 slice per well, solution volume of 500µL per well, covered with parafilm and aluminium foil). Sections were rinsed three times (2×30 min, 1×60 min) in PBS then incubated in dilutions of secondary antibody, conjugated to different fluorophores, for 4 h at room temperature under gentle agitation. Presubicular layers and borders were defined using specific cytoarchitectonic features identified by DAPI staining. Stained sections were mounted on glass slides, coverslipped with anti-fade Prolong Gold (Life technologies).

During my PhD, I was confronted to a difficulty in staining SOM immunopositive interneurons. I came to find a reliable and specific SOM staining protocol that differs from the usual one in the time of incubation both for the primary and secondary antibodies. Thus, for SOM single labeling, I increased the incubation time with the primary antibody to 48–72 h and with the secondary antibody to 24 h, both at 4°C. For SOM and PV co-labeling, these long incubation times were applied as well. The sources and dilutions of primary and secondary antibodies used are described in details in the method section in Nassar et al., (2015).

Analysis and quantification of labeled neurons

Stained slices were visualized with a QImaging Retiga EXI camera (Qimaging Surrey, BC, Canada), and scanned with an Optigrid II (Thales Optem, Qioptik, Rochester, NY, USA) on an inverted Olympus IX81 microscope. Stacks of 50–80 images (*z*-step, 0.7 µm) were acquired per slice, using an oil immersion objective (20X, NA 0.9). Presubicular layers and borders were defined using specific cytoarchitectonic features identified by DAPI staining. Images were uniformly adjusted for contrast and brightness.

Identification of presubicular layers with DAPI staining allowed layer specific quantification of GABAergic interneurons of the total number of neurons as well as the number of PV or SOM expressing interneurons subpopulations within each presubicular layer. Delimitated layers were cropped out of the image. Layer volume was a product of the layer area and the

number of optical sections in which cells were counted plus the spacing between acquired sections (z-step, 0.5µm). Cells divided by the predefined layers were not considered.

For each brain slice, fluorescent tdTomato+ or GFP+ cells from all layers of the presubiculum were identified visually by complete scans of optical sections. Cell counting was performed using Volocity software (Improvision, Perkin-Elmer, Coventry, UK) to measure cell numbers in defined volumes. Counts were made only from slices with optimal signal to noise levels and very low background fluorescence. Visual checks only revealed very rare ambiguities for weakly fluorescent neurons. Cell density was calculated as the number of fluorescent cells/volume of each presubicular layer (nb/mm^3).

Antibody fluorescence was examined for each tdTomato+ or GFP+ cell. A cell was regarded as positive for a given antibody when somatic fluorescence was clearly higher than background levels. Colocalization of antibody labeling was confirmed from observations at all levels of a stack of optical sections for the soma of a neuron. Percentages of single and dual-immuno labeled fluorescent neurons were obtained by dividing the number of immuno-labeled fluorescent neurons by the total number of GFP+ or tdTomato+ neurons.

Stereotactic injections

When Bertrand Mathon, a neurosurgeon, came to our lab to realize a Master 2 internship, we established a protocol that improved the effectiveness and safety and saved time for stereotaxic injection in adult and neonatal mice. The procedure is fully described in Mathon et al., 2015 for further detailed information.

Mice were anesthetized by intraperitoneal injection of ketamine hydrochloride and xylazine (100 and 15 mg.kg−1, respectively). When the animals showed no response to nociceptive stimulation (pinching of the toes), ophthalmic ointment was applied in order to prevent eye drying. A straight midline incision that runs far enough along the anterior-posterior axis was made through the skin.

The mice were placed in a custom stereotaxic apparatus (Stoelting; Model 900 Small Animal Stereotaxic Instrument). After fixing the animal's head onto the ear bars, an incisor adapter is inserted into the animal's mouth. A snout clamp is then placed just below the eyes to perfectly fix the animal's head. In the right position, the animal's head is straight and symmetrical to the ear bars and cannot move laterally. By measuring the dorsal-to-ventral (Z) coordinates of bregma and lambda and adjusting the height of the head, the animal's head became horizon-

tally flat. Injection coordinates were chosen according to the antero-posterior, medio-lateral and dorso-ventral axis to bregma determined from Paxinos Mouse Brain Atlas (Paxinos and Franklin. 2004) and confirmed by post hoc histological analysis. All injections were performed on the right hemisphere with a rigid 33-gauge needle. With a small drill (Dremel Stylus™ Lithium-ion Cordless drill), a single burr-hole was made into the skull, allowing the insertion of the needle.

One critical point is to make sure that the needle is not clogged by ejecting a small volume of fluid at the same rate as the one for the injection. For all injections, the flow rate was set to 50-60nL/min. The rate should not be either too slow or too fast but has to be adjusted according to the nature (viscous or fluid): higher rate could be used for more viscous molecules. The volume of injection is dependent on the volume of the brain area to be injected, and whether spillover can be tolerated or not, or whether the injection volume is needed to cover a certain area entirely. Before withdrawing the needle from the brain after the injection, the injector was left in place for 5 min in order to allow tracer diffusion and to avoid backflow in the puncture channel. After removing the injection needle, the skin was sutured with a non-absorbable 4/0 filament (Vicryl®) and the animal kept at 37°C in heated chamber until full recovery.

For double injections, two double burr-hole were made one after another. I used the same syringe and needle when AAV virus were injected but not the same syringe and needle when AAV and beads were injected. I determined Bregma again between the two injection sites.

Verification of injection site

An adjustment of the injection site had to be realized before injecting any neuronal tracers or vectors. The inactive tracer Fluoruby (red) or Chicago blue (blue) was therefore injected in the PrS, RSC, ATN and MEC. Afterward, animals were sacrificed directly after surgery. Correctness of injection site was verified by comparing bright field images of 100-300µm thick coronal or horizontal slices comparing the targeted area with plates from atlas “The Mouse Brain in Stereotaxic Coordinates” (Paxinos). In a second time, the retrograde tracers and/or viral vectors were injected with help of the adjusted coordinates. Animals were sacrificed after at least 48h for Retrobeads and Choleratoxin B, and after 2 to 6 weeks depending on the serotypes of AAV virus for anatomical characterization and slice recordings. For every electrophysiological experiment, specificity of the injection site was always checked during the

slicing or later with left over whole-brain representing horizontal slices containing the ATN, PrS and MEC, mounted on glass slides and coverslipped with anti-fade Prolong Gold (Life technologies).

Coordinates (mm from Bregma)	AP	MV	DV
ATN	-0.82	0.75	-3.2
RSC	-2.10	0.71	-0.6
MEC	-4.7	3	4
PrS	-4.06	2	-2.15

Table 4: Stereotaxic coordinates

Injection site	Nature	Volume (nL)	Mouse age	Time before recordings
ATN	AAV9.hSyn.hChR2(H134R)-eYFP.WPRE.hGH,(Addgene26973P)	150	25-35	2 weeks
ATN	AAV5.hSyn.hChR2(H134R)-eYFP.WPRE.hGH ,(Addgene26973P)	350	25-35	3 weeks
RSC	AAV9.hSyn.hChR2(H134R)-eYFP.WPRE.hGH,(Addgene26973P)	150	25-35	2 weeks
ATN	Cholera toxin B	250-300	25-35	2-4 days
ATN	Retrobeads	300	25-35	2-4 days
MEC	Retrobeads	300	25-35	2-4 days
PrS	AAV1.EF1a.DIO.eNpHR3.0-eYFP.WPRE.hGH, (Addgene26966)	350	25-35	6 weeks

Table 5: List of all viruses and tracers injected in different areas

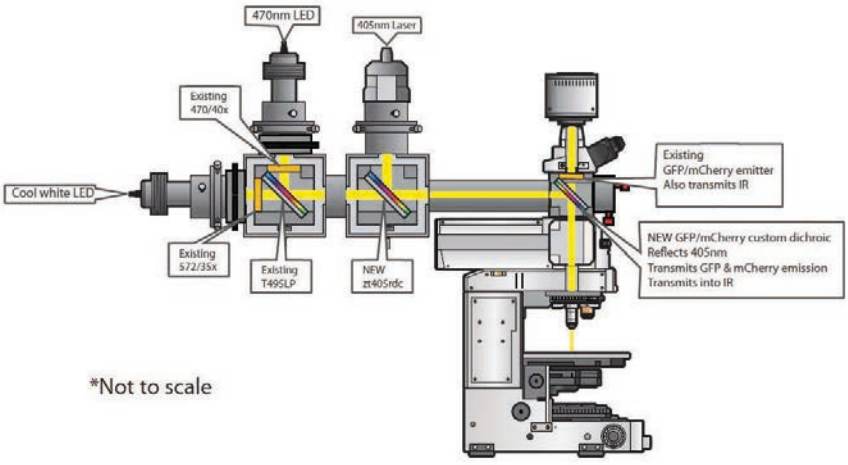

Figure 27: Triple port configuration from Cairn
Filter names-catalogue numbers
ET-GFP (FITC, Cy2) exciter-DC/ET470/40x
ET-Halorhodopsin exciter-DC/ET572/35x
Microscope coupling dichroic-DC/T495LPXR
ET-405nm laser dichroic-DC/ZT405rdc
"Existing" ET Series GFP/mCherry Dual Band Emitter-DC/59022m
"New" ET-dual band dichroic for Channel and Halo-Rhodopsin-DC/59022bs

RESULTS

Article 1

Diversity and overlap of parvalbumin and somatostatin expressing interneurons in mouse presubiculum

The presubiculum as part of the parahippocampal cortex, is involved in spatial orientation. It contains head direction cells that discharge as a function of the animal's preferential head orientation in the horizontal plane. Vestibular and visual inputs are thought to be major contributors to the head direction signals as they generate and update the head directional information converging in the Presubiculum. Presubicular head directional firing appears to be refined, with a more narrowly tuned firing range compared to more upstream regions. In spite of its functional importance in spatial coding, information processing in the presubiculum has remained little studied. What are the neuronal components that compose the different layers of the presubicular microcircuit? What are their intrinsic electrophysiological properties and anatomical features compared to that of the hippocampal and cortical areas?

Our lab had previously characterized the diversity of principal neurons in the presubiculum (Simonnet et al., 2013). My thesis has been devoted to determine the cellular basis of the inhibitory microcircuit. GABAergic interneurons generally regulate activity by balancing excitation, selecting incoming information and synchronizing the activity of neuronal assemblies, and thus, are likely to control the timing, sensitivity and selectivity of head directional signals. I took advantage of transgenic mouse lines by using the Pvalb-Cre mice for the identification of PV interneurons and Sst-IRES-Cre and X98-SST for identifying SOM expressing interneurons. Using whole-cell patch clamp technique in the in vitro slice preparations, I characterized the anatomo-functional properties of these interneurons. In collaboration with Jean Simonnet, we performed the unsupervised cluster analysis of 19 electrophysiological parameters based on the passive, active and action potential properties. We identified typical groups of interneurons resembling those of the neocortex: (1) the PV fast-spiking basket-cells and (2) the SOM low-threshold spiking Martinotti cells. A third group emerged as an intermediate group between (1) and (2) composed of half Pvalb-Cre and half SST-Cre neurons with quasi-fast spiking properties and heterogeneous axo-dendritic trees. Finally, by performing double immunohistochemistry for PV and SOM molecular markers, I revealed the existence of double-labelled PV and SOM interneurons that are likely to be part of the atypical third group described here.

These results have brought fundamental knowledge about presubicular interneuron anatomy and physiology, which as we show share common features with interneurons in other cortical areas. The next steps will be to identify the connectivity motifs of PV and SOM interneurons as well as their involvement in the integration of afferent synaptic inputs. This will provide an essential level of comprehension concerning the information flow in the presubicular microcircuit and more specifically how the head direction signal is treated in this area.

frontiers in Neural Circuits

ORIGINAL RESEARCH
published: 08 May 2015
doi: 10.3389/fncir.2015.00020

Diversity and overlap of parvalbumin and somatostatin expressing interneurons in mouse presubiculum

*Mérie Nassar[1‡], Jean Simonnet[1†‡], Roxanne Lofredi[1], Ivan Cohen[2], Etienne Savary[1], Yuchio Yanagawa[3,4], Richard Miles[1] and Desdemona Fricker[1]**

[1] Institut du Cerveau et de la Moelle Epinière, Sorbonne Universités, UPMC Université Paris 06 UM 75, CHU Pitié-Salpêtrière INSERM U1127, CNRS UMR7225, Paris, France, [2] Neuroscience Paris Seine Paris, Sorbonne Universités, UPMC Université Paris 06 UM CR 18, CNRS UMR 8246, INSERM U1130, Paris, France, [3] Department of Genetic and Behavioral Neuroscience, Gunma University Graduate School of Medicine, Maebashi, Japan, [4] Japan Science and Technology Agency, Tokyo, Japan

OPEN ACCESS

Edited by:
Erika E. Fanselow, Neuroscience Consultant, USA

Reviewed by:
Gianmaria Maccaferri, Northwestern University, USA
Anne-Marie Oswald, University of Pittsburgh, USA

***Correspondence:**
Desdemona Fricker, Institut du Cerveau et de la Moelle Epinière, Sorbonne Universités, UPMC Université Paris 06 UM 75, CHU Pitié-Salpêtrière INSERM U1127, CNRS UMR7225, 47 Boulevard de l'Hôpital, 75013 Paris, France desdemona.fricker@upmc.fr

†Present address:
Jean Simonnet, Bernstein Center for Computational Neuroscience, Humboldt-Universität zu Berlin, Berlin, Germany

‡These authors have contributed equally to this work.

Received: *02 March 2015*
Accepted: *20 April 2015*
Published: *08 May 2015*

Citation:
Nassar M, Simonnet J, Lofredi R, Cohen I, Savary E, Yanagawa Y, Miles R and Fricker D (2015) Diversity and overlap of parvalbumin and somatostatin expressing interneurons in mouse presubiculum. Front. Neural Circuits 9:20. doi: 10.3389/fncir.2015.00020

The presubiculum, located between hippocampus and entorhinal cortex, plays a fundamental role in representing spatial information, notably head direction. Little is known about GABAergic interneurons of this region. Here, we used three transgenic mouse lines, Pvalb-Cre, Sst-Cre, and X98, to examine distinct interneurons labeled with tdTomato or green fluorescent protein. The distribution of interneurons in presubicular lamina for each animal line was compared to that in the GAD67-GFP knock-in animal line. Labeling was specific in the Pvalb-Cre line with 87% of labeled interneurons immunopositive for parvalbumin (PV). Immunostaining for somatostatin (SOM) revealed good specificity in the X98 line with 89% of fluorescent cells, but a lesser specificity in Sst-Cre animals where only 71% of labeled cells were immunopositive. A minority of ∼6% of interneurons co-expressed PV and SOM in the presubiculum of Sst-Cre animals. The electrophysiological and morphological properties of fluorescent interneurons from Pvalb-Cre, Sst-Cre, and X98 mice differed. Distinct physiological groups of presubicular interneurons were resolved by unsupervised cluster analysis of parameters describing passive properties, firing patterns and AP shapes. One group consisted of SOM-positive, Martinotti type neurons with a low firing threshold (cluster 1). Fast spiking basket cells, mainly from the Pvalb-Cre line, formed a distinct group (cluster 3). Another group (cluster 2) contained interneurons of intermediate electrical properties and basket-cell like morphologies. These labeled neurons were recorded from both Sst-Cre and Pvalb-Cre animals. Thus, our results reveal a wide variation in anatomical and physiological properties for these interneurons, a real overlap of interneurons immunopositive for both PV and SOM as well as an off-target recombination in the Sst-Cre line, possibly linked to maternal cre inheritance.

Keywords: inhibition, excitability, morphology, postsubiculum, head direction

Abbreviations: AHP, afterhyperpolarization; AP, action potential; GFP, green fluorescent protein; InsF, instantaneous frequency; PV, parvalbumin; R_{in}, input resistance; RMP, resting membrane potential; SOM, somatostatin.

Introduction

The presubicular cortex, located between the hippocampus and the medial entorhinal cortex, plays a major role in spatial navigation. It contains "head direction" cells which discharge according to the orientation of the animal's head in the environment (Taube et al., 1990; Van Strien et al., 2009; Boccara et al., 2010). Visual information from visual and retrosplenial cortices, and directional information from vestibular nuclei converge in the presubiculum (Calton et al., 2003; Taube, 2007). Presubicular output neurons project directional information to grid cells in the entorhinal cortex (van Groen and Wyss, 1990a; van Haeften et al., 1997; Honda and Ishizuka, 2004; Yoder et al., 2011; Kononenko and Witter, 2012; Rowland et al., 2013).

Three types of pyramidal cells have been distinguished in superficial and deep layers of presubiculum (Simonnet et al., 2013). They all receive frequent inhibitory synaptic events. Spatial information processing in the presubiculum involves local interactions between excitatory glutamatergic neurons and inhibitory GABAergic interneurons. The physiological and anatomical features of presubicular interneurons and their distribution in superficial and deep layers are not yet well defined. In hippocampus and neocortex, distinct subsets of interneurons are believed to play distinct roles. In particular, soma targeting inhibitory neurons control timing and frequency of AP discharge in pyramidal cells (Miles et al., 1996; Fricker and Miles, 2001) and may contribute to the generation of fast oscillations (Cobb et al., 1995; Chrobak and Buzsaki, 1996; Somogyi and Klausberger, 2005; Schlingloff et al., 2014). Dendrite targeting interneurons rather control input signals to pyramidal neurons (Isaacson and Scanziani, 2011). Do analogous interneuron types with comparable functions contribute to represent head direction in the presubicular microcircuit?

Different interneuron functions are mediated by heterogeneous GABAergic cells of multiple embryonic sources (Kepecs and Fishell, 2014). Interneurons may be subdivided according to their somato-dendritic form, synaptic connectivity, electrophysiology and neurochemistry (Freund and Buzsáki, 1996; Cauli et al., 1997; Kawaguchi and Kubota, 1997; Parra et al., 1998; Markram et al., 2004; Rudy et al., 2010; Defelipe et al., 2013; Kubota, 2014). The definition of an interneuron type is still open to debate. Classification by unsupervised clustering has been used to define neuronal classes through sets of common features (Dumitriu et al., 2006; Ma et al., 2006; Karagiannis et al., 2009; McGarry et al., 2010; Perrenoud et al., 2012; Helm et al., 2013). Even so, Battaglia et al. (2013) note that a continuum of phenotypes may exist.

We therefore characterized the electrophysiology and anatomy of two well-defined groups of presubicular interneurons. Interneurons were recorded in slices from three transgenic mouse lines. In Pvalb-Cre tdTomato animals, cells expressing the calcium binding protein PV should be fluorescent, and neurons expressing the neuropeptide SOM should be labeled in Sst-Cre tdTomato and X98 GFP mice. Unsupervised cluster analysis of physiological parameters revealed three main groups of interneurons. These subsets did not coincide perfectly with neurochemical marker expression. Our results establish a dichotomy between Pvalb and X98 interneurons in presubiculum, while Sst-Cre neurons showed similarities with both the X98 and the Pvalb interneurons, partially depending on the parent-of-origin for cre transmission.

Materials and Methods

Animals

Experiments were performed on male and female Pvalb-Cre mice (Jax 008069; Hippenmeyer et al., 2005) and Sst-IRES-Cre mice (Jax 013044; Taniguchi et al., 2011) crossed with the Ai14 Cre reporter line (Jax 007914; Madisen et al., 2010). Cre-mediated recombination resulted in the expression of red fluorescent tdTomato labeling in subsets of GABAergic neurons. The terms "Sst-Cre" or "Pvalb-Cre" will be used when referring to the mouse line. "SOM" and "PV" will be used to refer to the expression of the neuropeptide or Ca-binding protein marker. We will show that these terms are not always equivalent. We also used a transgenic mouse line X98 (Jax 006340), in which GFP expression driven by the GAD67 short promoter, labels a subset of SOM positive neurons. With axons arborizing in layer I, these cells resemble neocortical Martinotti cells (Ma et al., 2006). The total number of interneurons in all presubicular layers was quantified using GAD67-GFP knock-in mice, in which GFP was specifically expressed in GABAergic neurons under the control of the endogenous GAD67 promoter (Tamamaki et al., 2003). Our care and use of animals conformed to the European Community Council Directive of 22 September 2010 (2010/63/EU) and French law (87/848). Our study was approved by the local ethics committee Charles Darwin N°5 and the French Ministry for Research.

Immunohistochemistry

Mice were anesthetized intraperitoneally with ketamine hydrochloride and xylazine (100 and 15 $mg.kg^{-1}$, respectively). They were then perfused transcardially with 0.9% saline containing heparin (100–200 UI/ml followed by 30–50 ml of a fixative solution containing 4% paraformaldehyde in 0.1 M phosphate buffer (PB). Dissected brains were post-fixed overnight in the same solution at 4°C, rinsed three times for 3 min, and then placed in a 30% sucrose solution at 4°C for at least 24 h. Horizontal sections of thickness 60 μm were cut in 0.1 M PBS using a slicing vibratome (Microm HM650 V). Membranes were permeabilized by three cycles of freeze-thawing slices on dry ice in a 30% sucrose containing solution. Sections were washed three times (2 × 30 min, 1 × 60 min) in PBS 0.1M (BupH^{TM} Phosphate Buffered Saline Packs, Thermo Fisher Scientific), then transferred to a saturation buffer containing 2% milk powder and 0.3–0.4% Triton X-100 in PBS 0.1M, and agitated for 2 h at room temperature. Sections were then transferred into primary antibody solution of 0.1M PBS and 0.3% Triton X-100 and gently agitated, overnight at 4°C. Sections were rinsed three times (2 × 30 min, 1 × 60 min) in PBS then incubated in dilutions of secondary antibody, conjugated to different fluorophores, for 4 h at room temperature under gentle agitation.

4′,6-diamidino-2-phenylindole (DAPI, Sigma) was always added to secondary antibodies containing solutions (1:1000) to stain cellular nuclei. For SOM immunostaining, we increased the incubation time with the primary antibody to 48–72 h and with the secondary antibody to 24 h, both at 4°C. For SOM and PV co-labeling, these long incubation times were applied as well.

The following primary antibodies were used: Goat Anti-PV (Swant, PVG-214, 1:500), Rat Anti-Somatostatin (Chemicon #MAB357, 1:200), Mouse Anti-NeuN (Millipore #MAB377, 1:500), rabbit anti-GFP (Millipore #AB3080, 1:500). Secondary antibodies were: Donkey Anti-Mouse (Cy3, Jackson ImmunoResearch, 1:500), Donkey Anti-Rat (Millipore, A488, 1:500), Donkey Anti-Rabbit (Cy2, Jackson, 1:500), Donkey Anti-Goat (Life technologies A647 or A488, 1:500). Stained sections were mounted on glass slides, coverslipped with anti-fade Prolong Gold (Life technologies).

Image Acquisition and Analysis

Stained slices were visualized with a QImaging Retiga EXI camera (Qimaging Surrey, BC, Canada), and scanned with an Optigrid II (Thales Optem, Qioptik, Rochester, NY, USA) on an inverted Olympus IX81 microscope. The Optigrid system permitted the acquisition of structured images Stacks of 50–80 images (*z*-step, 0.7 μm) were acquired per slice, using an oil immersion objective (20x, NA 0.9). Presubicular layers and borders were defined using specific cytoarchitectonic features identified by DAPI staining. Images were uniformly adjusted for contrast and brightness.

For each brain slice, fluorescent tdTomato+ or GFP+ cells from all layers of the presubiculum were identified visually by complete scans of optical sections. Cell counting was performed using Volocity software (Improvision, Perkin-Elmer, Coventry, UK) to measure cell numbers in defined volumes. Counts were made only from slices with optimal signal to noise levels and very low background fluorescence. Visual checks only revealed very rare ambiguities for weakly fluorescent neurons. Cell density was calculated as the number of fluorescent cells/volume of each presubicular layer (nb/mm^3).

Antibody fluorescence was examined for each tdTomato+ or GFP+ cell. A cell was regarded as positive for a given antibody when somatic fluorescence was clearly higher than background levels. Colocalization of antibody labeling was confirmed from observations at all levels of a stack of optical sections for the soma of a neuron. Percentages of single and dual-immuno labeled fluorescent neurons were obtained by dividing the number of immuno-labeled fluorescent neurons by the total number of GFP+ or tdTomato+ neurons. Data are given as mean ± SEM.

Slice Preparation for Patch-Clamp Recording

Acute slices containing the hippocampus, subicular complex and entorhinal cortex were prepared from 21 to 45 days-old mice. After ketamine hydrochloride and xylazine anesthesia (100 and 15 mg.kg^{-1}, respectively), animals were perfused through the heart with a solution containing 125 NaCl, 25 sucrose, 2.5 KCl, 25 $NaHCO_3$, 1.25 NaH_2PO_4, 2.5 D-glucose, 0.1 $CaCl_2$, 7 $MgCl_2$ (in mM) cooled to 4°C and equilibrated with 5% CO_2 in O_2. Animals were decapitated and horizontal, 280–320 μm thick brain sections were cut in the same solution using a vibratome (Leica VT1000S or Microm HM650V). They were stored for at least 1 h at 22–25° C in a holding chamber filled with ACSF containing (in mM): 124 NaCl, 2.5 KCl, 26 $NaHCO_3$, 1 NaH_2PO_4, 2 $CaCl_2$, 2 $MgCl_2$, and 11 D-glucose, bubbled with 5% CO_2 in O_2 (pH 7.3, 305–315 mOsm/L). Slices were then transferred to a recording chamber (volume 2–3 ml, temperature 33–35°C) mounted on either an Axioskop 2 FS plus microscope (Zeiss, France) or a BX51WI microscope (Olympus, France).

Whole-Cell Patch-Clamp Recordings

Recordings were made with glass pipettes pulled using a Brown–Flaming electrode puller (Sutter Instruments) from borosilicate glass of external diameter 1.5 mm (Clark Capillary Glass, Harvard Apparatus). Electrode resistance was 3–6 MΩ after filling with a solution containing (in mM): 135 K-gluconate, 1.2 KCl, 10 HEPES, 0.2 ethylene glycol tetraacetic acid (EGTA), 2 $MgCl_2$, 4 MgATP, 0.4 Tris-GTP, 10 Na_2-phosphocreatine and 2.7–7.1 biocytin. The pH of the pipette solution was adjusted to 7.3 with KOH and the osmolarity was 290 mOsm. Slices were visualized using infrared-differential interference contrast optics. Fluorescently labeled PV, SST or X98 interneurons were identified using LED illumination with appropriate emission/excitation filters (OptoLED, Cairn Research, Faversham, UK). Whole-cell current-clamp recordings were made using a MultiClamp 700B amplifier and pCLAMP software (Molecular Devices, Union City, CA, USA). Potential signals were filtered at 6 kHz and digitized at 20–50 kHz and an estimated junction potential of ∼15 mV was not corrected.

Electrophysiological Analysis

Recorded signals were analyzed with Axograph X and routines written in MATLAB (The Mathwork). Cellular parameters were measured at least 3–5 min after whole-cell records were established. RMP was the mean potential over at least 10 s. Most electrophysiological parameters were measured from responses to step current injections of 800 ms duration applied from a fixed membrane potential of −65 mV. Injected currents increased from negative to positive values, with a range of amplitudes that resulted in hyperpolarization to about −100 mV during the first step and depolarizations to maximum sustained firing frequency. Depending on the resistance of the recorded neuron, the first hyperpolarizing step was in the range of −50 pA to −500 pA with a step change of 5–50 pA. Neuronal R_{in} was determined as the slope of the current-voltage (I-V) relationship between −71 and −64 mV. Membrane time constants (τ) were estimated from a double exponential fit to the negative deflection of membrane voltage (Levenberg–Marquardt algorithm; Golowasch et al., 2009) in response to a 800 ms hyperpolarizing current injection inducing a voltage change of up to 15 mV. A "sag ratio," indicative of I_h expression, was calculated for steps in which the voltage deflection reached values between −105 and −90 mV, as the ratio of the maximal negative potential, typically from 0 to 200 ms, divided by the mean steady state voltage deflection, between 400 and 800 ms.

Action potentials of amplitude at least 20 mV were detected from continuous periods of rising membrane potential. Rheobase (or threshold current for firing) was defined as the smallest current step of 800 ms that elicited at least one AP. Firing frequency (Hz) was deduced either by averaging all instantaneous frequencies of a given step (MeanInsF) or dividing the number of APs over time (*APs/sec*). Input–output (I–O) curves were constructed by plotting firing frequency (either *MeanInsF* or *APs/sec*) as a function of injected current. The I–O gain was measured from a linear fit to frequencies measured from the nine current steps after rheobase. The coefficient of variation (CV) of firing frequency was calculated as SD divided by the mean of InsF when at least three APs were elicited. This value gave an index of firing regularity; values were higher when firing was more irregular. First AP-Latency was calculated from the first AP in spike trains induced by injecting a current of amplitude twice rheobase. The adaptation index (AI) was defined as the ratio of the mean of the three last instantaneous frequencies divided by the first InsF, measured from a step with minimum CV.

Action potential waveform features were obtained by averaging the measures from the first AP elicited, at latency less than 100 ms, by three consecutive depolarizing steps. AP threshold (threshold) was defined as the membrane potential when dV/dt > 30 mV/ms. AP peak was its maximum potential. The AP rising amplitude (amplitude) was the difference between the threshold and the peak AP voltage. AP width (width) was measured from the half-height of the AP rising phase. *Max depolarization rate* and *max repolarization rate* were defined as the maximum and minimum dV/dt, during rising and falling phases of APs, respectively. The AHP was the voltage minimum after the AP peak and its amplitude (AHP) was defined as the difference from the threshold.

Cluster Analysis

We performed unsupervised cluster analysis using 17 electrophysiological parameters from 159 neurons recorded in superficial and deep layers of the presubiculum. The parameters were: (1) RMP, (2) R_{in}, (3) tau, (4) sag ratio, (5) rheobase, I–O gain ((6) *MeanInsF* or (7) *APs/sec);* (8) *MeanInsF* at 2 times rheobase, (9) CV, (10) latency, (11) AI; AP properties including (12) threshold, (13) width, (14) amplitude, (15) AHP, (16) maximum depolarization rate and (17) maximum repolarization rate.

Interneurons were grouped on similarities of these parameters, using Ward's method (Ward, 1963), with Euclidean distances measured as previously described (Simonnet et al., 2013). Cluster analysis was implemented using the statistics toolbox of MATLAB (The Mathwork). The Thorndike procedure (Thorndike, 1953), where jumps in distances within clusters indicate prominent differences between groups, was used to examine resulting clusters.

Neuronal Morphology: Staining, Image Acquisition, and 3D Reconstruction

After recordings with pipettes containing biocytin (1–3 $mg.ml^{-1}$), slices were fixed in 4% paraformaldehyde in 0.1 M PB at 4°C for 24 h. Slices were then rinsed in PBS (3 × 3 min) and cryoprotected in 30% sucrose mixture at 4°C overnight. Membranes were permeabilized by three cycles of freeze-thawing over dry ice and then washed three times with PBS (2 × 30, then 1 × 60 min). Slices were agitated in saturation buffer containing 2% milk powder and 1% Triton X-100 in PBS 0.1M for 3 h at room temperature. Then, section were gently agitated with Streptavidin–Cy3 or Cy5 conjugate (1:500, Invitrogen, Eugene, OR, USA) and DAPI in the blocking solution overnight at 4°C. After washing with PBS (2 × 30 min, 1 × 60 min). Slices were mounted on coverslips using anti-fade Prolong Gold medium (Life technologies). Filled cells were visualized with a QImaging Retiga EXI camera on an inverted Olympus IX81 microscope. Structured images were acquired with an Optigrid system and Volocity software (Improvision, Perkin-Elmer, Coventry, UK). Stacks of 75–250 images (*z*-step 0.7 μm) were acquired with a 20X, 0.9NA oil immersion objective. Stacks were then imported to the Neurolucida software (Microbrightfield, Williston, VT, USA) for three-dimensional reconstruction. The "layer length" analysis feature of the Neurolucida software was used to measure dendritic and axonal lengths in specific layers of the presubiculum as previously (Simonnet et al., 2013). DAPI staining was used to define boundaries and layers of the presubiculum. We did not correct for tissue shrinkage.

Statistics

Results are given as mean ± SEM. Statistical analysis was performed with Prism (GraphPad Software, Inc.) and MATLAB (The Mathwork). The Wilcoxon signed rank test for matched pairs was used to compare non-parametric data in matched samples. The Kruskal–Wallis one-way analysis of variance (ANOVA) test followed by Dunn's *post hoc* comparison was used for comparison between more than two groups. Significance levels are indicated as *p* values.

Results

Layer Distribution and Immunohistochemistry of GABAergic and non-GABAergic Neurons in Mouse Presubiculum

Figure 1A shows the presubiculum in the context of the mouse hippocampal formation. Six cytoarchitectonic layers can be recognized. The high density of cell bodies in layer II serves as a good marker to define the proximal transition to the subiculum and the distal border with parasubiculum. In ventral horizontal sections, the presubiculum is small with a triangular shape; it becomes broader in dorsal sections. Dorsal presubiculum is also termed postsubiculum (van Groen and Wyss, 1990a; **Figures 1A–C**). Most presubicular neurons are glutamatergic and a smaller proportion are GABAergic. We measured the densities and distributions of GABAergic and non-GABAergic neurons at mid-dorsal level (**Figure 1A**). In 12 slices from 3 adult GAD67-GFP knock-in animals (**Figures 1D–F**), NeuN labeled neurons and GFP+ neurons were counted in superficial (I, II, and III) and deep layers (IV, V/VI). NeuN labeling was sparse in layer I, contrasting with a high neuronal density in layer

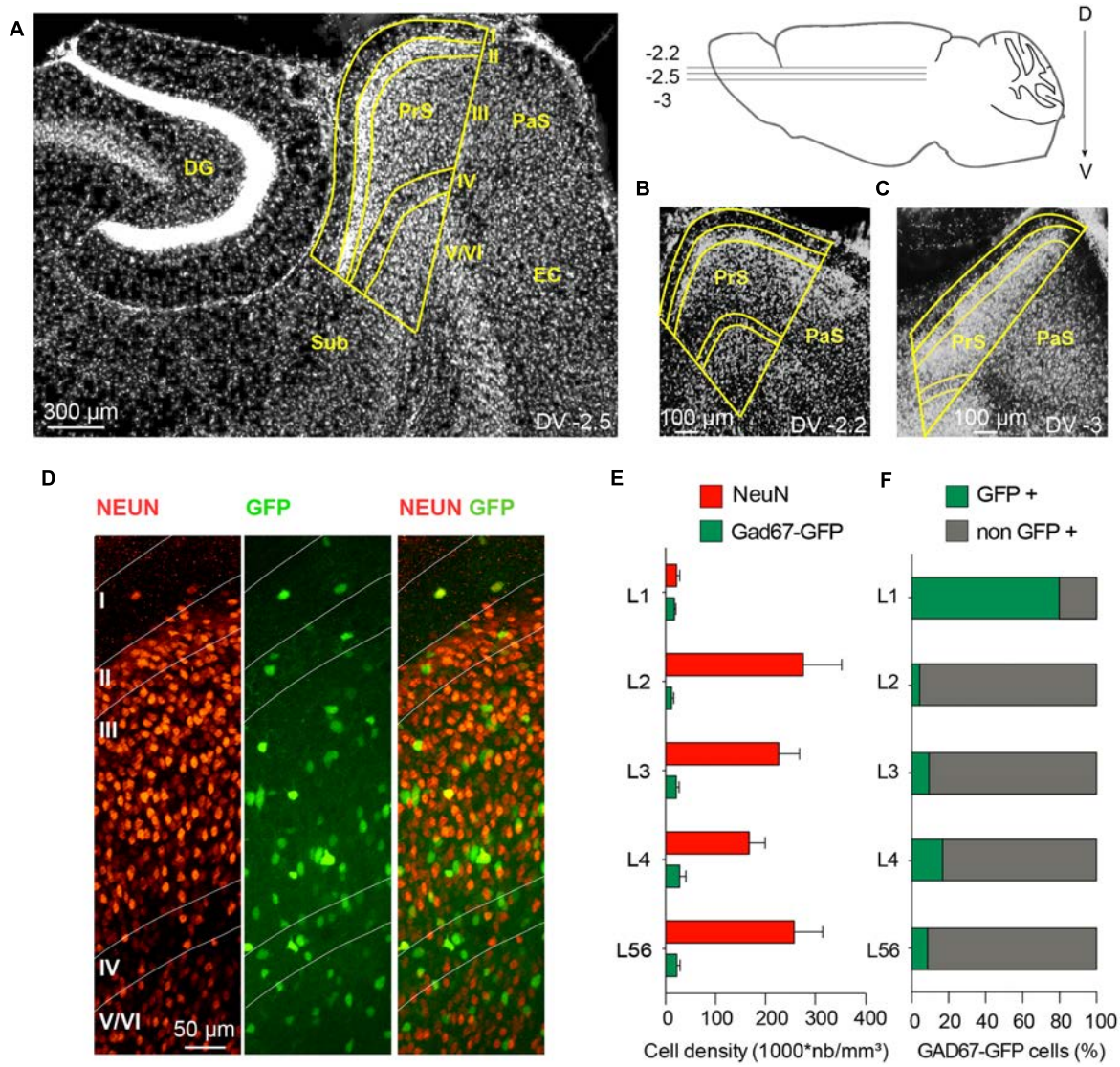

FIGURE 1 | Spatial distribution of GABAergic and non-GABAergic neuron somata in mouse presubiculum. (A) Horizontal section of mouse presubiculum (PrS) stained with DAPI. Dorso-ventral (DV) level −2.5 mm. The presubiculum continues from the subiculum (Sub), faces the dentate gyrus (DG), and is adjacent to parasubiculum (PaS) and entorhinal cortex (EC). Changes in the disposition of these regions at DV −2.2 mm **(B)** and DV −3 mm **(C)**. **(D)** NeuN staining (left), GFP fluorescence (middle), and an overlay (right) of all layers of presubiculum in a slice from a GAD67-GFP mouse. **(E)** Mean density of NeuN stained neurons (red) and GAD67-GFP+ neurons (green) for each layer. Mean neuronal density and its standard error were measured from 12 horizontal slices from 3 mice. **(F)** Proportions of GAD67-GFP+ neurons (green) and non-GABAergic neurons (NeuN+, GFP-, gray) in each layer. Scale bars: **(A)** 300 µm; **(B,C)** 100 µm; **(D)** 50 µm.

II (275 651 ± 134 225 cells/mm^3). Neuronal density in layer III was apparently lower and that in layer IV even lower (167 484 ± 55 674 cells/mm^3). Neuronal density in layers V and VI, which are not readily distinguished, increased toward levels similar to those of layer III. We assume that GFP-labeled neurons of the GAD67 knock-in line represent all GABAergic neurons of the presubiculum. Overall, 11% of all neurons were GFP-positive. This ratio is similar to the proportion of interneurons in hippocampus and neocortex. GABAergic cell somata were present in all layers, including layer I. The highest laminar density of about 30 000 GFP+ neurons/mm^3 was detected in layer IV. GABAergic GFP+ neurons were a majority, ~80%, of all NeuN labeled neurons in layer I. Lower proportions of GABAergic to NeuN labeled neurons were found in all other layers: 4% in layer II, 9% in layer III, 16% in layer IV and 9% in layers V/VI.

We examined the presubicular distribution of labeled neurons in transgenic mice created to label cells expressing PV or SOM: female Pvalb-Cre (Hippenmeyer et al., 2005) and female Sst-IRES-Cre mice (Taniguchi et al., 2011) were crossed with a reporter line expressing a red fluorescent protein, tdTomato (Ai14, Madisen et al., 2010). We also examined the X98 mouse

line (Ma et al., 2006), where a subset of SOM expressing interneurons is labeled with GFP.

The distribution of interneurons in these mouse lines was quantified as the density of fluorescently labeled cells, in different layers of the presubiculum, and compared to that of interneurons in GAD67-GFP mice. Pvalb-Cre interneurons were absent from layer I. Their mean density was higher in layer III than in layer II or in layers V/VI (**Figures 2A,D**). Pvalb cell bodies were smaller and neurite staining less intense than in neighboring parasubiculum (not shown). tdTomato-labeled Sst-Cre interneurons were more abundant in deep than in superficial layers, with maximal densities in layer IV and upper layer V/VI (**Figures 2B,D**). No Sst-Cre interneurons were found in layer I. GFP-labeled neurons of the X98 line were sparse, with less cells labeled than in the Pvalb or Sst-Cre line. The density of labeled interneurons was highest in layer IV, and no cells were labeled in layer I (**Figures 2C,D**). We noted that the density of Sst-Cre tdTomato labeled neurons in layers V/VI exceeded that of GAD67-GFP+ neurons. This was unexpected, since all GABAergic neurons should be labeled in GAD67-GFP animals (Tamamaki et al., 2003) and in the Sst-Cre line only a subset of SOM expressing interneurons should be labeled.

We therefore used antibodies against PV and SOM to explore the specificity of labeled cells in the Pvalb-Cre and Sst-Cre lines and in X98 mice. The numbers of tdTomato+ or GFP+ fluorescent presubicular cells that were also immunopositive for PV or SOM were quantified in at least three non-adjacent slices from at least three animals for each line (**Figures 3A–D**). As expected, the great majority of tdTomato+ neurons in the Pvalb-Cre line were immunopositive for PV (326/374); very few were positive for SOM (7/374). Also, most GFP+ neurons of the X98 line were positive for SOM (155/175); none were labeled for PV (0/175). However for the Sst-Cre line, while 403 out of 570 tdTomato+ presubicular cells were positive for SOM, 154 out of 674 Sst-Cre tdTomato+ cells were positive for PV (**Figures 3C,D**). The SOM immuno-labeling was significantly lower in deep layers (IV–VI) of presubiculum (66 ± 5%) than in superficial layers (78 ± 3%; Wilcoxon matched-pairs signed rank test, $P < 0.05$), while PV labeling was significantly higher in deep layers (28 ± 3%) than in superficial layers (16 ± 3%; Wilcoxon matched-pairs signed rank test, $P < 0.01$).

We next asked if PV labeled neurons of the Sst-Cre mouse line might reflect the off-target recombination that has been described

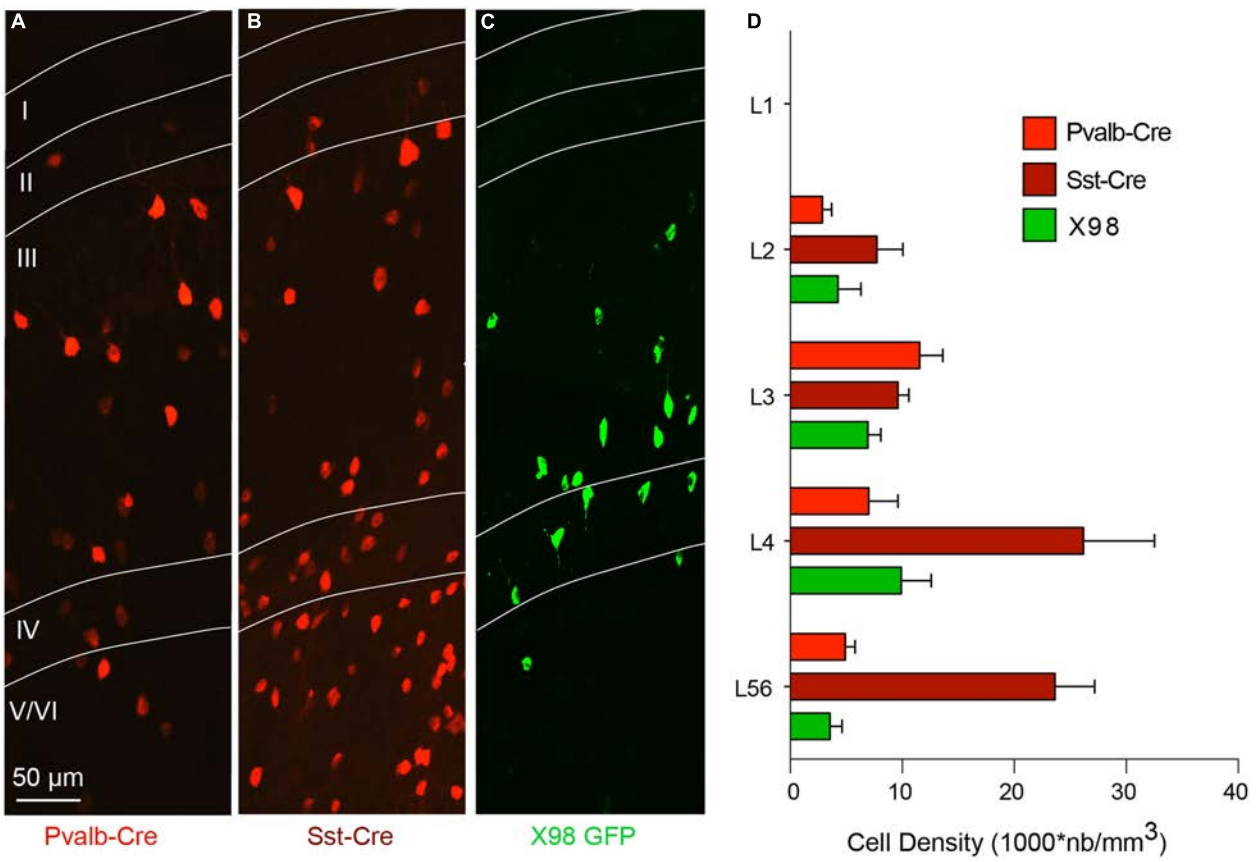

FIGURE 2 | Layer-specific distribution of presubicular interneurons in three mouse lines. (A–C) show horizontal sections of presubiculum, with fluorescently labeled neurons from the Pvalb-Cre line **(A)**, the Sst-Cre line **(B)**, both with maternal cre inheritance and tdTomato as reporter (red), and GFP+ interneurons from an X98 animal (green; **C**). Layers are indicated and the scale bar is 50 µm **(D)** Densities (mean ± SEM) of labeled neurons from these three lines in different layers of presubiculum. Data from 6 slices of three mice for each strain.

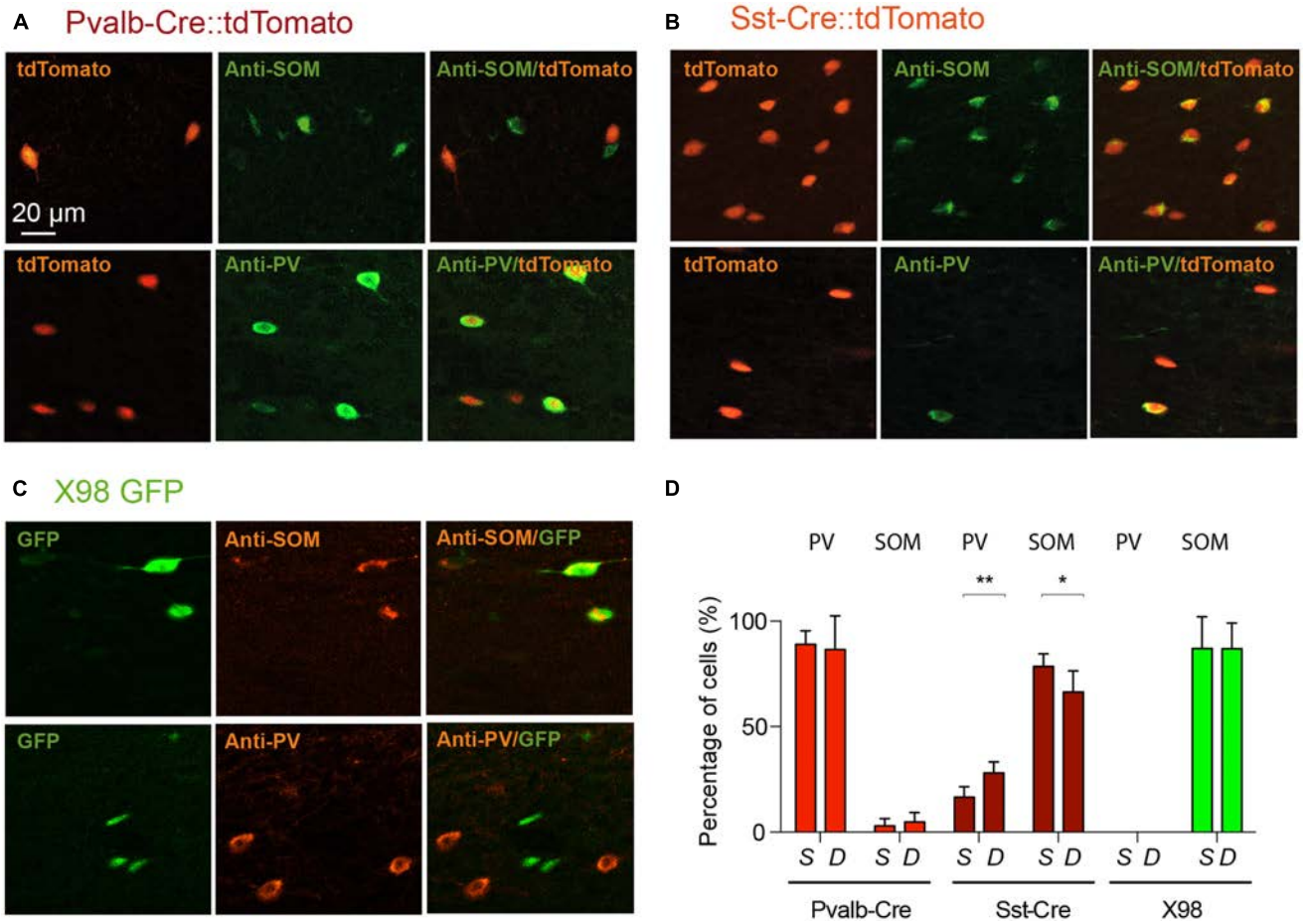

FIGURE 3 | Verification by PV or SOM immunostaining of the identity of labeled neurons from Pvalb-Cre tdTomato, Sst-Cre tdTomato, or X98 GFP animals. Presubicular sections from **(A)**, Pvalb-Cre tdTomato mice and **(B)** Sst-Cre tdTomato mice, both with maternal cre inheritance, and **(C)**, X98 GFP mice, immunostained with anti-SOM (top) and anti-PV antibodies (bottom). For each panel fluorescent labeled neurons of the cell line are on the right, immunostaining in the middle and merge on the left. The scale bar is 20 µm. **(D)** Bar graphs indicate percentages of antibody labeling of fluorescent (tdTomato or GFP) neurons (mean ± SEM) from each mouse line. Data from at least 6 slices from 3 animals of each mouse line and each antibody (Wilcoxon's test, $*P < 0.05$, $**P < 0.01$).

in this Cre line (Hu et al., 2013), or whether some presubicular interneurons truly express both PV and SOM. **Figure 4** shows the results of double-labeling with anti-PV and anti-SOM antibodies in slices from Pvalb-Cre and from Sst-Cre tdTomato mice. We confirmed that a small proportion of interneurons were immuno-positive for both markers. In the Pvalb-Cre line 2 ± 1% of labeled cells were stained by both antibodies, and in Sst-Cre mice 6 ± 3% of labeled neurons expressed both PV and SOM. This fully accounts for the SOM expressing cells detected in the Pvalb-Cre line. However, neurons co-expressing both PV and SOM only partly account for the numbers of PV expressing neurons detected in Sst-Cre tdTomato+ labeled cells.

Furthermore a number of tdTomato+ cells were not immunopositive for either PV or SOM. Such neither SOM nor PV expressing somata were detected in 7% of Pvalb-Cre tdTomato+ cells (12/181), more frequently in superficial than in deep layers (8 vs. 4% respectively). In the Sst-Cre mice, 19% (85/449) of tdTomato+ cell bodies were not immunopositive for either SOM or PV. These double immunonegative neurons were more numerous in deep (22%) than in superficial layers (14%).

Cluster Analysis of Electrophysiological Parameters Reveals Groups of Presubicular Interneurons

We measured passive membrane properties, AP waveforms and firing patterns of 142 presubicular interneurons for a classification based on electrophysiological criteria alone. All recordings were made from labeled neurons in slices from the mid-to-dorsal portion of presubiculum. Dorso-ventral depths ranged from −3 to −2.2 mm, with most interneurons recorded from a level close to −2.5 mm (cf. **Figure 1A**). Fluorescent neurons, 46 from Pvalb-Cre tdTomato+ mice, 61 from the Sst-Cre tdTomato+ line and 35 GFP+ neurons of the X98 line, were recorded randomly from either superficial or deep layers of presubiculum. The same physiological parameters were measured for 17 superficial layer

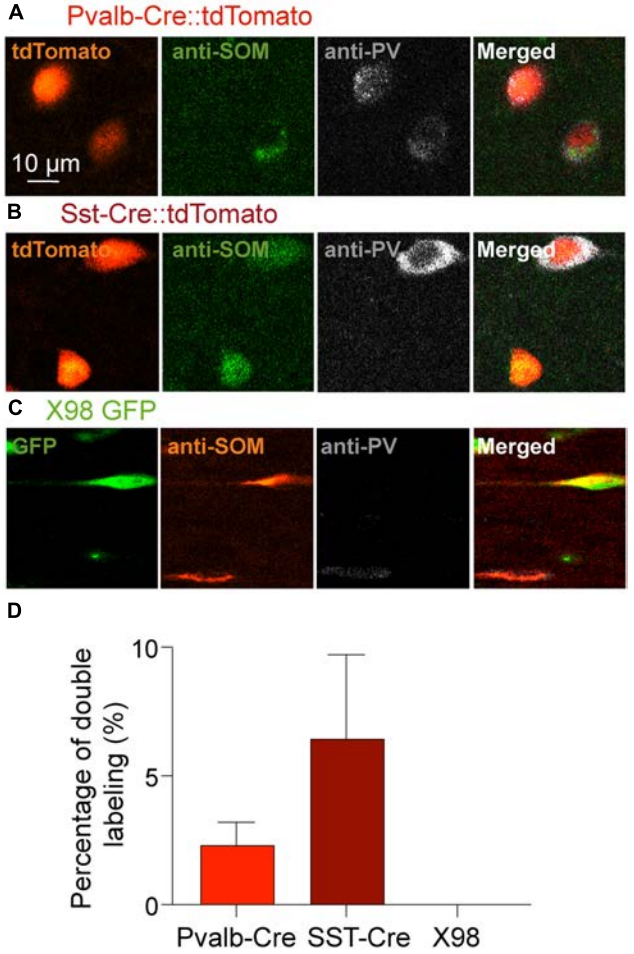

FIGURE 4 | Double immunostaining of mouse presubicular sections for PV and SOM. Staining of tissue from **(A)** Pvalb-Cre tdTomato, **(B)** Sst-Cre tdTomato and **(C)** X98 GFP animals with antibodies against SOM (green or red) and PV (gray). **(A–C)** show fluorescent signals from labeled neurons of each mouse line (left), immunostaining for SOM, for PV and a merged image (right). **(D)** 2% of Pvalb-Cre tdTomato+ cells were immunopositive for both PV *and* SOM. 6% of Sst-Cre tdTomato+ cells were positive for both PV *and* SOM. Co-marked cells were found in both deep and superficial layers. Since X98 GFP+ cells were never immunopositive for PV, there was no co-labeling.

pyramidal neurons as an external reference. Unsupervised cluster analysis using Ward's method (Ward, 1963) was based on 17 electrophysiological variables as listed in **Table 1**.

Figure 5A shows the hierarchical tree diagram of clusters that emerged. The tree diagram initially separated two populations: the first branch (I) included all principal neurons, all X98 GFP+ cells, and some Sst-Cre tdTomato+ cells; the second branch (II) included all Pvalb-Cre tdTomato+ cells and some Sst-Cre tdTomato+ cells. Decreasing the cut-off value for cluster separation completely isolated the pyramidal neurons, as a highly homogenous population of cells, in cluster 0 (**Figure 5A**). **Figure 5B** shows a typical pyramidal cell. This separation validates the clustering method. While the pyramidal neurons were not considered further, they served as an external reference for the interneuron containing clusters. Three interneuron-containing clusters point to the existence of three main cell types in recorded presubicular interneurons. X98 GFP+ neurons (cluster 1) were strictly segregated from Pvalb-Cre tdTomato+ neurons (clusters 2 and 3). While labeled cells from these two mouse lines were expected to be distributed in distinct clusters, we found a different situation for tdTomato+ interneurons recorded from Sst-Cre mice. A majority of them (55%) clustered together with SOM expressing X98 GFP+ neurons (cluster 1) but a large minority (45%) were grouped together with Pvalb-Cre tdTomato+ interneurons (in clusters 2 and 3). Within-cluster Euclidean distances for clusters 1, 2, and 3 were similar (13, 12, and 15, respectively) even though the Thorndike procedure suggested clusters 2 and 3 might be combined. We explore interneurons in the three clusters in detail below.

Cluster 1: Mainly Somatostatin Expressing, Low Rheobase Adapting Interneurons

Cluster 1 comprised 65 interneurons, 35 of them GFP+ cells from the X98 mouse line (54%), and 30 Sst-Cre tdTomato+ cells (46%). **Figure 5C** shows a cell of this cluster, a Martinotti type interneuron from the X98 line, with an adapting firing pattern and broad APs. The soma of this SOM expressing, adapting interneuron, typical for cluster 1, was located in layer III.

Cluster 1 interneurons typically fired spontaneously both in the whole-cell mode and in cell-attached records made before rupturing the membrane. Mean RMP was -54 ± 1 mV ($n = 65$; mean ± SEM), significantly more positive than for the other clusters ($P < 0.001$), and the AP threshold was -38.6 ± 0.4 mV. R_{in} was 374 ± 17 MΩ, twice as high as for cluster 2 cells, and membrane time constant, tau, was 32 ± 2 ms, almost three times longer than in the other two clusters. Hyperpolarizing current injections induced a marked voltage sag (**Figure 6B**; sag ratio 1.22 ± 0.01). Cluster 1 cells could fire regularly or irregularly, with the highest CV at twofold rheobase current levels (0.24 ± 0.02) and a stronger frequency adaptation (AI, 0.70 ± 0.01) than cluster 2 and cluster 3 cells. **Figures 6A,B** (left column) show distinct firing patterns of three cells of cluster 1. Injected currents initiated APs easily, with a mean rheobase of 40 ± 3 pA. Input–output curves, obtained by plotting AP frequency against injected current (**Figure 6C**), had a mean initial slope of 778 ± 28 Hz.nA^{-1}. The firing frequency at double rheobase current level was 35 ± 2 Hz, the first AP latency was 21 ± 1 ms. AP mean amplitude was 82 ± 1 mV and width was 0.29 ± 0.01 ms. The maximum AP depolarization and repolarization rates were 567 ± 11 and -329 ± 9 V.s^{-1} respectively. Spike AHPs were sometimes complex or bi-phasic (**Figure 5C**), with mean maximal amplitude of -23.8 ± 0.5 mV.

Cluster 3: Mostly Fast-Spiking Interneurons from the Pvalb-Cre Line

The 29 neurons of cluster 3 comprised 22 (76%) tdTomato+ neurons of the Pvalb-Cre line, and 7 (24%) from the Sst-Cre line. **Figure 5E** shows a basket shaped interneuron from the Pvalb-Cre line with fast-spiking (FS) firing pattern typical for this cluster. The cell body of this neuron was located in layer III, and all

TABLE 1 | Electrophysiological parameters (mean ± SEM) of presubicular pyramidal cells (PC, *n* = 17) and interneurons recorded from the three mouse lines (X98 GFP, 35; Sst-Cre tdTomato, 61; Pvalb-Cre tdTomato, 46). Using these parameters for Ward's unsupervised cluster analysis permitted separation of clusters 0, 1, 2, and 3. Values (mean ± SEM) for each parameter are given for each cluster in (B).

	PC			X98 GFP			Sst Cre tdTomato			Pvalb Cre tdTomato		
	Mean	**SEM**	***n***	**Mean**	**SEM**	***n***	**Mean**	**SEM**	***n***	**Mean**	**SEM**	***n***
(A)												
RMP (mV)	−78	1	17	−54	1	35	−58	1	61	−65	1	46
R_{in} (MΩ)	250	24	17	376	22	35	285	20	61	148	9	46
Time constant (ms)	28	4	17	36	3	35	21	2	61	10	1	46
Sag	1.04	0.00	17	1.25	0.02	35	1.15	0.01	61	1.10	0.01	46
Rheobase (pA)	84	9	17	40	4	35	72	9	61	175	14	46
I-O gain (Hz/nA; MeanInsF)	275	23	17	748	38	35	917	54	61	1015	92	46
I-O gain (Hz/nA; APs/sec)	270	22	17	732	46	35	885	59	61	1065	98	46
MeanInsF (Hz)	33	3	17	33	3	35	74	8	61	247	19	46
Coefficient of variation	0.21	0.02	17	0.28	0.03	35	0.15	0.01	61	0.06	0.00	46
Latency (ms)	27	3	17	21	2	35	15	1	61	13	2	46
Adaptation Index	0.72	0.04	17	0.66	0.02	35	0.86	0.02	61	0.94	0.02	46
Threshold (mV)	−35.5	0.5	17	−38.2	0.4	35	−38.5	0.5	61	−39.6	0.6	46
Width (ms)	0.56	0.02	17	0.27	0.01	35	0.27	0.01	61	0.20	0.01	46
Amplitude (pA)	84	2	17	83	1	35	77	1	61	72	1	46
AHP (mV)	−14.7	0.6	17	−23.8	0.7	35	−23.5	0.5	61	−23.7	0.6	46
Max depol. rate ($V.s^{-1}$)	517	22	17	598	14	35	571	13	61	637	18	46
Min depol. rate ($V.s^{-1}$)	−134	6	17	−355	11	35	−353	14	61	−498	22	46
	Cluster 0			**Cluster 1**			**Cluster 2**			**Cluster 3**		
	Mean	**SEM**	***n***	**Mean**	**SEM**	***n***	**Mean**	**SEM**	***n***	**Mean**	**SEM**	***n***
(B)												
RMP (mV)	−78	1	17	−54	1	65	−60	1	48	−70	1	29
R_{in} (MΩ)	250	24	17	374	17	65	189	11	48	137	17	29
Time constant (ms)	28	4	17	32	2	65	11	1	48	13	2	29
Sag	1.04	0.00	17	1.22	0.01	65	1.11	0.01	48	1.09	0.01	29
Rheobase (pA)	84	9	17	40	3	65	113	8	48	202	23	29
I–O gain (Hz/nA; MeanInsF)	275	23	17	778	28	65	762	41	48	1437	131	29
I–O gain (Hz/nA; APs/sec)	270	22	17	746	35	65	747	43	48	1525	132	29
MeanInsF (Hz)	33	3	17	35	2	65	128	7	48	297	27	29
Coefficient of variation	0.21	0.02	17	0.24	0.02	65	0.07	0.00	48	0.08	0.02	29
Latency (ms)	27	3	17	21	1	65	14	2	48	8	2	29
Adaptation Index	0.72	0.04	17	0.70	0.01	65	0.92	0.02	48	1.00	0.02	29
Threshold (mV)	−35.5	0.5	17	−38.4	0.4	65	−37.4	0.5	48	−42.2	0.7	29
Width (ms)	0.56	0.02	17	0.29	0.01	65	0.23	0.00	48	0.18	0.01	29
Amplitude (pA)	84	2	17	82	1	65	76	1	48	69	2	29
AHP (mV)	−14.7	0.6	17	−23.8	0.5	65	−23.8	0.5	48	−22.9	0.8	29
Maximum depolarization rate ($V.s^{-1}$)	517	22	17	567	11	65	627	14	48	623	26	29
Minimum depolarization rate ($V.s^{-1}$)	−134	6	17	−329	9	65	−409	15	48	−547	30	29

anatomically recovered neurons in this cluster were superficial layer cells.

The mean resting potential of cluster 3 interneurons was −70 ± 1 mV (n = 29, mean ± SEM), more negative than values for clusters 1 or 2. Their mean firing threshold was −42.2 ± 0.7 mV, and these cells never fired spontaneously. R_{in} was 137 ± 17 MΩ, half the value of cluster 2 and three times less than cluster 1. The membrane time constant, tau, was 13 ± 2 ms, similar to cluster 2, but almost three times less than for cluster 1. Virtually no voltage sag was observed, even during large hyperpolarizations (**Figure 4B**, right column; sag ratio 1.09 ± 0.01). Induced to discharge by current injection, cluster 3 cells fired with a non-accommodating, FS pattern characteristic of basket cells. **Figures 6A,B** show the stereotyped firing patterns for three neurons from cluster 3 (right column). The CV was low (0.08 ± 0.02) and the AI was 1.00 ± 0.02. The rheobase current to induce firing was 202 ± 23 pA, higher than for clusters 1 or 2. The input–output curves rose steeply, with

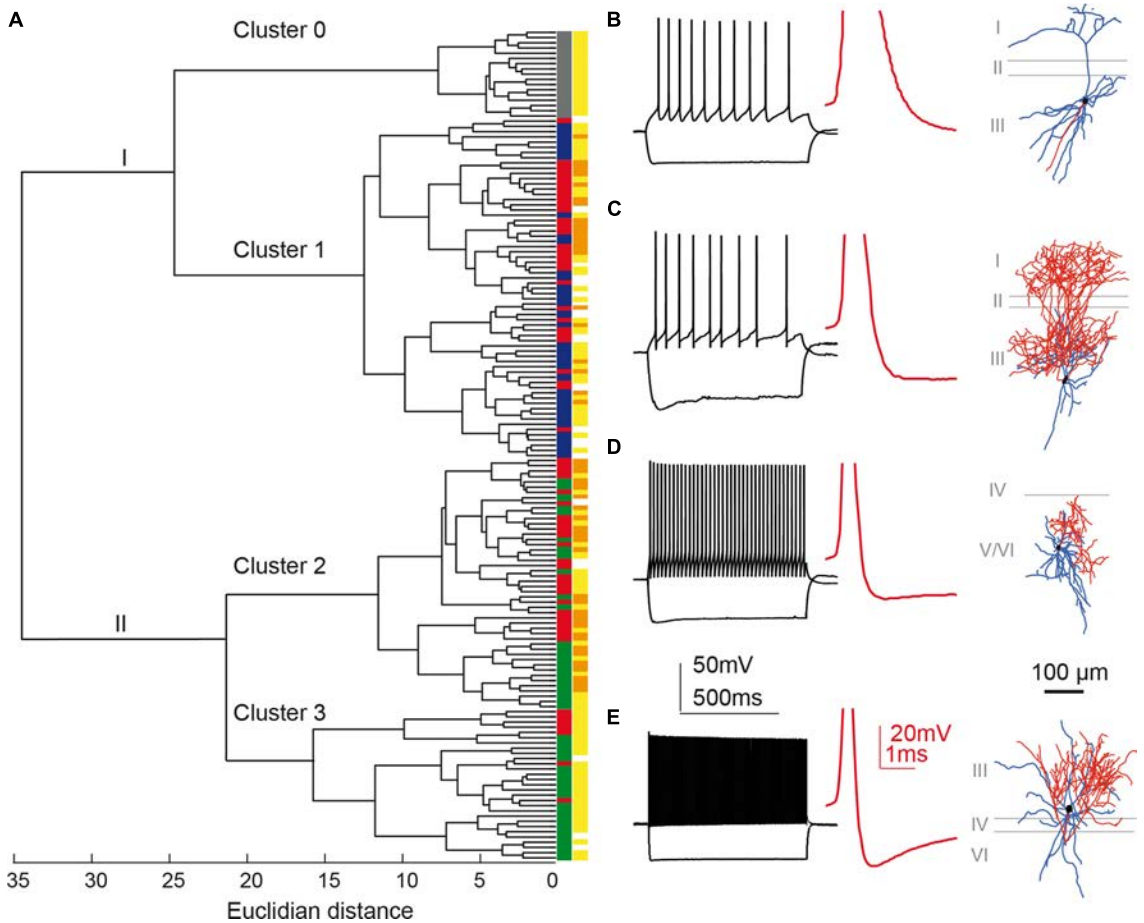

FIGURE 5 | Cluster analysis classification of presubicular interneurons and pyramidal cells. Ward's unsupervised analysis was used with physiological parameters from **Table 1** to classify 17 unlabeled pyramidal cells and 142 fluorescent interneurons from the three mouse lines. **(A)** Dendrogram. Pyramidal cells are isolated in cluster 0 (labeled gray). **(B)** shows a typical pyramidal cell firing pattern and morphology. A cut-off at a Euclidean distance of 20, separated interneurons into clusters 1, 2, and 3. Cluster 1 includes putative SST interneurons from the X98 (blue) and Sst-Cre (red) mouse lines. Cluster 2 includes both Sst-Cre (red) and Pvalb-Cre (green) interneurons. Cluster 3 contains mostly fast-spiking Pvalb-Cre (green) cells. Somatic location was either superficial (yellow) or deep (orange). **(C–E)** show representative neurons from each of these clusters. **(C)**, Martinotti type adapting neuron of cluster 1, recorded from the X98 line. **(D)**, quasi fast-spiking interneuron form cluster 2, recorded from a Sst-Cre tdTomato mouse. **(E)**, fast-spiking interneuron from cluster 3, recorded from a Pvalb-Cre tdTomato mouse. **(B–E)** show current-clamp responses to a negative current pulse that hyperpolarizes the cell to −100 mV and to a positive, twice rheobase current pulse. Insets: details of the first AP repolarization phase (red trace). Morphologies with axons in red and dendrites in blue.

a high I–O gain of 1437 ± 131 Hz.nA^{-1}. Firing frequency at double rheobase current was very high at 297 ± 27 Hz, and AP latency was short (8 ± 2 ms). Single APs of cluster 3 neurons possessed very short half widths (0.18 ± 0.01 ms) with amplitudes of 69 ± 2 mV. Maximum rates of depolarization and repolarization were 623 ± 26 and -547 ± 30 V.s^{-1} respectively. Spike afterhyperpolarization was typically simple with an AHP amplitude of −22.9 ± 0.8 mV.

Cluster 2: Quasi Fast-Spiking Interneurons from Either Pvalb or Sst-Cre Lines

The 48 neurons of cluster 2 comprised 24 (50%) tdTomato+ neurons of the Pvalb-Cre line, and 24 (50%) from the Sst-Cre line. **Figure 5D** shows a small basket shaped interneuron from the Sst-Cre line with quasi FS properties. The cell body of this neuron was located in layer V/VI, as were many neurons in this cluster.

The membrane potential of cluster 2 cells was −60 ± 1 mV (n = 48, mean ± SEM), with a firing threshold of −37.4 ± 0.5 mV. They did not fire spontaneously. R_{in} was 189 ± 11 MΩ and membrane time constant tau was 11 ± 1 ms. The voltage sag upon hyperpolarization was moderate (sag ratio, 1.11 ± 0.01). These values are all intermediate between those of clusters 1 and 3. Cluster 2 neurons fired in regular or quasi-fast patterns (**Figures 6A,B**). CV was low (0.07 ± 0.00), as for cluster 3, and the AI was 0.92 ± 0.02. APs were elicited at a rheobase current of 113 ± 8 pA. Firing gain of mean InsF was 762 ± 41 Hz.nA^{-1}, similar to cluster 1 (**Figure 6C**). At double rheobase, the firing frequency was moderate to high (128 ± 7 Hz), and the first AP latency was 14 ± 2 ms. AP

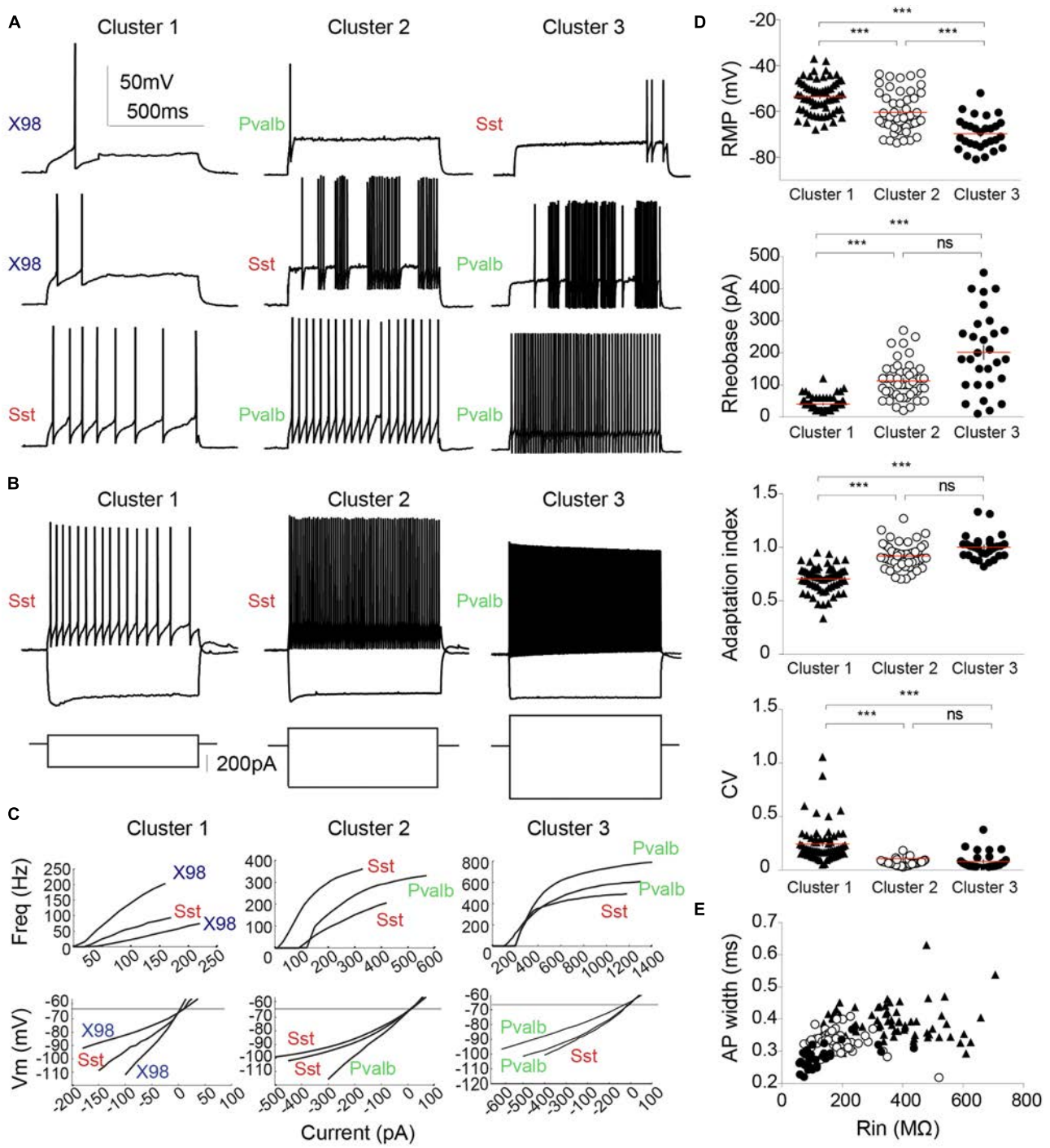

FIGURE 6 | Electrophysiological diversity of PV or SOM expressing interneurons. (A) Examples of firing patterns of three different interneurons from each cluster in response to a 800 ms rheobase current pulse. **(B)** Firing induced by a twice rheobase depolarizing current and the trajectory of hyperpolarization to −100 mV induced by a negative current pulse. Note the low R_{in} of neurons in cluster 1 compared with that of neurons in clusters 2 and 3 (larger current steps are needed to elicit similar voltage changes). Most pronounced voltage sags in response to hyperpolarization were exhibited by neurons of cluster 1. **(C)** Input–output curves (upper) and current–voltage relations at sub-threshold potentials (lower) are plotted for three interneurons from each cluster. Left column, Cluster 1; middle, Cluster 2; right column, Cluster 3. Neurons from different mouse lines are identified as: green, Pvalb-Cre tdTomato+; red, Sst-Cre tdTomato+; blue, X98 GFP+. **(D)** RMP, rheobase, AI and CV for each cluster. Each cell is represented by a dot. Horizontal lines (red) indicate mean values. **(E)** AP width plotted against R_{in} for each neuron. Cluster 3 interneurons are characterized by low values for AP width and R_{in}. Each cell is represented by a symbol. Cluster 1, filled triangles; Cluster 2, empty circles; Cluster 3, filled circles. Red lines indicate mean values. ***Kruskal–Wallis and Dunn's multiple comparison *post hoc* test, ***$P < 0.001$, ns: non-significant.

amplitude was 76 ± 1 mV and half width 0.23 ± 0.01 ms. Maximal AP depolarization and repolarization rates were 627 ± 14 and −409 ± 15 $V.s^{-1}$ respectively. After-potential waveforms were simple or complex with a mean amplitude of −23.8 ± 0.5 mV.

Maternal versus Paternal Inheritance of the cre Transgene

Differential activity of the cre allele may depend on the parent-of-origin (Heffner et al., 2012). We therefore examined the distribution of neurons in each of the three clusters with respect to cre transmission by the male or female parent (**Table 2**). In the Pvalb-Cre tdTomato mice, cre transmission was paternal for 27 recorded neurons (59%) and maternal for 19 recorded neurons (41%). Cluster 3 with its typical FS cells, contained 22 Pvalb-Cre tdTomato+ neurons, all of which had inherited cre paternally. The intermediate cluster 2 contained 24 Pvalb-Cre tdTomato+ neurons, 20% with cre inherited paternally, and 80% with cre inherited maternally: all Pvalb-Cre tdTomato+ neurons from animals with maternal cre inheritance were grouped in cluster 2, together with five neurons from animals with paternal cre transmission. For the Sst-Cre tdTomato line, cre transmission was paternal for 46 recorded neurons (75%) and maternal for 15 recorded neurons (25%). For the 30 Sst-Cre tdTomato+ neurons of cluster 1, cre transmission was paternal in 87%, and maternal in 13%. For the great majority of the 24 Sst-Cre tdTomato+ neurons in intermediate cluster 2, cre transmission was paternal (79%), and it was maternal in 21%. In cluster 3, the FS cluster, there were seven Sst-Cre tdTomato+ neurons. Only one neuron came from an animal with paternal cre transmission, whereas six of these Sst-Cre tdTomato+ cells in cluster 3 were from animals with maternal cre inheritance (86%).

Morphology

All recorded neurons were filled with biocytin to reveal their anatomy. Axonal and dendritic morphologies of 16 well-filled cells were completely reconstructed with Neurolucida. We compared the morphologies of neurons from all electrophysiologically defined interneuron clusters, and with features of SOM or PV positive interneurons from other cortical areas.

Figure 7A shows the somatodendritic form of four cluster 1 neurons. Somata of these putative SOM expressing cells, either X98 GFP or Sst-Cre tdTomato+ labeled, were ovoid, and located in both superficial and deep layers. Axons emerged from the soma or from an ascending dendritic trunk and their arbors were compact. Some branches ramified immediately above the soma in layer III, while multiple collaterals ascended to layer I and branched densely and horizontally for distances as long as 300 μm (Martinotti type interneurons, cf. Wang et al., 2004). Similarly, axons of Sst-Cre tdTomato+ neurons formed a local arbor in the vicinity of the cell body while other axon collaterals projected to, and ramified in layer I (Sst1, "GIN like," cf. Ma et al., 2006), or, axons avoided layer I (Sst2, "X94 like," cf. Ma et al., 2006). Axonal Sholl plots accordingly show a complex distribution of axon intersections, with a peak at a distance of 100 μm from the soma, and a plateau between 200 and 300 μm, due to the axonal cluster in layer I (**Figure 8A**). The mean number of primary dendrites for cluster 1 neurons was 4 ± 0.4 ($n = 4$). X98-labeled neurons possessed multipolar dendritic arbors. Sst-Cre tdTomato+ neuron dendrites occupied a radius of 150–200 μm around the soma and were preferentially oriented toward deeper layers. The mean total axonal length of cluster 1 interneurons was 9804 ± 2103 μm, significantly higher than that for cluster 2 and 3 interneurons. A high proportion of the total axon length ramified in layer I (35 ± 12%). The mean axonal length of cluster 1 interneurons was almost 6 times greater than the dendritic length (1764 ± 397 μm; $n = 4$).

Figure 7B shows seven completely reconstructed cluster 2 interneurons. Their somata were located either in superficial or deep layers. The mean total axonal length for all interneurons of cluster 2 was 7100 ± 1180 μm ($n = 13$). 6 ± 0.3 primary dendrites projected from the soma of cluster 2 interneurons, usually in all directions for distances up to 500 μm and with a total dendritic length of 2299 ± 160 μm ($n = 13$).

Axonal and dendritic arbors of some superficial cluster 2 neurons, with somata in layers II/III, were entirely limited to superficial layers (see Pvalb3 of axo-axonic like morphology, and Sst5). Reciprocally, axons and dendrites of other neurons with somata in deep layers, were restricted to deep layers, (see Pvalb2, Sst4, and eight other neurons not shown). Axons typically ramified symmetrically around the soma with no specific directional bias as for cortical basket cells. Of the reconstructed neurons shown in **Figure 7B**, some dendrites of cell Sst3 extended away from the somatic layer V to superficial layers II and III. Conversely, the axon of Pvalb1, with a soma in layer V, projected to both deep and superficial layers and ramified especially densely in layer II. Atypically, the axon of Sst6, with soma in layer III, ramified sparsely over large volumes of deep layers almost completely distinct from zones occupied by the dendrites of the neuron. Axons of six cluster 2 interneurons projected into nearby parasubiculum (**Figure 7B**, black vertical lines) where they could ramify extensively (Sst4, axonal length 3063 μm, 45% of total length; Pvalb1, length 2187 μm, 24% of total length) and Pvalb3 (1569 μm, 17% of total length). Only 2 ± 1% of the total axonal length was in layer I. The Sholl analysis for axons of cluster 2 interneurons showed a peak in the number of intersections at a distance of 100 μm, which then decreased gradually to the extremities of the axon at ∼450 μm from the soma (**Figure 8B**).

TABLE 2 | Mouse lines and parent-of-origin for Cre lines.

Mouse line and parent-of-origin for Cre lines	Cluster 1	Cluster 2	Cluster 3	Total
X98	35	0	0	35
Sst-Cre paternal	26	19	1	46
Sst-Cre maternal	4	5	6	15
Pvalb-Cre paternal	0	5	22	27
Pvalb-Cre maternal	0	19	0	19

For each cluster, the number of recorded neurons stemming from each mouse line is given, together with the paternal or maternal cre inheritance for the Sst-Cre and Pvalb-Cre mice.

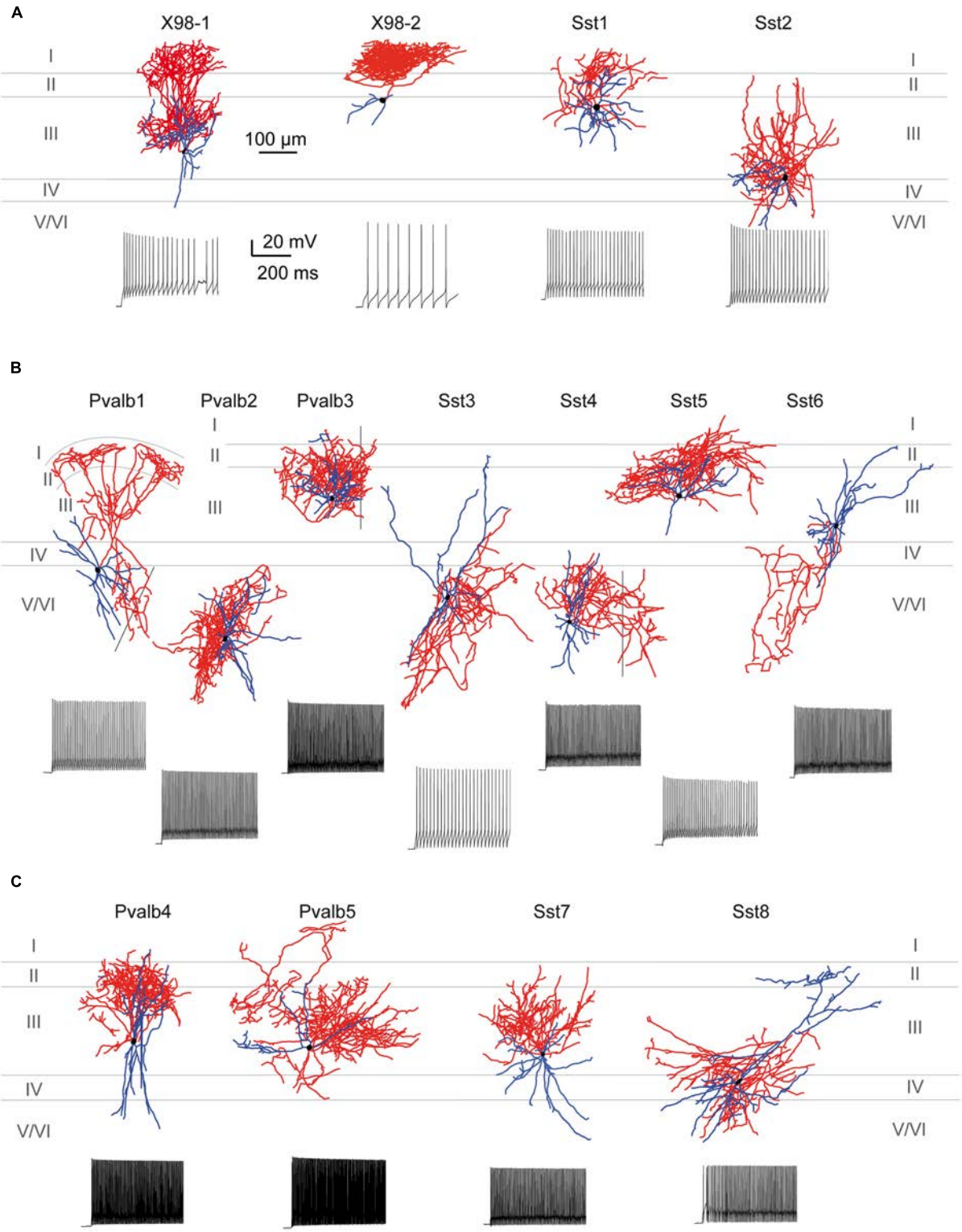

FIGURE 7 | Morphological variability of presubicular interneurons and firing patterns. (A–C) Axo-dendritic arbors of 15 biocytin-filled, reconstructed interneurons typical for clusters 1, 2, and 3. Neurons were recorded from the X98, Sst-Cre or Pvalb-Cre mouse lines as indicated. Axons are shown in red, dendrites in blue and cell bodies in black. Firing patterns are shown for each neuron for a double rheobase current injection. **(A)** Cluster 1 comprised putative SOM-expressing interneurons including Martinotti-like (X98-1 and X98-2), GIN-like (Sst1) and X94-like (Sst2) cells. **(B)** Cluster 2 contained interneurons with variable morphology, including basket (Pvalb-1, Pvalb2, Sst3, Sst4) and chandelier-like (Pvalb3) cells as well as GIN-like (Sst5) and atypical SOM-like (Sst6) neurons. **(C)** Cluster 3 contained mainly multipolar basket-cell like interneurons.

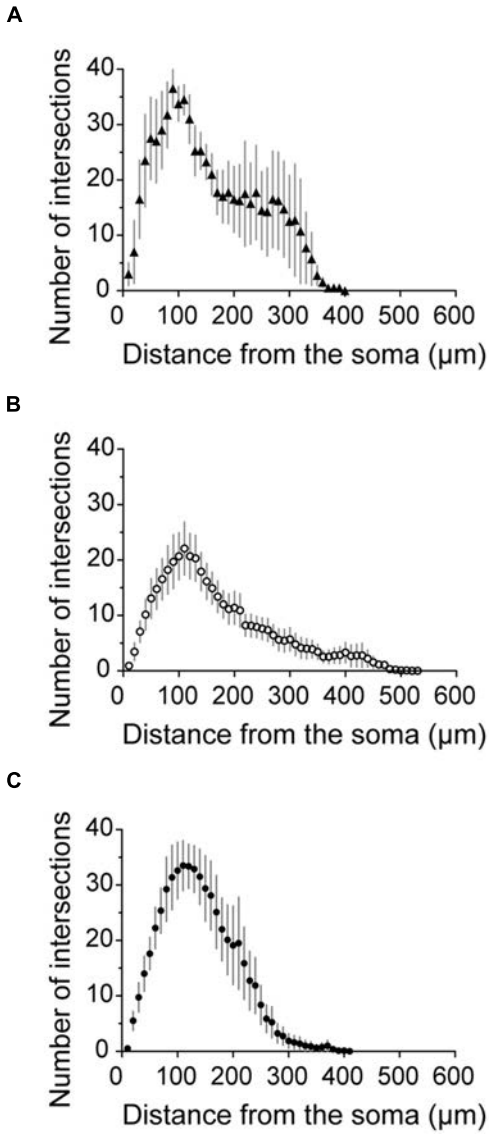

FIGURE 8 | Axonal Sholl plots. (A–C) Sholl plots of the number of axon crossings for concentric circles against distance from the soma for neurons from cluster 1 (**A**, filled triangles, $n = 4$), cluster 2 (**B**, empty circles, $n = 13$) and cluster 3 (**C**, filled circles, $n = 8$). Error bars indicate mean ± SEM.

Figure 7C shows four interneurons of cluster 3, with somata all located in superficial layers. The mean total axonal length of reconstructed cluster 3 interneurons was 8511 ± 1488 μm and mean total dendritic length 2370 ± 344 μm ($n = 8$). Axons were typically restricted to superficial layers and collaterals tended to ascend rather than descend (Pvalb4, Pvalb5, and Sst7). Axonal arbors could be dense, such as that of Pvalb5 which projected long axon collaterals in all directions, as do large basket cells (Wang et al., 2002). Sholl analysis of axon distributions showed a peak at 100 μm from the soma, and axons typically did not project more than 300 μm from the soma (**Figure 8C**). There were 6 ± 0.6 primary dendrites in cluster 3 interneurons. Dendritic arbors were typically multipolar, ramifying evenly in all directions from the soma, as for neurons of cluster 2. Other dendritic arbors such as that of Pvalb4 (and one similar neuron not shown) possessed vertically biased dendrites projecting to both deep and superficial layers or just toward superficial layers (Pvalb5) or deep layers (Sst8). Similar to cluster 2, cluster 3 was characterized by a low proportion of the total axonal length in layer I (1 ± 1%).

Discussion

This study provides a first classification of mouse presubicular interneurons. Our data show about 11% of mouse presubicular neurons are GABAergic. We used transgenic animals to identify subtypes of these cells that express the peptide SOM or the Ca-binding protein PV. We measured physiological parameters and somato-dendritic form and also verified the chemical content of labeled neurons from Pvalb-Cre, Sst-Cre and X98 mice. Immunohistochemical verification of these interneuron markers revealed both a true overlap – about 5% of presubicular interneurons were co-labeled by antibodies against SOM and PV – and an imperfect specificity for one of the animal lines – only about 70% of labeled cells in Sst-Cre animals were immunopositive for SOM. We therefore used physiological parameters alone for a cluster analysis. Three groups of interneurons emerged. Cells conforming to classical archetypes of adapting SOM neurons and FS PV neurons occupied two distinct clusters (1 and 3). A third cluster (cluster 2) contained quasi fast spiking neurons with intermediate properties. Neurons from the cluster of FS cells (3) often possessed a basket-cell like anatomy, those from the cluster of neurons with adapting firing (1) could display a Martinotti cell like anatomy, but neurons with intermediate physiology (2) tended to possess intermediate somato-dendritic forms.

Mouse Lines and Neurochemical Marker Expression Pattern in Presubiculum

Labeled cells from genetically modified mouse lines revealed a specific distribution of interneuron subtypes in distinct layers of presubiculum, with the exceptions for mislabeling. The overall density of GABAergic interneurons in different layers was measured using the GAD67-GFP line. Pvalb-Cre tdTomato+ labeled neurons were preferentially located in superficial layers (II/III) innervated by thalamic afferents while the density of Sst-Cre tdTomato+ cells was highest in deeper layers (V/VI) of the presubiculum. Layer specific distributions of distinct types of interneurons may differ in other cortical regions. In mouse visual cortex, PV, and SOM interneurons are more evenly distributed across superficial and deep layers (Gonchar et al., 2007). However, higher SOM positive cell densities in deep cortical layers, as here, were previously described by Ma et al. (2006) and Xu et al. (2010). In contrast to our results, PV cell density has been found to be higher in deep than in superficial cortical layers (Xu et al., 2010). There may be differences between visual, frontal and somatosensory cortical areas, as well as differences between mouse and rat cortex (Ma et al., 2006; Xu et al., 2010).

Immunohistochemistry showed that ∼90% of labeled cells from Pvalb-Cre animals were positive for PV and ∼2% were SOM positive. Double immunolabeling demonstrated a co-expression of SOM *and* PV. Even though PV and SOM expression do not overlap in neocortical adult interneurons of rodents (Gonchar and Burkhalter, 1997; Kawaguchi and Kubota, 1997; Xu et al., 2010; Kubota et al., 2011), mRNAs coding for both PV and SOM have been detected in the same interneuron (Cauli et al., 2000). PV and SOM co-expression has been detected by immunolabeling of bistratified neurons or oriens-locunosum-moleculare interneurons of the hippocampus (Jinno and Kosaka, 2000; Klausberger et al., 2003; Somogyi and Klausberger, 2005; Fishell and Rudy, 2011; Katona et al., 2014).

Immunostaining showed that ∼70% of labeled Sst-Cre tdTomato+ cells were SOM positive, while 23% were PV positive. Cre-mediated recombination in this mouse line had been assumed to be largely restricted to SOM interneurons (Gentet et al., 2012; Cottam et al., 2013; Kvitsiani et al., 2013; Xu et al., 2013). Data of Hu et al. (2013) suggest though that 6–10% of labeled interneurons in different cortical areas of Sst-Cre tdTomato+ mice possess a fast spiking PV-like phenotype. This result may be explained by off-target recombination in PV cells that transiently express SOM during development (Hu et al., 2013), possibly at high levels in the presubiculum. Off-target recombination may occur preferentially for maternal cre inheritance. However, PV and SOM are co-expressed in 6% of Sst-Cre tdTomato+ neurons. This special population of PV+SOM+ cells does not entirely account for all (23%) PV labeled Sst-Cre tdTomato+ neurons. The 16% of Sst-Cre neurons that expressed neither SOM nor PV, could correspond to other types of interneurons. Some Sst-Cre tdTomato+ cells could be labeled with anti Calbindin antibody for instance (data not shown). Alternatively they might be non-GABAergic which could explain how the Sst-Cre tdTomato+ neuron density exceeded that of GAD67-GFP neurons in layers V/VI. Indeed we also noted some clusters of pyramidal shaped Sst-Cre tdTomato+ neurons in adjacent subiculum (unpublished observation).

The X98 mouse line is specific for a subset of infragranular, SOM containing interneurons in neocortex (Ma et al., 2006). In the presubiculum, ∼90% of labeled cells were immunopositive for SOM and 0% for PV. The somata of labeled cells from X98 mice were located in both deep and superficial layers, with a highest density in layer IV.

Interneuron Classification

Classical anatomical studies of Cajal (1911) and Lorente de No (1933) established that short-axon cells possess diverse forms. More recently, interneurons have been classified into distinct groups on the basis of electrophysiological, morphological, molecular and developmental criteria (Markram et al., 2004; Petilla Interneuron Nomenclature Group et al., 2008; Druckmann et al., 2012). But the fundamental question of how to define different classes of interneurons (Parra et al., 1998) or how to treat a structured continuum (Battaglia et al., 2013) remains open. Here we used Ward's unsupervised classification method to analyze interneuron types based on multiple physiological parameters. The resulting groups were then correlated with the maternal versus paternal inheritance of the cre transgene and the neuronal anatomy.

Ward's method requires no preliminary supposition on the number of cell types, even if it may separate neuronal classes less efficiently than K-mean clustering (Cauli et al., 2000; Karagiannis et al., 2009). We included unlabeled presubicular pyramidal cells as a control of our cluster analysis. Their clear separation from all labeled interneurons, as cluster 0, validates our clustering procedures. Application of the Thorndike procedure to Ward's clustering method should provide an optimal threshold to maximize information content. With this threshold, adapting SOM interneurons (**Figure 5C**) labeled from X98 mice were found in cluster 1, while classical FS interneurons (**Figure 5E**) from the Pvalb-Cre line were grouped in main branch II of the dendrogram. These two interneuron classes have been defined in both hippocampus and neocortical areas (Cauli et al., 1997; Kawaguchi and Kubota, 1997; Markram et al., 2004; Somogyi and Klausberger, 2005; Petilla Interneuron Nomenclature Group et al., 2008; Fishell and Rudy, 2011). Lowering the cluster separation threshold permitted resolution of two distinct clusters 2 and 3. Interneurons of cluster 2 possessed intermediate, physiological and anatomical properties. We were surprised to note that interneurons labeled in the Sst-Cre line were found in all interneuron containing clusters (cluster 1, 2, and 3).

Two Main Types of GABAergic Interneurons in Presubiculum

Cluster 1 interneurons fired regularly with a consistent frequency adaptation. APs were characterized by a large amplitude and half-duration. These cells were the most excitable of the three groups with depolarized membrane potentials, high R_{ins} and pronounced voltage sags. All cells in this cluster were from SOM expressing X98 interneurons or from the Sst-Cre line, in majority with paternal cre inheritance. Similar adapting-SOM type interneurons are described in hippocampus as oriens-lacunosum-moleculare cells and in neocortex as Martinotti cells (Wang et al., 2004; Halabisky et al., 2006; Ma et al., 2006; Uematsu et al., 2007; Karagiannis et al., 2009; Xu et al., 2013).

Anatomically, X98 GFP+ labeled cells of cluster 1 resembled Martinotti cells. They possessed multipolar dendrites, with few primary dendrites as for cortical SOM Martinotti cells (Kawaguchi et al., 2006). Axons sent collaterals to layers II/III and particularly to layer I, where they could branch over horizontal distances up to 300 μm (Wang et al., 2004; Ma et al., 2006). Axonal arborizations of Sst-Cre tdTomato+ labeled neurons were more sparse and ramified locally around their soma, as do some SOM neurons of the GIN mouse line (McGarry et al., 2010). Cluster 1 interneurons are well suited to control inputs from retrosplenial cortex and thalamus which excite principal cell apical dendrites in presubicular layers I and III (van Groen and Wyss, 1990b; Kononenko and Witter, 2012).

Cluster 3 comprised FS cells, similar to those of hippocampus (Somogyi and Klausberger, 2005) and neocortex (Kawaguchi, 1995). Neurons of this group were the least excitable in responses to current injection. They possessed hyperpolarized

resting potentials, low R_{in} and short membrane time constants (**Figure 6**). Stronger stimuli induced sustained high-frequency firing of fast spikes with little or no frequency adaptation, linked to fast, delayed rectifier Kv3-mediated currents (Martina et al., 1998; Erisir et al., 1999). Hence, the AP firing pattern can be described as fast spiking, with continuous delayed or stuttering dynamics (Druckmann et al., 2012).

Most interneurons of cluster 3 were recorded from Pvalb-Cre animals, with paternal cre inheritance only, and others from the Sst-Cre line with mostly maternal inheritance (**Table 2**). Possibly the second group corresponds to off-target recombination (**Figure 3B**). Anatomically, archetypal FS-PV interneurons include basket cells and chandelier cells of neocortical superficial layers (Kawaguchi, 1995; Wang et al., 2002) and of the hippocampus (Freund and Buzsáki, 1996; Somogyi and Klausberger, 2005). Dendritic arbors of filled neurons of cluster 3 FS cells were typically multipolar, with more primary dendrites than SOM cells of cluster 1 (cf. Kawaguchi et al., 2006). Axonal distributions conformed to those of these cell types although we did not confirm a perisomatic site of postsynaptic targets. Axonal arbors could be small or large and while some projections remained local, others might mediate a translaminar or transcolumnar inhibition (Wang et al., 2002; Karube et al., 2004; Markram et al., 2004). The tdTomato+ cells of the Sst-Cre line in this cluster had basket like morphologies similar to the Pvalb-Cre tdTomato+ neurons.

. . . and An Intermediate Cluster

Cluster 2 grouped together some Sst-Cre tdTomato+ interneurons with similar numbers of Pvalb-Cre tdTomato+ interneurons (**Figure 5A**). *Cre* inheritance could be either paternal or maternal, but all Pvalb-Cre cells from animals that inherited cre maternally were found solely in this cluster. Electrically, neurons of this cluster possessed intermediate values of membrane potential, a relatively small resistance and a short time constant approaching that of FS cells. The APs of cluster 2 cells from both Cre mouse lines were of short duration and firing patterns included single spiking, stuttering and regular spiking (**Figure 6**). At higher firing frequencies, neurons of this cluster displayed a quasi-FS firing pattern with a weak to absent frequency adaptation. Cluster 2 cells in presubiculum are thus clearly distinct from the classical adapting SOM-archetype of cluster 1. In other neocortical areas, SOM positive neurons comprise several subtypes, including the Martinotti type cells (Wang et al., 2004), the SOM cells in the X94 line (Ma et al., 2006), and others (Halabisky et al., 2006; McGarry et al., 2010). It is possible that the subpopulation of interneurons co-expressing SOM and PV (**Figure 4**) were included in cluster 2, even though with restricted numbers, they seem unlikely to account for all of the cells.

The somato-dendritic morphology of labeled neurons from both Sst-Cre and the Pvalb-Cre lines grouped into cluster 2 was often similar to that of basket cells (Wonders and Anderson, 2006; Kubota, 2014). Neurites of these cells tended to branch within their home layer with also intra-laminar axonal projections that may mediate early and late blanket inhibition (Karnani et al., 2014). Other neurons of cluster 2 did not follow this pattern, with dendrites oriented toward superficial (layer II/III) or deep layers (V/VI). Conversely, other neurons with dendritic arbors in superficial layers projected axons into deep layers, and presumably mediate translaminar inhibition (Bortone et al., 2014).

Interneuron Diversity

Presubicular interneurons examined here included both typical SOM adapting cells and classical FS PV cells. However, we also distinguished a group of interneurons with intermediate physiology and anatomy. Labeled neurons of this cluster (2) comprised all Pvalb-Cre tdTomato+ neurons with maternal cre inheritance, some with paternal inheritance, as well as Sst-Cre tdTomato+ neurons with either paternal or maternal cre inheritance. These interneurons seem to represent a convergence of traits of archetypical SOM- and PV-containing cells. Such a continuum of properties has been evoked in the context of interneuron classification and linked to fuzzy set theory (Battaglia et al., 2013).

How might cells with intermediate traits emerge? Interneuron properties are specified during development. Both PV and SOM interneurons, along with the majority of neocortical interneurons, originate from the medial ganglionic eminence (Xu et al., 2004; Wonders and Anderson, 2006; Batista-Brito and Fishell, 2009; Miyoshi et al., 2010; Kepecs and Fishell, 2014). While adapting-SOM and FS PV cells may be archetypal, a common developmental origin might also produce transitional "edge cells" reflecting a shared embryonic origin. Clones of the same progenitor lineage include both SOM- and PV-expressing interneurons rather than a single subtype (Kepecs and Fishell, 2014). Could that explain the presence of Sst-Cre and Pvalb-Cre tdTomato+ cells in a same interneuron class? Even transient SOM expression in Sst-Cre cells should induce a persistent tdTomato+ signal due to Cre-recombinase expression and Cre-mediated recombination (Hu et al., 2013). This point should be pursued by a molecular characterization, including calcium binding protein and neuropeptide content, of Sst-Cre tdTomato+ interneurons with quasi-FS properties. Further studies on parent-of-origin effect for *cre* transmission should examine why different interneuron phenotypes are labeled or whether maternal cre inheritance could modify interneuron phenotype.

Parvalbumin and somatostatin expressing neurons both originate in the MGE. They are presumably subject to similar chemical cues during migration and when they arrive in the presubiculum similar local cues control interneuron phenotype and neurite branching pattern (Adams and Eichmann, 2010; Battaglia et al., 2013). Even if the six-layered cytoarchitecture of the presubiculum is similar to that of neocortex, the heterogeneous, atypical populations of presubicular PV and SOM interneurons may be linked to the transitional nature of the region (O'Mara et al., 2001; Simonnet et al., 2013). Possibly similar features of Sst-Cre and Pvalb-Cre tdTomato+ cells in cluster 2 originate from local presubicular signals.

Implication of Interneurons in Presubicular Microcircuit Function

GABAergic neurons of the presubiculum seem likely to control the timing, sensitivity and selectivity of head directional signals.

Synapses of FS basket-like cells of cluster 3 presumably target perisomatic regions of principal cells and act to enforce precisely timed firing as in hippocampus or somatosensory cortex (Miles et al., 1996; Fricker and Miles, 2000; Pouille and Scanziani, 2001; Gabernet et al., 2005). In contrast, inhibition due to Martinotti cells of cluster 1, targets dendritic sites in layer I and may act to counter layer-specific excitatory inputs from retrosplenial cortex and thalamus in a graded fashion. Martinotti cells are often reciprocally connected with presubicular pyramidal cells (unpublished observations), and their recruitment should tend to limit excitatory inputs or mediate lateral inhibition onto nearby cells (Silberberg and Markram, 2007). Mapping by two-photon glutamate uncaging showed that inhibition by both PV and SOM cortical interneurons induces a "blanket" of inhibitory actions rather than locally selective effects (Fino and Yuste, 2011; Packer and Yuste, 2011). Presubicular PV or SOM interneurons with sparse or profuse local axonal arborisations seem likely also to target postsynaptic targets non-selectively and spread a "blanket of inhibition" over the microcircuit (Karnani et al., 2014). Dual records from interneurons and principal cells will be needed to establish connectivity motifs of distinct groups of presubicular interneurons for comparison with inhibitory circuits in other regions of the cortex.

Acknowledgments

We thank Alberto Bacci and Caroline Mailhes for help and support, and Yoshiyuki Kubota for comments on an earlier version of the manuscript. This work was supported by ANR Grant JCJC R10206DD (DF); the French Ministry for Research (MN); the Région Ile-de-France and the Fondation pour la Recherche Médicale (JS), INSERM and Grant-in-Aids for Scientific Research from the MEXT, Japan (YY). The research leading to these results also benefitted from the program "Investissements d'avenir" ANR-10-IAIHU-06.

References

Adams, R. H., and Eichmann, A. (2010). Axon guidance molecules in vascular patterning. *Cold Spring Harb. Perspect. Biol.* 2:a001875. doi: 10.1101/cshperspect.a001875

Batista-Brito, R., and Fishell, G. (2009). The developmental integration of cortical interneurons into a functional network. *Curr. Top. Dev. Biol.* 87, 81–118. doi: 10.1016/S0070-2153(09)01203-4

Battaglia, D., Karagiannis, A., Gallopin, T., Gutch, H. W., and Cauli, B. (2013). Beyond the frontiers of neuronal types. *Front. Neural Circuits.* 7:13. doi: 10.3389/fncir.2013.00013

Boccara, C. N., Sargolini, F., Thoresen, V. H., Solstad, T., Witter, M. P., Moser, E. I., et al. (2010). Grid cells in pre- and parasubiculum. *Nat. Neurosci.* 13, 987–994. doi: 10.1038/nn.2602

Bortone, D. S., Olsen, S. R., and Scanziani, M. (2014). Translaminar inhibitory cells recruited by layer 6 corticothalamic neurons suppress visual cortex. *Neuron* 82, 1–12. doi: 10.1016/j.neuron.2014.02.021

Cajal, R. S. (1911). *Histologie du Systeme Nerveux De L'Homme et des Vertébrés*. Paris: Maloine.

Calton, J. L., Stackman, R. W., Goodridge, J. P., Archey, W. B., Dudchenko, P. A., and Taube, J. S. (2003). Hippocampal place cell instability after lesions of the head direction cell network. *J. Neurosci.* 23, 9719–9731.

Cauli, B., Audinat, E., Lambolez, B., Angulo, M. C., Ropert, N., Tsuzuki, K., et al. (1997). Molecular and physiological diversity of cortical nonpyramidal cells. *J. Neurosci.* 17, 3894–3906.

Cauli, B., Porter, J. T., Tsuzuki, K., Lambolez, B., Rossier, J., Quenet, B., et al. (2000). Classification of fusiform neocortical interneurons based on unsupervised clustering. *Proc. Natl. Acad. Sci. U.S.A.* 97, 6144–6149. doi: 10.1073/pnas.97.11.6144

Chrobak, J. J., and Buzsaki, G. (1996). High-frequency oscillations in the output networks of the hippocampal-entorhinal axis of the freely behaving rat. *J. Neurosci.* 16, 3056–3066.

Cobb, S. R., Buhl, E. H., Halasy, K., Paulsen, O., and Somogyi, P. (1995). Synchronization of neuronal activity in hippocampus by individual GABAergic interneurons. *Nature* 378, 75–78. doi: 10.1038/378075a0

Cottam, J. C. H., Smith, S. L., and Hausser, M. (2013). Target-specific effects of somatostatin-expressing interneurons on neocortical visual processing. *J. Neurosci.* 33, 19567–19578. doi: 10.1523/JNEUROSCI.2624-13.2013

Defelipe, J., López-Cruz, P. L., Benavides-Piccione, R., Bielza, C., Larrañaga, P., Anderson, S., et al. (2013). New insights into the classification and nomenclature of cortical GABAergic interneurons. *Nat. Rev. Neurosci.* 14, 202–216. doi: 10.1038/nrn3444

Druckmann, S., Hill, S., Schürmann, F., Markram, H., and Segev, I. (2012). A hierarchical structure of cortical interneuron electrical diversity revealed by automated statistical analysis. *Cereb. Cortex* 23, 2994–3006. doi: 10.1093/cercor/bhs290

Dumitriu, D., Cossart, R., Huang, J., and Yuste, R. (2006). Correlation between axonal morphologies and synaptic input kinetics of interneurons from mouse visual cortex. *Cereb. Cortex* 17, 81–91. doi: 10.1093/cercor/bhj126

Erisir, A., Lau, D., Rudy, B., and Leonard, C. S. (1999). Function of specific K(+) channels in sustained high-frequency firing of fast-spiking neocortical interneurons. *J. Neurophysiol.* 82, 2476–2489.

Fino, E., and Yuste, R. (2011). Dense inhibitory connectivity in neocortex. *Neuron* 69, 1188–1203. doi: 10.1016/j.neuron.2011.02.025

Fishell, G., and Rudy, B. (2011). Mechanisms of inhibition within the telencephalon: "where the wild things are." *Annu. Rev. Neurosci.* 34, 535–567. doi: 10.1146/annurev-neuro-061010-113717

Freund, T. F., and Buzsáki, G. (1996). Interneurons of the hippocampus. *Hippocampus* 6, 347–470. doi: 10.1002/(SICI)1098-1063(1996)6:4<347::AID-HIPO1>3.0.CO;2-I

Fricker, D., and Miles, R. (2000). EPSP amplification and the precision of spike timing in hippocampal neurons. *Neuron* 28, 559–569. doi: 10.1016/S0896-6273(00)00133-1

Fricker, D., and Miles, R. (2001). Interneurons, spike timing, and perception. *Neuron* 32, 771–774. doi: 10.1016/S0896-6273(01)00528-1

Gabernet, L., Jadhav, S. P., Feldman, D. E., Carandini, M., and Scanziani, M. (2005). Somatosensory integration controlled by dynamic thalamocortical feed-forward inhibition. *Neuron* 48, 315–327. doi: 10.1016/j.neuron.2005.09.022

Gentet, L. J., Kremer, Y., Taniguchi, H., Huang, Z. J., Staiger, J. F., and Petersen, C. C. H. (2012). Unique functional properties of somatostatin-expressing GABAergic neurons in mouse barrel cortex. *Nat. Neurosci.* 15, 607–612. doi: 10.1038/nn.3051

Golowasch, J., Thomas, G., Taylor, A. L., Patel, A., Pineda, A., Khalil, C., et al. (2009). Membrane capacitance measurements revisited: dependence of capacitance value on measurement method in nonisopotential neurons. *J. Neurophysiol.* 102, 2161–2175. doi: 10.1152/jn.00160.2009

Gonchar, Y., and Burkhalter, A. (1997). Three distinct families of GABAergic neurons in rat visual cortex. *Cereb. Cortex* 7, 347–358. doi: 10.1093/cercor/7.4.347

Gonchar, Y., Wang, Q., and Burkhalter, A. (2007). Multiple distinct subtypes of GABAergic neurons in mouse visual cortex identified by triple immunostaining. *Front. Neuroanat.* 1:3. doi: 10.3389/neuro.05.003.2007

Halabisky, B., Shen, F., Huguenard, J. R., and Prince, D. A. (2006). Electrophysiological classification of somatostatin-positive interneurons in mouse sensorimotor cortex. *J. Neurophysiol.* 96, 834–845. doi: 10.1152/jn.01079.2005

Heffner, C. S., Pratt, C. H., Babiuk, R. P., Sharma, Y., Rockwood, S. F., Donahue, L. R., et al. (2012). Supporting conditional mouse mutagenesis

with a comprehensive cre characterization resource. *Nat. Comms.* 3:1218. doi: 10.1038/ncomms2186

Helm, J., Akgul, G., and Wollmuth, L. P. (2013). Subgroups of parvalbumin-expressing interneurons in layers 2/3 of the visual cortex. *J. Neurophysiol.* 109, 1600–1613. doi: 10.1152/jn.00782.2012

Hippenmeyer, S., Vrieseling, E., Sigrist, M., Portmann, T., Laengle, C., Ladle, D. R., et al. (2005). A developmental switch in the response of DRG neurons to ETS transcription factor signaling. *PLoS Biol.* 3:e159. doi: 10.1371/journal.pbio.0030159

Honda, Y., and Ishizuka, N. (2004). Organization of connectivity of the rat presubiculum: I. Efferent projections to the medial entorhinal cortex. *J. Comp. Neurol.* 473, 463–484. doi: 10.1002/cne.20093

Hu, H., Cavendish, J. Z., and Agmon, A. (2013). Not all that glitters is gold: off-target recombination in the somatostatin-IRES-Cre mouse line labels a subset of fast-spiking interneurons. *Front. Neural. Circuits.* 7:195. doi: 10.3389/fncir.2013.00195

Isaacson, J. S., and Scanziani, M. (2011). How inhibition shapes cortical activity. *Neuron* 72, 231–243. doi: 10.1016/j.neuron.2011.09.027

Jinno, S., and Kosaka, T. (2000). Colocalization of parvalbumin and somatostatin-like immunoreactivity in the mouse hippocampus: quantitative analysis with optical dissector. *J. Comp. Neurol.* 428, 377–388. doi: 10.1002/1096-9861(20001218)428:3<377::AID-CNE1>3.0.CO;2-L

Karagiannis, A., Gallopin, T., Dávid, C., Battaglia, D., Geoffroy, H., Rossier, J., et al. (2009). Classification of NPY-expressing neocortical interneurons. *J. Neurosci.* 29, 3642–3659. doi: 10.1523/JNEUROSCI.0058-09.2009

Karnani, M. M., Agetsuma, M., and Yuste, R. (2014). Science Direct A blanket of inhibition: functional inferences from dense inhibitory connectivity. *Curr. Opin. Neurobiol.* 26, 96–102. doi: 10.1016/j.conb.2013.12.015

Karube, F., Kubota, Y., and Kawaguchi, Y. (2004). Axon branching and synaptic bouton phenotypes in GABAergic nonpyramidal cell subtypes. *J. Neurosci.* 24, 2853–2865. doi: 10.1523/JNEUROSCI.4814-03.2004

Katona, L., Lapray, D., Viney, T. J., Oulhaj, A., Borhegyi, Z., Micklem, B. R., et al. (2014). Sleep and movement differentiates actions of two types of somatostatin-expressing GABAergic interneuron in rat hippocampus. *Neuron* 82, 872–886. doi: 10.1016/j.neuron.2014.04.007

Kawaguchi, Y. (1995). Physiological subgroups of nonpyramidal cells with specific morphological characteristics in layer II/III of rat frontal cortex. *J. Neurosci.* 15, 2638–2655.

Kawaguchi, Y., Karube, F., and Kubota, Y. (2006). Dendritic branch typing and spine expression patterns in cortical nonpyramidal cells. *Cereb. Cortex* 16, 696–711. doi: 10.1093/cercor/bhj015

Kawaguchi, Y., and Kubota, Y. (1997). GABAergic cell subtypes and their synaptic connections in rat frontal cortex. *Cereb. Cortex* 7, 476–486. doi: 10.1093/cercor/7.6.476

Kepecs, A., and Fishell, G. (2014). Interneuron cell types are fit to function. *Nature* 505, 318–326. doi: 10.1038/nature12983

Klausberger, T., Márton, L. F., Baude, A., Roberts, J. D. B., Magill, P. J., and Somogyi, P. (2003). Spike timing of dendrite-targeting bistratified cells during hippocampal network oscillations in vivo. *Nat. Neurosci.* 7, 41–47. doi: 10.1038/nn1159

Kononenko, N. L., and Witter, M. P. (2012). Presubiculum layer III conveys retrosplenial input to the medial entorhinal cortex. *Hippocampus* 22, 881–895. doi: 10.1002/hipo.20949

Kubota, Y. (2014). Untangling GABAergic wiring in the cortical microcircuit. *Curr. Opin. Neurobiol.* 26, 7–14. doi: 10.1016/j.conb.2013.10.003

Kubota, Y., Shigematsu, N., Karube, F., Sekigawa, A., Kato, S., Yamaguchi, N., et al. (2011). Selective coexpression of multiple chemical markers defines discrete populations of neocortical GABAergic neurons. *Cereb. Cortex* 21, 1803–1817. doi: 10.1093/cercor/bhq252

Kvitsiani, D., Ranade, S., Hangya, B., Taniguchi, H., Huang, J. Z., and Kepecs, A. (2013). Distinct behavioural and network correlates of two interneuron types in prefrontal cortex. *Nature* 498, 363–366. doi: 10.1038/nature12176

Lorente de No, R. (1933). Studies on the structure of the cerebral cortex. *J. für Psychol. Neurol.* 45, 381–438.

Ma, Y., Hu, H., Berrebi, A. S., Mathers, P. H., and Agmon, A. (2006). Distinct subtypes of somatostatin-containing neocortical interneurons revealed in transgenic mice. *J. Neurosci.* 26, 5069–5082. doi: 10.1523/JNEUROSCI.0661-06.2006

Madisen, L., Zwingman, T. A., Sunkin, S. M., Oh, S. W., Zariwala, H. A., Gu, H., et al. (2010). A robust and high-throughput cre reporting and characterization system for the whole mouse brain. *Nat. Neurosci.* 13, 133–140. doi: 10.1038/nn.2467

Markram, H., Toledo-Rodriguez, M., Wang, Y., Gupta, A., Silberberg, G., and Wu, C. (2004). Interneurons of the neocortical inhibitory system. *Nat. Rev. Neurosci.* 5, 793–807. doi: 10.1038/nrn1519

Martina, M., Schultz, J. H., Ehmke, H., Monyer, H., and Jonas, P. (1998). Functional and molecular differences between voltage-gated K+ channels of fast-spiking interneurons and pyramidal neurons of rat hippocampus. *J. Neurosci.* 18, 8111–8125.

McGarry, L. M., Packer, A. M., Fino, E., Nikolenko, V., Sippy, T., and Yuste, R. (2010). Quantitative classification of somatostatin-positive neocortical interneurons identifies three interneuron subtypes. *Front. Neural. Circuits.* 4:12. doi: 10.3389/fncir.2010.00012

Miles, R., Tóth, K., Gulyás, A. I., Hajos, N., and Freund, T. F. (1996). Differences between somatic and dendritic inhibition in the hippocampus. *Neuron* 16, 815–823. doi: 10.1016/S0896-6273(00)80101-4

Miyoshi, G., Hjerling-Leffler, J., Karayannis, T., Sousa, V. H., Butt, S. J. B., Battiste, J., et al. (2010). Genetic fate mapping reveals that the caudal ganglionic eminence produces a large and diverse population of superficial cortical interneurons. *J. Neurosci.* 30, 1582–1594. doi: 10.1523/JNEUROSCI.4515-09.2010

O'Mara, S. M., Commins, S., Anderson, M., and Gigg, J. (2001). The subiculum: a review of form, physiology and function. *Prog. Neurobiol.* 64, 129–155. doi: 10.1016/S0301-0082(00)00054-X

Packer, A. M., and Yuste, R. (2011). Dense, unspecific connectivity of neocortical parvalbumin-positive interneurons: a canonical microcircuit for inhibition? *J. Neurosci.* 31, 13260–13271. doi: 10.1523/JNEUROSCI.3131-11.2011

Parra, P., Gulyás, A. I., and Miles, R. (1998). How many subtypes of inhibitory cells in the hippocampus? *Neuron* 20, 983–993. doi: 10.1016/S0896-6273(00)80479-1

Perrenoud, Q., Rossier, J., Geoffroy, H., Vitalis, T., and Gallopin, T. (2012). Diversity of GABAergic interneurons in layer VIa and VIb of mouse barrel cortex. *Cereb. Cortex* 23, 423–421. doi: 10.1093/cercor/bhs032

Petilla Interneuron Nomenclature Group, Ascoli, G. A., Alonso-Nanclares, L., Anderson, S. A., Barrionuevo, G., Benavides-Piccione, R., et al. (2008). Petilla terminology: nomenclature of features of GABAergic interneurons of the cerebral cortex. *Nat. Rev. Neurosci.* 9, 557–568. doi: 10.1038/nrn2402

Pouille, F., and Scanziani, M. (2001). Enforcement of temporal fidelity in pyramidal cells by somatic feed-forward inhibition. *Science* 293, 1159–1163. doi: 10.1126/science.1060342

Rowland, D. C., Weible, A. P., Wickersham, I. R., Wu, H., Mayford, M., Witter, M. P., et al. (2013). Transgenically targeted rabies virus demonstrates a major monosynaptic projection from hippocampal area CA2 to medial entorhinal layer II neurons. *J. Neurosci.* 33, 14889–14898. doi: 10.1523/JNEUROSCI.1046-13.2013

Rudy, B., Fishell, G., Lee, S., and Hjerling-Leffler, J. (2010). Three groups of interneurons account for nearly 100% of neocortical GABAergic neurons. *Dev. Neurobio.* 71, 45–61. doi: 10.1002/dneu.20853

Schlingloff, D., Kali, S., Freund, T. F., Hájos, N., and Gulyás, A. I. (2014). Mechanisms of sharp wave initiation and ripple generation. *J. Neurosci.* 34, 11385–11398. doi: 10.1523/JNEUROSCI.0867-14.2014

Silberberg, G., and Markram, H. (2007). Disynaptic inhibition between neocortical pyramidal cells mediated by Martinotti cells. *Neuron* 53, 735–746. doi: 10.1016/j.neuron.2007.02.012

Simonnet, J., Eugène, E., Cohen, I., Miles, R., and Fricker, D. (2013). Cellular neuroanatomy of rat presubiculum. *Eur. J. Neurosci.* 37, 583–597. doi: 10.1111/ejn.12065

Somogyi, P., and Klausberger, T. (2005). Defined types of cortical interneurone structure space and spike timing in the hippocampus. *J. Physiol.* (*Lond*) 562, 9–26. doi: 10.1113/jphysiol.2004.078915

Tamamaki, N., Yanagawa, Y., Tomioka, R., Miyazaki, J.-I., Obata, K., and Kaneko, T. (2003). Green fluorescent protein expression and colocalization with calretinin, parvalbumin, and somatostatin in the GAD67-GFP knock-in mouse. *J. Comp. Neurol.* 467, 60–79. doi: 10.1002/cne.10905

Taniguchi, H., He, M., Wu, P., Kim, S., Paik, R., Sugino, K., et al. (2011). A resource of cre driver lines for genetic targeting of GABAergic eurons in cerebral cortex. *Neuron* 71, 995–1013. doi: 10.1016/j.neuron.2011.07.026

Taube, J. S. (2007). The head direction signal: origins and sensory-motor integration. *Annu. Rev. Neurosci.* 30, 181–207. doi: 10.1146/annurev.neuro.29.051605.112854

Taube, J. S., Muller, R. U., and Ranck, J. B. (1990). Head-direction cells recorded from the postsubiculum in freely moving rats. II. Effects of environmental manipulations. *J. Neurosci.* 10, 436–447.

Thorndike, R. L. (1953). Who belongs in the family? *Psychometrika* 18, 267–276. doi: 10.1007/BF02289263

Uematsu, M., Hirai, Y., Karube, F., Ebihara, S., Kato, M., Abe, K., et al. (2007). Quantitative chemical composition of cortical GABAergic neurons revealed in transgenic venus-expressing rats. *Cereb. Cortex* 18, 315–330. doi: 10.1093/cercor/bhm056

van Groen, T., and Wyss, J. M. (1990a). The connections of presubiculum and parasubiculum in the rat. *Brain Res.* 518, 227–243. doi: 10.1016/0006-8993(90)90976-I

van Groen, T., and Wyss, J. M. (1990b). The postsubicular cortex in the rat: characterization of the fourth region of the subicular cortex and its connections. *Brain Res.* 529, 165–177. doi: 10.1016/0006-8993(90)90824-U

van Haeften, T., Wouterlood, F. G., Jorritsma-Byham, B., and Witter, M. P. (1997). GABAergic presubicular projections to the medial entorhinal cortex of the rat. *J. Neurosci.* 17, 862–874.

Van Strien, N. M., Cappaert, N. L. M., and Witter, M. P. (2009). The anatomy of memory: an interactive overview of the parahippocampal-hippocampal network. *Nat. Rev. Neurosci.* 10, 272–282. doi: 10.1038/nrn2614

Wang, Y., Gupta, A., Toledo-Rodriguez, M., Wu, C. Z., and Markram, H. (2002). Anatomical, physiological, molecular and circuit properties of nest basket cells in the developing somatosensory cortex. *Cereb. Cortex* 12, 395–410. doi: 10.1093/cercor/12.4.395

Wang, Y., Toledo-Rodriguez, M., Gupta, A., Wu, C., Silberberg, G., Luo, J., et al. (2004). Anatomical, physiological and molecular properties of Martinotti cells in the somatosensory cortex of the juvenile rat. *J. Physiol.* (*Lond*) 561, 65–90. doi: 10.1113/jphysiol.2004.073353

Ward, J. H. Jr. (1963). Hierarchical grouping to optimize an objective function. *J. Am. Stat. Assoc.* 58, 236–244. doi: 10.1080/01621459.1963.10500845

Wonders, C. P., and Anderson, S. A. (2006). The origin and specification of cortical interneurons. *Nat. Rev. Neurosci.* 7, 687–696. doi: 10.1038/nrn1954

Xu, H., Jeong, H.-Y, Tremblay, R., and Rudy, B. (2013). Neocortical somatostatin-expressing GABAergic interneurons disinhibit the thalamorecipient layer 4. *Neuron* 77, 155–167. doi: 10.1016/j.neuron.2012.11.004

Xu, Q., Cobos, I., La Cruz De, E., Rubenstein, J. L., and Anderson, S. A. (2004). Origins of cortical interneuron subtypes. *J. Neurosci.* 24, 2612–2622. doi: 10.1523/JNEUROSCI.5667-03.2004

Xu, X., Roby, K. D., and Callaway, E. M. (2010). Immunochemical characterization of inhibitory mouse cortical neurons: three chemically distinct classes of inhibitory cells. *J. Comp. Neurol.* 518, 389–404. doi: 10.1002/cne.22229

Yoder, R. M., Clark, B. J., and Taube, J. S. (2011). Origins of landmark encoding in the brain. *Trends Neurosci.* 34, 561–571. doi: 10.1016/j.tins.2011.08.004

Conflict of Interest Statement: The authors declare that the research was conducted in the absence of any commercial or financial relationships that could be construed as a potential conflict of interest.

Article 2

Anterior thalamic nuclei provide excitation and PV mediated feed-forward inhibition onto presubicular layer 3 neurons

In my previous study, I characterized the interneuron diversity in all layers of the presubiculum. Both excitatory and inhibitory components of the microcircuit have now been identified and we found that they share similar features with neuronal populations in other cortical areas. Vestibular inputs are the major contributors to the head directional firing of neurons in the anterior thalamic nuclei (ATN) that project to the presubiculum. Presubicular head direction cells in turn project to the entorhinal cortex and contribute to spatial firing of grid cells. However, little is known about the influence of thalamic inputs onto presubicular neurons, the nature of their postsynaptic target cells within presubiculum as well as the existence of feedforward and feedback inhibitory motifs.

The second part of my thesis consisted in examining the long-range inputs from the anterior thalamic nuclei to the presubicular principal neurons and interneurons. In the present work, I addressed the functional connectivity of the thalamic head directional input to superficial layer 3 neurons of the presubiculum combining double patch-clamp whole-cell recordings, optogenetics (ChR2 and NphR) and stereotaxic retrobeads injections. By injecting a viral vector containing channelrhodopsin (ChR2) and a fluorescent reporter protein (eYFP) in the anterior thalamic nuclei (ATN), I revealed that ATN selectively innervated superficial layers of the presubiculum with dense axonal projections observed in layers 1 and 3. Then, I combined the retrograde labelling of MEC projecting neurons of the presubiculum with the viral expression of ChR2-eYFP in thalamic axons. My result showed that ATN inputs provide direct excitation onto MEC projecting pyramidal neurons and FS-PV interneurons but not onto LTS-SST interneurons in superficial layer 3. Interestingly, evoked excitation onto pyramidal neurons was typically followed by a disynaptic inhibitory component likely arising from a feedforward inhibitory circuit. Using dual-patch-clamp recordings, I demonstrated a high degree of interconnections between pyramidal neurons and FS-PV interneurons. By specifically expressing NphR in Pvalb-Cre mice, I confirmed that FS-PV interneurons are the major elements of the feedforward inhibition, as optogenetic silencing of PV greatly suppressed, and in most cases abolished, feedforward inhibition onto principal neurons.

Taken together, my finding suggested two distinct roles of PV and SOM presubicular interneurons. The directly recruited PV interneurons are responsible for the feedforward inhibition onto pyramidal neurons and thus, are likely to control the temporal precision of head direction signalling during fast head turns. On the contrary, SST interneurons are not excited by long-range inputs from the thalamus, but rather are recruited indirectly by presubicular pyramidal cells and potentially form a feedback inhibitory loop during persistent firing in the absence of head movements. In the future, in vivo recordings of presubicular

head direction cells combined with silencing of either PV or SST interneurons will enable to confirm these hypotheses.

Title :

Anterior thalamic nuclei provide excitation and PV mediated feed-forward inhibition onto presubicular layer 3 neurons

Authors :

Mérie Nassar, Jean Simonnet, Bertrand Mathon, Li-Wen Huang, Ivan Cohen, Michael H.K. Bendels, Richard Miles and Desdemona Fricker

Keywords: optogenetics, feed-forward, presubiculum, thalamus, head-direction

Introduction

The presubiculum (Prs) is part of the parahippocampal cortex, located between the hippocampus and the entorhinal cortex (Amaral and Witter, 1989 ; van Strien et al., 2009). It plays a fundamental role in spatial orientation as most presubicular neurons in layer 3 and some in deep layers are head direction cells (Boccara et al., 2010; Preston-Ferrer et al., 2016). These neurons fire persistently when the head of the animal is oriented in a specific direction. Vestibular inputs make a major contribution to head directional firing of neurons in the anterior thalamic nucleus (ATN) of the thalamus (Taube. 2007), which in turn projects to the presubiculum (van Groen and Wyss, 1990; Peyrache et al., 2015). Lesions of the anterior thalamus abolish head direction firing and impair grid cell signals in parahippocampal cortex (Goodridge and Taube, 1997; Winter et al., 2015). Head direction signals transmitted via the thalamus (Taube et al., 1995), together with visual information from visual (Vogt and Miller, 1983) and retrosplenial cortices (van Groen and Wyss, 1990) are integrated in the presubiculum. In terms of functional connectivity, direct synaptic connections of retrosplenial cortex to presubicular MEC projecting neurons have been demonstrated (Kononenko and Witter. 2011). In addition, ATN has been shown to contribute to spatial firing of grid cells in the MEC (McNaughton et al., 2006; Langston et al., 2010, Winter et al., 2015). But whether thalamic axons also contact directly the presubicular MEC projecting neurons remains to be shown.

Recently, we have identified a diversity of principal cells and interneurons in the presubiculum (Nassar et al., 2015; Simonnet et al., 2013). However, little is know about how thalamic information is processed by presubicular microcircuit. More fundamentally, the identity of their main postsynaptic target types within presubiculum remains uncertain, i.e., pyramidal (Pyr) dendrites or inhibitory interneurons such as parvalbumin (PV) or somatostatin (SST) expressing neurons. A key feature of thalamocortical interactions is the feedforward inhibition mediated by cortical inhibitory interneurons (INs) (Agmon and Connors, 1991; Swadlow, 2002) that is thought to control the temporal precision of cortical responses to sensory stimuli (Beierlein et al., 2003; Gabernet et al., 2005; Sun et al., 2006; Cruikshank et al., 2007). It is unclear whether a similar process operates within the ATN-PrS pathway.

In the current study, we examine the long-range inputs from ATN to principal neurons and interneurons of presubiculum using a combination of electrophysiology, optogenetics and retrograde labeling techniques. Our results reveal that ATN axons selectively innervate

superficial layers and most densely superficial layer 3. SST interneurons are not excited by thalamic inputs, but rather are recruited indirectly in a facilitating and frequency dependent manner by presubicular pyramidal cells. On the contrary, ATN axons make direct synaptic contacts with pyramidal MEC projecting neurons as well as with PV interneurons in superficial layer 3. While pyramidal cell-Martinotti cell interactions may support sustained firing of head direction cells (Simonnet et al., under review), PV mediated feed-forward inhibition could limit the "window of opportunity" during which pyramidal neurons integrate excitatory inputs and gate spike output during fast head turns.

Material and Methods

Animals

Experiments were performed on male Pvalb-Cre mice (Jax 008069 ; Hippenmeyer et al., 2005) and Sst-IRES- Cre mice (Jax 013044; Taniguchi et al., 2011) crossed with the Ai14 Cre reporter line (Jax 007914; Madisen et al., 2010). Cre-mediated recombination resulted in the expression of red fluorescent tdTomato labeling in Pvalb-Cre and SST-Cre neurons, which can be visualized without activating ChR2. Wild-type BL6 and Pvalb-Cre males were used for double injections. Our care and use of animals conformed to the European Community Council Directive of 22 September 2010 (2010/63/EU) and French law (87/848). Our study was approved by the local ethics committee Charles Darwin N◦5 and the French Ministry for Research.

Viral vectors

AAV2.hSyn.hChR2(H134R)-eYFP.WPRE.hGH (PennVector core, University of Pennsylvania School of Medicine, Addgene 26973P) with serotypes 5 or 9, containing an enhanced ChR2-EYFP fusion gene, driven by a hSynapsin promoter were used for injections. We also used AAV1.EF1a.DIO.eNpHR3.0-eYFP.WPRE.Hgh (PennVector core, University of Pennsylvania School of Medicine, Addgene 26966) an adeno-associated virus serotype 1 (AAV1) carrying Cre-inducible halorhodopsin-3.0 (eNpHR3.0)-enhanced yellow fluorescent protein (eYFP) transgene driven by EF1a promoter for optogenetic inhibition. Viral vectors were stored in aliquots at -80°C until use.

Stereotaxic surgery

Mice were anesthetized intraperitoneally with ketamine hydrochloride and xylazine (100 and 15 mg.kg−1, respectively) and positioned in a stereotaxic frame. Mice aged postnatal day 25-35 were used for all surgeries. Unilateral viral injections were performed using previously described procedure (Mathon et al., 2015). Anterior-thalamic nuclei were targeted for AAV injections. Typical coordinates from Bregma for ATN were lateral, +0.75 mm; posterior, -0.82 mm; and depth, 3.2 mm. The final volume for hSyn-ChR2 AAV2/5 or 2/9 vectors was between 150 nL and 350nL. AAV vector was delivered with a Hamilton syringe in a syringe Pump Controller (Harvard Apparatus, Pump 11 elite) at 60nL/min. We waited 2 weeks with AVV9 and 3 weeks with AAV5 to allow maximal and complete viral expression. Viral titers for AAV2/5 and AAV2/9 vectors were respectively $1.3^{e}10^{13}$ and $3.39^{e}10^{13}$ virus particles/ml. Light-evoked responses were similar for ChR2 expression by either of the two serotypes and results were pooled (Supplementary Fig. 2). Double injections of AAV in ATN and retrograde tracer in MEC were also performed. Presubicular projecting neurons were retrogradely labeled by injecting red fluorescent latex microspheres (Lumafluor) in the ipsilateral MEC. Coordinates from Bregma for MEC were lateral, +3 mm; posterior, -4.7 mm; and depth, 4 mm. A volume of 300nL microspheres was injected. Finally, we combined a double injection of AAV-ChR2 in ATN and AAV-eNpHR3.0 in the presubiculum in Pvalb-Cre mice to allow specific expression of halorhodpsin in PV interneurons. AAV-EF1a-DIO-eNpHR3.0-EYFP was injected into the presubiculum. Coordinates from Bregma for presubiculum were lateral +2 mm; posterior -4.06 mm; and depth 2.15 mm. Final volume of AAV-eNpHR3.0 was 350nL. We waited 5 weeks for viral expression. The titer for the virus was $1.09^{e}13$ virus particles /ml. To ensure minimal leak into surrounding brain areas, injection pipettes remained in the brain for 5 min after injection before being slowly withdrawn.

Preparation of brain slices

Acute slices containing the hippocampus, subicular complex and entorhinal cortex were prepared 2–5 weeks after virus and/or tracer injections. Animals were anesthetized with ketamine hydrochloride and xylazine (100 and 15 mg.kg−1, respectively), then perfused through the heart with a solution containing 125 NaCl, 25 sucrose, 2.5 KCl, 25 $NaHCO_3$, 1.25 NaH_2PO_4, 2.5 D-glucose, 0.1 $CaCl_2$, 7 $MgCl_2$ (in mM) cooled to 4°C and equilibrated with 5% CO_2 in O_2. Animals were decapitated and horizontal, 300-320 µm thick brain sections

were cut in the same solution using a vibratome (Leica VT1000S). They were stored for at least 1 h at 22–25°C in a holding chamber filled with ACSF containing (in mM): 124 NaCl, 2.5 KCl, 26 $NaHCO_3$, 1 NaH_2PO_4, 2 $CaCl_2$, 2 $MgCl_2$, and 11 D-glucose, bubbled with 5% CO_2 in O_2 (pH 7.3, 305–315 mOsm/L). Slices were then transferred to a recording chamber (volume 2–3 ml, temperature 33–35°C) mounted on a BX51WI microscope (Olympus, France). Mice were excluded if the extent of transfection at the injection site was too small or too large and leaking into surrounding brain regions.

Whole-Cell Patch-Clamp Recordings

Recordings were made with glass pipettes pulled using a Brown-Flaming electrode puller (Sutter Instruments) from borosilicate glass of external diameter 1.5 mm (Clark Capillary Glass, Harvard Apparatus). Electrode resistance was 4–8 MOhm after filling with a solution containing (in mM) : 135 K-gluconate, 1.2 KCl, 10 HEPES, 0.2 ethylene glycol tetra-acetic acid (EGTA), 2 $MgCl_2$, 4 MgATP, 0.4 Tris-GTP, 10 Na_2-phosphocreatine and 2.7–7.1 biocytin. 2 mM of QX 314 bromide (Tocris) a blocker of voltage-activated Na+ channels was added to the intra-pipette solution to measure the inhibitory (I) and excitatory (E) synaptic currents at depolarized holding potentials (Fig. 3 and Fig. 9). pH of the pipette solution was adjusted to 7.3 with KOH and the osmolarity was 290 mOsm. Fluorescently labeled PV or SST were identified using LED illumination with appropriate emission/excitation filters (OptoLED, Cairn Research, Faversham, UK) using a Luca CCD Camera (Andor). Whole-cell current-clamp recordings were made using a MultiClamp 700B amplifier and pCLAMP software (Molecular Devices, Union City, CA, USA). Potential signals were filtered at 6 kHz and digitized at 20–50 kHz and an estimated junction potential of 15 mV was not corrected. Pyramidal cells were identified as non-fluorescent regular-spiking neurons, Parvalbumin-expressing and Somatostatin-expressing interneurons were identified from PvalbCre::tdTomato and Sst-Cre::tdTomato mice as red fluorescent neurons. Typical properties of each cell type are listed in Table 1 (cf. Nassar et al., 2015). PV interneurons recorded from PvalbCre::tdTomato exhibited a typical fast-spiking firing pattern. Given the heterogeneous population of presubicular SST interneurons labelled in Sst-Cre::tdTomato mouse line (Nassar et al., 2015), we always checked for the typical low threshold firing patterns (LTS-SST).

Optical stimulation

The optical stimulation of ChR2-expressing ATN axons, was achieved via a single-wavelength LED system (470 nm; Cairn OptoLED) or laser illumination (405 nm ; LuxX, Omicron), connected to the microscope via a custom made triple port (Cairn). Synaptic responses were recorded in whole-cell current- and voltage-clamp mode from postsynaptic presubicular neurons. Double recordings of neighboring pyramidal neurons and interneurons were performed for most experiments. The LED illumination gave a 200µm-diameter spot through a 60X 1.0 NA plan-Apochromat objective. 0.5–20 ms flashes were delivered locally near or over the recorded somata. LED light intensity was calibrated (Supplementary Fig. 1), then for most experiments, we chose a "low intensity stimulation" that ranged from 0.1 to 0.5 mW, set such that neuronal responses were near threshold, reducing network activation following ATN axons stimulation. Excitatory and inhibitory post-synaptic responses were evoked by 10Hz and 30Hz trains of photostimulation (light pulse duration, 0.5 ms). We tested for direct, monosynaptic excitation as decribed previously (Petreanu et al., 2007; Cruikshank et al., 2010) by optical stimulation in the presence of 1 µM TTX (Tocris) to remove polysynaptic excitation, and 100 µM 4-AP (Sigma) to enhance axonal depolarization. NBQX (10µm, Tocris), D-AP5 (100µm, Tocris) and Gabazine (10µm, Tocris) were used to block AMPA, NMDA and $GABA_A$ receptors respectively.

In experiments where PV interneurons were inhibited while the thalamic pathway was photostimulated, a second, yellow LED (572nm) was used to activate eNpHR3.0 in PV neurons, and combined with the blue light (470nm) illumination in the lightpath. The light intensity at the sample was set at 0.3mW. A yellow light pulse (20 ms in duration) was triggered 5 ms before the onset of the blue light pulse (0.5 ms in duration) to ensure that the PV interneurons were inhibited before and during thalamic axon stimulation. For each injected mouse, we verified the efficacy of yellow LED-triggered hyperpolarization in at least one PV interneuron.

To determine the excitatory-inhibitory balance for activation of thalamic fibers at different stimulation sites in the presubiculum, pyramidal cells in layer 3 were voltage-clamped at –30mV while a focused 405 nm laser beam (LuxX, Omicron) scanned the across the presubiculum. After acquiring a planning image at 4X, we switch back to 60X objective for focal point illumination (spot size 5-10µm). A motorized platform (Luigs and Neumann, Ratingen, Germany) was used to move the stage with custom written software (Morgentau Solutions, Munich, Germany ; Bendels et al., 2008; Beed et al., 2010) across a scanning field

with a hexagonal grid of optical stimulation sites. The 40 to 80 stimulation sites were separated from each other at 40µm distance.

The spatial resolution for laser illumination is given by the single photon illumination cone, and diffraction limited by light scattering in the slice (Trigo et al., 2009). A light spot of diameter ~ 10 µm in 100 µM pyranine (HPTS) solution was measured at the focus using the Luca CCD camera. The duration of the light pulse was gated so as to deliver brief (0.5-2ms) pulses of light at each stimulation site. Laser power was adjusted to nominally 0.4-2mW, to record EPSC-IPSC sequences from the activation of a small number of fibers. Grids were repeated three times for each recorded neuron.

We took multiple precautions to limit experimental variability arising from variation in the amount of virus taken up and/or expressed across animals. First, we only recorded from slices exhibiting ChR2-eYFP expression visible under ×4 magnification. Second, we limited recordings to superficial layer 3 where ChR2 expression was high. Third, we included data only from animals in which at least one significant excitatory response in a pyramidal neuron was recorded in control and remained present in TTX/4AP. Fourth, we performed double-recording of neighboring pyramidal neuron and PV or SST interneuron such that we could normalize the photo-stimulation–evoked response in a given interneuron type to the response in the pyramidal neuron.

Data analysis and Statistics

Peak amplitudes of light-evoked PSCs were calculated from average traces (typically 30-40 traces per trial) for PV and pyramidal cells. Failures and additional or later peaks only occurred in LTS-SST interneurons for evoked EPSC responses. If multiple peaks were detected, the amplitude of the first peak was calculated from individual traces. A cell was considered to have received an input if the peak response was > 3 times the standard deviation of the noise level of resting membrane potential. Success rate was determined as the number of detected evoked EPSCs divided by the total number of episodes. We recorded EPSCs close to -60 mV holding potential. IPSCs were recorded at 0 mV. ESPC onset latency was calculated from the stimulation onset to 5 % of the rising amplitude of the evoked current from individual traces and then averaged. If multiple peaks were detected, only the onset of the first peak was considered. For analysis of synaptic dynamics, response amplitudes were calculated for each pulse then normalized to the first value. IPSCs were recorded at 0 mV, in

the presence of D-AP5. Gabazine abolished the outward current, confirming its inhibitory nature. To detect the onset of the IPSC, we measured the 5% rising amplitude starting from the peak of the outward current. Onset jitter was defined as the SD of the 5% rise onset, measured across individual sweeps per cell. Paired-pulse ratio (PPR) was defined as the amplitude ratio of the second to the first postsynaptic response after repetitive stimulations, and was calculated from averaged traces (typically 10 traces per trial). Current-clamp recordings of postsynaptic evoked responses were performed at resting membrane potential. Because LTS-SST interneurons tended to fire spontaneously, they were held at a slightly hyperpolarized membrane potential near -50-55 mV to avoid spontaneous AP firing. Action potential latency was calculated as the latency from the stimulation onset to the peak of the action potential. Spiking probability corresponded to the number of action potentials during a train of 10 stimulations for a given intensity, divided by 10. The input resistance was constantly monitored by applying small current step (-50 pA) to the patch pipette. If the input resistance changed more than 20% the recording was discarded.

Signals were analyzed with AxoGraphX, and custom written software (Labview, National Instruments; MATLAB, The Mathwork). Algorithms to detect action potentials and measure active and passive neuronal properties are described fully in Simonnet et al. (2013) and Nassar et al. (2015). Results are given as mean ± SEM (n = number of cells, slices, or animals as indicated). Statistical analysis was performed with Prism (GraphPad Software, Inc.) and MATLAB (The Mathwork).

Paired recordings

During paired whole-cell patch-clamp recordings of synaptically connected neurons in voltage clamp mode, single action current were evoked by a brief depolarizing injection in the presynaptic neuron (1–2 ms, 100-200mV). uIPSCs and uEPSCs were respectively recorded at -50 mV and -70 mV holding potentials in the postsynaptic cell. Excitatory and inhibitory postsynaptic currents were detected and measured automatically from low-pass filtered records (1-1.5 KHz). Thresholds for detection were 4-6 pA for EPSCs and IPSCs. Functional properties of unitary IPSCs and EPSCs were determined from averages of 30–60 traces, including failures. Peak amplitudes were calculated as the mean amplitude of responses including failures (failure amplitude = 0). The synaptic latency was determined as the time interval between the peak of the presynaptic action current and the onset of the postsynaptic uIPSC; the onset point was determined as 5% of the postsynaptic peak event. Rise time was

defined as the time from 20 to 80% of the peak response. Decay time constant was defined as the time from 100 to 50% of the peak response. PSC trains were normalized to the amplitude of the first EPSC or IPSC before analyzing them for short-term plasticity. Synaptic transfer rate was calculated from paired records as the number of detected post-synaptic events divided by the number of presynaptic spikes. Failure rate was 1-transfer rate.

Image acquisition and Analysis

Stained slices were visualized with a QImaging Retiga EXI camera (Qimaging Surrey, BC, Canada), and scanned with an Optigrid II (Thales Optem, Qioptik, Rochester, NY, USA) on an inverted Olympus IX81 microscope. The Optigrid system permitted the acquisition of structured images. Stacks of 50–80 images (*z*-step, 0.7 µm) were acquired per slice, using an oil immersion objective (20x, NA 0.9). Presubicular layers and borders were defined using specific cytoarchitectonic features identified by DAPI staining. For a better resolution (cf fig. 2b), sections were visualized using an Olympus FV-1000 Upright Confocal Microscope. *Z* series of optical sections was performed at 0.3-µm increments for qualitative analysis. Blue, green, red, fluorescence was acquired sequentially. Images were uniformly adjusted for contrast and brightness using Image J software (NIH).

Morphological 3D reconstructions

As described in detail previously (Nassar et al., 2015; Simonnet et al., 2013), neurons were filled with 0.3% (3mg/mL) of biocytin during whole-cell recordings for post-hoc revelation of the morphology. Axo-dendritic morphology was reconstructed from z-stacks of acquired images with Neurolucida software (Microbrightfield, Williston, VT, USA).

Results

Selective ChR2 expression in the anterior thalamic nuclei

To investigate the funtional connectivity of the ATN to the presubiculum, we performed unilateral *in vivo* injection of adeno-associated viruses (AAV) to express the light-gated Channelrhodopsin2-green fluorescent protein (ChR2-EYFP) in the anterior thalamic nuclei (ATN). Two to three weeks after incubation, horizontal slices were prepared, and the thalamic injection site was examined. An example illustrating the ChR2-eYFP expression in the ATN

is show in fig. 1A, B. Fluorescent (eYFP) labeled thalamic axons innervated superficial layers of presubiculum, more densely in layers 1 and 3 than layer 2. They did not project into deep presubiculum layers, adjacent subiculum or entorhinal cortex (Fig. 1C, D; Fig. 2A). When a ChR2-eYFP expressing thalamic neuron was illuminated with a blue light pulse in the presence of the inotropic glutamatergic antagonists CNQX and D-AP5, it depolarized and generated a spike in current clamp (Fig. 1F, upper). In voltage clamp mode, an inward ChR2-mediated photocurrent was detected (Fig. 1F, lower). ChR2-eYFP positive thalamic neurons always responded immediately to light onset (latency to onset < 0.1 ms; n=4 neurons).

ATN axon terminals directly contact MEC projecting pyramidal neurons

To test whether ATN axons directly target MEC projecting pyramidal neurons, we combined the retrograde labeling of MEC projecting neurons of the presubiculum with the viral expression of ChR2-eYFP in thalamic axons (Fig. 2A). Retrograde labeling showed beads in the somata of presubicular layer 3 neurons (Fig. 2B, C). A few labeled neurons were also observed in deep layers consistent with our previous work (Huang et al., in prep). We performed whole-cell recordings of retrobeads labeled neurons and measured the postsynaptic responses evoked by photo-stimulation of ChR2-expressing thalamic axons. Low intensity light stimulation (0.1-0.5mW) of ATN axons led to excitatory postsynaptic currents (Fig. 2D, F, same neuron as in 2C.). The delay to the onset of the EPSCs was 2±0.15 ms (n=11, Fig. 2E), compatible with monosynaptic activation.

Postsynaptic responses to light stimulation were highly reproducible, with little variation in amplitude across trials and no failures. All retrobeads labeled neurons recorded from slices with channelrhodopsin expressing axons surrounding the cell body responded to light stimulation. Amplitudes varied for different neurons in different slices (289±43 pA, mean± sem, n=11 neurons/5 animals; Fig. 2E). The activation of ATN fibers with a 30 Hz light stimulus evoked action potentials in the beads labeled neuron at resting membrane potential. TTX (1μm) and 4-AP (100μM) were used to prevent recurrent excitation (Mao et al. 2011), established that the observed EPSCs originated from direct connection of ChR2-expressing ATN axon terminals (n=11). The stimulation of ATN terminals generated glutamatergic postsynaptic currents in retrobeads labeled neurons, and evoked EPSCs recorded in beads labeled neurons were sensitive to AMPA receptor and NMDA receptor antagonists (Fig 2. G, n=2 neurons/2 animals). The glutamatergic nature of neurotransmission was confirmed in

layer 3 pyramidal neurons in mice without retrobeads injection (not shown, n=4 neurons/4 animals).

Activation of ATN inputs drives feedforward inhibition in the presubiculum

We next asked if in addition to direct glutamatergic excitation ATN axons also mediate disynaptic inhibition. To test this, light-evoked postsynaptic currents were recorded at a depolarized holding potential of 0 mV. Under this recording condition, responses to photostimulation were biphasic with an excitatory inward current that rapidly transitioned to an inhibitory outward current. Photostimulation of ATN axons reliably elicited both EPSCs and IPSCs in all L3 pyramidal neurons tested (n=9 neurons/9 animals) comprising retrobeads labeled MEC projecting neurons (n=3 neurons/3 animals). The onset latencies of the IPSCs were significantly longer (Fig. 3A, B; 3.3±0.11 ms; mean±sem; n=12/4 animals ; $p < 0.001$, Wilcoxon signed rank test) than those of the EPSCs (1.7±0.09 ms; mean±sem; n=12/4 animals.). The IPSCs were abolished by bath application of GABA receptor antagonist Gabazine or AMPA receptor antagonist NBQX, indicating that they were disynaptic inhibitory currents. The delay between the onset of the EPSC and IPSC onto principal neurons was 1.6 ± 0.09 ms. The variability of onset latency of the EPSCs was significantly smaller than that of IPSCs (EPSCs, 0.12±0.03 ms; IPSCs 0.23±0.03 ms; mean±sem; n=12 cells/4 animals; $p <0.05$, Wilcoxon signed-rank test, Fig. 3C, D). These observations suggests that inputs from ATN provide disynaptic feedforward inhibition onto L3 pyramidal neurons in the presubiculum.

ATN provides excitatory inputs to principal neurons and PV interneurons but not SST interneurons

What are the inhibitory interneuron types that mediate this disynaptic feed-forward inhbition ? To investigate the ATN inputs onto excitatory and different inhibitory cellular elements of superficial layer L3, we performed double-recordings of a principal neuron and a neighboring interneuron to measure the evoked postsynaptic EPSCs (Fig. 4). Recordings of fluorescently labeled PV or SST interneurons were performed in two distinct transgenic mouse lines expressing tdTomato that we previously characterized (Nassar et al. 2015). Low intensity stimulation was set so that synaptic responses could be evoked in at least one of the double recorded neurons. PV interneurons had significantly higher absolute reponse amplitudes

compared to pyramidal neurons (PV, 800 ± 109 pA, n=10 neurons/5 animals; Pyr, 178 ± 55 pA, n=10 neurons/ 5 mice; $p<0.01$ Wilcoxon matched-pairs signed rank test, Fig. 4C, D). LTS-SST had significantly lower absolute amplitudes compared to pyramidal neurons (Pyr, 306±41 pA; LTS-SST, 58±17 pA; mean±sem; n=12 neurons /10 mice ; $p<0.001$ Wilcoxon matched-pairs signed rank test; Fig. 4D, H). EPSC onset latencies were similar in simultaneouly recorded pyramidal neurons and PV neurons (PV, 2.0±0.1ms; Pyr, 2.4±0.1ms; mean±sem; n=10 neurons/5 animals), but they were significantly shorter for pyramidal neurons compared to LTS-SST neurons (Pyr, 2.0±0.2 ms; LTS-SST, 5.3±0.4 ms; mean±sem; n=11 recordings/9 animals, *** $p<0.001$ (Wilcoxon matched-pairs signed rank test; Fig. 4E). While light activation of ATN inputs reliably elicited EPSCs in all Pyr and PV interneurons tested, this was not the case in all LTS-SST interneurons. LTS-SST interneurons responded at least once for repeated trials, but the responses to light stimulation had a 30 % probability of failure across trials (success rate, 0.70 ± 0.06; mean±sem; n=11 neurons/11 animals, Fig. 4I, J). These results were obtained in control conditions, where evoked synaptic responses followed presynaptic action potentials. In pyramidal neurons and PV interneurons synaptic responses persisted during TTX perfusion if 4-AP was simultaneously present (1µM TTX and 100µM 4-AP; n=5 pairs/5 animals; Fig. 4C, H), indicating direct monosynaptic connectivity. In LTS-SST interneurons, evoked responses were completely abolished in the presence of TTX/4-AP. Taken together, our results show that ATN fibers make direct contact with principal neurons and PV interneurons while LTS-SST interneurons are indirectly contacted.

Action potential timing in principal neurons and interneurons is consistent with direct vs. indirect thalamic connectivity.

Next we examined the timing of action potential initiation following light activation of thalamic fibers. As expected, AP latency varied as a function of the light intensity, higher light intensities leading to shorter AP latencies by recruiting more thalamic fibers (n=26 Pyr, 13 PV and 16 SST neurons; Fig. 5A). The light intensity was then adjusted to the lowest level initiating action potentials in simultaneously recorded pairs of Pyr–PV or Pyr-SST neurons. Pairwise comparison showed that pyramidal neurons always fired before SST interneurons with significantly shorter latencies (Pyr, 3.7±0.2 ms; LTS-SST, 7±0.3 ms, mean±sem, n=7 pairs/5 mice, * $p<0.05$ Wilcoxon matched-pairs signed rank test, Fig. 5B, D). On the contrary, PV interneurons always fired earlier than pyramidal neurons with significantly shorter latency

for the first action potential (Pyr, 3.5±0.2 ms; PV, 1.9±0.33 ms, mean±sem, n=8 pairs / 5 mice, ** $p<0.01$ Wilcoxon matched-pairs signed rank test, Fig. 5C, E).

Short-term dynamics of ATN inputs are dependent on post-synaptic cell types

We then investigated the dynamic properties of repetitive ATN fiber stimulation at 10 Hz or 30 Hz using low light intensity (0.1-0.5mW). In both PV and pyramidal neurons, light evoked excitatory postsynaptic currents became smaller over time at both frequencies (Fig 6 A-D); PV interneuron EPSCs tended to depress more strongly (Pair pulse ratio (PPR); 10Hz, 0.63±0.03; 30 Hz, 0.58±0.04, n=12, mean±sem) than pyramidal neuron EPSCs (PPR; 10Hz, 0.93±0.04, n=26; 30Hz, 0.96±0.05, n=25, mean±sem; Fig. 6G, H). On the contrary, the magnitude of the evoked EPSCs displayed short-term facilitation in SST interneurons, between the 2nd and 4th pulse of 30Hz stimulations (PPR; 10Hz, 1.56±0.32, n=14; 30Hz, 5.3±1.19, n=15, mean±sem; Fig. 6 E, F, I). Very small or no responses were detected in SST interneurons during 10Hz trains.

Light evoked spiking dynamics for pyramidal neurons and interneurons

How do differences in synaptic input dynamics impact the spiking behavior of the excitatory and inhibitory neurons ? We examined how spiking probability evolved along repetitive stimuli in each cell type (Fig. 7). We first examined action potential firing probabilities over a range of increasing light intensities (Fig. 7A). For PV interneurons, the transition from 0 to 100% spiking probability occurred over a narrow range in power levels. The spiking probability even exceeded 100% for 12/13 PV cells for high intensities, meaning that a single high intensity light pulse could initiate more than one AP.. In comparison with PV interneurons (10Hz, 1.5±0.1, n=13; 30Hz, 1.4±0.1, n=11; mean±sem), pyramidal neurons and LTS-SST interneurons had much lower spiking probabilities even for maximal intensity stimulations (LTS-SST, 10Hz, 0.3±0.1, n=15; Pyr, 10Hz, 0.5±0.1, n=22; mean±sem) and 30Hz (LTS-SST, 0.4±0.1, n=14; Pyr, 0.5±0.1, n=22; mean±sem). Most Pyr and SST neurons did not sustain firing until the 10th pulse in a train.

To compare the dynamics of spiking probabilities during repetitive stimulations, the intensity of photostimulation was adjusted to intermediate values for each experiment, in order to evoke at least one action potential in the postsynaptic neuron, but to avoid saturating

responses with 100% spiking probability. This intermediate intensity varied from cell to cell, and was in the range of 0.2 to 1 mW. In PV interneurons, the probability to initiate an action potential was highest for the first pulse of both 10 Hz (n=5 neurons/5 animals) or 30 Hz stimuli (n=9 neurons/9 animals, Fig. 7B,C, D), then spiking probabilities decreased for repetitive stimulations. For Pyr cells, spiking probabilities depended on the frequency: at 10 Hz, the probability was highest for the first pulse (n=12 neurons/14 animals), while at 30 Hz, it was highest for the second pulse (Pyr, n=10 neurons/18 animals, Fig. 7B,E,F). Thereafter, spiking probability decreased strongly at both 10Hz and 30Hz (Fig. 7D,F). Pyramidal neurons and even more so LTS-SST interneurons did not always discharge at the beginning of a train of stimulations. In LTS-SST cells, spiking facilitation was observed for the 2nd to the 4th pulse (LTS-SST, n= 9 neurons/15 animals) for 10Hz stimulations and even more for 30Hz stimulations (Fig. 7B, G, H).

L3 PV interneurons are highly interconnected with pyramidal neurons in presubiculum

PV interneurons appeared to be good candidates for feed-forward inhibition of presubicular pyramidal cells. We therefore examined whether L3 FS interneurons make inhibitory synaptic contacts onto nearby pyramidal cells using double recordings (n = 40 pairs tested). The morphology and the corresponding traces obtained from a typical reciprocally connected PV-Pyr pair are shown in Fig. 8. In 50% of tested connections (Fig. 8B), action currrents initiated by depolarizing voltage steps in the PV cell caused IPSCs with monosynaptic latency (0.68±0.03 ms, n=19, table 2) in the pyramidal cell. Conversely, APs in the pyramidal cell initiated unitary excitatory postsynaptic currents (uEPSCs) with monosynaptic latencies (0.74 ± 0.03 ms, n=17; table 2) in PV cells in 52.5% of PV-Pyr pairs tested, and 37.5% of pairs were reciprocally connected (Fig. 8B). PV cells are therefore well suited to mediate feed-forward inhibition, and could also mediate feedback inhibition. Consistent with the idea that PV cells target the perisomatic compartment, unitary IPSCs from PV cells onto pyramidal cells had rapid rise times (uIPSCs: 0.52±0.07 ms, n=19; table 2) compared to the longer unitary EPSC rise times from Pyr-to-PV cells (uEPSCs: 0.31±0.02 ms, n=17; table 2). Under our recording conditions, the mean absolute amplitude of uEPSCs onto PV cells was 72.92±20.15 pA (n=17; Fig. 8D, top) and the mean decay time constant was 0.91±0.07 ms (n=17; table 2). The mean amplitude of uIPSCs in pyramidal cells was 13.76±2.23 pA (n=19; Fig. 8D, top) and the mean decay time constant was 2.9±0.2 ms (n=19; table 2). The probability that a single spike triggered a postsynaptic event, the transfer rate, was high for

both uEPSCs (0.79±0.06, n=17; table 2) and uIPSCs (0.71±0.07, n=19; table 2). In response to 50Hz trains of APs initated in pyramidal cells or in interneurons, the amplitudes of uEPSCs or uIPSCs, respectively, slightly depressed (paired pulse ratio, uEPSCs 0.82±0.07, n=15; uIPSCs 0.85±0.03, n=18; Fig. 8D, E, F). These results show that L3 FS cells mediate widespread inhibition of neighbouring pyramidal neurons and are biased to inhibit those pyramidal cells that directly excite them.

ATN provide PV interneuron mediated feedforward inhibition in the presubiculum

Several elements suggest that PV interneurons mediate ATN-driven feedforward inhibition in the presubiculum. First, our results show that ATN axons directly project to and make functional synapses onto L3 PV interneurons and principal neurons in the presubiculum (Fig. 2 to 7). Second, these two cell types are highly interconnected with each other in the presubicular microcircuit (Fig. 8). To directly test the hypothesis that PV mediate ATN-driven feedforward inhibition, we sought to inhibit them while monitoring the ATN-driven synaptic responses in superficial layer 3 pyramidal cells (Fig. 9A). To achieve this goal, we injected the ATN of PV-Cre mice with AAV.hSyn.hChR2-eYFP and injected the Presubiculum in the same mice with AAV.Ef1a.DIO.eNpHR3.0-eYFP. The cre-dependent expression of the light-gated chloride pumping halorhodopsin (eNpHR3.0) permitted to selectively silence PV neurons in response to yellow light via a potent hyperpolarization (Fig. 9B, n=4 cells/2 animals). We next demonstrated in cell-attached recordings that PV cells fire in response to blue light stimulation of thalamic afferents, and that the evoked action potential can be inhibited during the concommitant activation of eNpHR3.0 (Fig. 9C). In L3 pyramidal neurons, voltage-clamped at 0 mV, a sequence of inward (EPSC) and outward (IPSC) currents was activated in response to optical activation of thalamic fibers. Light mediated silencing of PV interneurons dramatically reduced the ATN-driven feedforward inhibitory current component (at 0 mV, n=6 cells/2 mice, *$p<0.05$, **$p<0.01$, Kruskal–Wallis and Dunn's multiple comparison *post hoc* test) (Fig. 8D, E), and this effect was reversible (Fig. 8D, E). As a control, we checked that the peak amplitude of ATN-driven EPSCs was not affected during yellow light stimulation (-60mV; light off, n=6 cells/2 animals, Kruskal–Wallis and Dunn's multiple comparison *post hoc* test) (Fig. 8F).

Spatial specificities of the feed-forward inhibitory circuit

Whole field LED illumination consistently evoked EPSC-IPSC sequences when stimulating ChR2 expressing thalamic fibers. To better compare with the physiologically sparse activation of head directional inputs, we selectively activated a small subset of thalamic fibers using low intensity focal laser illumination. Presubicular layer 3 pyramidal neurons were recorded in voltage-clamp configuration at -30 mV. Laser scanning photostimulation determined the spatial distribution of activation sites that gave direct excitatory and indirect feed-forward inhibitory responses (Fig. 10A, B). When directing the laser spot close to the soma of the recorded layer 3 pyramidal neuron, the optical activation of ATN axons initiated an inward current followed by an outward current similar to the EPSC-IPSC sequence initiated by whole-field LED illumination (Fig. 10C). The outward currents were abolished in the presence of Gabazine (GZ, n=3/3 tested cells ; Fig. 10 C, D, E), confirming their GABAergic nature, and both inward and outward currents were sensitive to Glutamate receptor antagonists (not shown).

In a radius of up to 200 µm around the soma, synaptic responses were observed for most of the photostimulation sites (80.5±4% of non-null responses in n=9 cells from 3 mice). For distances > 200µm the overall probability to initiate any synaptic responses dropped (28 ± 2.6 % of non-null responses) and the average amplitudes for both inward and outward currents tended to be smaller. Interestingly, depending on the exact site of the laser stimulation, blue light gave either balanced excitatory-inhibitory responses (Fig. 10C), or, only disynaptic inhibitory responses (Fig. 10D), or only direct excitation (Fig. 10E). Frequently, evoked pure IPSCs were found for stimulation sites in superficial layer 2 (Fig. 10D, n=4/9 pyr neurons). IPSC amplitudes generally tended to become smaller for light stimulations at greater distance from the perisomatic region. Responses were consistent across multiple trials (not shown).

Discussion

Here, we characterized the synaptic connections of the axonal projections from ATN to superficial layer 3 of mouse presubiculum by combining electrophysiology, retrograde tracing and optogenetics. We show for the first time that ATN inputs provide direct excitation onto MEC projecting pyramidal neurons and PV interneurons but not onto LTS-SST interneurons. The activation of ATN inputs may lead to disynaptic inhibition of layer 3 pyramidal neurons and PV are a major mediator of this feedforward inhibition. Pyramidal neurons and FS

interneurons in superficial layer 3 are highly interconnected, and optogenetic silencing of PV neurons greatly reduced, and in most cases abolished, feedforward inhibition onto principal neurons.

ATN inputs onto presubicular layer 3 pyramidal neurons and PV interneurons provided strong glutamatergic excitation with short-term depression in response to repetitive photostimulation of ChR2 expressing thalamic fibers. PV interneurons were readily recruited and fired at least one action potential even for low stimulation intensities. Our results indicate that single incoming stimuli activate PV mediated feedforward inhibitory circuitry more effectively than excitation onto principal neurons. ATN inputs onto LTS-SST interneurons were indirect with longer latencies and small amplitudes of responses characterized by a high probability of failures. They showed frequency dependent short-term synaptic facilitation during 30Hz trains and an increased action potential firing probability for repetitive stimulations. Our findings suggest that while LTS-SST interneurons provide a delayed source of inhibition in the presence of sustained high-frequency inputs, PV inteneurons are responible for rapid feed-forward inhibition in the presubiculum. This could play an important role in filtering head directional information as soon as it reaches the presubicular microcircuit.

Optical activation of long-range axon terminals using ChR2

The presubiculum is a 6-layered neocortical area and receives fibers from several afferent brain regions, including the thalamus, and also retrosplenial cortex, visual cortex, neighboring subiculum, parasubiculum and EC among others (Van Groen and Wyss, 1990 a,b,c; Van Groen et al., 1992a; Van Groen and Wyss, 2003; Jones et al., 2007; Sugar et al., 2011). Afferent fibers are intermingled across the different layers and the *ex vivo* slice preparation does not allow to electrically stimulate fibers from only one afferent area. The targeted injection of AAV expressing channelrhodopsin in the ATN allowed us to specifically stimulate those afferent fibers with light, and dissect their functional connectivity.

One potential complication associated with the use of AAV-ChR2 is artificial depression of synaptic transmission (Cruickshank et al., 2010). Artificial depression can be more or less pronounced and might depend not only on the molecular pattern of the synapse or the number of available vesicles but also on the stimulation protocol and the AAV serotype. A recent report by Jackman et al. (2014) comparing optical and electrical stimulation showed that AAV9 mediated expression of ChR2 gave responses that are more similar to electrical

stimulation than with AAV5 and AAV1. In our experiments, due to the overlap of thalamic axonal fibers with others that converge also to the presubiculum, we could not compare optical stimulation of ChR2 expressing thalamic fibers with electrical stimulation. We note, however, that both AAV5 and AAV9 serotypes evoked similar short-term depression in principal neurons and PV interneurons, and "indirect" facilitation in LTS-SST **(**Supplementary Fig. 2**).** The calcium permeability of ChR2 may be problematic (Nagel et al., 2003), because calcium influx through ChR2 might modulate transmitter release and alter synaptic dynamics (Neher and Sakaba, 2008). This issue could be resolved by mutations of ChR2 (Lin et al., 2009) which would reduce its calcium permeability. For now, synaptic dynamics reported using ChR2 dependent optical stimulation must be interpreted with caution. Nevertheless, our results show cell-type specific, distinct profiles of synaptic activation in responses to thalamic input activation onto principal neurons, PV and LTS-SST interneurons.

Anterior thalamic inputs to excitatory and inhibitory neurons in Presubiculum

Strong excitatory synaptic responses with short monosynaptic latencies and high amplitudes were recorded from pyramidal neurons and PV interneurons. We qualified these inputs as direct synaptic connections, and indeed responses persisted in the presence of TTX, ie. independent of action potential generation. The light induced opening of the ChR2 cationic ion channel assured a sufficient depolarization of the presynaptic terminal, that – in the presence of 4-AP - led to neurotransmitter liberation. Light evoked postsynaptic responses in LTS-SST interneurons were relatively small, displayed longer latencies and failures. Despite their greater intrinsic excitability (high input resistance and depolarized resting potentials, cf. Table 1) relative to PV interneurons, LTS-SST interneurons had much lower probability of firing action potentials at all stimulation intensities. In contrast to the light-induced responses observed in PV interneurons and pyramidal neurons that both passed the TTX/4AP test for monosynaptic transmission, this was not the case for postsynaptic responses recorded on LTS-SST interneurons, indicating that they were obtained through indirect disynaptic excitation. Presumably, LTS-SST interneurons were activated by local principal neurons, in turn mediating feedback inhibition onto PC (see also Simonnet et al., 2016, under review). Overall, our findings are similar to results obtained in neocortical areas (Cruikshank et al., 2010 ; Lee et al., 2013, Keshavarzi et al., 2014) where PV cells receive stronger excitatory inputs and are more easily recruited than pyramidal cells or LTS-SST. Latencies calculated

from light onset to postsynaptic responses are shorter in PV than in pyramidal neurons, which could be due to the location of thalamic excitatory synapses on the soma of PV cells, ensuring fast signaling, while in pyramidal cells excitatory synapses may be located on dendritic spines at some distance from the soma. Compared to other cortical areas (Lee et al., 2013 ; Haley et al., 2016 ; Keshavarzi et al., 2014) the latencies of synaptic excitation after photostimulation of afferent fibers on PV and Pyr neurons seem to be rather similar to presubiculum, even though this comparison is across different experimental preparations.

The presubiculum is known to project to neighboring MEC (Van Groen and Wyss, 1990c ; Honda and Ishizuka, 2008, Honda et al., 2011). Preston-Ferrer et al. (2016) have shown recently that these projection neurons are located in layer 3 of presubiculum and that they are head direction cells. Here, we demonstrate that labeled MEC projecting neurons in presubicular layer 3 receive direct thalamic inputs. ATN inputs onto MEC projecting neurons had similar amplitudes, latencies, spiking probability and disynaptic inhibition as in the overall population of superficial layer 3 principal neurons. The passive and active intrinsic properties (table 1) of retrogradely labeled layer 3 MEC projecting pyramidal neurons are also similar to the overall population of pyramidal layer 3 neurons, and we thus suggest that pyramidal neurons in superficial layer 3 are a rather homogenous cell population (cf. also Simonnet et al., 2013). A difference in AP threshold was noted, possibly due to retrobeads labeling that could possibly alter the gating properties of Na+ channels. The fact that the presubicular head direction neurons are crucial in the sequential transmission of the ATN head directional signal to the MEC establishes this area as an obligatory node in the information flow required for undisrupted grid cell signaling (Tukker et al., 2015; Winter et al., 2015).

Strong activation of PV cells by thalamic inputs is likely to result in widespread disynaptic inhibition within superficial layer 3 of the presubiculum consistent with their typically dense axons (Nassar et al., 2015). The anatomical features and firing patterns of layer 3 PV interneurons resemble those of parvalbumin-positive, somatic-targeting interneurons found in many brain regions (Markram et al., 2004; Rudy et al., 2010, Nassar et al., 2015). In the presubiculum, they make unitary inhibitory connections onto a large fraction (37.5%) of nearby pyramidal cells, similar to the high connectivity rates reported for somatic targeting FS cells in other circuits (Holmgren et al., 2003; Yoshimura and Callaway, 2005). They are likely

to form a « blanket inhibition » characterized by an unspecific, homogenous matrix covering pyramidal neurons, as do neocortical PV+ interneurons (Packer and Yuste, 2011). The majority of unitary excitatory connections from pyramidal cells onto PV cells were reciprocated by inhibitory connections, as previously found in visual cortex (Yoshimura and Callaway, 2005; Yoshimura et al., 2005).

We took advantage of an optogenetic tool that consists in silencing PV interneurons in a Cre-dependent manner. Indeed, silencing PV interneurons greatly suppressed or reduced disynaptic inhibition in Pyr neurons. PV interneurons thus are at the origin of fast and reliable inhibition in response to thalamic signals. Latency from excitation to inhibition (1.65±0.1 ms, n=12) onset in the ATN-PrS circuit was similar to that in sensory thalamocortical pathways (Pouille and Scanziani, 2001; Gabernet et al., 2005; Cruikshank et al., 2010; Stokes and Isaacson, 2010). ATN fiber excitation induced excitation–feed forward inhibition sequences most of the time. Even minimal laser stimulation of ATN fibers typically activated a balanced excitation-feed-forward-inhibition sequence. For focal optical stimulations at distances over 200 µm away from the soma of a recorded layer 3 pyramidal neuron disynaptic inhibitory events could also occur in the absence of direct excitation. In the presubicular microcircuit, PV neurons may therefore mediate both, feed-forward inhibition, or, a lateral disynaptic inhibition. The broad inhibitory innervation is consistent with the axonal arborization of layer 3 PV neurons described previously (Nassar et al., 2015).

Functional implications

During sensory information processing, feed-forward inhibition is thought to play an important role for the timing of spikes of principal neurons by filtering out the stimulus-evoked responses of cortical neurons for “a non-preferred stimulus” and enforcing a precise time window for evoked spiking (Pouille and Scanziani, 2001). In the medial entorhinal cortex, PV modulate the overall firing rate of grid cells and head-direction cells without affecting their grid-firing pattern and direction selectivity (Buetfering et al., 2014). Royer et al. (2012) showed that PV cells have a major impact at the beginning of the place-field whereas SOM cells have a stronger effect at the end. These latter results are consistent with our findings showing early recruitment of PV interneurons and late and indirect activation of LTS-SST cells.

Presubicular principal cells showed depressing dynamics for 10Hz activation of thalamic fibers, while, at least initially, 30Hz activation of thalamic fibers resulted in facilitated recruitment of pyramidal cell spikes. We therefore suggest that presubicular pyramidal cells could function as a filter, preferentially selecting relevant thalamic information, and contributing to presubicular refinement of head direction signals. The direct excitation followed by disynaptic inhibition could ensure temporally precise directional signaling in the current direction. Cells with different tuning from the currently active direction may receive only disynaptic inhibition, and it is tempting to speculate that such a « lateral inhibition » could be a mechanism for sharpening of the head directional signal in presubiculum. FS interneurons are modulated by angular velocity (Preston-Ferrer et al., 2016), that is, they are activated during fast head turns, when the set of active afferent fibers continuously shifts. When the same fibers are active for longer times periods, as is the case for sustained head directional signaling during immobility and zero angular velocity, then the responses of PV cells will depress. PV cells will therefore probably not fire for sustained head direction signaling. The fact that ATN-PV synapse depresses might indirectly contribute to a facilitation of pyramidal cell recuitment for the second or later action potentials, easing excitation from thalamic inputs.

In our previous study (Simonnet et al., 2016, under review), we demonstrated a strong recurrent connectivity between the presubicular somatostatin expressing Martinotti type interneurons and layer 3 pyramidal cells that form a feedback inhibitory circuit. The inhibitory feedback effect on pyramidal cell activity depended on the precise IPSP timing relation to the pyramidal cell firing phase. Delayed inhibition could well provide lateral inhibition, while reciprocal, short latency inhibition rather helps spike repolarization and so preserves sustained firing. In the future, connectivity between PV and SOM will be tested. LTS-SST interneurons may be inhibited by FS interneurons during fast head-turns, but this inhibition might fade during sustained head-directional firing in the absence of head motion (Ma et al., 2010, Simonnet et al., 2016, under review). In vivo recording of presubicular head direction cells during optical silencing of PV or LTS-SST interneurons should give insight in the resultant effect when fast inhbition or delayed inhibition is specifically suppressed.

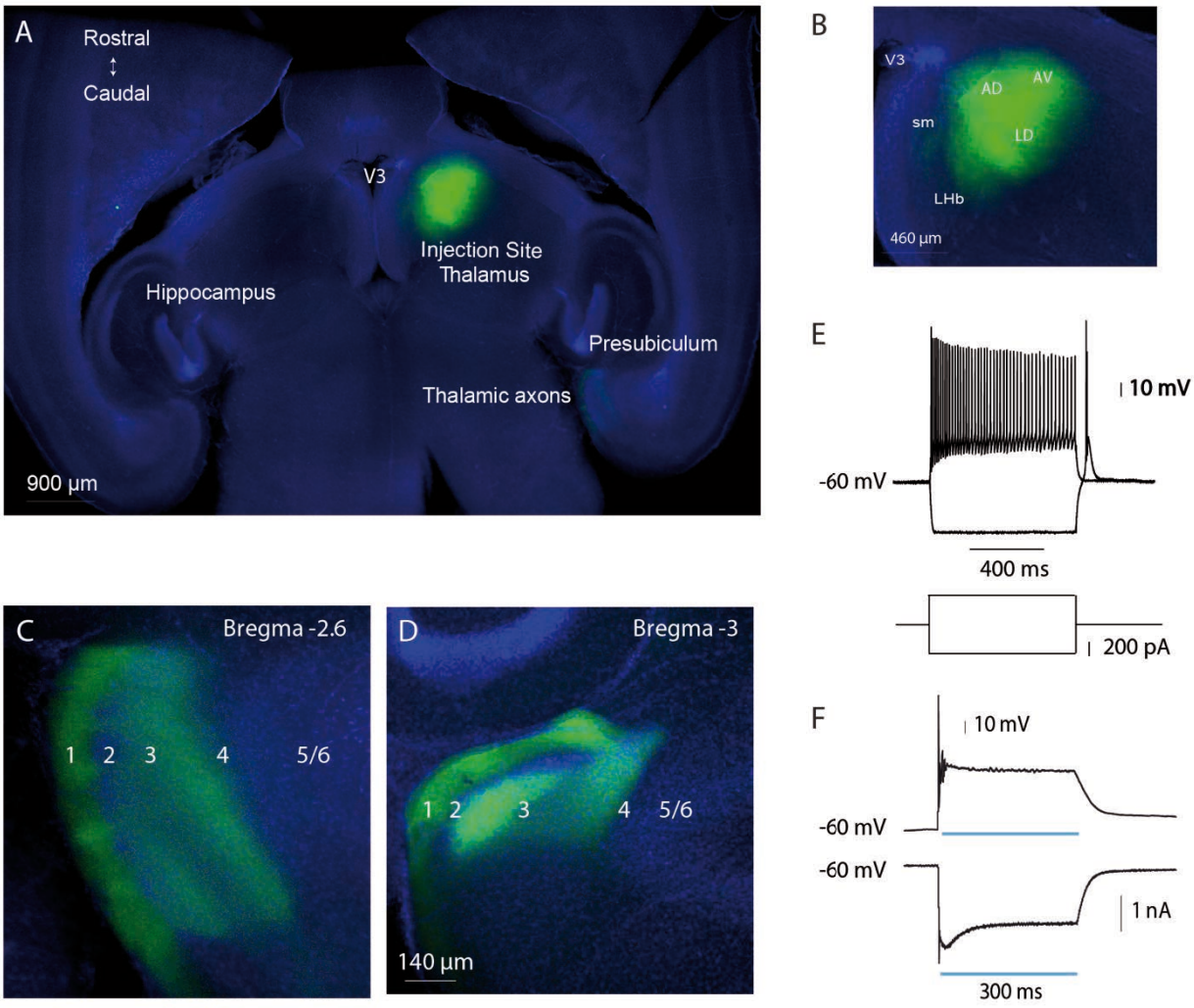

Figure 1: ChR2-eYFP expression in the anterior thalamic nuclei and axon terminals ramifying in the presubiculum. **(A)** Fluorescence image of a 320 µm-thick horizontal brain slice from a mouse unilaterally injected with viral vector AAV5-ChR2-eYFP in the ATN. **(B)** Enlargement of the ChR2-eYFP expression at the injection site: AD antero-dorsal nucleus, AV antero-ventral nucleus, LD latero-dorsal nucleus, sm stria medullaris, V3 third ventricle, LHb lateral habenula. **(C)**, **(D)** ChR2-eYFP expressing axon terminals in the presubiculum at different dorso-ventral levels, Bregma -2.6 and -3 mm. DAPI staining in blue. AAV-ChR2-eYFP in green. **(E)** Firing of a thalamic cell induced by a two-fold rheobase depolarizing current. Hyperpolarization induced by a negative current pulse is followed by a rebound burst. **(F)** Top, photostimulation (0.1 mW, 300 ms) evoked spikes and depolarization block in the same thalamic cell in current clamp mode. Bottom, a ChR2-mediated photocurrent was recorded in voltage-clamp upon same duration and intensity of stimulation as in current-clamp. The blue bar indicates the light pulse. Recordings were performed in the presence of CNQX and APV.

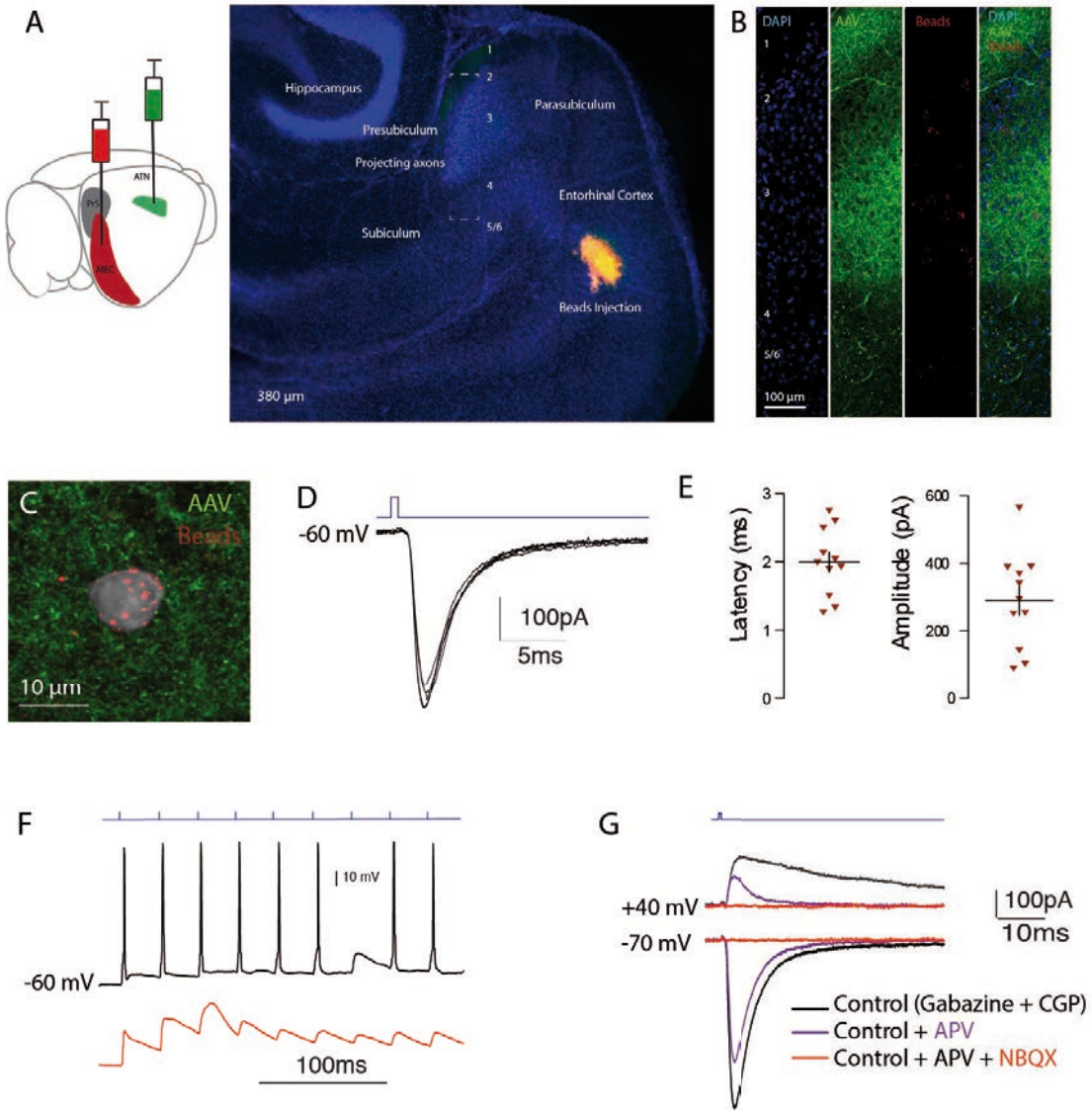

Figure 2: ATN axons contact directly MEC projecting neurons. **(A)** Left, schematic 3D mouse brain illustrating unilateral double injections of AAV5-ChR2 in ATN (green) and retrobeads (red) in the MEC. PrS, presubiculum. Right, fluorescent image of a horizontal section of the parahippocampal formation showing the Retrobeads injection site in the MEC in yellow. Axons from thalamus expressing ChR2-eYFP (green) target the presubiculum. DAPI staining in blue. **(B)** Magnification of the presubiculum (rectangle in A) stained with DAPI (blue), ChR2-eYFP expressing thalamic axons (green), retrobeads (red) and the merged image (right). **(C)** Confocal image at higher magnification (60x) of a biocytin-filled neuron in superficial layer 3 (soma in grey), that contains retrobeads (red), and is surrounded by thalamic axons (green). **(D)** Light-evoked EPSCs recorded from the same neuron. Holding potential Vh = -60 mV**. (E)** EPSC latencies (left) and amplitudes (right) from n=11 beads-labeled neurons. Each dot represents the average for one neuron. Population mean ± SEM are indicated by horizontal and vertical traits. **(F)** A train of light stimulations at 30 Hz initiated action potential firing (upper trace, black; same beads labeled neuron as in **(C).** Application of TTX/4-AP (1 µM/ 100 µM) abolished spikes, while direct EPSPs persisted (bottom trace, red). **(G)** Light evoked synaptic currents at +40 and at -70mV revealed glutamatergic neurotransmission with a NMDA and AMPA receptor mediated component. EPSCs were recorded in the presence of 10µm Gabazine and 10µm CGP, and entirely abolished by co-application of both APV and NBQX.

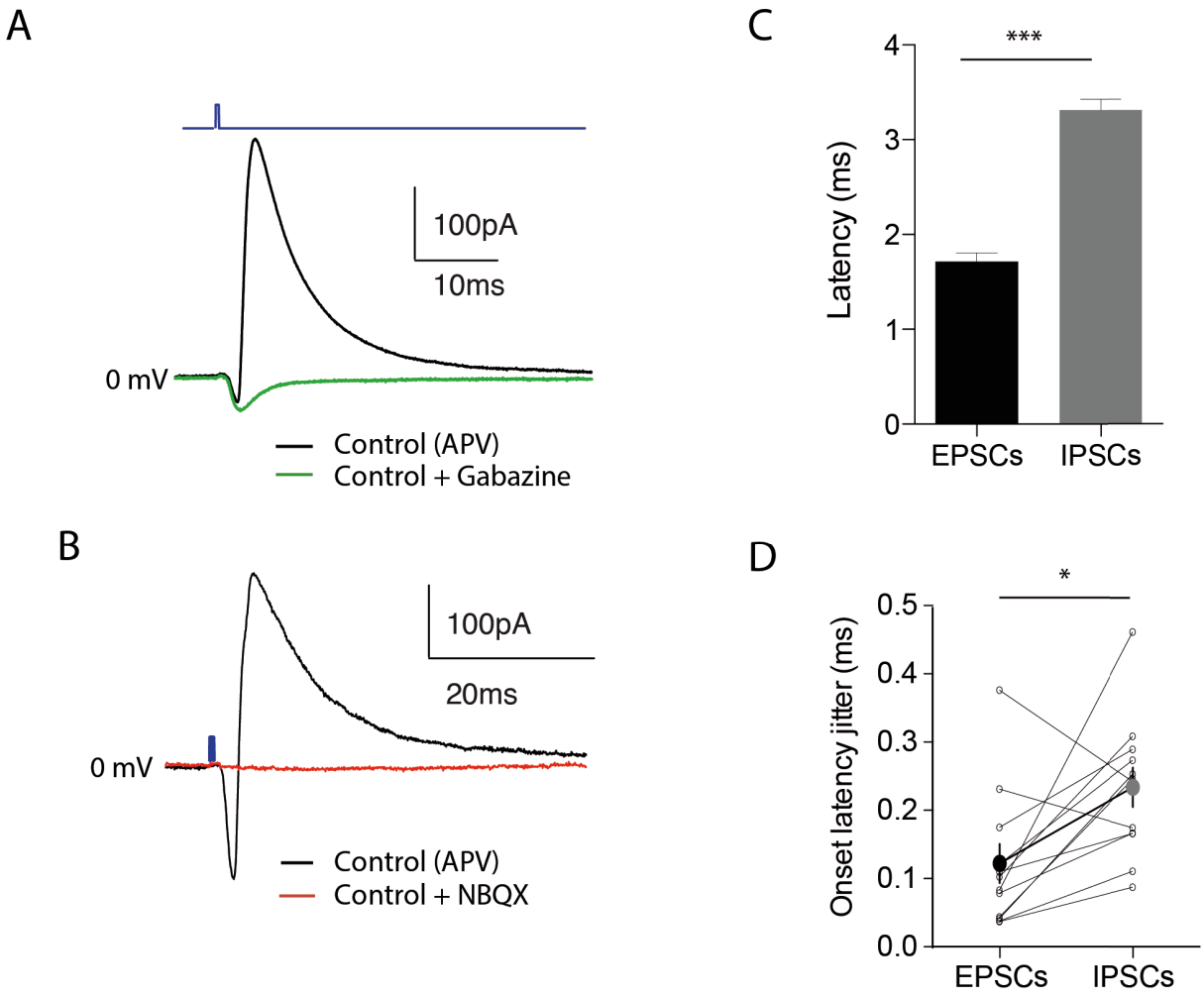

Figure 3: ATN driven feed-forward inhibition onto layer 3 principal neurons in the presubiculum. **(A), (B)** ATN-evoked currents recorded from presubicular pyramidal neurons at 0 mV holding potential, in the presence of APV. The current was biphasic, the initial inward current being followed by an outward current component. **(A)** The outward current was mediated by $GABA_A$ receptors, and entirely blocked by application of gabazine. **(B)** NBQX abolished both the inward current and the disynaptic GABAergic component. **(C), (D)** The ATN-driven disynaptic IPSCs exhibit higher onset latency and jitter than the ATN-driven EPSCs. ***p< 0.001, *p<0.05, Wilcoxon matched-pairs signed rank test. Values are given as mean ± SEM.

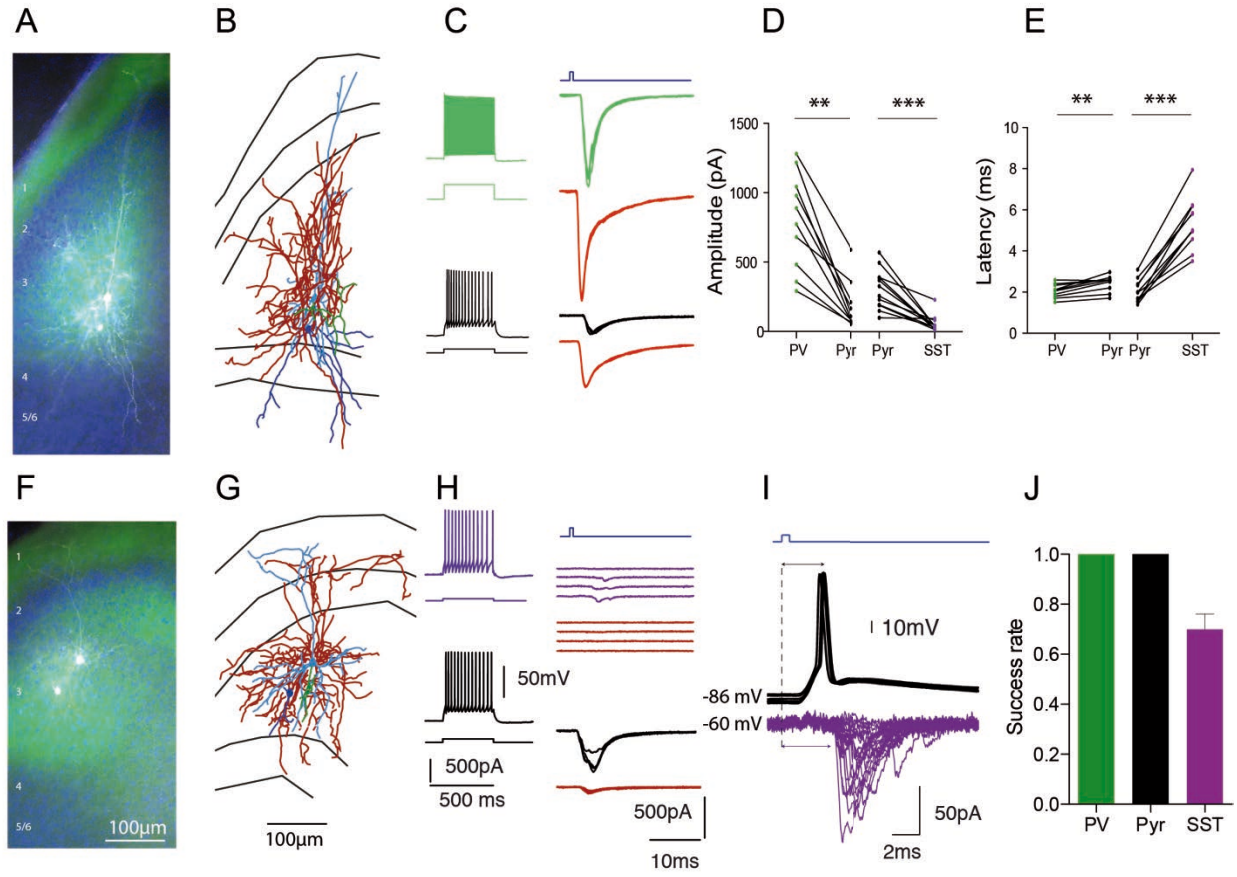

Figure 4: Long-range excitatory inputs from ATN to interneurons and principal neurons in superficial layer 3. **(A)**, **(F)** Fluorescent images of biocytin-filled and **(B)**, **(G)** anatomically reconstructed double-recorded principal neurons and PV interneurons or LTS-SST interneurons respectively **(C)**, **(H)** Left, firing patterns in response to a two-fold rheobase current injection. Right, light-evoked EPSCs recorded from the illustrated pair of simultaneously recorded neurons. **(D)** Amplitude and **(E)** latency from double-recorded principal neurons and interneurons. **(I)** Brief whole-field illumination reliably generated action potentials in a pyramidal neuron and indirectly evoked EPSCs in simultaneously voltage-clamp recorded LTS-SST neurons. In about 30% of trials no EPSC was evoked in the LTS-SST interneuron (30 trials). **(J)** Bar plots representing success rate as a function of cell type (calculated from 30 trials from n=13 PV, n=13 Pyr and n=11 SST neurons). PV interneurons in green, LTS-SST interneurons in purple, Pyr cells in black. **p<0.01, ***p<0.001, Wilcoxon matched-pairs signed rank test. Values are given as mean ± SEM.

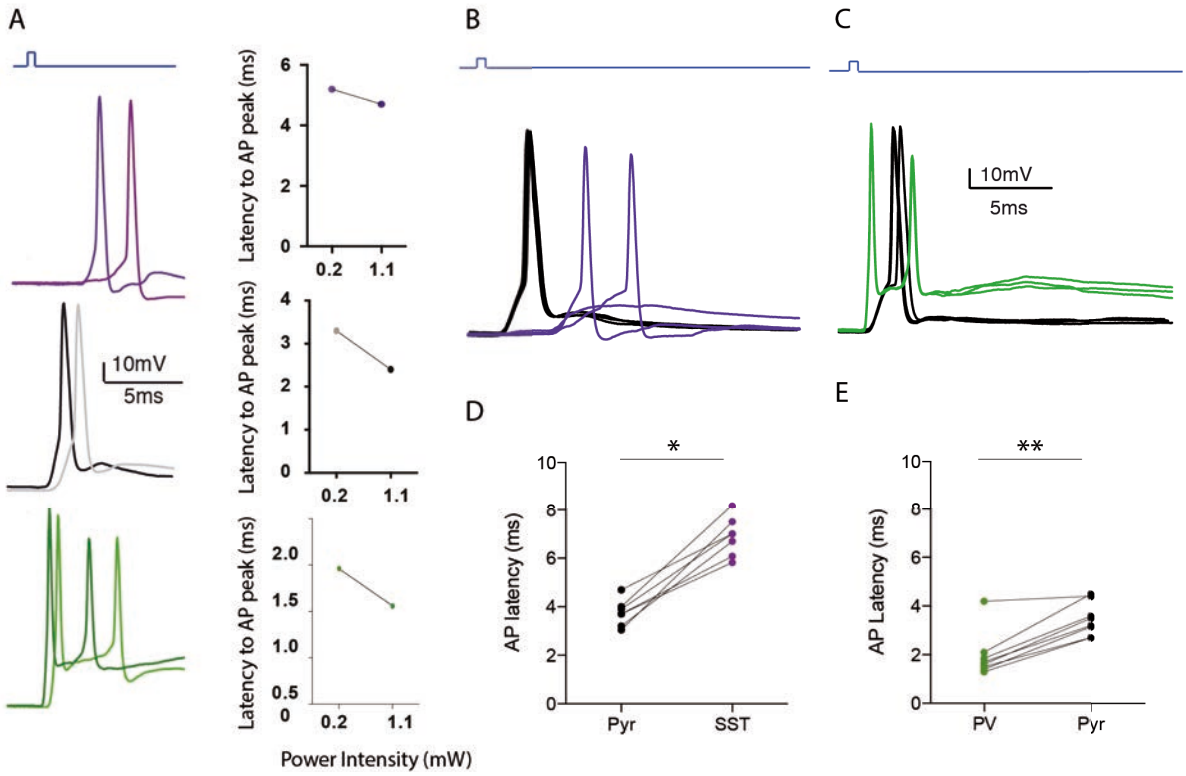

Figure 5: Sequence of activation of principal neurons and interneurons. **(A)** Left, traces showing simultaneous current-clamp recording of Pyr, SST and PV neurons at two different intensities of stimulation. Right, AP latencies measured from traces with 0.2 mW and 1.1 mW stimulation intensities. A brief pulse generated action potentials in simultaneous current-clamp recording of **(B)** Pyr and LTS-SST interneurons or **(C)** pyr and PV interneurons interneurons. **(D)** and **(E)** summary data showing that AP latency in Pyr cells are shorter than in LTS-SST and longer than in PV interneurons. Black, purple and green filled circles for Pyr, LTS-SST and PV neurons respectively. Black, violet and green filled circles for Pyr, SST and PV neurons respectively. * $p<0.05$, ** $p<0.01$, Wilcoxon matched-pairs signed rank test. Values are given as mean ± SEM.

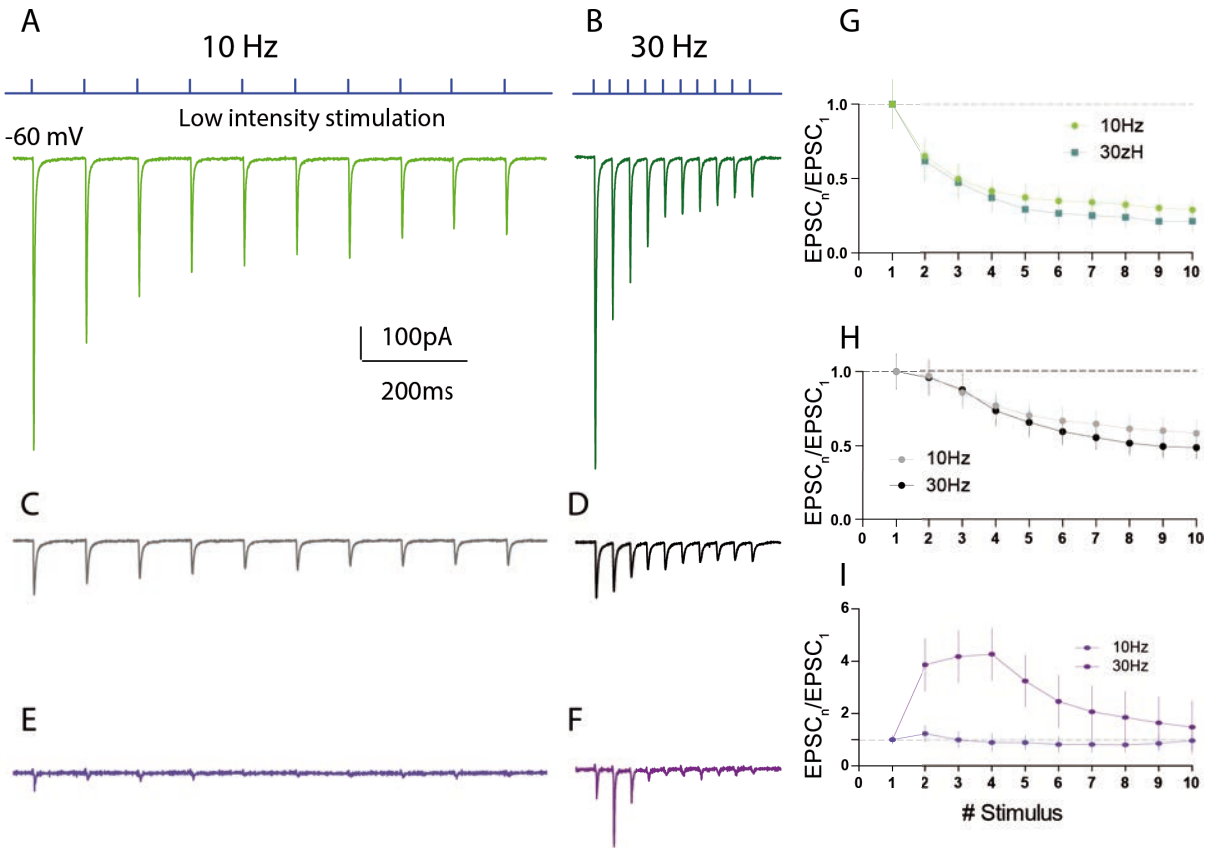

Figure 6: Synaptic dynamics of responses to photostimulation of ATN inputs in layer 3 pyramidal neurons and interneurons. Trains of photo-stimuli **(A)**, **(C)**, **(E)** at 10Hz and **(B)**, **(D)**, **(E)** at 30Hz evoked EPSCs in PV interneurons (top, green), Pyr cells (middle, grey, black) and LTS-SST interneurons (purple, bottom). **(G)**, **(H)**, **(I)** Average normalized EPSC amplitudes to stimulations at 10Hz and 30Hz for the three cell types respectively. Amplitudes of EPSCs are normalized to 1st ESPC. Values are given as mean ± SEM.

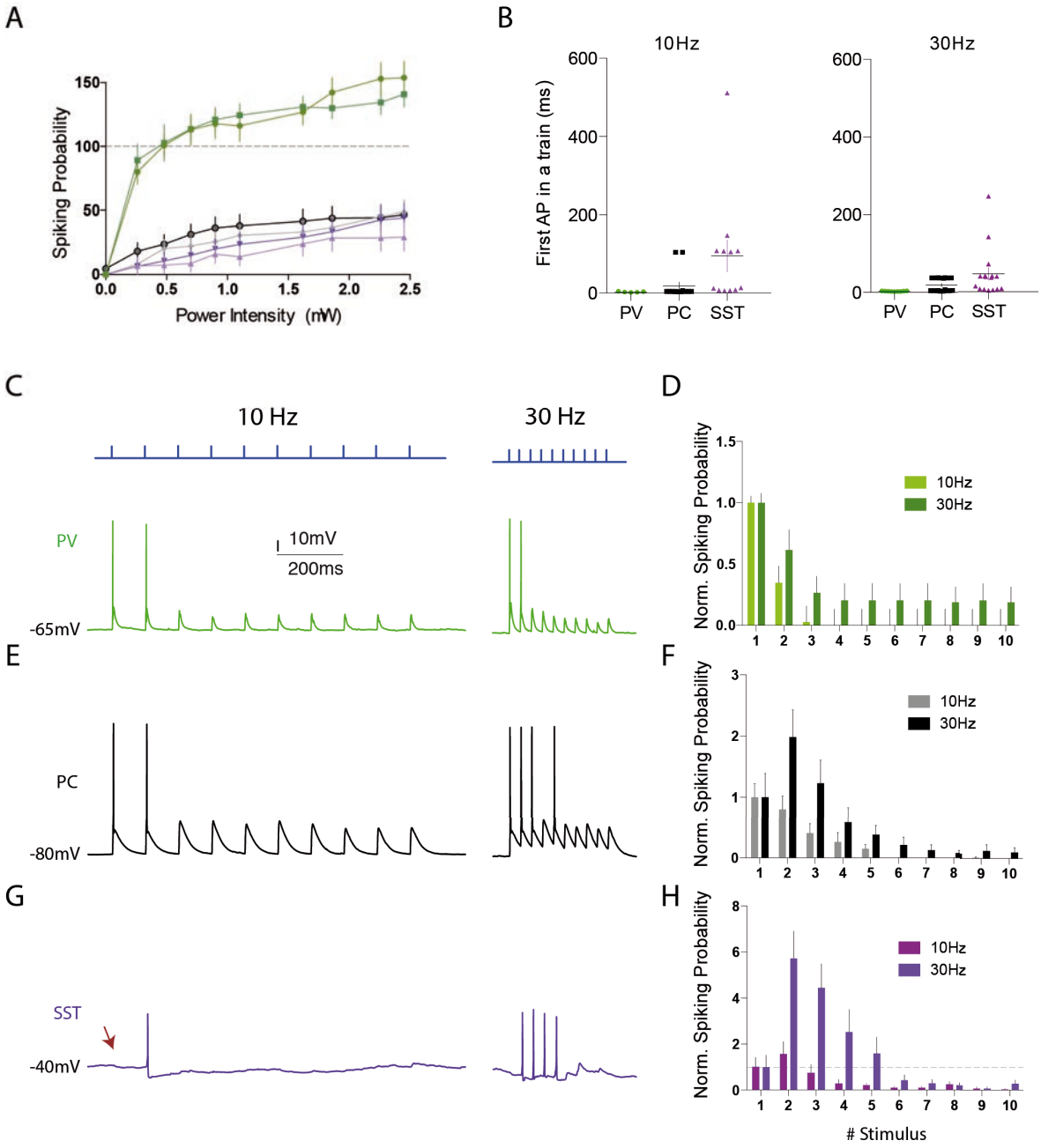

Figure 7: Cell-type specific spiking probability in responses to optical stimulation of ChR2 expressing ATN fibers. **(A)** The probability of spiking as a function of the light intensity. 100% probability corresponds to 10 spikes for a train of 10 stimulations. For increasing light intensities, PV neurons (green) sometimes responded with multiple spikes per pulse. Pyr neurons in black, LTS-SST neurons in purple. **(B)** Timing of the first action potential during a 10Hz or 30Hz train at intermediate stimulation intensities (0.2 – 1 mW). PV interneurons always fired on the first pulse in a train. Pyramidal cells and LTS-SST neurons occasionally fired the first spike on the second pulse in a train. Representative examples of membrane potential responses from a PV interneuron **(C)** pyramidal neuron **(E)** LTS-SST interneuron **(G)** for 10Hz and 30Hz stimulations from resting membrane potential or near AP threshold. Red arrow in **(G)** indicates the absence of a spike for the 1st pulse. **(D)**, **(F)**, **(H)** AP spiking probabilities normalized to the first pulse for each cell type for 10Hz and 30Hz.

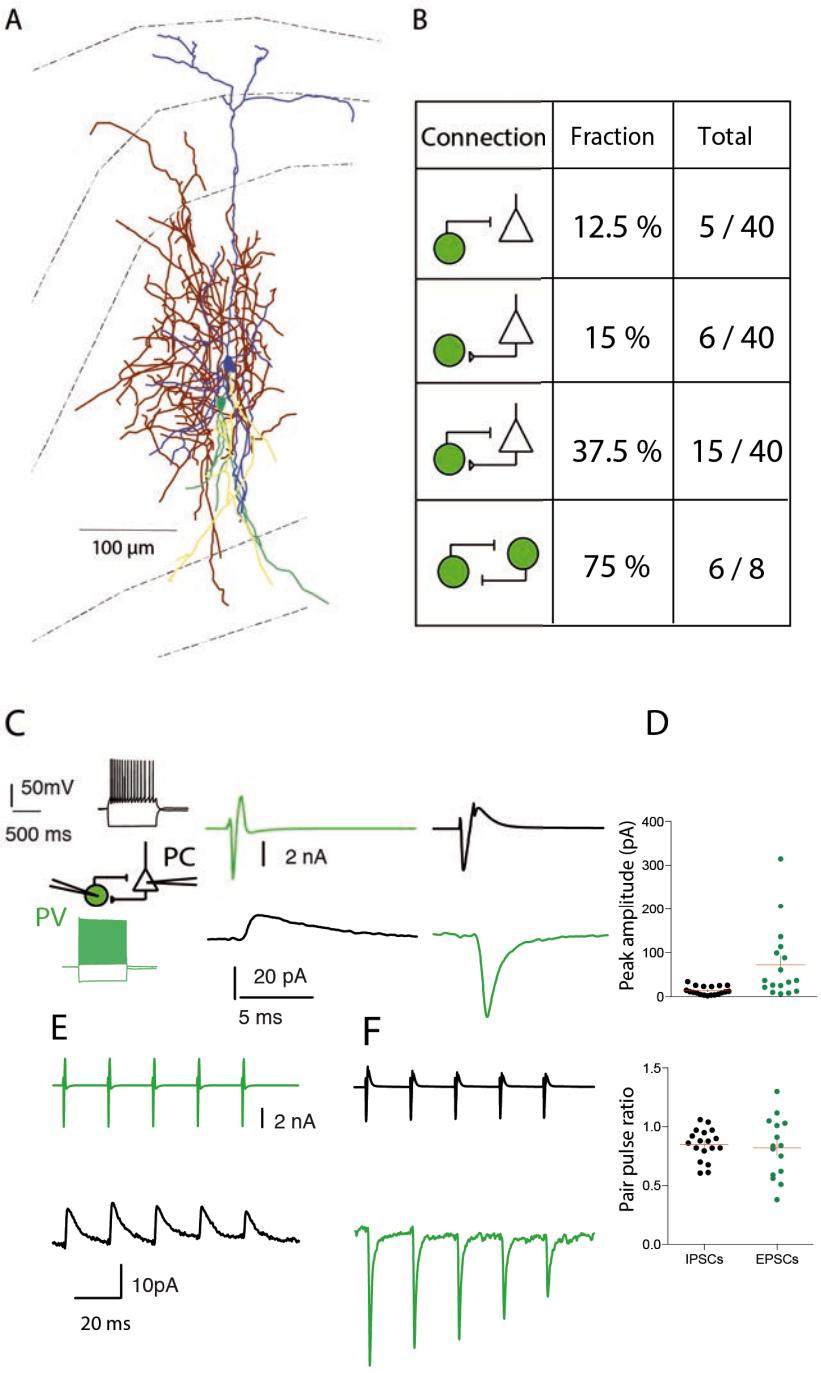

Figure 8: L3 FS cells are highly interconnected with local pyramidal cells. **(A)** Anatomical reconstruction of a reciprocally connected pair of PV and Pyr neurons in layer 3. Pyr dendrites (blue) and PV axon (red). Pyr axon (yellow) and PV dendrites (green). Subiculum is to the left and the parasubiculum to the right. **(B)** Summary of connectivity between L3 FS and pyramidal cells. **(C)** Average traces from paired recording of a L3 PV interneuron (green) and reciprocally connected pyramidal cell (black). A single action current in the L3 FS cell (-70mV in voltage-clamp) produced a short-latency IPSC in the voltage-clamped (-50mV) pyramidal cell. A single action current in the pyramidal cell produced a short-latency EPSC in the FS cell. **(D)** summary data showing average peak amplitudes (top) and pair pulse ratio (bottom) of EPSCs (green) in PV interneurons and IPSCs (black) in Pyr neurons. **(E, F)** Unitary EPSCs (green) and IPSCs (black) from the same reciprocally connected pair obtained during 5 pulses at 50 Hz.

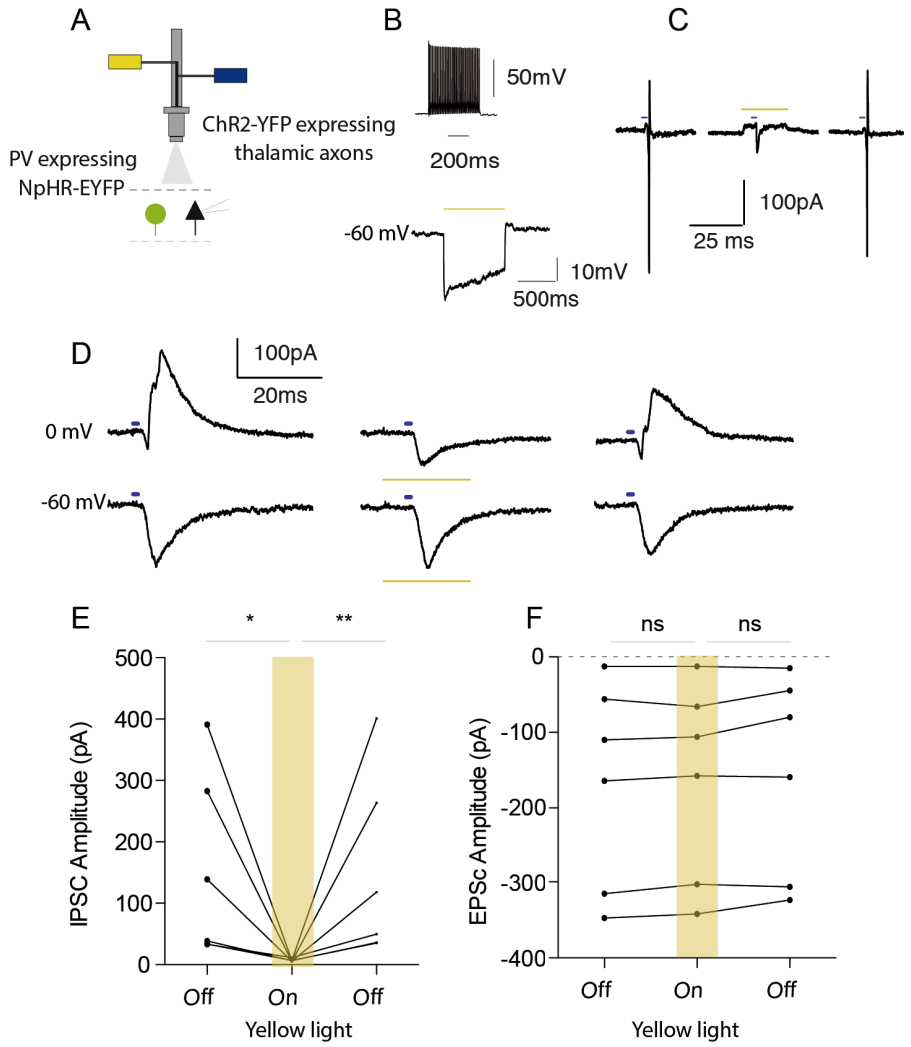

Figure 9: PV interneurons mediate ATN driven feed-forward inhibition in the Presubiculum. (**A)** Schematic of the experimental setup. Blue (470 nm) and yellow wavelength illumination (585 nm) were combined in the light path to either activate ChR2 alone, or together with the activation of NpHR3.0, respectively. (**B)** Photostimulation caused potent hyperpolarization in PV interneurons expressing eNpHR3.0. Inset, fast-spiking firing pattern in response to depolarising current step in an eNpHR-expressing PV cell. (**C)** Sample traces of action potentials recorded in cell-attached mode from a PV neuron expressing eNpHR in response to photoactivation of ATN inputs with blue light pulses (blue bars), before, during, and after the presentation of yellow light (yellow bar) to activate eNpHR3.0. Yellow light was triggered 5 ms before the onset of the 0.5 ms blue light pulse and remained on for 20 ms. (**D)** Sample traces of synaptic currents recorded from a layer 3 Pyr neuron in the presubiculum in response to photostimulation (blue bars) of fibers from the ATN, in the absence, in the presence, and again in the absence of yellow light illumination (yellow bars). The presentation of yellow light reversibly inhibited PV interneurons and suppressed the evoked IPSCs recorded at 0 mV holding potential (pipette contained QX-314). (**E)** The peak outward current amplitude of IPSCs recorded from pyramidal neurons at 0 mV was reduced to zero when PV interneurons were silenced, *p<0.05, **p < 0.01, Kruskal–Wallis and Dunn's multiple comparison *post hoc* test. (F) The amplitudes of EPSCs recorded in Pyr cells at -60mV holding potential were not affected by the yellow light presentation. ns: non significant.

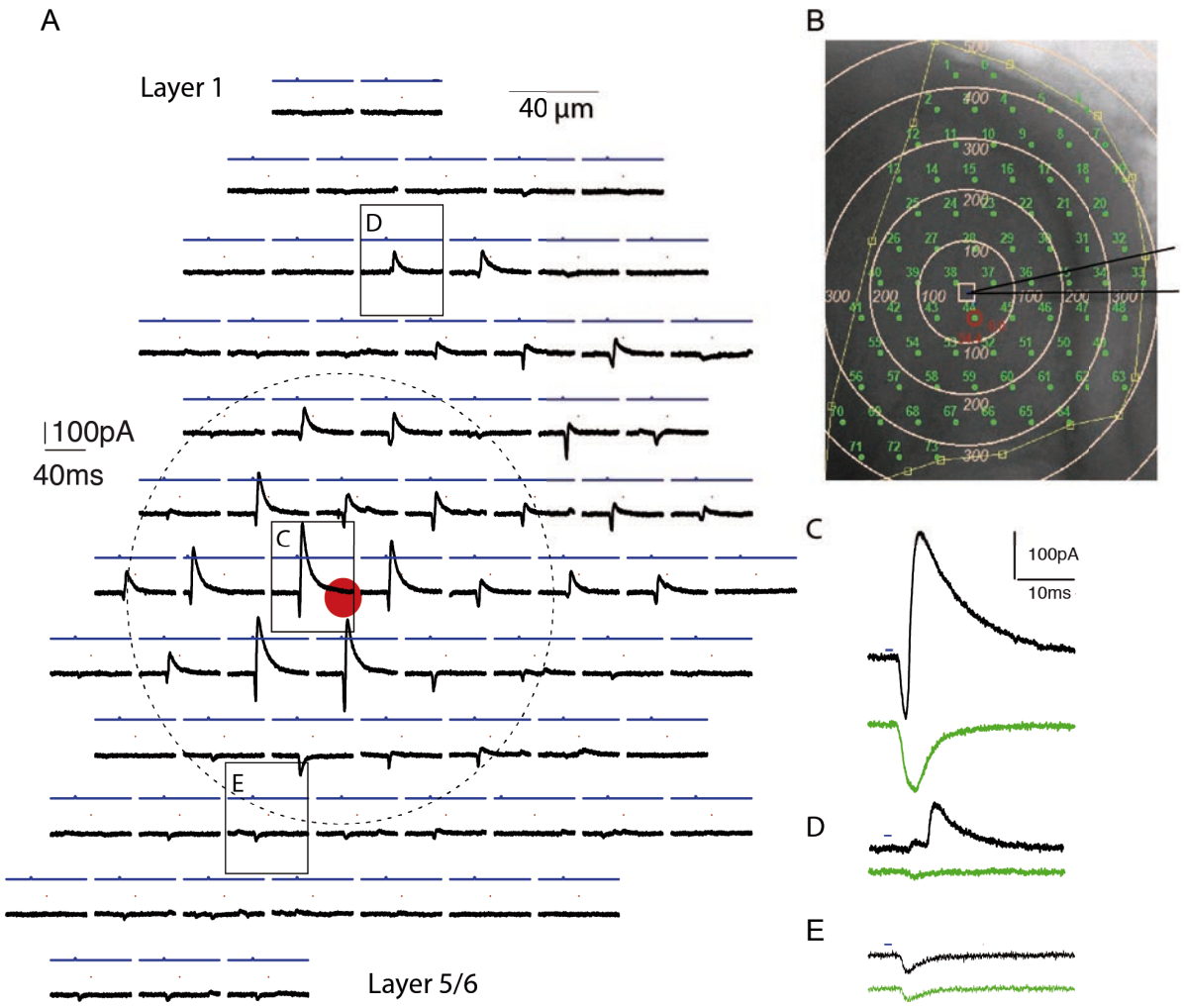

Figure 10: Spatial specificities of feed-forward inhibition across the Presubiculum. **(A)** Responses of layer 3 pyramidal neuron to light activation of ATN inputs (1ms, 1.5mW) at different locations (in the presence of 100µM APV). Red circle represents pyramidal neuron somatic location. Each trace corresponds to a response evoked by a laser photostimulus delivered to ChR2-expressing ATN axon terminals at specific locations (40µm spacing) across layers 1 (top) to 5/6 (bottom). Responses for the same photostimulation grid across multiple runs were highly consistent. **(B)** photograph of the presubiculum during the recording with the recording pipette (black) and an overlay of the grid points (green). Example traces are shown at a higher magnification in **(C)**, **(D)** and **(E)** respectively. Green traces correspond to responses after Gabazine application.

Table 1: Electrophysiological properties of presubicular interneurons and principal neurons

	PV			SST			PC			Beads +		
	mean	sem	n	mean	sem	n	mean	sem	n	mean	sem	n
Membrane Potential (mV)	-67	1.1	13	-54	2	15	-72	3	17	-74	1,1	15
Time Constant (ms)	19	3,0	10	38	8	10	28	6	8	27	4	11
Sag ratio	1.1	0.006	12	1.2	0.02	15	1.04	0.005	16	1.05	0,005	16
Rin (MΩ)	147	12,0	13	438	58	14	362	68	15	359	34	14
Threshold current (pA)	183	18	13	59	19	15	63	18	13	70	11	16
I-O initial gain (Hz/pA)	1.06	0.09	13	0.90	0.07	15	0.36	0.06	16	0,27	0,02	15
Firing Frequency at 2x threshold current	191	12	8	40	6.2	14	28	3.3	14	27	1,4	16
AP threshold (mV)	-39	1.2	13	-34	0.9	15	-38	0.8	17	-30	0.6	16
AP amplitude (mV)	77	1.1	13	76	1.8	15	81	1.03	17	80	1,4	16
AP half duration (ms)	0.2	0.007	13	0.3	0.01	15	0.6	0.01	17	0,65	0,02	16
AP rising phase speed (V/s)	624	22,0	13	507	23	15	478	17	17	452	22	16
AP falling phase speed (V/s)	-464,0	22,0	13	-272	14	15	-127	4	17	-121	4	16

Table 2: Summary of uPSCs parameters

	EPSC			IPSC		
	Mean	Sem	n	Mean	Sem	n
Rise time (ms)	0.31	0.02	17	0.52	0.07	19
Decay time (ms)	0.91	0.07	17	2.89	0.19	19
Latency Onset (ms)	0.74	0.03	17	0.68	0.03	19
Transfer rate	0,79	0,06	17	0.71	0.07	19

Supplementary figures

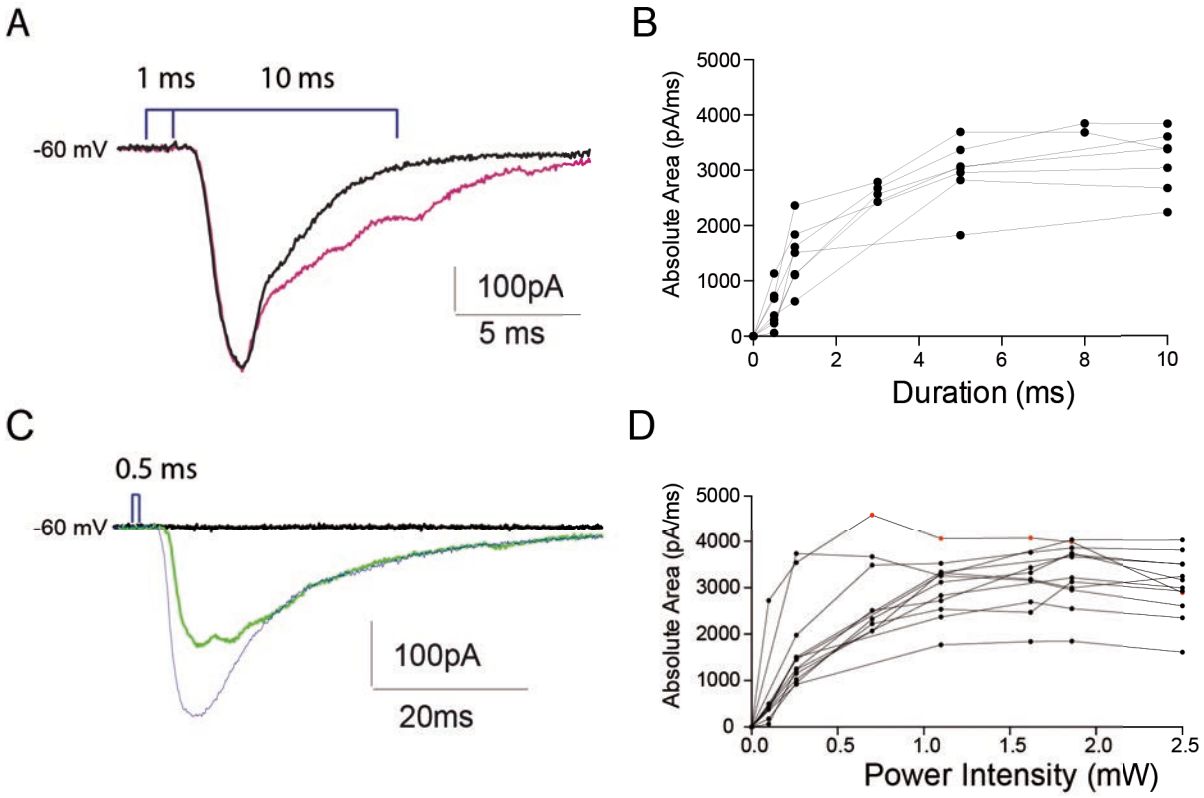

Supplementary figure 1: Calibration of the LED light duration and intensity. **(A)** Single evoked traces from a pyramidal neuron at -60mV following LED stimulation with same intensity (0.3 mW) and 1 ms (black trace) or 10 ms duration (pink trace). **(B)** Calculated area of the light-evoked event plotted as a function of the duration for 6 pyramidal neurons. **(C)** Single evoked traces at 0 (black), 0.7 (green) or 2 (blue) mW recorded from a presubicular layer 3 principal neuron following light stimulation. **(D)** Calculated area of the light evoked events as a function of the power intensity for n=11 pyramidal neurons.

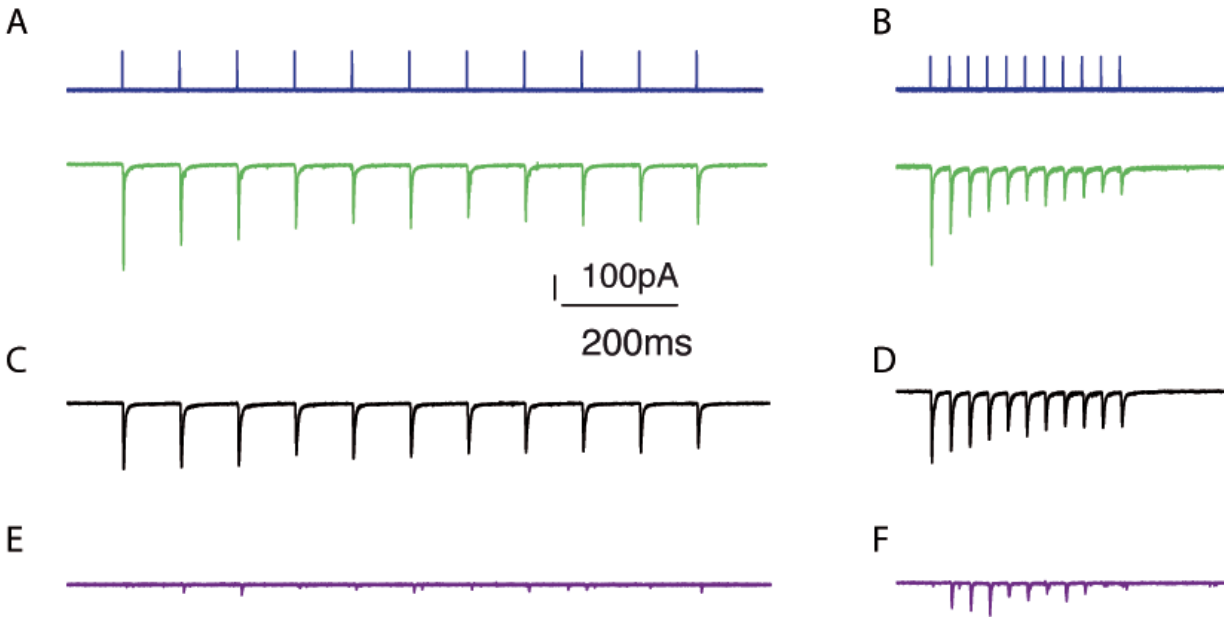

Supplementary figure 2: Synaptic dynamics of responses to photostimulation of AAV2/9-ChR2 expressing ATN inputs in layer 3 pyramidal neurons and interneurons. Trains of photostimuli **(A)**, **(C)**, **(E)** at 10Hz and **(B)**, **(D)**, **(E)** at 30Hz evoked EPSCs from PV interneurons (top, green), Pyr cells (middle, grey, black) and LTS-SST interneurons (purple, bottom). 3 traces are superimposed for each cell type and frequency. Neurons were recorded at -60mV holding potential at low intensity stimulation (pulse duration 0.5 ms)

References

Agmon, A., and Connors, B. W. (1991). Thalamocortical responses of mouse somatosensory (barrel) cortex in vitro. *Neuroscience*, *41*(2-3), 365–379.

Amaral, D. G. and Witter, M. P. (1989). The three-dimensional organization of the hippocampal formation: a review of anatomical data. *Neuroscience*, 31(3):571–591.

Beed, P., Bendels, M. H. K., Wiegand, H. F., Leibold, C., Johenning, F. W., and Schmitz, D. (2010). Analysis of excitatory microcircuitry in the medial entorhinal cortex reveals cell-type-specific differences. *Neuron*, *68*(6), 1059–1066.

Beierlein, M., Gibson, J. R., and Connors, B. W. (2003). Two dynamically distinct inhibitory networks in layer 4 of the neocortex. *Journal of Neurophysiology*, *90*(5), 2987–3000.

Bendels, M. H. K., Beed, P., Leibold, C., Schmitz, D., and Johenning, F. W. (2008). A novel control software that improves the experimental workflow of scanning photostimulation experiments. *The Journal of Neuroscience Methods*, *175*(1), 44–57.

Buetfering, C., Allen, K., and Monyer, H. (2014). Parvalbumin interneurons provide grid cell–driven recurrent inhibition in the medial entorhinal cortex. *Nature Publishing Group*, *17*(5), 710–718.

Cruikshank, S. J., Lewis, T. J., and Connors, B. W. (2007). Synaptic basis for intense thalamocortical activation of feedforward inhibitory cells in neocortex. *Nature Neuroscience*, *10*(4), 462–468.

Cruikshank, S. J., Urabe, H., Nurmikko, A. V., and Connors, B. W. (2010). Pathway-specific feedforward circuits between thalamus and neocortex revealed by selective optical stimulation of axons. *Neuron*, *65*(2), 230–245.

Gabernet, L., Jadhav, S. P., Feldman, D. E., Carandini, M., and Scanziani, M. (2005). Somatosensory integration controlled by dynamic thalamocortical feed-forward inhibition. *Neuron*, *48*(2), 315–327.

Goodridge, J. P. and Taube, J. S. (1997). Interaction between the postsubiculum and anterior thalamus in the generation of head direction cell activity. *The Journal of Neuroscience,* 17(23):9315–9330

Haley, M. S., Fontanini, A., and Maffei, A. (2016). Laminar- and target-specific amygdalar inputs in rat primary gustatory cortex. *The Journal of Neuroscience, 36*(9), 2623–2637.

Hippenmeyer, S., Vrieseling, E., Sigrist, M., Portmann, T., Laengle, C., Ladle, D. R., et al. (2005). A developmental switch in the response of DRG neurons to ETS transcription factor signaling. *PLoS Biol.* 3:e159.

Holmgren, C., Harkany, T., Svennenfors, B., and Zilberter, Y. (2009). Pyramidal cell communication within local networks in layer 2/3 of rat neocortex. *The Journal of Physiology*, *551*(1), 139–153.

Honda, Y. and Ishizuka, N. (2004). Organization of connectivity of the rat presubiculum: I. Efferent projections to the medial entorhinal cortex. *The Journal of Comparative Neurology*, 473(4):463–484.

Honda, Y., Furuta, T., Kaneko, T., Shibata, H., and Sasaki, H. (2011). Patterns of axonal collateralization of single layer V cortical projection neurons in the rat presubiculum. *The Journal of Comparative Neurology*, *519*(7), 1395–1412.

Honda, Y., and Ishizuka, N. (2004). Organization of connectivity of the rat presubiculum: I. Efferent projections to the medial entorhinal cortex. *The Journal of Comparative Neurology*, *473*(4), 463–484.

Keshavarzi, S., Sullivan, R. K. P., Ianno, D. J., and Sah, P. (2014). Functional properties and projections of neurons in the medial amygdala. *Journal of Neuroscience*, *34*(26), 8699–8715.

Kononenko, N. L., and Witter, M. P. (2011). Presubiculum layer 3 conveys retrosplenial input to the medial entorhinal cortex. *Hippocampus*, *22*(4), 881–895.

Jackman, S. L., Beneduce, B. M., Drew, I. R., and Regehr, W. G. (2014). Achieving high-frequency optical control of synaptic transmission. *The Journal of Neuroscience*, *34*(22), 7704–7714.

Jones, B. F. and Witter, M. P. (2007). Cingulate cortex projections to the parahippocampal region and hippocampal formation in the rat. *Hippocampus*, 17(10):957–976.

Langston, R. F., Ainge, J. A., Couey, J. J., Canto, C. B., Bjerknes, T. L., Witter, M. P., Moser, E. I., and Moser, M. B. (2010). Development of the spatial representation system in the rat. *Science*, 328(5985):1576–1580.

Lee, S., Kruglikov, I., Huang, Z. J., Fishell, G., and Rudy, B. (2013). A disinhibitory circuit mediates motor integration in the somatosensory cortex. *Nature Publishing Group*, *16*(11), 1662–1670.

Lin, J. Y., Lin, M. Z., Steinbach, P., and Tsien, R. Y. (2009). Characterization of engineered channelrhodopsin variants with improved properties and kinetics. *Biophysical Journal*, *96*(5), 1803–1814.

Ma, W.-P., Liu, B.-H., Li, Y.-T., Huang, Z. J., Zhang, L. I., and Tao, H. W. (2010). Visual representations by cortical somatostatin inhibitory neurons--selective but with weak and delayed responses. *The Journal of Neuroscience*, *30*(43), 14371–14379.

Madisen, L., Zwingman, T. A., Sunkin, S. M., Oh, S. W., Zariwala, H. A., Gu, H., et al. (2010). A robust and high-throughput Cre reporting and characterization system for the whole mouse brain. *Nature Publishing Group*, *13*(1), 133–140.

Mao, T., Kusefoglu, D., Hooks, B. M., Huber, D., Petreanu, L., and Svoboda, K. (2011). Long-range neuronal circuits underlying the interaction between sensory and motor cortex. *Neuron*, *72*(1), 111–123.

McNaughton, B. L., Battaglia, F. P., Jensen, O., Moser, E. I., and Moser, M.-B. (2006). Path integration and the neural basis of the 'cognitive map'. *Nature Reviews Neuroscience*, 7(8):663– 678.

Markram, H., Toledo-Rodriguez, M., Wang, Y., Gupta, A., Silberberg, G., and Wu, C. (2004). Interneurons of the neocortical inhibitory system. *Nature Reviews Neuroscience*, *5*(10), 793–807.

Nagel, G., Szellas, T., Huhn, W., Kateriya, S., Adeishvili, N., Berthold, P., et al. (2003). Channelrhodopsin-2, a directly light-gated cation-selective membrane channel. *Proceedings of the National Academy of Sciences*, *100*(24), 13940–13945.

Nassar, M., Simonnet, J., Lofredi, R., Cohen, I., Savary, E., Yanagawa, Y., et al. (2015). Diversity and overlap of parvalbumin and somatostatin expressing interneurons in mouse presubiculum. *Frontiers in Neural Circuits*, *9*(a001875), 81–19.

Neher, E., and Sakaba, T. (2008). Multiple roles of calcium ions in the regulation of neurotransmitter release. *Neuron*, *59*(6), 861–872.

Packer, A. M., and Yuste, R. (2011). Dense, unspecific connectivity of neocortical parvalbumin-positive interneurons: a canonical microcircuit for inhibition? *The Journal of Neuroscience*, *31*(37), 13260–13271.

Pouille, F., and Scanziani, M. (2001). Enforcement of temporal fidelity in pyramidal cells by somatic feed-forward inhibition. *Science*, *293*(5532), 1159–1163.

Preston-Ferrer, P., Coletta, S., Frey, M., and Burgalossi, A. (2016). Anatomical organization of presubicular head-direction circuits. *eLife*, *5*, e14592.

Royer, S., Zemelman, B. V., Losonczy, A., Kim, J., Chance, F., Magee, J. C., and Buzsáki, G. (2012). Control of timing, rate and bursts of hippocampal place cells by dendritic and somatic inhibition. *Nature Publishing Group*, *15*(5), 769–775.

Rudy, B., Fishell, G., Lee, S., and Hjerling-Leffler, J. (2011). Three groups of interneurons account for nearly 100% of neocortical GABAergic neurons. *Developmental Neurobiology*, *71*(1), 45–61.

Simonnet, J., Lofredi, R., Cohen, I., Miles, R., and Fricker, D. (2013). Cellular neuroanatomy of rat presubiculum. *The European Journal of Neuroscience*, *37*(4), 583–597.

Simonnet, J., Nassar, M., Stella, F., Cohen, I., Mathon, B., Boccara, C.N., Miles, R., and Fricker, D. (under review). Activity dependent feedback inhibition supports head direction coding in the presubiculum. *Nature Communications*

Stokes, C. C. A., and Isaacson, J. S. (2010). From dendrite to soma: dynamic routing of inhibition by complementary interneuron microcircuits in olfactory cortex. *Neuron*, *67*(3), 452–465.

Sugar, J., Witter, M. P., van Strien, N. M., and Cappaert, N. L. M. (2011). The retrosplenial cortex: intrinsic connectivity and connections with the (para)hippocampal region in the rat. An interactive connectome. *Frontiers in Neuroinformatics*, 5, 7.

Sun, Q.-Q., Huguenard, J. R., and Prince, D. A. (2006). Barrel cortex microcircuits: thalamocortical feedforward inhibition in spiny stellate cells is mediated by a small number of fast-spiking interneurons. *The Journal of Neuroscience*, *26*(4), 1219–1230.

Swadlow, H. A. (2002). Thalamocortical control of feed-forward inhibition in awake somatosensory "barrel" cortex. *Philosophical Transactions of the Royal Society B: Biological Sciences*, *357*(1428), 1717–1727.

Taniguchi, H., He, M., Wu, P., Kim, S., Paik, R., Sugino, K., et al. (2011). A resource of Cre driver lines for genetic targeting of GABAergic neurons in cerebral cortex. *Neuron*, *71*(6), 995–1013.

Taube, J. S. (1995). Head direction cells recorded in the anterior thalamic nuclei of freely moving rats. *The Journal of Neuroscience*.

Taube, J. S. (2007). The head direction signal: origins and sensory-motor integration. *Annual Review of Neuroscience*, *30*(1), 181–207.

Trigo, F. F., Corrie, J. E. T., and Ogden, D. (2009). Laser photolysis of caged compounds at 405nm: Photochemical advantages, localisation, phototoxicity and methods for calibration. *Journal of Neuroscience Methods*, *180*(1), 9–21.

Tukker, J. J., Tang, Q., Burgalossi, A., and Brecht, M. (2015). Head-directional tuning and theta modulation of anatomically identified neurons in the presubiculum. *The Journal of Neuroscience*, *35*(46), 15391–15395.

Van Strien, N. M., Cappaert, N. L. M., and Witter, M. P. (2009). The anatomy of memory: an interactive overview of the parahippocampal–hippocampal network. *Nature Reviews Neuroscience*, *10*(4), 272–282.

Van Groen, T. and Wyss, J. M. (1990a). Connections of the retrosplenial granular a cortex in the rat. *The Journal of Comparative Neurology*, 300(4):593–606.

Van Groen, T. and Wyss, J. M. (1990b). The connections of presubiculum and parasubiculum in the rat. *Brain research*, 518(1-2):227–243.

Van Groen, T. and Wyss, J. M. (1990c). The postsubicular cortex in the rat: characterization of the fourth region of the subicular cortex and its connections. *Brain research*, 529(1-2):165–177.

Van Groen, T. and Wyss, J. M. (1992a). Connections of the retrosplenial dysgranular cortex in the rat. *The Journal of Comparative Neurology*, 315(2):200–216.

Van Groen, T. and Wyss, J. M. (1995). Projections from the anterodorsal and anteroventral nucleus of the thalamus to the limbic cortex in the rat. *The Journal of Comparative Neurology*, 358(4):584–604.

Vogt, B. A. and Miller, M. W. (1983). Cortical connections between rat cingulate cortex and visual, motor, and postsubicular cortices. *The Journal of Comparative Neurology*, 216(2):192–210.

Winter, S. S., Clark, B. J., Taube, J. S. (2015) Disruption of the head-direction cell network impairs the parahippocampal grid cell signal. *Science* 347: 870 – 874.

Yoshimura, Y., and Callaway, E. M. (2005). Fine-scale specificity of cortical networks depends on inhibitory cell type and connectivity. *Nature Neuroscience*, *8*(11), 1552–1559.

Yoshimura, Y., Dantzker, J. L. M., and Callaway, E. M. (2005). Excitatory cortical neurons form fine-scale functional networks. *Nature*, *433*(7028), 868–873.

Article 3

Activity dependent feedback inhibition supports head direction coding in the presubiculum

Our previous studies characterized the principal neuron and interneuron diversity in different layers of presubiculum. The electrophysiological and morphological properties of excitatory and inhibitory presubicular neurons are now well established. In vivo, presubicular pyramidal cells can generate persistent firing with little adaptation over tens of seconds as a necessary feature for maintaining the head direction signal. However, connectivity between neurons and their recruitment by long-range excitatory inputs are crucial elements to understand head direction information processing in the presubicular network that so far, remains unknown.

Work by a former student in our lab, Jean Simonnet, had focused on the interaction between the dendrite targeting Martinotti cells and principal neurons in superficial layers 2/3 of the presubiculum. I contributed to this study by exploring presubicular targets of afferents by *in vivo* stereotaxic injections of viral vectors to transduce channelrhodopsin-2 fused to eYFP in the ATN. Our data demonstrated a direct innervation of layer 3 pyramidal neurons of the presubiculum by thalamic fibers whereas Martinotti type interneurons received no direct excitation.

Concerning the connectivity, using dual patch-clamp recordings, Jean had shown a strong recurrent connectivity between pyramidal cells and Martinotti cells that form a feedback inhibitory circuit. Importantly, the excitation of Martinotti cells by pyramidal cells displayed an activity-dependent facilitation. In turn, the feedback inhibitory effect of Martinotti cells onto pyramidal cells was dependent on the exact timing of the IPSP with respect to the pyramidal cell-firing phase. This feedback circuit appeared well suited to refine and preserve the sustained firing of in-tune head direction cells while mediating lateral inhibition onto nearby principal cells. Our experimental data allowed to generate an autonomous attractor model based on recurrent inhibition that mimics head direction activity comparable to the presubicular records in vivo.

Activity dependent feedback inhibition supports head direction coding in the presubiculum

running title:
Activity dependent recruitment of Martinotti cells

Jean Simonnet[1,*], Mérie Nassar[1], Federico Stella[2], Ivan Cohen[3], Bertrand Mathon[1], Charlotte N. Boccara[2], Richard Miles[1] and Desdemona Fricker[1,*]

(1) Inserm U1127, CNRS UMR7225, Sorbonne Universités, UPMC Univ Paris 6 UMR S1127, Institut du Cerveau et de la Moelle épinière, Paris 75013, France; (2) Institut of Science and Technology Austria, 3400 Klosterneuburg, Austria ; (3) INSERM U1130, CNRS UMR8246, Sorbonne Universités, UPMC Univ Paris 6 UM CR 18, Neuroscience Paris Seine, 75005 Paris, France

*Correspondence: Desdemona Fricker: desdemona.fricker@upmc.fr
Jean Simonnet: jean.simonnet@bccn-berlin.de

J. Simonnet's present address : Bernstein Center for Computational Neuroscience, Humboldt University of Berlin, 10115 Berlin, Germany

SUMMARY

Orientation in space is represented in specialized brain circuits. Persistent head direction signals are transmitted from anterior thalamus to the presubiculum, but the identity of the presubicular target neurons, their connectivity and function in local microcircuits are unknown. Here we examine how thalamic afferents recruit presubicular principal neurons and Martinotti interneurons and the ensuing synaptic interactions between these cells. Pyramidal neuron activation of Martinotti cells in superficial layers is strongly facilitating such that high frequency head directional stimulation efficiently unmutes synaptic excitation. Martinotti cell feedback plays a dual role: precisely timed spikes may not inhibit the firing of in-tune head direction cells, while exerting lateral inhibition. Autonomous attractor dynamics emerge from a modeled network implementing wiring motifs and timing sensitive synaptic interactions in the pyramidal - Martinotti cell feedback loop. This inhibitory microcircuit is therefore tuned to refine and maintain head direction information in the presubiculum.

INTRODUCTION

The neural head direction signal is processed over several interconnected brain areas, and similarly to other sensory systems, it is relayed through the thalamus[1]. From there it reaches the presubicular cortex, located between the hippocampus and the entorhinal cortex[2]. About half of presubicular principal neurons signal head direction[3,4]. They fire persistently when the head of the animal faces a specific direction. The dorsal presubiculum, also termed postsubiculum (Brodmann area 48), controls the accuracy of the head direction signal and links them to specific features of the environment thus enabling a role for the hippocampal formation in landmark-based navigation[5,6].

Vestibular inputs make a decisive contribution to head directional firing of neurons in the anterodorsal nucleus of the thalamus[1,7,8] and lesions of this thalamic region abolish head direction firing in presubiculum[6]. Head direction signals transmitted via the thalamus are integrated in the presubiculum with visual information[5] from visual[9] and retrosplenial cortices[7], and information from the hippocampal formation[2]. Presubicular head direction cells project to the entorhinal cortex[10] and may contribute to spatial firing of grid cells[11-13].

The properties of presubicular microcircuits that signal head direction are less clear than the long-range outputs from the region. The electrophysiological and morphological properties of excitatory and inhibitory presubicular neurons have been described[14,15]. Pyramidal cells can generate persistent firing with little adaptation over tens of seconds[16] as needed to signal a maintained head direction. However, less is known of the connectivity and dynamics of inter- and intralaminar presubicular synapses[17]. Such data are crucial to understand how signals are transformed within the presubiculum and how this structure gates the flow of head direction information to the entorhinal cortex.

The roles of presubicular interneurons are presumably multiple: they provide global inhibition to restrain over-excitation[18] and, as suggested by continuous attractor theories, could induce selective inhibition of pyramidal cells, ensuring head direction signal specificity over time[13,19-22]. Yet, details of the recruitment of inhibitory cells are unknown. In somatosensory cortex, high frequency pyramidal cell firing is needed to recruit Martinotti interneurons. These cells then initiate a feedback inhibition of distal pyramidal cell dendrites[23,24], to exert a local control on excitatory synapses made at these sites[25]. Facilitating excitation of interneurons may be critical for the treatment of the persistent head direction signal, however, there is no data on the functional effects of Martinotti cells in the presubiculum.

We report here that strong recurrent connectivity between the presubicular Martinotti cells and layer III pyramidal cells form a feedback inhibitory circuit. Importantly, the excitation of Martinotti cells by pyramidal cells exhibits a dramatic activity-dependent facilitation. The feedback effects of Martinotti cell inhibition on pyramidal cell activity depend on IPSP timing, suggesting they could provide a source of lateral inhibition that enforces directionally selective firing. Testing these hypotheses by

modelling connectivity and synaptic dynamics of recurrent Martinotti-cell mediated inhibition revealed features of an attractor network generating activity patterns comparable to presubicular records *in vivo*. Our results demonstrate autonomous dynamic activity in the presubicular cortex emerging from the local circuits that process head direction signals *in vivo*.

RESULTS

Electrophysiology of presubicular Martinotti and pyramidal cells

Martinotti (MC) and pyramidal cells (PC) were recorded from superficial layer 3 of mouse presubiculum in horizontal slices (Fig. 1). MCs were identified as GFP positive neurons in tissue from X98-SST and Sst-Cre::tdTomato transgenic mice[15]. Martinotti cells often discharged spontaneously from a relatively depolarized membrane potential above -60 mV (Fig. 1a-c, Supplementary Table 1; ref.[15]). They exhibited low threshold spiking in response to current pulses and their axons ramified extensively in layer 1 as for other neocortical Martinotti cells[26] (Fig. 1a,d,e). Pyramidal cells, in contrast, typically did not discharge spontaneously and membrane potentials were more hyperpolarized, below -70 mV, than those of MCs (Fig. 1a-c and Supplementary Table 1). PCs fired regularly in response to injected current[14] with a higher threshold current (92.3 ± 6.3 pA) than that of MCs (51.5 ± 4.9 pA). The input-output gain was lower in PCs (0.373 ± 0.016 $Hz.pA^{-1}$) than in MCs (0.845 ± 0.040 $Hz.pA^{-1}$, Fig. 1e).

Anterior thalamic fibers directly excite principal neurons in superficial layers of presubiculum

Head directional inputs to the presubiculum originate in part from the Anterior Thalamic Nuclei[6,27] (ATN). We sought to define presubicular targets of these afferents by *in vivo* stereotaxic, intra-thalamic injection of viral vectors to transduce channelrhodopsin-2 fused to eYFP (Fig. 2; n = 5 SstCre::tdTomato mice). Fluorescent (eYFP) labeled thalamic axons innervated superficial layers of presubiculum, more densely in layers 1 and 3 than layer 2. They did not project to deep layers, to the adjacent subiculum or entorhinal cortex (Fig. 2a,b). Optical stimulation of ATN axons *in vitro* let us compare synaptic responses of PCs and MCs to thalamic input (Fig. 2c,d). At -65 mV, 11 out of 14 layer 3 pyramidal cells were made to fire by optical stimulation, while 4 out of 9 Martinotti-like cells of layer 3 discharged action potentials in response to identical stimuli. The latencies of optically evoked EPSCs in pyramidal cells were short and mono-synaptic (1.5 ± 0.3 ms) with a charge transfer of -2.647 ± 0.211 nC over 25 ms. In Martinotti-like neurons optically evoked EPSCs occurred with longer, more variable latencies (3.5 ± 0.7 ms) with lower charge transfer (charge transfer, -0.463 ± 0.174 nC) indicating a weaker excitatory drive (Fig. 2c,e,f). TTX (1 μM) and 4AP (100 μM) let us examine synaptic excitation mediated by thalamic afferents in isolation. Optical stimulation continued to excite PCs (-1.324 ± 0.046 nC, Fig. 2d,g) showing they are directly innervated by ATN fibers, but light-evoked responses in MCs were suppressed (charge transfer, -0.019 ± 0.009 nC, Fig. 2d,g). These data suggest that optical excitation of Martinotti cells is mediated indirectly via synapses made by presubicular pyramidal cells. We examined this recurrent inhibitory control of thalamic inputs to

pyramidal cells in dual patch clamp records from presubicular PCs and MCs in X98-SST mice (n = 54).

A feedback loop: pyramidal cells activate Martinotti cells and are inhibited in return

Pyramidal cells and Martinotti cells were highly interconnected (Fig. 3) as expected from the spatial overlap of their axons and dendrites (Fig. 1a). The proportion of connected pairs was 58% (82 of 142 tested) for Martinotti cell to pyramidal cell (MC-to-PC) and 37% (56 of 152 tested) for pyramidal cell to Martinotti cell (PC-to-MC). 28% of cell pairs (38 of 137) were reciprocally connected. 85% of PC-to-MC connections were reciprocal, and 52% of MC-to-PC pairs were reciprocally innervated. Connectivity between pyramidal neurons (PC-to-PC) was very low (1 of 48 tested). At -50 mV, the mean amplitude of inhibitory postsynaptic currents or potentials (IPSCs or IPSPs) triggered by Martinotti cells was 9.01 ± 1.19 pA (n = 45) or -0.56 ± 0.07 mV (n = 21). The probability that a single spike triggered a postsynaptic event was high (transfer rate 0.86 ± 0.05, mean ± sem; median = 0.925; n = 11; Fig. 3C, D), and for multiple trials, at least one postsynaptic event was observed for each connected pair. PC-to-MC transmission was much less reliable. For single spikes, the transfer rate from pyramidal cells to Martinotti cells was very low, 0.12 ± 0.02 (median = 0.08; n = 44, Fig. 3e,f). In 6 pairs, successful synaptic transmission occurred only during high frequency trains, which allowed us to identify them as functionally connected pairs, but single presynaptic spikes never initiated a postsynaptic response (at least 30 trials for each pair). In 38 PC-to-MC pairs, single pyramidal cell spikes, or first spikes in a train, occasionally initiated excitatory postsynaptic responses. Their potency, that is, the mean amplitude of single successful responses for PC-to-MC synapses, was -20.1 ± 1.94 pA (median = -20.4 pA; n = 31) or 1.44 ± 0.21 mV (median = 1.37 mV; n = 8). The efficacy, the potency multiplied by the transfer rate, was -2.36 ± 0.58 pA (median = -1.24.; n = 38) or 0.24 ± 0.05 mV (median = 0.27; n = 9) for the first spike; Fig. 3e,f; Supplementary Fig. 1).

We have shown a significant asymmetry in synaptic reliability in the recurrent inhibitory loop between pyramidal cells and Martinotti interneurons in superficial layers of the presubiculum: inhibitory synapses are much more reliable than excitatory connections. Since the dynamic behavior of both synapses in this feedback circuit will govern its operation[28,29], we examined postsynaptic responses at different rates of pre-synaptic firing. Transfer rate, potency and efficacy were analysed for synaptic responses to trains of 30 action potentials at either 10 Hz or 30 Hz, repeated with an inter-stimulus interval of at least 20 seconds (Fig. 4a and 5a). We detected all postsynaptic events and classed those following pre-synaptic spikes at mono-synaptic latencies (see methods) as spike-induced events.

Stable Martinotti cell inhibition during repetitive stimulation.

Information transfer at MC-to-PC connections was reliable and stable during synaptic activation at 10 or 30 Hz (Supplementary Table 2 and Fig. 4a-d). The synaptic efficacy for the first five action

potentials (early efficacy) and that of the last five action potentials (late efficacy) in trains of 30 pre-synaptic spikes were similar, for 10 Hz and 30 Hz stimulations (early 10 Hz, 16.97 ± 3.58 pA; late 10 Hz, 17.33 ± 3.32 pA; early 30 Hz, 16.13 ± 3.73 pA; late 30 Hz, 15.47 ± 2.76 pA, n = 8; Friedman test, P = 0.5222). Changes in efficacy during repetitive firing were mostly due to changes of potency and less to alterations in transfer rate (Fig. 4e). Cumulative efficacy evolved linearly during repetitive stimulations (Fig. 4f). Changes in synaptic frequency (see methods) were proportional to changes in presynaptic firing frequency (Fig. 4g). Thus, the dynamic behavior of MC-to-PC inhibitory synapses is relatively stable with little dependence on the history of pre-synaptic firing.

Repetitive stimulation unmutes the PC-to-MC connection in a frequency dependent manner

In contrast, PC-to-MC excitatory synapses displayed remarkable facilitating dynamic behavior (n = 55/56 pairs). Figure 5 shows an example of excitatory postsynaptic currents (EPSCs) elicited by 10 Hz and 30 Hz stimulations (Fig. 5a). Synaptic efficacy was low at first, but increased greatly with both the number and frequency of pre-synaptic action potentials, even though spike-to-spike responses varied between trials (Fig. 5a-d, Friedman test, P = 0.0002). At 10 Hz, late efficacy (6.51 ± 2.99 pA) was more than double early efficacy (2.99 ± 0.99 pA). At 30 Hz, late efficacy (17.34 ± 5.14 pA) was four times higher than early efficacy (4.41 ± 0.88 pA). Efficacy increased for 6/9 pairs tested at 10 Hz (Fig. 5d left, Dunn's multiple comparison, n.s.) and for 9/9 pairs at 30 Hz (Fig. 5d right, Dunn's multiple comparison P < 0.05). The extent of the increase varied between connections especially at 30 Hz (Fig. 5d). In contrast to the MC-to-PC synapse, changes in efficacy at the PC-to-MC synapse during activation at 30 Hz were due to variations in response probability and not in potency (Fig. 5e, n = 15 pairs). Increased efficacy implies a greater reliability of PC-to-MC synaptic transmission for increasing numbers and frequencies of pre-synaptic spikes. Furthermore the synaptic frequency increased supra-linearly with presynaptic spike frequency. After one second, the cumulative efficacy was 11 times higher at 30 Hz than at 10 Hz (Fig. 5f). The synaptic frequency was 5.9 times faster for early spikes and 7.9 times faster for late spikes, when presynaptic firing rate increased from 10 to 30 Hz (Fig. 5f,g), thus largely exceeding expected changes due to a three-fold increase in the rate of synaptic activation.

Increase of transfer rate at the PC-to-MC synapse as a medium term memory process

Presubicular Martinotti cells are reliably excited only when pyramidal cells fire at high frequency, as when they signal a preferred head direction. These frequency dependent changes do not reflect long-term synaptic plasticity since synaptic efficacy returned to previous values within ~20 s (Fig. 5a).

Several paired records nevertheless revealed medium term effects on the PC-to-MC excitatory synaptic transmission (n = 10, Fig. 6 and Supplementary Fig. 2). When synaptic unmuting was

induced after initial 30-40 Hz high frequency firing of the pyramidal neuron, synaptic transfer at the PC-to-MC synapse remained enhanced even as PC firing adapted to lower frequencies of firing (Supplementary Fig. 2a-c, blue lines). Similarly, after a high frequency spike train had unmuted the PC-to-MC synapse, a subsequent 10 Hz test stimulation maintained transfer rates well above those during a 10 Hz control spike train (Supplementary Fig. 2d-e). These results show that the unmuting effect of high frequency synaptic activation outlasts the high frequency stimulation itself. We then determined the time course of decay of synaptic enhancement. Following synaptic unmuting by a 30 Hz spike train of duration 2 seconds, synaptic responses to subsequent 2 Hz test stimuli revealed a double exponential decay of synaptic efficacy and transfer, with a fast time constant of 0.63 - 0.84 seconds accounting for reductions of about 70 %, followed by a slower decrease to baseline level, with a time constant of 7 – 11 s (n = 4, Fig. 6a-c).

How in vivo head direction signaling activates the PC-MC loop

How do these findings relate to head direction signaling *in vivo*? We recorded firing of presubicular head direction (HD) cells from animals running in an open field in order to test their effects at the PC-MC synapse. Firing of presubicular head direction cells *in vivo* was very irregular and instantaneous frequencies fluctuated widely[3]. Neurons with typical mean direction specific firing rates of ~15 Hz, could have peak instantaneous firing frequencies up to 250 Hz (n = 5; Fig. 7a,b). While the head remained within range of preferred directions (here 200° - 240°), the neuron shown in Fig. 7a fired in a sustained manner.

We used spike trains from isolated single head direction units within their preferred range *in vivo* as depolarizing current commands to presynaptic PCs in paired PC-MC recordings (Fig. 7c,d). As expected, excitatory transmission induced at the start of high frequency *in vivo* spike patterns was poor. The PC-to-MC synaptic efficacy increased considerably during sustained high frequency firing (from 0.9 ± 0.6 to 21.7 ± 11.9 pA; n = 5), and synaptic unmuting persisted during later sparse firing, even after a silent period of several hundred milliseconds (Fig. 7e,f). We noted not only an increase in synaptic events "locked" to presynaptic spikes with latencies < 3 ms, but also an increase in the frequency of delayed excitatory postsynaptic events after sustained high frequency firing (Fig. 7e). Firing of Martinotti cells induced by pyramidal cell firing was consistent with facilitating synaptic dynamics. Synchronous and asynchronous EPSPs summed to reach Martinotti cell firing threshold during repetitive high frequency firing (Fig. 7g,h).

For comparison, we also examined the synaptic transmission of the same spike train onto fast-spiking parvalbumin (PV) expressing interneurons in paired PC-PV recordings (Supplementary Fig. 3). Quite opposite to Martinotti cells, PV+ neurons responded with highest efficacy at the onset of a high

frequency spike train, then displayed depression. The facilitating pattern of synaptic recruitment was therefore specific to Martinotti cells but not PV+ interneurons.

Spike timing dependent inhibitory effect favoring lateral inhibition over self-induced inhibition

We next asked how Martinotti cell mediated feedback IPSPs affected post-synaptic pyramidal cells. Pyramidal cell spikes typically initiated Martinotti cell firing at a less than 10 ms delay (Fig. 8a; n = 4). In reciprocally connected cell pairs, Martinotti-cell mediated IPSPs coincided with the spike afterhyperpolarization (AHP) of the triggering pyramidal cell. These feedback IPSPs summed with the AHP, resulting in a larger pyramidal cell hyperpolarization and enhancing the peak amplitude of the next pyramidal cell action potential (Fig. 8a), but exerted little inhibitory effect on pyramidal cell firing.

However, Martinotti cells also mediate lateral inhibition. IPSPs in neighboring, but not reciprocally connected, pyramidal cells tend to occur with timing unrelated to preceding pyramidal cell spikes. We tested the hypothesis that such lateral inhibition has distinct effects to reciprocal inhibition in records from unidirectionally connected MC-to-PC pairs with mean IPSP amplitude greater than -0.3 mV at -50 mV (n = 7; Fig. 8b-e). MC action potentials were timed to initiate IPSPs at different times during the PC firing cycle (n = 7, 30-50 Hz). We then compared the effects of IPSPs of latencies <10 ms or >10 ms between PC and MC firing. We measured values for the pyramidal cell AHP (AHP_{TEST}) together with the peak of the next spike (PK_{TEST}) and the inter-spike interval (ISI_{TEST}). Since these parameters can adapt during spike trains, observed values were compared to extrapolated values. Pyramidal cell AHPs were more hyperpolarized for short latencies (-0.49 ± 0.13 mV, Fig. 8h, Wilcoxon signed rank test, P = 0.0313) than for long latencies (0.02 ± 0.02 mV; Fig. 8h, Wilcoxon signed rank test, P = 0.6875). PC action potential amplitude was increased for short latencies (0.31 ± 0.11 mV) compared to delayed MC spike timing (-0.06 ± 0.05 mV; Fig. 8h). Interspike intervals were significantly longer when MC-spikes were delayed >10ms rather than at short-latency (111.6 ± 2.6 % vs. 103.3 ± 0.95 %; Fig. 8i, unilateral Wilcoxon matched-pairs signed rank test, P < 0.01). Thus, the inhibitory effect of Martinotti cell IPSPs depends on when they are initiated during a PC firing cycle. Short latency feedback IPSPs are induced when persistent PC firing recruits a MC - these IPSPs have little inhibitory effect and may even encourage PC firing. In contrast, delayed IPSPs impinging on non-reciprocally connected PCs tend to delay subsequent PC discharges.

Inhibitory attractor network model reproduces presubicular head direction signaling

Head direction signals are organized internally, such that neurons with similar preferred head directions fire together in a correlated way[27]. Computational models of the head direction signal suggest that this activity profile may emerge from an attractor network[19,22,30,31]. We asked whether a

model based on experimentally measured connectivity, strength and dynamic behavior of synapses in recurrent Martinotti-cell circuits could generate attractor network dynamics.

Presubicular pyramidal cell and Martinotti cell interactions were simulated in a firing rate model, with the interneurons and principal cells represented as a two-layer network (Fig. 9a). Each pyramidal cell was assigned a preferred firing direction, so that the entire population evenly spanned 360°. The network was modeled after five key experimental findings of this study. 1. Each pyramidal unit contacted multiple Martinotti units, and vice-versa, with a high number of reciprocal connections (local dependency on phase similarity of head direction cells; cf. Methods). 2. Martinotti mediated inhibition was stable. 3. Slow, facilitating excitation of Martinotti neurons was implemented as a high threshold for Martinotti unit activation. Highly active pre-synaptic pyramidal cells compete for the control over inhibitory activity (winner takes all). 4. For simplicity, spike timing dependent inhibition was not modeled in terms of timing. Instead, we mimicked the essence of our experimental findings, that is, Martinotti recruitment only by the most active pyramidal unit, and reciprocal feedback inhibition leaving the driving pyramidal unit largely unaffected. Full, lateral inhibition was exerted on less active pyramidal units (Fig. 9a, right panel). 5. The transmission of directional information from the thalamus was simulated as a selective external input activating pyramidal units directly, but not Martinotti units.

We show that, in the absence of correlated inputs, the model network spontaneously generated a directionally selective increase in activity, thus satisfying attractor network dynamics (Fig. 9b). The model neurons coding for a certain direction forcedly mirrored the thalamic directional input, and when the external drive was reduced and the system relaxed, the neuronal activity profiles were mostly maintained (Fig. 9c). Polar plots of the activity of representative pyramidal cells were similar to those of finely tuned head direction cells *in vivo*, while Martinotti cells were very little directionally modulated (Fig. 9d). The precision of the pyramidal cell tuning could be controlled by varying the range α of the inhibition suppression around an existing connection between a pyramidal cell and a Martinotti cell (Supplementary Fig. 4). Finally the model allowed us to test the importance of the facilitating synaptic dynamics of Martinotti cell recruitment for the formation of a coherent activity bump. When facilitating synapses were replaced with depressing or stable synapses, the system rapidly fell apart, underscoring the key importance of the facilitating PC-to-MC synaptic properties for a maintained head directional signal (Fig. 9e). Thus recurrent excitatory synapses made with PV interneurons, which exhibit a dynamic depression, are not part of the attractor that maintains the head directional information in the presubiculum. In conclusion, an inhibitory feedback triggered exclusively at high firing frequencies with spike-timing dependent inhibitory effects on pyramidal cells will suffice to refine and sustain head direction signals in the presubiculum.

DISCUSSION

We have described activity-dependent dynamic properties of the Martinotti cell inhibitory feedback loop in the presubiculum. These properties underlie a self-sustained processing of head direction information in presubicular microcircuits. Superficial pyramidal cells are directly excited by thalamic inputs. Martinotti type interneurons are excited by these pyramidal cells and reliably inhibit pyramidal cell dendrites in layers 1 and 3. Feedback excitatory transmission from pyramidal cells to Martinotti cells is greatly facilitated during sustained high frequency presynaptic firing. Synaptic transfer may be enhanced for several seconds after a PC-to-MC connection is "unmuted". The behavior of this feedback inhibitory circuit is directly relevant to patterns of head direction activity. Natural firing patterns of these cells, recorded *in vivo,* recruited Martinotti cells very effectively *in vitro* whereas lower firing frequencies had little effect. Firing of these interneurons had distinct timing-dependent effects. In reciprocal connections, MCs fired at short latencies after PC action potentials. Inhibition by such precisely timed, spike-locked IPSPs was less effective than for randomly timed IPSPs, such that Martinotti cells provide a strong lateral inhibition. This feedback circuit is well-adapted to refine head direction signals in the presubiculum and to robustly preserve sustained firing of in-tune head direction cells.

Head direction signals are thought to be generated in subcortical nuclei and relayed via the thalamus to the parahippocampal region[1,6]. Neurons of anterior thalamus (ATN) project specifically to the presubiculum[7] (Fig. 1). A monosynaptic connection from ATN to presubicular head direction cells has been recently inferred *in vivo* based on short latency, reliable spike transmission[27]. Here we examined the effects of optogenetic activation of anterior thalamic axon terminals on single presubicular neurons *in vitro*. Our data provide functional evidence for a direct innervation of layer 3 pyramidal neurons of the presubiculum by thalamic fibers. Martinotti type interneurons received no direct excitation. Pyramidal cells of superficial layers project directly to the MEC (data not shown; cf. also[10,32]). While grid cell activity of MEC neurons depends on head direction information[33], the ATN does not project directly to the MEC. Thus integration of head direction code in presubicular superficial layers seems to be an essential element in the construction of inputs to MEC grid cells.

Recurrent feedback circuits of Martinotti cells and pyramidal cells are highly interconnected. The probability of PC-to-MC connections was 37%. The MC-to-PC connection probability was even higher: 58%. Such estimates from paired recordings are probably underestimates since all connections may not be preserved in slices. Our pipette solution was designed to enhance the driving force for chloride, increasing our ability to detect inhibitory synaptic events and to distinguish them from

failures. Nevertheless, we may have missed low amplitude inhibitory synaptic events generated at very distal dendritic sites. Martinotti cells of other cortical areas also have high connection probabilities with local pyramidal cells to provide a dense, reliable and non-specific inhibition[34], with both convergent and divergent connectivity[23,35]. We detected no direct activation of Martinotti cells by thalamic afferents reinforcing the feedback role of MCs in a presubiculum circuit. With a very low rate of recurrent connection between pyramidal cells (~ 2%), the PC-MC pathway becomes especially important to mediate interactions between presubicular pyramidal cells, similar to layer 5 pyramidal cells in neocortex[23] or to layer 2 stellate cells in medial entorhinal cortex[36,37].

We found MCs were only excited to fire by summed EPSPs induced after synaptic unmuting when PCs fired at high frequencies for prolonged periods. Single PC spikes never led to MC discharge (Fig. 7g, 8a). The short-term dynamics of pyramidal cell synapses vary between fast-spiking, parvalbumin expressing or low threshold spiking, somatostatin expressing interneurons in neocortex and hippocampus[23,38-40] (cf. also Supplementary Fig. 3). The facilitation during repeated activation shown here at synapses that excite Martinotti cells, is similar to that of synapses made with SST immunopositive interneurons in hippocampus[39] and neocortex[23,40,41]. Presubicular PC-to-MC synapses were often silent during paired pulse stimuli. We therefore analyzed synaptic dynamics from responses to trains of action potentials at 10 or 30 Hz. Enhanced synaptic efficacy during these trains resulted from increased transfer rate rather than potency (Fig. 5e). This phenomenon persisted for a time after high frequency stimuli (Fig. 6 and Supplementary Fig. 2) as at some other synapses[29,42]. Nevertheless even after unmuting, the transfer rate remained quite low at this synapse, compared to responses elicited by similar stimuli at neocortical PC-to-MC synapses in layer 3[41] or layer 5[23]. Possibly presubicular PC-to-MC transmission is regulated by an activity dependent mechanism, distinct from short term facilitation[29,43], situated at either axonal or presynaptic sites, and affecting spike waveform or the release machinery[24,44,45]. Transfer rate depends on both the probability of neurotransmitter release p_r, and the number of release sites. Data on numbers of terminals and active zones as well as the location of synapses on post-synaptic membrane will necessitate ultrastructural work. Further, since basal and dynamic values for p_r may differ at individual PC-MC synaptic boutons[46], a full description would also require information on vesicle pool size and replenishment. This work has rather presented an average picture of PC-MC synapses. Functionally, activity dependent synaptic unmuting and asynchronous release provide a medium term synaptic memory[47]. Such a trace of recent head directions at this synapse would permit comparison with incoming visual and hippocampal information converging in the presubiculum.

About half of presubicular principal neurons are directionally modulated[3]. Head direction cells sustain firing at high frequencies with weak adaptation while an animal maintains its head in a preferred direction[4]. PC-to-MC synapses are perfectly tuned to activate recurrent inhibition for sustained HD

signals. With very low initial transfer rates they act as a high pass filter[28], insensitive to sharp increases, but enhanced over time. Unlike fast-spiking parvalbumin expressing interneurons, MCs may therefore not be recruited during fast head turns when head direction cells do not fire persistently. MC inhibition of pyramidal cell dendrites seems likely to control the genesis of regenerative dendritic events[25] as well as to prevent over-excitation and control network activity[18,48] during persistent head direction firing. MC feedback inhibition would provide a common time window for dendritic excitation and so synchronize firing in neurons with similar head direction tuning, even if its influence on somatic and axonal processes of spike generation may be relatively minor. The effects of inhibition vary with timing during the pyramidal cell firing cycle (Fig. 8; ref [49,50]). In reciprocally connected cell pairs, when PCs drive MC firing, an IPSP is generated at short latency during the PC AHP. These IPSPs enhance repolarization which may facilitate initiation of the next PC action potential. Short latency feedback inhibition is therefore functionally less inhibitory than randomly timed lateral inhibition. Because well-tuned head direction cells fire maximally, and poorly-tuned cells fire less[13], PC-to-MC synapse dynamics clearly favor MC recruitment by well-tuned direction cells. Lateral feedback then preferentially inhibits poorly-tuned cells.

Experimental data let us propose a modified continuous attractor model based on recurrent inhibition to mimic head direction activity. The build-up of strong principal neuron activation as a necessary condition for interneuron recruitment is essential to the model. We suggest that activity-dependent unmuting of Martinotti cells and their facilitating synapse dynamics are key for autonomous circuit dynamics in the presubiculum. In contrast to primary visual cortex[51], the presubiculum could, in this way, sustain activity. PV neurons with depressing synapses (Supplementary Fig. 3) are not part of the attractor. We suggest that during fast head turns, when Martinotti cells are not recruited, the system may switch to a relay type function. However they become active during maintained directional signaling, and support a form of working presubicular memory. Our data on a one-dimensional head direction system might suggest that equivalent dynamics exist in the medial entorhinal grid-cell system[36,52]. We note the model network requires no directional tuning of presubicular interneurons and the efficacy of synapses they make depends exclusively on the timing of interneuron firing with respect to firing in the presynaptic principal neuron, simulated as a connection sign switch. In conclusion, the recruitment of Martinotti cells by differentially active, randomly connected pyramidal cells provides an economic way to refine and sustain presubicular head direction signal representations.

METHODS

Animals

Most work was done on slices from transgenic mice (X98-SST line, JAX 006340) that express GFP in a subpopulation of somatostatin-positive (SST) neocortical Martinotti cells[26]. X98-SST mice were maintained by breeding heterozygous males with C57BL/6J females (CERJ Janvier). Sst-Cre::tdTomato mice were used in experiments involving the light activation of Channelrhodopsin-2 (ChR2). They were obtained by crossing Sst-IRES-Cre mice[53] (Jax 013044) with an Ai14 Cre reporter line[54] (Jax 007914). SST positive neurons of these mice express the red fluorescent protein tdTomato, which can be visualized without activating ChR2. Pvalb-Cre::tdTomato mice were used for comparing synapse dynamics. They were obtained by crossing Pvalb-Cre mice[55] (Jax 008069) with the Ai14 Cre reporter line. Animal care and use conformed to the European Communities Council Directive of 2010 (2010/63/EU) and French law (87/848). Our study was approved by the local ethics committee Charles Darwin N°5.

Stereotactic Virus Injections

Adeno-associated viral vectors carrying genes for ChR2-EYFP fusion proteins (AAV2/9.hSyn.hChR2 (H134R)-EYFP.WPRE.hGH; University of Pennslvania Vector Core) were injected into the anterior thalamic nucleus (ATN) at postnatal age P28. For surgery, mice were deeply anesthetized with intraperitoneal injection of ketamine hydrochloride and xylazine (100 and 15 $mg.kg^{-1}$, respectively) following stereotaxic procedures described previously[56]. 50-150 nl of virus was delivered via a 33-gauge needle with a Hamilton syringe in a syringe Pump Controller (Harvard Apparatus, Pump 11 elite) at 20 $nl.min^{-1}$. ATN was targeted at coordinates from Bregma: lateral, 0.75 mm; posterior, -0.82 mm; depth, -3.2 mm. Slices were prepared at 12-16 days after vector injection.

Slice preparation, in vitro electrophysiology and photostimulation

Under ketamine and xylazine anesthesia, animals were perfused via the heart with 30 ml or more of a solution containing (in mM): 125 NaCl, 25 sucrose, 2.5 KCl, 25 $NaHCO_3$, 1.25 NaH_2PO_4, 2.5 D-glucose, 0.1 $CaCl_2$ and 7 $MgCl_2$, cooled to 2–6 °C and equilibrated with 5% CO_2 in O_2. The forebrain was dissected, and horizontal slices of thickness 260-320 µm were cut with a vibratome (Leica VT1200S). They were transferred to a storage chamber containing warmed (37°C) artificial cerebrospinal fluid (ACSF) of : 124 NaCl, 2.5 KCl, 26 $NaHCO_3$, 1 NaH_2PO_4, 2 $CaCl_2$, 2 $MgCl_2$, and 11 D-glucose (mM), gently bubbled with 5% CO_2 in O_2 (pH 7.3, 305–310 mOsm/L). ACSF in the storage chamber cooled towards room temperature (22-25°C) as slices were kept for at least 1 hr before transfer to a recording chamber.

The recording chamber, of volume ~ 2 ml, was heated to 33 – 35 °C. Neurons were visualized with an EMCCD Luca-S camera (Andor) on an Axioskop 2 FS plus microscope (Zeiss, France) with infrared differential interference contrast. Glass recording pipettes were pulled from borosilicate glass of external diameter 1.5 mm (Clark Capillary Glass, Harvard Apparatus) using a Brown-Flaming electrode puller (Sutter Instruments). A low-chloride potassium gluconate-based (Low-Cl K-gluc) internal solution contained (in mM): 145 K-gluconate, 2 KCl, 10 HEPES, 0-0.2 ethylene glycol tetra-acetic acid (EGTA), 2 $MgCl_2$, 4 MgATP, 0.4 Tris-GTP, 10 Na_2-phosphocreatine. The cesium gluconate-based internal solution (Cs-gluc) contained (in mM): 135 Cs-gluconate,5 KCl, 10 HEPES, 0-0.2 ethylene glycol tetra-acetic acid (EGTA), 2 $MgCl_2$, 4 MgATP, 0.4 Tris-GTP, 10 Na_2-phosphocreatine. Recordings were made with low-Cl K-gluc solution unless specified. Tip resistance of filled pipettes was 3–7 MΩ. Whole-cell records were made with a Multiclamp 700B amplifier and acquired with pClamp software (Molecular Devices). Recordings were filtered at 6-12 KHz in current clamp mode and at 2-6 KHz in voltage clamp mode. No correction was made for junction potential (~15 mV). Access resistance was continuously monitored and records were excluded if variations exceeded 15 %.

Pyramidal cells were identified as non-fluorescent regular spiking neurons with typical properties[14]; Martinotti-like cells (MC) of tissue from X98-SST mice were defined as green fluorescent neurons, and those from Sst-Cre::tdTomato mice as red fluorescent neurons. In both mouse lines, MC possessed resting membrane potential above -65 mV. Discharges were either adapting or low threshold firing and biocytin filling revealed typical Martinotti cell axonal and dendritic morphologies (Fig. 2).

Channelrhodopsin expressing terminals from the AT thalamic nucleus were excited with blue light from a source (Cairn OptoLED, white) coupled to the epifluorescence microscope port, filtered (BP 450-490, FT 510) and fed into a 60X 1.0 NA plan-Apochromat objective. Light pulses of 0.5 ms duration and intensity 2 mW were delivered at 20 s intervals. 1 µM TTX and 40 µM 4AP were added to the bath to check for direct vs. indirect optical activation. Salts and anesthetics were all obtained from Sigma, except TTX from Tocris.

In vivo electrophysiology

Head direction firing was sampled from presubicular neurons in 4 months old Long-Evans rats *in vivo* (cf. ref.[3]). Briefly, tetrodes were implanted at AP 2.2 mm in front of the transverse sinus, ML 3.7 mm from the midline, and DV 1.5 mm below the dura. Tetrodes were lowered progressively until reaching presubicular layers. Recording sites in presubiculum were confirmed from post-hoc Nissl, parvalbumin and calbindin stained sections. Head direction was tracked with two light-emitting diodes while the animal collected randomly distributed food crumbs from a 100 cm wide square box. Spikes were sorted offline with cluster cutting Axona software. Head direction was calculated from projections of the relative position of the two LEDs on the horizontal plane. Directional tuning for

each cell was obtained by plotting firing rate against the rat head direction, divided into bins of 3 degrees and smoothed with a 14.5 degrees mean window filter (14 bins on each side). Command protocols for slice records were generated from these spike trains imported into pClamp.

Data analysis

Signals were analyzed with AxoGraphX, and locally-written software (Labview, National Instruments; MATLAB, The Mathwork). Algorithms to detect action potentials and measure active and passive neuronal properties were described previously[14,15].

Detection of postsynaptic events

Excitatory and inhibitory postsynaptic currents and potentials were detected and measured automatically from low-pass filtered records adapted to the recording mode (0.4 KHz for EPSPs, 1 KHz for EPSCs and 500-750 KHz for IPSCs). Spontaneous or spike-associated events were detected as continuous rising signals exceeding a threshold set for records from each cell to minimize both false positive and negative detection. Thresholds were 0.3-0.6 mV for EPSPs, 4-7 pA for EPSCs and IPCSs recorded in K-gluconate and 4-12 pA for IPSCs recorded with Cs-gluconate solution.

Spike-locked postsynaptic events were defined as first events occurring within a monosynaptic latency (generally 0.5-3 ms for an EPSC and 0.5-4 ms for an IPSC). Delayed postsynaptic events were those that occurred later than the spike-locked events or outside the monosynaptic window but still within 10 ms after the spike. PSC latencies were calculated from the action potential peak to the mid-rise of the postsynaptic event.

Spontaneous activity can bias values for synaptic transfer. We estimated “false positives” which might exaggerate monosynaptic transfer rates. Presynaptic firing patterns were aligned to a “control window”, before stimulation, and transfer rate, corresponding to a noise value, was calculated. This procedure was applied multiple (250 - 300) times using different starting points in the same control window. The number of “false positive” rarely exceeded 0.05. It depended on the level of background synaptic activity, but not on presynaptic firing frequency.

Synapse dynamics in repetitive stimuli

Synaptic transfer rate was calculated from paired records as the number of detected post-synaptic events divided by the number of presynaptic spikes. Failure rate was 1 – transfer rate. Synaptic potency (pA or mV) was defined as the amplitude of detected events. Efficacy (pA or mV) was the mean amplitude of responses including failures (failure amplitude = 0). Efficacy may be deduced as potency x transfer rate. Synaptic transmission during repeated presynaptic activation was analyzed in these terms to derive transfer rate, potency and efficacy for either (1) a given spike across different trials of a standard stimulus, or (2) groups of successive spikes elicited during a defined time. For

spike trains, the first five spikes and the last five spikes were grouped to increase measurement precision (Figs. 4 and 5) when trial-to-trial variability was high. Changes of transfer rate, potency and efficacy over time are measured as the ratio of late/early values. Cumulative efficacy over time provides a temporal dynamic. The derivative of this cumulative efficacy, that we called "synaptic frequency", corresponds to the information transferred per second.

Inhibitory effect

Functional MC-mediated inhibition was quantified as the ability of an IPSP to delay PC-discharge (ISI modulation). We also measured effects of IPSPs induced after pyramidal cell firing. In an effective recurrent circuit, pyramidal cells may induce MC-spike firing evoking in turn an IPSP in the initiating pyramidal cell. This effect was quantified as an enhanced pyramidal cell AHP (AHP modulation) or change in peak amplitude of a PC-spike (Peak modulation). Both parameters could be affected by intrinsic properties such as adaptation, peak accommodation and an AHP depolarization during repetitive firing. We therefore determined the effect of inhibition as changes from predicted pyramidal cell repetitive firing behavior (Fig. 8).

Cellular anatomy

Biocytin (1mg/ml) was added to the pipette solution to reveal the morphology of some recorded cells as described[14,15]. Axo-dendritic morphology was reconstructed from z-stacks of acquired images with Neurolucida software (Microbrightfield, Williston, VT, USA).

Computational model

The model aims at building on previous work on the head direction system by studying a network whose function is dominated by inhibitory interactions between pyramidal cells and where the interneurons mediating such interactions are explicitly included in the dynamics of the system[20,57,58].

Network Wiring. We simulated the activity of a layer of N_{Pyr} pyramidal units interacting through a population of $N_{Inh} = \rho N_{Pyr}$ Martinotti units. Each pyramidal unit was assigned a preferred direction Θ, evenly spaced to cover the $0-2\pi$ interval, while Martinotti units were identified with an index *j*. Excitatory connections from pyramidal to Martinotti units ($W_{\Theta,j}^{OUT}$) and inhibitory connections from Martinotti units back to the pyramidal layer ($W_{j,\Theta}^{IN}$) were established as follows (cf. Fig. 9a). Initially, each Martinotti unit randomly connected to pyramidal units with a 0.7 probability. A sub-set N_{Conn} of these inhibitory connections was randomly selected as "main connections". Inhibitory connections contacting neighboring pyramidal cells were pruned. Consequently, for each main connection between a Martinotti unit $\tilde{j}$ and a pyramidal unit $\tilde{\Theta}$, connections from the Martinotti unit to pyramidal units with directional preference close to $\tilde{\Theta}$ were pruned. The number of main

connections N_{Conn} for each Martinotti unit depended on the range of pruning, α. The number of pruned connections for each main connection was a constant fraction Λ of all the possible connections for any range of the pruning, that is $\alpha N_{Conn} = \Lambda N_{Pyr}$. Therefore :

$$N_{Conn} = \frac{\Lambda * N_{Pyr}}{\alpha}$$

After establishing the inhibitory connectivity, the excitatory wiring was established as follow. Each main connection was associated with a reciprocal excitatory connection. For the remaining inhibitory connections, excitatory connections were created with a 0.4 probability and a reduced strength compared to those associated with the main connections.

As a last step, the strength of the inhibitory connections converging on each pyramidal cell was normalized according to:

$$\sum_j W^{IN}_{j,\Theta} = w^{IN}$$

Ultimately, three different groups of connections could be found: 1) strong main excitatory connections from pyramidal to Martinotti, with strength $\overline{w}^{OUT}$, 2) background excitatory connections with strength w^{OUT} and 3) inhibitory connections (Network parameters are given in Supplementary Table 4).

Unit Dynamics. A pyramidal unit assigned with preferred direction Θ was described by its firing rate at time *t,* $r_E(\Theta,t)$, regulated through the following dynamics:

$$\tau_E \dot{r}_E(\Theta,t) = -r_E(\Theta,t) + f(h(\Theta,t) + I(\Theta,t))$$

where $f[I] = g[I]_+$ is a threshold linear f-I curve and τ_E is the neuronal time constant. The input to the unit consisted of an external input term, *h* (see below), and the contribution coming from feedback inhibition, *I.* In turn, the inhibition term consisted of the combined effect of the presynaptic Martinotti units:

$$I(\Theta,t) = \sum_j w^{IN}_{j,\Theta} r_I(j,t)$$

where $w^{IN}_{j,\Theta}$ is the strength of the inhibitory connection between Martinotti unit *j* and pyramidal unit Θ. Similarly, for Martinotti units firing rate was regulated by the equation

$$\tau_I \dot{r}_I(j,t) = -r_I(j,t) + f(E(j,t) - T)$$

that includes an activation threshold *T* and a time constant $\tau_I > \tau_E$ generating slower input integration times. The excitatory current E was not the sum of pre-synaptic inputs but instead the maximum of the pre-synaptic components:

$$E(j,t) = \max_{\Theta}\{W^{OUT}_{\Theta,j} r_E(\Theta,t)\}$$

Therefore, at any time each Martinotti unit was controlled by a single excitatory pyramidal unit, and became locked to it. The reciprocal feedback inhibition for the locked pair was:

$$W^{IN}_{\tilde{j},\tilde{\Theta}} \rightarrow \lambda W^{IN}_{\tilde{j},\tilde{\Theta}}$$

where $\tilde{j}$ was a given Martinotti unit and $\tilde{\Theta}$ was the preferred direction of the dominating pre-synaptic unit. For all simulations in Fig. 9, λ was set to 0, so that feedback inhibition between the locked pair was absent, as long as $\tilde{\Theta}$ remained the dominating input. To test the effect of a moderate degree of feedback inhibition, λ was varied over a range of values from 0 to 1 (Supplementary Fig. 4b).

External Input. Each pyramidal unit in the network received an independent, time-dependent, activation current $h(\Theta,t)$ from an external source. Since all the internal effective interactions between pyramidal units were inhibitory, this external source of excitation was necessary for activity in the network. In our simulations, each unit was fed with a random input, uncorrelated across units, but correlated in time:

$$\tau_N \dot{h}(\Theta,t) = -h(\Theta,t) + \eta(\mu,\sigma)$$

where η was a normal distributed random variable with mean μ and standard deviation σ. This random background input could be combined with an additional direction selective component, restricted to a sub-set of the units, centered around a given direction φ,

$$h(\Theta,t) = \beta \exp(-(\Theta-\varphi)^2 / 2\kappa^2)$$

where β controlled the strength of this component (with respect to the background one) and κ regulated the degree of selectivity around the central selected direction φ (cf. Supplementary Table 4 for network parameters values).

Dynamic properties of synapses. In order to examine the influence of synapse dynamics on the ability of the system to form a coherent bump of activity, we modified the previous dynamics equation,

$$\tau_I \dot{r}_I(j,t) = -r_I(j,t) + f(\tilde{E}(j,t) - T)$$

so that the term $\tilde{E}(j,t)$ reflected depressing synaptic dynamics mediated by the equations:

$$\tau_{A1} \dot{\tilde{E}}(j,t) = -\tilde{E}(j,t) + (E(j,t) - G(j,t))$$

$$\tau_{A2} \dot{G}(j,t) = -G(j,t) + (E(j,t)$$

The unit's responsiveness to its input from the pyramidal units was being regulated over time, forcing it into periods of low activity. The time-scale of depression and following recovery was determined by the parameters τ_{A1} and τ_{A2}. Only τ_{A1} was varied, and $\tau_{A2} = 3\tau_{A1}$.

Activity Bump Coherence. The degree of concentration of the pyramidal cell activity was measured as

$$\Omega = \frac{\left| \sum_{k=1}^{N_{Pyr}} e^{i\Theta_k} r_E(\Theta_k) \right|}{\sum_{k=1}^{N_{Pyr}} r_E(\Theta_k)}$$

Simulations. Simulations consisted in integrating the network dynamics during 200 time steps of 1-ms. When only white noise was fed into the system, the simulation consisted in reproducing network dynamics starting from a random activity configuration. When studying the effect of directionally selective external inputs, the network received random and selective external inputs to the pyramidal cell layer for the first 30 time steps with the latter then gradually fading away between time steps 30 and 40. This procedure was repeated with the directional input sequentially centered over each of the cells preferred directions.

When studying the effect of inhibition strength on the bump size (Supplementary Fig 4b), the procedure was the same, just repeated with different connection strength w^{IN}. The size of the bump was calculated as the angle spanned by the range of units with non-zero activity.

All simulations were performed using MATLAB custom code.

SUPPLEMENTAL INFORMATION

Supplemental information includes three Tables and five Supplementary Figures and can be found with this article online at http://dx.doi.org/

ACKNOWLEDGEMENTS

This work was supported by the Région Ile-de-France and Fondation pour la recherché Medicale (J.S.) and by ANR Grant JCJC R10206DD (D.F.). The research leading to these results also benefitted from the program "Investissements d'avenir" ANR-10-IAIHU-06. We thank Karl Deisseroth for making available AAV-hSyn-hChR2(H134R)-EYFP. We thank Dominique Debanne for discussions, and

Matthew Nolan and Bruno Delord for comments on the manuscript. *In vivo* spike train data were collected in the lab of Edvard and May-Britt Moser (Trondheim, Norway).

AUTHOR CONTRIBUTIONS

J.S. and D.F. conceived and designed research, interpreted the data and supervised the experiments. All *in vitro* recordings were carried out and analyzed by J.S., with the help of M.N. for recordings with optical stimulations and experiments on parvalbumin interneurons. B.M., M.N. and J.S. performed stereotaxic viral injections. I.C. provided tools for analysis. F.S. implemented the model and run the simulations. C.B. performed *in vivo* recordings and co-coordinated the study. J.S., F.S., C.B., R.M. and D.F. wrote the paper.

References

1. Taube, J. S. The head direction signal: origins and sensory-motor integration. *Annu. Rev. Neurosci.* **30,** 181–207 (2007).
2. Van Strien, N. M., Cappaert, N. L. M. & Witter, M. P. The anatomy of memory: an interactive overview of the parahippocampal-hippocampal network. *Nat. Rev. Neurosci.* **10,** 272–282 (2009).
3. Boccara, C. N. *et al.* Grid cells in pre- and parasubiculum. *Nat. Neurosci.* **13,** 987–994 (2010).
4. Taube, J. S., Muller, R. U. & Ranck, J. B. Head-direction cells recorded from the postsubiculum in freely moving rats. II. Effects of environmental manipulations. *J. Neurosci.* **10,** 420–435 (1990).
5. Yoder, R. M., Peck, J. R. & Taube, J. S. Visual landmark information gains control of the head direction signal at the lateral mammillary nuclei. *J. Neurosci.* **35,** 1354–1367 (2015).
6. Goodridge, J. P. & Taube, J. S. Interaction between the postsubiculum and anterior thalamus in the generation of head direction cell activity. *J. Neurosci*. **17,** 9315–9330 (1997).
7. van Groen, T. & Wyss, J. M. The postsubicular cortex in the rat: characterization of the fourth region of the subicular cortex and its connections. *Brain Res.* **529,** 165–177 (1990).
8. Valerio, S. & Taube, J. S. Head direction cell activity is absent in mice without the horizontal semicircular canals. *J. Neurosci*. **36,** 741–754 (2016).
9. Vogt, B. A. & Miller, M. W. Cortical connections between rat cingulate cortex and visual, motor, and postsubicular cortices. *J. Comp. Neurol.* **216,** 192–210 (1983).
10. Tukker, J. J., Tang, Q., Burgalossi, A. & Brecht, M. Head-directional tuning and theta modulation of anatomically identified neurons in the presubiculum. *J. Neurosci.* **35,** 15391–15395 (2015).
11. Wills, T. J., Cacucci, F., Burgess, N. & O'keefe, J. Development of the hippocampal cognitive map in preweanling rats. *Science* **328,** 1573–1576 (2010).
12. Langston, R. F. *et al.* Development of the spatial representation system in the rat. *Science* **328,** 1576–1580 (2010).
13. McNaughton, B. L., Battaglia, F. P., Jensen, O., Moser, E. I. & Moser, M.-B. Path integration and the neural basis of the 'cognitive map'. *Nat. Rev. Neurosci.* **7,** 663–678 (2006).
14. Simonnet, J., Eugène, E., Cohen, I., Miles, R. & Fricker, D. Cellular neuroanatomy of rat presubiculum. *Eur. J. Neurosci.* **37,** 583–597 (2013).
15. Nassar, M. *et al.* Diversity and overlap of parvalbumin and somatostatin expressing interneurons in mouse presubiculum. *Front. Neural Circuits* **9,** 1–19 (2015).
16. Yoshida, M. & Hasselmo, M. E. Persistent firing supported by an intrinsic cellular mechanism in a component of the head direction system. *J. Neurosci.* **29,** 4945–4952 (2009).
17. Funahashi, M. & Stewart, M. Presubicular and parasubicular cortical neurons of the rat: functional separation of deep and superficial neurons in vitro. *J. Physiol.* **501,** 387–403 (1997).
18. Isaacson, J. S. & Scanziani, M. How inhibition shapes cortical activity. *Neuron* **72,** 231–243 (2011).
19. Skaggs, W. E., Knierim, J. J., Kudrimoti, H. S. & McNaughton, B. L. A model of the neural basis of the rat's sense of direction. *Adv. Neural Inf. Process Syst.* **7,** 173–180 (1995).
20. Zhang, K. Representation of spatial orientation by the intrinsic dynamics of the head-direction cell ensemble: a theory. *J. Neurosci.* **16,** 2112–2126 (1996).
21. Song, P. & Wang, X.-J. Angular path integration by moving 'hill of activity': a spiking neuron model without recurrent excitation of the head-direction system. *J. Neurosci.* **25,** 1002–1014 (2005).
22. Goodridge, J. P. & Touretzky, D. S. Modeling attractor deformation in the rodent head-direction system. *J. Neurophysiol.* **83,** 3402–3410 (2000).
23. Silberberg, G. & Markram, H. Disynaptic inhibition between neocortical pyramidal cells

mediated by Martinotti cells. *Neuron* **53,** 735–746 (2007).
24. Zhu, J., Jiang, M., Yang, M., Hou, H. & Shu, Y. Membrane Potential-dependent modulation of recurrent inhibition in rat neocortex. *PLoS Biol.* **9,** e1001032 (2011).
25. Murayama, M., Pérez-Garci, E., Nevian, T., Bock, T., Senn, W. & Larkrum, ME. Dendritic encoding of sensory stimuli controlled by deep cortical interneurons. *Nature* **457,** 1137–1141 (2009).
26. Ma, Y., Hu, H., Berrebi, A. S., Mathers, P. H. & Agmon, A. Distinct subtypes of somatostatin-containing neocortical interneurons revealed in transgenic mice. *J. Neurosci.* **26,** 5069–5082 (2006).
27. Peyrache, A., Lacroix, M. M., Petersen, P. C. & Buzsáki, G. Internally organized mechanisms of the head direction sense. *Nat. Neurosci.* **18,** 569–575 (2015).
28. Abbott, L. F. & Regehr, W. G. Synaptic computation. *Nature* **431,** 796–803 (2004).
29. Regehr, W. G. Short-Term Presynaptic Plasticity. *Cold Spring Harb. Perspect. Biol.* **4,** a005702 (2012).
30. Knierim, J. J. & Zhang, K. Attractor dynamics of spatially correlated neural activity in the limbic system. *Annu Rev Neurosci* **35,** 267–285 (2012).
31. Redish, A. D., Elga, A. N. & Touretzky, D. S. A coupled attractor model of the rodent head direction system. *Netw. Comput. Neural Syst.* **7**,671–685 (1996).
32. Rowland, D. C. *et al.* Transgenically targeted rabies virus demonstrates a major monosynaptic projection from hippocampal area ca2 to medial entorhinal layer ii neurons. *J. Neurosci*. **33,** 14889–14898 (2013).
33. Winter, S. S., Clark, B. J. & Taube, J. S. Spatial navigation. Disruption of the head direction cell network impairs the parahippocampal grid cell signal. *Science* **347,** 870–874 (2015).
34. Fino, E. & Yuste, R. Dense inhibitory connectivity in neocortex. *Neuron* **69,** 1188–1203 (2011).
35. Kapfer, C., Glickfeld, L. L., Atallah, B. V. & Scanziani, M. Supralinear increase of recurrent inhibition during sparse activity in the somatosensory cortex. *Nat. Neurosci.* **10,** 743–753 (2007).
36. Couey, J. J. *et al.* Recurrent inhibitory circuitry as a mechanism for grid formation. *Nat. Neurosci*. **16,** 318–324 (2013).
37. Pastoll, H., Solanka, L., van Rossum, M. C. W. & Nolan, M. F. Feedback inhibition enables θ-nested γ oscillations and grid firing fields. *Neuron* **77,** 141–154 (2013).
38. Ali, A. B., Deuchars, J., Pawelzik, H. & Thomson, A. M. CA1 pyramidal to basket and bistratified cell EPSPs: dual intracellular recordings in rat hippocampal slices. *J. Physiol.* **507,** 201–217 (1998).
39. Ali, A. B. & Thomson, A. M. Facilitating pyramid to horizontal oriens-alveus interneurone inputs: dual intracellular recordings in slices of rat hippocampus. *J. Physiol.* **507,** 185–199 (1998).
40. Beierlein, M., Gibson, J. R. & Connors, B. W. Two dynamically distinct inhibitory networks in layer 4 of the neocortex. *J. Neurophysiol.* **90,** 2987–3000 (2003).
41. Fanselow, E. E., Richardson, K. A. & Connors, B. W. Selective, state-dependent activation of somatostatin-expressing inhibitory interneurons in mouse neocortex. *J. Neurophysiol.* **100,** 2640–2652 (2008).
42. Gupta, A., Wang, Y. & Markram, H. Organizing principles for a diversity of GABAergic interneurons and synapses in the neocortex. *Science* **287,** 273–278 (2000).
43. Jackman, S. L., Turecek, J., Belinsky, J. E. & Regehr, W. G. The calcium sensor synaptotagmin 7 is required for synaptic facilitation. *Nature* **529,** 88–91 (2016).
44. Debanne, D., Bialowas, A. & Rama, S. What are the mechanisms for analogue and digital signalling in the brain? *Nat. Rev. Neurosci.* **14,** 63–69 (2013).
45. Rama, S. *et al.* Presynaptic hyperpolarization induces a fast analogue modulation of spike-evoked transmission mediated by axonal sodium channels. *Nat. Commun.* **6,** 10163 (2015).
46. Branco, T. & Staras, K. The probability of neurotransmitter release: variability and feedback control at single synapses. *Nat. Rev. Neurosci*. **10,** 373–383 (2009).
47. Mongillo, G., Barak, O. & Tsodyks, M. Synaptic theory of working memory. *Science* **319, 1543-1546** (2008).

48. Beed, P. *et al.* Inhibitory gradient along the dorsoventral axis in the medial entorhinal cortex. *Neuron* **79,** 1197–1207 (2013).
49. Cobb, S. R., Buhl, E. H., Halasy, K., Paulsen, O. & Somogyi, P. Synchronization of neuronal activity in hippocampus by individual GABAergic interneurons. *Nature* **378,** 75–78 (1995).
50. Mann, E. O. & Paulsen, O. Role of GABAergic inhibition in hippocampal network oscillations. *Trends Neurosci.* **30,** 343–349 (2007).
51. Reinhold, K., Lien, A. D. & Scanziani, M. Distinct recurrent versus afferent dynamics in cortical visual processing. *Nat. Neurosci.* **18,** 1789–1797 (2015).
52. Roudi, Y. & Moser, E. I. Grid cells in an inhibitory network. *Nat. Neurosci.* **17,** 639–641 (2014).
53. Taniguchi, H. *et al.* A resource of Cre driver lines for genetic targeting of GABAergic neurons in cerebral cortex. *Neuron* **71,** 995–1013 (2011).
54. Madisen, L. *et al.* A robust and high-throughput Cre reporting and characterization system for the whole mouse brain. *Nat. Neurosci.* **13,** 133–140 (2010).
55. Hippenmeyer, S. *et al.* A developmental switch in the response of DRG neurons to ETS transcription factor signaling. *PLoS Biol.* **3,** e159 (2005).
56. Mathon, B. *et al.* Increasing the effectiveness of intracerebral injections in adult and neonatal mice: a neurosurgical point of view. *Neurosci. Bull.* **6**, 685-696 (2015).
57. Stringer, S. M., Trappenberg, T. P., Rolls, E. T. & de Araujo, I. E. T. Self-organizing continuous attractor networks and path integration: one-dimensional models of head direction cells. *Network* **13,** 217–242 (2002).
58. Boucheny, C., Brunel, N. & Arleo, A. A continuous attractor network model without recurrent excitation: maintenance and integration in the head direction cell system. *J. Comput. Neurosci.* **18,** 205–227 (2005).

FIGURE LEGENDS

Figure 1. Morphology and electrophysiological intrinsic properties of Martinotti interneurons and pyramidal cells in superficial layers of presubiculum

(a) Anatomical reconstruction of reciprocally connected PC and MC in layer 3. PC dendrites (blue) and MC axon (red) covered layer 1 and 3, PC axon (yellow) and MC dendrites (green) mainly occupied layer 3 (inset). Subiculum is to the left and the parasubiculum to the right.

(b) Current clamp recordings of a MC (green) and a PC (blue). The MC fired spontaneously, the PC, with a more hyperpolarized membrane potential, was silent.

(c) Membrane potential values for 80 MCs (circles, X98-SST, green; SstCre, orange) and 87 PCs (triangles, X98-SST, blue; SstCre, purple). The horizontal bar indicates the mean value.

(d) Typical responses of a MC and a PC to negative and positive current step injections of duration 800 ms from -65 mV.

(e) Plotting input-output (I-O) gain against threshold current separates of PCs (triangles) and MCs (circles; same color code as in **(c)**).

Figure 2. Pyramidal cells, but not Martinotti cells, are directly innervated by the anterior thalamus.

(a) Channelrhodopsin2-eYFP expression in Anterior Thalamus (AT) of SstCre::tdTomato mice fifteen days after stereotaxic injections of an AAV vector. Injection site in AT and projecting thalamic axons in the ipsilateral presubiculum (horizontal brain section, 20° angle; dorso-ventral depth 2.5 - 3).

(b) Enlarged view of the parahippocampal cortex. Thalamic axons specifically target the superficial layers of presubiculum. DG: dentate gyrus; S: subiculum; PrS: presubiculum, PaS: parasubiculum; EC: entorhinal cortex;

(c) Presubicular responses to illumination (470 nm LED, 0.5 ms, 2 mW) of ChR2-expressing thalamic fibers, in simultaneous records from a PC and MC. Top, action potentials were evoked in three trials following a blue light flash in the PC but not in the MC. Below, light evoked EPSCs from three trials, and average responses (40 trials) in red.

(d) In TTX-4AP containing ACSF, EPSCs were still elicited in PCs, indicating that thalamic axons made direct synaptic contacts onto PCs. Responses were mostly abolished in MCs, suggesting indirect, di-synaptic excitation of MCs. *** Mann-Whitney test, P = 0.001.

(e) Onset latencies of PC EPSCs are significantly shorter than for MC EPSCs. Charge transfer over 25 ms after the light stimulus in **(f)** standard and **(g)** TTX-4AP containing ACSF is significantly higher in PCs than MCs. *** Mann-Whitney test, P = 0.001. Horizontal bars indicate mean values. Data from n = 14 PC and 9 MCs (from 5 mice)

Figure 3. Pyramidal and Martinotti cells form an inhibitory feedback loop.

(a) Connectivity between PC and MCs, determined from dual patch clamp recordings, showing the percentage of connected pairs (%) and the number of tested paired records (n). Very few PC-PC connections were detected.

(b) Single spikes of MCs (green) reliably evoked small IPSPs in a PC (blue). Action potentials were initiated by brief current injections (1-2.5 nA for 1-2.5 ms; **(b)** and **(d)**). Average current traces in red, stimulation artifacts on the MC voltage trace blanked.

(c) Transfer rate (n = 11), IPSC amplitude (n = 45 pairs) and IPSP amplitude (n = 21 pairs) from responses to single spikes at MC-to-PC synapses. Red horizontal bars are median values. Transfer rates from automatically detected synaptic events, recorded with a Cs-Glu based internal solution. Amplitudes from averages of responses recorded using a low-Cl K-Glu internal solution (cf. methods).

(d) Single spikes of PCs (blue) did not reliably evoke EPSPs in a MC (green). The mean EPSP amplitude (red) was very low.

(e) Transfer rate (n = 44), EPSC amplitude (n = 38) and EPSP amplitude (n = 8) from responses to single spikes at a PC-to-MC synapse. Red horizontal bars give median values. Transfer rate and potency from automatically detected synaptic events, recorded with a low-Cl K-Glu internal solution (methods). Efficacy was calculated as transfer rate x potency and used as measure of average amplitude.

Figure 4. Stable inhibitory control by Martinotti cells

(a) 30 action potentials elicited at 10 or 30 Hz in a MC (green traces). Voltage clamp traces from a connected PC (blue traces) recorded at +40 mV, with a Cs-Glu internal solution. Three successive trials in blue, average of 8 trials in red. The inter-trial-interval here was 40 sec. Below, raster plots of synaptic transfer for 8 successive trials, showing presynaptic action potentials (green bar) and IPSCs (red dots) triggered at monosynaptic latencies (0 - 3 ms). Transmission failed only infrequently (cf. Supplementary Table 2).

(b) Detail of early and late MC-spikes and IPSCs in 30 Hz trains. Stimulus artifacts blanked.

(c) Poststimulus-histograms of IPSCs at monosynaptic latencies in the range 0 – 3 ms show peaks at 1.63 for trains at 10 Hz and 1.67 ms for trains at 30 Hz.

(d) MC-to-PC synaptic efficacy (transfer rate x absolute potency) was unrelated to the spike position in a train or to firing frequency (n = 8, Friedman test, P = 0.5222).

(e) Late/early transfer rate and potency plotted against late/early efficacy (n = 8 pairs, 30 Hz stimulation). These synapses are highly reliable with a low dynamic range (0.8 – 1.4). Slope of linear regressions show a small variation in synaptic efficacy is related to change in potency, rather than transfer rate.

(f) The cumulative efficacy (mean ± sem) of MC-to-PC synapses reveals stable dynamics during long stimulus trains.

(g) Synaptic frequency for early and late spikes of 10 and 30 Hz trains, normalized to 10 Hz. The increase in synaptic frequency corresponds to the 3-fold increase in presynaptic spike frequency.

Figure 5. Repetitive stimulation progressively unmutes PC – MC excitatory synapses.

(a) 30 action potentials elicited at 10 Hz and at 30 Hz in a PC (blue traces). Voltage clamp traces from a connected MC at -65 mV. Three successive trials in green, average of 8 trials in red. The inter-trial-interval here was 40 sec. Below, raster plots of synaptic transfer for 8 trains show presynaptic action potentials (blue bars), and EPSCs (red dots) triggered at monosynaptic latencies (0-3 ms). More EPSCs were elicited during the 30 Hz than the 10 Hz train and by late (last five) compared to early spikes (first five).

(b) Detail of early and late PC-spikes and MC-responses in 30 Hz trains. The transmission transfer rate was higher for late stimuli.

(c) Poststimulus-histogram of EPSCs at monosynaptic latencies, of 0–3 ms, show peaks at 1.16 and 1.14 ms (median) for trains at 10 and 30 Hz. Total counts were higher for 30 than 10 Hz, due to the frequency dependence of release.

(d) PC-MC synaptic efficacy (transfer rate x absolute potency) showed a strong dependence on spike number during a train and spike frequency (n = 9, Friedman test, P=0.0002). Facilitation occurred at 30 Hz but not at 10 Hz (* Dunn's Multiple comparison test, P< 0.05).

(e) Late/early transfer rate and potency plotted against late/early efficacy (n = 15 pairs, 30 Hz stimulation). Increased efficacy resulted from a higher transfer rate rather than changes in potency.

(f) Non-linear cumulative efficacy (mean ± sem) plotted against time shows facilitation dynamics and frequency dependence.

(g) The synaptic frequency increased more than the 3-fold change in presynaptic spike frequency, for both early and late spikes, during 10 and 30 Hz trains. Stimulus artifacts blanked in **(a-b)**.

Figure 6. Enhancement of PC-to-MC synaptic transmission outlasts train of high frequency stimulation.

(a) Synaptic efficacy and transfer rate were monitored (at 2 Hz) before and after unmuting induced by a 30 Hz presynaptic spike train of 2 seconds.

(b) Synaptic efficacy and **(c)** transfer rate for n = 4 pairs normalized to the maximal level reached during unmuting and averaged. Decay of these parameters was fitted with a dual exponential function (blue line):

$$\boldsymbol{Decay = UM - Span_{FAST}.e^{-\frac{t}{Tau_{FAST}}} + Span_{SLOW}.e^{-\frac{t}{Tau_{SLOW}}}}.$$

$Span_{FAST}$ and $Span_{FAST}$ indicate the relative contributions of Tau_{FAST} and Tau_{SLOW}. Baseline was constrained to the mean value for the spikes preceding unmuting (broken line).

Figure 7. PC-to-MC synaptic unmuting and Martinotti cell recruitment by head direction spike trains.

(a) Polar plot showing firing frequency (spike/sec) as a function of head direction (°) for a head direction cell recorded *in vivo.*

(b) Detected spikes for this unit plotted against instantaneous head direction and frequency.

(c) The spike train was injected as a current command into a presubicular pyramidal cell *in vitro*.

(d) The shaded part of the trace in **(c)** extended (total trace time 1.4 sec).

(e) Three successive responses recorded from a connected MC in voltage clamp at -65 mV (green traces) show unmuting and facilitation.

(f) Synaptic strength for EPSCs from 5 pairs. Transfer was null at first and increased progressively after sustained high frequency firing. Transfer rate remained high during subsequent lower frequency firing (at right).

(g) Current clamp recording of MC cell in (**e**) at resting potential. Four successive traces show reliable firing towards the end of high-frequency head direction derived spiking.

(h) MC firing probability (200 ms bins) was maximal after persistent high frequency PC firing (from 5 pairs). Error bars are S.E.M.

Figure 8. Timing dependence of inhibition

(a) MC recruitment by a PC in a reciprocally connected pair (top). Magnification of a MC-spike evoked by PC firing at short latency (bottom). The MC-spike alters the PC-spike AHP (AHP_{TEST}), the PC-spike peak (PK_{TEST}) and the PC ISI (ISI_{TEST}) according to the delay after the PC-spike PK_{INT}. Dotted lines indicate the extrapolated level for PK_{TEST} and for AHP_{TEST}.

(b) Spike timing dependent MC-inhibition was tested in unidirectionally connected MC-to-PC pairs. Drifting single MC-spikes were triggered during sustained PC firing (30-50 Hz). Two sweeps of PC firing are shown (one in blue, one in red), with the corresponding MC spikes at the bottom. For the blue voltage trace, the PC-spike to MC-spike delay was short ("time locked"; delay < 10 ms, similar to reciprocal connections as in (**a**)). For the red voltage trace ("delayed"), the MC spike delay exceeded 10 ms.

(c-e) Differential effect of short latency vs long latency inhibitory modulation of AHP, peak and ISI of PC spikes (30-50 Hz; n = 7). **(c)** The PC AHP was more hyperpolarized for short latency, time-locked MC-spikes but not for delayed MC-spikes (n = 7, * $p < 0.05$). The modulation of the PC-spike AHP was calculated as $(AHP_{TEST}\text{-}AHP_{INT})\text{-}(AHP_{INT}\text{-}AHP_{REF})$. **(d)** The PC-spike peak after a MC-spike was higher for timed locked but not for delayed inhibition (n = 7, ** $p < 0.01$). Peak modulation was calculated as $(PK_{TEST}\text{-}PK_{INT})\text{-}(PK_{INT}\text{-}PK_{REF})$. **(e)** The PC ISI increased more for delayed than for time-locked inhibition (n = 7, ** $p < 0.01$). ISI change was calculated as $100*(ISI_{TEST}/$

ISI_{INT})/(ISI_{INT}/ISI_{REF}). Each dot indicates the mean for one pair. Horizontal bars are medians. The median-null difference was assessed with a Wilcoxon signed rank test († $p < 0.05$) and the relative difference between short- and long-latency inhibition with a Wilcoxon match-pairs signed rank test (*, **). ISI, inter-spike interval; AHP, after-hyperpolarization; PK, peak.

Figure 9. Structure and activity patterns of the neural network model.

(a) Schematic representation of the network wiring process. Left: Initial random connectivity between each Martinotti cell (green circle) and the pyramidal cell population (blue triangles). Middle panels: Establishment of final connectivity by selecting and strengthening the main connections (for simplicity only 1 Main Connection is shown; inhibitory strength $\lambda = 0$). Connections with neighboring units are removed (pink area), reciprocal excitatory connections are added (blue). Right: resulting inhibitory effect of each pyramidal cell on the rest of the population. Phase selective suppression of activity is mediated by collective Martinotti cell activity.

(b) Spontaneous activity profile formation in pyramidal cells. In blue, example of raw activity over time of the pyramidal cell population (arranged according to directional selectivity) in the absence of selective external input. Fed with white noise input, the system evolves over time from an initial random configuration (left) towards a stable configuration of concentrated activity ("bump" formation, right). In green, same as above, but for simultaneous activity of Martinotti cells (positions on the circle are randomly assigned).

(c) Persistence of directional tuning after external input removal. Starting from random activity (left), pyramidal cells around a given direction are transiently provided with an additional external input (red arrows). The final state of the network is then observed after removing this additional input (grey background). No directional selectivity appears in Martinotti cells.

(d) Example tuning curves for a pyramidal neuron in blue and a Martinotti cell in green. Obtained from networks with an intermediate size of the connection-pruning range (α). For larger α, pyramidal cell directional tuning curves become broader while Martinotti cells preserve their lack of directional selectivity (cf. Supplementary Fig. 4).

(e) Coherent activity in the pyramidal layer depends on PC-to-MC synapse dynamics. Bump coherence (Ω) deteriorates quickly when simulating depressing excitatory synapses, as for PC-to-PV synapses. Shown are synapse dynamics that vary from stable on the left (Martinotti like) to depresssing on the right ($\tau_{A1} = 10$ ms; PV like).

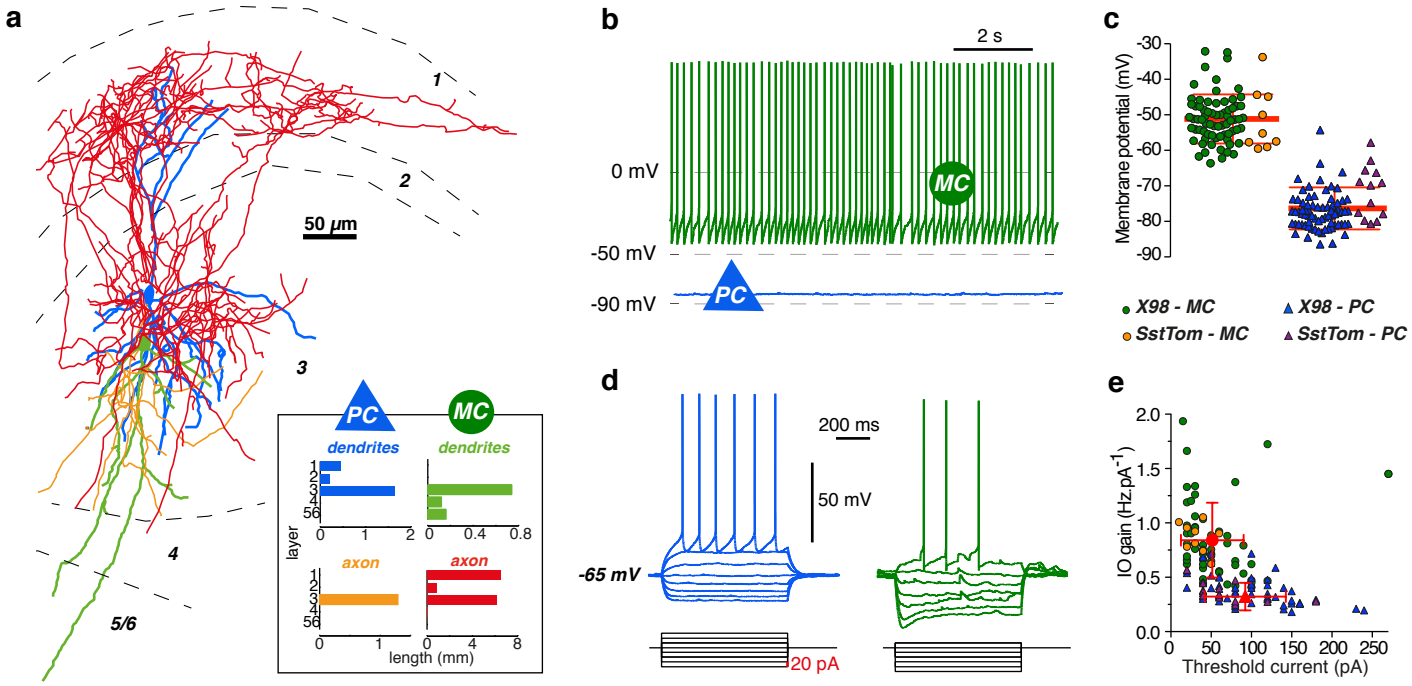

Figure 1. Morphology and electrophysiological intrinsic properties of Martinotti interneurons and pyramidal cells in superficial layers of presubiculum

(a) Anatomical reconstruction of reciprocally connected PC and MC in layer 3. PC dendrites (blue) and MC axon (red) covered layer 1 and 3, PC axon (yellow) and MC dendrites (green) mainly occupied layer 3 (inset). Subiculum is to the left and the parasubiculum to the right.

(b) Current clamp recordings of a MC (green) and a PC (blue). The MC fired spontaneously, the PC, with a more hyperpolarized membrane potential, was silent.

(c) Membrane potential values for 80 MCs (circles, X98-SST, green; SstCre, orange) and 87 PCs (triangles, X98-SST, blue; SstCre, purple). The horizontal bar indicates the mean value.

(d) Typical responses of a MC and a PC to negative and positive current step injections of duration 800 ms from -65 mV.

(e) Plotting input-output (I-O) gain against threshold current separates of PCs (triangles) and MCs (circles; same color code as in (c)).

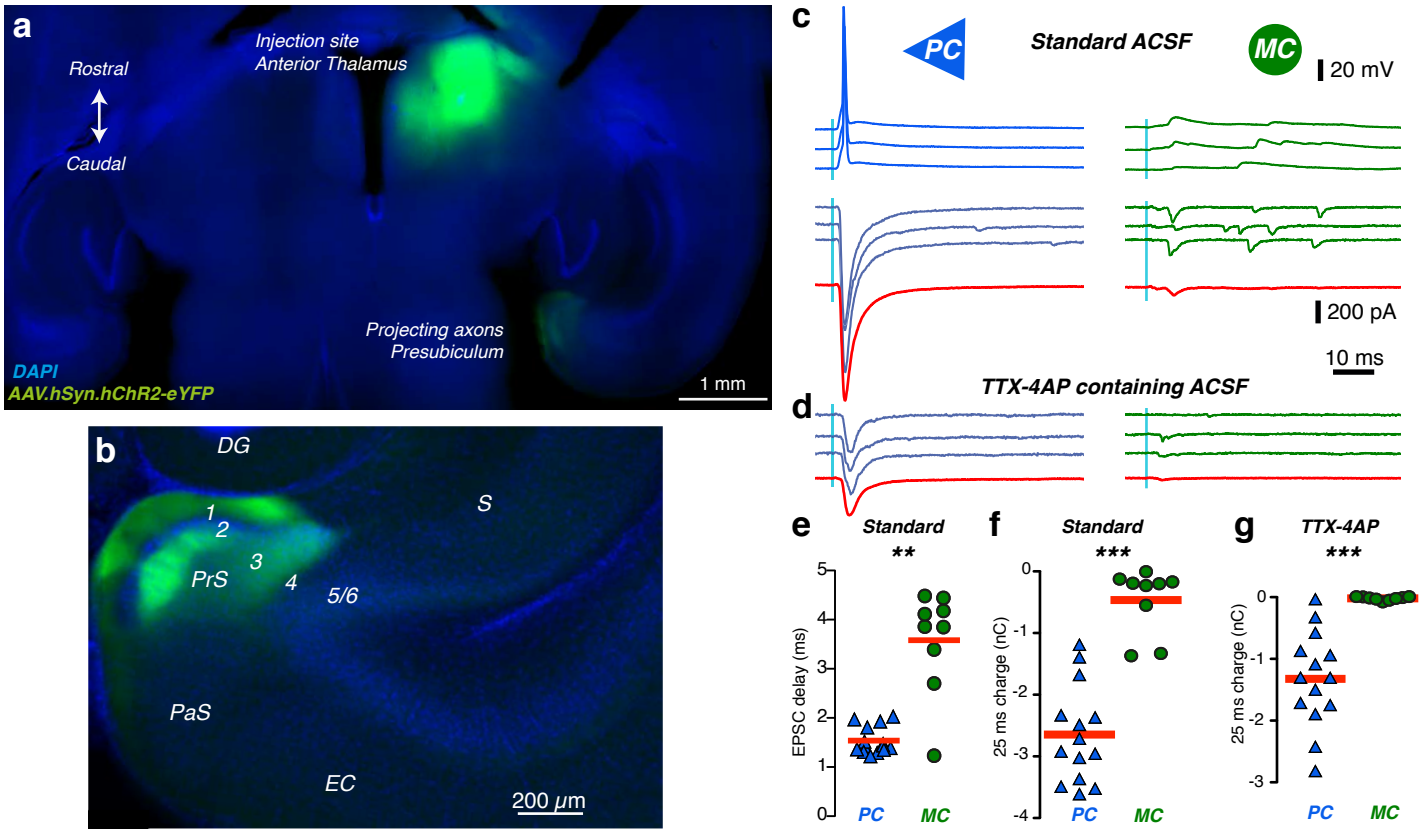

Figure 2. Pyramidal cells, but not Martinotti cells, are directly innervated by the anterior thalamus.

(a) Channelrhodopsin2-eYFP expression in Anterior Thalamus (AT) of SstCre::tdTomato mice fifteen days after stereotaxic injections of an AAV vector. Injection site in AT and projecting thalamic axons in the ipsilateral presubiculum (horizontal brain section, 20° angle; dorso-ventral depth 2.5 - 3).

(b) Enlarged view of the parahippocampal cortex. Thalamic axons specifically target the superficial layers of presubiculum. DG: dentate gyrus; S: subiculum; PrS: presubiculum, PaS: parasubiculum; EC: entorhinal cortex;

(c) Presubicular responses to illumination (470 nm LED, 0.5 ms, 2 mW) of ChR2-expressing thalamic fibers, in simultaneous records from a PC and MC. Top, action potentials were evoked in three trials following a blue light flash in the PC but not in the MC. Below, light evoked EPSCs from three trials, and average responses (40 trials) in red.

(d) In TTX-4AP containing ACSF, EPSCs were still elicited in PCs, indicating that thalamic axons made direct synaptic contacts onto PCs. Responses were mostly abolished in MCs, suggesting indirect, di-synaptic excitation of MCs. *** Mann-Whitney test, P = 0.001.

(e) Onset latencies of PC EPSCs are significantly shorter than for MC EPSCs. Charge transfer over 25 ms after the light stimulus in **(f)** standard and **(g)** TTX-4AP containing ACSF is significantly higher in PCs than MCs. *** Mann-Whitney test, P = 0.001. Horizontal bars indicate mean values. Data from n = 14 PC and 9 MCs (from 5 mice)

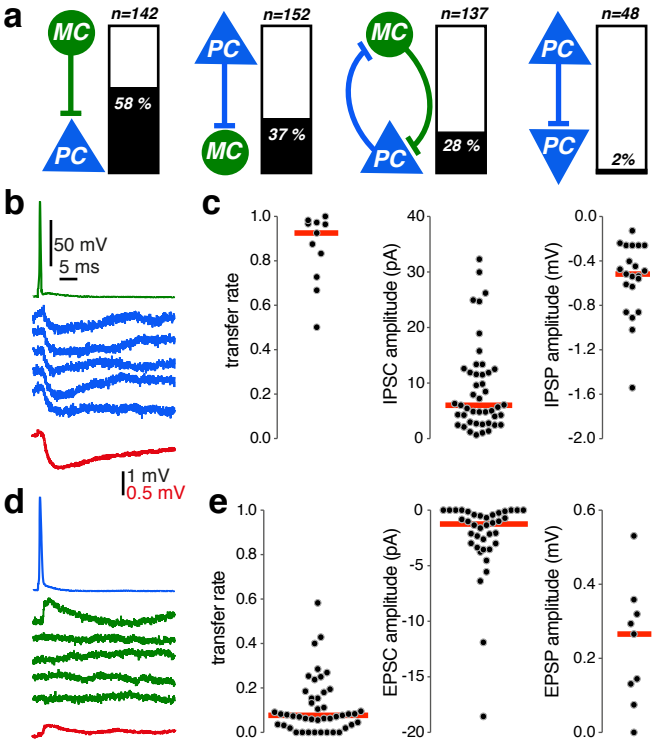

Figure 3. Pyramidal and Martinotti cells form an inhibitory feedback loop.

(a) Connectivity between PC and MCs, determined from dual patch clamp recordings, showing the percentage of connected pairs (%) and the number of tested paired records (n). Very few PC-PC connections were detected.

(b) Single spikes of MCs (green) reliably evoked small IPSPs in a PC (blue). Action potentials were initiated by brief current injections (1-2.5 nA for 1-2.5 ms; (b) and (d)). Average current traces in red, stimulation artifacts on the MC voltage trace blanked.

(c) Transfer rate (n = 11), IPSC amplitude (n = 45 pairs) and IPSP amplitude (n = 21 pairs) from responses to single spikes at MC-to-PC synapses. Red horizontal bars are median values. Transfer rates from automatically detected synaptic events, recorded with a Cs-Glu based internal solution. Amplitudes from averages of responses recorded using a low-Cl K-Glu internal solution (cf. methods).

(d) Single spikes of PCs (blue) did not reliably evoke EPSPs in a MC (green). The mean EPSP amplitude (red) was very low.

(e) Transfer rate (n = 44), EPSC amplitude (n = 38) and EPSP amplitude (n = 8) from responses to single spikes at a PC-to-MC synapse. Red horizontal bars give median values. Transfer rate and potency from automatically detected synaptic events, recorded with a low-Cl K-Glu internal solution (methods). Efficacy was calculated as transfer rate x potency and used as measure of average amplitude.

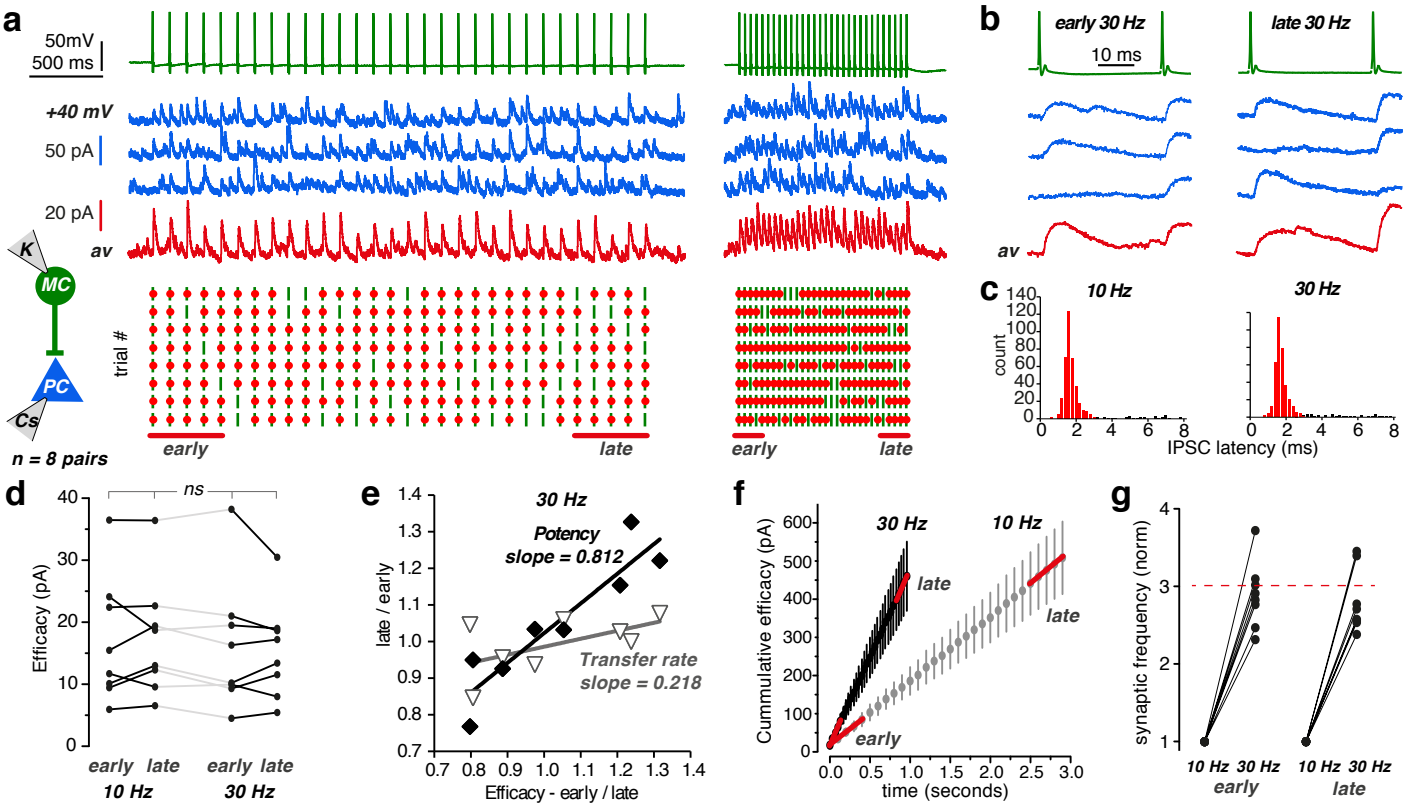

Figure 4. Stable inhibitory control by Martinotti cells

(a) 30 action potentials elicited at 10 or 30 Hz in a MC (green traces). Voltage clamp traces from a connected PC (blue traces) recorded at +40 mV, with a Cs-Glu internal solution. Three successive trials in blue, average of 8 trials in red. The inter-trial-interval here was 40 sec. Below, raster plots of synaptic transfer for 8 successive trials, showing presynaptic action potentials (green bar) and IPSCs (red dots) triggered at monosynaptic latencies (0 - 3 ms). Transmission failed only infrequently (cf. Supplementary Table 2).

(b) Detail of early and late MC-spikes and IPSCs in 30 Hz trains. Stimulus artifacts blanked.

(c) Poststimulus-histograms of IPSCs at monosynaptic latencies in the range 0 – 3 ms show peaks at 1.63 for trains at 10 Hz and 1.67 ms for trains at 30 Hz.

(d) MC-to-PC synaptic efficacy (transfer rate x absolute potency) was unrelated to the spike position in a train or to firing frequency (n = 8, Friedman test, P = 0.5222).

(e) Late/early transfer rate and potency plotted against late/early efficacy (n = 8 pairs, 30 Hz stimulation). These synapses are highly reliable with a low dynamic range (0.8 – 1.4). Slope of linear regressions show a small variation in synaptic efficacy is related to change in potency, rather than transfer rate.

(f) The cumulative efficacy (mean ± sem) of MC-to-PC synapses reveals stable dynamics during long stimulus trains.

(g) The synaptic frequency for early and late spikes of 10 and 30 Hz trains, normalized to 10 Hz. The increase in synaptic frequency corresponds to the 3-fold increase in presynaptic spike frequency

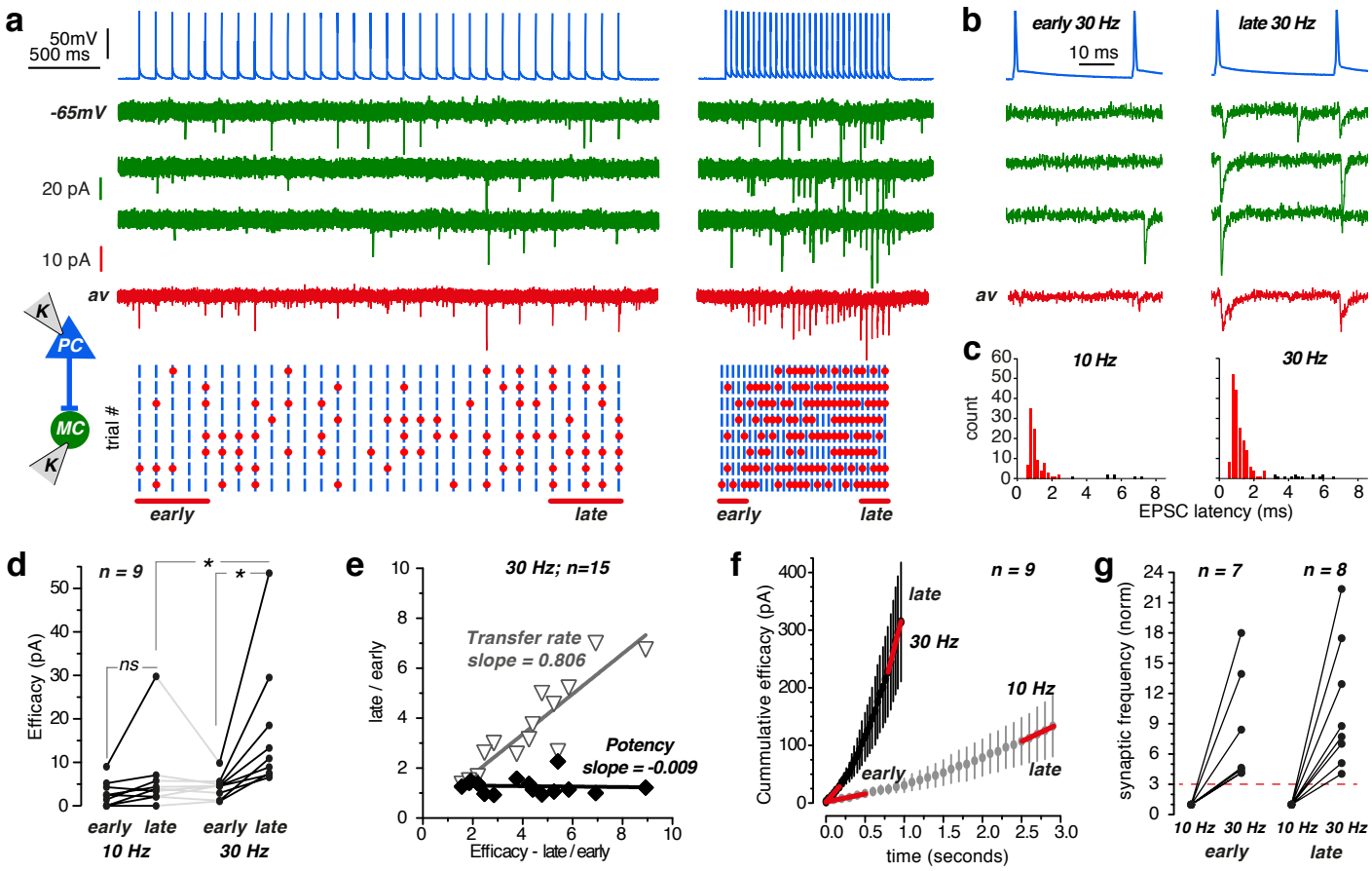

Figure 5. Repetitive stimulation progressively unmutes PC – MC excitatory synapses.

(a) 30 action potentials elicited at 10 Hz and at 30 Hz in a PC (blue traces). Voltage clamp traces from a connected MC at -65 mV. Three successive trials in green, average of 8 trials in red. The inter-trial-interval here was 40 sec. Below, raster plots of synaptic transfer for 8 trains show presynaptic action potentials (blue bars), and EPSCs (red dots) triggered at monosynaptic latencies (0-3 ms). More EPSCs were elicited during the 30 Hz than the 10 Hz train and by late (last five) compared to early spikes (first five).

(b) Detail of early and late PC-spikes and MC-responses in 30 Hz trains. The transmission transfer rate was higher for late stimuli.

(c) Poststimulus-histogram of EPSCs at monosynaptic latencies, of 0–3 ms, show peaks at 1.16 and 1.14 ms (median) for trains at 10 and 30 Hz. Total counts were higher for 30 than 10 Hz, due to the frequency dependence of release.

(d) PC-MC synaptic efficacy (transfer rate x absolute potency) showed a strong dependence on spike number during a train and spike frequency (n = 9, Friedman test, P=0.0002). Facilitation occurred at 30 Hz but not at 10 Hz (* Dunn's Multiple comparison test, P< 0.05).

(e) Late/early transfer rate and potency plotted against late/early efficacy (n = 15 pairs, 30 Hz stimulation). Increased efficacy resulted from a higher transfer rate rather than changes in potency.

(f) Non-linear cumulative efficacy (mean ± sem) plotted against time shows facilitation dynamics and frequency dependence.

(g) The synaptic frequency increased more than the 3-fold change in presynaptic spike frequency, for both early and late spikes, during 10 and 30 Hz trains. Stimulus artifacts blanked in (a-b).

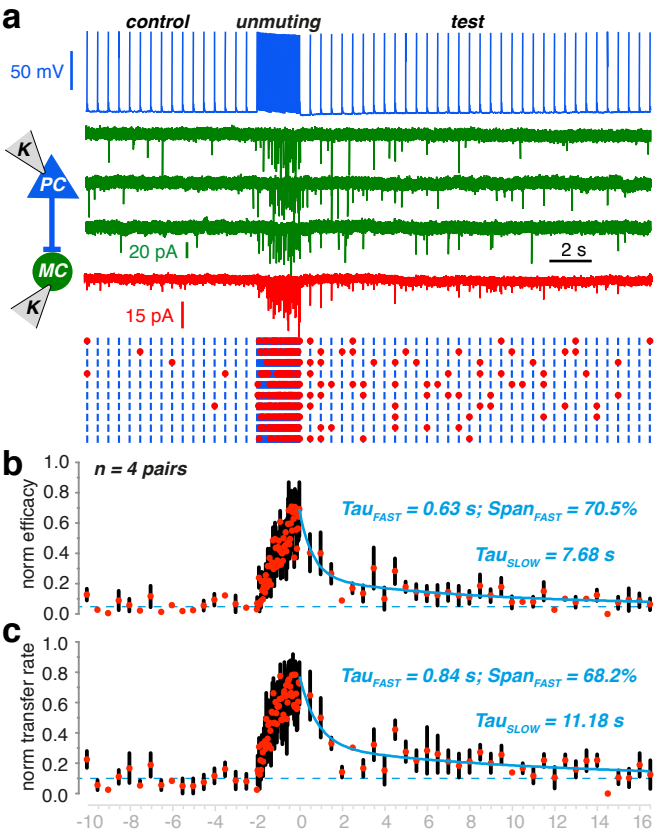

Figure 6. Enhancement of PC-to-MC synaptic transmission outlasts train of high frequency stimulation.

(a) Synaptic efficacy and transfer rate were monitored (at 2 Hz) before and after unmuting induced by a 30 Hz presynaptic spike train of 2 seconds.

(b) Synaptic efficacy and **(c)** transfer rate for n = 4 pairs normalized to the maximal level reached during unmuting and averaged. Decay of these parameters was fitted with a dual exponential function (blue line):

$$Decay = UM - Span_{FAST}.exp(-t/Tau_{FAST}) + Span_{SLOW}.exp(-t/Tau_{SLOW})$$

$Span_{FAST}$ and $Span_{FAST}$ indicate the relative contributions of Tau_{FAST} and Tau_{SLOW}. Baseline was constrained to the mean value for the spikes preceding unmuting (broken line).

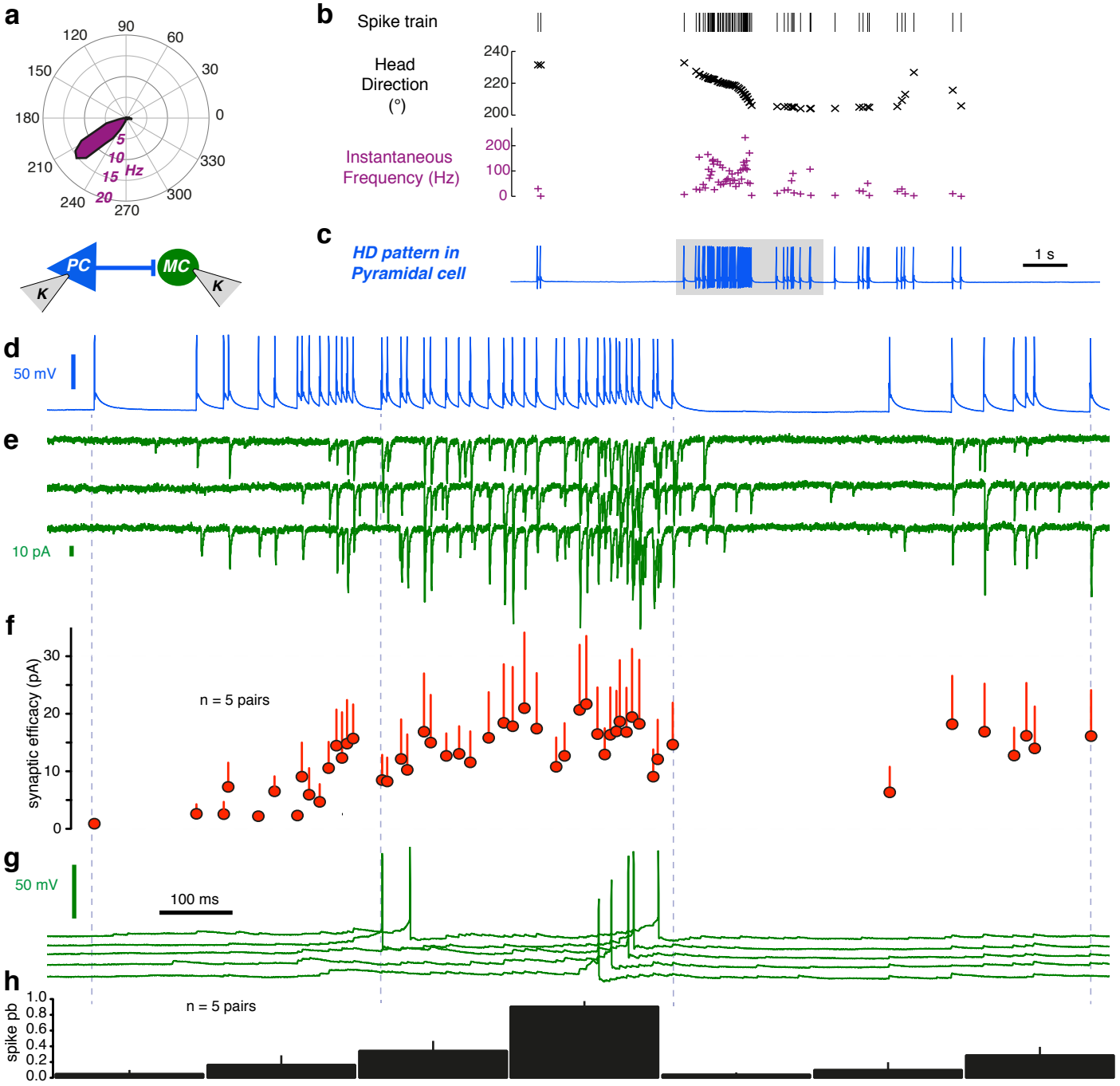

Figure 7. PC-to-MC synaptic unmuting and Martinotti cell recruitment by head direction spike trains.
(a) Polar plot showing firing frequency (spike/sec) as a function of head direction (°) for a head direction cell recorded in vivo.
(b) Detected spikes for this unit plotted against instantaneous head direction and frequency.
(c) The spike train was injected as a current command into a presubicular pyramidal cell in vitro.
(d) The shaded part of the trace in (c) extended (total trace time 1.4 sec).
(e) Three successive responses recorded from a connected MC in voltage clamp at -65 mV (green traces) show unmuting and facilitation.
(f) Synaptic strength for EPSCs from 5 pairs. Transfer was null at first and increased progressively after sustained high frequency firing. Transfer rate remained high during subsequent lower frequency firing (at right).
(g) Current clamp recording of MC cell in (e) at resting potential. Four successive traces show reliable firing towards the end of high-frequency head direction derived spiking.
(h) MC firing probability (200 ms bins) was maximal after persistent high frequency PC firing (from 5 pairs). Error bars are S.E.M.

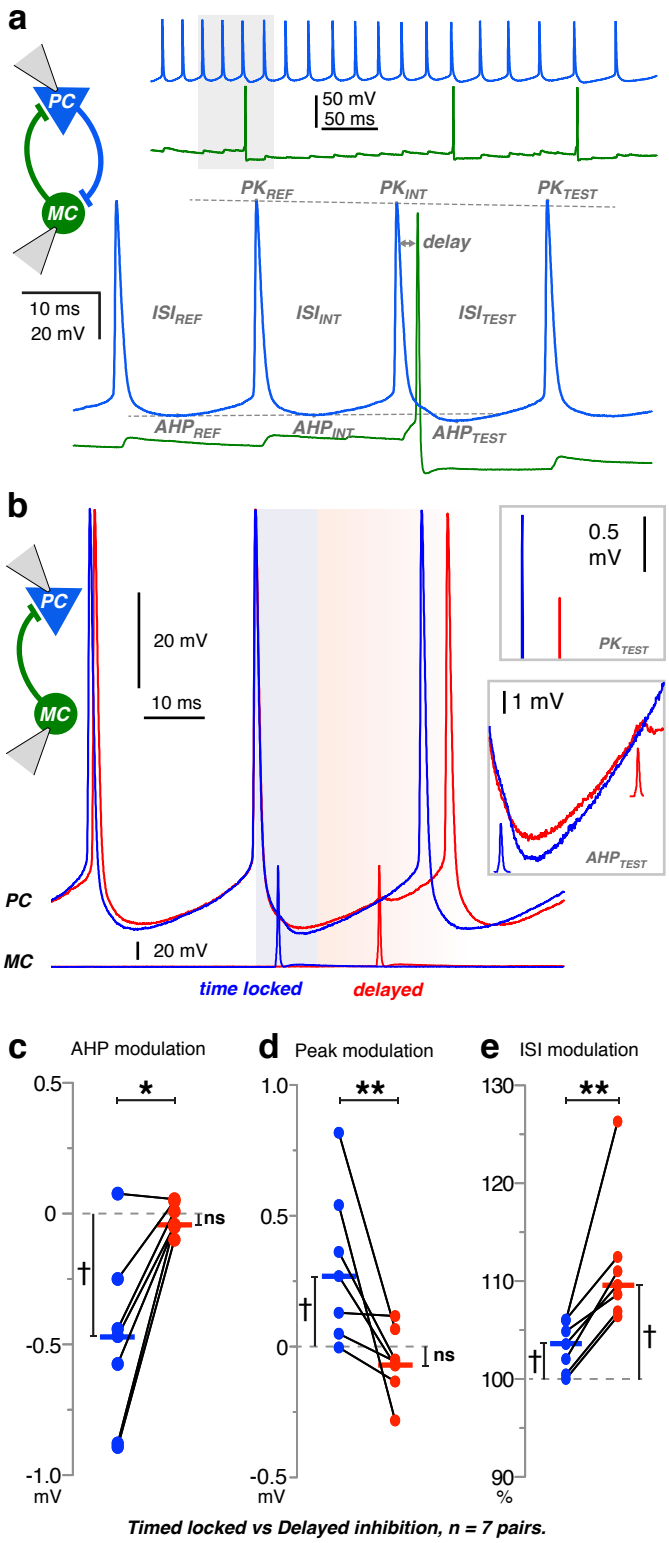

Timed locked vs Delayed inhibition, n = 7 pairs.

Figure 8. Timing dependence of inhibition

(a) MC recruitment by a PC in a reciprocally connected pair (top). Magnification of a MC-spike evoked by PC firing at short latency (bottom). The MC-spike alters the PC-spike AHP (AHP_{TEST}), the PC-spike peak (PK_{TEST}) and the PC ISI (ISI_{TEST}) according to the delay after the PC-spike PK_{INT}. Dotted lines indicate the extrapolated level for PK_{TEST} and for AHP_{TEST}.

(b) Spike timing dependent MC-inhibition was tested in unidirectionally connected MC-to-PC pairs. Drifting single MC-spikes were triggered during sustained PC firing (30-50 Hz). Two sweeps of PC firing are shown (one in blue, one in red), with the corresponding MC spikes at the bottom. For the blue voltage trace, the PC-spike to MC-spike delay was short ("time locked"; delay < 10 ms, similar to reciprocal connections as in (a)). For the red voltage trace ("delayed"), the MC spike delay exceeded 10 ms.

(c-e) Differential effect of short latency vs long latency inhibitory modulation of AHP, peak and ISI of PC spikes (30-50 Hz; n = 7). (c) The PC AHP was more hyperpolarized for short latency, time-locked MC-spikes but not for delayed MC-spikes (n = 7, * $p < 0.05$). The modulation of the PC-spike AHP was calculated as (AHP_{TEST}-AHP_{INT})-(AHP_{INT}-AHP_{REF}). (d) The PC-spike peak after a MC-spike was higher for timed locked but not for delayed inhibition (n = 7, ** $p < 0.01$). Peak modulation was calculated as (PK_{TEST}-PK_{INT})-(PK_{INT}-PK_{REF}). (e) The PC ISI increased more for delayed than for time-locked inhibition (n = 7, ** $p < 0.01$). ISI change was calculated as 100*(ISI_{TEST}/ISI_{INT})/(ISI_{INT}/ISI_{REF}). Each dot indicates the mean for one pair. Horizontal bars are medians. The median-null difference was assessed with a Wilcoxon signed rank test († $p < 0.05$) and the relative difference between short- and long-latency inhibition with a Wilcoxon match-pairs signed rank test (*, **). ISI, inter-spike interval; AHP, after-hyperpolarization; PK, peak.

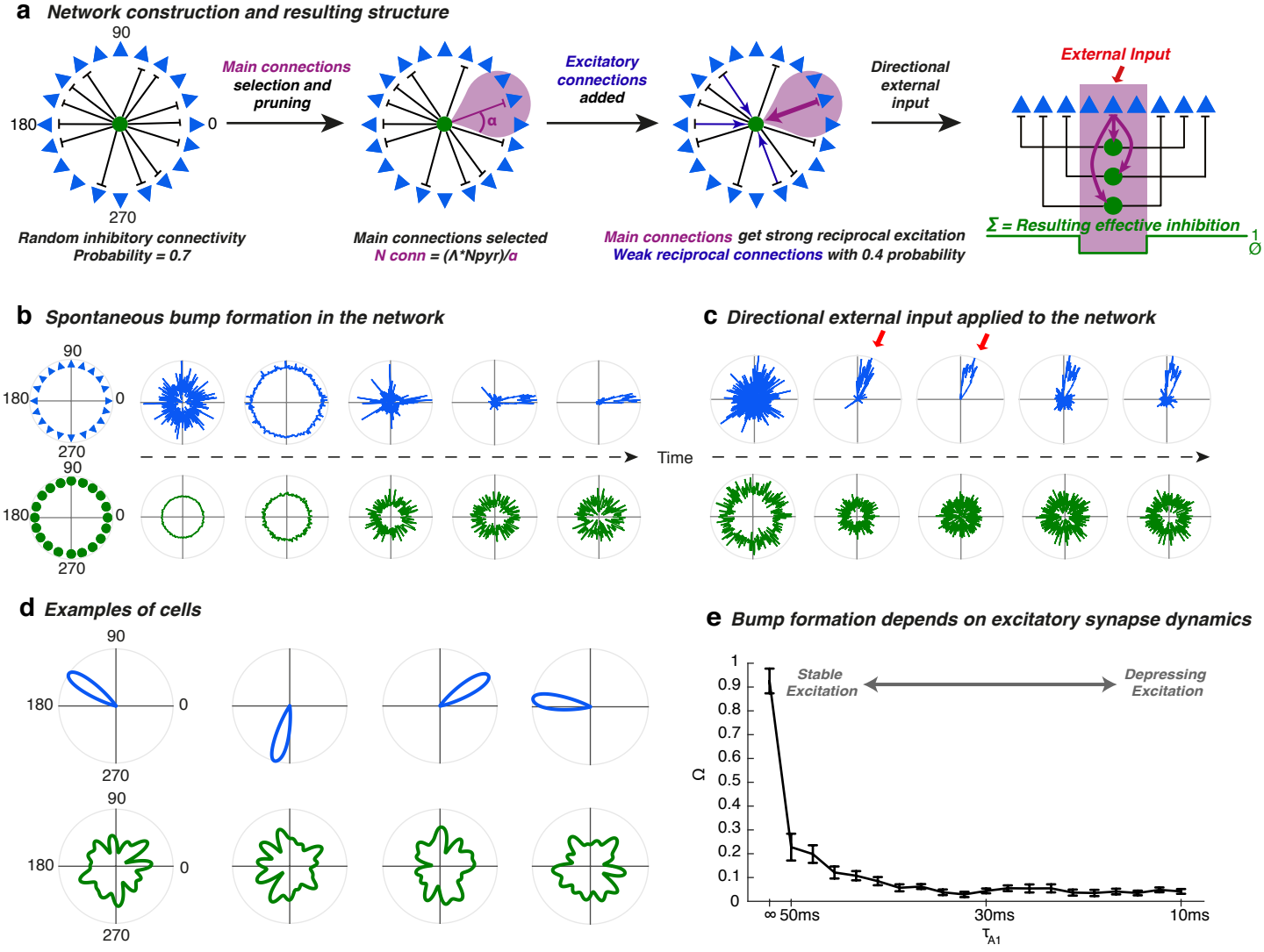

Figure 9. Structure and activity patterns of the neural network model.

(a) Schematic representation of the network wiring process. Left: Initial random connectivity between each Martinotti cell (green circle) and the pyramidal cell population (blue triangles). Middle panels: Establishment of final connectivity by selecting and strengthening the main connections (for simplicity only 1 Main Connection is shown; inhibitory strength λ = 0). Connections with neighboring units are removed (pink area), reciprocal excitatory connections are added (blue). Right: resulting inhibitory effect of each pyramidal cell on the rest of the population. Phase selective suppression of activity is mediated by collective Martinotti cell activity.

(b) Spontaneous activity profile formation in pyramidal cells. In blue, example of raw activity over time of the pyramidal cell population (arranged according to directional selectivity) in the absence of selective external input. Fed with white noise input, the system evolves over time from an initial random configuration (left) towards a stable configuration of concentrated activity ("bump" formation, right). In green, same as above, but for simultaneous activity of Martinotti cells (positions on the circle are randomly assigned).

(c) Persistence of directional tuning after external input removal. Starting from random activity (left), pyramidal cells around a given direction are transiently provided with an additional external input (red arrows). The final state of the network is then observed after removing this additional input (grey background). No directional selectivity appears in Martinotti cells.

(d) Example tuning curves for a pyramidal neuron in blue and a Martinotti cell in green. Obtained from networks with an intermediate size of the connection-pruning range (α). For larger α, pyramidal cell directional tuning curves become broader while Martinotti cells preserve their lack of directional selectivity (cf. Supplementary Fig. 4).

(e) Coherent activity in the pyramidal layer depends on PC-to-MC synapse dynamics. Bump coherence (Ω) deteriorates quickly when simulating depressing excitatory synapses, as for PC-to-PV synapses. Shown are synapse dynamics that vary from stable on the left (Martinotti like) to depres s rsg ion on the right (τ A = 10 ms PV lik e).

Supplementary Information

Activity dependent feedback inhibition supports head direction coding in the presubiculum

Jean Simonnet, Mérie Nassar, Federico Stella, Ivan Cohen
Bertrand Mathon, Charlotte N. Boccara, Richard Miles and Desdemona Fricker

	MC			PC		
	mean	sd	n	mean	sd	n
Membrane Potential (mV)	-51.1	6.9	80	-76.3	5.9	87
Time constant (ms)	37.1	17.6	84	22.5	12	90
R_{in} (MOhm)	343	129	74	251	112	85
Sag ratio	1.22	0.01	72	1.05	0.02	74
Threshold current (pA)	51.5	38.9	64	92.3	50.4	65
I-O initial gain (Hz/pA)	0.845	0.040	64	0.373	0.127	65
Firing frequency @ 2x Threshold current (Hz)	37.5	26.0	64	32.25	11.51	64
AP rising amplitude (mV)	79.8	6.2	86	81.69	5.86	95
AP half duration (ms)	0.293	0.039	86	0.578	0.103	95
AP rising phase speed (V/s)	565	87	86	508	86	95
AP falling phase speed (V/s)	-319	59	86	-131	19	95

Supplementary Table 1. Electrophysiological properties of presubicular pyramidal cells and Martinotti interneurons. Values are given as mean ± sd.

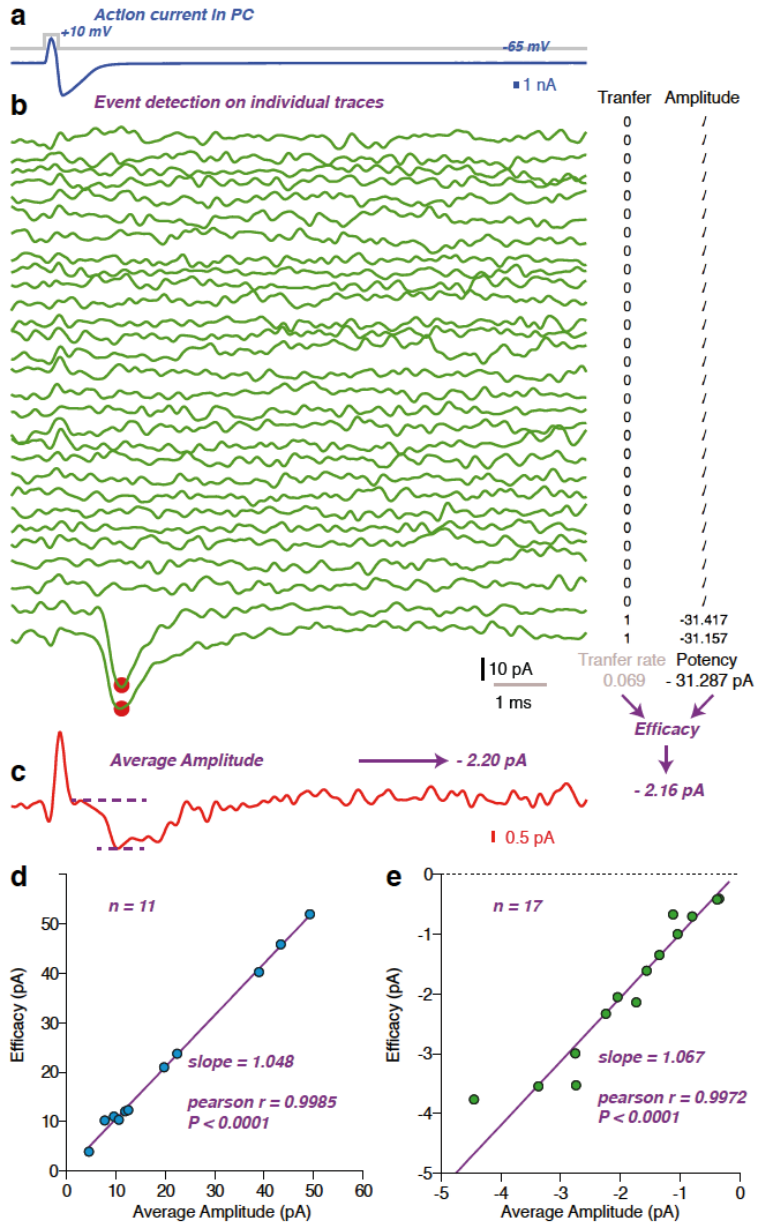

Supplementary Figure 1. Two reliable methods to determine synaptic strength: measures of average amplitude or trial-by-trial analysis to calculate efficacy give equivalent results.
(a) A single action current was evoked in a pyramidal cell with a very high (-65 to +10 mV) and short (0.2 ms) voltage pulse.
(b) Martinotti cell was recorded in voltage clamp mode at -65 mV. The postsynaptic currents in the Martinotti cell (green traces) following the stimulation are shown for twenty-nine trials. EPSCs were evoked within a monosynaptic time window (0.5 to 3 ms) only in two trials. Transfer (1 when an EPSC is detected and 0 otherwise) and amplitude of events (nothing when transfer equals 0) is indicated on the right. The mean transfer rate (0.069), potency (-31.287) and the calculated efficacy (-2.16 pA) are indicated.
(c) The average current response of the Martinotti cell is shown in red and its maximum downward amplitude of – 2.20 pA was determined within the monosynaptic window. The upward deflection at the beginning is a stimulation artifact. Note the similarity between trial-by-trial calculation of efficacy and the average trace amplitude.
(d-e) These two methods were applied for n = 11 MC-to-PC synapses **(b)** and n = 17 PC-to-MC synapses **(c)** to test their agreement. Efficacy and Average amplitude were highly correlated for both synapses.

N = 8	Efficacy (pA)						
	10 Hz	10 Hz	10 Hz	30 Hz	30 Hz	30 Hz	late
	early	late	late/early	early	late	late/early	30Hz/10Hz
MCtoPC#1	5.95	6.55	1.1	4.50	5.44	1.2	0.8
MCtoPC#2	9.45	12.31	1.3	9.33	11.54	1.2	0.9
MCtoPC#3	10.13	13.01	1.3	10.20	13.43	1.3	1.0
MCtoPC#4	11.73	9.60	0.8	9.94	8.01	0.8	0.8
MCtoPC#5	15.49	19.40	1.3	16.33	17.21	1.1	0.9
MCtoPC#6	22.43	22.64	1.0	21.02	18.65	0.9	0.8
MCtoPC#7	24.13	18.71	0.8	19.51	19.02	1.0	1.0
MCtoPC#8	36.50	36.40	1.0	38.22	30.48	0.8	0.8
Mean	**16.97**	**17.33**	**1.1**	**16.13**	**15.47**	**1.0**	**0.9**
sd	**10.12**	**9.40**	**0.2**	**10.54**	**7.81**	**0.2**	**0.1**
sem	**3.58**	**3.32**	**0.1**	**3.73**	**2.76**	**0.1**	**0.0**
N = 8	Transfer rate						
	10 Hz	10 Hz	10 Hz	30 Hz	30 Hz	30 Hz	late
	early	late	late/early	early	late	late/early	30Hz/10Hz
MCtoPC#1	0.60	0.59	1.0	0.49	0.51	1.0	0.9
MCtoPC#2	0.67	0.77	1.1	0.67	0.67	1.0	0.9
MCtoPC#3	0.66	0.74	1.1	0.74	0.80	1.1	1.1
MCtoPC#4	0.75	0.69	0.9	0.71	0.60	0.8	0.9
MCtoPC#5	0.75	0.86	1.1	0.77	0.82	1.1	0.9
MCtoPC#6	0.96	0.96	1.0	0.97	0.93	1.0	1.0
MCtoPC#7	0.88	0.80	0.9	0.84	0.79	0.9	1.0
MCtoPC#8	0.97	0.93	1.0	0.93	0.97	1.0	1.0
Mean	**0.78**	**0.79**	**1.0**	**0.77**	**0.76**	**1.0**	**1.0**
sd	**0.14**	**0.12**	**0.1**	**0.15**	**0.16**	**0.1**	**0.1**
sem	**0.05**	**0.04**	**0.0**	**0.05**	**0.06**	**0.0**	**0.0**
N = 8	Potency (pA)						
	10 Hz	10 Hz	10 Hz	30 Hz	30 Hz	30 Hz	late
	early	late	late/early	early	late	late/early	30Hz/10Hz
MCtoPC#1	9.94	11.19	1.1	9.24	10.66	1.2	1.0
MCtoPC#2	13.94	16.31	1.2	13.64	18.10	1.3	1.1
MCtoPC#3	15.29	17.55	1.1	13.66	16.69	1.2	1.0
MCtoPC#4	15.74	13.94	0.9	13.98	13.28	0.9	1.0
MCtoPC#5	20.45	22.55	1.1	20.40	21.05	1.0	0.9
MCtoPC#6	23.54	23.61	1.0	21.68	20.07	0.9	0.8
MCtoPC#7	27.60	23.31	0.8	23.09	23.86	1.0	1.0
MCtoPC#8	37.58	39.23	1.0	40.92	31.42	0.8	0.8
Mean	**20.51**	**20.96**	**1.0**	**19.58**	**19.39**	**1.1**	**0.9**
sd	**8.91**	**8.67**	**0.1**	**9.86**	**6.44**	**0.2**	**0.1**
sem	**3.15**	**3.07**	**0.0**	**3.49**	**2.28**	**0.1**	**0.0**

Supplementary Table 2. Transmission at the Martinotti cell to pyramidal cell synapses.

N = 9	Efficacy (pA)						
	10 Hz	10 Hz	10 Hz	30 Hz	30 Hz	30 Hz	late
	early	late	late/early	early	late	late/early	30Hz/10Hz
PCtoMC#1	0.00	0.00	+*inf*	1.09	7.54	6.9	+*inf*
PCtoMC#2	0.00	3.90	+*inf*	2.99	6.58	2.2	1.7
PCtoMC#3	0.14	2.12	15.1	1.22	10.92	9.0	5.2
PCtoMC#4	1.46	5.75	3.9	5.63	29.53	5.2	5.1
PCtoMC#5	2.54	4.39	1.7	4.58	7.17	1.6	1.6
PCtoMC#6	2.55	2.13	0.8	4.67	13.31	2.9	6.2
PCtoMC#7	4.35	3.42	0.8	4.67	8.94	1.9	2.6
PCtoMC#8	5.22	7.09	1.4	4.93	18.52	3.8	2.6
PCtoMC#9	9.00	29.78	3.3	9.90	53.52	5.4	1.8
Mean	**2.81**	**6.51**	**3.9**	**4.41**	**17.34**	**4.3**	**3.4**
sd	**2.99**	**8.97**	**5.1**	**2.63**	**15.42**	**2.5**	**1.9**
sem	**1.00**	**2.99**	**1.9**	**0.88**	**5.14**	**0.8**	**0.7**
N = 9	Transfer rate						
	10 Hz	10 Hz	10 Hz	30 Hz	30 Hz	30 Hz	late
	early	late	late/early	early	late	late/early	30Hz/10Hz
PCtoMC#1	0.00	0.00	+*inf*	0.03	0.20	6.67	+*inf*
PCtoMC#2	0.00	0.16	+*inf*	0.10	0.17	1.70	1.06
PCtoMC#3	0.02	0.16	8.00	0.09	0.60	6.67	3.75
PCtoMC#4	0.08	0.18	2.25	0.14	0.64	4.57	3.56
PCtoMC#5	0.16	0.29	1.81	0.36	0.49	1.36	1.69
PCtoMC#6	0.17	0.30	1.76	0.20	0.60	3.00	2.00
PCtoMC#7	0.27	0.18	0.67	0.31	0.44	1.42	2.44
PCtoMC#8	0.26	0.48	1.85	0.28	0.72	2.57	1.50
PCtoMC#9	0.32	0.66	2.06	0.36	0.96	2.67	1.45
Mean	**0.14**	**0.27**	**2.63**	**0.21**	**0.54**	**3.40**	**2.18**
sd	**0.12**	**0.20**	**2.42**	**0.12**	**0.25**	**2.09**	**1.00**
sem	**0.04**	**0.07**	**0.92**	**0.04**	**0.08**	**0.70**	**0.35**
N = 9	Potency (pA)						
	10 Hz	10 Hz	10 Hz	30 Hz	30 Hz	30 Hz	late
	early	late	late/early	early	late	late/early	30Hz/10Hz
PCtoMC#1	/	/	/	38.08	38.04	1.00	+*inf*
PCtoMC#2	/	27.56	+*inf*	29.63	41.16	1.39	1.49
PCtoMC#3	6.40	14.24	2.23	15.11	18.46	1.22	1.30
PCtoMC#4	18.24	29.84	1.64	43.64	46.11	1.06	1.55
PCtoMC#5	14.82	15.32	1.03	12.19	15.40	1.26	1.01
PCtoMC#6	15.31	9.62	0.63	23.80	22.02	0.93	2.29
PCtoMC#7	16.60	19.02	1.15	13.26	19.71	1.49	1.04
PCtoMC#8	22.24	14.50	0.65	16.48	26.00	1.58	1.79
PCtoMC#9	27.38	45.44	1.66	24.73	56.06	2.27	1.23
Mean	**17.28**	**21.94**	**1.12**	**24.10**	**31.44**	**1.36**	**1.46**
sd	**6.54**	**11.74**	**0.71**	**11.22**	**14.32**	**0.41**	**0.43**
sem	**2.47**	**4.15**	**0.25**	**3.74**	**4.77**	**0.14**	**0.15**

Supplementary Table 3. Transmission at the pyramidal cell to Martinotti cell synapses.

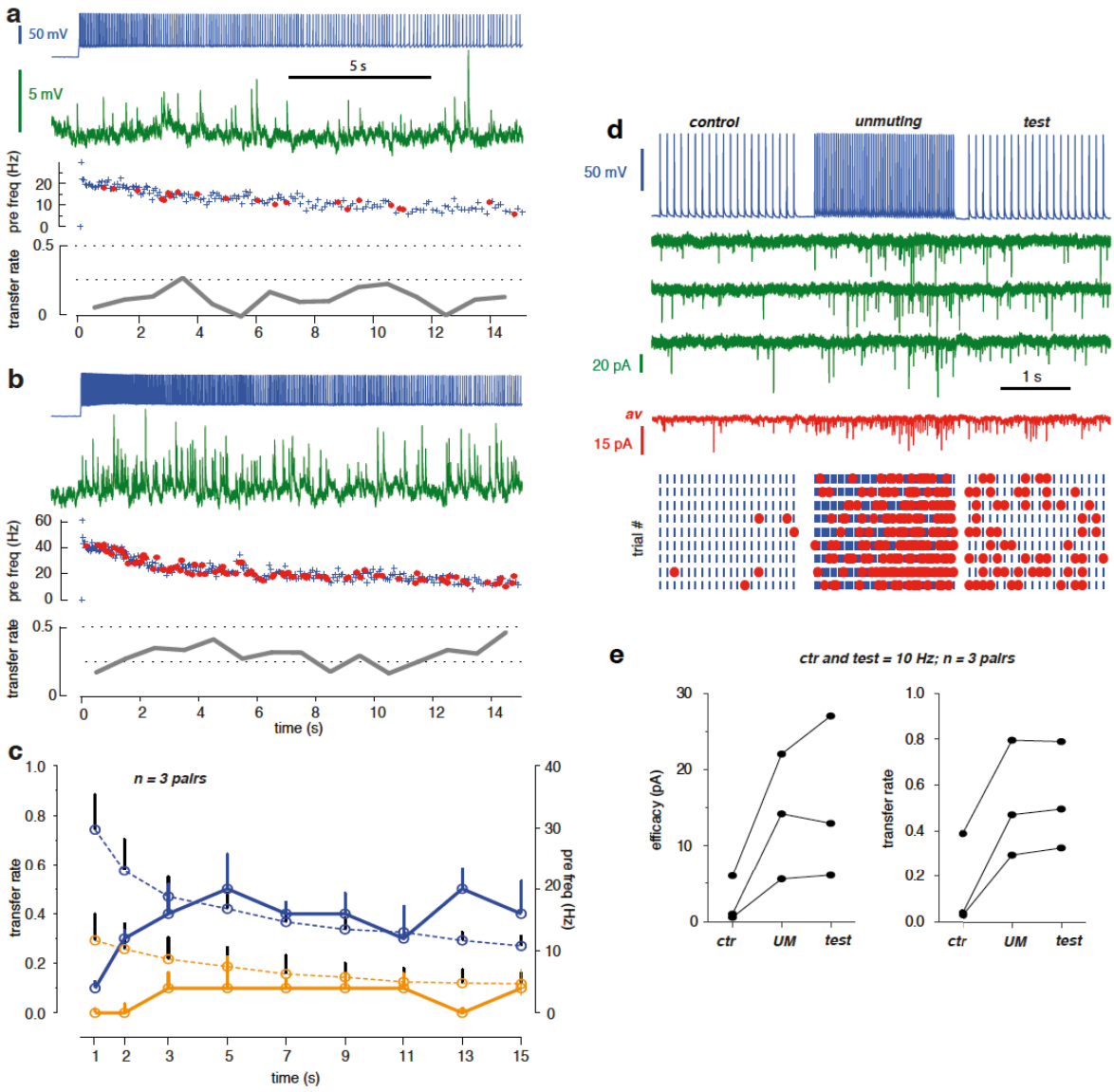

Supplementary Figure 2. Moderate firing can maintain synaptic un-muting following initial high frequency firing.

(**a,b,c**) Maintained current injections were applied to induce maintained firing in a presynaptic PC while a MC was recorded in current clamp mode. The top graphs show the presynaptic instantaneous frequency over time (blue +). Red dots indicate monosynaptic EPSPs in the postsynaptic MC. The lower graphs show transfer rate over time.

(a) Presynaptic firing frequency adapted from 50 to 20 Hz. The initial 50 Hz spiking activity un-muted the synaptic connection and synaptic transfer remained enhanced (0.2 - 0.5) even as presynaptic firing frequency progressively slowed.

(b) Presynaptic firing frequency adapted from 20 Hz to 10 Hz over several seconds. The initial 20 Hz frequency did not enhance transfer rate, and transfer remained low (0 – 0.25).

(c) For initially high firing frequencies (blue broken line), synapses were un-blocked and transfer rates (blue line) stayed high even as presynaptic firing frequencies progressively decreased. For initially low firing frequency stimulation (orange broken line), synapses remained un-efficient with low transfer rates (orange line). Summary data from n = 3 pairs, mean ± SEM.

(d) PC-stimulation (blue) and MC-EPSCs recorded at -65 mV. Three trials (green) and average in red (low pass filtered at 1 Hz). Below, raster plots of synaptic transfer. The PC was stimulated with a control train at 10 Hz, followed by an unmuting train at 30 Hz and then a test stimulus at 10 Hz. The

raster plot shows a low synaptic efficacy during the control 10 Hz train, unmuting and facilitation during the 30 Hz train followed by enhanced transfer during the subsequent 10 Hz test train.
(e) Summary data from n = 3 pairs where synaptic unmuting was successful and synaptic efficacy and transfer rate had doubled at the end of the 30 Hz spike train.

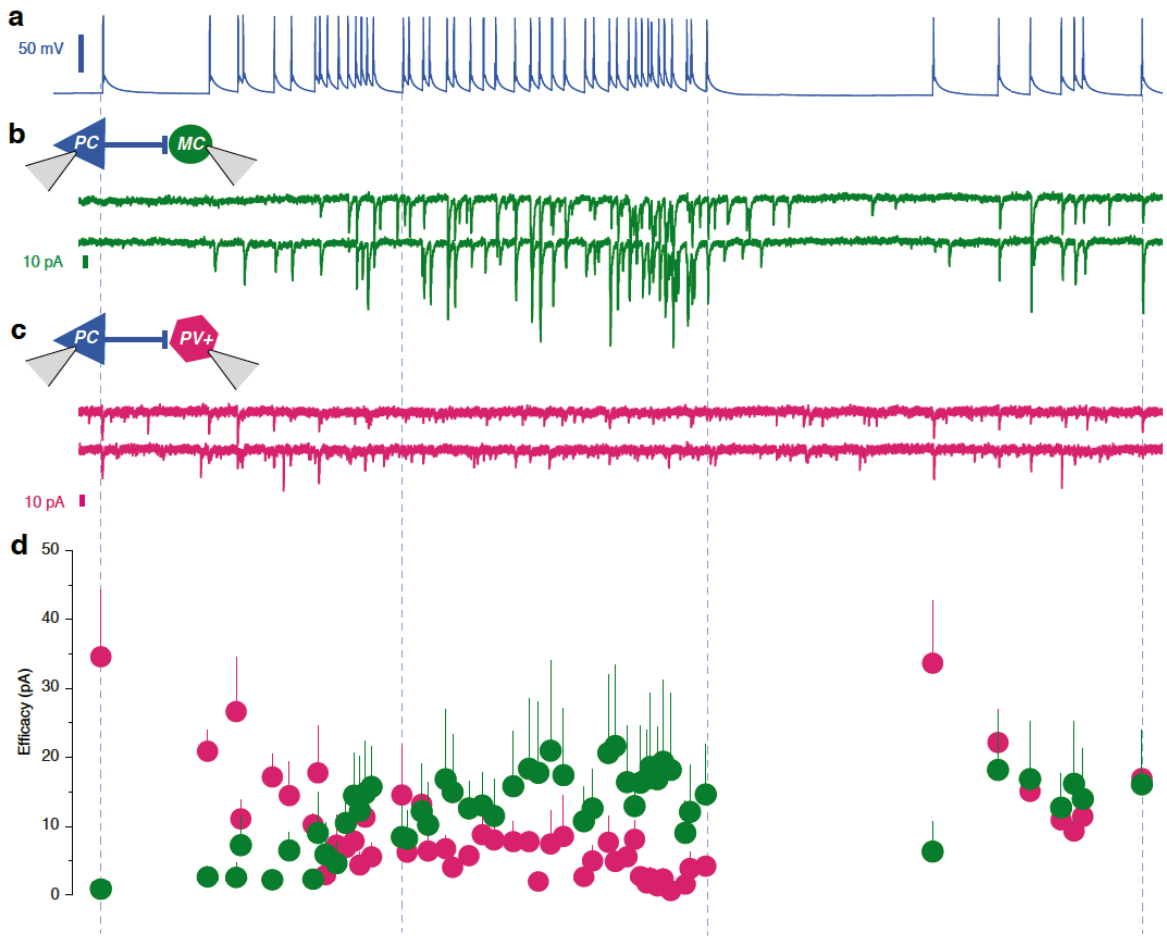

Supplementary Figure 3. Synaptic responses to HD spike train in Martinotti vs parvalbumin (PV) expressing cells.
(a) Head direction firing pattern injected in a pyramidal neuron.
(b) The recordings from a postsynaptically connected Martinotti cell show EPSCs in response to the spike train, with facilitating dynamics (shown are two consecutive trials).
(c) The recording from a postsynaptically connected parvalbumin positive fast-spiking neuron also show EPSCs in response to the same spike train, but with depressing dynamics (shown are two consecutive trials).
(d) Summary graph of the average efficacy of evoked EPSCs for the Martinotti cells (in green; n = 5 pairs) and the average efficacy of evoked EPSCs in parvalbumin positive cells (in pink; n = 5 pairs). Note how the first spike evoked the largest response in PV cells, while Martinotti neurons didn't respond to the first spike.

N_{Pyr}	500
ρ	0.5
$\bar{w}^{OUT}$	0.9
w^{OUT}	0.7
w^{IN}	5
τ_E	22 ms
τ_I	37 ms
τ_N	5 ms
T	0.05
μ	0.2
σ	0.02
β	0.3
κ	36^o
Λ	0.6668

Supplementary Table 4. Table of model network parameters.

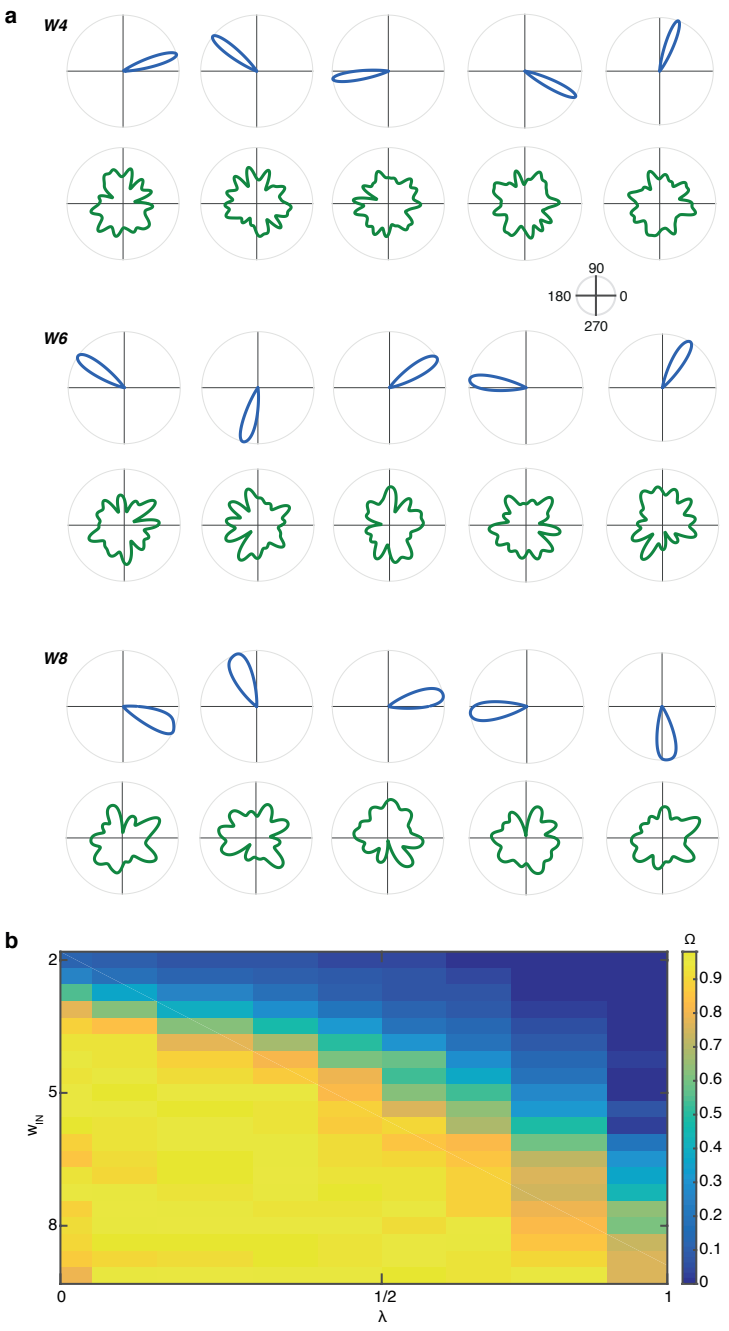

Supplementary Figure 4.
(a) Examples of tuning curves from running the network simulation. A series of 5 examples for Pyramidal cell polar plots (blue) and Martinotti cell polar plots (green) for different values (W4, W6, W8) of the range α of the inhibition suppression. The larger α, the broader the head directional tuning of pyramidal cell. Martinotti cells are not directionally tuned.
(b) Bump coherence Ω can be achieved with a range of values for λ.

Article 4

Different intrinsic properties of presubicular projection neurons: pathway-specific transmission of head direction related information

The head directional signal that originates from vestibular information is generated subcortically, in the reciprocally connected dorsal tegmental nuclei (DTN) and lateral mammillary nucleus (LMN). It is then transferred consecutively to the anterodorsal thalamus (ADN) and the presubiculum. The presubiculum is continuously updated by visual cues arising from both visual and retrosplenial cortices. Then, the presubiculum itself, exerts a visual landmark control on the subcortical head direction signal via direct projections to ADN and LMN. In addition, the presubiculum has been showed to contribute to the generation of grid cell activity by sending axons to the downstream MEC.

While these projection areas (e.g. MEC, thalamus and LMN) of the presubiculum have been already described in anatomical tracing studies, at the physiological level, single neuron connectivity of these projections has remained unclear. In this study, we investigate the morphology and physiology of retrogradely labeled presubicular neurons projecting to MEC, LMN and ATN using an *in vivo* labeling approach followed by *in vitro* patch clamp recordings. Analysis of electrophysiological parameters based on principal component analysis demonstrates projection-specific subpopulations with distinct intrinsic properties.

Different Intrinsic Properties of Presubicular Projection Neurons : Pathway-specific Transmission of Head Direction Related Information

running title:
Presubicular projection neurons

Li-Wen Huang[1,2,*], Jean Simonnet[1,3,*], Mérie Nassar[1,4], Roxanne Lofredi[1] and Desdemona Fricker[1,4]

(1) Inserm U1127, CNRS UMR7225, Sorbonne Universités, UPMC Univ Paris 6 UMR S1127, Institut du Cerveau et de la Moelle épinière, Paris 75013, France; (2) Centre for Integrative Physiology, University of Edinburgh, Hugh Robson Building, Edinburgh, EH8 9XD, UK (3) Bernstein Center for Computational Neuroscience, Humboldt University Berlin, 10115 Berlin, Germany (4) CNRS UMR 8119, Université Paris Descartes, France.

* these authors contributed equally to this work

Correspondence:
Desdemona Fricker, MD, PhD
CNRS UMR8119 Université Paris Descartes
45 rue des Saint Pères
75006 Paris, FRANCE
desdemona.fricker@parisdescartes.fr
Phone +33 617590592

Number of pages:
Number of figures: 4
Total number of words (abstract, introduction, materials and methods, results, discussion, in text references and figure legends) : (now : 4152)

Abstract

The presubiculum is part of an interconnected network of distributed brain regions where individual neurons signal the animals heading direction. In particular, presubiculum sends axons to medial entorhinal cortex (MEC), it is reciprocally connected with anterior thalamic nuclei (ATN) and it sends projections to the Lateral Mammillary Nucleus (LMN). Here we used projection specific labeling of presubicular neurons to identify MEC projecting neurons, preferentially located in superficial layers II-III and to a lesser degree in deep layers. MEC projecting neurons were regular spiking neurons. LMN projecting neurons were anatomically distinct pyramidal neurons located in layer IV. We show for the first time that LMN projectors are also physiologically distinct, characterized by an intrinsic bursting discharge behavior, which may be uniquely adapted to transmit visual landmark information. Neurons projecting to the thalamus were located in deep layers V/VI, and were regular spiking neurons. Mathematical cluster analysis of intrinsic properties suggested that the three categories of projection neurons correspond to different subgroups of neurons, with some similarities between MEC and thalamus projecting neurons. Projection-specific neuronal subpopulations may therefore subserve separate functions in the presubiculum and may be engaged differently in transmitting head direction related information.

Significance statement

The presubiculum is part of a brain wide network of head direction cells. It contributes to the generation of grid cell activity in the downstream medial entorhinal cortex, and it also feeds back information to immediate and indirect subcortical input regions. Here we identify projection specific subpopulations of presubicular neurons. We show how they differ in their laminar location and in their intrinsic neuronal properties. These distinct cell types may provide specific coding capacities for distinct output channels of presubiculum.

Introduction

Spatial navigation relies on extended brain circuits, including the hippocampal and parahippocampal network that support grid cell (Hafting et al., 2005), place cell (O'Keefe and Nadel, 1978) and head direction cell firing (Taube, 2007). The head directional signal is generated subcortically, probably in the reciprocally connected dorsal tegmental nuclei (DTN) and lateral mammillary nucleus (LMN), where vestibular sensory information contribute to its generation (Bassett et al., 2007; Clark and Taube, 2012; Yoder and Taube, 2014). It is then conveyed sequentially to the anterior thalamic nuclei (ATN) (Blair et al., 1998) and the dorsal part of the presubiculum, also termed postsubiculum (van Groen and Wyss, 1990a; Goodridge and Taube, 1997; Peyrache et al., 2015). In addition to thalamic head direction inputs, the presubiculum also receives inputs from visual cortex and retrosplenial cortex (Vogt and Miller, 1983; van Groen and Wyss, 1990a; Jones and Witter, 2007). Self-motion and visual cues continually update the head direction signal (Taube, 2007), and when available, visual landmarks control the preferred firing direction (Zugaro et al., 2003).

It has been shown recently that the transmission of the head direction signal from the ATN is necessary for the generation and function of the grid cell activity in the medial entorhinal cortex (MEC) (Winter et al., 2015). In the absence of direct projections from the ATN to the MEC (Nassar 2015 Soc neurosci abstract #445.07), the presubicular projection may be essential for relaying the head direction signal to the medial entorhinal grid cell system (Rowland et al., 2013). Other known projection areas of the presubiculum include feedback projections to the thalamus (van Groen and Wyss, 1990b; 1990a; Ishizuka, 2001) and LMN (Allen and Hopkins, 1989; Gonzalo-Ruiz et al., 1992). The cellular elements of the presubicular microcircuit projecting to these two subcortical areas, ATN and LMN, have been identified as two non-overlapping populations (Yoder and Taube, 2011). However, the physiology and single neuron connectivity of presubicular projection neurons have not been elucidated.

In this study, we examine the morphology and physiology of retrogradely labeled presubicular neurons projecting to MEC, ATN and LMN. Principal component analysis revealed distinct intrinsic properties of projection-specific neuronal subpopulations.

Materials and Methods:

Animals. Experiments were performed on 22 male and female young adult C57BL/6 wild type mice (P29-P35 for stereotaxic injection and P31-P40 for recording), as well as 6 GAD67-GFP mice and 2 Sst^{CRE}::tdTomato mice (Nassar et al., 2015). Our care and use of animals conformed to the European Community Council Directive of 22 September 2010 (2010/63/EU) and French law 587/848). Our study was approved by the local ethics committee Charles Darwin N°5 and the French Ministry for Research.

Stereotaxic injections. Retrograde fluorescent tracers (Retrobeads, Lumafluor) were injected unilaterally into MEC, LMN or ATN. Stereotaxic coordinates were: MEC, -4.65, 3.08, -4 (mm); LMN, -2.8, 0.75, -5.35 (mm); ATN, -0.8, 0.75, -3.2 (mm) (anterior-posterior, medial-lateral, dorsal-ventral to bregma). The protocol for injections was described in detail previously (Mathon et al., 2015). Briefly, mice were deeply anesthetized with a mixture of ketamine and xylazine (*80mg/kg-20mg/kg*). 150-300 nl of Retrobeads were injected with a Hamilton syringe at a speed of 40-60 nl/min. The animals were allowed to recover for at least 48 hours.

Slice electrophysiology. Horizontal slices (300-320 µm) containing presubiculum were prepared from mice that had been previously injected with Retrobeads. The cutting solution contained (in mM): 125 NaCl, 25 sucrose, 2.5 KCl, 1.25 NaH_2PO_4, 25 $NaHCO_3$, 2.5 glucose, 0.5 $CaCl_2$, 7 $MgCl_2$ (cooled to 2-6 ºC, bubbled with 95% O_2 /5% CO_2). Slices were incubated for 15 min at 36 °C in a holding chamber with aCSF composed of (in mM): 124 NaCl, 2.5 KCl, 10 NaH_2PO_4, 26 $NaHCO_3$, 11 glucose, 2 $CaCl_2$, 2 $MgCl_2$ (bubbled with 95% O_2 /5% CO_2). Post incubation, slices were stored at room temperature. For whole-cell recordings, slices were bathed in carbogenated aCSF at 32-34 °C. Retrobeads containing neurons of presubiculum were identified under a Axioscope 2FS plus microscope (Zeiss), equipped with appropriate LED illumination (Cairn). Pipettes were pulled into patch electrodes with 4-6 MΩ resistance and filled with a potassium-based intracellular solution, pH 7.3, composed of (in mM): 140 Kgluconate, 1.2 KCl, 10 HEPES, 0.2 EGTA, 2 $MgCl_2$, 4 MgATP•$2H_2O$, 0.4 Na_3GTP•$2H_2O$, 10 Na phosphocreatine. Biocytin (3 mg/ml) was added for posthoc revelation of cellular morphology. Pipette capacitance was compensated. Electrophysiological signals were sampled at 50 kHz and filtered at 5-6 kHz (Multiclamp 700B or Axopatch 200A amplifier, Molecular Devices) in whole-cell current-clamp mode. Data acquisition and analysis were performed respectively in pClamp (Molecular Devices), Axograph® and MATLAB®.

The ***resting membrane potential*** was determined in voltage-follower mode after breaking in and averaging the membrane potential over 20 s. During the step current injection protocol, baseline membrane potential was maintained at -65 mV. Membrane responses in current clamp were elicited by injecting hyperpolarizing to depolarizing current steps of 800 ms duration (typically starting at -300

pA; 10 to 20 pA increments). The membrane voltage was plotted as a function of current commands, and a linear fit was created between -70 to -60 mV, the slope of which indicated ***input resistance***, R_{input}. The membrane time constant, ***tau***, was calculated by fitting a double exponential function to an averaged membrane response to a small negative current (potential difference $\Delta V < 10$ mV) (Golowasch et al., 2009). The shorter of the two time constants was used. ***Sag ratio*** was measured by averaging the ratio $\Delta V_{min}/\Delta V_{steady\text{-}state}$ of three data points around -100 mV ($\Delta V_{min} = V_{min} - V_{baseline}$; $\Delta V_{steady\text{-}state} = V_{steady\text{-}state} - V_{baseline}$).

The properties of the first action potential (AP) at rheobase (the minimal current required to discharge action potentials) were characterized: ***AP threshold*** (a point at the foot of the AP where dV/dt > 30 V/sec), ***AP amplitude*** (from threshold to peak), ***AP width*** (width at half-maximum amplitude), afterhyperpolarization amplitude (***AHP***, from threshold to the trough of the afterhyperpolarization), and ***AP maximum depolarization*** and ***repolarization rates***. The ***latency*** of the first AP was measured from the onset of the current step to the peak of the AP. The ***firing rate at twice rheobase*** was determined. The current step that gave the AP firing rate closest to 15 Hz was analyzed for bursting behavior of spiking, quantified by ***fast-doublet index*** (the averaged inter-spike interval over the first interval; only applicable for neurons that fired > 2 spikes during positive current steps). Firing rate increases were quantified by calculating the initial (4-5 current points from rheobase) slope of the frequency-current relationship (***f-I slope***).

Histology and anatomy. Slices were fixed in 4% paraformaldehyde overnight, then incubated with a blocking solution (2% milk in PB supplemented with 0.3-1% Triton-X-100). Streptavidin-Cy3 or Cy5 conjugate (1:500; Life Technologies) was used for biocytin revelation, and DAPI (1/1000) to stain nuclei. Sections were imaged using a pseudo-confocal Olympus IX81 microscope, and Volocity® software for analysis. Automated fluorescence quantification of retrobeads after MEC injection was done on the contralateral presubiculum, to avoid overshadowing by strong fluorescence from the nearby MEC injection site. Retrobeads fluorescence density of each layer was measured and normalized to averaged density across layers. In one mouse injected in the MEC, Retrobeads-labeled neurons of the presubiculum were visualized in stacks of confocal images of NeuN-stained 60 µm sections and counted manually. The Neurolucida software was used for 3-D computer-aided morphological reconstruction of biocytin-filled neurons (Simonnet et al., 2013).

Statistical analysis. The Principal component analysis (PCA) and Ward's unsupervised cluster analysis (Ward, 1963; Simonnet et al., 2013) of presubicular projection neurons was implemented using MATLAB, and based on 11 electrophysiological parameters (cf. Table 1): resting membrane potential, input resistance, tau, sag ratio, AP threshold, AP amplitude, AP width, AP AHP, AP latency, firing rate at double rheobase, f-I slope. Measurements for each variable in our data set were transformed to standard scores across all cells based on the formula (x_i - mean/s) (Romesburg, 1984).

To avoid artificially weighting highly correlated variables, the AP maximum depolarization rate and repolarization rate were not included, because they were highly correlated with AP amplitude and AP width respectively ($r > 0.8$ in the correlation matrix), and their value was lower in the principal component loadings table (Tsiola et al., 2003).

Results

Anatomical segregation of LMN, ATN and MEC projectors in the presubiculum

Retrograde fluorescent tracer was injected in MEC (10 mice), LMN (9 mice) or ATN (7 mice), in order to identify presubicular projection neurons. Injection sites were confirmed posthoc in horizontal sections for MEC (Fig. 1A), and in coronal sections for LMN (Fig. 1B) and ATN (Fig. 1C). MEC injections targeted the superficial layers of the MEC, and in some cases deep layers were also hit. Cases where MEC injections were not entirely restricted to the MEC were excluded from analysis. LMN injection sites and ATN injection sites were confirmed in three cases by slicing the rostral half of the brain in the coronal plane, while the distribution of retrogradely labeled neurons was observed in horizontal sections of presubiculum, contained in the caudal half of the brain (illustrations in Figure 1).

Retrobeads injection into MEC resulted in bilateral retrograde labeling in the presubiculum. Labeled neurons were most numerous in layer II/III, and some were located in deep layers (Fig. 1D). The layer distribution of Retrobeads fluorescence in the contra-lateral presubiculum was similar to ipsi-lateral Retrobeads-labeled cell counts. The density of Retrobeads fluorescence was significantly higher in layer III of the presubiculum compared with layer IV ($p < 0.05$) or layer V/VI ($p < 0.01$; 9 slices from 3 mice injected in MEC). Retrobeads-labeled neuron counts resulted in highest numbers in layer III (911 of 1323 cells, total number counted in 3 slices). Retrobeads-labeled neurons were also observed in other brain regions known to project to the MEC, including the parasubiculum, subiculum, CA1 and postrhinal cortex.

For Retrobeads injections into LMN, labeled neurons were limited to layer IV of the presubiculum (Fig. 1E). For ATN injections, Retrobeads-labeled neurons were found exclusively in layers V/VI (Fig. 1F).

Morphology and intrinsic electrophysiological properties of presubicular projecting neurons

Retrogradely labeled presubicular neurons projecting to MEC, LMN or ATN were targeted for *in vitro* whole-cell recordings. The injection sites into MEC or ATN were routinely checked in horizontal sections. LMN injections were estimated to be correct, if labeled neurons were present specifically in

layer IV of presubiculum. Active spiking behaviors and passive membrane properties of 57 projecting neurons were measured and quantified.

MEC projectors in superficial layers: regular firing pyramidal neurons

Reconstruction of cell morphology revealed that MEC projecting neurons were layer II/III pyramidal neurons, with apical dendrites arborizing in layer I, basal dendrites in layer III, and axons branching across deep layers (Fig. 2A). Following positive current injections, MEC projecting neurons fired at high frequency with little adaptation (n = 18; Fig. 2E). The firing frequency at double rheobase current in MEC projectors was 25 ± 1 Hz, significantly higher than that in LMN projectors (13 ± 3 Hz; $p < 0.05$). Negative current injections revealed very little voltage sag, with a sag ratio of 1.06 ± 0.01, significantly smaller than for LMN or ATN projectors ($p < 0.001$ and $p < 0.01$ respectively; cf. Table 1 or Fig. 4).

MEC projecting Martinotti-type interneuron

Interestingly, one Retrobeads-labeled MEC projecting neuron was non-pyramidal, with a typical Martinotti type morphology (Fig. 2B), indicating that this was a long-range projecting GABAergic neuron. The axon of the Martinotti cell arborized densely in superficial layers and its dendrites extended across deep layers. Voltage recordings of the Martinotti cell are shown in Fig. 2F. Positive current injections led to action potential firing with prominent AP afterhyperpolarizations. The AHP was -26.8 mV in the MEC projecting Martinotti cell, standing out from the average AHP in pyramidal MEC projecting neurons (-17.0 ± 0.7 mV). This MEC projecting Martinotti cell was not included in subsequent PCA or cluster analysis. We then injected Retrobeads in MEC in 2 transgenic mice where all GABAergic neurons (GAD67-GFP line) or a subpopulation of Somatostatin expressing neurons (SstCre::tdTomato line) can be identified by their green or red fluorescence: 6 GABAergic presubicular neurons in one GAD67-GFP mouse, and 6 presubicular tomato expressing neurons in one SstCre::tdTomato mouse were also found to contain Retrobeads.

LMN projectors: bursting pyramidal neurons in layer IV

LMN projecting neurons were layer IV pyramidal neurons, with apical dendrites arborizing in layer I, basal dendrites mainly in layer IV, some in layer V/VI, and their axons branching across deep layers (Fig. 2C). Following positive current injections, LMN projectors tended to discharge in an initial burst of two spikes (n = 18; Fig. 2G). This bursting tendency was quantified by the fast-doublet index, which was 29 ± 2 for LMN projectors (n = 11), while MEC projectors (n = 18) and ATN projectors (n = 20) both had very low average fast-doublet indices of 2 ± 0. The bursting behavior of LMN projectors was associated with a smaller AHP following the first spike ($p < 0.0001$, comparison with MEC or AND projectors, Table 1 or Fig. 4). Most LMN projectors displayed prominent sag during

negative current steps, and rebound depolarization after the offset (Fig. 2G). The sag ratio was 1.21 ± 0.28 (n = 18), significantly higher than in MEC projectors ($p < 0.001$).

ATN projectors: regular firing pyramidal neurons in layer V/VI

ATN projecting neurons were deep layer pyramidal neurons with dendrites distributed across all layers in the presubiculum (Fig. 2D). The latency to spike onset was quite long at rheobase current (281 ± 62 ms, n = 20) for ATN projectors, while this latency was significantly shorter for LMN projectors or MEC projectors ($p < 0.001$; Table 1 or Fig. 4). For larger current injections, ATN projectors fired with little adaptation (n = 20; Fig. 2H). For negative current injections, ATN projecting neurons showed large sag (sag ratio, 1.18 ± 0.04), which appeared somewhat slower compared to LMN projecting neurons. The maximum depolarization/repolarization rates in ATN projectors were significantly slower compared to LMN projectors ($p < 0.05$). The membrane time constant of ATN projectors was 21 ± 1 ms, significantly longer than LMN projectors (13 ± 1 ms; $p < 0.0001$).

Physiological segregation of projection-specific presubicular neurons

We examined the range of intrinsic properties of presubicular projection neurons using unsupervised principal component analysis (PCA). PCA selected variables that contributed most to the overall variability, and, thus, were most important in distinguishing different physiological cell groups. The first principal component (PC1) captured most of the variability (34 %). The parameters that were positively correlated with PC1 included passive properties, tau and input resistance, and action potential properties, f-I slope, firing rate at double rheobase, AP width, AP threshold, latency to spike. PC2 mostly correlated with sag ratio, f-I slope, firing rate at double rheobase, and PC3, mostly AP width, captured additional 15.9 % and 14.7 % of the total variability, respectively. Thus about 64.6 % of the total variability could be explained by the first three principal components. PCA revealed a separation between LMN projecting neurons (red dots) and ATN/MEC projecting neurons (green dots/blue dots; Fig. 3A). Then the same data set was submitted to un-supervised cluster analysis. The projection–specific subpopulations of neurons were reflected in the dendrogram as two major clusters, separating LMN projectors (red) from MEC projectors (blue) and ATN projectors (green; Fig. 3B). The two subclusters in the LMN projecting group corresponded to two subpopulations in PCA as well. ATN projecting neurons were separated into two different subclusters with one subcluster sharing some similarity with MEC projecting neurons.

Discussion (<1500 words): now 858 words

We have shown that presubicular neurons fall into projection-specific neuronal subpopulations, that segregate in their anatomical distribution and also in physiological intrinsic properties.

Our retrograde tracing from MEC had targeted layer III, and some cases also involved layers I-IV. All injections rendered similar distribution pattern in presubiculum: retrogradely labeled neurons were densely distributed in layer II/III of presubiculum, with much fewer distribution in deep layers. This finding is coherent with previous tracing studies showing that layer II-III of presubiculum project bilaterally to layer I-IV of the MEC (van Groen and Wyss, 1990b; Caballero-Bleda and Witter, 1993; van Haeften et al., 1997; Honda and Ishizuka, 2004; Rowland et al., 2013). A few MEC projecting neurons (< 1%) were GABAergic, and those cells were strictly located in layer II/III of the ipsilateral presubiculum. Previous reports had estimated 20-30% of MEC projection neurons to be GABAergic (Van Haeften et al., 1997). This difference could be due to a species difference (mouse vs. rat), or to a lesser uptake of Retrobeads by interneurons. Retrobeads-labeled neurons were also observed in other brain regions known to project to the MEC, including parasubiculum, subiculum, CA1 and postrhinal cortex, which underscores the specificity and efficacy of our retrograde tracing.

LMN projecting neurons were exclusively distributed in layer IV of the presubiculum and ATN projecting neurons were only found in layer V/VI. We thus confirm for mice a previous report from rats, showing that these projections neurons constitute non-overlapping populations in distinct cell layers presubiculum (Yoder and Taube, 2011). In addition to this anatomical segregation of the two projection-specific subpopulations, we reported for the first time that LMN projecting neurons and ATN projecting neurons are also physiologically distinct.

Rodent LMN and ATN are small brain structures, and stereotaxic injections of tracers may spill over to adjacent regions. Adjacent to the LMN lies the lateral part of the medial mammillary nucleus, which also receives presubicular inputs (van Groen and Wyss, 1990b). This might explain the two separated LMN-projecting groups in our PCA and clustering results. Some heterogeneity of thalamic projection neurons might also be due to the fact that there are several thalamic target nuclei: The presubicular projection to the thalamus targets densely the anterodorsal nucleus, but also the anteroventral and laterodorsal nucleus (van Groen and Wyss, 1990a). The heterogeneity of thalamic projecting neurons found with unsupervised clustering might therefore reflect the heterogeneity of neurons projecting to specific thalamic nuclei. It will be interesting to use genetic or immunohistochemical tools to test whether the group that is more intrinsically similar to MEC projecting neurons corresponds specifically to the anterodorsal thalamic nucleus, which is the core nucleus receiving and relaying head direction signals (Taube, 2007).

Our classification based on electrophysiological properties revealed three main subgroups of presubicular projection neurons: regular-firing MEC projecting neurons, burst-firing LMN projecting neurons and heterogeneous ATN projecting neurons. Interestingly, those specific projection groups correspond well with the cellular neuroanatomy classification reported previously in rat (Simonnet et al., 2013): layer II/III neurons were regular-firing neurons with no prominent sag, layer IV neurons were intrinsically bursting with large sag, and layer V/VI neurons were heterogeneous regular-firing neurons with significantly larger sags than superficial layer cells. The preserved cell layer structure across species, mouse and rat, very possibly explains the important functional roles they play in the head direction circuits. The presubicular projection to the LMN helps relay visual information to the head direction system and further gain head direction signal stability and accuracy (Yoder et al., 2015), the bursting nature of LMN projecting neurons may ensure the visual feedback is sent effectively and efficiently with little delay. To unveil the specific functional roles of each projection group in head direction signaling, it will be interesting to combine retrograde labeling techniques or modern genetic tracing tools with *in vivo* whole-cell recordings.

Despite the fact that LMN projectors are burst firing neurons, the three projection groups can sustain high-frequency firing and fire regularly without adaptation, which allows all of them to be good candidates for transmitting head directional information (Taube, 2007). While in the *in vivo* study head direction cells were recorded across superficial and deep layers of presubiculum (Boccara et al., 2010), we revealed for the first time different functional groups of presubicular cells that project to specific circuits in head direction system, namely the upstream LMN, the intermediate ATN, and the output grid cell signaling MEC.

Figure Legends

Figure 1. Anatomical segregation of presubicular neurons that project to MEC, LMN or ATN. **A,** Injection of retrobeads into layer III of MEC. Low magnification image of a horizontal section of the temporal lobe. **B**, Injection of retrobeads into LMN (coronal section). **C**, Injection of retrobeads into ATN (coronal section). **D**, Higher magnification image of the presubiculum (rectangle in **A**). Retrogradely labeled MEC projecting neurons are mostly found in superficial layers of presubiculum. **E**, LMN projecting neurons are confined to layer IV of presubiculum (horizontal section, same animal as in **B**). **F**, ATN projecting neurons are present in layers V-VI of presubiculum (horizontal section, same animal as in **C**). Retrobeads in red, DAPI staining in blue. Abbreviations: MEC, medial entorhinal cortex; LMN, lateral mammillary nucleus; ATN, anterior thalamic nucleus; PrS, presubiculum; PaS, parasubiculum; DG, dentate gyrus; 3Vd, dorsal third ventricle. Scale bars in **A, B, C** = 200µm; scale bars in **D, E, F** = 100µm.

Figure 2. Morphology and firing patterns of retrogradely labeled presubicular projecting neurons. **A, E**, MEC-projecting pyramidal neuron. **B, F**, MEC-projecting Martinotti interneuron. **C, G**, LMN-projecting neuron. **D, H**, ATN-projecting neuron. **A-D**: Reconstruction of cell morphology with dendrites in blue and axons in red. Scale bars, 50µm. **E-H**: Firing patterns at rheobase (upper traces) and at double rheobase (lower traces). Membrane voltage responses to hyperpolarizing current steps of -150 pA are shown in light blue. Insets show larger scale traces of the first action potential.

Figure 3. Segregation of MEC projectors (blue), LMN projectors (red) and ATN projectors (green) in presubiculum based on electrophysiological parameters. **A**, Score plot of presubicular projecting neurons on principal component (PC) 1, PC 2, and PC 3 planes. **B**, Cluster analysis of presubicular projecting neurons.

Figure 4. Comparison of intrinsic properties of presubicular neurons that project to MEC (blue), LMN (red) or ATN (green). **A**, resting membrane potential. **B**, Input resistance. **C,** Time constant. **D,** Sag ratio. **E**, f-I slope. **F,** Firing rate at double rheobase. **G**, AP threshold. **H**, AP width. **I**, Afterhyperpolarization. **J**, AP macimum depolarization rate. **K**, AP maximum repolarization rate. **L**, Latency to first spike at rheobase. Kruskal wallis and Dunn's multiple comparison post hoc test were performed for significance between projecting neurons, *$p < 0.05$, **$p < 0.01$, ***$p < 0.001$****$p < 0.0001$.

References

Allen GV, Hopkins DA (1989) Mamillary body in the rat: Topography and synaptology of projections from the subicular complex, prefrontal cortex, and midbrain tegmentum. J Comp Neurol 286:311–336.

Bassett JP, Tullman ML, Taube JS (2007) Lesions of the tegmentomammillary circuit in the head direction system disrupt the head direction signal in the anterior thalamus. Journal of Neuroscience 27:7564–7577.

Blair HT, Cho J, Sharp PE (1998) Role of the lateral mammillary nucleus in the rat head direction circuit: a combined single unit recording and lesion study. Neuron 21:1387–1397.

Boccara CN, Sargolini F, Thoresen VH, Solstad T, Witter MP, Moser EI, Moser M-B (2010) Grid cells in pre- and parasubiculum. Nature Publishing Group 13:987–994.

Caballero-Bleda M, Witter MP (1993) Regional and laminar organization of projections from the presubiculum and parasubiculum to the entorhinal cortex: an anterograde tracing study in the rat. J Comp Neurol 328:115–129.

Clark BJ, Taube JS (2012) Vestibular and attractor network basis of the head direction cell signal in subcortical circuits. Front Neural Circuits 6:7.

Golowasch J, Thomas G, Taylor AL, Patel A, Pineda A, Khalil C, Nadim F (2009) Membrane capacitance measurements revisited: dependence of capacitance value on measurement method in nonisopotential neurons. Journal of Neurophysiology 102:2161–2175.

Gonzalo-Ruiz A, Alonso A, Sanz JM, Llinás RR (1992) Afferent projections to the mammillary complex of the rat, with special reference to those from surrounding hypothalamic regions. J Comp Neurol 321:277–299.

Goodridge JP, Taube JS (1997) Interaction between the postsubiculum and anterior thalamus in the generation of head direction cell activity. J Neurosci 17:9315–9330.

Hafting T, Fyhn M, Molden S, Moser M-B, Moser EI (2005) Microstructure of a spatial map in the entorhinal cortex. Nature 436:801–806.

Honda Y, Ishizuka N (2004) Organization of connectivity of the rat presubiculum: I. Efferent projections to the medial entorhinal cortex. J Comp Neurol 473:463–484.

Ishizuka N (2001) Laminar organization of the pyramidal cell layer of the subiculum in the rat. J Comp Neurol 435:89–110.

Jones BF, Witter MP (2007) Cingulate cortex projections to the parahippocampal region and hippocampal formation in the rat. Hippocampus 17:957–976

Mathon B, Nassar M, Simonnet J, Le Duigou C, Clemenceau S, Miles R, Fricker D (2015) Increasing the effectiveness of intracerebral injections in adult and neonatal mice: a neurosurgical point of view. Neurosci Bull.

Nassar M, Simonnet J, Lofredi R, Cohen I, Savary E, Yanagawa Y, Miles R, Fricker D (2015) Diversity and overlap of parvalbumin and somatostatin expressing interneurons in mouse presubiculum. Front Neural Circuits 9:1–19

O'keefe J, Nadel L (1978) The hippocampus as a cognitive map. :1–296.

Peyrache A, Lacroix MM, Petersen PC, Buzsáki G (2015) Internally organized mechanisms of the head direction sense. Nature Publishing Group 18:569–575.

Romesburg HC (1984) Cluster Analysis For Researchers, Lulu Press. Belmont.

Rowland DC, Weible AP, Wickersham IR, Wu H, Mayford M, Witter MP, Kentros CG (2013) Transgenically Targeted Rabies Virus Demonstrates a Major Monosynaptic Projection from Hippocampal Area CA2 to Medial Entorhinal Layer II Neurons. Journal of Neuroscience 33:14889–14898.

Simonnet J, Eugène E, Cohen I, Miles R, Fricker D (2013) Cellular neuroanatomy of rat presubiculum. Eur J Neurosci 37:583–597.

Taube JS (2007) The head direction signal: origins and sensory-motor integration. Annu Rev Neurosci 30:181–207.

Tsiola A, Hamzei-Sichani F, Peterlin Z, Yuste R (2003) Quantitative morphologic classification of layer 5 neurons from mouse primary visual cortex. J Comp Neurol 461:415–428.

van Groen T, Wyss JM (1990a) The postsubicular cortex in the rat: characterization of the fourth region of the subicular cortex and its connections. Brain Res 529:165–177.

van Groen T, Wyss JM (1990b) The connections of presubiculum and parasubiculum in the rat. Brain Res 518:227–243.

van Haeften T, Wouterlood FG, Jorritsma-Byham B, Witter MP (1997) GABAergic presubicular projections to the medial entorhinal cortex of the rat. J Neurosci 17:862–874.

Vogt BA, Miller MW (1983) Cortical connections between rat cingulate cortex and visual, motor, and postsubicular cortices. J Comp Neurol 216:192–210.

Ward JH Jr (1963) Hierarchical grouping to optimize an objective function. Journal of the American statistical association:236–244.

Winter SS, Clark BJ, Taube JS (2015) Spatial navigation. Disruption of the head direction cell network impairs the parahippocampal grid cell signal. Science 347:870–874.

Yoder RM, Peck JR, Taube JS (2015) Visual Landmark Information Gains Control of the Head Direction Signal at the Lateral Mammillary Nuclei. Journal of Neuroscience 35:1354–1367.

Yoder RM, Taube JS (2011) Projections to the anterodorsal thalamus and lateral mammillary nuclei arise from different cell populations within the postsubiculum: implications for the control of head direction cells. Hippocampus 21:1062–1073.

Yoder RM, Taube JS (2014) The vestibular contribution to the head direction signal and navigation. Front Integr Neurosci 8:32.

Zugaro MB, Arleo A, Berthoz A, Wiener SI (2003) Rapid spatial reorientation and head direction cells. Journal of Neuroscience 23:3478–3482.

Figure 1.

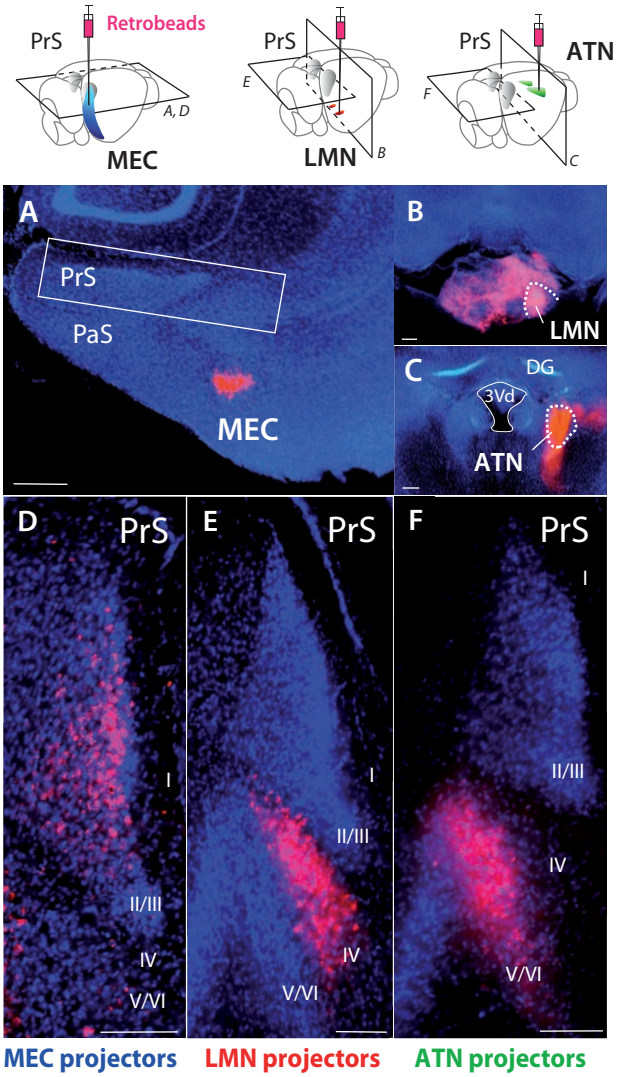
PrS
Retrobeads
A, D
MEC
PrS
E
LMN
B
PrS
ATN
F
C
A
PrS
PaS
MEC
B
LMN
C
DG
3Vd
ATN
D
PrS
I
II/III
IV
V/VI
E
PrS
I
II/III
IV
V/VI
F
PrS
I
II/III
IV
V/VI
MEC projectors
LMN projectors
ATN projectors

Figure 2.

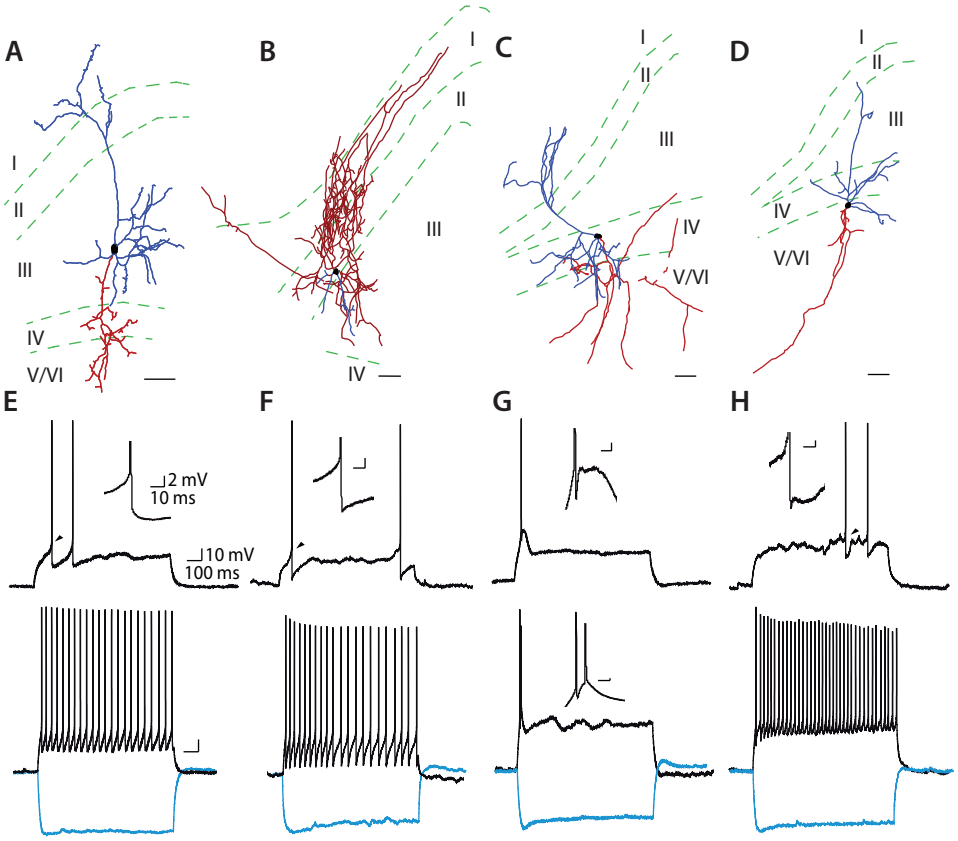

Figure 3.

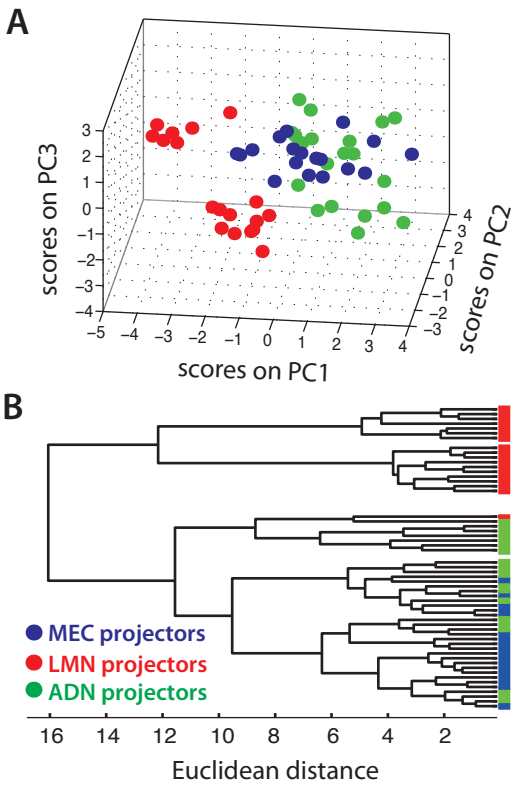
A
scores on PC3
scores on PC1
scores on PC2
B
MEC projectors
LMN projectors
ADN projectors
16 14 12 10 8 6 4 2
Euclidean distance

Figure 4.

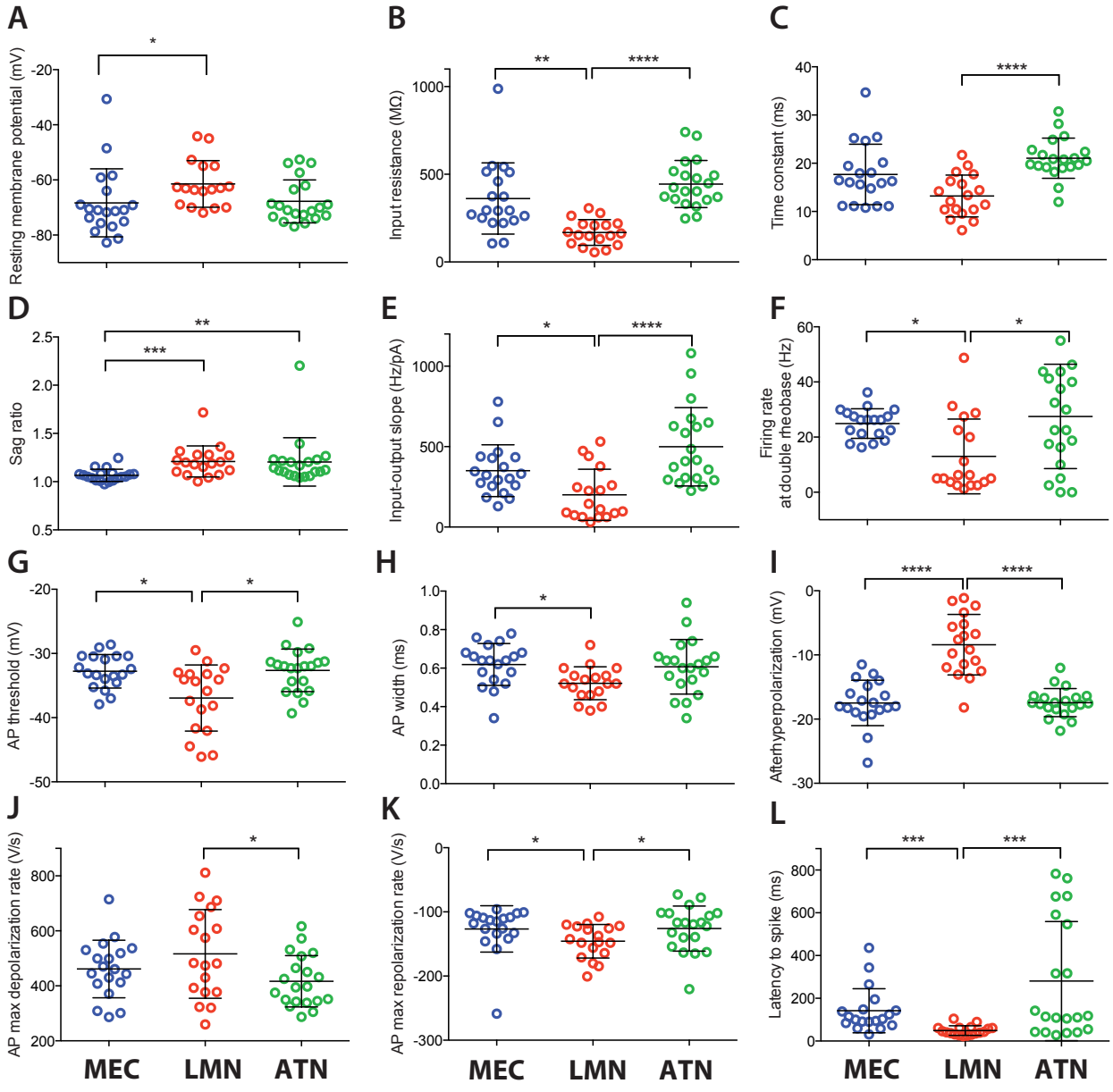
A
Resting membrane potential (mV)
B
Input resistance (MΩ)
C
Time constant (ms)
D
Sag ratio
E
Input-output slope (Hz/pA)
F
Firing rate at double rheobase (Hz)
G
AP threshold (mV)
H
AP width (ms)
I
Afterhyperpolarization (mV)
J
AP max depolarization rate (V/s)
K
AP max repolarization rate (V/s)
L
Latency to spike (ms)
MEC
LMN
ATN

Table 1. Comparison of intrinsic properties of identified projection-specific presubicular neurons.

	MEC projectors			LMN projectors			ATN projectors			MEC proj.	
	mean	sem	N	mean	sem	N	mean	sem	N	Martinotti	N
resting membrane potential (mV)	-70	2	18	-62	2	18	-68	2	20	-31	1
time constant tau (ms)	18	1	18	13	1	18	21	1	20	11	1
sag ratio	1.06	0.01	18	1.22	0.04	18	1.18	0.04	20	1.16	1
input resistance (MΩ)	367	49	18	166	17	18	444	30	20	262	1
firing rate at twice rheobase current (Hz)	25	1	18	13	3	18	28	4	20	26	1
f-I slope (Hz/nA)	334	34.8	18	190	37	18	499	54	20	654	1
AP threshold (mV)	-33	1	18	-37	1	18	-33	1	20	-32	1
AP amplitude (mV)	80	1	18	81	3	18	76	1	20	84	1
AP width (ms)	0.63	0.02	18	0.53	0.02	18	0.61	0.03	20	0.34	1
AP AHP (mV)	-17.0	0.7	18	-8.1	1.1	18	-17.4	0.5	20	-26.8	1
latency at rheobase	146	25	18	48	5	18	281	62	20	74	1
AP max. depol. (V/s)	457	25	18	524	38	18	417	21	20	537	1
AP max. repol. (V/s)	-119	4	18	-144	6	18	-126	8	20	-259	1

The underlined parameters (line 1-11) are used for PCA and cluster analysis in Fig. 3.

Article 5

Direct excitatory inputs from retrosplenial cortex onto pyramidal neurons and PV interneurons in layer 3 of the presubiculum

In addition to thalamic head direction inputs, the presubiculum also receives inputs from visual cortex and retrosplenial cortex providing a visual control that continually updates the head direction signal in the presubiculum. The present study is part of an ongoing work that aims to elucidate the long-range inputs from the retrosplenial cortex to both principal neurons and interneurons of the presubiculum.

I used the same approach as in my previous work (cf. Article 2) by injecting a viral vector containing ChR2-eYFP in the RSC. Similar to the ATN projections patterns, RSC axons target specifically superficial layers of the presubiculum. My preliminary data show typical monosynaptic latencies in principal neurons and PV interneurons after light onset with variable amplitude of EPSCs responses. Application of TTX/4AP did not abolish light-evoked EPSCs thus confirming the direct monosynaptic recruitment of these neurons. For the same intensity of stimulation, PV interneurons are likely to be activated more efficiently and rapidly than principal neurons by earlier evoked action potentials. All together, these results suggest that RSC inputs are likely to provide direct excitation onto double-recorded principal neurons and PV expressing interneurons.

ATN and RSC are both important contributors to the head direction signaling. However, at the presubicular microcircuit level, so far it remains unknown how the ATN-Prs and the RSC-PrS circuit differ from each other. Are the key components of feed-forward and feedback inhibitory patterns different from the one described in ATN-PrS circuit? Do the thalamic and retrosplenial axons converge on the same neuronal elements in the presubicular microcircuit? In the future, I wish to compare more precisely the ATN and RSC inputs onto principal neurons, PV interneurons as well as SST interneurons to answer these questions.

Direct excitatory inputs from retrosplenial cortex onto pyramidal neurons and PV interneurons in layer 3 of the presubiculum

Authors: Mérie Nassar, Bertrand Mathon and Desdemona Fricker

Introduction

The presubiculum, at the transition between the hippocampal archicortex and the six-layered neocortex, is involved in spatial orientation as it contains head direction cells that discharge as a function of the animal's directional heading. The generation and update of the presubicular head direction signal involves the integration of visual information. Indeed, the presubicular head direction signal is continuously updated by visual cues (Taube et al., 1990), receiving cortical projections from both visual (Vogt and Miller, 1983) and retrosplenial cortex (RSC; Vogt and Miller, 1983; Van Groen and Wyss, 1990a,b; Jones and Witter, 2007).

Anatomically, the RSC is divided in two parts, the dorsally located dysgranular retrosplenial cortex (Van Groen and Wyss, 1992), and the ventrally located granular retrosplenial cortex (Van Groen and Wyss, 1990a; Van Groen and Wyss, 2003). The projections of the dysgranular RSC terminate in layers 1, 2, 3 and 5/6 of the PrS (Van Groen and Wyss, 1992; Shibata, 1994; Jones and Witter, 2007; Sugar et al. 2011). The granular RSC projects to the same layers expect layer 2 of the PrS (Van Groen and Wyss, 1990a,b, 2003; Jones and Witter, 2007; Sugar et al. 2011). The projections of RSC to PrS show a topographical organization such that the rostrocaudal axis of origin in RSC correlates to a septotemporal terminal distribution in PrS (Sugar et al. 2011, 2016). Recently, direct inputs from the granular RSC have been shown to target preferentially layer 3 presubicular neurons which provide inputs to the superficial layers of MEC (Kononenko and Witter, 2012). Functionally, the presence of head direction cells in the RSC (Chen et al., 1994; Cho and Sharp, 2001) along with lesions of RSC (Clark et al. 2010; Harker and Whishaw, 2004; Nelson et al., 2015) that result in impairments in navigational tasks, support its functional importance in spatial cognition (Sutherland et al. 1988; Vann et al., 2009; Van Groen et al., 2004; Hindley et al., 2014; Alexander and Nitz, 2015).

The functional relevance of the RSC and its connectivity with the presubiculum strongly suggests a functional relationship between these areas. However, at the microcircuit level, how presubiculum processes retrosplenial information is still unresolved. In the present study, we

examined the long range inputs of RSC axons (both dysgranular and agranular parts) to the presubicular excitatory and fast-spiking inhibitory neurons in superficial layer 3 using opto-genetic tools and in vitro patch-clamp recordings.

Methods

Experiments were performed on four male Pvalb-Cre mice (Jax 008069; Hippenmeyer et al., 2005) crossed with the Ai14 Cre reporter line (Jax 007914; Madisen et al., 2010). Cre-mediated recombination resulted in the expression of red fluorescent tdTomato labeling in PV expressing interneurons. Mice aged postnatal day 25-35 were anesthetized intraperitoneally with ketamine hydrochloride and xylazine (100 and 15 mg.kg−1, respectively) and positioned in a stereotaxic frame for AAV2/9.hSyn.hChR2(H134R)-eYFP.WPRE.hGH in vivo unilateral injections. Both the granular and agranular retropslenial cortices were targeted with a single AAV injection (volume of virus 150nL). Typical coordinates from Bregma for RSC were lateral, +0.71mm; posterior -2.1 mm and depth 0.6 mm. After allowing 2 weeks for ChR2 expression, horizontal acute slices containing the hippocampus, subicular complex and ento-rhinal cortex were prepared for further patch-clamp recordings following the methods de-scribed in our previous study (Article 2, Nassar et al., in prep.).

Results

Selective ChR2 expression in the retrosplenial cortex

Two weeks after incubation, coronal slices were prepared to assess the effectiveness of the AAV-ChR2-EYFP injection in the RSC. An example illustrating the ChR2-eYFP fusion ex-pression with the corresponding fluorescence injection pattern in RSC is shown in fig. 1A. Consistent with previous studies (Van Groen and Wyss, 1990a,b; Van Groen and Wyss, 1992), ChR2-eYFP expressing RSC fibers project to ipsilateral ATN (both the dorsal and ventral part) as well as to the contralateral AV (Van Groen and Wyss, 1990a) (Fig. 1A). The fluorescently labeled axonal projections in the PrS is showed in horizontal slices for different dorso-ventral levels (Fig. 1B). Fluorescent (eYFP) labeled retrosplenial axons innervated superficial layers of presubiculum, more densely in layers 1 and 3 than layer 2. Layer 2 was characterized by the presence of patches separated from each other by RSC eYFP fibers at more dorsal levels. A few labeled axons were also found in deep pre-subicular layers, adjacent subiculum, parasubiculum and entorhinal cortex (Fig. 1B).

RSC axons directly excite principal neurons and PV expressing interneurons

To investigate the RSC inputs onto the different cellular elements of superficial layer L3, we performed double-recordings of neighboring principal neurons and PV expressing interneurons (Fig. 2) to measure the evoked EPSCs. At low intensity stimulations, post-synaptic EPSCs responses in pyramidal neurons (PNs) and PV expressing interneurons could be evoked reliably in control (n=5 neurons/n=2 mice) and during TTX perfusion if 4-AP was simultaneously present (Fig. 2A; n=2 double-recordings/n= 2 mice). Peak amplitude and latency of the light-evoked EPSCs were calculated for 2 double recordings of a PV cell and a PN (Fig. 2B, left panels). Mean amplitudes and latencies from single recorded PV (N=13, 103±41 pA, 2.2±0.15 ms) cells and PNs (N=21, 209±50 pA; 2.3±0.1 ms) after light onset were also calculated (Fig.2B, right panels). These initial data clearly indicate that RSC inputs provide direct excitatory inputs onto PNs and PV-FS interneurons. In the two double-recorded pyramidal neurons and interneurons, we also checked the spiking probability and timing of light-evoked action potentials. For the same minimal intensity of stimulation that made both recorded neurons fire, FS-PV cells always fired earlier than PNs (Fig. 2D-E; n=3 double-recordings/n=2 mice). At the beginning of a train of stimulations, PV neurons discharged in spike doublets in 3 out of 3 PV neurons tested.

Discussion

Here, we showed for the first time that RSC axons make direct functional contacts onto PN and PV neurons using optogenetic methods and pharmacological blockers. Our anatomical and functional connectivity data are consistent with previous reports (Sugar et al., 2011; Kononenko and Witter, 2012). Our initial results demonstrate that PV cells fire before PNs discharge which is then followed by another PV cell spike. Thus, inhibition might define a narrow window for pyramidal neuron discharge. The precise timing relation could play an important role in coordinating the head directional signal across different regions. The reciprocal connections between ATN, RSC and PrS may be crucial for parallel processing by maintaining the HD signal in working memory and updating it with visual information.

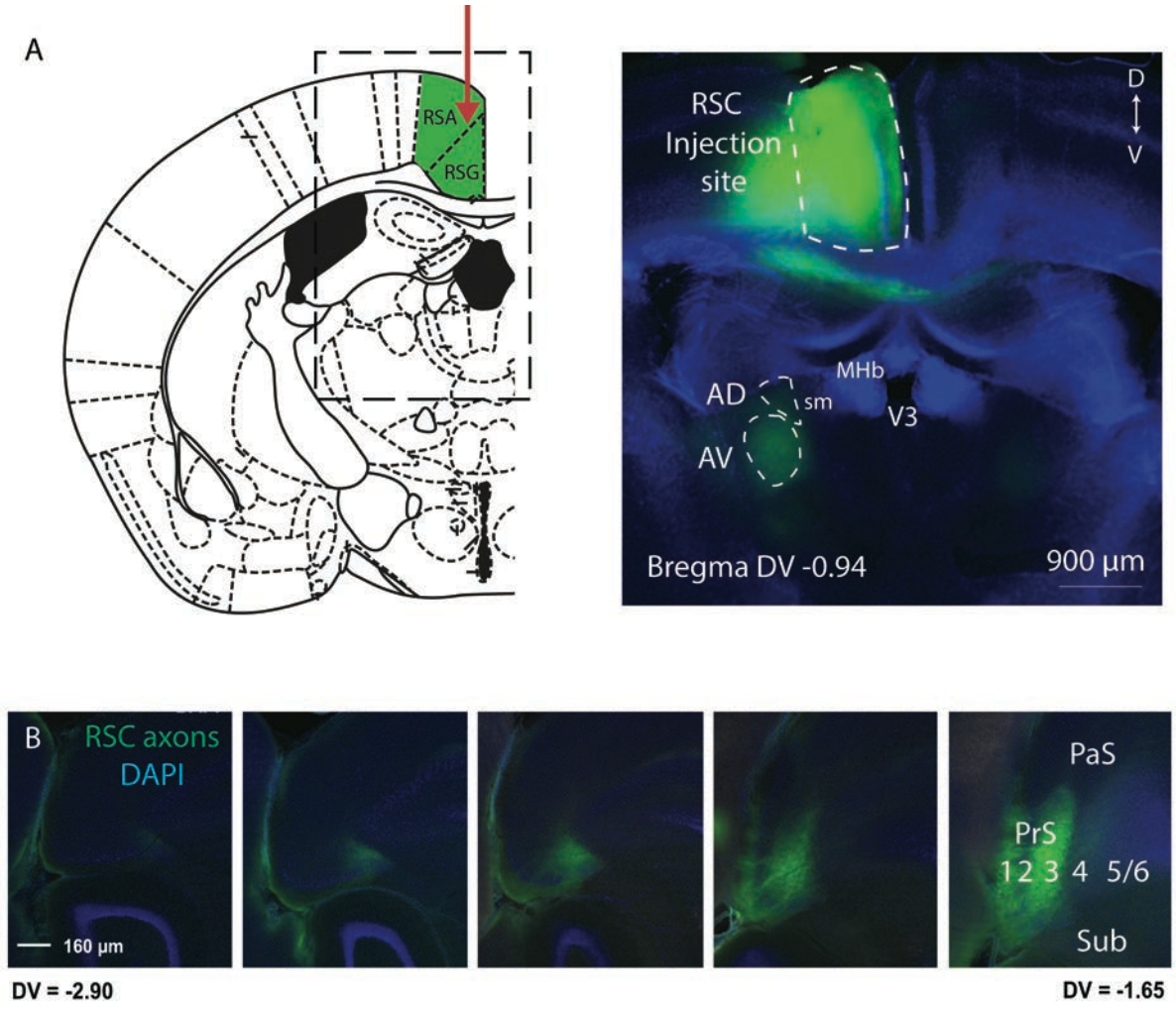

Figure 1: ChR2 expression in the retrosplenial cortex. **A**. Left, drawing of coronal slice at the level of the retrosplenial cortex (RSC) injection (0.94 from bregma). From Paxinos Mouse Atlas. Right, fluorescent image of a 300µm-thick coronal slice from unilaterally injected mouse with AAV2/9-ChR2-eYFP in the RSC. RSC projects ipsilaterally to the AD and bilaterally to AV of the ATN. **B**: Projection pattern of the ChR2 expressing retrosplenial axons in the presubiculum along the dorso-ventral axis in 150µm horizontal thick slices. PrS: presubiculum; Sub: subiculum; PaS: parasubiculum; sm: stria medullaris.

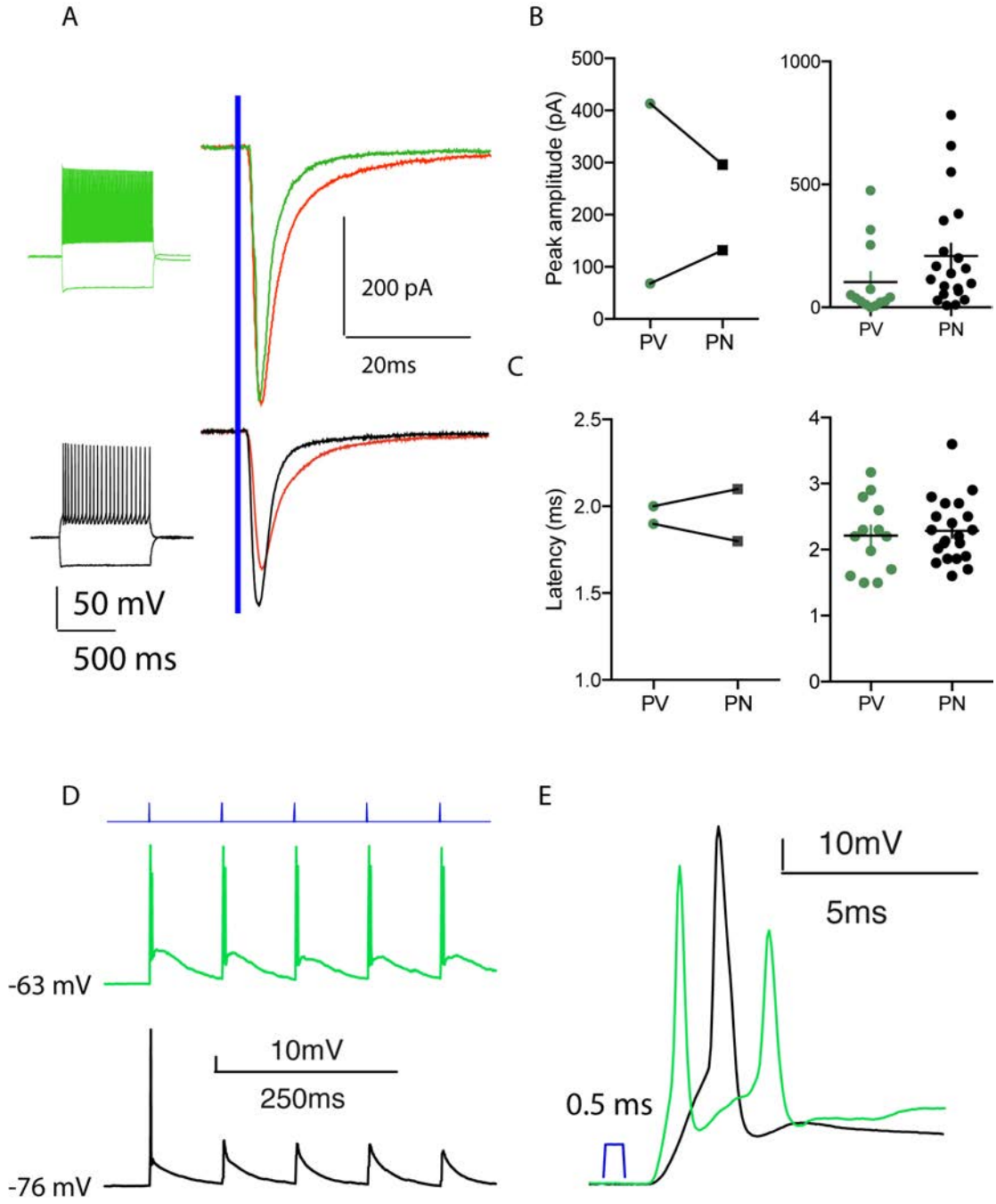

Figure 2: Retrosplenial inputs directly contact pyramidal neurons and PV expressing interneurons in the presubiculum. **A**. Left, firing patterns in response to hyperpolarizing and two-fold rheobase current injection of double recorded PV (top, green) and pyramidal neurons (PN, bottom, black) at -65mV holding potential. Right, single light-evoked EPSCs recorded at -60mV from the same neurons in control (Top, PV, green; Bottom, PN, black) and in the presence of TTX/4AP (Top, PV, red; bottom, PN, red) at -60mV following whole field LED stimulation (470nm, 0.5ms, 0.3mW). **B.** Absolute peak amplitude and (**C**) latency calculated from recorded PV cells and PNs in control condition. Left graphs are obtained from double recordings from PV cells and PNs. Right, graphs obtained from single recordings of PV cells and PNs **D**. Light-evoked action potentials or EPSPs in the same PV cell and PN recorded at their resting membrane potential in response to light pulses with the lowest stimulus intensity (0.3mW) at 10Hz. **E**. Enlargement of the first pulse in response in (**D**) to retrosplenial fiber light activation.

References

Alexander, A. S., and Nitz, D. A. (2015). Retrosplenial cortex maps the conjunction of internal and external spaces. *Nature Publishing Group*, *18*(8), 1143–1151.

Cho, J., and Sharp, P. E. (2001). Head direction, place, and movement correlates for cells in the rat retrosplenial cortex. *Behavioral Neuroscience*, 115, 3–25.

Chen, L. L., Lin, L. H., Barnes, C. A. and McNaughton, B. L. (1994). Head-direction cells in the rat posterior cortex - II. Contributions of visual and ideothetic information to the directional firing. *Experimental Brain Research*, 101(1):24–34.

Clark, B. J., Bassett, J. P., Wang, S. S., and Taube, J. S. (2010). Impaired head direction cell representation in the anterodorsal thalamus after lesions of the retrosplenial cortex. *The Journal of Neuroscience*, 30(15), 5289–5302.

Harker, K. T., and Whishaw, I. Q. (2004). A reaffirmation of the retrosplenial contribution to rodent navigation: reviewing the influences of lesion, strain, and task. *Neuroscience and Biobehavioral Reviews*, 28(5), 485–496.

Hindley, E. L., Nelson, A. J. D., Aggleton, J. P., and Vann, S. D. (2014). The rat retrosplenial cortex is required when visual cues are used flexibly to determine location. *Behavioural Brain Research*, 263, 98–107.

Hippenmeyer, S., Vrieseling, E., Sigrist, M., Portmann, T., Laengle, C., Ladle, D. R., et al. (2005). A developmental switch in the response of DRG neurons to ETS transcription factor signaling. *PLoS Biology*. 3:e159.

Jones, B. F. and Witter, M. P. (2007). Cingulate cortex projections to the parahippocampal region and hippocampal formation in the rat. *Hippocampus*, 17(10):957–976.

Kononenko, N. L., and Witter, M. P. (2012). Presubiculum layer 3 conveys retrosplenial input to the medial entorhinal cortex. *Hippocampus*, *22*(4), 881–895.

Nelson, A. J. D., Hindley, E. L., Haddon, J. E., Vann, S. D., and Aggleton, J. P. (2014). A novel role for the rat retrosplenial cortex in cognitive control. *Learning and Memory, 21*(2), 90–97.

Nelson, A. J. D., Hindley, E. L., Pearce, J. M., Vann, S. D., and Aggleton, J. P. (2015). The effect of retrosplenial cortex lesions in rats on incidental and active spatial learning. *Frontiers in Behavioral Neuroscience*, *9*, 11.

Shibata, H. (1994). Terminal distribution of projections from the retrosplenial area to the retrohippocampal region in the rat, as studied by anterograde transport of biotinylated dextran amine. *Neuroscience Research*, 20(4), 331–336.

Sugar, J., Witter, M. P., van Strien, N. M., and Cappaert, N. L. M. (2011). The retrosplenial cortex: intrinsic connectivity and connections with the (para)hippocampal region in the rat. An interactive connectome. *Frontiers in Neuroinformatics*, *5*, 7.

Sugar, J., and Witter, M. P. (2016). Postnatal development of retrosplenial projections to the parahippocampal region of the rat. *eLife*, *5*, 1–58

Sutherland, R. J., Whishaw, I. Q., and Kolb, B. (1988). Contributions of cingulate cortex to two forms of spatial learning and memory. *The Journal of Neuroscience,* 8, 1863–1872.

Taube, J. S., Muller, R. U., and Ranck, J. B. (1990). Head-direction cells recorded from the postsubiculum in freely moving rats. II. Effects of environmental manipulations. *The Journal of Neuroscience*, *10*(2), 436–447.

Vann, S. D., Aggleton, J. P., and Maguire, E. A. (2009). What does the retrosplenial cortex do? *Nature Reviews Neuroscience*, *10*(11), 792–802.

Van Groen, T. and Wyss, J. M. (1990a). Connections of the retrosplenial granular a cortex in the rat. *The Journal of Comparative Neurology*, 300(4):593–606.

Van Groen, T. and Wyss, J. M. (1990b). The postsubicular cortex in the rat: characterization of the fourth region of the subicular cortex and its connections. *Brain Research*, 529(1-2):165–177.

Van Groen, T. and Wyss, J. M. (1992). Connections of the retrosplenial dysgranular cortex in the rat. *The Journal of Comparative Neurology*, 315(2):200–216.

Van Groen, T. and Wyss, J. M. (2003). Connections of the retrosplenial granular b cortex in the rat. *The Journal of Comparative Neurology*, 463:249–263.

Van Groen, T., Kadish, I., and Wyss, J. M. (2004). Retrosplenial cortex lesions of area Rgb (but not of area Rga) impair spatial learning and memory in the rat. *Behavioral Brain Research*, 154(2), 483–491.

Vogt, B. A. and Miller, M. W. (1983). Cortical connections between rat cingulate cortex and visual, motor, and postsubicular cortices. *The Journal of Comparative Neurology*, 216(2):192–210.

Article 6

Presubicular principal neurons and Parvalbumin expressing neurons send long-range projections to the anterior thalamic nuclei

Head direction (HD) signaling is generated in the presubiculum from head direction information arising from subcortical areas via the ATN. Anatomically, the ATN projects to layers 1 and 3 of the presubiculum. In turn, neurons in the presubicular deep layers project back to the ATN, forming a feedback loop circuit that is likely to have subtle but measurable effect on the HD signal in the ATN. While I was studying the long-range thalamic projections onto the presubiculum (cf. Article 2), I noticed that some presubicular PV neurons could respond quasi-immediately to light activation of thalamic fibers. Knowing that AAV2/9 may be retrogradely transported, I wanted to test whether long-range presubicular PV interneurons could exist.

My preliminary data point to the existence of long-range PV interneurons from the presubiculum to the anterior thalamic nuclei. My evidence is based on retrograde labeling with retrobeads and retrograde viral tracers combined with optogenetics. These findings are surprising, even though long-range projecting GABAergic neurons have already been described in the hippocampal-entorhinal circuit as well.

I next wish to confirm evidence from tracing experiments with physiological evidence. This will be done by recording PSCs from thalamic neuron during light activation in the thalamus of Pvalb-Cre neuron axon terminals that have been transfected with AAV-FLEX-ChR2 in the presubiculum. Using immunohistochemistry, I will investigate the nature of these synapse using VGAT and VglutT1 staining. Further electron microscope studies will help us to reinforce this finding. In the future, it will be interesting to understand the functional impact of this reciprocal connection in the head direction signalling. Some other long-range inhibitory inputs that connect the presubiculum with the MEC should also be searched.

Article 6

Presubicular principal neurons and Parvalbumin expressing neurons send long-range projections to the anterior thalamic nuclei

Authors: Mérie Nassar and Desdemona Fricker

Introduction

The Head Direction (HD) signal is generated in subcortical regions, and then transmitted to the Anterior Thalamic Nuclei (ATN; Taube et al., 2007). The ATN conveys the head direction information to presubicular neurons, which in turn project to medial entorhinal cortex (MEC), where head direction cells and also grid cells are found. ATN and presubiculum are reciprocally connected, and this loop could be a key element in maintaining, refining and synchronizing head direction signals.

From combined lesion and recording studies it is known that the ATN transmits the head direction signal to the cortex, since ATN lesion abolishes head direction cell activity in presubiculum (Goodridge and Taube, 1997) and other downstream areas including parasubiculum and superficial layers of the medial entorhinal cortex (Clark and Taube, 2012; Winter et al., 2015). In contrast, lesion of the PrS has little effect on direction-specificity of ATN neurons. Presubicular lesions do however influence ATN HD neurons by increasing the extent of anticipation in ADN (Blair and Sharp, 1995) and disrupting visual landmarks based cue control in the ATN (Goodridge and Taube, 1997). The PrS-to-ATN projection therefore seems to provide feedback control and sensory update to the predictive thalamic HD signal. Coherent activity both within and across ATN and presubiculum is suggested to rely on an internally organized attractor network structure (Peyrache et al., 2015).

At the anatomical level, ATN projects to layers 1, 3 and 5 in the presubiculum (Van Groen and Wyss, 1995; Nassar et al., in prep). Conversely, most of the presubiculum-to-ATN projection arises from pyramidal neurons in the deep layers of the ipsilateral presubiculum (Van Groen and Wyss, 1990; Huang et al., in prep). We know already that the ATN-to-Presubiculum projection is glutamatergic in nature (Nassar et al., in prep). The presubicular feedback projection to ATN may include both glutamatergic and GABAergic elements. Superficial layer 3 fast-spiking interneurons are significantly modulated by angular velocity

(Preston-Ferrer et al., 2016). The activity of GABAergic neurons can extend well beyond local circuit regulation. Long-range projecting GABAergic neurons have been described in the hippocampal-entorhinal formation and are well suited to precisely coordinate theta activity between the hippocampus and the entorhinal cortex (Mizuseki et al., 2009, Melzer et al., 2012). Direct GABAergic projections mediated by PV or CB interneurons from the medial septum to the MEC (Mitchell et al., 1982; Gonzalez-Sulser et al., 2014; Fuchs et al., 2016) are likely to contribute to generation of theta oscillations and thus grid cell activity (Brandon et al., 2011; Koenig et al., 2011). In the present study, we investigate the possible contribution of long-range PV GABAergic neurons to the projection from the presubiculum to the anterior thalamic nuclei, using retrograde tracers and AAV aided anterograde tracing methods.

Methods

Experiments were performed on 14 Pvalb-Cre mice (Hippenmeyer et al., 2005) crossed (Fig. 1, 2 and 3) or not (Fig. 4) with the Ai14 Cre reporter line (Madisen et al., 2010). Cholera toxin B (CTB, Life Technologies) was used as a retrograde tracer for the visualization of projecting neurons. For AAV mediated eYFP labeling of presubicular PVcre neurons, we used AAV2/1.EF1a.DIO.eNpHR3.0-eYFP.WPRE.hGH (UPenn Vector core) carrying Cre-inducible halorhodopsin-3.0 (eNpHR3.0)-enhanced yellow fluorescent protein (eYFP) transgene driven by EF1a promoter. For ChR2-eYFP expression in ATN neurons, we used AAV2/9.hSyn.hChR2(H134R)-eYFP.WPRE.hGH (UPenn Vector core) containing an enhanced ChR2-eYFP fusion gene, driven by a hSynapsin promoter. The AAV serotype 9 exhibit a strong anterograde and also retrograde expression (Castle et al., 2014). Mice aged postnatal day 25-35 were anesthetized intraperitoneally with ketamine hydrochloride and xylazine (100 and 15 mg.kg−1, respectively). Unilateral stereotaxic injections of 250-300nL of 1% of Choleratoxin B, 150nL of AAV2/9-ChR2-eYFP or 350nL of AAV2/1-NpHR-eYFP were performed using previously described procedure (Mathon et al., 2015). The ATN was targeted for AAV2/9-ChR2-eYFP or CTB injections and typical coordinates from Bregma were lateral, +0.75 mm; posterior, -0.82 mm; and depth, 3.2 mm. Presubiculum was targeted for AAV2/1-NphR-eYFP injections and typical coordinates from Bregma were lateral +2mm; posterior -4.06mm; and depth 2.15 mm. After allowing 48h, 2 or 6 weeks for CTB, AAV2/9 or AAV2/1 incubation respectively, 60 µm thick horizontal slices were prepared for anatomical studies and 320µm thick slices for electrophysiological recordings. Procedures for electrophysiology and light stimulation were described previously (Nassar et al., in prep).

Results

To assess the identity and layer distribution of presubicular neurons projecting to the thalamus, we injected the retrograde tracer Cholera toxin B into the ATN of PVcre*::*dtTomato mice (n=2 mice; Fig. 1A). As expected, putative pyramidal neurons in deep layers of presubiculum were strongly labeled. Fig. 1B reveals the position of their cell bodies in layers V/VI, and in addition, green fluorescent labeling appears in layers 1 and 3, probably corresponding to ramifications of their dendritic arbors. We also detected some retrogradely labeled CTB+ neurons colocalized with PVcre::tdTomato+ labeling (Fig. 1C, D; total of 3 neurons in 1 out of 2 mice).

We next used injection of AAV2/9-ChR2-eYFP in the anterior thalamic nuclei of PVcre*::*dtTomato mice. The anterograde and retrograde expression of the AAV9 serotype gave 2 types of labeling in horizontal slices of presubiculum: (i) we observed anterograde ChR2-eYFP expression in thalamic axons that projected to superficial layers of the presubiculum, and (ii) we distinguished several retrogradely labeled cell bodies of Prs-to-ATN projecting neurons (Fig. 2). We found that overall, most of AAV2/9 retrogradely labeled cell bodies were also PVcre::tdTomato positive neurons. Further cell counting's will be needed to assess the number of retrogradely labelled PV neurons with both AAV-eYFP and dtTomato.

We recorded from 22 presubicular PV and 24 pyramidal neurons in the presubiculum, while applying a blue light stimulation to activate ChR2. Light-evoked inward currents were observed in all recorded neurons. The latency from light onset to 5% of peak amplitude was > 0.5 ms for n=22 pyramidal neurons (black dots) and n=11 PV interneurons (green dots) indicating that these neurons received short-latency monosynaptic inputs from thalamic axons. In the remaining n=2 pyramidal neurons and n=11 PV neurons, evoked inward currents were activated quasi-instantaneously at light onset with a latency from light onset to 5% of peak amplitude <0.5 ms and the currents persisted as a plateau as long as the duration of light stimulation (Fig. 3A, light duration 1, 5 or 10ms). These immediately activated currents could correspond to non-synaptic currents in neurons that directly express ChR2. To better distinguish between directly activated, ChR2-mediated, non-synaptic currents and monosynaptically activated short latency responses, we plotted their amplitudes, as measured at 0.5ms after the beginning of light stimulation, as a function of their onset latency (Fig. 3C). Interestingly, most dtTomato+ PV neurons recorded from animals with maternal Cre

(n=11/18 neurons) transmission exhibited directly activated, non-synaptic ChR2-mediated currents, while neurons with current responses with latency >0.5 ms were either recorded from animals with paternal (n=4/4) or maternal (n=7/18) Cre transmission.

To provide direct evidence for the presence of PV+ neurons projecting to the ATN, we injected the adeno-associated viral (AAV) vector AAV DIO NpHR-eYFP into the presubiculum of PVCre mice (Fig. 4A) allowing specific expression of the fluorescent fusion protein NphR-eYFP in presubicular PV neurons (Fig. 4B-C-D). We confirmed the fast-spiking phenotype from recording of a transfected, eYFP expressing PV neuron in presubiculum (Fig. 4B-D). EYFP-labeled axons of PV+ presubicular neurons projected to the ATN, where they appeared as basket-like structures around the soma of thalamic neurons (Fig. 4E-F; n=1 mouse).

Discussion

The head direction circuit is not a one-way street, but it involves crucial back projections, which intriguingly may rely on different neuron types. Here, we provide evidence that, in addition to principal neurons in deep layers of presubiculum, PV expressing neurons may also contribute to the presubicular-to-ATN projections. In a next step, we will need to confirm that presubicular dtTomato+ PV neurons expressing ChR2 make functional GABAergic synapses onto thalamic neurons. In order to answer this question, we will (i) stereotactically inject the AAV.FLEX. ChR2.eYFP virus into the presubiculum of PVCre mice, (ii) record in thalamic neurons surrounded by YFP labeled axons terminals, and (iii) stimulate them with blue light. It is unclear why CTB labelled very few dtTomato+ PV neurons while retrograde labelling with AAV9 revealed more dtTomato+ PV neurons but few dtTomato- PV neurons. We speculate that this could be due to a cell-type preference of the AAV9 itself or its promotor. Possibly the dtTomato+ labelling also depends on the parent-of-origin (Heffner et al., 2012) of the Cre allele, which could contribute to variability. What could be the consequence of the previously found, mixed excitatory-inhibitory feedback connection to the ATN? Eventually, *in vivo* optogenetic experiments should help to dissect the specific role of those PV long-range projecting neurons. Do they signal angular velocity (Preston-Ferrer et al. 2016)? We suggest that silencing of the inhibitory PV+ component of the presubicular-to-ATN projection might alter the precision and synchrony of the head direction signal across the brain.

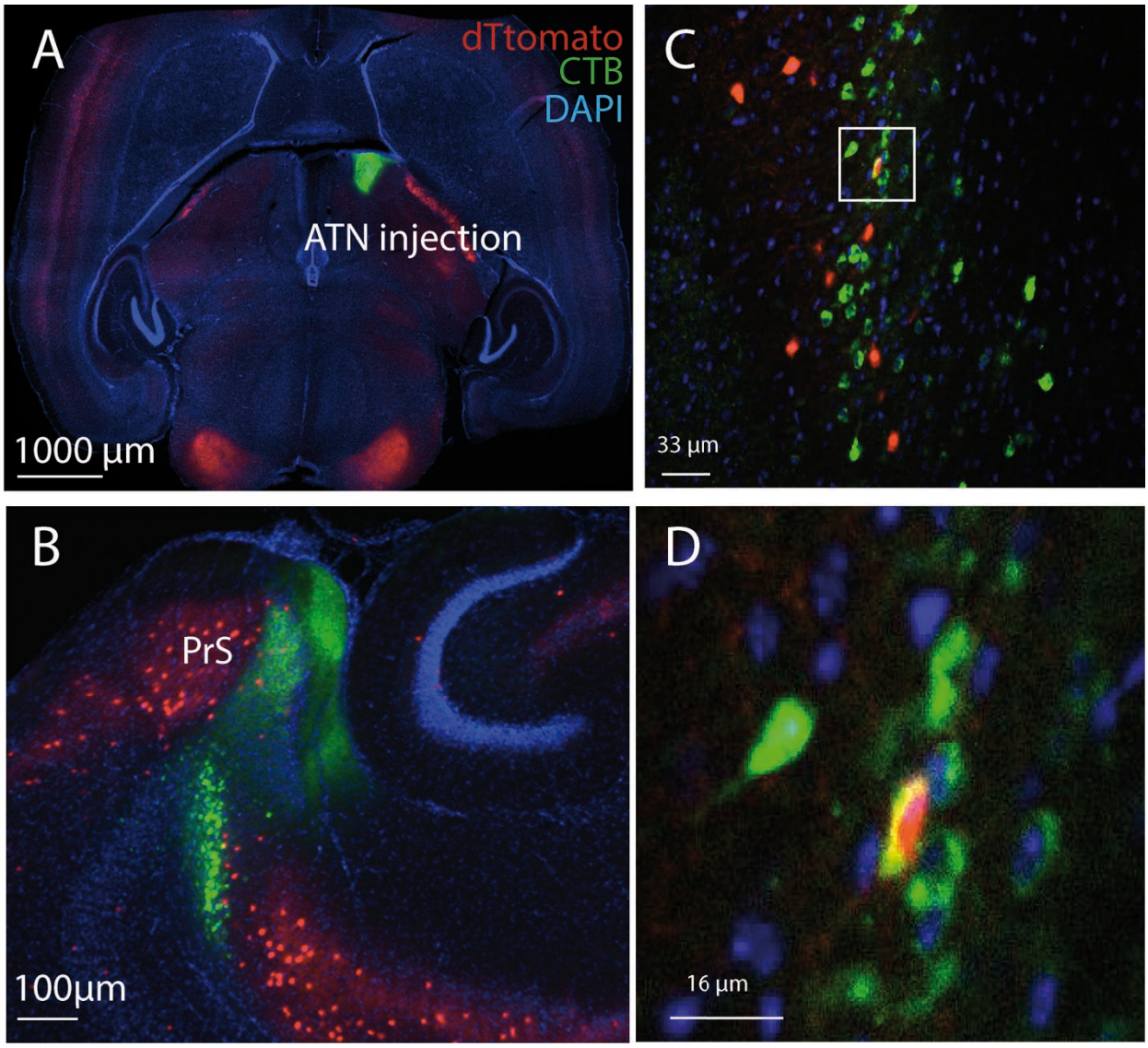

Figure 1: Retrograde labeling of presubicular neurons projecting to the thalamus. **A**. Fluorescent horizontal section (60µm-thick) showing the unilateral injection site of the retrograde tracer CTB in the ATN of PVCre::dtTomato mouse. **B**. Magnified image of the hippocampal formation showing ATN projectors in deep layers of the ipsilateral presubiculum, with apical dendrites extending to layer 1. **C.** 20X image stack of presubicular deep layer projecting neurons. **D.** Enlargement of the white box in (**C**) showing co-labeling of one dTtomato+ PV neuron with CTB. Tomato in red. CTB in green. DAPI in blue.

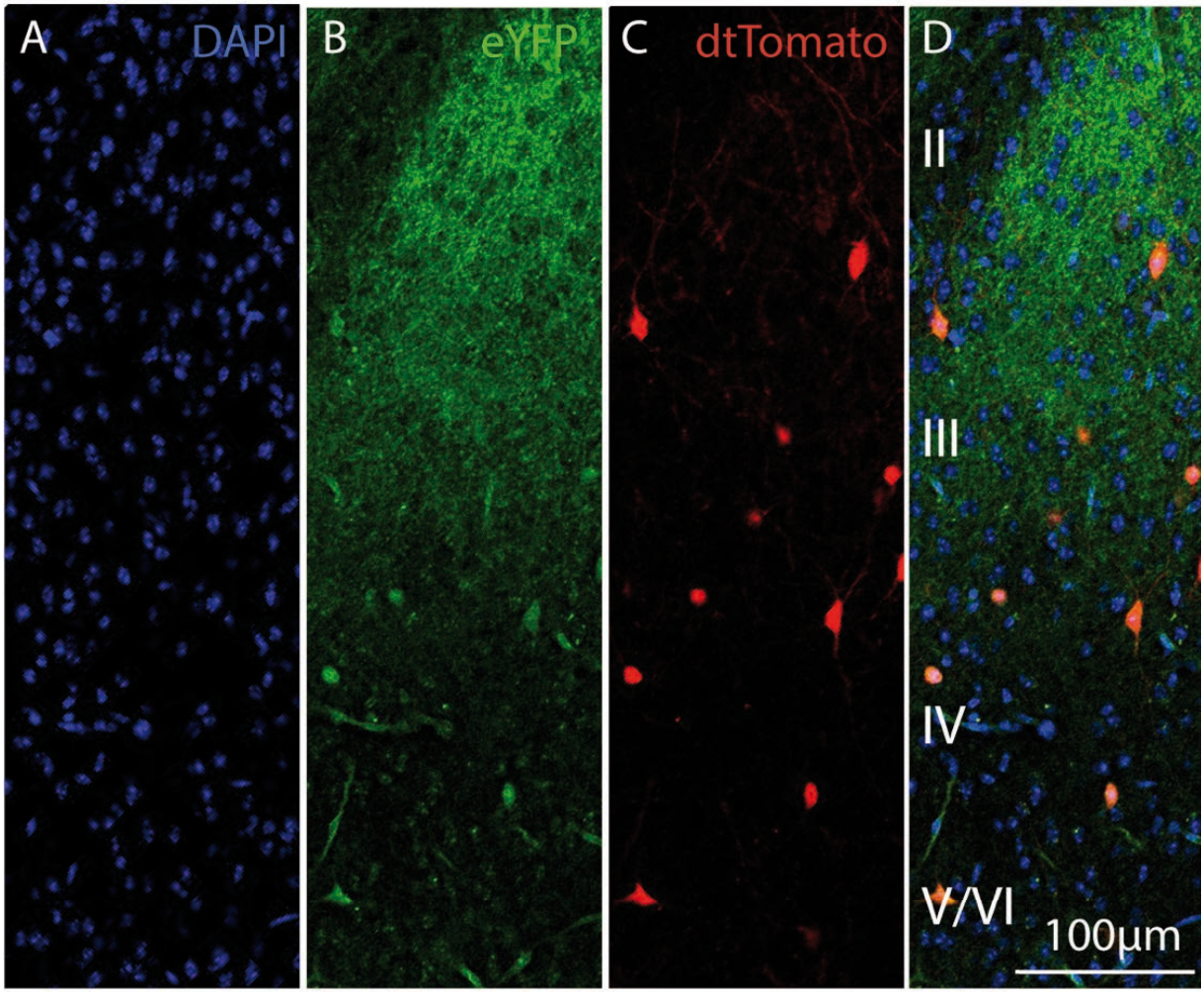

Figure 2: Anterograde labeling of thalamic axons and retrograde expression following AAV2/9 injection in the anterior thalamic nuclei. Confocal image from a horizontal section of presubiculum showing (**A**) presubicular layers with DAPI staining (blue), (**B**) thalamic axons expressing ChR2-eYFP (green) mostly in layer 3, **(C)** dtTomato labelled neurons from Pvalb-Cre line, and (D) merged image showing retrogradely labeled cell bodies which are mostly dtTomato+.

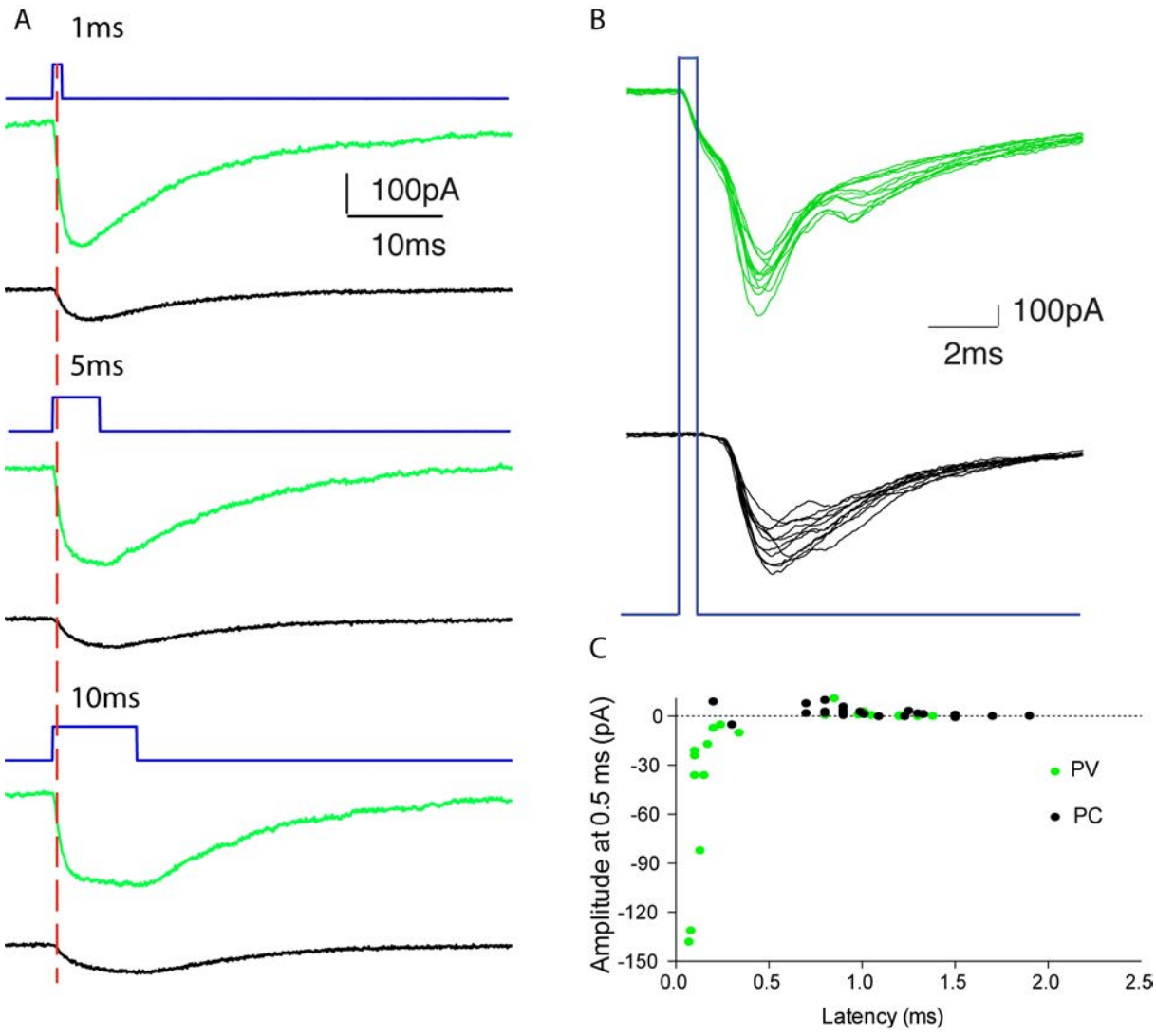

Figure 3: Monosynaptic vs immediate, non-synaptic activation of PV interneuron and pyramidal neuron after light activation of thalamic fibers with ChR2. **A**. Activation of double recorded PV (green traces) and Pyr (black traces) concurrently to 1 (top), 5 (middle) and 10 (bottom) ms light activation of ATN fibers. Evoked currents showed a persistent plateau all along the duration of the stimulation. **B**. 10 superimposed traces of monosynaptically activated pyramidal neuron (latency > 0.5ms) and immediately activated PV cell (< 0.5 ms) recorded at -70 mV with intra-pipette solution containing QX (2mM). **C**. Amplitude of light-evoked currents measured 0.5 ms after light onset. Some PV interneurons and pyramidal neurons are activated quasi immediately after light onset (amplitude ranges from -130 to -5 pA at 0.5ms), while monosynaptic activation of EPSCs occurs with a delay, with a close-to-zero current amplitude at time point 0.5ms. PV interneurons (green dots) and Pyr neurons (black dots).

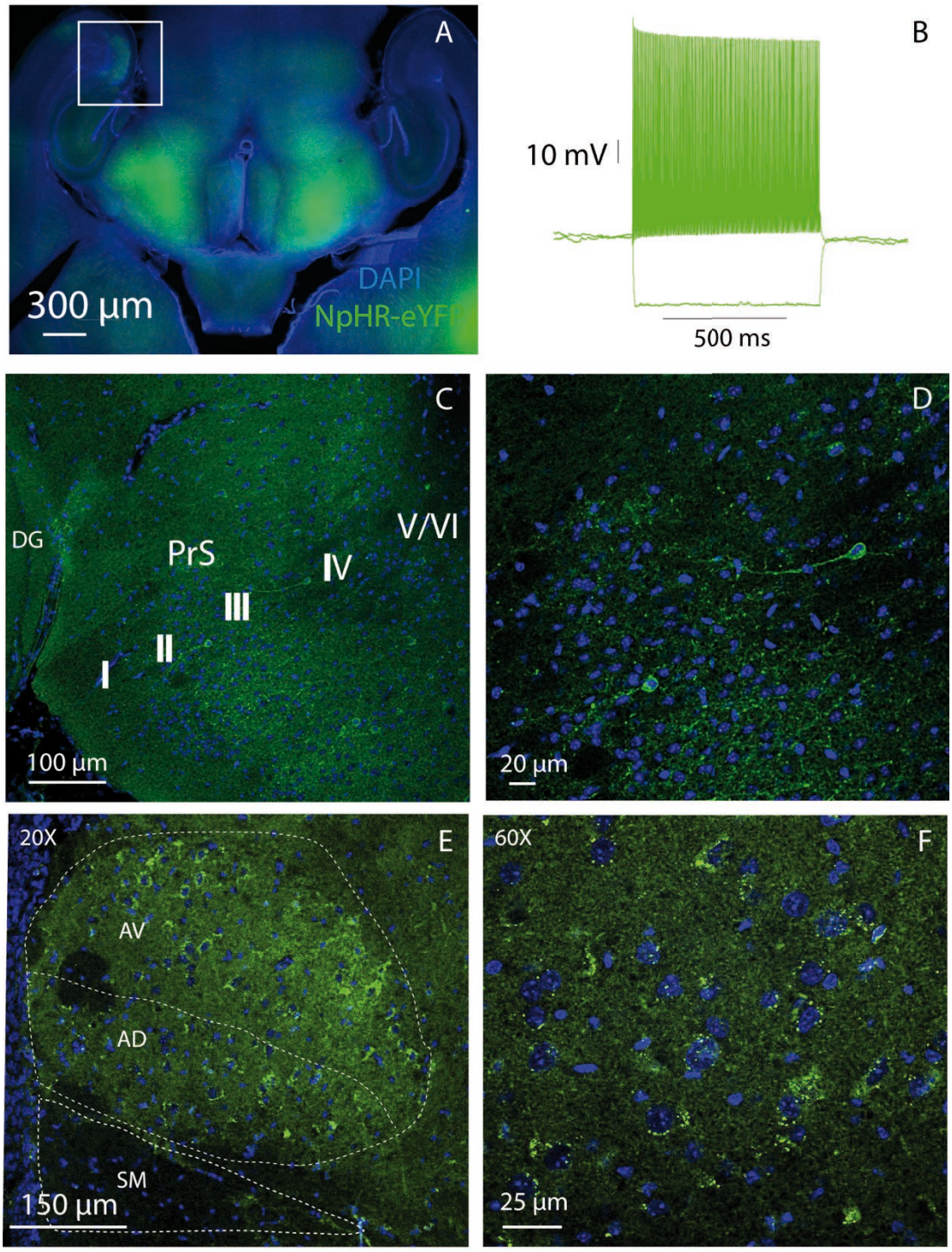

Figure 4: Long-range projecting presubicular FS-PV interneurons target the anterior thalamic nuclei. **A**. AAV.DIO.NpHR-eYFP was unilaterally injected in the presubiculum of PVCre mice. The injection site is indicated with a white box and shown as magnified image in (**C**) and (**D**). Structures are labeled with DAPI staining (blue). B. Firing pattern from a recorded NpHR-eYFP labelled neuron with typical fast-spiking properties. **C**. Confocal image of PV+ labeled neurons in all layers of the presubiculum shown in higher magnification in (**D**). Note the somatic, dendritic and axonal expression of eYFP (green) labelled neurons. **E**. eYFP axons of long-range projecting presubicular cells in ipsilateral ATN (AD and AV). **F**. Higher magnification image in AD reveals basket like structures surrounding the somata of thalamic neurons.

REFERENCES

Blair, H. T., and Sharp, P. E. (1995). Anticipatory head direction signals in anterior thalamus: evidence for a thalamocortical circuit that integrates angular head motion to compute head direction. *The Journal of Neuroscience*, *15*(9), 6260–6270.

Brandon, M. P., Bogaard, A. R., Libby, C. P., Connerney, M. A., Gupta, K., and Hasselmo, M. E. (2011). Reduction of theta rhythm dissociates grid cell spatial periodicity from directional tuning. *Science*, *332*(6029), 595–599.

Castle, M. J., Gershenson, Z. T., Giles, A. R., Holzbaur, E. L. F., and Wolfe, J. H. (2014). Adeno-associated virus serotypes 1, 8, and 9 share conserved mechanisms for anterograde and retrograde axonal transport. *Human Gene Therapy*, *25*(8), 705–720.

Clark, B. J. and Taube, J. S. (2012). Vestibular and attractor network basis of the head direction cell signal in subcortical circuits. *Frontiers in neural circuits*, 6:7.

Fuchs, E. C., Neitz, A., Pinna, R., Melzer, S., Caputi, A., and Monyer, H. (2016). Local and distant input controlling excitation in layer 2 of the medial entorhinal cortex. *Neuron*, *89*(1), 194–208.

Gonzalez-Sulser, A., Parthier, D., Candela, A., McClure, C., Pastoll, H., Garden, D., et al. (2014). GABAergic projections from the medial septum selectively inhibit interneurons in the medial entorhinal cortex. *The Journal of Neuroscience*, *34*(50), 16739–16743.

Goodridge, J. P. and Taube, J. S. (1997). Interaction between the postsubiculum and anterior thalamus in the generation of head direction cell activity. *The Journal of Neuroscience*, 17(23): 9315–9330.

Heffner, C. S., Pratt, C. H., Babiuk, R. P., Sharma, Y., Rockwood, S. F., Donahue, L. R., et al. (2012). Supporting conditional mouse mutagenesis with a comprehensive cre characterization resource. *Nature Communications*, *3*, 1218–9.

Hippenmeyer, S., Vrieseling, E., Sigrist, M., Portmann, T., Laengle, C., Ladle, D. R., and Arber, S. (2005). A developmental switch in the response of DRG neurons to ETS transcription factor signaling. *PLoS biology*, 3(5):e159.

Koenig, J., Linder, A. N., Leutgeb, J. K., and Leutgeb, S. (2011). The Spatial Periodicity of Grid Cells Is Not Sustained During Reduced Theta Oscillations. *Science*, *332*(6029), 592–595.

Madisen, L., Zwingman, T. A., Sunkin, S. M., Oh, S. W., Zariwala, H. A., Gu, H., Ng, L. L., Palmiter, R. D., Hawrylycz, M. J., Jones, A. R., Lein, E. S., and Zeng, H. (2010). A robust and high-throughput Cre reporting and characterization system for the whole mouse brain.

Nature Publishing Group, 13(1):133–140.

Mathon, B., Nassar, M., Simonnet, J., Le Duigou, C., Clemenceau, S., Miles, R., and Fricker, D. (2015). Increasing the effectiveness of intracerebral injections in adult and neonatal mice: a neurosurgical point of view. *Neuroscience Bulletin*, 1–12.

Melzer, S. (2012). Long-Range–Projecting Gabaergic Neurons Modulate Inhibition in Hippocampus and Entorhinal Cortex. *Science*, *335*(6075), 1503–1506.

Mitchell, S. J., Rawlins, J. N., Steward, O., and Olton, D. S. (1982). Medial septal area lesions disrupt theta rhythm and cholinergic staining in medial entorhinal cortex and produce impaired radial arm maze behavior in rats. *The Journal of Neuroscience*, *2*(3), 292–302.

Mizuseki, K., Sirota, A., Pastalkova, E., and Buzsáki, G. (2009). Theta oscillations provide temporal windows for local circuit computation in the entorhinal-hippocampal loop. *Neuron*, *64*(2), 267–280.

Peyrache, A., Lacroix, M. M., Petersen, P. C., and Buzsáki, G. (2015). Internally organized mechanisms of the head direction sense. *Nature Publishing Group*, *18*(4), 569–575.

Preston-Ferrer, P., Coletta, S., Frey, M., and Burgalossi, A. (2016). Anatomical organization of presubicular head-direction circuits. *eLife*, *5*, e14592.

Taube, J. S. (2007). The head direction signal: origins and sensory-motor integration. *Annual Review of Neuroscience*, *30*, 181–207.

Van Groen T, and Wyss, J. M. (1990). The postsubicular cortex in the rat: characterization of the fourth region of the subicular cortex and its connections. *Brain Research*, *529*(1-2), 165–177.

Van Groen, T. and Wyss, J. M. (1995). Projections from the anterodorsal and anteroventral nucleus of the thalamus to the limbic cortex in the rat. *The Journal of Comparative Neurology*, 358(4):584–604.

Winter, S. S., Clark, B. J., and Taube, J. S. (2015). Disruption of the head direction cell network impairs the parahippocampal grid cell signal. *Science*, *347*(6224), 870–874.

Article 7

Increasing the effectiveness of intracerebral injections in adult and neonatal mice: a neurosurgical point of view

Stereotaxic surgery is an advantageous tool in systems neuroscience that has been used in many experiments for the creation of site-targeted lesions, injection of anatomical tracers or viral constructs as well as the implantation of electrodes. Intracerebral stereotaxic injections of tracers or viruses provides a useful approach to label and study long-range projections.

In this protocol, we describe intracerebral injections optimized for gene delivery by recombinant adeno-associated viruses and tracers in adult mice. Moreover, we describe a two-handed procedure for stereotaxic injections in neonatal mice. Overall, our protocol is optimized to provide reproducible results with high probability of success in targeting the injection site in a very short time and safe manner.

·Method·

Increasing the effectiveness of intracerebral injections in adult and neonatal mice: a neurosurgical point of view

Bertrand Mathon[1, 2], Mérie Nassar[2], Jean Simonnet[2], Caroline Le Duigou[2], Stéphane Clemenceau[1], Richard Miles[2], Desdemona Fricker[2]

[1]*Department of Neurosurgery, Groupe Hospitalier Universitaire de La Pitié-Salpêtrière, APHP, F-75013, Paris, France*

[2]*Inserm, U 1127, F-75013, Paris, France; CNRS, UMR 7225, F-75013, Paris, France; Sorbonne Universités, UPMC Univ Paris 06, UMR S 1127, F-75013, Paris, France; Institut du Cerveau et de la Moelle épinière, ICM, F-75013, Paris, France*

Corresponding author: Bertrand Mathon. E-mail: bertrand.mathon@neurochirurgie.fr

ABSTRACT

Intracerebral injections of tracers or viral constructs in rodents are now commonly used in the neurosciences and must be executed perfectly. The purpose of this article is to update existing protocols for intracerebral injections in adult and neonatal mice. Our procedure for stereotaxic injections in adult mice allows the investigator to improve the effectiveness and safety, and save time. Furthermore, for the first time, we describe a two-handed procedure for intracerebral injections in neonatal mice that can be performed by a single operator in a very short time. Our technique using the stereotaxic arm allows a higher precision than freehand techniques previously described. Stereotaxic injections in adult mice can be performed in 20 min and have >90% efficacy in targeting the injection site. Injections in neonatal mice can be performed in 5 min. Efficacy depends on the difficulty of precisely localizing the injection sites, due to the small size of the animal. We describe an innovative, effortless, and reproducible surgical protocol for intracerebral injections in adult and neonatal mice.

Keywords: rodents; surgery; neurosciences; stereotaxic injection; newborn mice; neonatal brain

INTRODUCTION

Intracerebral injections of tracers or viral constructs in rodents have contributed much to our understanding of the nervous system by targeting specific areas of the brain. These techniques are now commonly used in the neurosciences[1, 2]. Because experimental results depend on intracerebral injections, they have to be perfectly executed. Although intracerebral injection procedures in adult[3] and newborn[4-6] mice have already been described, the purpose of this article is to update these protocols. Our aim is to detail, step by step, an easy and reproducible procedure to allow the investigator to improve the effectiveness and safety of this surgery, and save time. Using our neurosurgical experience in humans, we apply the principles to rodents and propose tips to circumvent the difficulties of the procedures. Furthermore, for the first time, we describe a two-handed procedure for intracerebral injections in neonatal mice.

MATERIALS

Stereotaxic Intracerebral Injections in Adult Animals

REAGENTS

- -Experimental mice (use of live mice must conform to institutional rules)
- -Sterile saline (0.9% NaCl)
- -Distilled water
- -Ophthalmic gel
- -Anesthetics: ketamine hydrochloride / xylazine hydrochloride solution (Sigma®) [or ketamine (Imalgene®) + xylazine (Rompun®)] or isoflurane

(Iso-Vet®) (ketamine is a narcotic and should be used according to the regulations of the host institution). Some investigators use tribromoethanol (Avertin®) as the anesthetic for rodents (it is not a narcotic).
-Analgesics: buprenorphine (Vetergesic®; this is a narcotics and should be used according to the regulations of the host institution), ketoprofene (Ketoprofene Arrow®)
-Injection fluid: virus, enzyme, tracer…
-Crushed ice
-Lidocaine (Xylovet®) (local anesthetic, optional)
-Iodine-based wash (Betadine®, optional)
-Hydrogen peroxide (optional)

EQUIPMENT (Fig. 1)
-Stereotaxic apparatus (e.g., Stoelting®, Digital Lab Standard for mouse, or David Kopf Instruments® for mouse or rat)
-Stereotaxic injection system (Harvard Apparatus®, Pump 11 Elite)
-Dissecting microscope (Leica® S6E)
-Temperature-controlled heating cage (VetTech Solutions® HE011),
-Surgical tools: surgical scissors, fine forceps, surgical hook or 26-gauge needle, black leader for human spinal anesthesia (Braun, Spinocan 4509900), needle holder
-Surgical braided absorbable suture (Vicryl 3-0, Ethicon®)
-High-speed dental drill with small drill-bits (Foredom® 38,000 rpm)
-10 μL injection syringe (Hamilton® 1700) with flexible (silica) 33-gauge needle (Phymep®), or rigid 33-gauge needle (Hamilton® 7762-03)
-10 μL calibrated micropipettes (Eppendorf® Research Plus)
-Container of crushed ice to preserve injection fluid
-Cotton swab
-Laboratory film (Parafilm®)
-Precision wipes (Kimtech Science®)
-10 mL-syringes,
-Isoflurane vaporizer (optional)
-Electric shaver (optional)

Intracerebral Injections in Neonatal Animals

REAGENTS

-Experimental new-born mice (postnatal days 0-1 (P0-P1); use of live mice must conform to institutional regulations),
-Crushed ice
-Sterile saline (NaCl 0.9%)
-Distilled water
-Injection fluid: virus, enzyme, tracer…
-Iodine-based wash (Betadine®; optional)
-Mineral oil (optional)

EQUIPMENT (Fig. 1)
-Stereotaxic apparatus (Stoelting®, Digital Lab Standard)
-Stereotaxic injection system (Harvard Apparatus®, Pump 11 Elite)
-Dissecting microscope (Leica® S6E)
-Temperature-controlled heating cage (VetTech Solutions® HE011)
-Surgical tools: 30-gauge needle
-10 μL injection syringe (Hamilton® 1700) with rigid 33-gauge needle (Hamilton® 7762-03)
-10 μL calibrated micropipettes (Eppendorf® Research Plus)
-Polystyrene foam stage
-Container of crushed ice to preserve the injection fluid and induce anesthesia
-Petri dish
-Cotton swab
-Laboratory film (Parafilm®)
-Precision wipes (Kimtech Science®)
-Aluminum foil
-Syringes

PROCEDURES

Stereotaxic Intracerebral Injections in Adult Animals

Step 1: Anesthesia

Weigh the animal and calculate the appropriate dose for anesthesia. We use a mixture of ketamine and xylazine given intraperitoneally. Doses are summarized in Table 1. To inject the ketamine-xylazine mixture, restrain the animal with one hand, abdomen up. Inject the mixture intraperitoneally through a 21-gauge needle inserted into the lower left or right abdominal quadrant (Fig. 2A). Immediately place the animal in the heating cage to

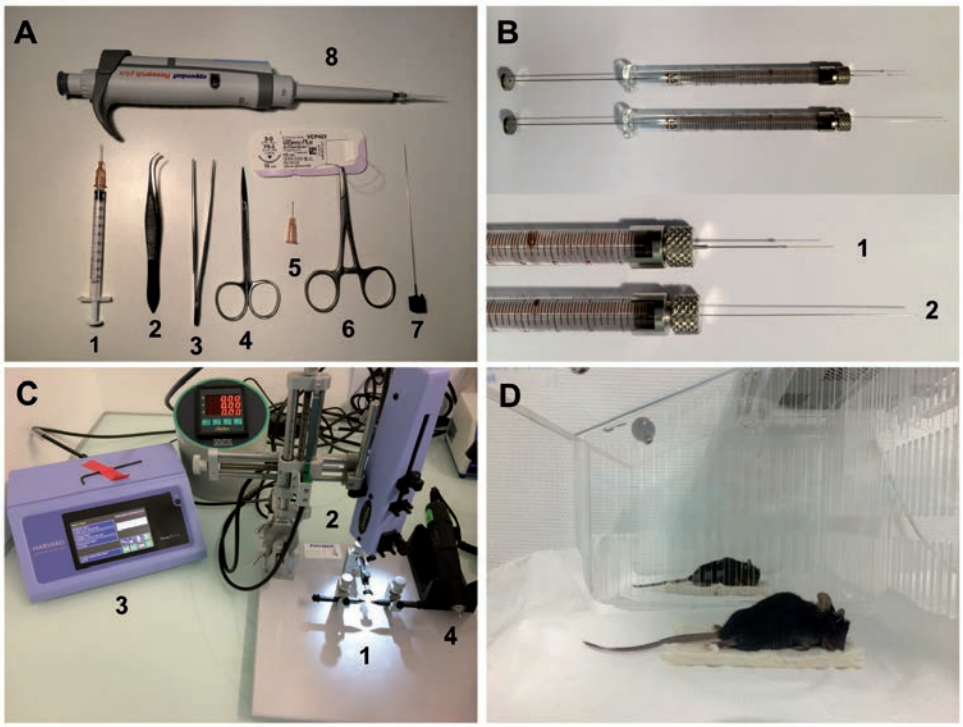

Fig. 1. Equipment required for intracerebral injections in mice. (A) Surgical tools. 1, 1 mL syringe for anesthesia; 2 and 3, fine forceps; 4, surgical scissors; 5, surgical hook; 6, needle holder with surgical braided absorbable suture; 7, black leader for human spinal anesthesia; 8, 10 µL calibrated micropipette. (B) 10 µL injection syringes with 1, flexible or 2, rigid 33-gauge needle. (C) Surgical area. 1 and 2, Stereotaxic apparatus with stereotaxic arm; 3, Stereotaxic injection system; 4, High-speed dental drill with small drill-bits. (D) Temperature-controlled heating cage.

maintain body temperature. The animal should reach deep anesthesia within ~10 min. Check the lack of response to nociceptive stimuli to confirm depth of anesthesia by pinching the tail. Instead of ketamine-xylazine mixture, vaporized isoflurane may be used to obtain surgical anesthesia (Table 1). *Pre-anesthesia with atropine is unnecessary for adult animals, but you may perform local anesthesia using lidocaine given subcutaneously (optional) (Table 1).*

Step 2: Preparation of the Animal

Shave the fur on the skull, clean the skin with iodine-based wash (optional because infection in rodents is almost nonexistent)[7]. Apply lubricant ophthalmic gel to both eyes to avoid keratitis during surgery. Pull out the tongue using forceps to facilitate breathing (Fig. 2B). Make a straight midline incision through the skin with surgical scissors from the back of the neck to the interpupillary line (the incision must run far enough along the anterior–posterior axis to expose stereotaxic markers). Softly push aside the connective tissue on top of the skull as needed for a clear view.

Step 3: Fixation of the Animal in the Stereotaxic Apparatus (for Right-handers)

To place the animal in the stereotaxic apparatus, fix the left ear bar to a predefined scale (e.g., 4 mm). Position the animal's head to lead its left ear canal onto the ear bar; the tip of the ear bar should pull the skin to expose the skull. An auxiliary ear bar (EB-5N, Narishige Co. Ltd., Tokyo, Japan) may assist the investigator in fixing the animal's head. Keep the animal's head in place using your left index finger to sustain the head and position the right ear bar to the same scale applying soft pressure to complete the fixation (Fig. 2C). In the right position, the animal's head is straight and symmetrical to the ear bars and cannot move laterally. If the animal's head position looks incorrect or is unstable, repeat the procedure.

With your right hand, insert the incisor adapter into the animal's mouth until the animal's incisors 'fit' in the opening

of the adapter. The animal's head can be freely moved up by using your left index finger on the back of its neck to facilitate the insertion of the incisor adapter (Fig. 2D). Then slightly pull back the incisor adapter to check its correct position and allow moderate extension of the animal's head. Fix the incisor adapter in place. Finally, place the snout clamp just below the eyes using low pressure. At this point in the procedure, the animal's head should be perfectly fixed in the stereotaxic apparatus. *For left-handers, reverse the sides of the procedure.*

Step 4: Alignment of Bregma and Lambda ("Flat-Skull" Step)

Make sure that the top of the animal's skull is in the horizontal plane. For this, the head position may be adjusted using the screw at the incisor adapter. Then place the injection syringe into the holder of the stereotaxic arm.

The following step is optional if your target injection is neocortical or superficial. Use a dissecting microscope at ×20 magnification. Make sure that bregma and lambda are easily distinguishable (Fig. 2E). Level the animal's head horizontally by measuring the dorsal-to-ventral (Z) coordinates of bregma and lambda and adjusting the head position so that they become equal using the adjustment screw at the incisor adapter (Fig. 2F). A 50-μm difference between bregma and lambda can be tolerated.

Step 5: Craniotomy and Opening the Dura

Use a dissecting microscope at ×20 to ×40 magnification. Consider the position of bregma as the reference (stereotaxic zero) of the *X* and *Y* coordinates. Using predefined stereotaxic coordinates, mark on the skull the intended site of injection. Adjust the drill to 20,000 rpm. Make a single burr-hole in the skull at the injection site. For this purpose, refine the bone by circular movements of a small drill-bit while applying very gentle pressure on the skull. Too much pressure may cause the drill to penetrate the skull and directly damage the brain parenchyma. Keep the drill-bit moist with sterile saline, applied drop-wise throughout the drilling to avoid heat generation and make the bone transparent. Stop when the drill-bit reaches the internal cortical layer of the skull. A thin layer of skull may remain. Using a 26-gauge surgical hook, remove the small pieces of any remaining skull to expose the dura. Flush the site with sterile saline to remove bone dust and possible blood. Open the dura by making a small incision with the leader for spinal anesthesia (*opening of the dura is optional if you use a rigid needle or micropipette, but necessary if you use a flexible needle*). Finally, position the syringe over the craniotomy and check that it is not diverted by the edge of the burr-hole. If the syringe is diverted, widen the craniotomy.

Step 6: Preparation for Injection

Adjust the features of fluid aspiration on the injection system (the aspirated volume should be 10% larger than the injected volume, or at least +100 nL, for small volumes). Pipet the desired volume of fluid onto a precut square of laboratory film; then bring the needle of the syringe into the drop under visual control with the dissecting microscope and suck up the fluid. If you are not comfortable with this, you can place the laboratory film on top of the skull or directly apply aspiration into the tube containing the fluid. Aspiration speed can be up to 38 μL/min (slower aspiration is preferred for viscous fluid). Check that the drop has been aspirated on the laboratory film. *Critical*: Make sure that the needle is not clogged by ejecting a small volume of fluid (e.g. 50 nL) under visual control. A droplet should be seen forming at the tip.

Step 7: Injection

Position the syringe over the burr-hole. Lower the syringe until the needle touches the cortical surface and use this point as "zero" (*Z zero*). Lower the syringe needle to the desired depth (*Z* coordinate of the injection site) in the brain parenchyma (Fig. 2G). Adjust the features of fluid injection on the injection system. The injection of the fluid should be very slow to avoid an acute increase of intracranial pressure and facilitate diffusion of the fluid (rate of injection should not be >100 nL/min). Depending on the total volume injected, this step may take up to 10 min. We limit the maximal injection volume to no more than 1500 nl in one session.

Step 8: Anesthesia of the Next Animal (Ketamine-Xylazine Anesthesia Only)

During the intracerebral injection, perform anesthesia of the next animal by injecting the ketamine-xylazine mixture intraperitoneally, and immediately place the animal in the temperature-controlled cage.

Step 9: Withdrawal of the Syringe and End of the Procedure

When the injection is completed, allow a minimum of 2

additional minutes rest time before starting to withdraw the syringe from the brain. Withdraw the syringe slowly, in two stages, allowing another 2 min rest time at the halfway point to avoid backflow of the fluid to the surface. The burr-hole does not need to be covered. Remove the animal from the stereotaxic apparatus. *Clean the skin with iodine-based wash (optional).* Pull the edges of the skin together and suture the skin at 3 separate points.

Immediately (before suturing) rinse the syringe to avoid clot formation in the needle, by alternating aspiration and ejection of distilled water several times (in most stereotaxic apparatus this can be easily done using the "withdraw/inject" program). Check the patency of the syringe by ejecting a large volume of distilled water.

Step 10: Postoperative Management

Place the animal in the temperature-controlled cage until full recovery. Subcutaneous rehydration is unnecessary but provided free access to food by putting wet chow in the cage. Once the animal recovers, analgesic treatment may be administered, according to the protocol of your institution, for at least 2 days after surgery (Table 2). CAUTION: do not administer analgesic before the animal has fully recovered. Then return the animal to its home cage. Monitor the well-being of the animal for at least 3 days or according to local regulations.

Clean and disinfect tools and the surgical area with 70% ethanol. This surgical procedure (steps 2–9) can easily be performed in 20 minutes.

Intracerebral Injections in Neonatal Animals

No stereotaxic coordinates: the skull is too soft for fixation in a stereotactic apparatus.

Step 1: Preparation of Surgical Area

Put crushed ice into the Petri dish and cover it with aluminum foil (this is necessary to maintain hypothermia-induced anesthesia during surgery). As previously described[4], a homemade stage is used to position the body and stabilize the head. However, the dimensions of

Table 1. Features of systemic and local anesthetics used in adult mice

Anesthetics		Dose			Anesthesia duration	Sleep duration
		Concentration	Volume	Dose		
Ketamine (Imalgene®)	Ketamine	100 mg/mL	1.5 mL	150 mg/kg		
+ Xylazine (Rompun®)	Xylazine	20 mg/mL	0.75 mL	15 mg/kg	10 min	60-120 min
	Saline	sterile	7.75 mL	-		
	Mixture	-	10 mL	0.1 mL/10 g (IP)		
Tribromoethanol (Avertin®)				250 mg/kg	2 min	40-90 min
				0.1 mL/5 g (IP)		
Isoflurane (Iso-Vet®)				3% - 200 mL/h induction	Unlimited	Unlimited
				1.5% - 200 mL/h maintenance		
Lidocaine (Xylovet®)				17.5 mg/kg (SC)	3 min	Local anesthesia

IP, intraperitoneal; SC, subcutaneous.

Table 2. Management of postoperative analgesia

Analgesics	Dose	Analgesia duration	Protocol
Buprenorphine (Vetergesic®)	0.1 mg/kg SC	12 h	2/day for at least 2 days
Ketoprofene (Ketoprofene Arrow®)	5 mg/kg SC	12 h	2/day for at least 2 days (optional)

SC, subcutaneous.

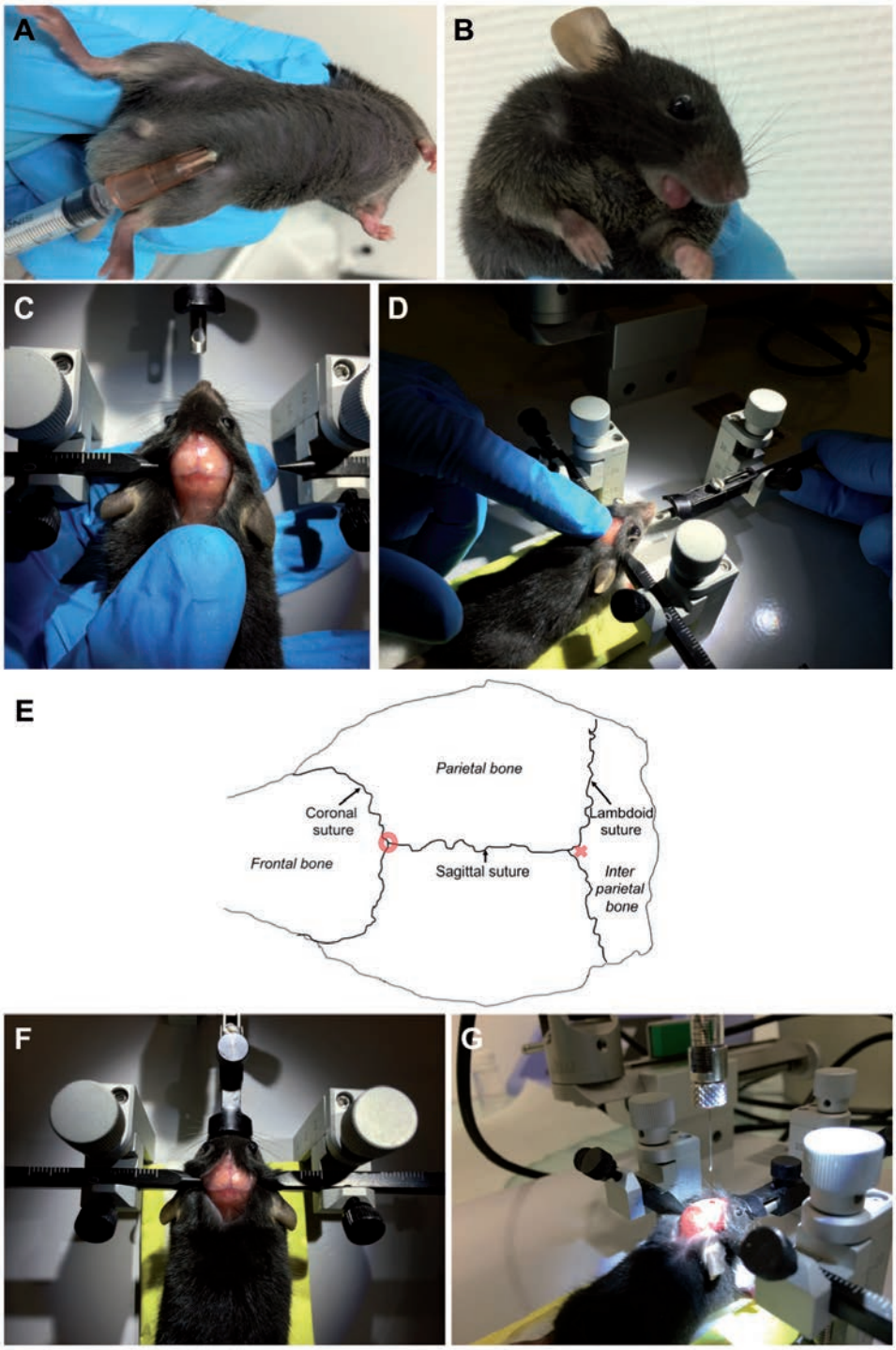

Fig. 2. Procedure of stereotaxic intracerebral injection in adult mice. (A) The ketamine-xylazine mixture is injected intraperitoneally through a 21-gauge needle inserted into the lower right abdominal quadrant. (B) The tongue of the mouse is pulled out to facilitate breathing. Lubricant ophthalmic gel is applied on both eyes to avoid keratitis during surgery. (C) The head of the mouse is held in place to allow positioning of the right ear bar. (D) The head of the mouse is moved up to insert the incisor adapter. (E) Stereotaxic landmarks on the skull of the mouse. Bregma is represented by the red circle and lambda by the red cross. (F) The snout clamp is placed just below the eyes. Before beginning injection, the skull is perfectly flat. (G) The syringe needle is lowered through the craniotomy to the desired depth; then the injection is started.

the stage should be adjusted according to the strain and size (or weight) of the mouse. For example, we used P0 C57BL6 mice (mean weight: 1.3 g) and precut the stage according to the features shown in Fig. 3A. Place and fix the stage to the center of the Petri dish. Finally, place the Petri box on the stereotaxic apparatus and keep it movable. Position the injection syringe on the stereotaxic arm and fix the stereotaxic arm above the Petri dish (Fig. 3B).

Step 2: Anesthesia

Place the newborn mouse in a container of crushed ice for ~2 min until the onset of hypothermia-induced anesthesia. When anesthesia is sufficient to start surgery, the skin becomes slightly blue and the animal does not move (Fig. 3C). This type of anesthesia can only be used for very young pups, until P2–P4 [4].

Step 3: Preparation for Injection

While waiting for anesthesia to set in, adjust the features of fluid aspiration on the injection system (aspirated volume should be slightly larger than injected volume). Pipet the desired volume of fluid onto a precut square of laboratory film; then bring the needle of the syringe into the drop under visual control with the dissecting microscope and suck up the fluid. If you are not comfortable with this, you can place the laboratory film on the stage or directly apply aspiration into the tube containing the fluid. Check that the drop has been aspirated. Make sure that the 33-gauge needle is patent by ejecting a very small volume of fluid (e.g. 50 nL) outside of the brain, under visual control, before proceeding. Adjust the features of fluid injection on the injection system.

Step 4: Preparation and Positioning of the Animal

Once anesthetized, place the newborn on the stage in the appropriate orientation for injection to obtain a “flat skull”.

Step 5: Injection (for Right-Handers)

Hold the animal’s head with your left index finger by applying moderate pressure to the back of its neck, and slightly stretch the head skin to facilitate penetration of the needle through the skin and the skull. Importantly, the animal’s head should remain held in this position by your left index finger throughout the injection. The edge of the Petri dish should be blocked between your left third and fourth fingers (Fig. 3D). With your right hand, draw a dot on the skin surface at the desired needle insertion point under a dissecting microscope. First use a 30-gauge needle to make a small puncture at the needle insertion point (Fig. 3E). Slide the Petri dish so that the syringe is above the puncture site. With your right hand, lower the syringe until the needle touches the cortical surface and use this point as the “zero” (*Z zero*) on the stereotaxic apparatus. Lower the syringe needle to the desired depth (*Z* coordinate of the injection site) in the brain parenchyma (Fig. 3F and G). Inject the desired volume of injection fluid in one minute. We use a maximum volume of 1000 nL per session in our experiments. *For left-handers, reverse the sides of the procedure.*

Step 6: Withdrawal of the Syringe and End of the Procedure

When the injection is completed, allow a minimum of one additional minute rest time before beginning to withdraw the syringe from the brain. Withdraw the syringe slowly. Remove the animal from the surgical area.

Step 7: Postoperative Management

Immediately place the newborn in the heating cage until full recovery. After ~2 min, the skin appears pink and reaction to touch is normal. Once the newborn recovers, return it to its home cage with its mother and litter. Newborns do not need to be treated with analgesics (buprenorphine and ketoprofene can be toxic in newborn animals) or cleaned with iodine-based wash. Monitor the health and well-being of the animal for at least 7 days.

While performing hypothermia-induced anesthesia of another newborn animal, rinse the syringe to avoid clot formation in the needle by alternating aspiration and ejection of distilled water (in most stereotaxic apparatus this can easily be done using the “withdraw/inject” program). Check the patency of the syringe by ejecting of a large volume of distilled water (>5 µL).

Clean and disinfect the tools and surgical area with 70% ethanol. This surgical procedure (steps 2–6) can be performed in 5 min.

RESULTS

We performed 300 intracerebral injections (270 in adult mice and 30 in neonates) and retrospectively analyzed the targeting of the injection site. Stereotaxic intracerebral injections in adult mice gave 92% (249/270) efficacy in targeting the injection site (Fig. 4A). Concerning injections in neonatal mice, we demonstrate that surgery can be

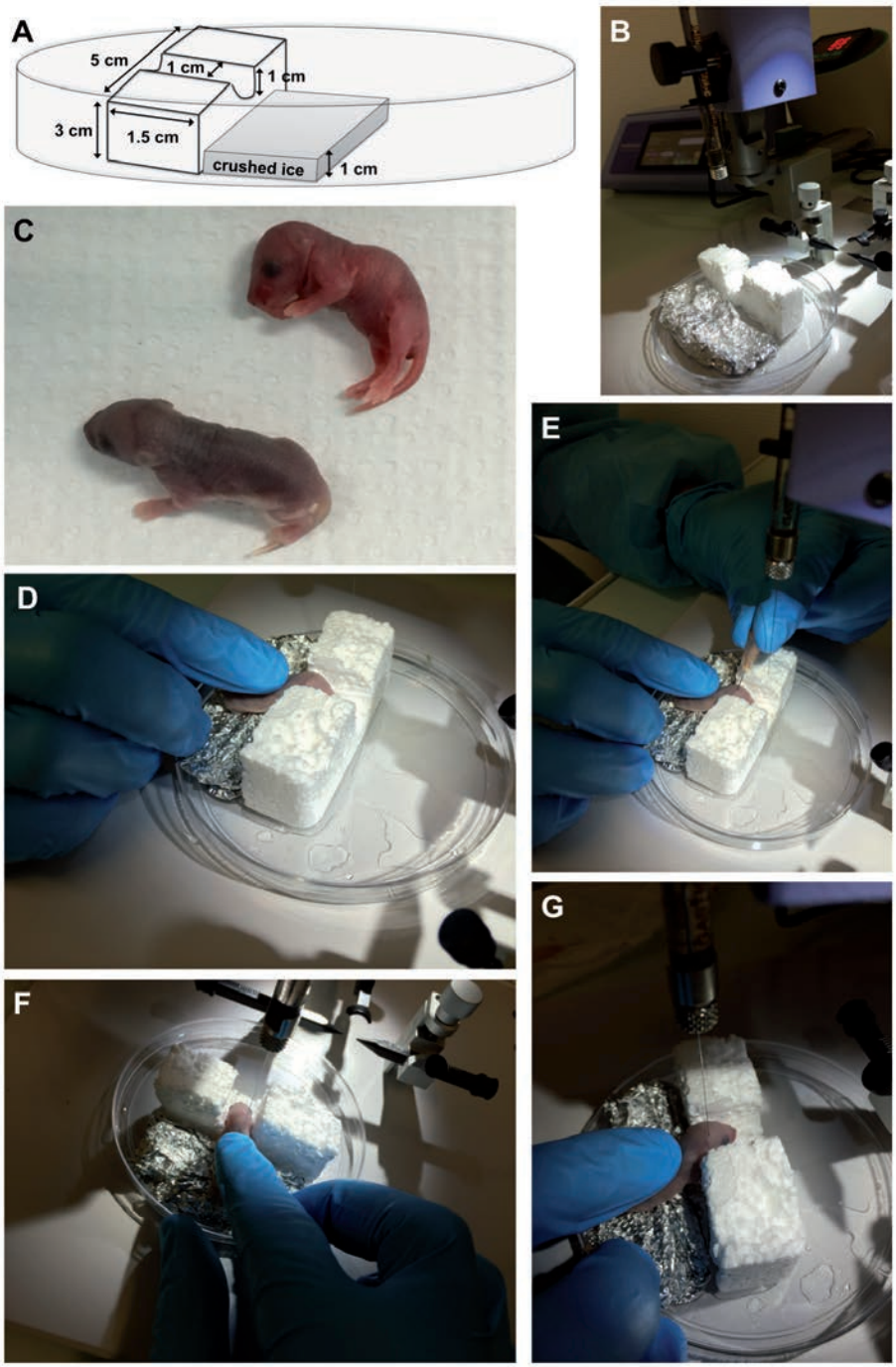

Fig. 3. Procedure of intracerebral injection in neonatal mouse. (A and B) Surgical area. The tailored stage is placed and fixed into the Petri dish. A carpet made with crushed ice surrounded by aluminum foil is placed in front of the stage. The Petri dish remains movable on the stereotaxic apparatus while the syringe is positioned above. (C) At the top of the picture, the neonatal mouse is awake (skin is pink). At the bottom of the picture, the neonatal mouse is under hypothermia-induced anesthesia (skin appears slightly blue). (D) The mouse's head is held with the index finger by applying moderate pressure on the back of its neck while the edge of the Petri dish is blocked between the third and fourth fingers. (E) A small puncture is made in the skull at the syringe needle insertion point with a 30-gauge needle. (F and G) The syringe needle is lowered through the puncture to the desired depth; then the injection is started. The mouse's head remains held by the operator's index finger throughout the injection. *The procedure shown on pictures D-G is performed by a left-handed operator.*

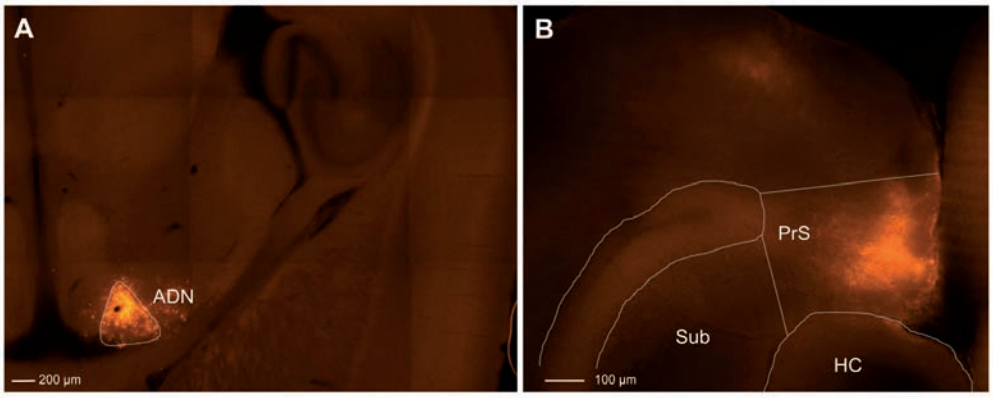

Fig. 4. Accuracy of injection sites. (A) Horizontal slice (DV = -2.85 mm). Stereotaxic injection of m-cherry expressing anterograde glycoprotein-deleted rabies virus (RABV ΔG (VSV G^{RtmC}); 300 nL)[13] in the anterodorsal nucleus of the thalamus (ADN) in an adult mouse (P28). The animal was sacrificed at P36. (B) Horizontal slice (DV = -2.00 mm). Injection of adeno-associated virus AAV1.CAGGS.Flex.ChR2-tdTomato (Addgene® 18917; 500 nL)[14] in the presubiculum (PrS) in a neonatal mouse (P0) which was sacrificed at P21. The virus expresses tdTomato in a cre-dependent fashion, here in an Sst-IRES-Cre mouse (Jax #013044). AAV, adeno associated virus; ChR2, channelrhodopsin-2; DV, dorsoventral; HC, hippocampus; IRES, internal ribosome entry site; PrS, presubiculum; RABV, rabies virus; Sst, somatostatin; Sub, subiculum.

performed by a single operator in a very short time (a litter of 8 neonates was injected in <1 h). Efficacy depends on the precision with which injection sites can be defined, due to the small size of the animal (Fig. 4B).

DISCUSSION

Surgical Tips

Stereotaxic Intracerebral Injections in Adult Animals

Planning the injection (coordinates and trajectory)

-Define the injection site that allows the easiest trajectory. The injection site should be as superficial as possible; in the best case, the trajectory should avoid ventricles; when the needle enters the cortex, it should be orthogonal to the cortical surface (it is possible to work with oblique trajectories depending on the stereotaxic apparatus).

-Calculate tailored coordinates. After choosing coordinates using *The Mouse Brain in Stereotaxic Coordinates* (George Paxinos and Keith B.J. Franklin, Academic Press, 2005), verify the injection site by injecting an inert tracer (e.g. 300 nL of Fluororuby or Chicago blue) in several animals and assess the reproducibility of your injections under a microscope. If your injection site is incorrect, correct it by calculating deviation between the expected site and the current site.

-Privilege one-phase injections. Should you need to inject two different fluids (e.g. virus and tracer) in the same animal, inject them during the same procedure (if possible) because postsurgical fibrosis can mask skull sutures rendering a second injection more difficult.

Preparation of surgical area and tools

-Careful handling of injection syringe and needle. Make sure that the needle is correctly inserted and fits tightly into the syringe. If you observe air bubbles inside the syringe, remove the needle, reinsert it into the syringe, replace the hub, and tighten. While the syringe is unused, we strongly suggest keeping it fully filled with distillated water (do not use sterile saline which can crystallize in the syringe). To avoid clogging of the syringe, use the procedure described above (aspiration and ejection of distilled water) and avoid direct contact between the needle and blood during the surgical procedure (stop bleeding and wash the craniotomy with sterile saline if necessary). Finally, make sure that the needle is not bent, and if so, replace it.

-Isolate stereotaxic apparatus. Vibrations of the environment can be transmitted to the syringe during intracerebral injection and lead to damage of the brain

parenchyma. To avoid transmission of vibrations, the base of the stereotaxic apparatus may be isolated by setting it up on an air table.

Anesthesia

-Choose anesthetics: The advantages of isoflurane are: speed of induction and recovery, greater control of depth of anesthesia, less metabolism of the drug in the liver and significantly less sensitization of the heart to catecholamines. The disadvantages of isoflurane include the cost and logistics of using precision vaporizers, the risk of fatal overdose if an open system is used instead of a precision vaporizer, as well as depressed respiratory rate and decreased blood pressure. In addition, once animals awaken from gas anesthesia, there is no residual analgesic activity[8, 9]. The advantages of ketamine-xylazine combinations are that they may be combined in one syringe, and that they produce short-term surgical anesthesia with good analgesia[10]. The disadvantages of ketamine-xylazine combinations are that they do not reliably reach the surgical level of anesthesia in all cases, and that they can cause profound cardiac depression[8]. Tribromoethanol induces anesthesia rapidly and provides good surgical analgesia for about one hour. However, tribromoethanol is an irritant, especially at high doses or with repeated use, and can cause intestinal ileus several weeks after injection. Tribromoethanol degrades in the presence of heat or light to produce toxic byproducts. Degraded solutions can be both nephrotoxic and hepatotoxic and can lead to death. The effects of tribromoethanol are also somewhat unpredictable in mice younger than 16 days[11, 12].

-Manage anesthesia. If the animal is not anesthetized after 10 min using the ketamine-xylazine combination, inject an additional 20% of the dose intraperitoneally and wait 5 min. If a ketamine-xylazine combination is used for surgery longer than 20 min, animals will likely require additional anesthetic. Inject an additional 20% dose intraperitoneally and closely monitor if the anesthesia deepens. It is possible to redose with a lower dose of ketamine rather than the combination. However, redosing repeatedly with ketamine alone does not produce a surgical level of anesthesia. Preferably, isoflurane should be used for procedures longer than 30 minutes.

Surgical procedure

-Choose the needle. The choice of the appropriate needle should be made according to the advantages of each type: a rigid steel needle is not diverted by the ependyma for a transventricular trajectory and perforates the dura without prior opening; a flexible silica needle allows for the best healing of brain parenchyma after withdrawal of the syringe.

-Select the right skull landmarks. If bregma and lambda are not distinguishable, apply oxygenated water to the skull, and the sutures appear white and easily visible. If the sagittal suture is shifted from the superior sagittal sinus (only visible in young rodents), consider that the zero of the medial-to-lateral (*X*) coordinate is located above the superior sagittal sinus (Fig. 5A and B).

-Open the dura. Be careful not to push the dura too strongly downward while trying to penetrate it; this will cause intracerebral hemorrhage or an epidural hematoma. The leader for human spinal anesthesia is the safest tool for opening the dura and avoid injuring the brain surface.

-Stop bleeding. To stop epidural or cortical bleeding, dab the injured vessel for at least 10 s with a cotton swab, then wash out the blood clot with sterile saline.

-Manage the transventricular trajectory. Several injection sites are located below the ventricle (e.g. thalamus). For these specific sites, we strongly suggest using a rigid needle in order to avoid deflection of the needle by the ventricular ependyma (Fig. 5C-E). After injection, withdraw the syringe slowly, in two stages, allowing 2 min rest time at a point located below the ventricle to avoid intraventricular diffusion of the fluid (Fig. 5E).

-Manage multisite injection. To avoid clot formation in the needle during multisite injection, replace the syringe after performing the first injection. Then, after positioning the new syringe on the stereotaxic arm, return to bregma to define the reference (stereotaxic zero) of the *X* and *Y* coordinates.

Intracerebral injections in Neonatal Animals

All surgical tips described above also apply to injections in

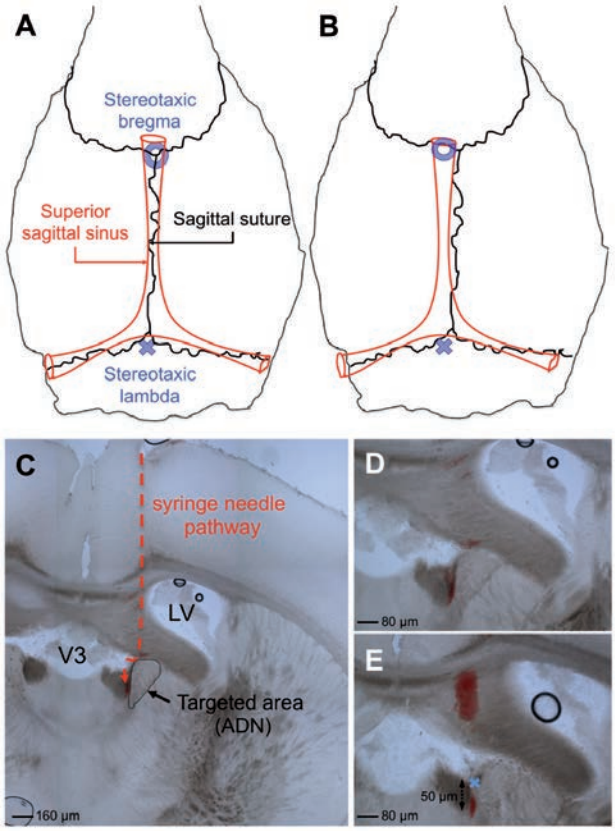

Fig. 5. Surgical tips. (A) Typical anatomical localization of the sagittal suture above the superior sagittal sinus. Correct stereotaxic landmarks are represented by the blue circle (bregma) and cross (lambda). (B) Frequent anatomical variation. The sagittal suture is shifted from the superior sagittal sinus. Correct zero of the medial-to-lateral (*X*) coordinate (stereotaxic bregma) is located above the superior sagittal sinus. (C-E) LV, lateral ventricle; V3, third ventricle; ADN, anterodorsal nucleus of thalamus. Coronal slice of mouse brain after injection of Fluororuby (red inert tracer) targeting the ADN. (C and D) Injection using a flexible 33-gauge needle. The flexible needle is deflected by the ventricular ependyma leading to an incorrect injection site. (E) Injection using a rigid 33-gauge needle. The rigid needle is not deflected resulting in a correct injection site. The blue cross represents the point where the operator should wait 2 min before continuing the withdrawal of the syringe to avoid intraventricular diffusion of the tracer.

newborn animals where relevant.

-Perform surgery at P0. The superior sagittal and lateral sinuses are used as landmarks to identify the desired needle insertion point. In mice, the sinuses become difficult to discern and the skull becomes less flexible after P3. Thus, to facilitate the procedure, we recommend, as much as possible, to perform surgery at P0. Likewise, the local diffusion of most tracers throughout the neonatal brain is greater at P0 tha that seen later in postnatal development.

-Define landmarks. After determining the coordinates of the injection site and the best entry point with the assistance of the *Atlas of the Developing Mouse Brain* (Paxinos *et al*., Elsevier, 2007), in addition to natural landmarks (sinuses), use the stereotaxic arm to increase the precision of the location of the entry point into the skull.

-Manage the postoperative period. To avoid parent mice killing their litters, minimize the total time away from the mother, ideally to <15 min [5].

CONCLUSIONS

We describe an innovative, effortless, and reproducible surgical protocol for stereotaxic intracerebral injections in adult mice that should give >90% efficacy in targeting an injection site. This procedure should allow any researcher to master these experiments quickly. Concerning injections in neonatal mice, we demonstrate that surgery can be performed by a single operator in a short time. The efficacy depends on the precision with which injection sites can be defined, due to the small size of the animal. However, our technique using the stereotaxic arm allows a higher precision than the freehand techniques previously described.

ACKNOWLEDGMENTS

This work was supported by the French Society of Neurosurgery (B.M.) and by an ANR Grant JCJC R10206DD (D.F.). The research leading to these results also benefitted from the program “Investissements d’avenir” ANR-10-IAIHU-06. The authors thank Andreas Frick and Matthias Haberl (Neurocentre Magendie, Bordeaux, France) for providing the rabies virus, and Jonathan Bradley, Ivan Cohen, Audrey Hay, Carole Morel, and Alan Urban for advice and discussions on surgical procedures. The authors thank Scott Sternson for authorizing use of plasmid 18917.

Received date: 2015-04-25; Accepted date: 2015-05-25

REFERENCES

[1] Cardin JA, Carlen M, Meletis K, Knoblich U, Zhang F,

Deisseroth K*, et al*. Targeted optogenetic stimulation and recording of neurons in vivo using cell-type-specific expression of Channelrhodopsin-2. Nat Protoc 2010, 5: 247–254.

[2] Puntel M, Kroeger KM, Sanderson NS, Thomas CE, Castro MG, Lowenstein PR. Gene transfer into rat brain using adenoviral vectors. Curr Protoc Neurosci 2010, Chapter 4: Unit 4 24.

[3] Cetin A, Komai S, Eliava M, Seeburg PH, Osten P. Stereotaxic gene delivery in the rodent brain. Nat Protoc 2006, 1: 3166–3173.

[4] Davidson S, Truong H, Nakagawa Y, Giesler GJ, Jr. A microinjection technique for targeting regions of embryonic and neonatal mouse brain in vivo. Brain Res 2010, 1307: 43–52.

[5] Li J, Daly TM. Adeno-associated virus-mediated gene transfer to the neonatal brain. Methods 2002, 28: 203–207.

[6] Pilpel N, Landeck N, Klugmann M, Seeburg PH, Schwarz MK. Rapid, reproducible transduction of select forebrain regions by targeted recombinant virus injection into the neonatal mouse brain. J Neurosci Methods 2009, 182: 55–63.

[7] Shurey S, Akelina Y, Legagneux J, Malzone G, Jiga L, Ghanem AM. The rat model in microsurgery education: classical exercises and new horizons. Arch Plast Surg 2014, 41: 201–208.

[8] Albrecht M, Henke J, Tacke S, Markert M, Guth B. Effects of isoflurane, ketamine-xylazine and a combination of medetomidine, midazolam and fentanyl on physiological variables continuously measured by telemetry in Wistar rats. BMC Vet Res 2014, 10: 198.

[9] Redfors B, Shao Y, Omerovic E. Influence of anesthetic agent, depth of anesthesia and body temperature on cardiovascular functional parameters in the rat. Lab Anim 2014, 48: 6–14.

[10] Hartsfield SM. Advantages and guidelines for using ketamine for induction of anesthesia. Vet Clin North Am Small Anim Pract 1992, 22: 266–267.

[11] McDowell A, Fothergill JA, Khan A, Medlicott NJ. A cyclodextrin formulation to improve use of the anesthetic tribromoethanol (Avertin((R))). J Pharm Bioallied Sci 2014, 6: 16–21.

[12] Meyer RE, Fish RE. A review of tribromoethanol anesthesia for production of genetically engineered mice and rats. Lab Anim (NY) 2005, 34: 47–52.

[13] Haberl MG, Viana da Silva S, Guest JM, Ginger M, Ghanem A, Mulle C*, et al*. An anterograde rabies virus vector for high-resolution large-scale reconstruction of 3D neuron morphology. Brain Struct Funct 2014.

[14] Atasoy D, Aponte Y, Su HH, Sternson SM. A FLEX switch targets Channelrhodopsin-2 to multiple cell types for imaging and long–range circuit mapping. J Neurosci 2008, 28: 7025–7030.

DISCUSSION

1- Interneuron diversity in the presubicular microcircuit

Cortical inhibitory interneurons can be divided into two major categories. Perisomatic interneurons synapse on the soma and proximal dendrites of pyramidal cells and are thus positioned to control their output. Dendrite-targeting interneurons send projections to the distal dendrites of the pyramidal cells, thus gating the incoming information. The two most prominent representatives of these classes are the PV and SOM expressing interneurons. In addition to being opposed by their differential morphology, PV interneurons are fast-spiking cells whereas SOM interneurons are adapting cells. The segregation in two distinct subclasses according to the anatomy and electrophysiology is however an oversimplification. Indeed, they constitute a very heterogeneous population in terms of electrophysiological properties, dendritic and axonal projections, molecular expression, synaptic targets and afferent inputs (Cauli et al., 1997; Parra et al., 1998; Markram et al., 2004; Klausberger and Somogyi, 2008). Depending on these features and the cortical area considered, they exhibit various functions in the brain circuitry.

My PhD work constitutes the first extensive study of electrophysiological and morphological properties of interneuron populations in the presubicular cortex. Indeed, little had been known about the cellular and anatomical substrates of presubicular inhibitory components (Fricker et al., 2009; Funahashi and Stewart, 1997a; Menendez de la Prida et al., 2003; Simonnet et al., 2013; Abbassi et al., 2014). I characterized the electrophysiological and morphological properties of the two major interneuron subtypes in the presubiculum (Nassar et al., 2015) using transgenic mouse lines that allow the identification of PV and SOM expressing interneurons.

I recorded from identified fluorescent interneurons in the slice and reconstructed their anatomy. In collaboration with Jean Simonnet, I performed unsupervised clustering based on electrophysiological parameters describing firing pattern, spike waveform and passive properties. I identified three groups of interneurons. I found SST low-threshold adapting interneurons (cluster 1) and archetypal PV fast-spiking cells (cluster 3). An intermediate group (cluster 2) of quasi-fast spiking cells lied at the transition between the two groups. Anatomical features were not included as parameters for cluster analysis, but the post-hoc comparison showed that the physiological classification of presubicular interneurons was quite consistent with their morphological features, as the two archetypal groups displayed typical morphologies, while the third one was more diverse.

The choice of significant and reliable parameters used for unsupervised cluster analysis is critical for the resulting classification. Our classification was based only on electrophysiological properties of neurons. Anatomical features were not included in the cluster analysis because of the insufficient number of complete neuronal reconstructions. Using more parameters may help to better define the populations (Cauli et al., 2000). Here, our asset for an efficient classification was the high quality of recordings and the reliability of the analysis.

Maybe most intriguing is the existence of the transitional cluster (cluster 2) that grouped together some Sst-Cre::tdTomato interneurons with similar numbers of Pvalb-Cre::tdTomato interneurons. Electrically, neurons of this cluster possessed intermediate values of membrane potential, a relatively small resistance and a short time constant approaching that of FS cells. At higher firing frequencies, neurons of this cluster displayed a quasi-FS firing pattern with a weak frequency adaptation. Anatomically, cluster 2 interneurons were often similar to basket cells (Wonders and Anderson, 2006; Kubota, 2014). Neurites of these cells tended to branch within their home layer with also intra-laminar axonal projections that may mediate early and late blanket inhibition (Karnani et al., 2014).

In cluster 1, I found all X98-GFP cells with mostly a typical Martinotti cell-like morphology, while some SST-Cre cells were basket like (Jiang et al., 2015). It is likely that the SSt-Cre::dtTomato mouse line labeled all subtypes of somatostatin positive interneurons in the presubiculum, including SOM interneurons that are not GFP labeled in the X98 line, but maybe labeled in the X94 (Ma et al., 2006) or in the GIN (Urban-Ciecko and Barth, 2016) mouse lines. Interneuron properties evolve during development: both PV and SOM interneurons originate from the medial ganglionic eminence (Wonders and Anderson, 2006; Kepecs and Fishell, 2014). Possibly their common developmental origin produces transitional “edge cells” reflecting the shared embryonic origin in the adult. The intermediate group, cluster 2, could represent a population of interneurons that sometimes co-express SOM and PV. Using ligand-dependent inducible Cre recombinase (CreER recombinases, Madisen et al., 2010), it would be interesting to study the physiological and anatomical properties of the genetically targeted cells during the neocortical development (Taniguchi et al., 2011) and possibly identify the timing of cluster 2 neurons generation.

I examined the specificity of fluorescently labeled neurons by using antibodies against PV and SOM in the Pvalb-Cre, Sst-Cre and X98 mouse lines. I found a minority of 2-6% of in-

terneurons that co-expressed PV and SOM in the presubiculum of adult Pvalb-Cre and Sst-Cre animals. This result is not enough to explain all cluster 2 interneurons, even though they could well be part of cluster 2. However, it clearly points out the existence of a little acknowledged subset of PV-SOM interneurons. These interneurons could correspond to a subpopulation of PV interneurons that is not surrounded by perineuronal nets, distinct in its electrophysiological properties from to the typical fast-spiking PV interneurons class that express metallopeptidases (Rossier et al., 2015).

The use of site-specific recombinases (SSRs) both *in vitro* and *in vivo*, have proven to be useful tools in the analysis of gene function. The Cre/lox system is the most widely SSRs system in mice to achieve cell-type-specific gene expression (Madisen et al., 2010). However, this system might have some limitations. In fact, the majority of Cre strains exhibit some degree of unreported recombinase activity. In addition, frequent mosaicism, inconsistent activity and parent-of-origin effects may be observed. Indeed, differential activity of the Cre allele may depend on the parent-of-origin (Heffner et al., 2012). In our study, Cre inheritance could be either paternal or maternal, but all Pvalb-Cre cells from animals that inherited Cre maternally were found solely in the intermediate cluster 2. During development, PV interneurons may transiently express SOM: in the SOM-Cre mouse line, cells that express transient SOM would also express Cre recombinase, thus inducing a persistent tdTomato+ signal after Cre-mediated recombination (Hu et al., 2013) even after the loss of SOM expression.

Another SSRs used is the Flp-frt system where Flp, or flippase, recombines DNA flanked by 2 FRT (Flp, recombinase target) sites (Dymecki et al., 2010). It could be interesting to compare the specificity of Pvalb-2A-Flp mouse line with the Pvalb-Cre one. Different variants of Flp have been described, referred to as wild-type Flp (Flp-wt), low-activity Flp (FlpL), enhanced Flp (Flpe), and optimized Flp (Flpo) (Dymecki et al., 2010). Interestingly, an increase in the specificity can be obtained by using dual-recombinase intersectional strategies with both recombinases Cre and Flp expressed from separate driver lines in order to doubly control reporter allele (Madisen et al., 2015).

The combinatorial expression of other molecular markers of SST and PV interneurons may be revealed using single-cell RNA sequencing (scRNA-seq) or using multiple-immunostaining (Gonchar et al., 2008). These techniques might help us to better identify different populations of PV and SOM interneurons in the presubiculum as well as other types of interneurons. Most

interneurons in the rodent cortex fall into three categories defined by expression of PV or SOM or vasoactive intestinal polypeptide (VIP) (Rudy et al., 2010). Consequently, in order to define the entire diversity of presubicular interneurons, the properties of VIP interneurons should also be addressed.

While GABAergic cells are mostly local interneurons, there are several recent studies on long-range GABAergic neurons connecting brain areas associated with different or similar functions (Freund and Antal, 1988; Melzer et al., 2012, Gonzalez-Sulser et al., 2014, Unal et al., 2015; Fuchs et al., 2016**).** In the presubiculum, my preliminary data show putative presubicular PV axons projecting to the thalamus (cf. Article 6). This study still needs to be pursued by combining immunostaining, electrophysiological techniques and optogenetic tools to prove or disprove the existence of such long-range inhibitory presubicular projections. RNA sequencing might help to identify molecular markers in PV or SOM long-range neurons that would segregate them from local PV neurons identified previously (Nassar et al., 2015).

The description of principal neurons (Simonnet et al., 2013) and interneurons (Nassar et al., 2015) of the presubicular microcircuit is the foundation for a better understanding of the presubicular cortex. To conclude, at least two components of inhibition exist in the presubiculum, the PV-mediated inhibition and SOM-mediated inhibition. Perisomatic versus dendritic targeting associated with PV and SOM respectively still need to be confirmed with high-resolution anatomical analysis in future studies. The entire interneuronal population has not been characterized yet, but the presubicular inhibitory microcircuit is likely to share the complexity of other cortical areas in terms of neuronal diversity.

2- From interneuron diversity to functional implications

The diversity of interneurons, with its range of electrophysiological properties as well as morphological features raises questions concerning the input-output transformation and the local connectivity between excitatory neurons and interneurons of the presubicular microcircuit. How interneurons and pyramidal neurons receive inputs and interact to convert input information into output is the key question that I have examined during my PhD.

Presubicular synaptic integration shares common features with other cortical areas (Cruikshank et al., 2010; Lee et al., 2013). However, while in barrel cortex the thalamo-recipient layer is mainly layer 4, I have shown that ATN axons selectively ramify in superficial layers of the presubiculum (Nassar et al. in prep, cf. article 2). More particularly, in superficial layer 3, thalamic inputs make direct synaptic contacts with pyramidal neurons and PV interneurons. The direct recruitment of PV interneurons by long-range afferents makes them important contributors to feedforward and feedback inhibition (Nassar et al., in prep.), whereas the SST interneurons provide feedback inhibition (Simonnet et al., under review). Occasionally recorded layer 4 bursting cells and deep layer 5/6 cells received indirect excitation (n = 2; data not shown). Deep layers are therefore likely to integrate input information indirectly, following feed-forward excitation from superficial layer neurons.

Excitatory principal neurons are also diverse. Our work has shown that presubicular neurons fall into projection-specific neuronal subpopulations, which segregate regarding their anatomical distribution and also their physiological intrinsic properties. Three main subgroups of presubicular neurons that project to specific brain areas of the head direction system, namely the upstream LMN, the ATN, and the downstream MEC with its grid cells, were retrogradely labeled and their electrophysiological properties were characterized. ATN projecting neurons were found in the heterogeneous layer 5/6, LMN projecting neurons were burst-firing neurons of layer 4 and layer 2/3 neurons were regular-firing neurons projecting to MEC (Huang et al. in prep). The preserved cell layer structure across species, mouse (Huang et al., in prep) and rat (Simonnet et al., 2013), underscores its functional importance in the head direction circuit. From a recent study by Preston-Ferrer et al. (2016), we now also know that calbindin-positive layer 2 neurons project to contralateral presubiculum, while calbindin-negative neurons in superficial layer 2 project to contralateral retrosplenial cortex. The spiking of both types of layer 2 neurons *in vivo* was largely unaffected by HD tuning, but rhythmically entrained by

theta oscillations. Superficial layer 3 neurons were highly tuned to a specific HD, and consistent with our results, they were found to project to the MEC (Preston-Ferrer et al., 2016). The presubicular projections to the ipsilateral and contralateral parasubiculum (Van Groen and Wyss, 1990b) still await further investigations. Taken together, the presubiculum is composed of molecularly, morphologically and functionally distinct principal cell populations, which can be differentiated according to their long-range projection targets. Similar to previous studies performed in deep layers of the MEC and neocortex (Sümerli et al., 2015, Woodworth et al., 2016), differences in molecular make-up of the distinct projecting neuronal populations should be addressed. Functional differences along the dorso-ventral axis of the presubiculum should also be tested. To reveal the specific functional roles of each projection class in head direction signaling, it might be interesting to combine retrograde labeling or optogenetic tools with *in vivo* whole-cell recordings of both presubicular projections neurons and the targeted neurons.

In the neocortex, principal neurons exhibit a remarkable degree of variability regarding their morphology, connectivity, firing properties and gene expression. As far as we can tell, this is also the case in presubiculum. Due to their heterogeneous properties, principal neurons may transform and transmit information in different ways, tailored to different functions, and adapted to the projection area of a given principal neuron population (Huang et al., in prep; Morishima and Kawaguchi, 2006; Mizuseki et al., 2011; Krook-Magnuson et al., 2012). Subgroups of principal cells exhibit different local connection properties as well as differences in their excitatory and inhibitory inputs, forming highly organized subnetworks with neighboring interneurons (Bannister, 2005; Brown and Hestrin, 2009; Krook-Magnuson et al., 2012). Interneuron subpopulations operate as groups. Indeed, PV networks, SOM populations and VIP populations accomplish within-population co-activity by means of conserved network mechanisms that receive each a distinct subset of local excitatory inputs (Karnani et al., 2016b).

Are populations of PV interneurons organized in a network manner in the presubicular microcircuit? When performing dual-recordings of nearby PV interneurons, I found a high reciprocal connection probability (75%, n=6 /8 pairs; Nassar et al. in prep; article 2). Presubicular PV cells are likely to share similar anatomical features (Nassar et al., 2015) with cortical PV interneurons and might form a network of inhibition providing a global “blanket of inhibition” (Packer and Yuste, 2011). I also found a high proportion of connectivity be-

tween PV interneurons and pyramidal cells (Nassar et al., in prep; article 2). In the presubiculum, feedback and feed-forward inhibitory circuits are formed between fast-spiking cells and layer 3 pyramidal cells, which are reciprocally connected and share common excitatory inputs, similar to connectivity motifs in some other neocortical areas (Yoshimura and Callaway, 2005; Yoshimura et al., 2005). In specific sets of subnetworks and given the very low rate of recurrent connection between layer 3 pyramidal cells (~2%; Simonnet et al., under review), presubicular PV-expressing interneurons could play a role in setting the gain and timing of responses within principal neuron populations (Gabernet et al., 2005; Pouille and Scanziani, 2001).

In many brain areas, PV interneurons make reciprocal contacts onto each other (Freund and Buzsáki, 1996; Gibson et al., 1999; Galarreta and Hestrin, 2002; Pfeffer et al., 2013) providing network synchrony and disinhibition. Inhibition of SOM by PV neurons is rare in visual cortex (Pfeffer et al., 2013; Jiang et al., 2015). However, SOM interneurons inhibit intensively PV neurons (Pfeffer et al., 2013; Jiang et al., 2015) suggesting that mixed subnetworks of cortical interneurons may also exist. The SOM-to-PV neuron connection could also be important for cortex assembly and functional maturation of PV interneurons during early postnatal stages (Tuncdemir et al., 2016).

Different kinds of plasticity may coexist in a same synaptic terminal, and the level of their relative expression determines the overall synapse dynamics (Markram et al., 1998; Regehr, 2012). The dynamics of excitatory glutamatergic synaptic transmission onto PV interneurons is depressing compared to the facilitating one onto SOM interneurons. Changes in synaptic efficiency can be due to different mechanisms involving vesicle pool dynamics and/or calcium signaling.

Further investigations into the strength of unitary excitatory and inhibitory connections will provide additional insight into whether the large inputs to some presubicular neurons result from a few very strong synaptic connections and/or a convergence of many synapses onto single postsynaptic neurons. Minimal stimulation techniques could be adapted for use with optical laser stimulation to address these questions in future studies. My preliminary data using low intensity laser stimulation of thalamic inputs suggest that PV cells receive larger unitary inputs than Pyr cells similarly to previous studies (Cruikshank et al., 2007). In simultaneously recorded nearby pyramidal neurons or PV interneurons, the probability of convergence and divergence of a same excitatory input should be tested.

The presubiculum receives fibers from several afferent brain regions, including thalamus, but also retrosplenial cortex (Wyss and Van Groen, 1992; Van Groen and Wyss, 1995). The targeted injection of AAV expressing Channelrhodopsin in the ATN or the RSC allowed us to specifically stimulate either set of those afferent fibers with light, and determine their functional connectivity. Both ATN and RSC fibers ramified in superficial layers and innervated layer 3 pyramidal neurons (Nassar et al., in prep; article 2 and 5). Do inputs from either the thalamus or the retrosplenial cortex converge on a same cell? Do RSC axons also target interneurons? And what is the subcellular distribution of long-range excitatory synapses on pyramidal neurons? It is now possible to independently activate two distinct sets of fibers in brain slices: Chronos and Chrimson are light-activated channelrhodopsins that allow independent two-color activation and synaptic release from different neural populations (Klapoetke et al., 2014). Chronos is similar to ChR2 but with faster kinetics and high sensitivity to blue and green light. Chrimson is a red light sensitive channelrhodopsin with spectra that are red shifted by 45 nm compared to those of previous channelrhodopsin variants. One experiment we could suggest is to co-activate the two ATN and RSC inputs, by expressing Chrimson in ATN and Chronos in RSC, and check for sub- or suprathreshold summation in the postsynaptic neuron. The mathematical sum of evoked responses following activation of each input separately and the simultaneous activation of both inputs will be compared.

Ultimately, the implication of the different subtypes of interneurons in tuning the head direction signal must be addressed *in vivo* using passive movement with head-restraining procedures (Preston-Ferrer et al., 2016), or, even better, in freely moving animals (Taube et al., 1990a; Taube, 1995; Tukker et al., 2015). Recent studies have shown that HD directional information is encoded by superficial layer 3 excitatory neurons in the presubiculum, but not by FS neurons, and our own work suggests that SOM interneurons might inhibit HD cells with different phase, consistent with an attractor model (Tukker et al., 2015; Preston-Ferrer et al., 2016; Simonnet et al., under review). Presubicular FS interneurons were modulated by angular velocity and fired at higher rates during fast head-turns compared to resting periods (Preston-Ferrer et al., 2016). Unlike FS-PV interneurons, properties of pyramidal neuron-to-SOM/Martinotti synapses (Simonnet et al., under review) make the Martinotti cells suitable to be recruited in the absence of head rotation when head direction cells fire persistently. Both PV (Preston-Ferrer et al., 2016) and SOM interneurons (our preliminary data, not shown) are likely to be little modulated by HD tuning. In a lateral-inhibition-type connectivity (Couey et al., 2013; Peyrache et al., 2015) cells signaling the current direction may inhibit all other cells

disynaptically during fast head-turns or in the absence of head movements respectively. SST interneurons are recruited with a facilitatory delay, and they may be transiently inhibited by PV interneurons during fast-head rotations. PV inhibition would fade out during sustained firing of in-tune head-direction cells in the absence of head motion (Ma et al., 2012, Simonnet et al., under review). The next step will be to examine *in vivo* how tuning properties of head direction cells are controlled by distinct interneuron types using specific silencing of either PV or SOM interneurons (with Arch or Halorhodopsin; Chow et al., 2010; Zhang et al., 2007a, b).

GENERAL CONCLUSION

During my PhD, I studied the mouse presubiculum, a transitional six-layered cortex situated between the hippocampus and the entorhinal cortex. Given the presence of head direction neurons which fire persistently as a function of an animal's directional heading, the presubiculum appears as a crucial component in spatial orientation. Local inhibition plays a major role in regulating information processing in cortical areas, and my work has contributed to a better comprehension of the presubicular inhibitory microcircuit physiology and anatomy, and the functional connectivity with local principal neurons as well as with upstream and downstream areas.

From my analysis of electrophysiological and morphological properties of the two major subtypes of GABAergic neurons, the PV- and the SOM- expressing interneurons, it becomes clear that the presubiculum is a complex cortical area, with a high degree of interneuron diversity. Different inhibitory neuron populations participate in information processing in the presubiculum in specific ways. My investigation of the input-output connectivity of excitatory and inhibitory elements of the presubiculum revealed the functional connectivity of ATN (and RSC) inputs to interneurons and pyramidal neurons of the presubiculum. My work demonstrates for the first time that thalamic inputs to the medial entorhinal cortex are serially transferred via presubicular principal neurons of layer 3. This has important functional implications for the genesis and the role of the HD signal in MEC. Given the high reciprocal connection probability between PV interneurons and presubicular pyramidal cells and the direct recruitment of these neurons by long-range afferent inputs, PV interneurons are likely to be responsible for feed-forward inhibition onto pyramidal neurons. On the contrary, SST interneurons are indirectly recruited only during persistent and high frequency firing of presubicular pyramidal cells and in turn, they mediate feed-back inhibition onto principal neurons. Initial data concerning the RSC inputs need to be more precisely characterized and further experiments should address the subcellular targeting of thalamic and retrosplenial inputs, as well as their putative convergence and rules for synaptic integration.

In addition to layer 3 regular-firing MEC projecting neurons, we identified two other main subgroups of presubicular neurons that project to specific areas of the head direction system. They corresponded to heterogeneous layer 5/6 ATN projecting neurons and layer 4 burst-firing LMN projecting neurons. We also found evidence for MEC projecting SOM interneurons, and, more surprisingly, for PV neurons projecting to ATN. The nature of their postsynaptic targets and their functional role for HD signaling and grid cell activity should be tested.

To conclude, my PhD work brought fundamental new knowledge about interneuron properties and the integration of afferent inputs in the presubicular microcircuit. The general design of the presubicular inhibitory microcircuit showed many similarities with anatomical, biophysical, synaptic and input integration features in hippocampus and neocortex. In combination with our computational modelling study, this work contributes to a better understanding of the functional impact of inhibition for head direction signaling.

REFERENCES

Abbasi, S. and Kumar, S. S. (2013). Electrophysiological and morphological characterization of cells in superficial layers of rat presubiculum. *The Journal of Comparative Neurology*, 521(13):3116– 3132.

Abbasi, S., and Kumar, S. S. (2014). Regular-spiking cells in the presubiculum are hyperexcitable in a rat model of temporal lobe epilepsy. *Journal of Neurophysiology*, *112*(11), 2888–2900.

Acsády, L., Görcs, T. J., and Freund, T. F. (1996). Different populations of vasoactive intestinal polypeptide-immunoreactive interneurons are specialized to control pyramidal cells or interneurons in the hippocampus. *Neuroscience*, *73*(2), 317–334.

Adesnik, H. and Scanziani, M. (2010). Lateral competition for cortical space by layer specific horizontal circuits. *Nature* 464, 1155-1160.

Adesnik, H., Bruns, W., Taniguchi, H., Huang, Z. J., and Scanziani, M. (2012). A neural circuit for spatial summation in visual cortex. *Nature*, *490*(7419), 226–231.

Ali, A. B. and Thomson, A. M. (1998). Facilitating pyramid to horizontal oriens-alveus interneurone inputs: dual intracellular recordings in slices of rat hippocampus. *The Journal of Physiology (Lond.)* 507, 185–199

Amaral, D. G. and Witter, M. P. (1989). The three-dimensional organization of the hippocampal formation: a review of anatomical data. *Neuroscience,* 31(3):571–591.

Amilhon, B., Huh, C. Y. L., Manseau, F., Ducharme, G., Nichol, H., Adamantidis, A., and Williams, S. (2015). Parvalbumin interneurons of hippocampus tune population activity at theta frequency. *Neuron*, *86*(5), 1277–1289.

Anderson, J. S., Carandini, M., and Ferster, D. (2000). Orientation tuning of input conductance, excitation, and inhibition in cat primary visual cortex. *Journal of Neurophysiology*, *84*(2), 909–926.

Angelucci, A., Clascá, F., and Sur, M. (1996). Anterograde axonal tracing with the subunit B of cholera toxin: a highly sensitive immunohistochemical protocol for revealing fine axonal morphology in adult and neonatal brains. *The Journal of Neuroscience Methods*, *65*(1), 101–112.

Aschauer, D. F., Kreuz, S., and Rumpel, S. (2013). Analysis of transduction efficiency, tropism and axonal transport of AAV serotypes 1, 2, 5, 6, 8 and 9 in the mouse brain. *PLoS ONE*, *8*(9), e76310.

Ascoli, G. A., Alonso-Nanclares, L., Anderson, S. A., Barrionuevo, G., Benavides-Piccione, R., Burkhalter, A. et al. (2008). Petilla terminology: nomenclature of features of GABAergic interneurons of the cerebral cortex. *Nature Reviews Neuroscience*, 9(7):557–568.

Asokan, A., Schaffer, D. V., and Jude Samulski, R. (2012). The AAV vector toolkit: poised at the clinical crossroads. *Molecular Therapy, 20*, 699–708.

Atallah, B. V., and Scanziani, M. (2009). Instantaneous modulation of gamma oscillation frequency by balancing excitation with inhibition. *Neuron*, *62*(4), 566–577.

Atallah, B. V., Bruns, W., Carandini, M., and Scanziani, M. (2012). Parvalbumin-expressing interneurons linearly transform cortical responses to visual stimuli. *Neuron*, *73*(1), 159–170.

Bannister, A. P. Inter- and intra-laminar connections of pyramidal cells in the neocortex. *Neuroscience research* **53**, 95-103 (2005).

Bartos, M., Vida, I., Frotscher, M., Geiger, J. R. P. and Jonas, P. (2001). Rapid signaling at inhibitory synapses in a dentate gyrus interneuron network. *The Journal of Neuroscience,* 21, 2687–2698

Bartos, M., Vida, I., Frotscher, M., Meyer, A., Monyer, H., Geiger, J. R. P., and Jonas, P. (2002). Fast synaptic inhibition promotes synchronized gamma oscillations in hippocampal interneuron networks. *Proceedings of the National Academy of Sciences*, *99*(20), 13222–13227.

Bartos, M., Vida, I., and Jonas, P. (2007). Synaptic mechanisms of synchronized gamma oscillations in inhibitory interneuron networks. *Nature Reviews Neuroscience*, *8*(1), 45–56.

Bassett, J. P., and Taube, J. S. (2001). Neural correlates for angular head velocity in the rat dorsal tegmental nucleus. *The Journal of Neuroscience, 21*(15), 5740–5751.

Bassett, J. P., Tullman, M. L., and Taube, J. S. (2007). Lesions of the tegmento-mammillary circuit in the head hirection system disrupt the head direction signal in the anterior thalamus. *The Journal of Neuroscience*, 27(28):7564–7577.

Battaglia, D., Karagiannis, A., Gallopin, T., Gutch, H. W., and Cauli, B. (2013). Beyond the frontiers of neuronal types. *Frontiers Neural Circuits.* 7:13.

Baude, A., Bleasdale, C., Dalezios, Y., Somogyi, P., and Klausberger, T. (2007). Immunoreactivity for the GABAA receptor 1 subunit, somatostatin and connexin36 distinguishes axoaxonic, basket, and bistratified interneurons of the rat hippocampus. *Cerebral Cortex*, *17*(9), 2094–2107.

Beed, P., Gundlfinger, A., Schneiderbauer, S., Song, J., Böhm, C., Burgalossi, A., et al. (2013). Inhibitory gradient along the dorsoventral axis in the medial entorhinal cortex. *Neuron*, *79*(6), 1197–1207.

Beierlein, M., Gibson, J. R., and Connors, B. W. (2000). A network of electrically coupled interneurons drives synchronized inhibition in neocortex. *Nature Neuroscience*, *3*(9), 904–910.

Beierlein, M., Gibson, J. R., and Connors, B. W. (2003). Two dynamically distinct inhibitory networks in layer 4 of the neocortex. *Journal of Neurophysiology*, *90*(5), 2987–3000.

Bendels, M. H. K., Beed, P., Leibold, C., Schmitz, D., and Johenning, F. W. (2008). A novel control software that improves the experimental workflow of scanning photostimulation experiments. *The Journal of Neuroscience Methods*, 175(1), 44–57.

Berger, T. W., Milner, T. A., Swanson, G. W., Lynch, G. S., and Thompson, R. F. (1980). Reciprocal anatomical connections between anterior thalamus and cingulate-retrosplenial cortex in the rabbit. *Brain Research*, *201*(2), 411–417.

Berger, T. K., Perin, R., Silberberg, G., and Markram, H. (2009). Frequency-dependent disynaptic inhibition in the pyramidal network: a ubiquitous pathway in the developing rat neocortex. *The Journal of Physiology*, *587*(Pt 22), 5411–5425.

Bett, D., Stevenson, C. H., Shires, K. L., Smith, M. T., Martin, S. J., Dudchenko, P. A., and Wood, E. R. (2013). The postsubiculum and spatial learning: the role of postsubicular synaptic activity and synaptic plasticity in hippocampal place cell, object, and object-location memory. *The Journal of Neuroscience*, *33*(16), 6928–6943.

Bjerknes, T. L., Langston, R. F., Kruge, I. U., Moser, E. I., and Moser, M.-B. (2015). Coherence among head direction cells before eye opening in rat pups. *Current Biology*, *25*(1), 103–108.

Blair, H. T. and Sharp, P. E. (1995). Anticipatory head direction signals in anterior thalamus: evidence for a thalamocortical circuit that integrates angular head motion to compute head direction. *The Journal of Neuroscience*, 15(9):6260–6270.

Boccara, C. N., Sargolini, F., Thoresen, V. H., Solstad, T., Witter, M. P., Moser, E. I., and Moser, M.-B. (2010). Grid cells in pre- and parasubiculum. *Nature Publishing Group*, 13(8): 987–994.

Boccara, C. N., Kjonigsen, L. J., Hammer, I. M., Bjaalie, J. G., Leergaard, T. B., and Witter, M. P. (2015). A three-plane architectonic atlas of the rat hippocampal region. *Hippocampus*, *25*(7), 838–857.

Bock, D. D., Lee, W.-C. A., Kerlin, A. M., Andermann, M. L., Hood, G., Wetzel, A. W., et al. (2011). Network anatomy and in vivo physiology of visual cortical neurons. *Nature*, *471*(7337), 177–182.

Bonnevie, T., Dunn, B., Fyhn, M., Hafting, T., Derdikman, D., Kubie, J. L., Roudi, Y., Moser, E. I., and Moser, M.-B. (2013). Grid cells require excitatory drive from the hippocampus. *Nature Neuroscience*, 16(3):309–317.

Borhegyi, Z., Varga, V., Szilágyi, N., Fabo, D., and Freund, T. F. (2004). Phase segregation of medial septal GABAergic neurons during hippocampal theta activity. *The Journal of Neuroscience, 24*(39), 8470–8479.

Boyden, E. S., Zhang, F., Bamberg, E., Nagel, G., and Deisseroth, K. (2005). Millisecond-timescale, genetically targeted optical control of neural activity. *Nature Neuroscience*, *8*(9), 1263–1268.

Bragin, A., Jandó, G., Nádasdy, Z., Hetke, J., Wise, K., and Buzsáki, G. (1995). Gamma (40-100 Hz) oscillation in the hippocampus of the behaving rat. *The Journal of Neuroscience*, *15*(1 Pt 1), 47–60.

Brandon, M. P., Bogaard, A. R., Libby, C. P., Connerney, M. A., Gupta, K., and Hasselmo, M. E. (2011). Reduction of theta rhythm dissociates grid cell spatial periodicity from directional tuning. *Science*, *332*(6029), 595–599.

Brodmann, K. (1909). Vergleichende Lokalisationslehre der Grosshirnrinde in ihren Prinzipien dargestellt aufgrund des Zellenbaues.

Brown, S. P. and Hestrin, S. (2009). Intracortical circuits of pyramidal neurons reflect their long-range axonal targets. *Nature* 457, 1133-1136

Buetfering, C., Allen, K., and Monyer, H. (2014). Parvalbumin interneurons provide grid cell–driven recurrent inhibition in the medial entorhinal cortex. *Nature Publishing Group*, *17*(5), 710–718.

Burak, Y., and Fiete, I. R. (2009). Accurate path integration in continuous attractor network models of grid cells. *PLoS Computational Biology*, 5(2), e1000291.

Burgalossi, A., Herfst, L., Heimendahl, von, M., Förste, H., Haskic, K., Schmidt, M., and Brecht, M. (2011). Microcircuits of functionally identified neurons in the rat medial entorhinal cortex. *Neuron*, *70*(4), 773–786.

Burger, C., Nash, K., and Mandel, R. J. (2005). Recombinant adeno-associated viral vectors in the nervous system. *Human Gene Therapy*, *16*(7), 781–791.

Bush, D., Barry, C., and Burgess, N. (2014). What do grid cells contribute to place cell firing? *Trends in Neurosciences*, *37*(3), 136–145.

Butt S. J., Fuccillo M., Nery S., Noctor S., Kriegstein A., Corbin J. G. and Fishell G. (2005). The temporal and spatial origins of cortical interneurons predict their physiological subtype. Neuron 48:591– 604.

Buzsáki, G. (1984). Feed-forward inhibition in the hippocampal formation. *Progress in Neurobiology*, *22*(2), 131–153.

Buzsáki, G., and Draguhn, A. (2004). Neuronal oscillations in cortical networks. *Science*, *304*(5679), 1926–1929.

Caballero-Bleda, M., and Witter, M. P. (1994). Projections from the presubiculum and the parasubiculum to morphologically characterized entorhinal-hippocampal projection neurons in the rat. *Experimental brain research*, *101*(1), 93-108.

Calton, J. L., Stackman, R. W., Goodridge, J. P., Archey, W. B., Dudchenko, P. A., and Taube, J. S. (2003). Hippocampal place cell instability after lesions of the head direction cell network. *The Journal of Neuroscience*, 23(30):9719–9731.

Calton, J. L., Turner, C. S., Cyrenne, D.-L. M., Lee, B. R., and Taube, J. S. (2008). Landmark control and updating of self-movement cues are largely maintained in head direction cells after lesions of the posterior parietal cortex. *Behavioral neuroscience*, 122(4):827–840.

Canto, C. B., Wouterlood, F. G., and Witter, M. P. (2008). What does the anatomical organization of the entorhinal cortex tell us? *Neural Plasticity*, *2008*, 381243.

Canto, C. B., Koganezawa, N., Beed, P., Moser, E. I., and Witter, M. P. (2012). All layers of medial entorhinal cortex receive presubicular and parasubicular inputs. *The Journal of Neuroscience*, 32(49):17620–17631.

Capogna, M. (2011). Neurogliaform cells and other interneurons of stratum lacunosum-moleculare gate entorhinal-hippocampal dialogue. *The Journal of Physiology*, *589*(8), 1875–1883.

Castle, M. J., Gershenson, Z. T., Giles, A. R., Holzbaur, E. L. F., and Wolfe, J. H. (2014). Adeno-associated virus serotypes 1, 8, and 9 share conserved mechanisms for anterograde and retrograde axonal transport. *Human Gene Therapy*, *25*(8), 705–720.

Cauli, B., Audinat, E., Lambolez, B., Angulo, M. C., Ropert, N., Tsuzuki, K., et al. (1997). Molecular and physiological diversity of cortical nonpyramidal cells. *The Journal of Neuroscience*, *17*(10), 3894–3906.

Cauli, B., Porter, J. T., Tsuzuki, K., Lambolez, B., Rossier, J., Quenet, B., and Audinat, E. (2000). Classification of fusiform neocortical interneurons based on unsupervised clustering. *Proceedings of the National Academy of Sciences*, 97(11), 6144–6149.

Celio M.R. (1986). Parvalbumin in most gamma-aminobutyric acid-containing neurons of the rat cerebral cortex. *Science* 231:995-997.

Cenquizca, L. A. and Swanson, L. W. (2007). Spatial organization of direct hippocampal field CA1 axonal projections to the rest of the cerebral cortex. *Brain Research Reviews*, 56(1):1–26.

Chamberland, S., Salesse, C., Topolnik, D., and Topolnik, L. (2010). Synapse-specific inhibitory control of hippocampal feedback inhibitory circuit. *Frontiers in Cellular Neuroscience*, *4*, 130.

Chen, L. L., Lin, L. H., Barnes, C. A. and McNaughton, B. L. (1994). Head-direction cells in the rat posterior cortex - II. Contributions of visual and ideothetic information to the directional firing. *Experimental Brain Research*, 101(1):24–34.

Chen and Aston-Jones, G. (1995). Evidence that cholera toxin B subunit (CTb) can be avidly taken up and transported by fibers of passage. *Brain Research*, *674*(1), 107–111.

Chen, X. and Johnston, D. (2004). Properties of single voltage-dependent K+ channels in dendrites of CA1 pyramidal neurones of rat hippocampus. *The Journal of Physiology*, 559(Pt 1):187–203.

Chevaleyre, V. and Siegelbaum, S. A. (2010). Strong CA2 pyramidal neuron synapses define a powerful disynaptic cortico-hippocampal loop. *Neuron*, 66(4):560–572.

Cho, J. and Sharp, P. E. (2001). Head direction, place, and movement correlates for cells in the rat retrosplenial cortex. *Behavioral neuroscience*, 115(1):3–25.

Chow, B. Y., Han, X., Dobry, A. S., Qian, X., Chuong, A. S., Li, M., et al. (2010). High-performance genetically targetable optical neural silencing by light-driven proton pumps. *Nature*, *463*(7277), 98–102.

Chow, B. Y., Han, X., and Boyden, E. S. (2012). Genetically encoded molecular tools for light-driven silencing of targeted neurons. *Progress in Brain Research*, *196*, 49–61.

Chrobak, J. J., and Buzsáki, G. (1998). Operational dynamics in the hippocampal-entorhinal axis. *Neuroscience and Biobehavioral Reviews*, *22*(2), 303–310.

Clark, B. J. and Taube, J. S. (2012). Vestibular and attractor network basis of the head direction cell signal in subcortical circuits. *Frontiers in neural circuits*, 6:7.

Clark, B. J., and Harvey, R. E. (2016). Do the anterior and lateral thalamic nuclei make distinct contributions to spatial representation and memory? *Neurobiology of Learning and Memory*, *133*, 69–78.

Cobb, S. R., Buhl, E. H., Halasy, K., Paulsen, O., and Somogyi, P. (1995). Synchronization of neuronal activity in hippocampus by individual GABAergic interneurons. *Nature*, *378*(6552), 75–78.

Connors, B. W., and Gutnick, M. J. (1990). Intrinsic firing patterns of diverse neocortical neurons. *Trends in Neurosciences*, *13*(3), 99–104.

Conte, W. L., Kamishina, H., and Reep, R. L. (2009a). The efficacy of the fluorescent conjugates of cholera toxin subunit B for multiple retrograde tract tracing in the central nervous system. *Brain Structure and Function*, *213*(4-5), 367–373.

Conte, W. L., Kamishina, H., and Reep, R. L. (2009b). Multiple neuroanatomical tract-tracing using fluorescent Alexa Fluor conjugates of cholera toxin subunit B in rats. *Nature Protocols*, *4*(8), 1157–1166.

Coogan, T. A., and Burkhalter, A. (1993). Hierarchical organization of areas in rat visual cortex. *Journal of Neuroscience*, *13*(9), 3749–3772.

Cottam, J. C. H., Smith, S. L., and Hausser, M. (2013). Target-specific effects of somatostatin-expressing interneurons on neocortical visual processing. *The Journal of Neuroscience*, *33*(50), 19567–19578.

Couey, J. J., Witoelar, A., Zhang, S.-J., Zheng, K., Ye, J., Dunn, B., Czajkowski, R., Moser, M.-B., Moser, E. I., Roudi, Y., and Witter, M. P. (2013). Recurrent inhibitory circuitry as a mechanism for grid formation. *Nature Publishing Group*, 16(3):318–324.

Crochet, S., and Petersen, C. C. H. (2006). Correlating whisker behavior with membrane potential in barrel cortex of awake mice. *Nature Neuroscience*, *9*(5), 608–610.

Cruikshank, S. J., Lewis, T. J., and Connors, B. W. (2007). Synaptic basis for intense thalamocortical activation of feedforward inhibitory cells in neocortex. *Nature Neuroscience*, *10*(4), 462–468.

Cruikshank, S. J., Urabe, H., Nurmikko, A. V., and Connors, B. W. (2010). Pathway-specific feedforward circuits between thalamus and neocortex revealed by selective optical stimulation of axons. *Neuron*, *65*(2), 230–245.

Csicsvari, J., Jamieson, B., Wise, K. D., and Buzsáki, G. (2003). Mechanisms of gamma oscillations in the hippocampus of the behaving rat. *Neuron*, *37*(2), 311–322.

DeFelipe, J., and Fariñas, I. (1992). The pyramidal neuron of the cerebral cortex: morphological and chemical characteristics of the synaptic inputs. *Progress in Neurobiology*, *39*(6), 563–607.

DeFelipe, J. (2002). Cortical interneurons: from Cajal to 2001. *Progress in Brain Research*, *136*, 215–238.

DeFelipe, J., López-Cruz, P. L., Benavides-Piccione, R., Bielza, C., Larrañaga, P., Anderson, S., et al. (2013). New insights into the classification and nomenclature of cortical GABAergic interneurons. *Nature Reviews Neuroscience*, *14*(3), 202–216.

Dhillon, A., and Jones, R. S. (2000). Laminar differences in recurrent excitatory transmission in the rat entorhinal cortex in vitro. *Neuroscience*, 99(3), 413–422.

Dickson, C. T., Magistretti, J., Shalinsky, M. H., Fransen, E., Hasselmo, M. E., and Alonso, A. (2000). Properties and role of Ih in the pacing of subthreshold oscillations in entorhinal cortex layer 2 neurons. *Journal of Neurophysiology*, *83*(5), 2562–2579.

Ding, S.-L. (2013). Comparative anatomy of the prosubiculum, subiculum, presubiculum, postsubiculum, and parasubiculum in human, monkey, and rodent. *The Journal of Comparative Neurology*, *521*(18), 4145–4162.

Ding, S.-L. and Rockland, K. (2001). Modular organization of the monkey presubiculum. *Experimental Brain Research*, 139(3):255–265.

Dingledine, R., Borges, K., Bowie, D., and Traynelis, S. F. (1999). The glutamate receptor ion channels. *Pharmacological Reviews*, *51*(1), 7–61.

Dong, H., Shao, Z., Nerbonne, J. M., and Burkhalter, A. (2004). Differential depression of inhibitory synaptic responses in feedforward and feedback circuits between different areas of mouse visual cortex. *The Journal of Comparative Neurology*, *475*(3), 361–373.

Douglas, R. J. and Martin, K. A. (2004). Neuronal circuits of the neocortex. *Annual review of neuroscience* **27**, 419-451

Douglas, R. J., and Martin, K. A. C. (2007). Recurrent neuronal circuits in the neocortex. *Current Biology*, *17*(13), R496–R500

Druga, R. (2009). Neocortical inhibitory system. *Folia Biologica*, *55*(6), 201–217.

Dumitriu, D., Cossart, R., Huang, J., and Yuste, R. (2007). Correlation between axonal morphologies and synaptic input kinetics of interneurons from mouse visual cortex. *Cerebral Cortex*, *17*(1), 81–91.

Dymecki, S. M., Ray, R. S., and Kim, J. C. (2010). Mapping cell fate and function using recombinase-based intersectional strategies. *Methods in Enzymology*, 477, 183–213.

Erisir A., Lau D., Rudy B., Leonard C.S. (1999). Function of specific K channels in sustained high-frequency firing of fast-spiking neocortical interneurons. *Journal of Neurophysiology*, 82:2476 –2489.

Ferrante, M., Shay, C. F., Tsuno, Y., William Chapman, G., and Hasselmo, M. E. (2016). Post-inhibitory rebound spikes in rat medial entorhinal layer 2/3 principal cells: in vivo, in vitro, and computational modeling characterization. *Cerebral Cortex,* 1-15

Finkelstein, R. A., and Dorner, F. (1985). Cholera enterotoxin (choleragen). *Pharmacology and Therapeutics*, *27*(1), 37–47.

Fino, E., and Yuste, R. (2011). Dense inhibitory connectivity in neocortex. *Neuron*, *69*(6), 1188–1203.

Fogarty M., Grist M., Gelman D., Marin O., Pachnis V., and Kessaris N. (2007). Spatial genetic patterning of the embryonic neuroepithelium generates GABAergic interneuron diversity in the adult cortex. *The Journal of Neuroscience*, 27:10935-10946.

Freund T. F., Magloczky Z., Soltesz I., Somogyi P. (1986). Synaptic connections, axonal and dendritic patterns of neurons immunoreactive for cholecystokinin in the visual cortex of the cat. *Neuroscience*, 19, 1133-1159

Freund, T.F., Antal, M., (1988). GABA-containing neurons in the septum control inhibitory interneurons in the hippocampus. *Nature,* 336, 170e173.

Freund, T. F. and Buzsáki, G. (1996). Interneurons of the hippocampus. *Hippocampus* **6**, 347-470.

Freund, T. F. (2003). Interneuron diversity series: rhythm and mood in perisomatic inhibition. *Trends in Neurosciences*, *26*(9), 489–495.

Freund, T. F., and Katona, I. (2007). Perisomatic Inhibition. *Neuron*, *56*(1), 33–42. 2

Fricker, D., Dinocourt, C., Eugène, E., Wood, J. N., Wood, J., and Miles, R. (2009). Pyramidal cells of rodent presubiculum express a tetrodotoxin-insensitive Na+ current. *The Journal of Physiology*, 587(Pt 17):4249–4264.

Frotscher, M., and Léránth, C. (1985). Cholinergic innervation of the rat hippocampus as revealed by choline acetyltransferase immunocytochemistry: a combined light and electron microscopic study. *The Journal of Comparative Neurology*, *239*(2), 237–246.

Fu, Y., Tucciarone, J. M., Espinosa, J. S., Sheng, N., Darcy, D. P., Nicoll, R. A., et al. (2014). A cortical circuit for gain control by behavioral state. *Cell*, *156*(6), 1139–1152.

Fuchs, E. C., Zivkovic, A. R., Cunningham, M. O., Middleton, S., LeBeau, F. E. N., Bannerman, D. M., et al. (2007). Recruitment of parvalbumin-positive interneurons determines hippocampal function and associated behavior. *Neuron*, *53*(4), 591–604.

Fuchs, E. C., Neitz, A., Pinna, R., Melzer, S., Caputi, A., and Monyer, H. (2016). Local and distant input controlling excitation in layer 2 of the medial entorhinal cortex. *Neuron*, *89*(1), 194–208.

Fuentealba, P., Begum, R., Capogna, M., Jinno, S., Márton, L. F., Csicsvari, J., et al. (2008). Ivy cells: a population of nitric-oxide-producing, slow-spiking gabaergic neurons and their involvement in hippocampal network activity. *Neuron*, *57*(6), 917–929.

Fukuda, T. (2007). Structural organization of the gap junction network in the cerebral cortex. *The Neuroscientist*, *13*(3), 199–207.

Funahashi, M. and Stewart, M. (1997a). Presubicular and parasubicular cortical neurons of the rat: electrophysiological and morphological properties. *Hippocampus*, 7(2):117–129.

Funahashi, M. and Stewart, M. (1997b). Presubicular and parasubicular cortical neurons of the rat: functional separation of deep and superficial neurons in vitro. *The Journal of Physiology*, 501 (Pt 2):387–403.

Fyhn, M., Molden, S., Witter, M. P., Moser, E. I., and Moser, M.-B. (2004). Spatial representation in the entorhinal cortex. *Science*, 305(5688):1258–1264.

Gabernet, L., Jadhav, S. P., Feldman, D. E., Carandini, M., and Scanziani, M. (2005). Somatosensory integration controlled by dynamic thalamocortical feed-forward inhibition. *Neuron*, *48*(2), 315–327.

Galarreta, M., and Hestrin, S. (2002). Electrical and chemical synapses among parvalbumin fast-spiking GABAergic interneurons in adult mouse neocortex. *Proceedings of the National Academy of Sciences*, *99*(19), 12438–12443.

Gatome, C. W., Slomianka, L., Lipp, H. P., and Amrein, I. (2010). Number estimates of neuronal phenotypes in layer 2 of the medial entorhinal cortex of rat and mouse. *Neuroscience*, *170*(1), 156–165.

Gelman, D. M., and Marín, O. (2010). Generation of interneuron diversity in the mouse cerebral cortex. *The European Journal of Neuroscience*, *31*(12), 2136–2141.

Gentet, L. J., Avermann, M., Matyas, F., Staiger, J. F., and Petersen, C. C. H. (2010). Membrane potential dynamics of GABAergic neurons in the barrel cortex of behaving mice. *Neuron*, *65*(3), 422–435.

Gentet, L. J., Kremer, Y., Taniguchi, H., Huang, Z. J., Staiger, J. F., and Petersen, C. C. H. (2012). Unique functional properties of somatostatin-expressing GABAergic neurons in mouse barrel cortex. *Nature Publishing Group*, *15*(4), 607–612.

Germroth, P., Schwerdtfeger, W. K., and Buhl, E. H. (1989). GABAergic neurons in the entorhinal cortex project to the hippocampus. *Brain Research*, *494*(1), 187–192.

Gibson, J. R., Beierlein, M., and Connors, B. W. (1999). Two networks of electrically coupled inhibitory neurons in neocortex. *Nature*, *402*(6757), 75–79.

Giocomo, L. M., and Hasselmo, M. E. (2009). Knock-Out of HCN1 subunit flattens dorsal-ventral frequency gradient of medial entorhinal neurons in adult mice. *The Journal of Neuroscience*, *29*(23), 7625–7630.

Giocomo, L. M., Hussaini, S. A., Zheng, F., Kandel, E. R., Moser, M.-B., and Moser, E. I. (2011). Grid cells use HCN1 channels for spatial scaling. *Cell*, *147*(5), 1159–1170.

Giocomo, L. M., Stensola, T., Bonnevie, T., Van Cauter, T., Moser, M.-B., and Moser, E. I. (2014). Topography of head direction cells in medial entorhinal cortex. *Current Biology*, *24*(3), 252–262.

Goldman-Rakic, P. S. (1995). Architecture of the prefrontal cortex and the central executive. *Annals of the New York Academy of Sciences*, *769*, 71–83.

Golob, E. J. and Taube, J. S. (1997). Head direction cells and episodic spatial information in rats without a hippocampus. *Proceedings of the National Academy of Sciences of the United States of America*, 94(14):7645–7650.

Gonchar, Y., and Burkhalter, A. (1997). Three distinct families of GABAergic neurons in rat visual cortex. *Cerebral Cortex*, *7*(4), 347–358.

Gonchar, Y., Turney, S., Price, J. L., and Burkhalter, A. (2002). Axo-axonic synapses formed by somatostatin-expressing GABAergic neurons in rat and monkey visual cortex. *The Journal of Comparative Neurology*, *443*(1), 1–14.

Gonchar, Y., and Burkhalter, A. (2003). Distinct GABAergic targets of feedforward and feedback connections between lower and higher areas of rat visual cortex. *The Journal of Neuroscience, 23*(34), 10904–10912.

Gonchar, Y., Wang, Q., and Burkhalter, A. (2008). Multiple distinct subtypes of GABAergic neurons in mouse visual cortex identified by triple immunostaining. *Frontiers in Neuroanatomy*, *1*, 3.

Gonzalez-Sulser, A., Parthier, D., Candela, A., McClure, C., Pastoll, H., Garden, D., et al. (2014). GABAergic projections from the medial septum selectively inhibit interneurons in the medial entorhinal cortex. *The Journal of Neuroscience, 34*(50), 16739–16743.

Goodridge, J. P. and Taube, J. S. (1997). Interaction between the postsubiculum and anterior thalamus in the generation of head direction cell activity. *The Journal of Neuroscience*, 17(23): 9315–9330.

Goodridge, J. P., Dudchenko, P. A., Worboys, K. A., Golob, E. J., and Taube, J. S. (1998). Cue control and head direction cells. *Behavioral Neuroscience*, 112(4):749–76.

Goutagny, R., Jackson, J., and Williams, S. (2009). Self-generated theta oscillations in the hippocampus. *Nature Neuroscience*, *12*(12), 1491–1493.

Gray, E. G. Axo-somatic and axo-dendritic synapses of the cerebral cortex: an electron microscope study. *Journal of anatomy* 93, 420-433 (1959).

Gulyás, A. I., Hájos, N., and Freund, T. F. (1996). Interneurons containing calretinin are specialized to control other interneurons in the rat hippocampus. *Journal of Neuroscience*, *16*(10), 3397–3411.

Gulyás, A. I., Megías, M., Emri, Z., and Freund, T. F. (1999). Total number and ratio of excitatory and inhibitory synapses converging onto single interneurons of different types in the CA1 area of the rat hippocampus. *The Journal of Neuroscience, 19*(22), 10082–10097.

Gunaydin, L. A., Yizhar, O., Berndt, A., Sohal, V. S., Deisseroth, K., and Hegemann, P. (2010). Ultrafast optogenetic control. *Nature Publishing Group*, *13*(3), 387–392.

Gupta, A., Wang, Y. and Markram, H. (2000). Organizing principles for a diversity of GABAergic interneurons and synapses in the neocortex. *Science* 287, 273–278.

Hafting T., Fyhn M., Molden S., Moser M-B., Moser E.I. (2005). Microstructure of a spatial map in the entorhinal cortex. *Nature*, 436(7052): 801–806.

Haider, B., Duque, A., Hasenstaub, A. R., and McCormick, D. A. (2006). Neocortical network activity in vivo is generated through a dynamic balance of excitation and inhibition. *The Journal of Neuroscience, 26*(17), 4535–4545.

Hájos N, Acsidy L, Freund TF. (1996). Target selectivity and neurochemical characteristics of VIP-immunoreactive interneurons in the rat dentate gyrus. *The European Journal of Neuroscience*, 8:1415-1431.

Hájos, N., and Paulsen, O. (2009). Network mechanisms of gamma oscillations in the CA3 region of the hippocampus. *Neural Networks*, *22*(8), 1113–1119.

Halabisky, B., Shen, F., Huguenard, J. R., and Prince, D. A. (2006). Electrophysiological classification of somatostatin-positive interneurons in mouse sensorimotor cortex. *Journal of Neurophysiology*, *96*(2), 834–845.

Han, X., and Boyden, E. S. (2007). Multiple-color optical activation, silencing, and desynchronization of neural activity, with single-spike temporal resolution. *PLoS ONE*, *2*(3), e299.

Hangya, B., Pi, H.-J., Kvitsiani, D., Ranade, S. P., and Kepecs, A. (2014). From circuit motifs to computations: mapping the behavioral repertoire of cortical interneurons. *Current Opinion in Neurobiology*, *26*, 117–124.

Harris, K. D., and Thiele, A. (2011). Cortical state and attention. *Nature Reviews Neuroscience*, *12*(9), 509–523.

Hartwich, K., Pollak, T., and Klausberger, T. (2009). Distinct firing patterns of identified basket and dendrite-targeting interneurons in the prefrontal cortex during hippocampal theta and local spindle oscillations. *The Journal of Neuroscience*, *29*(30), 9563–9574.

Hasselmo, M. E. (2014). Neuronal rebound spiking, resonance frequency and theta cycle skipping may contribute to grid cell firing in medial entorhinal cortex. *Philosophical Transactions of the Royal Society of London. Series B, Biological Sciences*, *369*(1635), 20120523.

Heffner, C. S., Herbert Pratt, C., Babiuk, R. P., Sharma, Y., Rockwood, S. F., Donahue, L. R., et al. (2012). Supporting conditional mouse mutagenesis with a comprehensive Cre characterization resource. *Nature Communications*, *3*, 1218.

Helm, J., Akgul, G., and Wollmuth, L. P. (2013). Subgroups of parvalbumin-expressing interneurons in layers 2/3 of the visual cortex. *Journal of Neurophysiology*, *109*(6), 1600–1613.

Hestrin, S., and Galarreta, M. (2005). Electrical synapses define networks of neocortical GABAergic neurons. *Trends in Neurosciences*, *28*(6), 304–309.

Higley, M. J., and Contreras, D. (2006). Balanced excitation and inhibition determine spike timing during frequency adaptation. *The Journal of Neuroscience, 26*(2), 448–457.

Hofer, S. B., Ko, H., Pichler, B., Vogelstein, J., Ros, H., Zeng, H., et al. (2011). Differential connectivity and response dynamics of excitatory and inhibitory neurons in visual cortex. *Nature Publishing Group*, *14*(8), 1045–1052.

Honda, Y. and Ishizuka, N. (2004). Organization of connectivity of the rat presubiculum: I. Efferent projections to the medial entorhinal cortex. *The Journal of Comparative Neurology*, 473(4):463–484.

Honda, Y., Umitsu, Y., and Ishizuka, N. (2008). Organization of connectivity of the rat presubiculum: II. Associational and commissural connections. *The Journal of Comparative Neurology*, 506(4):640–658.

Honda Y, Furuta T, Kaneko T, Shibata H, Sasaki H. Patterns of axonal collateralization of single layer V cortical projection neurons in the rat presubiculum. *The Journal of Comparative Neurology*, 2011; 519(7):1395–412.

Hosp, J. A., Strüber, M., Yanagawa, Y., Obata, K., Vida, I., Jonas, P., and Bartos, M. (2014). Morpho-physiological criteria divide dentate gyrus interneurons into classes. *Hippocampus*, *24*(2), 189–203.

Houser, C. R. (2007). Interneurons of the dentate gyrus: an overview of cell types, terminal fields and neurochemical identity. *Progress in Brain Research*, *163*, 217–232.

Hubel, D. H. and Wiesel, T. N. (1962). Receptive fields, binocular interaction and functional architecture in the cat's visual cortex. *The Journal of physiology* 160, 106-154.

Hu, H., Martina, M., and Jonas, P. (2010). Dendritic mechanisms underlying rapid synaptic activation of fast-spiking hippocampal interneurons. *Science*, *327*(5961), 52–58.

Hu, H., Ma, Y., and Agmon, A. (2011). Submillisecond firing synchrony between different subtypes of cortical interneurons connected chemically but not electrically. *The Journal of Neuroscience*, *31*(9), 3351–3361.

Hu, H., Cavendish, J. Z., and Agmon, A. (2013). Not all that glitters is gold: off-target recombination in the somatostatin-IRES-Cre mouse line labels a subset of fast-spiking interneurons. *Frontiers in Neural Circuits*, 7, 195.

Hu, H., and Jonas, P. (2014). A supercritical density of Na+ channels ensures fast signaling in GABAergic interneuron axons. *Nature Publishing Group*, *17*(5), 686–693.

Isaacson, J. S., and Scanziani, M. (2011). How inhibition shapes cortical activity. *Neuron*, *72*(2), 231–243.

Ishizuka, N. (2001). Laminar organization of the pyramidal cell layer of the subiculum in the rat. *The Journal of Comparative Neurology*, 435(1):89–110.

Jackson, J., Ayzenshtat, I., Karnani, M. M., and Yuste, R. (2016). VIP+ interneurons control neocortical activity across brain states. *Journal of Neurophysiology*, *115*(6), 3008–3017.

Janes, P. W., Ley, S. C., and Magee, A. I. (1999). Aggregation of lipid rafts accompanies signaling via the T cell antigen receptor. *The Journal of Cell Biology*, *147*(2), 447–461.

Jankowski, M. M., Islam, M. N., Wright, N. F., Vann, S. D., Erichsen, J. T., Aggleton, J. P., and O'Mara, S. M. (2014). Nucleus reuniens of the thalamus contains head direction cells. *eLife*, *3*.

Janusonis, S., Gluncic, V., and Rakic, P. (2004). Early serotonergic projections to Cajal-Retzius cells: relevance for cortical development. *The Journal of Neuroscience*, *24*(7), 1652–1659.

Jiang, X., Shen, S., Cadwell, C. R., Berens, P., Sinz, F., Ecker, A. S., et al. (2015). Principles of connectivity among morphologically defined cell types in adult neocortex. *Science*, *350*(6264), aac9462.

Jinno, S., and Kosaka, T. (2000). Colocalization of parvalbumin and somatostatin-like immunoreactivity in the mouse hippocampus: quantitative analysis with optical disector. *The Journal of Comparative Neurology*. 428(3):377-88.

Jinno, S., Klausberger, T., Márton, L. F., Dalezios, Y., Roberts, J. D. B., Fuentealba, P., et al. (2007). Neuronal diversity in GABAergic long-range projections from the hippocampus. *The Journal of Neuroscience*, *27*(33), 8790–8804.

Jones, B. F. and Witter, M. P. (2007). Cingulate cortex projections to the parahippocampal region and hippocampal formation in the rat. *Hippocampus*, 17(10):957–976.

Kapfer, C., Glickfeld, L. L., Atallah, B. V., and Scanziani, M. (2007). Supralinear increase of recurrent inhibition during sparse activity in the somatosensory cortex. *Nature Neuroscience*, *10*(6), 743–753.

Karagiannis, A., Gallopin, T., Dávid, C., Battaglia, D., Geoffroy, H., Rossier, J., et al. (2009). Classification of NPY-expressing neocortical interneurons. *The Journal of Neuroscience, 29*(11), 3642–3659.

Karnani, M. M., Agetsuma, M., and Yuste, R. (2014). A blanket of inhibition: functional inferences from dense inhibitory connectivity. *Current Opinion in Neurobiology*, *26*, 96–102.

Karnani, M. M., Jackson, J., Ayzenshtat, I., Hamzehei Sichani, A., Manoocheri, K., Kim, S., and Yuste, R. (2016a). Opening holes in the blanket of inhibition: localized lateral disinhibition by vip interneurons. *The Journal of Neuroscience*, *36*(12), 3471–3480.

Karnani, M. M., Jackson, J., Ayzenshtat, I., Tucciarone, J., Manoocheri, K., Snider, W. G., and Yuste, R. (2016b). Cooperative subnetworks of molecularly similar interneurons in mouse neocortex. *Neuron*, *90*(1), 86–100.

Karube, F., Kubota, Y., and Kawaguchi, Y. (2004). Axon branching and synaptic bouton phenotypes in GABAergic nonpyramidal cell subtypes. *The Journal of Neuroscience,* 24, 2853–2865.

Katona, L., Lapray, D., Viney, T. J., Oulhaj, A., Borhegyi, Z., Micklem, B. R., et al. (2014). Sleep and movement differentiates actions of two types of somatostatin-expressing GABAergic interneuron in rat hippocampus. *Neuron*, *82*(4), 872–886.

Katz L. C., Burkhalter A, Dreyer W.J. (1984). Fluorescent latex microspheres as a retrograde neuronal marker for in vivo and in vitro studies of visual cortex. *Nature*, 310(5977):498–500.

Katz L. C. and Iarovici D. M. (1990). Green fluorescent latex microspheres: A new retrograde tracer. *Neuroscience*, 34(2):511–20.

Kawaguchi, Y. (1993). Groupings of nonpyramidal and pyramidal cells with specific physiological and morphological characteristics in rat frontal cortex. *Journal of Neurophysiology*, *69*(2), 416–431.

Kawaguchi, Y. and Kubota, Y. (1993). Correlation of physiological subgroupings of nonpyramidal cells with parvalbumin- and calbindinD28k-immunoreactive neurons in layer V of rat frontal cortex. *Journal of neurophysiology* 70, 387-396

Kawaguchi, Y. and Kubota, Y. (1996). Physiological and morphological identification of so-matostatin- or vasoactive intestinal polypeptide-containing cells among GABAergic cell sub-types in rat frontal cortex. *The Journal of Neuroscience*, 16, 2701-2715

Kawaguchi, Y., and Kubota, Y. (1997). Gabaergic cell subtypes and their synaptic connections in rat frontal cortex. *Cerebral Cortex*, *7*(6), 476–486.

Kawaguchi, Y. (1995). Physiological subgroups of nonpyramidal cells with specific morphological characteristics in layer 2/3 of rat frontal cortex. *The Journal of Neuroscience,* 15, 2638-2655.

Kepecs, A., and Fishell, G. (2014). Interneuron cell types are fit to function. *Nature*, *505*(7483), 318–326.

Kerlin, A. M., Andermann, M. L., Berezovskii, V. K., and Reid, R. C. (2010). Broadly tuned response properties of diverse inhibitory neuron subtypes in mouse visual cortex. *Neuron*, *67*(5), 858–871.

Kitamura, T., Pignatelli, M., Suh, J., Kohara, K., Yoshiki, A., Abe, K., and Tonegawa, S. (2014). Island cells control temporal association memory. *Science*, *343*(6173), 896–901.

Klapoetke, N. C., Murata, Y., Kim, S. S., Pulver, S. R., Birdsey-Benson, A., Cho, Y. K., et al. (2014). Independent optical excitation of distinct neural populations. *Nature Methods*, 11(3), 338–346.

Klausberger, T., Magill, P. J., Márton, L. F., Roberts, J. D. B., Cobden, P. M., Buzsáki, G., and Somogyi, P. (2003). Brain-state- and cell-type-specific firing of hippocampal interneu-rons in vivo. *Nature*, *421*(6925), 844–848.

Klausberger, T., Márton, L. F., Baude, A., Roberts, J. D. B., Magill, P. J., and Somogyi, P. (2004). Spike timing of dendrite-targeting bistratified cells during hippocampal network oscillations in vivo. *Nature Neuroscience*, 7(1), 41–47.

Klausberger, T., Márton, L. F., O'Neill, J., Huck, J. H. J., Dalezios, Y., Fuentealba, P., et al. (2005). Complementary roles of cholecystokinin- and parvalbumin-expressing GABAergic neurons in hippocampal network oscillations. *The Journal of Neuroscience*, *25*(42), 9782–9793.

Klausberger, T., and Somogyi, P. (2008). Neuronal diversity and temporal dynamics: the unity of hippocampal circuit operations. *Science*, *321*(5885), 53–57.

Knierim, J. J., and Zhang, K. (2012). Attractor dynamics of spatially correlated neural activity in the limbic system. *Annual Review of Neuroscience*, *35*(1), 267–285.

Köbbert, C., Apps, R., Bechmann, I., Lanciego, JLy. J., Thanos, S. (2000). Current concepts in neuro-anatomical tracing. *Progress in Neurobiology*. 62(4):327–51.

Koenig, J., Linder, A. N., Leutgeb, J. K., and Leutgeb, S. (2011). The spatial periodicity of grid cells is not sustained during reduced theta oscillations. *Science*, *332*(6029), 592–595.

Kohara, K., Pignatelli, M., Rivest, A. J., Jung, H.-Y., Kitamura, T., Suh, J., et al. (2014). Cell type-specific genetic and optogenetic tools reveal hippocampal CA2 circuits. *Nature Publishing Group*, 17(2), 269–279.

Köhler, C., Chan-Palay, V., Wu, J.Y., (1984). Septal neurons containing glutamic acid decarboxylase immunoreactivity project to the hippocampal region in the rat brain. *Anatomy and Embryology*, 169, 41e44.

Kononenko, N. L., and Witter, M. P. (2012). Presubiculum layer 3 conveys retrosplenial input to the medial entorhinal cortex. *Hippocampus*, *22*(4), 881–895.

Kosaka, T., Katsumaru, H., Hama, K., Wu, J. Y., Heizmann C. W. (1987). GABAergic neurons con-taining the Ca2+-binding protein parvalbumin in the rat hippocampus and dentate gyrus. *Brain Research,* 419:119-130.

Krimer, L. S., Zaitsev, A. V., Czanner, G., Kröner, S., González-Burgos, G., Povysheva, N. V., et al. (2005). Cluster analysis-based physiological classification and morphological prop-erties of inhibitory neurons in layers 2-3 of monkey dorsolateral prefrontal cortex. *Journal of Neurophysiology*, *94*(5), 3009–3022.

Krook-Magnuson, E., Varga, C., Lee, S. H. and Soltesz, I. (2012). New dimensions of interneuronal specialization unmasked by principal cell heterogeneity. *Trends in neurosciences,* 35, 175-184

Kubota, Y., Hattori, R. and Yui, Y. (1994). Three distinct subpopulations of GABAergic neurons in rat frontal agranular cortex. *Brain Research,* 649, 159-173

Kubota, Y., and Kawaguchi, Y. (1997). Two distinct subgroups of cholecystokinin-immunoreactive cortical interneurons. *Brain Research*, *752*(1-2), 175–183.

Kubota, Y. (2014). Untangling GABAergic wiring in the cortical microcircuit. *Current Opinion in Neurobiology*, *26*, 7–14.

Kubota, Y., Karube, F., Nomura, M., and Kawaguchi, Y. (2016). The diversity of cortical inhibitory synapses. *Frontiers in neural circuits*, 10, 27.

Kuhlman, S. J., Olivas, N. D., Tring, E., Ikrar, T., Xu, X., and Trachtenberg, J. T. (2013). A disinhibitory microcircuit initiates critical-period plasticity in the visual cortex. *Nature*, *501*(7468), 543–546.

Langston, R. F., Ainge, J. A., Couey, J. J., Canto, C. B., Bjerknes, T. L., Witter, M. P., Moser, E. I., and Moser, M. B. (2010). Development of the spatial representation system in the rat. *Science*, 328(5985):1576–1580.

Lapray, D., Lasztoczi, B., Lagler, M., Viney, T. J., Katona, L., Valenti, O., et al. (2012). Be-havior-dependent specialization of identified hippocampal interneurons. *Nature Publishing Group*, *15*(9), 1265–1271.

Lee, S.-H., Kwan, A. C., Zhang, S., Phoumthipphavong, V., Flannery, J. G., Masmanidis, S. C., et al. (2012). Activation of specific interneurons improves V1 feature selectivity and visual perception. *Nature*, 488(7411), 379–383.

Lee, S.-H., Kruglikov, I., Huang, Z. J., Fishell, G., and Rudy, B. (2013). A disinhibitory cir-cuit mediates motor integration in the somatosensory cortex. *Nature Publishing Group*, *16*(11), 1662–1670.

Lee, S.-H., Marchionni, I., Bezaire, M., Varga, C., Danielson, N., Lovett-Barron, M., et al. (2014). Parvalbumin-positive basket cells differentiate among hippocampal pyramidal cells. *Neuron*, 1–16.

Leutgeb S, Ragozzino KE, Mizumori SJY. (2000). Convergence of head direction and place information in the CA1 region of hippocampus. *Neuroscience*, 100(1):11–9.

Lien C-C, Martina M, Schultz JH, Ehmke H, Jonas P (2002) Gating, modulation and subunit composition of voltage-gated K channels in dendritic inhibitory interneurons of rat hippocampus. *The Journal of Physiology* (Lond), 538:405– 419.

Lien, C.-C., and Jonas, P. (2003). Kv3 potassium conductance is necessary and kinetically optimized for high-frequency action potential generation in hippocampal interneurons. *The Journal of Neuroscience*, *23*(6), 2058–2068.

Liguz-Lecznar, M., Urban-Ciecko, J., and Kossut, M. (2016). Somatostatin and somatostatin-containing neurons in shaping neuronal activity and plasticity. *Frontiers in Neural Circuits*, *10*, 226–15.

Lin, J. Y., Lin, M. Z., Steinbach, P., and Tsien, R. Y. (2009). Characterization of engineered channelrhodopsin variants with improved properties and kinetics. *Biophysical Journal*, *96*(5), 1803–1814.

Liu, B.-H., Li, Y.-T., Ma, W.-P., Pan, C.-J., Zhang, L. I., and Tao, H. W. (2011). Broad inhi-bition sharpens orientation selectivity by expanding input dynamic range in mouse simple cells. *Neuron*, *71*(3), 542–554.

Lorente De Nó, R. (1933). Studies on the structure of the cerebral cortex. I. The area ento-rhinalis. *Journal für Psychologie und Neurologie*, pages 1–58.

Losonczy, A., Zhang, L., Shigemoto, R., Somogyi, P., and Nusser, Z. (2002). Cell type de-pendence and variability in the short-term plasticity of EPSCs in identified mouse hippocam-pal interneurones. *The Journal of Physiology*, *542*(Pt 1), 193–210.

Luppi, P. H., Fort, P., and Jouvet, M. (1990). Iontophoretic application of unconjugated chol-era toxin B subunit (CTb) combined with immunohistochemistry of neurochemical substanc-es: a method for transmitter identification of retrogradely labeled neurons. *Brain Research*, *534*(1-2), 209–224.

Ma, Y., Hu, H., Berrebi, A. S., Mathers, P. H., and Agmon, A. (2006). Distinct subtypes of somatostatin-containing neocortical interneurons revealed in transgenic mice. *The Journal of Neuroscience,* 26(19), 5069–5082.

Ma, W.-P., Liu, B.-H., Li, Y.-T., Huang, Z. J., Zhang, L. I., and Tao, H. W. (2010). Visual representations by cortical somatostatin inhibitory neurons--selective but with weak and delayed responses. *The Journal of Neuroscience*, *30*(43), 14371–14379.

Ma, Y., Hioki, H., Konno, M., Pan, S., Nakamura, H., Nakamura, K. C., et al. (2011). Expression of gap junction protein connexin36 in multiple subtypes of GABAergic neurons in adult rat somatosensory cortex. *Cerebral Cortex*, *21*(11), 2639–2649.

Maccaferri, G., and Dingledine, R. (2002). Control of feedforward dendritic inhibition by NMDA receptor-dependent spike timing in hippocampal interneurons. *The Journal of Neuroscience*, 22(13), 5462–5472.

Madisen, L., Zwingman, T. A., Sunkin, S. M., Oh, S. W., Zariwala, H. A., Gu, H., et al. (2010). A robust and high-throughput Cre reporting and characterization system for the whole mouse brain. *Nature Publishing Group*, 13(1), 133–140.

Madisen, L., Garner, A. R., Shimaoka, D., Chuong, A. S., Klapoetke, N. C., Li, L., et al. (2015). Transgenic mice for intersectional targeting of neural sensors and effectors with high specificity and performance. *Neuron*, 85(5), 942–958.

Major, G., and Tank, D. (2004). Persistent neural activity: prevalence and mechanisms. Current Opinion in Neurobiology, 14(6), 675–684.

Mann, E. O., Suckling, J. M., Hájos, N., Greenfield, S. A., and Paulsen, O. (2005). Perisomatic feedback inhibition underlies cholinergically induced fast network oscillations in the rat hippocampus in vitro. *Neuron*, *45*(1), 105–117.

Markram, H., Wang, Y., and Tsodyks, M. (1998). Differential signaling via the same axon of neocortical pyramidal neurons. *Proceedings of the National Academy of Sciences*, *95*(9), 5323–5328.

Markram, H., Toledo-Rodriguez, M., Wang, Y., Gupta, A., Silberberg, G., and Wu, C. (2004). Interneurons of the neocortical inhibitory system. *Nature Reviews Neuroscience*, *5*(10), 793–807.

Markram, H., Muller, E., Ramaswamy, S., Reimann, M. W., Abdellah, M., Sanchez, C. A., et al. (2015). Reconstruction and simulation of neocortical microcircuitry. *Cell*, *163*(2), 456–492.

Marozzi, E., and Jeffery, K. J. (2012). Place, space and memory cells. *Current Biology*, *22*(22), R939–R942.

Martina, M., Vida, I., and Jonas, P. (2000). Distal initiation and active propagation of action potentials in interneuron dendrites. *Science*, *287*(5451), 295–300.

Martin, D. L., and Rimvall, K. (1993). Regulation of gamma-aminobutyric acid synthesis in the brain. *Journal of Neurochemistry*, 60(2), 395–407.

Masamizu, Y., Okada, T., Kawasaki, K., Ishibashi, H., Yuasa, S., Takeda, S., et al. (2011). Local and retrograde gene transfer into primate neuronal pathways via adeno-associated virus serotype 8 and 9. *Neuroscience*, *193*, 249–258.

Mathon, B., Nassar, M., Simonnet, J., Le Duigou, C., Clemenceau, S., Miles, R., and Fricker, D. (2015). Increasing the effectiveness of intracerebral injections in adult and neonatal mice: a neurosurgical point of view. *Neuroscience Bulletin*, 31(6), 685–696.

McGarry, L. M., Packer, A. M., Fino, E., Nikolenko, V., Sippy, T., and Yuste, R. (2010). Quantitative classification of somatostatin-positive neocortical interneurons identifies three interneuron subtypes. *Frontiers in Neural Circuits*, *4*, 12.

McNaughton, B. L., Battaglia, F. P., Jensen, O., Moser, E. I., and Moser, M.-B. (2006). Path integration and the neural basis of the « cognitive map ». *Nature Reviews Neuroscience*, 7(8):663– 678.

Melzer, S., Michael, M., Caputi, A., Eliava, M., Fuchs, E. C., Whittington, M. A., and Monyer, H. (2012). Long-range-projecting GABAergic neurons modulate inhibition in hippocampus and entorhinal cortex. *Science*, *335*(6075), 1506–1510.

Menendez de la Prida, L., Suarez, F., and Pozo, M. A. (2003). Electrophysiological and morpholog- ical diversity of neurons from the rat subicular complex in vitro. *Hippocampus*, 13(6):728–744.

Meskenaite, V. (1997). Calretinin-immunoreactive local circuit neurons in area 17 of the cynomolgus monkey, *Macaca fascicularis*. *The Journal of Comparative Neurology* 379:113–132.

Mesik, L., Ma, W.-P., Li, L.-Y., Ibrahim, L. A., Huang, Z. J., Zhang, L. I., and Tao, H. W. (2015). Functional response properties of VIP-expressing inhibitory neurons in mouse visual and auditory cortex. *Frontiers in Neural Circuits*, *9*, 22.

Miles, R., Tóth, K., Gulyás, A. I., Hájos, N., and Freund, T. F. (1996). Differences between somatic and dendritic inhibition in the hippocampus. *Neuron*, *16*(4), 815–823.

Mitchell S.J., Rawlins J.N., Steward O., Olton D.S. (1982). Medial septal area lesions disrupt theta rhythm and cholinergic staining in medial entorhinal cortex and produce impaired radial arm maze behavior in rats. *The Journal of Neuroscience*, 2:292–302.

Miyashita, T. and Rockland, K. S. (2007), GABAergic projections from the hippocampus to the retrosplenial cortex in the rat. *The European Journal of Neuroscience*, 26: 1193–1204.

Miyoshi, G., Butt, S. J. B., Takebayashi, H., and Fishell, G. (2007). Physiologically distinct temporal cohorts of cortical interneurons arise from telencephalic Olig2-expressing precursors. *The Journal of Neuroscience, 27*(29), 7786–7798.

Mizumori, S. J. and Williams, J. D. (1993). Directionally selective mnemonic properties of neurons in the lateral dorsal nucleus of the thalamus of rats. *The Journal of Neuroscience,* 13(9):4015–4028.

Mizuseki, K., Sirota, A., Pastalkova, E., and Buzsáki, G. (2009). Theta oscillations provide temporal windows for local circuit computation in the entorhinal-hippocampal loop. *Neuron*, *64*(2), 267–280.

Mizuseki, K., Diba, K., Pastalkova, E., and Buzsáki, G. (2011). Hippocampal CA1 pyramidal cells form functionally distinct sublayers. *Nature Publishing Group*, *14*(9), 1174–1181.

Monier, C., Chavane, F., Baudot, P., Graham, L. J., and Fregnac, Y. (2003). Orientation and direction selectivity of synaptic inputs in visual cortical neurons: a diversity of combinations produces spike tuning. *Neuron*, *37*(4), 663–680.

Morishima, M. and Kawaguchi, Y. (2006). Recurrent connection patterns of corticostriatal pyramidal cells in frontal cortex. *The Journal of Neuroscience, 26*, 4394-4405

Moser, E. I. and Moser, M.-B. (2013). Grid cells and neural coding in high-end cortices. *Neuron*, 80(3):765–774.

Mott, D. D., Turner, D. A., Okazaki, M. M., and Lewis, D. V. (1997). Interneurons of the dentate-hilus border of the rat dentate gyrus: morphological and electrophysiological heterogeneity. *The Journal of Neuroscience*, *17*(11), 3990–4005.

Mountcastle, V. B., Davies, P. W. and Berman, A. L. (1957). Response properties of neurons of cat's somatic sensory cortex to peripheral stimuli. *Journal of Neurophysiology* 20, 374-407

Muir, G. M., Brown, J. E., Carey, J. P., Hirvonen, T. P., Della Santina, C. C., Minor, L. B., and Taube, J. S. (2009). Disruption of the head direction cell signal after occlusion of the semicircular canals in the freely moving chinchilla. *The Journal of Neuroscience*, 29(46):14521– 14533.

Muralidhar, S., Wang, Y., and Markram, H. (2014). Synaptic and cellular organization of layer 1 of the developing rat somatosensory cortex. *Frontiers in Neuroanatomy*, *7*, 1–17.

Murlidharan, G., Samulski, R. J., and Asokan, A. (2014). Biology of Adeno-Associated Viral Vectors in the Central Nervous System. *Frontiers in Molecular Neuroscience*, *7*(76).

Nagel, G., Szellas, T., Huhn, W., Kateriya, S., Adeishvili, N., Berthold, P., et al. (2003). Channelrhodopsin-2, a directly light-gated cation-selective membrane channel. *Proceedings of the National Academy of Sciences*, *100*(24), 13940–13945.

Nagel, G., M. Brauner, J. F. Liewald, N. Adeishvili, E. Bamberg, et al. (2005). Light activation of channelrhodopsin-2 in excitable cells of Caenorhabditis elegans triggers rapid behavioral responses. *Current Biology*, 15:2279–2284.

Nassar, M., Simonnet, J., Lofredi, R., Cohen, I., Savary, E., Yanagawa, Y., et al. (2015). Diversity and overlap of parvalbumin and somatostatin expressing interneurons in mouse presubiculum. *Frontiers in Neural Circuits*, *9*(a001875), 81–19.

Naumann, R. K., Ray, S., Prokop, S., Las, L., Heppner, F. L., and Brecht, M. (2016). Conserved size and periodicity of pyramidal patches in layer 2 of medial/caudal entorhinal cortex. *The Journal of Comparative Neurology*, *524*(4), 783–806.

Neske, G. T., Patrick, S. L., and Connors, B. W. (2015). Contributions of diverse excitatory and inhibitory neurons to recurrent network activity in cerebral cortex. *The Journal of Neuroscience, 35*(3), 1089–1105.

Nieuwenhuys, R. (1994). Comparative neuroanatomy: place, principles, practice and programme. *European journal of morphology* 32, 142-155.

Nishikawa, S., Goto, S., Hamasaki, T., Yamada, K., and Ushio, Y. (2002). Involvement of reelin and Cajal-Retzius cells in the developmental formation of vertical columnar structures in the cerebral cortex: evidence from the study of mouse presubicular cortex. *Cerebral cortex*, 12(10):1024–1030.

Nyíri, G., Stephenson, F. A., Freund, T. F., and Somogyi, P. (2003). Large variability in synaptic n-methyl-d-aspartate receptor density on interneurons and a comparison with pyramidal-cell spines in the rat hippocampus. *Neuroscience*, *119*(2), 347–363.

O'Keefe, J. and Dostrovsky, J. (1971). The hippocampus as a spatial map. Preliminary evidence from unit activity in the freely-moving rat. *Brain Research*, 34(1):171–175.

O'Keefe, J., and Recce, M. L. (1993). Phase relationship between hippocampal place units and the EEG theta rhythm. *Hippocampus*, *3*(3), 317–330.

Okun, M., and Lampl, I. (2008). Instantaneous correlation of excitation and inhibition during ongoing and sensory-evoked activities. *Nature Neuroscience*, *11*(5), 535–537.

Otsuka, T., and Kawaguchi, Y. (2009). Cortical inhibitory cell types differentially form intralaminar and interlaminar subnetworks with excitatory neurons. *The Journal of Neuroscience*, *29*(34), 10533–10540.

Packer, A. M., and Yuste, R. (2011). Dense, unspecific connectivity of neocortical parvalbumin-positive interneurons: a canonical microcircuit for inhibition? *The Journal of Neuroscience*, *31*(37), 13260–13271.

Parra, P., Gulyás, A. I., and Miles, R. (1998). How many subtypes of inhibitory cells in the hippocampus? *Neuron*, *20*(5), 983–993.

Pastoll, H., Ramsden, H. L., and Nolan, M. F. (2012). Intrinsic electrophysiological properties of entorhinal cortex stellate cells and their contribution to grid cell firing fields. *Frontiers in Neural Circuits*, *6*, 17.

Pastoll, H., Solanka, L., van Rossum, M. C. W., and Nolan, M. F. (2013). Feedback inhibition enables theta-nested gamma oscillations and grid firing fields. *Neuron*, *77*(1), 141–154.

Perrenoud, Q., Rossier, J., Geoffroy, H., Vitalis, T., and Gallopin, T. (2013). Diversity of GABAergic interneurons in layer VIa and VIb of mouse barrel cortex. *Cerebral*, *23*(2), 423–441.

Peterson, D. A., Lucidi-Phillipi, C. A., Murphy, D. P., Ray, J., and Gage, F. H. (1996). Fibroblast growth factor-2 protects entorhinal layer 2 glutamatergic neurons from axotomy-induced death. *The Journal of Neuroscience*, *16*(3), 886–898.

Petreanu, L., Mao, T., Sternson, S. M., and Svoboda, K. (2009). The subcellular organization of neocortical excitatory connections. *Nature*, *457*(7233), 1142–1145.

Peyrache, A., Lacroix, M. M., Petersen, P. C., and Buzsáki, G. (2015). Internally organized mechanisms of the head direction sense. *Nature Publishing Group*, *18*(4), 569–575.

Pfeffer, C. K., Xue, M., He, M., Huang, Z. J., and Scanziani, M. (2013). Inhibition of inhibition in visual cortex: the logic of connections between molecularly distinct interneurons. *Nature Publishing Group*, *16*(8), 1068–1076.

Pi, H.-J., Hangya, B., Kvitsiani, D., Sanders, J. I., Huang, Z. J., and Kepecs, A. (2013). Cortical interneurons that specialize in disinhibitory control. *Nature*, *503*(7477), 521–524.

Pillay, S., Meyer, N. L., Puschnik, A. S., Davulcu, O., Diep, J., Ishikawa, Y., et al. (2016). An essential receptor for adeno-associated virus infection. *Nature*, 530(7588), 108–112.

Polack, P.-O., Friedman, J., and Golshani, P. (2013). Cellular mechanisms of brain state–dependent gain modulation in visual cortex. *Nature Neuroscience*, *16*(9), 1331–1339.

Pouille, F., and Scanziani, M. (2001). Enforcement of temporal fidelity in pyramidal cells by somatic feed-forward inhibition. *Science*, *293*(5532), 1159–1163.

Pouille, F., and Scanziani, M. (2004). Routing of spike series by dynamic circuits in the hippocampus. *Nature*, *429*(6993), 717–723.

Preston-Ferrer, P., Coletta, S., Frey, M., and Burgalossi, A. (2016). Anatomical organization of presubicular head-direction circuits. *eLife*, *5*, e14592.

Ramon y Cajal, S. (1899). Textura del sistema nervioso del hombre y de los vertebrados. *Oxford University Press*.

Ramsden, H. L., Sürmeli, G., McDonagh, S. G., and Nolan, M. F. (2015). Laminar and dorsoventral molecular organization of the medial entorhinal cortex revealed by large-scale anatomical analysis of gene expression. *PLoS Computational Biology*, *11*(1), e1004032.

Ranck, Jr, J. B. (1984). Head direction cells in the deep cell layer of dorsal presubiculum in freely moving rats. *Society Neuroscience Abstracts*.

Ray, S., Naumann, R., Burgalossi, A., Tang, Q., Schmidt, H., and Brecht, M. (2014). Grid-layout and theta-modulation of layer 2 pyramidal neurons in medial entorhinal cortex. *Science*, *343*(6173), 891–896.

Redish, A. D., Elga, A. N., and Touretzky, D. S. (1996). A coupled attractor model of the rodent head direction system. *Network: Computation in Neural Systems* , 7(4):671–685.

Regehr, W. G. (2012). Short-term presynaptic plasticity. *Cold Spring Harbor Perspectives in Biology*, *4*(7), a005702–a005702.

Reyes, A., Lujan, R., Rozov, A., Burnashev, N., Somogyi, P., and Sakmann, B. (1998). Target-cell-specific facilitation and depression in neocortical circuits. *Nature Neuroscience*, *1*(4), 279–285.

Rogers, J. H**. (**1992). Immunohistochemical markers in rat cortex: co-localization of calretinin and calbindin-D28k with neuropeptides and GABA. *Brain Research,* 587: 147–157.

Rossier, J., Bernard, A., Cabungcal, J.-H., Perrenoud, Q., Savoye, A., Gallopin, T., et al. (2015). Cortical fast-spiking parvalbumin interneurons enwrapped in the perineuronal net express the metallopeptidases Adamts8, Adamts15 and Neprilysin. *Molecular Psychiatry*, *20*(2), 154–161.

Rothermel, M., Brunert, D., Zabawa, C., Díaz-Quesada, M., and Wachowiak, M. (2013). Transgene expression in target-defined neuron populations mediated by retrograde infection with adeno-associated viral vectors. *The Journal of Neuroscience* , 33(38), 15195–15206.

Roux, L., and Buzsáki, G. (2015). Tasks for inhibitory interneurons in intact brain circuits. *Neuropharmacology*, *88*, 10–23.

Rowland, D. C., Weible, A. P., Wickersham, I. R., Wu, H., Mayford, M., Witter, M. P., and Kentros, C. G. (2013). Transgenically targeted rabies virus demonstrates a major monosynaptic projection from hippocampal area CA2 to medial entorhinal layer 2 neurons. *The Journal of Neuroscience*, 33(37):14889–14898.

Royer, S., Zemelman, B. V., Losonczy, A., Kim, J., Chance, F., Magee, J. C., and Buzsáki, G. (2012). Control of timing, rate and bursts of hippocampal place cells by dendritic and somatic inhibition. *Nature Neuroscience*, *15*(5), 769–775.

Rudy, B., Fishell, G., Lee, S., and Hjerling-Leffler, J. (2010). Three groups of interneurons account for nearly 100% of neocortical GABAergic neurons. *Developmental Neurobiology*, *71*(1), 45–61.

Runyan, C. A., Schummers, J., Van Wart, A., Kuhlman, S. J., Wilson, N. R., Huang, Z. J., and Sur, M. (2010). Response features of parvalbumin-expressing interneurons suggest precise roles for subtypes of inhibition in visual cortex. *Neuron*, *67*(5), 847–857.

Runyan, C. A., and Sur, M. (2013). Response selectivity is correlated to dendritic structure in parvalbumin-expressing inhibitory neurons in visual cortex. *The Journal of Neuroscience*, *33*(28), 11724–11733.

Russell, D. W., and Kay, M. A. (1999). Adeno-associated virus vectors and hematology. *Blood*, 94(3), 864–874.

Salegio, E. A., Samaranch, L., Kells, A. P., Mittermeyer, G., San Sebastian, W., Zhou, S., et al. (2013). Axonal transport of adeno-associated viral vectors is serotype-dependent. *Gene Therapy*, *20*(3), 348–352.

Sargolini, F., Fyhn, M., Hafting, T., McNaughton, B. L., Witter, M. P., Moser, M.-B., and Moser, E. I. (2006). Conjunctive representation of position, direction, and velocity in entorhinal cortex. *Science*, 312(5774):758–762.

Sauer, J. F., Struber, M., and Bartos, M. (2012). Interneurons provide circuit-specific depolarization and hyperpolarization. *The Journal of Neuroscience*, *32*(12), 4224–4229.

Silberberg, G., Gupta, A., and Markram, H. (2002). Stereotypy in neocortical microcircuits. *Trends in Neurosciences*, *25*(5), 227–230.

Silberberg, G., and Markram, H. (2007). Disynaptic Inhibition between Neocortical Pyramidal Cells Mediated by Martinotti Cells. *Neuron*, *53*(5), 735–746.

Silberberg, G., Grillner, S., LeBeau, F. E. N., Maex, R., and Markram, H. (2005). Synaptic pathways in neural microcircuits. *Trends in Neurosciences*, 28(10):541–551.

Silberberg, G. and Markram, H. (2007). Disynaptic inhibition between neocortical pyramidal cells mediated by martinotti cells. *Neuron*, 53(5):735–746.

Simon, A., Oláh, S., Molnár, G., Szabadics, J., and Tamas, G. (2005). Gap-junctional coupling between neurogliaform cells and various interneuron types in the neocortex. *The Journal of Neuroscience, 25*(27), 6278–6285.

Simonnet, J., Eugène, E., Cohen, I., Miles, R., and Fricker, D. (2013). Cellular neuroanatomy of rat presubiculum. *The European Journal of Neuroscience*, 37(4):583–597.

Sharp, P. E., Blair, H. T., and Cho, J. (2001a). The anatomical and computational basis of the rat head-direction cell signal. *Trends in Neurosciences*, 24(5):289–294.

Sharp, P. E., Tinkelman, A., and Cho, J. (2001b). Angular velocity and head direction signals recorded from the dorsal tegmental nucleus of gudden in the rat: implications for path integration in the head direction cell circuit. *Behavioral neuroscience*, 115(3):571–588.

Shay, C. F., Ferrante, M., Chapman, G. W., and Hasselmo, M. E. (2016). Rebound spiking in layer 2 medial entorhinal cortex stellate cells: Possible mechanism of grid cell function. *Neurobiology of Learning and Memory*, *129*, 83–98.

Sheperd G. M., (2004). Synaptic Organization of the brain, Fifth Edition. O*xford University Press,* New York.

Shipston-Sharman, O., Solanka, L., and Nolan, M. F. (2016). Continuous attractor network models of grid cell firing based on excitatory-inhibitory interactions. *The Journal of Physiology*, 1-11

Skaggs, W. E., Knierim, J. J., Kudrimoti, H. S., and McNaughton, B. L. (1995). A model of the neural basis of the rat's sense of direction. Advances in neural information processing systems, 7:173–180.

Slomianka, L. and Geneser, F. A. (1991). Distribution of acetylcholinesterase in the hippocampal region of the mouse: I. Entorhinal area, parasubiculum, retrosplenial area, and presubiculum. *The Journal of Comparative Neurology*, 303(3):339–354.

Solanka, L., van Rossum, M. C. W., and Nolan, M. F. (2015). Noise promotes independent control of gamma oscillations and grid firing within recurrent attractor networks. *eLife*, 4.e06444

Solstad, T., Boccara, C. N., Krop, E., Moser, M.-B., and Moser, E. I. (2008). Representation of geometric borders in the entorhinal cortex. *Science*, 322(5909):1865–1868.

Somogyi, P. (1977). A specific "axo-axonal" interneuron in the visual cortex of the rat. *Brain research* 136, 345-350.

Somogyi, P., Tamas, G., Lujan, R., and Buhl, E. H. (1998). Salient features of synaptic organization in the cerebral cortex. *Brain Research Reviews*, *26*(2-3), 113–135.

Somogyi, J., Baude, A., Omori, Y., Shimizu, H., Mestikawy, S. E., Fukaya, M., et al. (2004). GABAergic basket cells expressing cholecystokinin contain vesicular glutamate transporter type 3 (VGLUT3) in their synaptic terminals in hippocampus and isocortex of the rat. *The European Journal of Neuroscience*, *19*(3), 552–569.

Stackman, R.W., and Taube, J. S. (1998). Firing properties of rat lateral mammillary single units: head direction, head pitch, and angular head velocity. *The Journal of Neuroscience*, 18(21):9020–37.

Staiger, J. F., Freund, T. F., and Zilles, K. (1997). Interneurons immunoreactive for vasoactive intestinal polypeptide (VIP) are extensively innervated by parvalbumin-containing boutons in rat primary somatosensory cortex. *The European Journal of Neuroscience*, *9*(11), 2259–2268.

Staiger, J. F., Masanneck, C., Schleicher, A., and Zuschratter, W. (2003). Calbindin-containing interneurons are a target for VIP-immunoreactive synapses in rat primary somatosensory cortex. *The Journal of Comparative Neurology*, *468*(2), 179–189.

Sugar, J., Witter, M. P., van Strien, N. M., and Cappaert, N. L. M. (2011). The retrosplenial cortex: intrinsic connectivity and connections with the (para)hippocampal region in the rat. An interactive connectome. *Frontiers in Neuroinformatics*, 5, 7.

Sugar, J., and Witter, M. P. (2016). Postnatal development of retrosplenial projections to the parahippocampal region of the rat. *eLife*, *5*, 1–58.

Sun, C., Kitamura, T., Yamamoto, J., Martin, J., Pignatelli, M., Kitch, L.J., Schnitzer, M.J., and Tonegawa, S. (2015). Distinct speed dependence of entorhinal island and ocean cells, including respective grid cells. *Proceedings of the National Academy of Sciences*, 112, 9466–9471.

Sürmeli, G., Marcu, D. C., McClure, C., Garden, D. L. F., Pastoll, H., and Nolan, M. F. (2015). Molecularly defined circuitry reveals input-output segregation in deep layers of the medial entorhinal cortex. *Neuron*, 88(5), 1040–1053.

Swadlow, H. A. (2002). Thalamocortical control of feed-forward inhibition in awake somatosensory barrel cortex. *Philosophical Transactions of the Royal Society B: Biological Sciences*, *357*(1428), 1717–1727.

Szabadics, J., and Soltesz, I. (2009). Functional specificity of mossy fiber innervation of GABAergic cells in the hippocampus. *The Journal of Neuroscience, 29*(13), 4239–4251.

Tan, Z., Hu, H., Huang, Z. J., and Agmon, A. (2008). Robust but delayed thalamocortical activation of dendritic-targeting inhibitory interneurons. *Proceedings of the National Academy of Sciences of the United States of America*, *105*(6), 2187–2192.

Tang, Q., Burgalossi, A., Ebbesen, C.L., Ray, S., Naumann, R., Schmidt, H., Spicher, D., and Brecht, M. (2014). Pyramidal and stellate cell specificity of grid and border representations in layer 2 of medial entorhinal cortex. *Neuron* 84, 1191–1197.

Taniguchi, H., He, M., Wu, P., Kim, S., Paik, R., Sugino, K., et al. (2011). A resource of Cre driver lines for genetic targeting of GABAergic neurons in cerebral cortex. *Neuron*, 71(6), 995–1013.

Taniguchi, H. (2014). Genetic dissection of GABAergic neural circuits in mouse neocortex. *Frontiers in Cellular Neuroscience*, *8*, 8.

Tasic, B., Menon, V., Nguyen, T. N., Kim, T. K., Jarsky, T., Yao, Z., et al. (2016). Adult mouse cortical cell taxonomy revealed by single cell transcriptomics. *Nature Neuroscience*, *19*(2), 335–346.

Taube, J. S., Muller, R. U., and Ranck, J. B. (1990a). Head-direction cells recorded from the postsubiculum in freely moving rats. I. Description and quantitative analysis. *The Journal of Neuroscience*, 10(2):420–435.

Taube, J. S., Muller, R. U., and Ranck, J. B. (1990b). Head-direction cells recorded from the postsubiculum in freely moving rats. II. Effects of environmental manipulations. *The Journal of Neuroscience*, 10(2):436–447.

Taube, J. S., Kesslak, J. P., and Cotman, C. W. (1992). Lesions of the rat postsubiculum impair performance on spatial tasks. *Behavioral and neural biology*, 57(2):131–143.

Taube, J. S. (1995). Head direction cells recorded in the anterior thalamic nuclei of freely moving rats. *The Journal of Neuroscience*, 15(1 Pt 1), 70–86.

Taube, J. S. (1998). Head direction cells and the neurophysiological basis for a sense of direction. *Progress in Neurobiology*, 55(3), 225–256.

Taube, J. S. (2007). The head direction signal: origins and sensory-motor integration. *Annual Review of Neuroscience*, 30(1), 181–207.

Thomson, A. M., and Deuchars, J. (1997). Synaptic interactions in neocortical local circuits: dual intracellular recordings in vitro. *Cerebral Cortex*, *7*(6), 510–522.

Toledo-Rodriguez, M. (2004). Correlation maps allow neuronal electrical properties to be predicted from single-cell gene expression profiles in rat neocortex. *Cerebral Cortex*, *14*(12), 1310–1327.

Tóth, K., Borhegyi, Z., Freund, T.F., (1993). Postsynaptic targets of GABAergic hippocampal neurons in the medial septum-diagonal band of broca complex. *The Journal of Neuroscience*, 13, 3712e3724.

Tóth, K., Freund, T. F., and Miles, R. (1997). Disinhibition of rat hippocampal pyramidal cells by GABAergic afferents from the septum. *The Journal of Physiology*, *500 (Pt 2)*, 463–474.

Tóth, K., and McBain, C. J. (1998). Afferent-specific innervation of two distinct AMPA receptor subtypes on single hippocampal interneurons. *Nature Neuroscience*, *1*(7),

Tricoire, L., Pelkey, K. A., Daw, M. I., Sousa, V. H., Miyoshi, G., Jeffries, B., et al. (2010). Common origins of hippocampal Ivy and nitric oxide synthase expressing neurogliaform cells. *The Journal of Neuroscience, 30*(6), 2165–2176.

Tsuno, Y., Chapman, G. W., and Hasselmo, M. E. (2015). Rebound spiking properties of mouse medial entorhinal cortex neurons in vivo. *The European Journal of Neuroscience*, *42*(11), 2974–2984.

Tukker, J. J., Tang, Q., Burgalossi, A., and Brecht, M. (2015). Head-directional tuning and theta modulation of anatomically identified neurons in the presubiculum. *The Journal of Neuroscience, 35*(46), 15391–15395.

Tuncdemir, S. N., Wamsley, B., Stam, F. J., Osakada, F., Goulding, M., Callaway, E. M., et al. (2016). Early somatostatin interneuron connectivity mediates the maturation of deep layer cortical circuits. *Neuron*, 89(3), 521–535.

Uematsu, M., Hirai, Y., Karube, F., Ebihara, S., Kato, M., Abe, K., et al. (2008). Quantitative chemical composition of cortical GABAergic neurons revealed in transgenic Venus-expressing rats. *Cerebral Cortex*, *18*(2), 315–330.

Unal, G., Joshi, A., Viney, T. J., Kis, V., and Somogyi, P. (2015). Synaptic targets of medial septal projections in the hippocampus and extrahippocampal cortices of the mouse. *The Journal of Neuroscience*, 35(48), 15812–15826.

Urban-Ciecko, J., and Barth, A. L. (2016). Somatostatin-expressing neurons in cortical networks. *Nature Reviews Neuroscience*, 17(7), 401–409.

Valerio, S., and Taube, J. S. (2016). Head direction cell activity is absent in mice without the horizontal semicircular canals. *The Journal of Neuroscience*, *36*(3), 741–754.

Van Groen, T. and Wyss, J. M. (1990a). Connections of the retrosplenial granular a cortex in the rat. *The Journal of Comparative Neurology*, 300(4):593–606.

Van Groen, T. and Wyss, J. M. (1990b). The connections of presubiculum and parasubiculum in the rat. *Brain research*, 518(1-2):227–243.

Van Groen, T. and Wyss, J. M. (1990c). The postsubicular cortex in the rat: characterization of the fourth region of the subicular cortex and its connections. *Brain research*, 529(1-2):165–177.

Van Groen, T. and Wyss, J. M. (1992a). Connections of the retrosplenial dysgranular cortex in the rat. *The Journal of Comparative Neurology*, 315(2):200–216.

Van Groen, T. and Wyss, J. M. (1992b). Projections from the laterodorsal nucleus of the thalamus to the limbic and visual cortices in the rat. *The Journal of Comparative Neurology*, 324(3):427– 448.

Van Groen, T. and Wyss, J. M. (1995). Projections from the anterodorsal and anteroventral nucleus of the thalamus to the limbic cortex in the rat. *The Journal of Comparative Neurology*, 358(4):584–604.

Van Groen T, Kadish, I., and Wyss, J. M. (1999). Efferent connections of the anteromedial nucleus of the thalamus of the rat. *Brain Research. Brain Research Reviews*, *30*(1), 1–26.

Van Groen, T., Miettinen, P., and Kadish, I. (2003). The entorhinal cortex of the mouse: organization of the projection to the hippocampal formation. *Hippocampus*, *13*(1), 133–149.

Van Groen, T. and Wyss, J. M. (2003). Connections of the retrosplenial granular b cortex in the rat. *The Journal of Comparative Neurology*, 463:249–263.

Van Strien, N. M., Cappaert, N. L. M., and Witter, M. P. (2009). The anatomy of memory: an interactive overview of the parahippocampal–hippocampal network. *Nature Reviews Neuroscience*, *10*(4), 272–282.

Varela, F., Lachaux, J. P., Rodriguez, E. and Martinerie, J. (2001). The brainweb: phase synchronization and large-scale integration. Nature reviews. *Neuroscience*, 2, 229-239

Varga, C., Golshani, P., and Soltesz, I. (2012). Frequency-invariant temporal ordering of interneuronal discharges during hippocampal oscillations in awake mice. *Proceedings of the National Academy of Sciences of the United States of America*, 109(40), E2726–34/

Vertes, R. P., and Kocsis, B. (1997). Brainstem-diencephalo-septohippocampal systems controlling the theta rhythm of the hippocampus. *Neuroscience*, 81(4), 893–926.

Vida, I., Halasy, K., Szinyei, C., Somogyi, P., and Buhl, E. H. (1998). Unitary IPSPs evoked by interneurons at the stratum radiatum-stratum lacunosum-moleculare border in the CA1 area of the rat hippocampus in vitro. *The Journal of Physiology,* 506 (Pt 3), 755–773.

Vida, I., Bartos, M., and Jonas, P. (2006). Shunting inhibition improves robustness of gamma oscillations in hippocampal interneuron networks by homogenizing firing rates. *Neuron*, *49*(1), 107–117.

Vogt, B. A. and Miller, M. W. (1983). Cortical connections between rat cingulate cortex and visual, motor, and postsubicular cortices. *The Journal of Comparative Neurology*, 216(2):192–210.

Wall, N. R., La Parra, De, M., Sorokin, J. M., Taniguchi, H., Huang, Z. J., and Callaway, E. M. (2016). Brain-wide maps of synaptic input to cortical interneurons. *The Journal of Neuro-science, 36*(14), 4000–4009.

Wang, X. J. (2001). Synaptic reverberation underlying mnemonic persistent activity. *Trends in Neurosciences*, *24*(8), 455–463.

Wang, Y. (2002). Anatomical, physiological, molecular and circuit properties of nest basket cells in the developing somatosensory cortex. *Cerebral Cortex*, *12*(4), 395–410.

Wang, Y., Toledo-Rodriguez, M., Gupta, A., Wu, C., Silberberg, G., Luo, J., et al. (2004). Anatomical, physiological and molecular properties of Martinotti cells in the somatosensory cortex of the juvenile rat. *Journal of Physiology (Lond*), 561, 65–90.

Watakabe, A., Ohtsuka, M., Kinoshita, M., Takaji, M., Isa, K., Mizukami, H., et al. (2015). Comparative analyses of adeno-associated viral vector serotypes 1, 2, 5, 8 and 9 in marmoset, mouse and macaque cerebral cortex. *Neuroscience Research*, 93, 144–157.

Wiener, S. I. (1993). Spatial and behavioral correlates of striatal neurons in rats performing a self-initiated navigation task. *The Journal of Neuroscience*, 13(9), 3802–3817.

Wiener, S. I. and Taube, J. S. (2005). Head direction cells and the neural mechanisms of spatial orientation. *The MIT Press*

Wilent, W. B., and Contreras, D. (2005). Dynamics of excitation and inhibition underlying stimulus selectivity in rat somatosensory cortex. *Nature Neuroscience,* 8(10), 1364–1370.

Wills, T. J., Cacucci, F., Burgess, N., and O'Keefe, J. (2010). Development of the hippocampal cognitive map in preweanling rats. *Science*, 328(5985):1573–1576.

Wilson, M. A., and McNaughton, B. L. (1993). Dynamics of the hippocampal ensemble code for space. *Science*, 261(5124), 1055–1058.

Wilson, N. R., Runyan, C. A., Wang, F. L., and Sur, M. (2012). Division and subtraction by distinct cortical inhibitory networks in vivo. *Nature*, 488(7411), 343–348.

Winter, S. S., Clark, B. J., Taube, J. S. (2015) Disruption of the head-direction cell network impairs the parahippocampal grid cell signal. *Science,* 347: 870 – 874.

Witter, M. P., Groenewegen, H. J., Lopes da Silva, F. H., and Lohman, A. H. (1989). Functional organization of the extrinsic and intrinsic circuitry of the parahippocampal region. *Progress in Neurobiology*, *33*(3), 161–253.

Witter, M. P., Wouterlood, F. G., Naber, P. A., and Van Haeften, T. (2000). Anatomical organization of the parahippocampal-hippocampal network. *Annals of the New York Academy of Sciences*, 911, 1–24.

Wonders, C. P., and Anderson, S. A. (2006). The origin and specification of cortical interneurons. Nature Reviews Neuroscience, 7(9), 687–696.

Woodworth, M. B., Greig, L. C., Liu, K. X., Ippolito, G. C., Tucker, H. O., and Macklis, J. D. (2016). Ctip1 regulates the balance between specification of distinct projection neuron subtypes in deep cortical layers. *Cell Reports*, *15*(5), 999–1012.

Wulff, P., Ponomarenko, A. A., Bartos, M., Korotkova, T. M., Fuchs, E. C., Bähner, F., et al. (2009). Hippocampal theta rhythm and its coupling with gamma oscillations require fast inhibition onto parvalbumin-positive interneurons. *Proceedings of the National Academy of Sciences of the United States of America*, *106*(9), 3561–3566.

Wyss, J. M. and van Groen, T. (1992). Connections between the retrosplenial cortex and the hippocampal formation in the rat: a review. *Hippocampus*, 2(1):1–11.

Xu, H., Jeong, H.-Y., Tremblay, R., and Rudy, B. (2013). Neocortical somatostatin-expressing GABAergic interneurons disinhibit the thalamorecipient layer 4. *Neuron*, 77(1), 155–167.

xu, Q., Cobos, I., La Cruz, De, E., Rubenstein, J. L., and Anderson, S. A. (2004). Origins of cortical interneuron subtypes. *The Journal of Neuroscience*, 24(11), 2612–2622.

Xu, X., Roby, K. D., and Callaway, E. M. (2006). Mouse cortical inhibitory neuron type that coexpresses somatostatin and calretinin. *The Journal of Comparative Neurology*, 499(1), 144–160.

Xu, X., Roby, K. D., and Callaway, E. M. (2010). Immunochemical characterization of inhibitory mouse cortical neurons: three chemically distinct classes of inhibitory cells. *The Journal of Comparative Neurology*,518, 389–404.

Yang, W., Carrasquillo, Y., Hooks, B. M., Nerbonne, J. M., and Burkhalter, A. (2013). Dis-tinct balance of excitation and inhibition in an interareal feedforward and feedback circuit of mouse visual cortex. *The Journal of Neuroscience*, *33*(44), 17373–17384.

Yoder, R. M. and Taube, J. S. (2009). Head direction cell activity in mice: robust directional signal depends on intact otolith organs. *The Journal of Neuroscience*, 29(4):1061–1076.

Yoder, R. M., Clark, B. J., and Taube, J. S. (2011). Origins of landmark encoding in the brain. *Trends in Neurosciences*.

Yoder, R. M. and Taube, J. S. (2011). Projections to the anterodorsal thalamus and lateral mammillary nuclei arise from different cell populations within the postsubiculum: implications for the control of head direction cells. *Hippocampus*, 21(10):1062–1073.

Yoder, R. M., Peck, J. R., and Taube, J. S. (2015). Visual landmark information gains control of the head direction signal at the lateral mammillary nuclei. *The Journal of Neuroscience*, *35*(4), 1354–1367.

Yoshida, M. and Hasselmo, M. E. (2009). Persistent firing supported by an intrinsic cellular mechanism in a component of the head direction system. *The Journal of Neuroscience*, 29(15):4945– 4952.

Yoshimura, Y., Dantzker, J. L. M., and Callaway, E. M. (2005). Excitatory cortical neurons form fine-scale functional networks. *Nature,* 433(7028), 868–873.

Zhang, F., Aravanis, A. M., Adamantidis, A., de Lecea, L., and Deisseroth, K. (2007a). Circuit-breakers: optical technologies for probing neural signals and systems. Nature Reviews Neuroscience, 8(8), 577–581.

Zhang, F., Wang, L.-P., Brauner, M., Liewald, J. F., Kay, K., Watzke, N., et al. (2007b). Multimodal fast optical interrogation of neural circuitry. Nature, 446(7136), 633–639.

Zhang, S. J., Ye, J., Miao, C., Tsao, A., Cerniauskas, I., Ledergerber, D., Moser, M. B., and Moser, E. I. (2013). Optogenetic dissection of entorhinal-hippocampal functional connectivity. Science, 340(6128):1232627–1232627.

Zilberter, Y., Kaiser, K. M. M., and Sakmann, B. (1999). Dendritic GABA release depresses excitatory transmission between layer 2/3 pyramidal and bitufted neurons in rat neocortex. Neuron, 24(4), 979–988.

Zugaro, M. B., Arleo, A., Berthoz, A., and Wiener, S. I. (2003). Rapid spatial reorientation and head direction cells. The Journal of Neuroscience, 23(8), 3478–3482.

Abstract

Spatial orientation and navigation are controlled by specific neuronal circuits and elements. The presubiculum, a transitional cortical area of the parahippocampal formation, is located between the hippocampus and the entorhinal cortex, and it participates in spatial navigation in animals and humans. More than half of presubicular neurons are head direction cells that fire as a function of the directional heading. The presubiculum is thought to be a crucial node for transferring directional heading information to the entorhinal-hippocampal network, and feeding back visual landmark information to upstream regions of the head directional circuit. Despite its functional importance, information processing within the 6-layered presubicular microcircuit remains not completely understood.

During my PhD, I studied inhibitory neurons of the presubicular microcircuit in the slice preparation using patch-clamp recordings. I characterized their anatomo-physiological properties as well as their functional connectivity with local principal neurons.

In the first part, I examined the diversity of two major populations of GABAergic neurons, the parvalbumin (PV) and somatostatin (SOM) expressing interneurons in mouse presubiculum. Using transgenic mouse strains Pvalb-Cre, Sst-Cre and X98, where interneurons were fluorescently labeled, I showed the existence of typical PV fast-spiking basket-like interneurons mainly in the Pvalb-Cre line and SOM low-threshold spiking Martinotti cell-like interneurons in the X98 and Sst-Cre line. Unsupervised cluster analysis based on electrophysiological parameters further revealed a transitional group containing interneurons from either Pvalb-Cre or Sst-cre lines with quasi-fast-spiking properties and heterogeneous morphologies. A small subpopulation of ~6% of interneurons co-expressed PV and SOM in mouse presubiculum. The presubiculum appears to share the whole complexity of other cortical areas in term of inhibition.

In the second part, I investigated the integration of thalamic inputs by principal neurons as well as PV and SST interneurons in the presubiculum using double patch-clamp recordings. I found that thalamic axons selectively innervated superficial layers and made direct synaptic contacts with pyramidal neurons that project to medial entorhinal cortex and also with PV interneurons in superficial layer 3. In contrast, SST interneurons were indirectly recruited by presubicular pyramidal cells in a facilitating and frequency dependent manner. They may mediate lateral inhibition onto nearby principal cells, and at the same time, preserve sustained firing of principal neurons. In paired recording experiments, I found that PV cells inhibit neighboring pyramidal neurons with a high connection probability. PV interneurons are rapidly recruited by thalamic excitation and mediate feed-forward inhibition in presubicular pyramidal neurons.

My PhD work brought fundamental knowledge about the presubicular inhibitory microcircuit. It has unraveled different populations of GABAergic interneurons and revealed canonical feedforward and feedback inhibitory motifs that are likely to be recruited at different times during head direction signaling.

Résumé

L'orientation spatiale et la fonction de navigation sont des processus contrôlés par des circuits et éléments neuronaux spécifiques. Le présubiculum, aire corticale de transition de la région parahippocampique, est situé entre l'hippocampe et le cortex entorhinal. Le présubiculum est impliqué dans la navigation spatiale à la fois chez l'animal et l'Homme. Plus de la moitié des neurones du présubiculum sont des cellules de direction de la tête qui déchargent en fonction de la direction prise par la tête de l'animal. Le présubiculum est un carrefour majeur pour le transfert d'information de direction de la tête et de l'information visuelle aux régions de la formation hippocampo-parahippocampique et aux aires sous-corticales. Malgré son importance fonctionnelle, le traitement de l'information au sein du circuit présubiculaire à 6 couches reste encore peu connu.

Au cours de ma thèse, j'ai étudié les éléments inhibiteurs qui composent le microcircuit présubiculaire à partir de tranches aigües de cerveau de souris en utilisant la technique du patch-clamp. J'ai caractérisé les propriétés anatomiques et électriques des interneurones ainsi que leur connectivité locale et à distance avec d'autres régions corticales.

Dans un premier temps, j'ai étudié la diversité des interneurones exprimant la parvalbumine et la somatostatine à partir de lignées de souris transgéniques exprimant une protéine fluorescente dans les interneurones. J'ai montré l'existence des cellules en panier à décharge rapide exprimant la parvalbumine et des cellules de Martinotti à bas seuil d'activation exprimant la somatostatine. J'ai également décrit un troisième groupe atypique avec des propriétés électriques intermédiaires et des morphologies hétérogènes. L'existence de ce groupe transitionnel pourrait s'expliquer par la présence d'interneurones exprimant à la fois la parvalbumine et la somatostatine. Ainsi, le microcircuit inhibiteur du présubiculum semble partager toute la complexité des autres aires corticales.

Dans un second temps, je me suis intéressée à l'intégration des entrées thalamiques par les neurones excitateurs et inhibiteurs dans les couches superficielles du présubiculum à l'aide de la technique du double patch-clamp. J'ai montré que les axones thalamiques innervent sélectivement les couches superficielles et plus particulièrement, contactent directement les cellules de projection vers le cortex entorhinal ainsi que les interneurones exprimant la parvalbumine dans la couche 3 du présubiculum. En revanche, les interneurones exprimant la somatostatine sont indirectement recrutés par les cellules pyramidales du microcircuit. Ces interneurones joueraient un double rôle à la fois dans l'inhibition latérale et le maintien d'une décharge soutenue des cellules principales. Du fait de la forte probabilité de connexion entre les cellules principales et les interneurones exprimant la parvalbumine, ces derniers seraient impliqués dans l'inhibition de type feed-forward.

Mon travail de thèse a permis d'apporter des connaissances fondamentales concernant l'inhibition au sein du présubiculum. Il a permis de dévoiler une diversité d'interneurones GABAergiques et de montrer l'existence de circuits neuronaux canoniques de type « feed-forward » et « feedback » qui seraient recrutés à différents moments de la signalisation de la direction de la tête.